CARDIFF UNIVERSITY

PRIFYSGOL CAERDYDD

ACME-UK 2016

24th Conference on Computational Mechanics

31 Mar – 1 Apr 2016 Cardiff

ACME

Association of Computational Mechanics in Engineering - UK

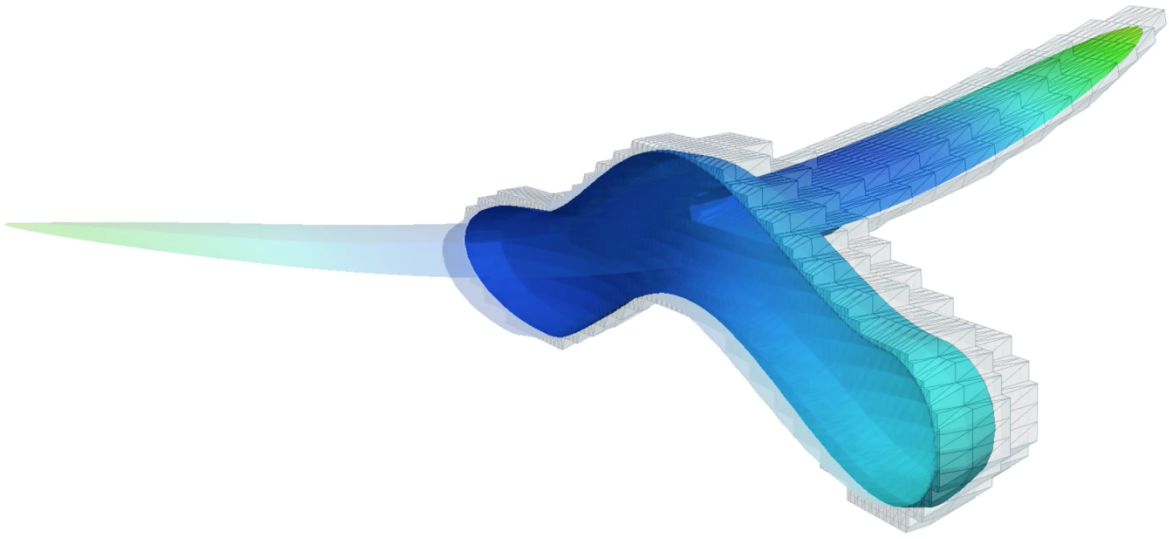

Proceedings

Table of contents

Optimisation and Inverse problems

A COMPARATIVE SIMULATION-OPTIMIZATION STUDY ON EFFECTIVE MANAGEMENT OF SALTWATER INTRUSION IN COASTAL AQUIFERS

***Akbar A. Javadi and Mohammed S. Hussain**

Department of Engineering, University of Exeter, Exeter, EX4 4QF, UK

*a.a.javadi@exeter.ac.uk

ABSTRACT

This study outlines the general performance of two different simulation-optimization (S/O) models developed to examine the capabilities of the new proposed management scenario to control seawater intrusion (SWI) in coastal aquifers. In the first S/O model, a finite element (FE) simulation model is directly linked with a multi-objective genetic model. In the second model a trained surrogate model is linked to the same optimization model. The simultaneous abstraction of saline water near the coast and artificial recharge of treated wastewater into the aquifer are the main principles used in the proposed management scenario. The recharge is implemented using a surface pond and therefore unsaturated flow theory is utilized in the simulation. The objective functions include minimization of the total economic cost of the management scenario and also the minimization of the total amount of salt in the aquifer. The results show that implementation of the surrogate model in the S/O framework results in a significant reduction in CPU time.

Keywords: *seawater intrusion; coastal aquifer; simulation-optimization; EPR*

1. Introduction

Saltwater intrusion is a common contamination problem in developed and urbanized coastal areas especially in arid and semi-arid regions of the world. In critical cases SWI may be followed by abandonment of production wells of freshwater, human health problems and damage to natural ecosystem [1,5]. Therefore, appropriate management strategies should be implemented to control SWI with acceptable limits of economic and environmental costs. In parallel with raising awareness of the concerns on management of coastal groundwater resources, there has been a growing need to find optimal solutions for controlling the SWI problem. The problem is a multi-objective optimization problem that aims to find the trade-off relationship between conflicting objectives. In the early stages of this advancement, different linear/nonlinear programing optimization tools were incorporated with simulation models. However, the problematic features of the traditional optimization techniques in attaining the correct optimal solutions for multi-objective complex problems have triggered the demand for innovation and use of other types of optimization tools such as evolutionary algorithms [5]. In the S/O process the numerical simulation model is linked with a chosen optimization model. In cases with computational complexity some works have attempted to link surrogate models with the optimization algorithms. A recent review of the research efforts related to the application of S/O modelling in management of SWI in coastal aquifers has been presented in [2] and [4].

This paper presents the development and application of two S/O models to assess the efficiency of a new management method for controlling saltwater intrusion while satisfying water demands, and with acceptable limits of economic and environmental costs. The first S/O model (FE-GA) is developed by direct linking of a finite element (FE) simulation model with a multi-objective genetic algorithm. In order to reduce the computational burden the numerical simulation model is replaced by an Evolutionary Polynomial Regression (EPR) based surrogate model in the next S/O model (EPR-GA). A comparison is made between the capabilities of both schemes in capturing the optimal results in hypothetical coastal aquifers.

2. Evolutionary Polynomial Regression (EPR)

EPR [7] is a relatively recent hybrid data mining method that integrates the best features of the conventional numerical regression with the effectiveness of genetic programming. In EPR, the created models are presented in the form of mathematical expressions which are easily accessible to the user. This important feature, however, is not available in other black box data driven methods such as artificial neural networks. The possibility of getting a set of models (not only one) for a complex phenomenon is the other important feature of EPR. The level of accuracy for each model is evaluated based on the coefficient of determination (*COD*):

$$COD = 1 - \frac{\sum_{N}(y_{EPR} - y_a)^2}{\sum_{N}(y_a - avg(y_a))^2} \quad (1)$$

where y_a is the actual output value; y_{EPR} is the predicted value that is computed by the trained EPR model; and N is the number of data points on which *COD* is computed. Detailed explanation of the EPR methodology can be found in [7].

3. Model Description

The studied aquifer system is a 2D hypothetical unconfined aquifer with 200 m × 40 m dimensions. A density dependent FE model SUTRA (Saturated-Unsaturated TRAnsport) [3] is used for the numerical simulation of this flow system. The hydrostatic water heads of 31 m and 30 m are assigned to the left and right sides of the domain respectively to represent the freshwater and seawater pressure boundaries of the aquifer system (Figure 1). The aquifer is discretised into 2000 elements and 2091 nodes. The presence of an unsaturated flow layer in the model requires simulating this layer with finer spatial and temporal discretization in order to limit the instability and oscillation resulting from calculated pressure and saturation values which may change drastically during wetting events [3]. To simulate a plan for future demand, a local production well screened at coordinates (40, 10) m is incorporated into the model (see Figure 1). It is assumed that 26 m^3/day of groundwater is continuously pumped from this well. The total calculated mass of solute in the aquifer would be raised from 27 tons prior the pumping to 98 tons after pumping. Consequently, a management action is required to comply with the planned demand for water while protecting the aquifer against SWI.

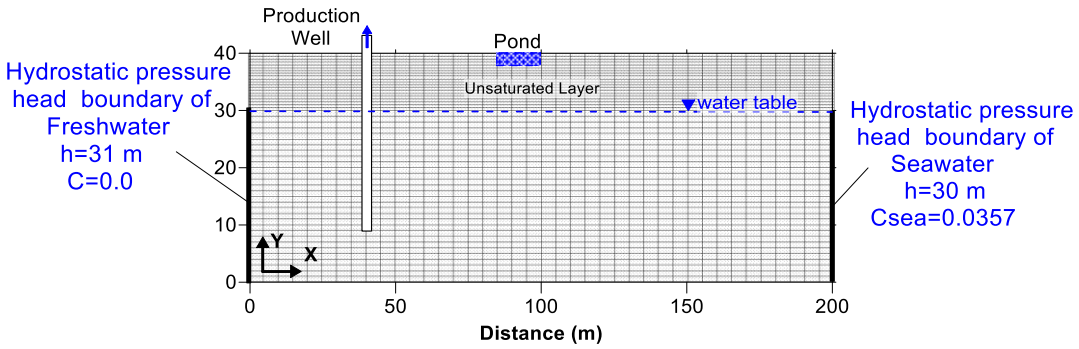

Figure 1: Model geometry and boundary conditions

A new management scenario called ADRTWW [1,6] is proposed to restrict the negative impacts of the intruded saline wedge and the pumping of freshwater from production well. This methodology consists of three steps; Abstraction of brackish water from the saltwater wedge, Desalination of the abstracted brackish water to meet a part of the projected water demand, and artificial Recharge of the aquifer using Treated Waste Water [1,6]. A pond system with dimensions 15m×2m located 65 m from the shoreline is used to collect the reclaimed water and then recharge the aquifer. The calculated recharge rate under this pond system is 0.35 m/day.

4. Simulation-Optimization models:

In order to investigate the cost-effectiveness of the ADRTWW management scenario in different arrangements of its recharge/abstraction components and also in a wider range of optimal solutions, two different S/O frameworks are developed. In the first S/O framework, so called FE-GA, the FE based numerical model (SUTRA code) is directly linked with non-dominated sorting genetic algorithm, NSGA-II [8]. NSGA-II is a popular, fast and elitist multi-objective genetic algorithm. In FE-GA, the numerical model (SUTRA) is repeatedly called by NSGA-II to calculate state variables (pressures and concentrations) in response to each set of generated design variables. After evaluating the corresponding fitness of the objective functions and passing through multiple elitism and evolutionary processes, the trade-off curve of optimal solutions is captured. In the second framework (EPR-GA) a suitably trained EPR is linked with the same multi-objective algorithm. Prior to its linking, the developed surrogate (EPR) model is trained and tested externally on the inputs/outputs of the SUTRA model describing the response of the aquifer system. The results of the EPR-GA model are compared with those obtained by direct integration of the numerical simulation model into the optimization (FE-GA) model. In both FE-GA and EPR-GA, the S/O process aims to minimize the total mass of salt (f_1) in the aquifer as well as minimizing the costs (f_2) of construction and operation of the management process subjected to several side constraints.

5. Results and Discussion

The values of the main parameters adjusted for the optimization algorithm in both developed S/O models are the population size = 50, total number of generations=100, probability of crossover = 0.9 and probability of mutation = 0.0025. Figure 2 shows the results of the trade-off between the two objectives of the management scenario using both FE-GA and EPR-GA models. It can be seen that the captured non-dominated fronts in both models are very close to each other. In the FE-GA model, the optimal points on the Pareto front correspond to abstraction rates in the range of 9.7-25.50 m^3/day and the location of the abstraction well at a distance of 10-20 m from the sea boundary and at the depth of 36-37 m. Figure 3 shows the final steady state distributions of salinity throughout the system for one of the optimal solutions selected based on engineering judgment in terms of the objective functions along the Pareto front (marked in Figure 2). In this selected solution, the optimal location of abstraction well, determined by FE-GA, is 15 m from the sea boundary abstracting the groundwater at the optimal rate of 15.5 m^3/day. The optimal depth of the well is 37 m below the top boundary. The great performance of this optimal solution in controlling SWI is compared with the no-management scenario. The 10%, 50% and 90% salinity contours of the no-management scenario are illustrated as dashed lines.

The total computational time of the analysis by FE-GA is 16 days on an Intel(R) Core(TM) i7-2600 CPU @ 3.40GHz (8 CPUs) with 16 GB RAM in this small aquifer system. The application of fine spatial and temporal discretization of the unsaturated flow zone increased the computational complexity of the simulation process. Under this circumstance, the multiple calls of the SUTRA in the optimization framework make the S/O method by FE-GA computationally inefficient. Consequently in the second scheme of the S/O framework it has been replaced by a metamodel (EPR). Horizontal (*Xa*) and vertical (*Ya*) coordinates of the abstraction well, and also its pumping rate (*Qa*) are the input parameters considered in EPR-GA. A database of 500 cases of these input variables is randomly generated with a uniform probability distribution. Then, by multiple runs of the SUTRA code the outputs (total mass of salinity, f_1) corresponding to each set of these data are calculated as the response of the system in each control scenario. The required database for training and validation of the EPR models is developed using the created sets of input and output. In each scenario 400 cases of data are used to train the EPR model and the remaining 100 cases (that are kept unseen to EPR during the model development process) are used for validation of the developed model. The following best EPR model (Equation 2) with high levels of fitness (*COD* values) is selected for prediction of total mass of solute (f_1) in ADRTWW scenario. The *COD* values of this EPR model are 94.9% and 93.1 % in training and testing datasets respectively. The input data of this equation were used concurrently to evaluate the second objective function (cost function, f_2) as well. The average time required to complete the analysis using EPR-GA (including the time to generate the database) is less that 10 % of

the time required by FE-GA on the same CPU core that can be considered as a very significant difference.

$$f_1 = 30.966\text{-}24.936Ya^{0.5} + 7.827Ya\text{-}(7.053\times10^{-2})Ya^2 + 56.411Qa^{-1}\text{-}12.204YA^{0.5}Qa^{-1}+343412.244Qa^{0.5}Xa^{-2}\text{-} 2.069Qa + (2.605\times10^{-2})Qa^2 - 105.069YA^{0.5}Qa^2Xa^{-2} \quad (2)$$

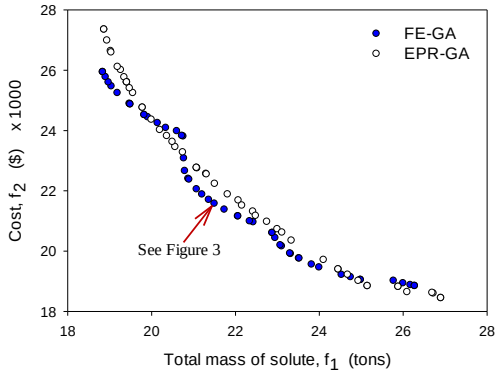

Figure 2: Optimal solutions obtained using both S/O models

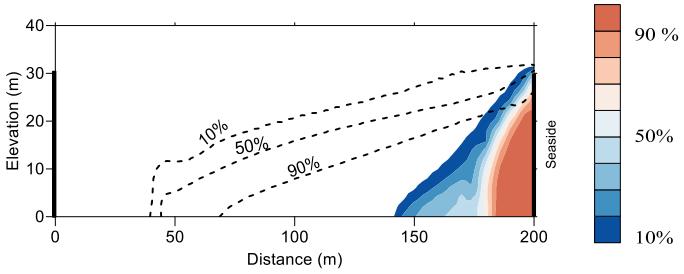

Figure 3: Steady state salinity map (%) of the system for the selected optimal solution compared with the case of no-management scenario (dashed lines)

6. Conclusions

This paper presented the results of an investigation into the capabilities of two different S/O models to find the set of optimal solutions for a new management scenario for controlling saltwater intrusion in coastal aquifers. The results showed that the two S/O schemes were in excellent agreement in terms of capturing the Pareto front of the system in the management scenario. The application of EPR-metamodel in the S/O framework (i.e linking of EPR with optimization tool) resulted in significant reduction of the overall computational complexity and CPU time compared with those obtained by direct linking of the numerical simulation model with the optimization tool.

References

[1] A. A. Javadi, M. S. Hussain, M. M. Sherif and R. Farmani. Multi-objective optimization of different management scenarios to control seawater intrusion in coastal aquifers. *Water Resources Management*, 29 (6), pp. 1843-1857, 2015.

[2] A. Singh. Optimization modelling for seawater intrusion management. *Journal of Hydrology*, 508, pp. 43-52, 2014.

[3] C. I. Voss and A. M., Provost. SUTRA-A model for saturated-unsaturated variable-density ground-water flow with solute or energy transport. *U.S. Geological Survey (USGS)*, Report 02-4231, 2010.

[4] H. Ketabchi and B. Ataie-Ashtiani. Review: Coastal groundwater optimization-advances, challenges, and practical solutions. *Hydrogeology Journal*, 23(6), pp. 1129-1154, 2015.

[5] M. S. Hussain. Numerical simulation and effective management of saltwater intrusion in coastal aquifers, *PhD thesis, University of Exeter*, 2015.

[6] M. S. Hussain, A. A. Javadi, A. Ahangar-Asr and R. Farmani. A surrogate model for simulation optimization of aquifer systems subjected to seawater intrusion, *Journal of Hydrology*, 523, pp. 542-554, 2015.

[7] O. Giustolisi and D. A. Savic. A symbolic data-driven technique based on evolutionary polynomial regression. *Journal of Hydroinformatics*, 8 (3), pp. 207-222, 2006.

[8] K. Deb, A. Pratap, S. Agarwal, and T. Meyarivan. A fast and elitist multiobjective genetic algorithm: NSGA-II. *Evolutionary Computation, IEEE Transactions on*, 6(2), pp. 182-197, 2002.

Proceedings of the 24th UK Conference of the
Association for Computational Mechanics in Engineering
31 March - 01 April 2016, Cardiff University, Cardiff

Topology optimisation using level set methods and the discontinuous Galerkin method

***Thomas Adams, Stefano Giani and William M. Coombs**

School of Engineering and Computing Sciences, University of Durham, South Road, Durham, DH1 3LE, UK.

*thomas.d.adams@durham.ac.uk

ABSTRACT

This paper presents a topology optimisation approach that combines an adjoint-based sensitivity analysis [1] with level set methods (LSM) [2] for front propagation, and the discontinuous Galerkin (DG) symmetric interior penalty (SIP) method [3]. The problems considered in this paper will be limited to the minimum compliance design of two-dimensional linear elastic structures.

Key Words: *topology optimisation; level set methods; discontinuous Galerkin method; symmetric interior penalty method.*

1. Introduction

One of the most challenging aspects of structural design is finding the optimal layout, or topology of a structure. Topology optimisation is the most general form of structural optimisation and is concerned with finding the boundary of a given problem domain which is optimal in that it minimises an objective functional while satisfying given constraints.

In this paper a topology optimisation is implemented by performing an adjoint-based sensitivity analysis to compute the gradient of the objective functional as described in [1]. The level set function (LSF) which defines the internal boundaries of the problem can then be advected along the steepest descent gradient towards an optima. The LSM developed by Osher and Sethian [2] is a simple and efficient method for computing the evolution of a moving interface. Since it was first used for structural optimisation in [4], the LSM has been used for boundary tracking in many shape optimisation implementations and has proven efficacy.

In this paper, the spatial domain of both the physical problem and the level set transport problem are discretised using the DGSIP method [3]. The DG method differs from the continuous Galerkin (CG) method in that it works over a trial space of functions which are only piecewise continuous. One of the main advantages of DG finite elements is that they are trivially parallelisable. As such this work is a first step towards exploiting parallel computing techniques to create an efficient shape optimisation method for large-scale problems.

Following this introduction, Section 2 will present and explain an algorithm for finding the solution to the minimum compliance problem for a cantilever beam. This will be followed by some numerical results for the given problem and conclusions in Section 3.

2. Topology optimisation algorithm and problem formulation

For the general case the proposed optimisation algorithm is as follows:

1. Define the problem domain.
2. Initialise the LSF as a signed distance function (SDF).
3. Until the value of the objective functional converges:
   (a) compute the current state and the adjoint state through the solution of the physical and adjoint problems;

(b) compute the advection velocity; and
(c) evolve the interface through the solution of the transport Hamilton-Jacobi equation.
    i. Reinitialise the LSF to a SDF through a geometric redistancing method.

The algorithm will now be explained through the use of an example optimisation problem. The objective of the optimisation process will be to determine the boundary, which for a given domain, load distribution and boundary conditions, will minimise the compliance of the system whilst satisfying a given weight constraint. Mathematically this can be stated as:

$$\inf J(\Omega) \quad \text{where:} \quad J(\Omega) = \int_{\partial\Omega_N} g \cdot u \, \mathrm{d}s + \ell \int_{\Omega} \mathrm{d}x \tag{1}$$

Where J is the objective functional, Ω is the domain, $\partial\Omega_N$ is the Neumann part of the boundary, g are the surface tractions, u is the displacement field, and ℓ is a penalty term enforcing the weight constraint.

2.1. Step 1: Defining the problem domain

The problem to be discussed in this paper aims to find the optimal topology of a 2D cantilever beam problem, the dimensions and the boundary/loading conditions are shown in Figure 1(a). The domain is discretised into a mesh of 100 by 50 first order, piecewise continuous, square elements. The domain has two sets of elastic properties which represent the material section and the void section. The material part of the domain has Young's modulus, $E = 1$Pa and Poisson's ratio, $\nu = 0.3$, and the void is modelled as a much more compliant material section which has a Young's modulus $E = 10^{-3}$Pa and Poisson's Ratio, $\nu = 0.3$. The value of Young's modulus varies smoothly across the interface between the two materials by applying a smoothed sign function to the LSF and using this as the input to a linear function which varies between the two values of Young's Modulus as the sign function varies between -1 and 1.

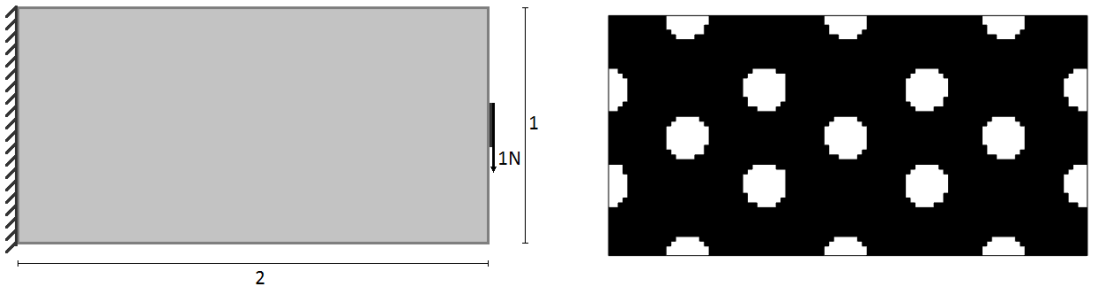

(a) Cantilever beam problem (b) Initial zero level set

Figure 1: Initialisation of the problem

2.2. Step 2: Initialisation of the LSF as an SDF

The interface between the material portion and the void portion of the domain is defined as the zero level set of the LSF, ϕ. Where the level set function is greater than zero the domain is filled with material and where the level set function is less than zero the domain is filled with the ersatz material which represents the void as further described in Section 2.1.

There are two main reasons for initialising the LSF as an SDF. First of all, numerical inaccuracies will occur during the transport process if there are large variations in the gradient of the LSF, especially in the region close to the zero level set. Secondly, initialising the LSF as an SDF and maintaining this property through frequent reinitialisation greatly simplifies the level set transport equation as discussed in Section 2.5.

When choosing the initial LSF, one must be sure to ensure that there are sufficient holes in the domain. This is because for a two dimensional problem being evolved with a time stepping scheme which satisfies a strict CFL condition, no holes can be created during the optimisation process [1]. The initial configuration can be seen in Figure 1(b), where black represents the material and white represents the voids.

2.3. Step 3(a): Computation of the state and the adjoint state through DG solution of the physical model

In order to compute the gradient of the objective functional, an adjoint-based sensitivity analysis is performed. The minimum compliance problem is self-adjoint and as such is simpler than the general case in which an adjoint state would also have to be computed at each iteration. The author points the reader towards [1] for the details of deriving the topological derivative and simply states the result that for the objective functional stated in (1) the topological derivative yields a vector field, V:

$$V = bn \quad \text{with} \quad b = \sigma(u) \cdot \varepsilon(u) - \ell \tag{2}$$

In order to compute this advection velocity field, it is necessary to first compute the displacement field for the current state of the cantilever beam problem. For a linear elastic stress analysis problem, the DG approximation for the displacement field, u, is given by:

$$\int_\Omega f v d\Omega = \int_\Omega vB \cdot DBu \, \mathrm{d}\Omega - \int_\Gamma [\![v]\!] \cdot D\{\{Bu\}\} \, \mathrm{d}\Gamma - \int_\Gamma \{\{Bv\}\} \cdot D[\![u]\!] \, \mathrm{d}\Gamma + \int_\Gamma \mu [\![v]\!] \cdot [\![u]\!] \, \mathrm{d}\Gamma \tag{3}$$

Where Γ denotes the element face, f are the body forces, v is the test function, B is the strain-displacement matrix, D is the elastic properties matrix, μ is a penalty parameter, $[\![q]\!]$ denotes the jump of q and $\{\{q\}\}$ denotes the average of q. For this problem, the boundary conditions are imposed strongly. Once again the author directs the reader to [3], for the details on the discretisation of elliptic problems using the DGSIP method.

2.4. Step 3(b): Computation of the advection velocity

The advection occurs only in the normal direction to the interface and so the advection velocity at each node is given by, b, defined in (2). The stress, σ, and strain, ε, can be recovered from the displacement solution of the linear elasticity problem described in Section 2.3. The ℓ term is a penalty term which describes the volume ratio, i.e. the ratio of material to void, at convergence. It is prescribed during the initial iteration, for the numerical example in this paper, $\ell = 150$.

2.5. Step 3(c): Evolution of the interface

The evolution of the LSF occurs through the solution of a Hamilton-Jacobi equation. However, as mentioned in Section 2.2, the maintenance of the LSF as an SDF ensures that the Euclidean norm of the spatial derivatives is always equal to unity and as such the level set transport equation can be greatly simplified as described in [5], which can be stated as follows:

$$\frac{\partial \phi}{\partial t} = b \tag{4}$$

Equation (4) is solved explicitly in time using a forward Euler method. The time step is constrained by the CFL condition and is inversely dependent on the maximum absolute value of the advection velocity field at each iteration and the size of the elements in the mesh. (4) is solved in space using DG finite elements once again. For this particular equation, both CG and DG formulations are the same, however, the DG formulation of (4) can be solved independently for each element, allowing for a much more efficient solution.

2.6. Step 3(c)i: Reinitialisation of the level set function

Maintaining the signed distance property of the LSF can be achieved through multiple methods. One method is known as geometric redistancing (or the brute force method). For this Yamasaki *et al.* [5] presented a method which involves discretising the zero level set and then computing the minimum distance from each node to the discretised interface and multiplying this by the sign of the level set at that node. When using a discontinuous LSF the multiplication by the sign can cause discontinuities at the interface which results in the LSF not being reinitialised as an SDF. To remedy this a smoothing is applied to the LSF prior to the reinitialisation whereby the value of the LSF at each node is taken to be the average of the values at each of the degrees of freedom at that node.

3. Numerical results and conclusions

The problem presented in the previous section was ran for 50 iterations. Figure 2(a) shows a smooth convergence of the objective functional until it reaches a minimum. The final shape after 50 iterations is shown in Figure 2(b).

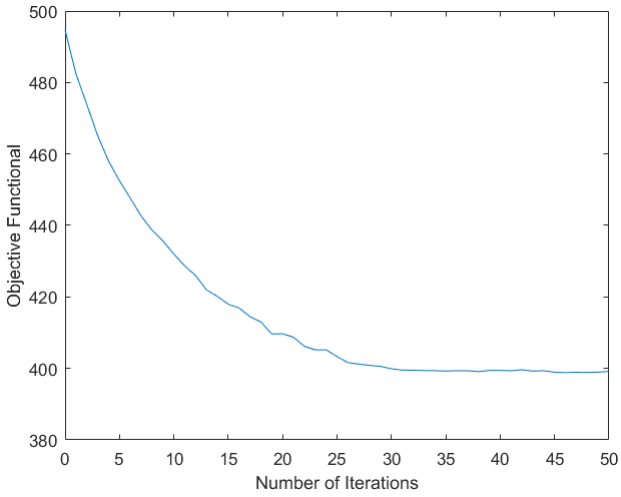

(a) Convergence of the objective functional

(b) Final topology after 50 iterations

Figure 2: Numerical results

To conclude, a topology optimisation algorithm using level set methods and the discontinuous Galerkin method has been presented and explained. The algorithm was implemented to find the optimal topology of a 2D linear elastic cantilever beam. The results show that the algorithm has good convergence and stability properties, and the optimal design shown is similar to that published in the literature.

Acknowledgements

The first author acknowledges financial support during the completion of this work by the UK Engineering and Physical Sciences Research (EPSRC) grant.

References

[1] G. Allaire, F. Jouve, and A. Toader. Structural optimization using sensitivity analysis and a level-set method. *J. Comput. Phys.*, 194(1):363–393, 2004.

[2] J. A. Sethian. *Level set methods and fast marching methods: evolving interfaces in computational geometry, fluid mechanics, computer vision, and materials science*, volume 3. Cambridge university press, 1999.

[3] D. N. Arnold, F. Brezzi, B. Cockburn, and L. Donatella Marini, Unified analysis of discontinuous galerkin methods for elliptic problems, *SIAM J. Numer. Anal.*, 39(5):1749–1779,2002, 2011.

[4] J. A. Sethian and Andreas Wiegmann, Structural Boundary Design via Level Set and Immersed Interface Methods. *J. Comput. Phys.*, 163, 489–528, 2000.

[5] S. Yamasaki, S. Nishiwaki, T. Yamada, K. Izui and M. Yoshimura, A structural optimization method based on the level-set method using a new geometry-based reinitialization scheme, *Int. J. Numer. Meth. Eng.*, 83(12), 1580–1624, 2010.

Proceedings of the 24th UK Conference of the
Association for Computational Mechanics in Engineering
31 March - 01 April 2016, Cardiff University, Cardiff

BAYESIAN STATISTICAL INFERENCE ON THE MATERIAL PARAMETERS OF A HYPERELASTIC BODY

***Jack S. Hale[1], Patrick E. Farrell[2,4] and Stéphane P.A. Bordas[1,3,5].**

[1]Research Unit in Engineering Science, Faculté des Sciences, de la Technologie et de la Communication, Université du Luxembourg, Campus Kirchberg, 6, rue Coudenhove-Kalergi, L-1359, Luxembourg.
[2]Mathematical Institute, University of Oxford, Andrew Wiles Building, Radcliffe Observatory Quarter, Woodstock Road, Oxford, OX2 6GG, UK.
[3]Cardiff University Institute of Mechanics & Advanced Materials The Queen's Building, The Parade, Cardiff, CF24 4AG, UK.
[4]Center for Biomedical Computing, Simula Research Laboratory, Oslo, Norway.
[5]University of Western Australia Intelligent Systems for Medicine Laboratory 35 Stirling Highway, Crawley, WA 6009, Australia.

*jack.hale@uni.lu

ABSTRACT

We present a statistical method for recovering the material parameters of a heterogeneous hyperelastic body. Under the Bayesian methodology for statistical inverse problems, the posterior distribution encodes the probability of the material parameters given the available displacement observations and can be calculated by combining prior knowledge with a finite element model of the likelihood.

In this study we concentrate on a case study where the observations of the body are limited to the displacements on the surface of the domain. In this type of problem the Bayesian framework (in comparison with a classical PDE-constrained optimisation framework) can give not only a point estimate of the parameters but also quantify uncertainty on the parameter space induced by the limited observations and noisy measuring devices.

There are significant computational and mathematical challenges when solving a Bayesian inference problem in the case that the parameter is a field (i.e. exists infinite-dimensional Banach space) and evaluating the likelihood involves the solution of a large-scale system of non-linear PDEs. To overcome these problems we use dolfin-adjoint to automatically derive adjoint and higher-order adjoint systems for efficient evaluation of gradients and Hessians, develop scalable maximum aposteriori estimates, and use efficient low-rank update methods to approximate posterior covariance matrices.

Key Words: *Bayesian inference, dolfin-adjoint, posterior, FEniCS, hyperelasticity.*

1. Theoretical framework

Following the infinite-dimensional presentation of Stuart [1], we introduce the parameter-to-observable map $\mathcal{G} : \mathcal{M} \to \mathcal{Y}$ as a deterministic function that maps the *parameters* $m \in \mathcal{M}$ to the observables $y \in \mathcal{Y}$, where $\mathcal{M}, \mathcal{Y}$ are Banach spaces:

$$y = \mathcal{G}(m). \tag{1}$$

In our case, every evaluation of this map $\mathcal{G}$ will involve solving a PDE governing the behaviour of a geometrically non-linear hyperelastic solid.

The parameter m we wish to infer is the (spatially-varying) shear-like parameter of the following Neo-Hookean energy potential W:

$$W(X, \mathrm{I}_C, \mathrm{III}_C) := \frac{m}{2}(\mathrm{I}_C - 2) - m \ln J + \frac{\lambda}{2}(\ln J)^2 \tag{2}$$

where $\mathrm{I}_C = \mathrm{tr}(C)$ and $\mathrm{III}_C = \det(C)$ are the first and third invariants of the right Cauchy-Green tensor $C = F^T F$, F is the deformation gradient and $J = \det F = (\mathrm{III}_C)^{1/2}$. The displacement field $u^* \in \mathcal{V}$ at equilibrium can then be found through a standard minimisation problem of the following form:

$$u^* = \underset{u \in \mathcal{V}}{\arg\min} \left\{ \int_{\Omega_0} W(X, \mathrm{I}_C, \mathrm{III}_C) \, \mathrm{d}x_0 - \int_{\partial_N \Omega_0} t \cdot u \, \mathrm{d}s \right\}, \tag{3}$$

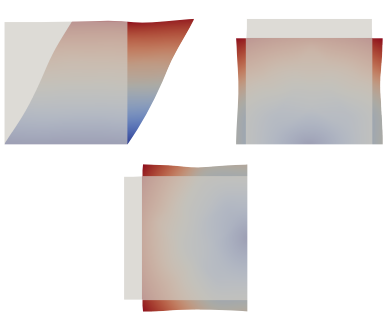

(a) Observed displacement fields y_{obs}.

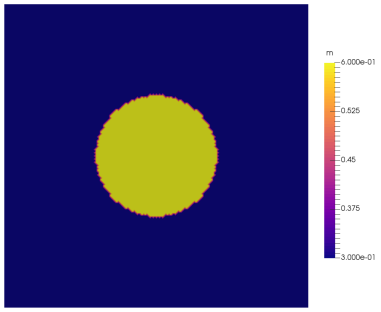

(b) Shear-related parameter m.

Figure 1: (a) Three virtual experiments (shear and two friction-free compression tests) on a hyperelastic body (b) with a parameter field m given by a circular inclusion in a softer matrix. Grey shape is the square undeformed configuration of the body. Colour shows magnitude of displacement at equilibrium. Note the warped deformation on the boundary - if we only have these limited observations, how much can we tell about the parameters in the centre of the domain? This is the question we attempt to answer with this work.

where $\mathrm{d}s$ and $\mathrm{d}x_0$ are measures on the undeformed configuration domain Ω_0 and its boundary $\partial_N\Omega_0$, respectively and t are the external applied tractions on $\partial_N\Omega_0$. Virtual experiments and the exact parameter field used to create them are shown in Figure 1.

We state the Bayesian solution to the infinite-dimensional inference problem as follows: We describe the observer's prior beliefs about the parameter m through the prior probability measure μ_0. Given the likelihood model π_{like}, which gives the probability that we will observe y given the parameters m, the goal of the inference problem is to find the posterior probability measure μ^{post} (Stuart [1], Theorem 6.2) as:

$$\frac{\mathrm{d}\mu^{\text{post}}}{\mathrm{d}\mu_{\text{prior}}} \propto \pi_{\text{like}}\left(y^{\text{obs}} - \mathcal{G}\left(u\right)\right) \tag{4}$$

where the Radon-Nikodym derivative (Stuart [1], Theorem 6.29) $\frac{\mathrm{d}\mu^{\text{post}}}{\mathrm{d}\mu_{\text{prior}}}$ is the derivative of the posterior probability measure μ^{post} with respect to the prior probability measure μ_0.

We further assume that our prior knowledge can be expressed by a Gaussian distribution with mean m_0 and covariance operator C_0, or more compactly $\pi_{\text{prior}} \sim \mathcal{N}(m_0, C_0)$. Again, following the well-posedness result of Stuart [1], we solve a Helmholtz-like PDE problem to generate actions of our prior covariance on a vector.

Furthermore we assume that our noise model is white-noise Gaussian with mean zero and covariance operator Γ_{noise}. We can then re-write the posterior more concretely as:

$$\pi_{\text{post}}(m|y^{\text{obs}}) \propto \exp\left(-\frac{1}{2}\left|\left|y_{\text{obs}} - \mathcal{G}(m)\right|\right|^2_{\Gamma^{-1}_{\text{noise}}} - \frac{1}{2}\left|\left|m - m_0\right|\right|^2_{C_0^{-1}}\right). \tag{5}$$

Taking the logarithm of the above equation results in the following weighted least-squares functional:

$$\hat{J}(m) := -\ln \pi_{\text{post}}(m|y_{\text{obs}}) = \frac{1}{2}\left|\left|y_{\text{obs}} - \mathcal{G}(m)\right|\right|^2_{\Gamma^{-1}_{\text{noise}}} + \frac{1}{2}\left|\left|m - m_0\right|\right|^2_{C_0^{-1}}, \tag{6}$$

We characterise the Bayesian posterior via extraction of two pieces of information. The maximum a posteriori point m_{MAP} is characterised by the maximum of the above functional:

$$m_{\text{MAP}} := \arg\max_{m\in\mathcal{M}} \pi_{\text{post}} = \arg\min_{m\in\mathcal{M}}(-\ln \pi_{\text{post}}) \tag{7}$$

This is a classical point estimate similar to those found in the PDE-constrained optimisation literature, but in that case the norms used are usually somewhat arbitrary. By formulating out problem in the Bayesian seting, our problem has rigorous statistical meaning [1].

An effective simplification in the case that the parameter-to-observable map $\mathcal{G}$ is a linear operator $A : \mathcal{M} \to \mathcal{Y}$ we can write the following semi-analytical expressions for the MAP point and the posterior covariance:

$$m_{\text{MAP}} = C(A^*\Gamma_{\text{noise}}^{-1} y^{\text{obs}} + C_0^{-1} m_0), \tag{8}$$

$$C = (A^*\Gamma_{\text{noise}}^{-1} A + C_0^{-1})^{-1}. \tag{9}$$

where * denotes the usual adjoint operation. After some some algebraic manipulation we can show that the posterior distribution is infact Gaussian and can be written:

$$\pi_{\text{post}} \sim \mathcal{N}(m_{\text{MAP}}, \mathcal{H}^{-1}). \tag{10}$$

where the Hessian operator $\mathcal{H} = C^{-1}$ is the second Fréchét derivative of the weighted least-squares functional $\hat{J}(m)$ defined above. It is worth pointing out at this stage that our hyperelastic forward problem does not lead to a linear parameter-to-observable map $\mathcal{G}$. Thus, the above result does *not* for our problem hold because the map $\mathcal{G}$ induces non-Gaussianity into the posterior.

However, a useful approximation, as long as the posterior is not too non-Gaussian, is to evaluate the Hessian of the functional around the MAP point and use it as an approximation to the true second moment of the distribution about the MAP point.

2. Solution approach

We implement our solver within the dolfin-adjoint package [3], which is based on the finite element solver DOLFIN from the FEniCS Project [4]. We express the forward model in the high-level Unified Form Language (UFL) before automatically deriving finite element cell tensors for the adjoint and higher-order adjoint equations using symbolic manipulations.

We first solve the problem of finding the MAP point using a mesh-independent bound-constrained quasi-Newton optimisation algorithm that uses the gradients from dolfin-adjoint to efficiently drive the optimisation.

Then once we have found the MAP point, we evaluate likelihood Hessian actions from dolfin-adjoint within a Krylov-Schur type eigenvalue solver to extract information about the directions in parameter space that are most constrained by the observations, with respect to the prior. We use an efficient low-rank update procedure from Spantini et al. [2] to construct an approximation to the posterior covariance.

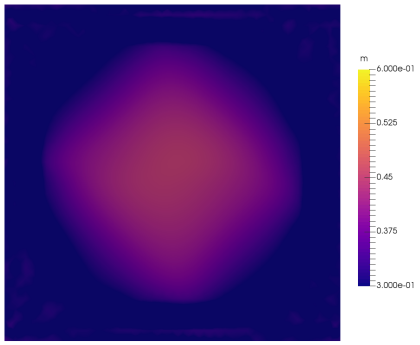

Figure 2: Maximum a posteriori (MAP) point of the Bayesian inference problem. We can detect the stiffness in the centre of the body, but the maximum value and precise radius are not recovered particularly well. This uncertainty is quantified by the information in the posterior covariance fig. 3.

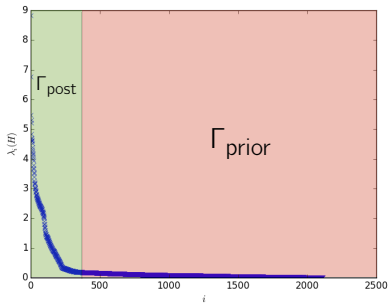

(a) Spectrum of the inverse of the posterior covariance.

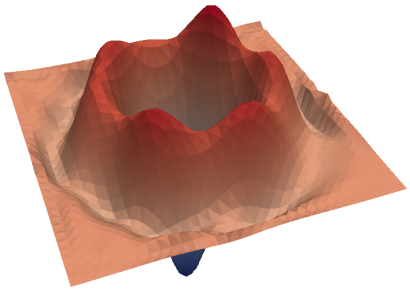

(b) Trailing eigenvector.

(c) Leading eigenvector.

Figure 3: (a) The leading eigenvalues $\lambda_i \gg 1$ (green) correspond to the directions in parameter space *most* informed by the observations via the likelihood. Conversely, the trailing eigenvalues $\lambda_i \ll 1$ (red) correspond to the directions in parameter space *least* informed, and thus correspond to the information originally contained in our prior. Plots of (b) trailing and (c) leading eigenvectors. The least constrained direction points towards the parameters in the centre. The most constrained direction points towards the parameters at the corner where in effect we have two independent 'sensors' touching one piece of material.

3. Results

We show our results along with full descriptions in Figures 2 and 3.

References

[1] A.M. Stuart. Inverse problems: a Bayesian perspective. Acta Numerica 19 (2010).

[2] Alessio Spantini, Antti Solonen, Tiangang Cui, James Martin, Luis Tenorio, Youssef Marzouk. Optimal low-rank approximations of Bayesian linear inverse problems. arXiv:1407.3463v2.

[3] Patrick E. Farrell, David A. Ham, Simon W. Funke and Marie E. Rognes. Automated derivation of the adjoint of high-level transient finite element programs, SIAM Journal on Scientific Computing 35.4, pp. C369-C393. doi:10.1137/120873558i (2013).

[4] M. S. Alnæs, J. Blechta, J. Hake, A. Johansson, B. Kehlet, A. Logg, C. Richardson, J. Ring, M. E. Rognes and G. N. Wells, The FEniCS Project Version 1.5, Archive of Numerical Software, 3(100), doi:10.11588/ans.2015.100.20553i (2016).

Self-learning finite element method and engineering applications

Ali Nassr[1], Akbar A. Javadi[1], Asaad Faramarzi[2]

[1]Department of Engineering, University of Exeter, North Park Road, Exeter, EX4 4QF

[2]Department of Engineering, School of Civil Engineering, University of Birmingham, Edgbaston, Birmingham, B15 2TT

*Adnn201@exeter.ac.uk

Key Words: *finite element, self-learning, data mining, evolutionary techniques*

Abstract

This paper presents the development of an automation process for the self-learning finite element method (FEM) and its application to a number of engineering problems. The self-learning FEM involves the integration of a suitably trained Evolutionary Polynomial Regression (EPR) model that represents the material constitutive behaviour in the framework of the finite element method. The automation algorithm was coded in Matlab environment using a new bespoke version of EPR. Two numerical examples are presented to illustrate the proposed methodology. The results show that using EPR in the self-learning finite element method provides very accurate predictions, simplifies the training of EPR and reduces the time required for analysis.

1 –Introduction

The self-learning simulation is an extension of the autoprogressive algorithm originally introduced by Ghaboussi et al. [1]. Hashash et al. [2] proposed a self-learning simulation methodology, also called inverse analysis technique. This methodology employs the auto-progressive algorithm that extracts material's constitutive behaviour (stress-strain relationship) using global load-displacement measurements. The self-learning finite element method introduced by Hashash [2] utilizes a neural network (ANN) based constitutive model to extract the materials behaviour [2]. Although there has been valuable research on the self-learning FEM using ANN, and demonstration of the advantages that ANN offers in constitutive modelling, however, it is also known that ANNs also suffer from a number of drawbacks. For example, the number of neurons, number of hidden layers, transfer function, etc. must be determined a priori, requiring a time-consuming trial and error procedure [3]. Faramarzi et al. [4] proposed an algorithm for training EPR models and their incorporation in the self-learning procedure and highlighted the advantages of EPR over ANN. In this paper the process of EPR based self-learning FEM has been applied to overcome the problems with the ANN approach and improve the way of EPR training.

2 – Evolutionary polynomial regression (EPR)

In recent years, by rapid developments in computational software and hardware alternative computer aided pattern recognition approaches have been extended beyond classical plasticity theories to modelling many engineering problems. Evolutionary polynomial regression (EPR) is a new hybrid technique based on evolutionary computing, aimed to search for polynomial structures representing the behaviour of a system [4]. EPR is a combination of genetic algorithm (GA) which searches for symbolic structures and least square (LS) regression which is used to estimate the constants values [5]. A typical formulation of EPR expression can be stated as:

$$y = \sum_{j=1}^{m} F(\mathbf{X}, f(\mathbf{X}), a_j) + a_0 \quad (1)$$

where y is the estimated output of the system; a_j is a constant value; F is a function constructed by the process; $\mathbf{X}$ is the matrix of input variables; f is a function defined by the user; and m is the number of terms of the expression excluding bias a_0.

3 – EPR based self-learning finite element method

The methodology of incorporating an EPR in finite element analysis was first presented by Javadi and Rezania [3]. They showed that a properly trained EPR on experimental data can be implemented in a finite element model with more simplicity compared with a conventional constitutive model [3]. However, this approach of training EPR needs a large number of experiments which is costly and may not be available in all cases. Therefore, training EPR within the self-learning FEM seems to be much more efficient. The framework of the self-learning FEM consists of two steps. In step 1, the applied load and constrained boundary conditions are implemented and the boundary forces and displacements are measured for each loading increment. Two finite elements analyses are considered in parallel (FEA and FEB) and an EPR model which represents the stress-strain relationship is trained. The FE model (A) simulates a structure and applies the forces while in parallel, the FE model (B) applies the corresponding displacements. The stresses and strains are determined at each integration point for both FE models. The methodology assumes that the stresses of FE (A) are accurate and strains of FE (B) are accurate and they are used to train the EPR model. Each cycle of self-learning that accomplishes the entire applied load is called a pass. Several passes may be required to complete the analysis. The flowchart of the EPR-based self-learning FEM is shown in Figure 1.

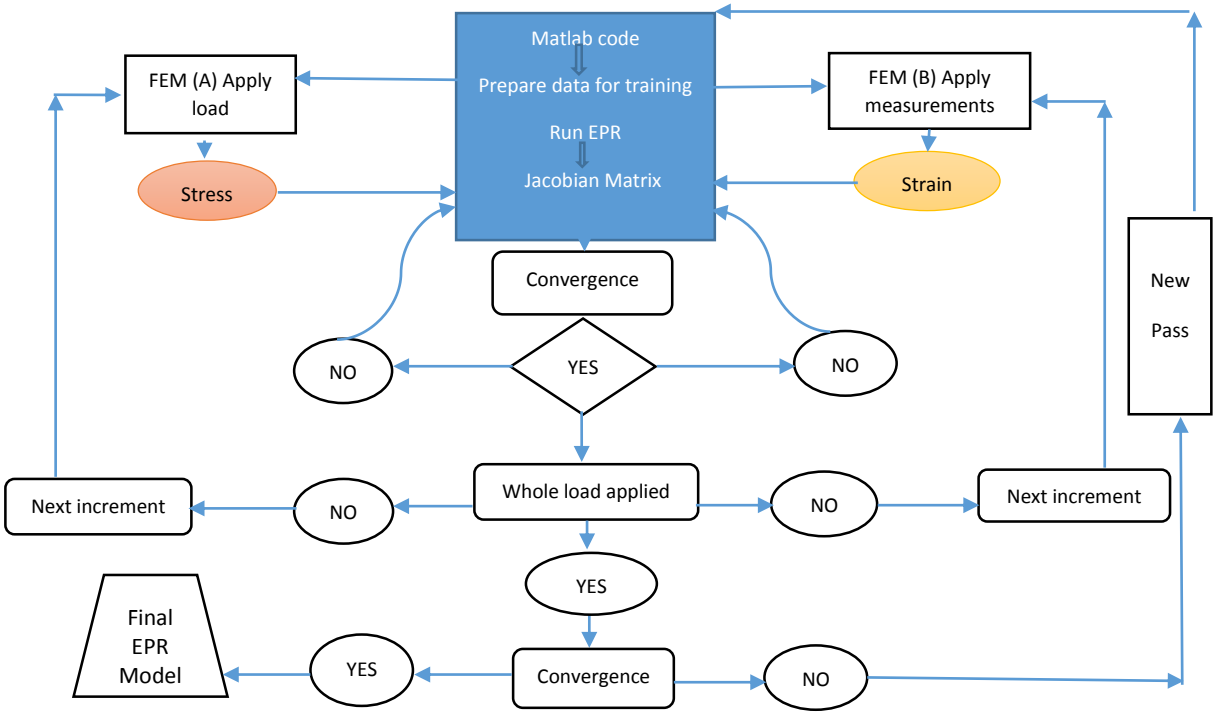

Figure 1. The flow chart of the proposed automation process of EPR-based self-learning FEM

4 – Numerical examples

4 – 1 Example 1

A 2D plane stress panel subjected to in-plane compression is considered. The geometry of the plate, boundary conditions and loading are shown in Figure 2. Due to the symmetry, only a quarter of the plate is simulated. The material of the plate is linear elastic with Young's modulus E = 500 pa and poison's ratio μ = 0.3 and the pressure applied is 10 pa. This example has been deliberately kept simple in order to verify the process of EPR based self-learning simulation.

The measurements are generated synthetically from a FE model using ABAQUS. It is assumed that during the experiment the displacements at the node on the right corner (node1) are recorded. Two finite elements models are created and three EPR models are used for the training process. Figure 3 shows the prediction of EPR-based self-learning FE model for the displacement at node (1) from one pass. Comparison is made between the results of the actual (linear elastic) model and the EPR based

self-learning FEM. It can be seen that the EPR-based FEM is able to provide an excellent agreement with the actual data.

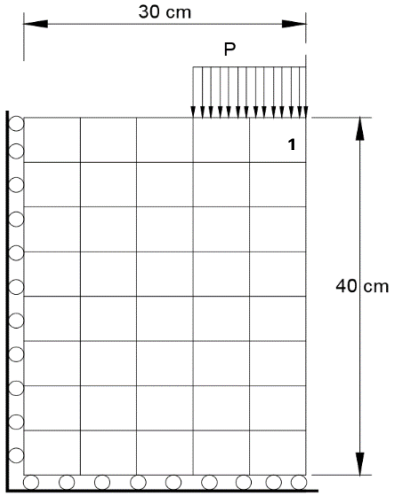

Fig.2 Geometry, loading, mesh and BC of the plate.

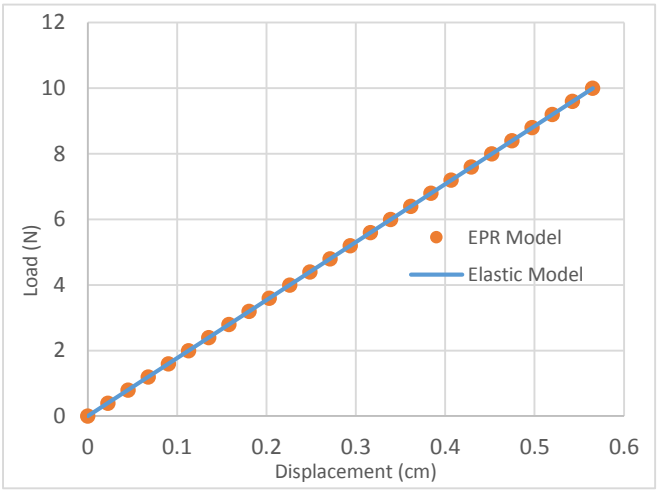

Fig. 3 EPR based self-learning FEM prediction at node1 1.

4 - 2 Example Two

A 2D truss structure with 13 axial force elements is considered in the second example. The geometry, boundary conditions and loading are illustrated in Figure 4. The truss is subjected to a concentrated load (100 KN) at node 3. The load–displacement data were generated using FE simulation with ABAQUS using the nonlinear Ramberg-Osgood model. The load and the corresponding displacement at node 3 are considered as the experimental measurements used in the self-learning process. The general form of the Ramberg-Osgood model is [6]:

$$\frac{\sigma}{E} + \frac{2\beta\sigma o}{3E}\left(\frac{\sigma}{\sigma o}\right)^{n} = \varepsilon \qquad (2)$$

Where E = $20.0\text{x}10^{9}$ pa, σ_o = $1.0\text{x}10^{7}$ pa, β = 2.34, n = 3.

The values of stresses were considered as input and strains as output. After training, in each run, an EPR model with the highest COD was chosen. It can be seen from Figure 5 that the EPR-based self–learning method is able to accurately capture the nonlinear behaviour of the truss from the first pass.

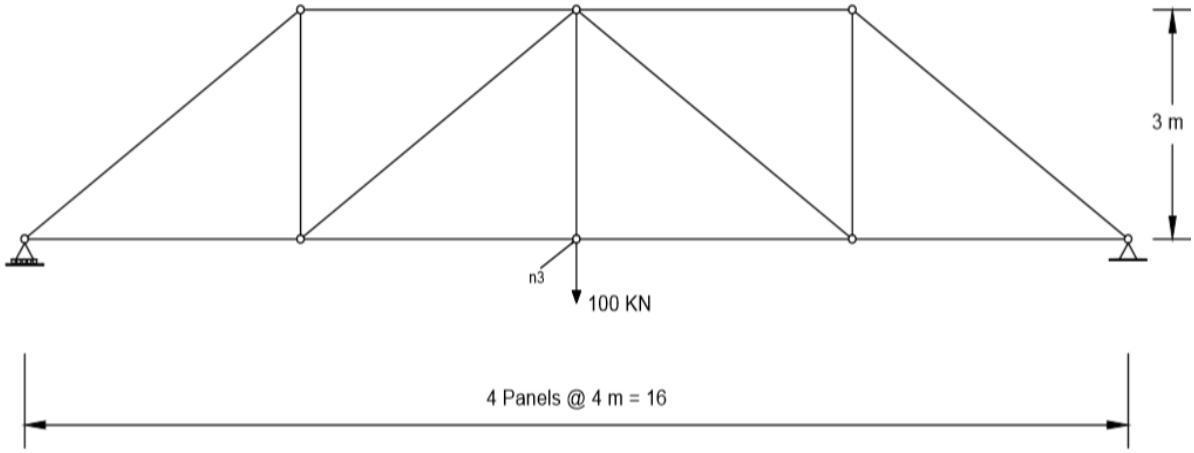

Fig. 4 Truss structure and the applied load

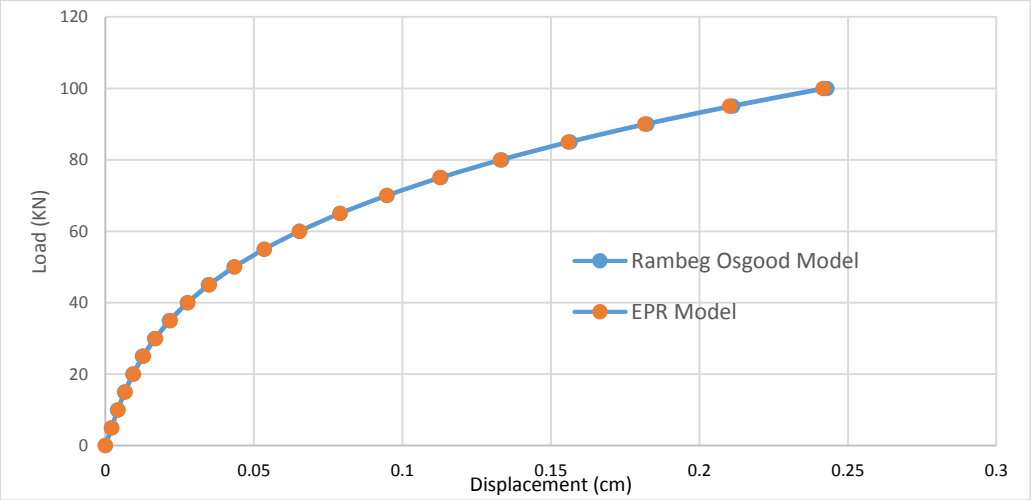

Fig. 5 Comparison between the Ramberg model and the EPR-based self-learning FEM (displacements at node 3)

5 – Conclusion

The conventional approach to constitutive modelling using data mining techniques requires a significant amount of data which could be costly and not available at all cases. Furthermore, obtaining a homogenous stress-strain state in experiments could be very challenging, especially for complex loading conditions. In this paper an EPR-based self-learning FE simulation model has been developed as an efficient approach for learning the constitutive behaviour of materials. The main advantage of using EPR in the self-learning FEM is that it gives transparent and structure equations representing the constitutive behaviour of material which can be readily implemented in FE code. The implementation EPR in the FE procedure is straightforward. In the self-learning FEM, there is no need to check yielding, to compute the gradients of plastic potential curve, to update the yield surface, etc.

The developed approach takes the advantages of the rich data buried in non-homogenous materials. It was shown that the EPR-based self-learning FEM is able to capture the material behaviour from one pass, reducing the overall computational time. In the two examples presented, the automation process was run only once and the EPR model captured the complete behaviour with very high accuracy. It should be noted that in more complex problems, more passes may be required to capture the more complex material behaviour. The proposed approach can be used in different boundary value problems.

Reference

[1] Ghaboussi, J. and Sidarta, D.E. (1998). "New nested adaptive neural networks (NANN) for constitutive modelling." Computers and Geotechnics, 22(1), 29-52.

[2] Hashash, Y.M.A., Maruland, C., Ghaboussi, J., & Jung, S. (2006). Novel Approach to integration of numerical modelling and field observations for deep excavations. ASCE Journal of Geotechnical and Geoenviromental Engineering, 132(8), pp. 1019–31.

[3] Javadi AA, Rezania M. (2009) intelligent finite element method: An evolutionary approach to constitutive modelling, Advanced Engineering Informatics, volume 23, no. 4, pages 442-451.

[4] Faramarzi, A. Javadi, A.A. and Alani, M. (2014). An EPR-based self-learning approach to material modelling. Computers and structures 137 (2014), pp.63-71.

[5] Giustolisi, O. & Savic, D. (2006). A symbolic data-driven technique based on evolutionary polynomial regression. Journal of Hydro informatics, 8(3), pp. 207-22.

[6] Ramberg W, Osgood WR. (1943). Description of stress-strain curves by three parameters. National advisory committee for aeronautics. [Technical Note No. 902].

Proceedings of the 24rd UK Conference of the
Association for Computational Mechanics in Engineering
31 March - 1 April 2016, Cardiff University, Cardiff

A NOVEL IMPLEMENTATION OF COMPUTATIONAL AERODYNAMIC SHAPE OPTIMISATION APPLIED TO A RACE CAR DIFFUSER AND A JET INTAKE DUCT

***D. S. Naumann[1], B. Evans[1] and O. Hassan[1]**

[1]College of Engineering, Swansea University, Swansea SA2 8PP, UK

*717761@swansea.ac.uk

ABSTRACT

The development of an automated aerodynamic optimisation algorithm using a novel method of parameterising a computational mesh by employing userdefined control nodes will be presented. The shape boundary movement is coupled to the movement of the novel concept of control nodes via a quasi-1D-linear deformation. Additionally, a discrete third order smoothing step has been integrated to act on the boundary during the mesh movement based on the change in its second derivative. By implementing the discrete boundary smoothing both linear and non-linear shape deformation is achievable dependent on the preference of the user. The domain mesh movement is then coupled to the shape boundary movement via a Delaunay graph mapping. An optimisation algorithm called Modified Cuckoo Search (MCS) is used acting within the prescribed design space defined by the allowed range of control node displacement. In order to obtain the aerodynamic design fitness a finite volume compressible Navier-Stokes solver is utilized. The resulting coupled algorithm is applied to a range of case studies in two dimensional space including the design of a race car diffuser and a subsonic, transonic and supersonic intake.

Key Words: *mesh movement, aerodynamic shape optimization, cuckoo search, shape parameterisation, computational fluid dynamics*

1. Motivation

During the last 30 years, Computational Fluid Dynamics (CFD) has become a very mature field now being the primary tool for aerodynamic design [1]. In light of this, computational aerodynamic shape optimisation has emerged aiming to replace the resource intensive manual optimisation process based on human expertise and intuition.

Despite these advancements, significant challenges for the modelling community remain in the parameterisation approach, the efficient transfer between CAD and CFD systems and improvements in the computationally expensive mesh re-generation process and CFD evaluation during optimisation [2, 1].

Aerodynamic designers have a clear preference towards tools that are intuitive, efficient and allow a wide ranging applicability. This paper presents a novel implementation of computational aerodynamic shape optimisation in which the parameterisation approach makes use of user–defined ‘control nodes’ in the mesh as the method for both defining the geometry movements and as the design parameters for the optimisation process. The ‘control nodes’ are linked to the rest of the discrete shape boundary via a a quasi-1D-linear boundary deformation. This is coupled to a ‘discrete boundary smoothing’. The Fast Dynamic Grid Deformation (FDGD) approach [24] has been applied to move the domain mesh and results in a self-contained algorithm formulated to propagate the effect of the ‘control node’ displacement throughout the discrete shape boundary and computational mesh making a mesh regeneration step redundant and allowing a flexible yet small design space. Also, there is no requirement to convert the geometry definition ‘stored’ in the mesh into any other format during the optimisation processs.

2. Methodology

2.1. Geometry Shape Parameterisation

The developed approach is a discrete parameterisation acting directly on the boundary mesh. Once the initial computational mesh has been created (which could have originated as a CAD geometry), the geometry is then parameterised by choosing 'control nodes' at critical positions defined by the user on the geometry. An important feature of the parameterisation is the dimensionality of the explorable design space which can be adjusted through the number of control nodes and the designers settings. The number and position of these control nodes is crucial in the evolution of the geometry. The total degrees of freedom are defined as $d = \sum_{k=1}^{N_{CN}} f_{cn}$ with f_{CN} being the degrees of freedom on each 'control node' [3].

2.2. Mesh Movement

A methodology involving three steps has been defined starting with the displacement of the 'control nodes' based on the fitness that has been evaluated by the optimization algorithm. In a second step, the boundary of the geometry is deformed given the 'control nodes' displacement. A new scheme was developed to propagate the displacement of the 'control nodes' throughout the boundary and was termed 'discrete boundary smoothing. Finally, the domain nodes are moved utilizing the FDGD method [5].

The 'discrete boundary smoothing' is inspired by the idea of artificial dissipation, a scheme applied to stabilize numerical solutions containing high gradients. The most common JST scheme applies a second and fourth order term for stabilisation. A modified approach applies a term $T\Omega = -(D^1 - D^3)\Omega$ exhibiting a third order and first order biharmonic and harmonic operator of the form $D^3\Omega = \nabla[\lambda\beta^{(3)}\nabla^2]\Omega$ and $D^1\Omega = \lambda\beta^{(1)}\nabla\Omega$ with λ and β being coefficients to scale and sense sharp gradients in the solution field [6]. This idea has been adapted. Let Ω be the discrete boundary so that $T\Omega$ may be discretized for a number of smoothing iterations $i = 2, 3, ..., N_s$ and yields

$$\Omega^{i+1} = \Omega^i + \beta^i\lambda\Big(\|\nabla^2\Omega^i\| - \|\nabla^2\Omega^{i=0}\|\Big) \tag{1}$$

$\|\quad\|$ is defining the norm operator in this paper. The smoothing iterations propagate the deformation of a boundary node and its respective change in $\nabla^2\Omega$ throughout the boundary. The first step $i = 1$ is reserved to perform an initial linear deformation step. β is applied to achieve mesh independence and is given as $\beta = \frac{\Delta s^2_{min}}{2}$.

A great advantage of the 'discrete boundary smoothing' is its flexible design space definition. This is greatly enhanced through the introduction of the scaling factor λ. In order to allow both linear and non–linear deformation along the same boundary , λ is set to be variable so equation 1 becomes

$$\Omega^{i+1}_j = \Omega^i_j + \beta^i\lambda_j[\|\nabla^2\Omega^i_j\| - \|\nabla^2\Omega^{i=0}_j\|] \tag{2}$$

with $j = 1, 2, ..., N_B$ whereas λ is selected by the user individually for each 'control node' and then linearly interpolated for the remaining boundary nodes. For $\lambda = 0$ the smoothing is disabled and only the linear deformation step occurred, for $\lambda > 0$ smoothing is applied resulting in a non–linear deformation. It also allows great local control and shape preservation capabilities when used in conjunction with the range of motion defined per 'control node'.

2.3. Computational Fluid Dynamics

The applied FLITE CFD system fluid solver is an edge–based, node–centred finite volume discretisation for solution of the compressible Reynolds Averaged Navier–Stokes equations [6]. All cases are fully viscous applying the Spallart-Allmaras turbulence model. In case of the jet intake case, the mass flow was fixed along the engine inlet face.

2.4. *Modified Cuckoo Search*

Modified Cuckoo Search [4] is an evolutionary algorithm applying the 'survival of the fittest' strategy to a given population. Each agent within the population exhibits a fitness value which is defined the objective function as for example Lift to Drag ratio. The population is separated into good and bad agents dictated by the fitness. All good agents are 'cross-bread' and the bad agents perform a random walk called Lévy flight in search of an improved agent. The process of replacing and creating eggs continues until a stopping criteria is met.

3. Case Studies

3.1. *Intake Duct Optimisation*

A common problem in aerodynamic design is the optimisation of an engine intake duct. In this case study a land–based supersonic vehicle has been optimised first for distortion and consequently for pressure recovery and distortion combined. Pressure recovery P_r measures the amount of restored total free stream pressure P_∞ $P_r = P_\infty / P_t$ to allow minimization of pressure losses. Distortion σ provides a measure of standard deviation of the total pressure P_t in relation to the mean total pressure $\bar{P}_t$ across a plane or line of interest using the integral $\sigma = -\int_0^L \frac{|P_t - \bar{P}_t|}{\bar{P}_t L} \, \mathrm{d}l$. Solutions to the fully viscous problem were sought at a range of Mach numbers $Ma = [0.5, 0.8, 1.1, 1.4]$. The applied mesh contains a total of 82868 mesh nodes and 163419 mesh elements including 7 boundary layers using four control nodes with a specified explorable design space of $x_C \in [-0.3, 0.3]$ and $y_C \in [-0.3, 0.3]$ for each control node C. The travel path as well as the fitness are illustrated in Figure 2. The utilized mesh as well as the initial and final pressure field for the case of $Ma = 0.5$ and optimization for Distortion only are visualized in Figure 1.

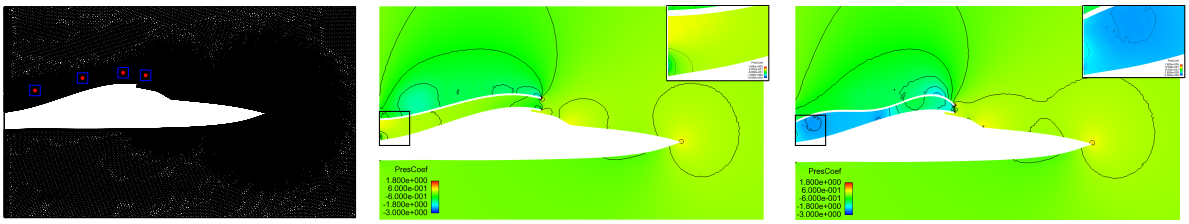

Figure 1: A supersonic vehicle with engine intake duct showing (a) detailed mesh including the control node locations and their range of motion (b) the pressure field of the initial geometry (c) the pressure field of the optimised geometry for Ma 0.5

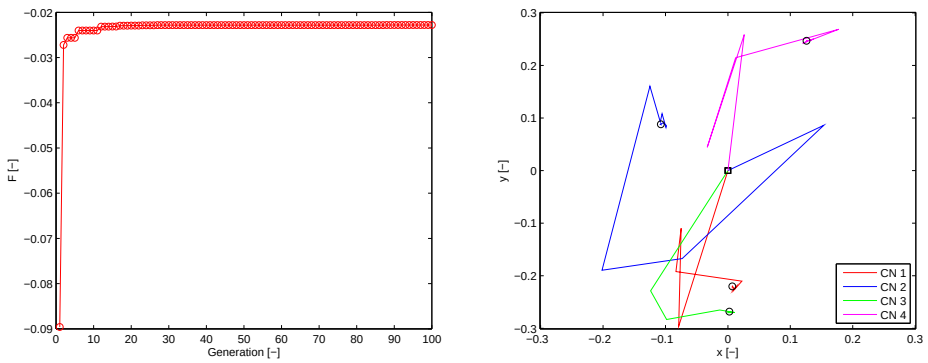

Figure 2: (a) The development of the fitness with increasing generations only considering distortion
(b) Control node movements of best egg starting from their initial position □ - start point o - end point

3.2. Race Car Diffuser

A 2D diffuser shape of a race car was optimised for down-force to drag ratio. Downforce has been measured as the negative lift according to $F = -\oint p(\boldsymbol{n} \bullet \boldsymbol{j})\,\mathrm{d}B$ and drag was determined by $D = \oint p(\boldsymbol{n} \bullet \boldsymbol{i})\,\mathrm{d}B$ with p is the non-dimensionalized static pressure, $\boldsymbol{n}$ is the normal unit vector directing into the surface and $\boldsymbol{i}$ and $\boldsymbol{j}$ are the parallel and vertical unit vectors in relation to the freestream velocity direction. Up to four control nodes were selected to determine a solution at a Mach number of $Ma = 0.1$ on a mesh with 41324 mesh nodes and 93564 mesh elements.

4. Conclusions

An automated aerodynamic shape optimisation algorithm has been developed making use of the concept of 'control nodes' in the mesh. The approach was coupled to the 'discrete boundary smoothing' technique allowing both linear and non–linear deformation along the same boundary. The approach is complemented with the FDGD domain mesh movement allowing to cut the mesh regeneration step and reduce the problem inherent in translating geometries from CAD-based geometry definitions to CFD meshes. Modified Cuckoo Search (MCS), an evolutionary optimisation approach, has been implemented to find the global optimum. The resulting algorithm is self-sufficient during the entire optimisation cycle and has been successfully applied to various different aerodynamic problems including a race car and subsonic, transonic and supersonic engine intake duct optimisation. It demonstrated to be robust in terms of the diverse applicability as well as its ease of implementation for all test cases and improvements in the fitness were achieved with a fast convergence in terms of number of generations. It has also demonstrated to be intuitive to use being able to include human expertise and allowing a flexible yet small design space.

For future work, the authors aim to extend the code into 3D. Additionally, 'dynamic' control nodes will be tested with the position being an optimisation by itself in order to increase the explorable design space whilst maintaining the rapid convergence. Also, enhancing the optimisation methodology may be exploited by implementing hybrid schemes combining this evolutionary approach with local gradient-based searching.

Acknowledgements

The authors would like to acknowledge the support provided by Fujitsu and the HPC Wales PhD scholarship scheme as well as the computational power provided to pursue such computationally expensive simulations.

References

[1] A. Jameson and J. C. Vassberg, "Computational fluid dynamics: Its current and future impact," *AIAA Paper 2001-0538*, 2001.

[2] S. Shahpar, "Challenges to overcome for routine usage of automatic optimisation in the propulsion industry," *The Aeronautical Journal*, vol. 115, no. 1172, 2011.

[3] E. B. W. S. H. O. Naumann, D. S., "A novel implementation of computational aerodynamic shape optimisation using modified cuckoo search," *Applied Mathematical Modelling*, 2015.

[4] S. Walton et al., "Modified cuckoo search: A new gradient free optimisation algorithm," *Chaos, Solitons and Fractals*, 2011.

[5] X. Liu, N. Qin, and H. Xia, "Fast dynamic grid deformation based on delaunay graph mapping," *Journal of Computational Physics*, vol. 211, pp. 405–423, 2006.

[6] K. A. Sørensen, "Phd thesis: A multigrid accelerated procedure for the solution of compressible fluid flows on unstructured hybrid meshes," *Swansea University*, 2001.

Waves and electromagnetics

hp FINITE ELEMENTS FOR THE SIMULATION OF COUPLED ACOUSTIC-MAGNETO-MECHANICAL SYSTEMS WITH APPLICATION TO MRI SCANNER DESIGN

***S. Bagwell[1], P.D. Ledger[1] and A.J. Gil[1]**
[1]Zienkiewicz Centre for Computational Engineering, College of Engineering,
Swansea University, Bay Campus, Swansea SA1 8EN, UK
*638988@swansea.ac.uk

ABSTRACT

In this paper, we focus on the generation of a strongly coupled monolithic system to describe the interaction of the magnetic field, generated mechanical vibrations and corresponding acoustic behaviour active in an MRI environment. We linearise the resulting nonlinear equations and consider both temporal and frequency dependant axisymmetric formulations of the full three dimensional problem. We also utilise a stress tensor approach for the electromagnetic forces, previously employed in [1, 2, 3]. This formulation allows the use of H^1 conforming *hp* finite elements, which when combined with *hp* refinement results in the possibility of accurate solutions. The fully discretised scheme is solved by a Newton-Raphson procedure, in an extension of [1], which employed a fixed-point algorithm. The results of our formulation are benchmarked against a series of numerical examples including an application to a realistic magnet geometry shown in Figure 1.

Key Words: *MRI Scanner; hp finite elements; Acoustic Magneto-Mechanical Coupling; Multi physics*

1. Introduction

Recently Magnetic Resonance Imaging (MRI) has become an important tool in the medical industry. The non-intrusive imaging capability and high resolution makes it desirable for identifying a range of medical ailments, such as tumours, damaged cartilage and internal bleeding. The most common type of magnet used in MRI scanners are superconducting magnets, consisting of superconducting wire cooled by liquid helium contained within a vessel known as a cryostat. Figure 1 shows a typical setup of an MRI scanner, which consists essentially of four main components. A set of main magnetic coils produce a strong uniform stationary magnetic field across the radial section of the scanner. The secondary magnetic coils are used to avoid large stray fields arising outside the scanner. The cryostat consists of a set of metallic vessels used to maintain the supercooled magnet temperatures and shield from radiation. A set of resistive coils inside the imaging volume, known as gradient coils, produce pulsed gradient magnetic fields to generate an image of the patient.

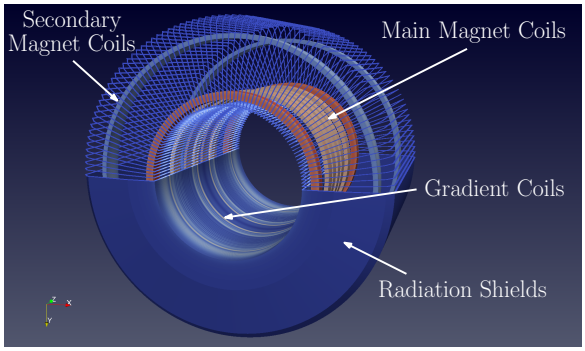

Figure 1: Primary Components of a typical MRI scanner

The presence of eddy currents in these conducting (metallic) vessels can be caused by changing magnetic fields, such as those generated by the pulsed gradient fields. These eddy currents can cause perturbations in the magnetic field. They also give rise to Lorentz forces and exert electro-mechanical stresses in the conducting components which cause them to vibrate and deform. These deformations cause the magnetic field to further perturb thus generating more eddy currents. The vibrations also cause perturbations of the surrounding air, which in turn produces an acoustic pressure field. These phenomena can have undesired effects causing imaging artefacts (ghosting), decreased component life and uncomfortable conditions for the patient, due to the noise from mechanical vibrations.

2. Coupled System

The aim of this work is to develop a computational analysis tool to aid in the magnet design by providing a better understanding of the induced vibrations and acoustic behaviour. These phenomena are described through the coupled set of Maxwell (eq. 1a and 1b) and linear elasticity (eq. 1c) equations. In the air the linear elasticity equations reduce to a scalar Helmholtz equation for the acoustic pressure (eq. 1d). Here ρ denotes the density of the material, μ the electromagnetic permeability, ϵ dielectric permittivity, γ the electric conductivity, λ and G the Lamé parameters, c the speed of sound through a medium, $\boldsymbol{E}$ the electric field vector, $\boldsymbol{H}$ the magnetic field vector, $\boldsymbol{u}$ the displacement field vector, $\hat{p}$ the acoustic pressure and $\boldsymbol{\sigma}^m$ is the cauchy stress tensor and the dot symbol ($\dot{}$) is used to represent a time derivative.

$$\nabla \times \boldsymbol{E} = \mu \dot{\boldsymbol{H}} \qquad \nabla \cdot \epsilon \boldsymbol{E} = \boldsymbol{0} \qquad \text{in } \Omega \tag{1a}$$

$$\nabla \times \boldsymbol{H} = \boldsymbol{J}\left(\dot{\boldsymbol{u}}, \boldsymbol{H}, \boldsymbol{E}\right) \qquad \nabla \cdot \mu \boldsymbol{H} = \boldsymbol{0} \qquad \text{in } \Omega \tag{1b}$$

$$\nabla \cdot \boldsymbol{\sigma}^m(\boldsymbol{u}) + \boldsymbol{b}\left(\boldsymbol{H}\right) = \rho \ddot{\boldsymbol{u}} \qquad \boldsymbol{\sigma}^m\left(\boldsymbol{u}\right) = \lambda\left(\nabla \cdot \boldsymbol{u}\right)\boldsymbol{I} + G\left(\nabla_{sym}\boldsymbol{u}\right) \qquad \text{in } \Omega_c \tag{1c}$$

$$\nabla^2 \hat{p} - \frac{1}{c^2}\ddot{\hat{p}} = 0 \qquad \text{in } \Omega_n \tag{1d}$$

The current term consists of $\boldsymbol{J}\left(\dot{\boldsymbol{u}}, \boldsymbol{H}, \boldsymbol{E}\right) = \boldsymbol{J}^s + \boldsymbol{J}^l\left(\dot{\boldsymbol{u}}, \boldsymbol{H}\right) + \boldsymbol{J}^o\left(\boldsymbol{E}\right)$, the source, Lorentz and Ohmic, or eddy currents. The magneto-mechanical coupling, shown in Figure 2, arises in the conductor due to the Lorentz currents and through body forces in terms of Maxwell stresses, $\boldsymbol{b}\left(\boldsymbol{H}\right) = \nabla \cdot \boldsymbol{\sigma}^e\left(\boldsymbol{H}\right)$ in continuation of [1, 2, 3], defined as

$$\boldsymbol{\sigma}^e\left(\boldsymbol{H}\right) = \mu\left(\boldsymbol{H} \otimes \boldsymbol{H} - \frac{1}{2}\left(\boldsymbol{H} \cdot \boldsymbol{H}\right)\boldsymbol{I}\right) \tag{2}$$

The acoustic pressure is coupled to the magneto-mechanical problem at the air-conductor interface boundary ($\partial\Omega_c$) through jump conditions in the tractions and accelerations.

$$[\![\boldsymbol{\sigma}]\!]\mathbf{n} = 0 \qquad \text{on } \partial\Omega_c \tag{3a}$$

$$[\![\ddot{\mathbf{u}}]\!] = 0 \qquad \text{on } \partial\Omega_c \tag{3b}$$

where $\boldsymbol{n}$ is the outward normal vector associated with the boundary and the double bracket symbol $[\![x]\!] = x_n - x_c$ defines the jump in the solution across a boundary. The subscripts c and n correspond to the conducting and non-conducting sub domains of our computational domain, shown in Figure 2.

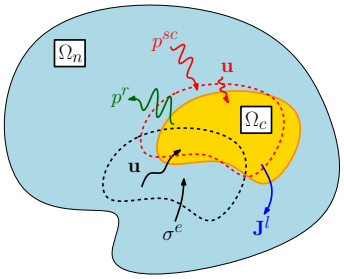

Figure 2: Computational domain of the coupled system

3. Computational Framework

3.1. Axisymmetric Problem

Given that the geometry of the MRI Cryostat is constant across the bore section of the cylinder and modelling only one set of gradient coils, the Z-gradient, the problem may be expressed in terms of an axisymmetric formulation. By expressing the geometry in cylindrical coordinates the fields are independent of the angular component and so the order of the geometry reduces from 3D to a 2D plane. The problem is solved on the r, z plane as opposed to the x, y, z Cartesian domain, whilst still resolving the full 3D nature of the fields. However this requires a more complex weak formulation, which takes account of the differential operators expressed in cylindrical coordinates. By introducing appropriately scaled variables the $1/r$ singularity at the radial axis can be eliminated and u_r and u_z the components of mechanical displacements along with the A_ϕ component of a vector potential for representing the electromagnetic fields can all be discretised by H^1 conforming hp finite elements.

3.2. Time Harmonic System

Computational speed is of great importance to the design process of an MRI scanner, as designers must test a large number of concept designs over a wide range of operational conditions. For this reason one would prefer to solve in the frequency domain, rather than the full time dependant problem. This formulation allows the designer to sweep quickly over the sourcing frequencies of the Z-gradient coil and compute the dissipated power as a function of the frequency. We have therefore chosen to adopt the approach taken in [1] of assuming a time harmonic, rather than pulsed, sourcing current in the gradient coil so that we can formulate the equations in the frequency domain.

3.3. Monolithic Scheme

Unlike the work previously carried out in [1], which involves the implementation of a fixed point iteration scheme, we have chosen to adopt a Newton-Raphson approach to solve the coupled system of non-linear equations (eq. 1). By forming the monolithic system, shown below in eq. 4, this method offers a more robust solver with quadratic rates of convergence.

$$\begin{bmatrix} \boldsymbol{K_{HH}} & \boldsymbol{K_{Hu}} & \boldsymbol{0} \\ \boldsymbol{K_{uH}} & \boldsymbol{K_{uu}} & \boldsymbol{K_{u\hat{p}}} \\ \boldsymbol{0} & \boldsymbol{K_{\hat{p}u}} & \boldsymbol{K_{\hat{p}\hat{p}}} \end{bmatrix} \begin{pmatrix} \boldsymbol{\delta}_H \\ \boldsymbol{\delta}_u \\ \boldsymbol{\delta}_{\hat{p}} \end{pmatrix} = - \begin{pmatrix} \boldsymbol{R}_H(\boldsymbol{H},\boldsymbol{u}) \\ \boldsymbol{R}_u(\boldsymbol{H},\boldsymbol{u},\hat{\boldsymbol{p}}) \\ \boldsymbol{R}_{\hat{p}}(\boldsymbol{u},\hat{\boldsymbol{p}}) \end{pmatrix} \tag{4}$$

Where $\boldsymbol{R}$ is the system residual vector, obtained from eq. 1, $\boldsymbol{\delta}$ is the solution update vector and $\boldsymbol{K}$ is the Tangent stiffness matrix, formed by taking the directional derivative of the residuals with respect to the solution fields, outlined in [4]. To obtain the solution $\boldsymbol{X} = [\boldsymbol{H},\boldsymbol{u},p]^T$ we define some initial guess $\boldsymbol{X}^{[0]}$ and update it by solving eq. 4 and iterating over $\boldsymbol{X}^{[k+1]} = \boldsymbol{X}^{[k]} + \boldsymbol{\delta}$ until convergence is acheived.

3.4. Perfectly Matched Layer

Due to the nature of acoustic wave propogation we must treat the infinite boundary of the computational domain with special consideration to allow for accurate results. We have chosen to employ a perfectly matched layer, or PML, to deal with the absorbtion of outgoing waves and avoid numerical pollution from artificial reflections at the boundary. The PML is analogous to a metamaterial where its parameters are artificial and are constructed through an exponential decay function in the complex plane (resulting in a complex coordinate stretching in the layer), in order to absorb incoming waves. A full PML construction and its behaviour in a *hp* finite element context is discussed in [5]. To demonstrate the effect of the PML a simple test problem is setup, shown in Figure 3, in which a sphere is located at the centre of an axisymmetric domain and an incident plane wave is propogated in the positive z direction (upwards) with a PML around the outer domain boundary. The acoustic pressure can be expressed as $\hat{p} = \hat{p}^{in} + \hat{p}^{sc}$, where $\hat{p}^{in}$ is an incident (known) plane wave and $\hat{p}^{sc}$ is the unknown scattered wave

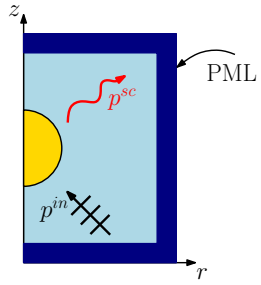

Figure 3: Problem Setup

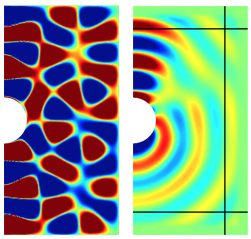

Figure 4: Pressure Field

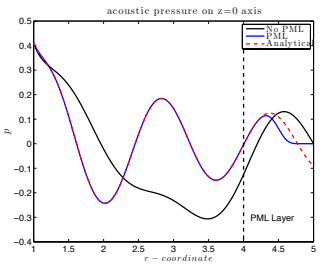

Figure 5: Solution Comparison

The contour plots of the computed scattered field $\hat{p}^{sc}$ is shown in Figure 4. The left plot shows the pressure field without the PML and the right plot with the PML implemented. Figure 5 is a line plot of the scattered field $\hat{p}^{sc}$ from the outer radius of the sphere at the centre of the domain to the edge of the PML. It is clear from the plots that without the PML the artificial reflections at the domain boundary cause numerical artefacts to emerge. With the PML implemented it is possible to absorb these waves and allow for accurate solutions within the computational domain. In the PML layer the solution decays to the defined boundary value and does not fully reflect the analytical solution.

4. Numerical Results

We present the following numerical example of a realistic cryostat geometry of an actual MRI scanner. Given that our axisymmetric formulation is still valid for a full 3D problem, Figure 6 shows the plots of the two magnetic field components, generated by the static and gradient coils, around the full 3D scanner.

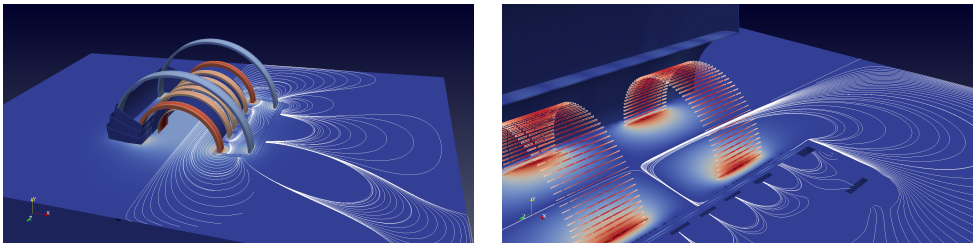

Figure 6: Static (left) and Gradient (right) Magnetic fields

The acoustic behaviour of the MRI magnet geometry is important for determining the noise levels generated during an imaging cycle. The high noise levels can be uncomfortable for patients undergoing a body scan, thus the need to accurately simulate the acoustic pressure generated by the scanner is of vital importance. In Figure 7 the effect of p, polynomial basis function, refinement on the acoustic distribution is visualised.

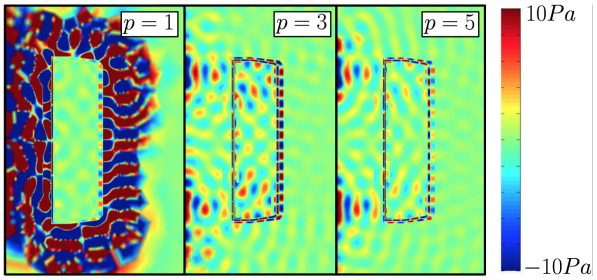

Figure 7: p effect on acoustic wave problem

The solution for linear, $p = 1$, basis functions varies significantly from those with higher order basis functions, $p = 3$ and $p = 5$. The linear shape functions result in numerical dispersion, which causes the amplitude to grow until steady state, whereas the higher order basis functions are much better at capturing the wave function and result in a more accurate solution.

5. Conclusions

The results presented here provide a framework to the set up of an analysis tool for the prediction of deformation and vibration in the conducting regions of an MRI scanner and the correponding acoustic patterns and sound levels that arise. The accuracy of the non-linear coupled *hp* finite element framework has been verified on a series of further benchmark industrial and academic examples, which will be presented in the talk at ACME conference Cardiff.

Acknowledgements

The authors gratefully acknowledge the support of EPSRC and Siemens Magnet Technology.

References

[1] P.D. Ledger, A.J. Gil, R. Poya, I. Wilkinson, M. Kruip, S. Bagwell. Solution of an industrially relevant coupled magneto-mechanical problem set on an axisymmetric domain, *Appl Math Model*, Vol. 40, Issue 3, 1959-1971, 2016

[2] D. Jin, P.D. Ledger, A.J. Gil. An *hp*-fem framework for the simulation of electrostrictive and magnetostrictive materials, *Comput Struct vol. 133*, 131-148, 2014

[3] A.J. Gil and P.D. Ledger, A coupled *hp*-finite element scheme for the solution of two-dimensional electrostrictive materials, *Int J Numer Meth Eng*, Vol. 91, Issue 11, 1158-1183, 2012

[4] J. Bonet and R.D.Wood, Nonlinear Continuum Mechanics for Finite Element Analysis, *Cambridge University Press*, ISBN 978-0-521-83870-2, 1997

[5] Improving the Performance of Perfectly Matched Layers by Means of hp-Adaptivity, *Numer Meth Part D E*, Vol. 23, Issue 4, 832-858, 2007

Proceedings of the 24th UK Conference of the
Association for Computational Mechanics in Engineering
31 March - 01 April 2016, Cardiff University, Cardiff

Solving short wave problems using high order finite elements

***K. Christodoulou[1], O. Laghrouche[1], M.S. Mohamed[1] and J. Trevelyan[2]**

[1]School of Energy, Geoscience, Infrastructure and Society, Heriot Watt University, Edinburgh, EH14 4AS
[2]School of Engineering and Computing Sciences, Durham University, Durham, DH1 3LE

*kc328@hw.ac.uk

ABSTRACT

In this paper, we study numerical solutions of Helmholtz problems using high order finite element formulations. These include the polynomial high-order finite element method (high-order FEM) and the partition of unity finite element method (PUFEM). The aim of the study is to solve efficiently and with high level of accuracy two dimensional problems at high frequencies. The performance of both methods is compared and analysed on test examples of practical interest.

Key Words: *Helmholtz equation ; weak variational formulation ; partition of unity finite element method ; high order finite element method ; propagation and evanescent waves*

1. Introduction

Numerical solutions to the Helmholtz problems depend significantly on the wave number k. Specifically, the accuracy of the solution of the Helmholtz equation using the conventional FEM deteriorates with increasing wave number, even if the number of elements per wavelength is kept constant. This is due to the *pollution* error [1].

With the aim to reduce the computational cost and improve the accuracy of wave problems, various methods based on field enrichment have been proposed. We addressed the literature on partition of unity finite element method (PUFEM) and other related methods. Another alternative to reduce the pollution error is to increase the interpolation polynomial order over each element. High order polynomial approximations reduce resolution requirements which results in lower number of parameters in the whole problem.

The current work assesses both PUFEM and high-order FEM for the solution of Helmholtz problems with increasing wave numbers. PUFEM has been thoroughly investigated for acoustic [2] wave problems and attempts have been made to compare its performance to that of the standard FEM. Given that only low order elements have been considered for FEM, it is intended here to increase the polynomial order p to hopefully claim a fair comparison.

2. Weak formulation and numerical approximation

Let $\Omega \subset \mathbb{R}^2$ be an open bounded domain with a smooth boundary Γ. We consider finite element discretizations for approximating the solution of the Helmholtz equation

$$-\Delta u - k^2 u = 0 \qquad \text{in} \quad \Omega, \tag{1a}$$

$$\nabla u.\mathbf{n} + \mathrm{i}ku = g \qquad \text{on} \quad \Gamma. \tag{1b}$$

The Galerkin finite element approximation is applied to the weak variational formulation of the Helmholtz problem. The weak formulation is obtained by multiplying the Helmholtz equation (1a) by a smooth test function $v = v(x, y)$ and integrating the resulting equation over the domain Ω such as

$$-\int_{\Omega} (\Delta u + k^2 u) v \, d\Omega = 0. \tag{2}$$

By applying the integration by parts to the integrand with second order derivatives and then introducing the Robin boundary condition (1b), the system of equations to solve is then

$$\int_{\Omega} (\nabla u.\nabla v - k^2 uv)\, d\Omega + \mathrm{i}k \oint_{\Gamma} u.v\, d\Gamma = \oint_{\Gamma} gv\, d\Gamma. \tag{3}$$

Our aim is to find an approximate solution u_h of the weak form (3) using either, high-order finite elements (FEM) or elements with plane wave enrichment functions (PUFEM).

In the high-order FEM model, the computational domain Ω is divided into N uniform non-overlapping quadrilateral elements Ω_e, $e = 1, ..., N$. The field unknown variable over each element Ω_e is then approximated by

$$u_h = \sum_{j=1}^{\#\text{vert}} u_j N_j(\boldsymbol{\xi}) \tag{4}$$

where N_j stands for the Lagrangian polynomial interpolation functions [3] and u_j represents the nodal values (unknowns of the problem) corresponding to the element vertices. The degree p of the polynomial interpolation functions N_j depends on the number of nodes assigned to each element. In general, for an approximation of degree p the number of vertices per element would be $(p+1)^2$.

In the PUFEM model, the elements are chosen to be quadrilateral with #vert = 4. At each vertex, the unknown variable u_j of expression (4) is expanded into a linear combination of q plane waves with directions encompassing the two dimensional space [2]. The PUFEM approximation of the unknown field variable within each element Ω_e is then given by

$$u_h = \sum_{j=1}^{4} \sum_{l=1}^{q} N_j\, e^{\mathrm{i}k\boldsymbol{d}.\boldsymbol{r}}\, A_j^l. \tag{5}$$

where N_j are the bi-linear basis functions corresponding to the mesh vertex, $\boldsymbol{d} = (\cos\theta_l, \sin\theta_l)^T$ and $\theta_l = 2\pi\ l/q$ for $l = 1, 2, ..., q$. The unknowns of the problem are no more the coefficients u_j but the amplitude factors A_j^l of the plane waves.

3. Numerical experiments

In this section, both PUFEM and high-order FEM models are assessed by considering test cases of practical interest. The first one involves an evanescent wave and the second case deals with the propagation of waves in a duct with rigid walls, which involves propagating and decaying modes. The performance of each method is measured through the relative error, in percent, using the L_2 norm. The discretization level in terms of degrees of freedom per wavelength is indicated by the paramter τ given by $\tau = \lambda \sqrt{totdof/area(\Omega)}$, where $totdof$ stands for the total number of degrees of freedom required for the solution and Ω_{area} is the area of the computational domain. Another parameter of interest is $totsys$ representing the total number of storage locations of the system matrix (x). Finally, the conditioning of the system matrix (x), denoted by $\kappa(A)$, is also considered. It is computed using the 1-norm and is given by $\kappa(A) = ||A||_1 ||A^{-1}||_1$. To conclude with, all the elementary integrals are evaluated numerically in a straight forward way by using Gauss-Legendre quadrature. The number of integration points is chosen to be enough so that the results are not affected by the integration errors.

3.1. Evanescent wave problem

The first test case deals with the numerical solution of an evanescent wave problem in a square domain $\Omega = [-1, 1] \times [-1, 1]$. The Robin boundary condition is applied on the boundary Γ through the boundary source term g. The exact solution of this problem can be found in [4].

The problem is solved for the wave number $ka = 100$ and $\beta = 1.001$. The results obtained with both approaches are given in Table 1. We list the L_2-error, the condition number κ and the total number

Table 1: Evanescent wave test case for $ka = 100$ and $\beta = 1.001$. Relative percentage L_2-error, $\epsilon_2[\%]$, conditioning, $\kappa(A)$, and total number of storage locations, $totsys$for different numbers of τ.

	p-FEM			PUFEM
	p=10	p=20	p=30	
$\epsilon_2[\%]$	3.44969 (4.5)	4.44105 (3.8)	1.55543 (3.8)	1.61219 (1.5)
	0.00053 (10.1)	0.00061 (6.4)	0.00025 (5.7)	0.08167 (1.6)
	0.00015(11.4)	0.00016 (7.6)	0.00023 (7.6)	0.00081 (1.7)
	0.00002 (13.9)	0.00002 (11.4)	0.00009 (9.5)	0.00080 (1.8)
$\kappa(A)$	0.80E+04 (4.5)	0.13E+05 (3.8)	0.23E+05 (3.8)	0.14E+09 (1.5)
	0.40E+05 (10.1)	0.38E+05 (6.4)	0.47E+05 (5.7)	0.97E+09 (1.6)
	0.54E+05 (11.4)	0.53E+05 (7.6)	0.85E+05 (7.6)	0.37E+10 (1.7)
	0.84E+05 (13.9)	0.12E+06 (11.4)	0.11E+06 (9.5)	0.5IE+14 (1.8)
$totsys$	1,973,161 (4.5)	2,386,381 (3.8)	3,520,981 (3.8)	102,870 (1.5)
	22,978,081 (10.1)	10,827,301 (6.4)	11,687,221 (5.7)	139,965 (1.6)
	32,645,341 (11.4)	18,614,761 (7.6)	27,471,961 (7.7)	182,760 (1.7)
	59,413,861 (13.9)	62,293,141 (11.4)	53,386,201 (9.5)	231,255 (1.8)

of storage locations of the final system matrix, $totsys$. The discretization level τ is also given and is presented between brackets.

The results from Table 1 show different aspects of the high-order FEM and PUFEM. As the order p increases in the FEM, the discretization level τ required to achieve a prescribed accuracy is decreased. But PUFEM seems to provide similar quality results for significantly lower values of the discretization level τ. For example, PUFEM provides 1.5% error with $\tau = 1.5$ whereas a similar error is obtained with $p = 30$ and $\tau = 3.8$. Moreover, PUFEM provides an error of order $10^{-4}\%$ with $\tau = 1.7$ whereas an error of the same order is achieved with $\tau = 10.1$ for $p = 10$, with $\tau = 6.4$ for $p = 20$ and finally, with $\tau = 5.7$ for $p = 30$. On the other hand, the lowest levels of L_2-error are achieved by the polynomial approach approach (FEM) but with a significantly higher discretization level. Moreover, the number $totsys$ of storage locations required by PUFEM is lower in comparison to the values required by high-order FEM. However, looking at the condition number κ, the values corresponding to high-order FEM are of the same order while the value corresponding to PUFEM is orders of magnitude higher.

3.2. Wave propagation in a duct

The second test example deals with the propagation of a wave in a duct with rigid walls. The computational domain $\Omega = [0,2] \times [0,1]$ is considered with the Robin condition (1b) on its boundary Γ through the source term g. The exact solution of this problem can be found in [5].

We solve the problem for the wave number $ka = 40$. Two different values of θ are considered which give the highest-propagating mode ($\theta = 12$) and the lowest-evanescent mode ($\theta = 13$). The computed L_2-errors, in percent, and the discretization levels are given in Table 2.

As shown in Table 2, the error decreases by refining the mesh grid for high-order FEM with a given order p and by increasing the number q of enriching plane waves for PUFEM. This is valid for both values of θ representing propagating and evanescent modes. Again, for all cases, PUFEM requires less degrees of freedom per wavelength in comparison to high-order FEM in order to reach a prescribed accuracy. While high-order FEM requires more degrees of freedom per wavelength, this number decreases as p increases. The results also show that the solution requires more degrees of freedom per wavelength to reach a certain accuracy for the evanescent wave problem in comparison to the propagating mode

Table 2: Wave propagation is a duct. Relative L_2-error [%] and discretization level for high-order FEM and PUFEM for $ka = 40$.

	p-FEM			PUFEM
	p=10	p=20	p=30	
$\theta = 12$	0.00380 (5.7)	0.00020 (4.6)	0.00101 (3.4)	1.24777 (1.9)
	0.00005 (9.0)	0.00006 (6.8)	0.00009 (6.8)	0.08853 (2.4)
	0.00005 (11.2)	0.00005 (11.2)	0.00007 (10.1)	0.00557 (2.7)
	0.00005 (13.4)	0.00006 (13.4)	0.00005 (13.4)	0.00019 (3.0)
$\theta = 13$	0.00870 (5.7)	0.00085 (4.6)	0.02018 (3.4)	39.14330 (1.9)
	0.00011 (9.0)	0.00010 (6.8)	0.00012 (6.8)	4.14675 (2.4)
	0.00010 (11.2)	0.00010 (11.2)	0.00010 (10.1)	0.41524 (2.7)
	0.00009 (13.4)	0.00010 (13.4)	0.00010 (13.4)	0.00121 (3.0)

problem. For example, PUFEM provides about 1.2% and 0.09% with $\tau = 1.9$ and 2.4, respectively, in the case of propagating mode. These errors increased to about 39.1% and 4.1% respectively in the case of evanescent mode. This observation is also valid for the high-order FEM approach.

4. Conclusions

In this work, two high order finite element formulations have been used to solve 2D Helmholtz problems. The methods chosen are the high-order polynomial finite element method (high-order FEM) and the partition of unity finite element method (PUFEM). The performance of each approach is assessed in terms of results quality and required degrees of freedom per wavelength. The condition number and total number of required storage locations are also considered.

PUFEM provides high quality results with a low number of degrees of freedom per wavelength, especially for relatively high frequencies where the element size incorporates many wavelengths. Errors lower than 1% were obtained with less than 2 degrees of freedom per wavelength. In such cases, the final system to solve is obviously drastically reduced in comparison to high-order FEM and hence the number of storage locations is also reduced. However, it is also shown that further increasing the discretization level by increasing the number of enriching plane waves does not always enhance the results beyond a certain level due to the ill-conditioning issue which is inherent to the plane wave enrichment technique.

References

[1] I. Frank and I. Babuska. Finite element solution of the Helmholtz equation with high wave number Part I: The h-version of the FEM. *Computers and Mathematics with Applications*, 30.9, 9-37, 1995.

[2] O. Laghrouche, P. Bettess and R. J. Astley. Modelling of short wave diffraction problems using approximating systems of plane waves. *International Journal for Numerical Methods in Engineering*, 54.10, 1501-1533, 2002.

[3] S. Petersen, D. Daniel and O. von Estorff. Assessment of finite and spectral element shape functions for efficient iterative simulations of interior acoustics. *Computer methods in applied mechanics and engineering*, 195.44, 6463-6478, 2006.

[4] T. Luostari, T. Huttunen and P. Monk. The ultra weak variational formulation using Bessel basis functions. *Communications in Computational Physics*, 11.02, 400-414, 2012.

[5] T. Huttunen, P. Gamallo and R.J. Astley. Comparison of two wave element methods for the Helmholtz problem. *Communications in Numerical Methods in Engineering*, 25.1, 35-52, 2009.

Proceedings of the 24th UK Conference of the
Association for Computational Mechanics in Engineering
31 March - 01 April 2016, Cardiff University, Cardiff

High fidelity computation of electromagnetic resonant modes in cavities

M. Dawson, R. Sevilla, O. Hassan and K. Morgan

Zienkiewicz Centre for Computational Engineering, College of Engineering, Swansea University, UK SA1 8EN

{743587,R.Sevilla,O.Hassan,K.Morgan}@swansea.ac.uk

ABSTRACT

We present a method of obtaining properties of electromagnetic cavities with frequency dependent materials, such as the resonant frequencies, quality factors and mode shapes, using a high-order discontinuous Galerkin (DG) time-domain solver. Optimal convergence in the resonant frequency has been achieved for all numerical examples. The accuracy of resonant frequencies obtained is quantified and we present a study of errors due to geometrical approximation. Advantages of a multi-processor computation using Message Passing Interface (MPI) are demonstrated.

Key Words: *Discontinuous Galerkin; Electromagnetics; Resonant Cavities; Time Domain*

1. Introduction

Recent advances in manufacturing techniques, such as electron beam lithography make it possible to manufacture resonant cavities on the scale of the wavelength of light. These devices frequently have desirable qualities such as high quality factors and well defined resonant frequencies [1]. However, the typical scale and the geometric complexity introduce several challenges for numerical simulation.

The behaviour of these resonators is described by Maxwells' equations of classical electromagnetics. For dispersive materials, an auxiliary ordinary differential equation based on the Drude model of solids [2] is coupled to the Maxwell system. Frequency domain solvers are traditionally employed to find the resonant frequencies and associated modes, but as the scale and geometric complexity of the devices increase, the large eigenvalue system that must be solved becomes computationally prohibitive.

We propose using the Discontinuous Galerkin method with explicit time marching, which only requires solving a block diagonal system of equations for each timestep [3]. The frequency spectrum, resonant frequencies and quality factors are then recovered by a Fourier transform of the time domain solution.

2. DG solution of the transient Maxwell's equations in dispersive media

Maxwell's equations of classical electromagnetics and the auxiliary ordinary different equation required for dispersive media in linear, dimensionless, conservation form by

$$\frac{\partial \mathbf{U}}{\partial t} + \sum_{k=1}^{\mathtt{n_{sd}}} \frac{\partial \mathbf{F}_k(\mathbf{U})}{\partial x_k} = \mathbf{S}(\mathbf{U}), \tag{1}$$

where $\mathtt{n_{sd}}$denotes the number of spatial dimensions. The vector of unknowns, $\mathbf{U}$, is given by $\mathbf{U} = (\epsilon E_1, \epsilon E_2, \epsilon E_3, \mu H_1, \mu H_2, \mu H_3, J_1, J_2, J_3)^T$, the flux vectors, $\mathbf{F}_k$, are given by $\mathbf{F}_1 = (0, H_3, -H_2, 0, -E_3, E_2, 0, 0, 0)^T$, $\mathbf{F}_2 = (-H_3, 0, H_1, E_3, 0, -E_1, 0, 0, 0)^T$ and $\mathbf{F}_3 = (H_2, -H_1, 0, -E_2, E_1, 0, 0, 0, 0)^T$ and the source term, $\mathbf{S}$, is given by $\mathbf{S} = (0, 0, 0, 0, 0, 0, \omega_d^2 E_1 - \gamma_d J_1, \omega_d^2 E_2 - \gamma_d J_2, \omega_d^2 E_3 - \gamma_d J_3)^T$. Here $\mathbf{E} = (E_1, E_2, E_3)$ is the electric field intensity, $\mathbf{H} = (H_1, H_2, H_2)$ is the magnetic field intensity and $\mathbf{J} = (J_1, J_2, J_3)$ is the polarisation current. The material parameters ϵ, μ, ω and γ are the electric permittivity, magnetic permeability, plasma frequency and electron damping coefficient respectively.

We discretise the computational domain Ω on an unstructured mesh. The DG weak formulation [4] of (1) on an element Ω_e can then be written as

$$\int_{\Omega_e} \mathbf{W} \cdot \frac{\partial \mathbf{U}_e}{\partial t} d\Omega + \int_{\Omega_e} \mathbf{W} \cdot \left(\sum_{k=1}^{\mathrm{n_{sd}}} \frac{\partial \mathbf{F}_k(\mathbf{U}_e)}{\partial x_k} - \mathbf{S}(\mathbf{U}_e) \right) d\Omega + \int_{\partial\Omega_e} \mathbf{W} \cdot \mathbf{A}_n^- [\![\mathbf{U}_e]\!] \, d\Gamma_e = 0 \,,$$

where $\mathbf{U}_e$ denotes the solution vector restricted to the element Ω_e, $\mathbf{W}$ is a vector of test functions and $[\![\mathbf{U}_e]\!] = \mathbf{U}_e - \mathbf{U}_{\mathrm{out}}$ denotes the jump of the solution across the element boundary $\partial\Omega_e$. The boundary term, derived after introducing the numerical flux on the boundary and using a flux-splitting technique, results in

$$\mathbf{A}_n^- [\![\mathbf{U}_e]\!] = \frac{1}{2} \begin{pmatrix} -\mathbf{n} \times [\![\mathbf{H}]\!] + \mathbf{n} \times (\mathbf{n} \times [\![\mathbf{E}]\!]) \\ \mathbf{n} \times [\![\mathbf{E}]\!] + \mathbf{n} \times (\mathbf{n} \times [\![\mathbf{H}]\!]) \\ \mathbf{0}_{3\mathrm{x}1} \end{pmatrix} ,$$

where $\mathbf{n}$ is the outward unit normal of the element and $\mathbf{0}_{3\mathrm{x}1}$ is a zero vector of dimension 3. After introducing the approximation of the solution and using a Galerkin formulation, the following system of ordinary differential equations is obtained

$$\mathbf{M} \frac{d\boldsymbol{U}}{dt} + \mathbf{R}(\boldsymbol{U}) = \mathbf{0} \,,$$

where $\boldsymbol{U}$ is the vector of nodal values, $\mathbf{M}$ is the block diagonal mass matrix and $\mathbf{R}(\boldsymbol{U})$ is the residual vector. The system of ordinary differential equations is advanced in time using a fourth-order explicit Runge-Kutta method.

3. Resonant frequencies and mode shapes

The engineering quantities of interest are the resonant frequencies and the associated modes shapes and quality factors. In order to obtain these quantities from time domain simulations, we begin with an intial field distribution containing a point excitation. Maxwells' equations are solved to advance the fields in time, and the amplitude of the solution field is recorded at fixed time intervals, Δt, at at least one point in space for a period of time, T. The resulting discrete field intensity signal is illustrated in Figure 1a. Taking the fast Fourier transform of the field intensity signal results in its frequency eigenspectrum, shown in Figure 1b for a 3-dimensional cubic cavity with a perfect electric conductory (PEC) boundary. The resonant frequencies of the cavity correspond to the locations of peaks in the spectrum, whilst the quality factors are related to peak widths. The mode shape associated to a given resonant frequency can be obtained as a postprocess, by taking the discrete Fourier transform at the desired frequency.

For a high fidelity computation of broadband spectrums, two properties of the fast Fourier transform must be taken into consideration: (1) the spectrum resolution is inversely proportional to T; (2) the highest resonant frequency that can be computed is inversely proportional to Δt. To alleviate the potentially large computational cost which results, we employ a high-order DG solver with a NEFEM [5] rationale. This enables the use of extremely coarse meshes that guarantee that the time step of the explicit time marching algorithm is not restricted by the stability condition, but by the maximum frequency that is to be resolved. In addition, an efficient parallel implementation using MPI has been developed, enabling to dramatically reduce the computational time required to advance the solution large periods of time.

4. Numerical Results

The solver was validated validated using a rectangular 2-dimensional cavity filled with a dispersive medium ($\epsilon_\infty = 1, \sigma = 1, \omega = 6.7433, \gamma = 0.0799$), surrounded by a perfect electric conductor, with a width twice its length. Figure 2a shows how error in the resonant frequency, calculated relative to a reference solution, converges with T to a final numerical error due to spatial discretisation. Optimal

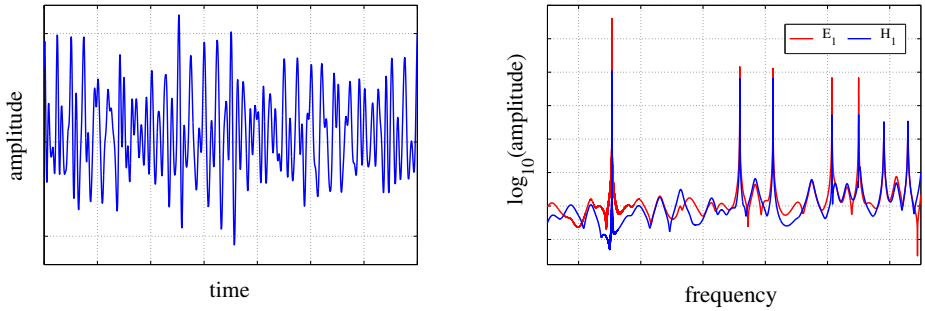

(a) Signal obtained from simulation run.

(b) Eigenspectrum obtained by FFT

Figure 1: Signal and corresponding eigenspectrum obtained from a time domain simulation for a cubic, free-space cavity with a PEC boundary.

convergence of the error in resonant frequency is shown in Figure 2b, the error convergences as the numerical dispersion error, at a rate $h^{2(p+2)}$.

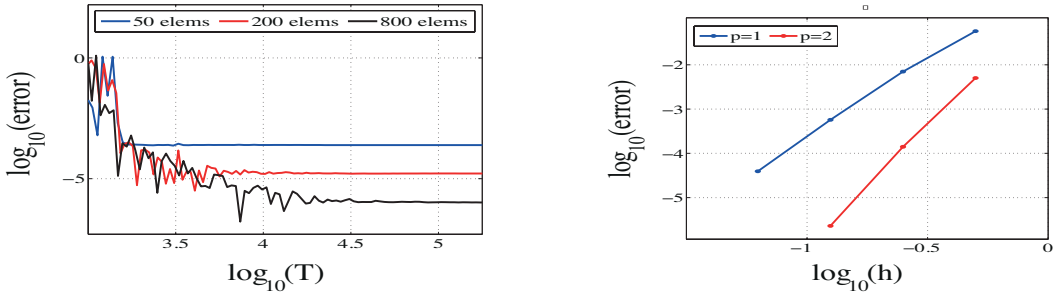

(a) Convergence of the error in calculated resonant frequency with T for three different meshes.

(b) h-convergence of the error in resonant frequency obtained for the fundamental frequency.

Figure 2: Results for a rectangular cavity filled with a dispersive medium, surrounded by a PEC boundary

A circular free-space cavity is used to illustrate the effect of boundary approximations on computed resonant frequencies. In Figure **??**, convergence of error for p- and h-refinement is shown for iosparametric elements and NEFEM elements. The geometrical error can be seen to have a significant effect for low-order planar elements.

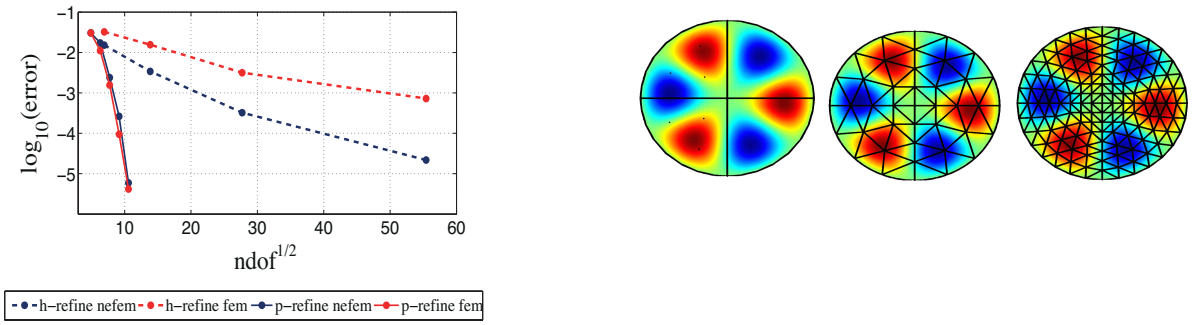

(a) Convergence of error in resonant frequency with square root of number of degrees of freedom for mode shown in (b).

(b) Meshes for resonant frequency error below 10^{-3}, left to right: planar isoparametric elements, $p = 1$ nefem elements, $p = 4$ isoparametric elements.

Figure 3: Results for a circular free-space cavity surrounded by a PEC boundary.

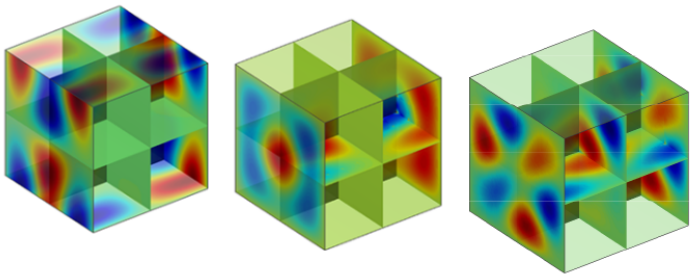

(a) Examples of mode shape obtained

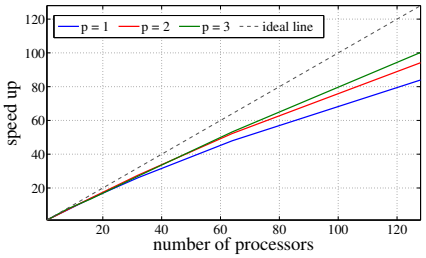

(b) Parallel speed up for a mesh of 12,288 planar hexahedral elements

Figure 4: Results for fully 3-dimensional cubic cavity with PEC boundaries

Parallel computation allows computation of resonant frequencies and mode shapes for challenging realistic 2- and 3-dimensional geometries with high accuracy, in a reasonable run time. Dramatic speed increases can be obtained for larger meshes, notable with higher-order elements, as illustrated by an almost linear speed up shown in Figure 4b.

5. Conclusions

A method has been presented for obtaining electromagnetic resonance properties of cavities using a parallelised discontinuous Galerkin time domain solver. We validated the method by showing h-convergence of the error in resonant frequencies. The method has been validated and optimal convergance rates in the resonant frequency error has been achieved. The effect of geometrical representation and high-order elements on resonant frequencies have been quantified and the advantages of parallelisation quantified.

Acknowledgements

The authors gratefully acknowledge the financial support provided by the Sêr Cymru National Research Network in Advanced Engineering and Materials.

References

[1] K. Busch, M. König, and J. Niegemann. Discontinuous Galerkin methods in nanophotonics. *Laser & Photonics Reviews*, 5(6):773–809, 2011.

[2] A. Taflove. *Computational Electrodynamics: The Finite-difference Time-domain Method*. Antennas and Propagation Library. Artech House, 1995.

[3] R. Sevilla, O. Hassan, and K. Morgan. The use of hybrid meshes to improve the efficiency of a discontinuous Galerkin method for the solution of Maxwells' equations. *Computers & Structures*, 137:2–13, 2014.

[4] J. Hesthaven and T. Warburton. *Nodal discontinuous Galerkin methods: algorithms, analysis, and applications*, volume 54. Springer Science & Business Media, 2007.

[5] R. Sevilla, S. Fernández-Méndez, and A. Huerta. Nurbs-enhanced finite element method (nefem). *International Journal for Numerical Methods in Engineering*, 76(1):56–83, 2008.

Proceedings of the 24th UK Conference of the
Association for Computational Mechanics in Engineering
31 March - 01 April 2016, Cardiff University, Cardiff

Novel Finite Elements for initial value problems of light waves in the time domain

***M. Drolia[1], M.S.Mohamed[1], O. Laghrouche[1], M. Seaid[2], and J. Trevelyan[2]**

[1]Institue for Infrastructure and Environment, Heriot Watt University, Edinburgh EH14 4AS
[2]School of Engineering and Computing Sciences, Durham University, Durham DH1 3LE

*md272@hw.ac.uk

ABSTRACT

This paper proposes a novel scheme for the solution of Maxwell equations in the time domain. A discretization scheme in time is developed to render implicit solution of system of equations possible. The scheme allows for calculation of the field values at different time slices in an iterative fashion. This facilitates us to tackle problems whose solutions have harmonic or even more general dependency on time.
The spatial grid is partitioned into finite number of elements with intrinsic shape functions to form the bases of solution. Furthermore, the finite elements are enriched with plane wave functions. This significantly reduces the number of nodes required to discretize the geometry, without compromising on the accuracy or allowed tolerance in the errors, as compared to that of classical FEM. Also, this considerably reduces the computational costs, viz. memory and processing time. Parametric studies, presented herewith, confirm the robustness and efficiency of the proposed method.
The numerical scheme can thus be further developed for solution of problems where analytical solutions cannot be developed, or even when the solution cannot be categorized as time-harmonic in nature.

Key Words: *Finite Element ; Partition of Unity ; Time domain ; Wave Equations*

1. Transverse Electric Mode of propagation

Let Ω be a unit square defined on a 2D Euclidean space, with its four edges as the boundary Γ. The boundary value problem be defined as follows

$$\frac{\partial^2 E}{\partial t^2} - c^2\nabla^2 E = f(t,x,y); \qquad \text{on } \Omega \tag{1a}$$

$$\frac{\partial E}{\partial \hat{\mathbf{v}}} + hE = g(t,x,y); \qquad \text{on } \Gamma \tag{1b}$$

$$E^0 = U_0 \tag{1c}$$

$$\frac{\partial E^0}{\partial t} = V_0 \tag{1d}$$

where E is the magnitude of the transverse electric field in the direction $\hat{\mathbf{z}}$ perpendicular to the Euclidean plane. The above equation can be approximated using finite element and finite difference schemes for numerical solution. Let's discretize the time derivative in the following way (in order to facilitate the development of time-dependent formulations [1] as seen in analyses for transient response [2] or diffusion problems [3])

$$\frac{\partial^2 E^n}{\partial t^2} = \frac{E^n - 2E^{n-1} + E^{n-2}}{\Delta t^2} \tag{2}$$

Where the superscript n stands for the value of the field at the time instance $t = n\Delta t$. Substituting in (1a) gives

$$\begin{aligned} \nabla^2 E^n &= \frac{E^n - 2E^{n-1} + E^{n-2}}{c^2\Delta t^2} - \frac{1}{c^2} f(t,x,y) \\ \Rightarrow E^n - (c^2\Delta t^2)\nabla^2 E^n &= 2E^{n-1} - E^{n-2} + (\Delta t^2) f(t,x,y) \end{aligned} \tag{3}$$

The equation (3) can be used to obtain a weak form which can be further solved over a finite number of elements in space as a linear system of equations. Let u be a test function multiplied to (3)

$$u(E^n - (c^2\Delta t^2)\nabla^2 E^n) = u\left(2E^{n-1} - E^{n-2} + (\Delta t^2) f(t, x, y)\right) \tag{4}$$

Integrating the left and right hand sides, over the domain Ω with boundary Γ, and applying the divergence theorem we get

$$\int_\Omega uE^n d\Omega + (c^2\Delta t^2)\left\{\int_\Omega \nabla u \cdot \nabla E^n d\Omega - \int_\Gamma u\, \hat{\mathbf{v}} \cdot \nabla E^n d\Gamma\right\} = \int_\Omega u\left(2E^{n-1} - E^{n-2} + (\Delta t^2) f(t, x, y)\right) d\Omega \tag{5}$$

Where $\hat{\mathbf{v}}$ is the normal unit vector to Γ. From (1b) and (5) we get the solvable weak form

$$\int_\Omega uE^n d\Omega \; + \; (c^2\Delta t^2)\int_\Omega \nabla u \cdot \nabla E^n d\Omega + (c^2\Delta t^2)\int_\Gamma u\; (hE^n) d\Gamma = \int_\Omega u\left(2E^{n-1} - E^{n-2} + (\Delta t^2) f(t, x, y)\right) d\Omega + (c^2\Delta t^2)\int_\Gamma u\; g(t_n, x, y)) d\Gamma \tag{6}$$

This equation (6) can be used to solve for E^n for the given set of boundary and initial conditions. The equation can then be iterated over n to obtain subsequent values of the fields for consecutive time steps.

This paper validates the proposed method against a transient wave problem on a 2D plane, where the solution is such that the magnitude of Electric field E is defined as $E = Ae^{\mathrm{i}wf_L^p}$ where $p = t - \frac{rk}{\omega}$. Here k is the wave number, ω angular frequency, r length of the position vector, e the natural exponent and i the imaginary number. Then the above constant c becomes the phase velocity defined such as $c = \frac{\omega}{k}$ while the function $g(t, x, y)$ is defined on each domain edge according to the relevant normal direction. The propagator function f_L^p (defined in the appendix) provides a means to control the initial condition of the problem, and can be used to manipulate the envelope of the moving wave, such that the solution is a wave expanding symmetrically about the origin as it evolves in time.
The problem is initialized with the solution E^0 (i.e. at $t = 0$), and for the boundaries we use appropriate derivatives.
To solve the weak form (6) using the finite element method we mesh the domain into a set of elements where the field E over each element is approximated in terms of a set of nodal values E_i and nodal shape functions N_i such as

$$E = \sum_{i=1}^{n} E_i N_i \tag{7}$$

Using the partition of unity [4] property one may further express the nodal values of the potential E_i as a combination of Q plane waves [5] such that

$$E = \sum_{i=1}^{n} N_i \left(B + \sum_{q=1}^{Q} A_i^q e^{\mathrm{i}(kx\cos\alpha_q + ky\sin\alpha_q)}\right) \tag{8}$$

where α_q is the angle of the qth plane wave. This ensures that we have the B term to capture variations which vary slowly (or don't vary at all, for example constants), and the plane wave enrichments that could form the basis for wave type solutions in the computational domain. Now by solving the linear system resulting from the above discrete representation we get the amplitudes A_i^q of the plane waves which is the qth plane wave contribution at the node i.

2. Analyses

A comparison of relative errors is conducted to study the behaviour of accuracy in solution obtained from the suggested PUFEM and classical FEM (figure 1). We test the accuracy of our method with the L_1 norm, computed as the relative error percentage given by $L_1 = \frac{\mathrm{abs}(\tilde{E} - E)}{\mathrm{abs}(E)} \times 100$, where $\tilde{E}, E$ are numerical and analytical solutions of the problem at hand.

The problems parameters are wave number $k = 8\pi$, angular frequency $\omega = 1$, and amplitude $A = 1$. The computational domain is a 2D unit square, with its bottom-left vertex shifted from the origin by a distance of $c \times 100\Delta t$ in each direction. This facilitates the wave, originating at the origin, to enter the computational domain by a 100 iterations in time, for the given step-size Δt. Note, the parameters assumed here are strictly numerical.

Table 1: : Parameters for PUFEM vs. FEM

Type	Δt	λ	DOF	Q	τ
PUFEM	10^{-2}	1/4	300	12	4.3
FEM	10^{-2}	1/4	3600	n/a	15

Table 1 shows the values of parameters studied. τ is the total number of degrees of freedom per wavelength, computed as $\tau = \lambda m\sqrt{Q}$ for PUFEM, and for FEM was calculated as $\tau = \lambda m$, where m is the number of nodes per direction on the computational grid. The total number of degrees of freedom (DOF) for PUFEM was computed as $m^2 Q$ and for FEM it's simply m^2.
Figure 1 below shows the plots of errors obtained from the analyses. The FEM stands at 50% error at the end of 5000 time steps (for a total time of 50 with $\Delta t = 10^{-2}$), as compared to the proposed PUFEM which showed less than 10% error with about one fourth the τ used in case of FEM.

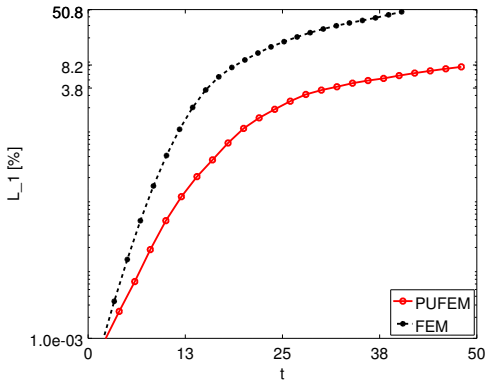

Figure 1: Semilog plot of L_1 norms in percentage to compare results from PUFEM and FEM for $k = 8\pi$. The wave covers the whole of computational domain by time $t \approx 36$.

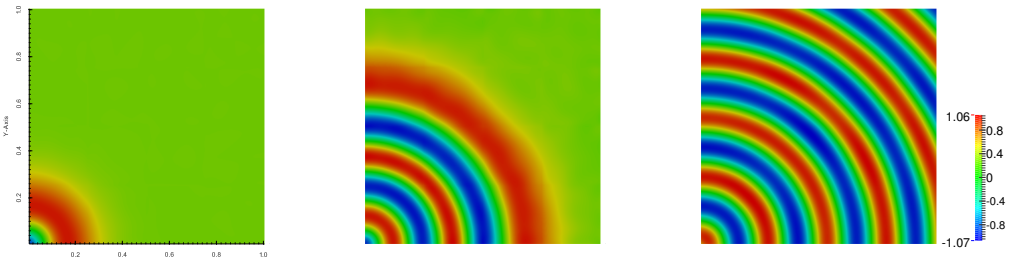

(a) $t = 14$ (b) $t = 27$ (c) $t = 50$

Figure 2: 2D Plots of the recovered wave ($k = 8\pi$), obtained using the proposed PUFEM. The computational domain was meshed into 4×4 elements. The number of plane wave enrichments used $Q(\tau) = 12(4.3)$, and $\Delta t = 10^{-3}$. The final L_1 norm percentage at the end of the simulation was 3.6%

Even though we know that, in theory, a smaller Δt would lead to better results, however, it becomes

increasingly impractical to use smaller Δt with FEM owing to the sheer computational costs to solve bigger systems. To provide an idea (and by no means a rigourous comparison), the FEM results presented here took multiple weeks to compute, compared to their PUFEM counter parts which finished all the computations over a few hours.
Figure 2 shows 2D plots for numerical solution obtained with PUFEM when we used the same $\tau = 4.3$ but with a smaller $\Delta t = 10^{-3}$, and the final error was about 4%.

3. Conclusions

An enriched Finite Element Method, utilising the property of partition of unity to enrich the nodal values in the classical FEM, is formulated for solution of Maxwell equations in the time domain. The proposed PUFEM is validated against a progressive wave problem as demonstrated in section 2, wherein the method is tested against analytical solution for the proposed problem, with the L_1 norm. A comparison of the suggested method with classical FEM is carried, and it is observed that the former outperforms the latter on the grounds of lesser computational cost (including the total simulation time) and accuracy.

References

[1] M. S. Mohamed, M. Seaid, J. Trevelyan, and O. Laghrouche, "An enriched finite element model with q-refinement for radiative boundary layers in glass cooling," *Journal of Computational Physics*, vol. 258, no. 0, pp. 718 – 737, 2014.

[2] M. S. Mohamed, M. Seaid, J. Trevelyan, and O. Laghrouche, "Time-independent hybrid enrichment for finite element solution of transient conductionâĂŞradiation in diffusive grey media," *Journal of Computational Physics*, vol. 251, no. 0, pp. 81 – 101, 2013.

[3] M. Shadi Mohamed, M. Seaid, J. Trevelyan, and O. Laghrouche, "A partition of unity fem for time-dependent diffusion problems using multiple enrichment functions," *International Journal for Numerical Methods in Engineering*, vol. 93, no. 3, pp. 245–265, 2013.

[4] J. Melenk and I. BabuÅąka, "The partition of unity finite element method: Basic theory and applications," *Computer Methods in Applied Mechanics and Engineering*, vol. 139, no. 1âĂŞ4, pp. 289 – 314, 1996.

[5] O. Laghrouche, P. Bettess, and R. J. Astley, "Modelling of short wave diffraction problems using approximating systems of plane waves," *International Journal for Numerical Methods in Engineering*, vol. 54, no. 10, pp. 1501–1533, 2002.

Appendix A. Definition for the propagator function

The function definition for f_L for parameters a and b is given as

$$f_L(x) = \frac{1}{1+a}\left\{\text{erf}\left(\frac{x}{b}\right)x + ax + \frac{b}{\sqrt{\pi}}e^{-\frac{x^2}{b^2}}\right\} \tag{A.1}$$

The parameters a and b can be set to control the smoothness of the slope of the function near the origin. The derivative of this function is given by

$$\frac{d}{dx}\{f_L(x)\} = \frac{\text{erf}\left(\frac{x}{b}\right) + a}{1+a} \tag{A.2}$$

That is, the derivative of the function is a shifted and normalised error funciton. The following notation is used for the function

$$f_L(p) = \frac{1}{1+a}\left\{\text{erf}\left(\frac{p}{b}\right)p + ap + \frac{b}{\sqrt{\pi}}e^{-\frac{p^2}{b^2}}\right\} = f_L^p \tag{A.3}$$

Proceedings of the 24th UK Conference of the
Association for Computational Mechanics in Engineering
31 March - 01 April 2016, Cardiff University, Cardiff

A Model Reduction Method for Boundary Element Method

***Shengze Li[1], Jon Trevelyan[2] and Weihua Zhang[1]**

[1]College of Aerospace Science and Engineering, National University of Defense Technology, 109 Deya Road, Changsha 410073, China
[2]School of Engineering and Computing Sciences, Durham University, South Road, Durham DH1 3LE

*lishengze12@gmail.com

ABSTRACT

The aim of this work is to provide a promising way to improve the computational efficiency for BEM. This study introduces an 'a priori' model reduction method in BEM analysis aiming to enhance efficiency by approximating the problem solution using the most appropriate set of basis functions, which depend on Karhunen-Loève decomposition. The calculation process will proceed making use of a precomputed basis function space if the norm of the residual is small enough; if not, it need to enrich the approximation basis and compute again some of the previous steps. Finally, an example is proposed which demonstrates fast resolution of BEM problem and illustrates the potential of this numerical technique. This work is preliminary work in a larger programme leading to optimisation using isogeometric BEM scheme accelerated with the Proper Orthogonal Decomposition.

Key Words: *BEM; model reduction; Karhunen-Loève decomposition*

1. Introduction

The Boundary Element Method (BEM) [1] is a domain discretization technique for solving partial differential equations; one major advantage of boundary integral equation approaches is to decrease the dimension by one, *i.e.*, only line integrals are required in 2D and surface integrals in 3D problems, from which a smaller system of equations will be generated. Hence, this alleviates the burden of mesh generation as a surface mesh generation is much easier, more rapid and (importantly) more robust than domain mesh. In spite of teh advances in FE mesh generation, these advantages of BEM remain considerable when the objective is to analyse many, similar geometries, such as in optimisation schemes, involving multiple remeshing operations. The drawbacks of BEM include the fully populated matrix structure; it also dos not lend itself as well as FEM to materially non-linear problems. In order to accelerate the solution (specifically, the re-solution) of the dense linear system, model reduction techniques present a promising strategy.

Model reduction techniques have been derived from some problems in random data processing, and further used in image processing. They have been successfully applied in some finite element frameworks [2, 3], the nonlinear mechanical problem [4, 5] and 2D BEM in fluid mechanics [6]. In the current work we assess their suitability for the BEM analysis process in 3D elasticity, updating solutions following geometric changes that might occur during an optimisation process. In the future this will be extended into an isogeometric BEM context.

1.1. Boundary Element Discretization

For a linear elastic problem, the structure occupies a continuous domain Ω, having boundary Γ, with the boundary conditions,

$$\begin{aligned} u &= \overline{u} \quad \text{on } \Gamma_u \\ t &= \overline{t} \quad \text{on } \Gamma_t \end{aligned} \tag{1}$$

where the domain boundary $\Gamma = \Gamma_u + \Gamma_t$.

The Boundary Integral Equation (BIE) can be written as follows,

$$u_i(s) + \int_\Gamma T_{ij}(s,x)u_j(x)d\Gamma(x) = \int_\Gamma U_{ij}(s,x)t_j(x)d\Gamma(x) \tag{2}$$

where s is the 'source' point and x the 'field' point. By using standard methods of discretisation of (2) and taking s as all nodes in turn, we arrive at the matrix form

$$\underline{\underline{H}}\,\underline{u} = \underline{\underline{G}}\,\underline{t} \tag{3}$$

where $\underline{u}$ contains the nodal displacements and $\underline{t}$ the nodal tractions. Both $\underline{u}$ and $\underline{t}$ include a combination of unknown values and prescribed boundary conditions. Rearrangement of (3) leads to the final form

$$\underline{\underline{A}}\,\underline{x} = \underline{F} \tag{4}$$

where the size of $\underline{\underline{A}}$ is $N \times N$.

1.2. The Karhunen-Loève Decomposition (KLD)

Also known as Proper Orthogonal Decomposition (POD), the KLD is a powerful and elegant method for data analysis aimed at obtaining low-dimensional descriptions of a high-dimensional process.

For an arbitrary evolution process, a certain field could be defined by a discrete form as $u^p(\underline{x}_i)$, $\forall p \in [1,\ldots,P]$, $\forall i \in [1,\ldots,N]$, describing the nodal displacement $(\underline{x}_i)$ at the calculation step p. The main idea of the KLD is to obtain a low dimensional space containing the most typical or characteristic behaviour among the displacement fields. This is equivalent to obtaining a function $\phi(\underline{x})$ maximizing α defined by

$$\alpha = \frac{\sum_{p=1}^{P}\left[\sum_{i=1}^{N}\phi(\underline{x}_i)u^p(\underline{x}_i)\right]^2}{\sum_{i=1}^{N}(\phi(\underline{x}_i))^2} \tag{5}$$

Introducing a vector notation, Eq.(5) takes the following matrix form

$$\underline{\underline{k}}\,\underline{\phi} = \alpha\underline{\phi} \tag{6}$$

The two point correlation matrix $\underline{\underline{k}}$ is given by

$$\underline{\underline{k}} = \sum_{p=1}^{P}\underline{u}^p(\underline{u}^p)^{\mathrm{T}} \tag{7}$$

which is symmetric and positive definite.

Here, the functions defining the characteristic structure of $u^p(\underline{x})$ are the eigenfunctions $\phi_k(\underline{x}) \equiv \underline{\phi}_k$ associated with the highest eigenvalues.

2. Reduced Model Construction

If some direct simulations have been carried out previously, the nodal displacement can be defined as $u(\underline{x}_i, s_p) \equiv u_i^p$, $\forall i \in [1,\ldots,N]$, $\forall p \in [1,\ldots,P]$. The eigenvalues are assumed ordered, if $\alpha_k > 10^{-10}\alpha_1$, $\forall k \in [1,\ldots,n]$, ($\alpha_1$ is the highest eigenvalue). Then, those n eigenvectors related to the eigenvalues above could be used for generating an approximating basis for further solutions. The matrix $\underline{\underline{B}}$ is defined as

$$\underline{\underline{B}} = \begin{bmatrix} \phi_1^1 & \phi_1^2 & \cdots & \phi_1^n \\ \phi_2^1 & \phi_2^2 & \cdots & \phi_2^n \\ \vdots & \vdots & \ddots & \vdots \\ \phi_N^1 & \phi_N^2 & \cdots & \phi_N^n \end{bmatrix} \tag{8}$$

where N is the DOF of the system and we take eigenvectors 1,...,n. The nodal displacement vector in Eq.(4) could be written as

$$\underline{x} = \sum_{i=1}^{n} \zeta_i \underline{\phi}_i = \underline{\underline{B}}\underline{\zeta} \tag{9}$$

which could be substituted to Eq.(4) to obtain

$$\underline{\underline{A}}\underline{\underline{B}}\underline{\zeta} = F \tag{10}$$

and we finally premultiply both sides by $\underline{\underline{B}}^{\mathrm{T}}$,

$$\underline{\underline{B}}^{\mathrm{T}}\underline{\underline{A}}\underline{\underline{B}}\underline{\zeta} = \underline{\underline{B}}^{\mathrm{T}}F \tag{11}$$

This procedure provides a final $n \times n$ matrix in a low dimension. While the generation of matrix $\underline{\underline{A}}$ is still time consuming, it can be accelerated by er-use of matrix coefficients that are unchanged from a previous design iteration. This process is likely to be made more powerful and general when the authors implement their future plans of bringing POD to an isogeometric BEM context.

3. An 'a priori' Model Reduction Strategy

As the geometry evolves during the design/optimisation process, the basis matrix B should be updated. The basis matrix $\underline{\underline{B}}$ is generated by the first P steps, and another S steps will be analysed with this basis. After each S steps, the residual of the system should be evaluated as

$$\underline{R} = \underline{\underline{A}}\underline{x} - \underline{F} = \underline{\underline{A}}\underline{\underline{B}}\underline{\zeta} - \underline{F} \tag{12}$$

If the norm of residual is sufficiently small, $\| \underline{R} \| < \epsilon$, with ϵ a threshold value, the next S steps will be continued; otherwise, the approximation basis should be enriched and the last S steps recomputed to ensure accuracy is maintained. The enrichment is built using the Krylov subspace, the new basis matrix being defined as

$$\underline{\underline{B}}^{*} = \{\underline{\underline{B}}\underline{\underline{V}}, \underline{R}, \underline{\underline{A}}\underline{R}, \underline{\underline{A}}^{2}\underline{R}\} \tag{13}$$

where $\underline{\underline{V}}$ is the combination of the most representative eigenvectors which is from the previous reduced result $\underline{\zeta}$. A new solution vector could be written as

$$\underline{\zeta}^{*} = \left[\underline{\underline{B}}^{*\mathrm{T}}\underline{\underline{B}}^{*}\right]^{-1} \underline{\underline{B}}^{*\mathrm{T}}\underline{\underline{B}}\underline{\zeta} \tag{14}$$

4. Numerical Example

In this preliminary study, the problem is defined as a simple cube (Fig. 1) which is under a uniaxial compressive pressure of 1MPa in the z-direction. The left, back and bottom surfaces have normal displacement constraints. The material properties of steel are used. As a design evolution process, the height h will be continuously increased in 0.02m increments. This problem is solved first $P = 25$ steps for generating the approximation matrix using the conventional BEM approach. The approximation is performed using 54 elements, giving 168 degrees of freedom. The eigenvalues and eigenvectors are derived from those pre-calculated displacements, and only 4 eigenvalues satisfy the selection criterion ($\alpha_k > 10^{-10}\alpha_1$). This means a 168×168 matrix will be reduced to a 4×4 matrix for solving the remaining design iterations. The next calculation step will be divided to $S = 35$ parts, for each part, including $S_{sub} = 5$ sub-calculation steps. In this case, the solution is performed starting from the reduced basis which is obtained previously and after each 5 steps, the quality of the solution is checked and follows the previous criterion for judging whether the basis should be enriched.

Fig. 2 compares the displacement result of the top surface in the z-direction; as the figure shows, the reduction model provides an accurate result with a lower dimensional computation, and the error is within 0.14%.

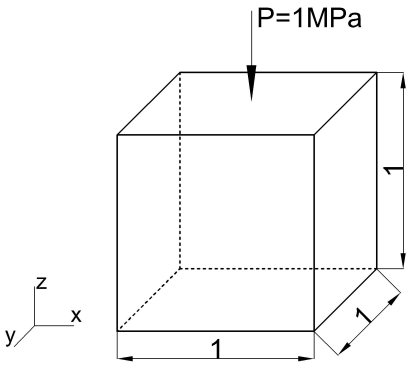

Figure 1: The cube under uniaxial compression

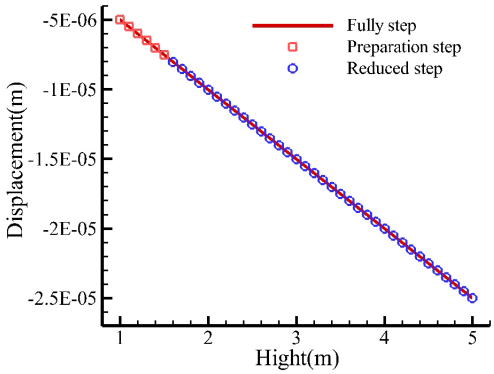

Figure 2: Displacement solutions

5. Conclusions

In this article, the Karhunen-Loève decomposition model reduction approach is combined with the Boundary Element Method for 3D elasticity. The size of linear system is dramatically decreased while mainitaining appropriate accuracy. The numerical example proves the potential of this method. Further work will demonstrate the extension of this method to isogeometric BEM, and linking with the optimisation process for more complicated structural components.

References

[1] T. A. Cruse. Numerical solutions in three dimensional elastostatics. International Journal of Solids and Structures, 5, 1259–1274, 1969.

[2] D. Ryckelynck. A priori hyperreduction method: an adaptive approach. Journal of Computational Physics, 202, 346-366, 2005.

[3] D. Ryckelynck, F. Chinesta, E. Cueto, A. Ammar. On the a priori model reduction: overview and recent developments. Archives of Computational Methods in Engineering, 13, 91-128, 2006.

[4] K. Carlberg, C. Bou-Mosleh, C. Farhat. Efficient non-linear model reduction via a least-squares Petrov-Galerkin projection and compressive tensor approximations. International Journal for Numerical Methods in Engineering, 86, 155-181, 2011.

[5] P. Kerfriden, P. Gosselet, S. Adhikari, S. Bordas. Bridging proper orthogonal decomposition methods and augmented Newton-Krylov algorithms: An adaptive model order reduction for highly nonlinear mechanical problems. Computer Methods in Applied Mechanics and Engineering, 200, 850-866, 2011.

[6] D. Ryckelynck, L. Hermanns, F. Chinesta, E. Alarcon. An efficient 'a priori' model reduction for boundary element models. Engineering Analysis with Boundary Elements, 29, 796-801, 2005.

Proceedings of the 24th UK Conference of the
Association for Computational Mechanics in Engineering
31 March - 01 April 2016, Cardiff University, Cardiff

An Isogeometric Boundary Element Method with Subdivision Surfaces for Helmholtz Analysis

***Z. Liu[1], R. Simpson[1] and F. Cirak[2]**

[1]School of Engineering,University of Glasgow, Glasgow G12 8QQ, United Kingdom
[2]Department of Engineering,University of Cambridge, Cambridge CB2 1PZ, United Kingdom

*z.liu.2@research.gla.ac.uk

ABSTRACT

The present work develops a new isogeometric Boundary Element Method with subdivision surfaces for solving Helmholtz problems. The work gives a brief overview of subdivision surfaces and their use in an analysis context highlighting the pertinent points for boundary element analysis. We find that by adopting the high order (quartic) basis functions of subdivision surfaces to perform Helmholtz analysis a higher accuracy per degree of freedom is obtained over equivalent Lagrangian discretisations. We demonstrate this through a Helmholtz problem with a closed-form solution in which a plane wave is impinged on a 'hard' sphere.
Key Words: *Isogeometric analysis; boundary element method; Helmholtz; subdivision surfaces*

1. Introduction

Isogeometric analysis (IGA) has rapidly expanded in recent years into a major research effort to link Computer Aided Design (CAD) and numerical methods driven by the need for more effcient industrial design tools. The central idea of IGA is that the same discretisation model is used for both design and analysis which eliminates costly model conversion processes encountered in traditional engineering design work flows. IGA was originally conceived by Hughes et al. [1] and has predominately focussed on the use of the Finite Element Method, but work has also applied the approach to the Boundary Element Method (BEM) where distinct advantages are found, stemming from the need for only a surface mesh. In the majority of IGA implementations the most commonly used CAD discretisation is the Non-Uniform Rational B-Spline (NURBS) due to its ubiquitous nature in CAD software. However, NURBS technology has limitations due to its tensor-product nature and a number of researchers have developed alternative CAD discretisations which overcome this limitation. One such example is T-spline technology which has been employed in an IGA setting by Bazilevs et al. [2] in 2010. Subdivision surfaces provide another alternative for overcoming the limitations of NURBS, initially introduced by Cirak [3] in 2000. The present work have developed an isogeometric Boundary Element Method with subdivision surfaces for solving acoustic problems.

2. Boundary Element Method for Helmholtz Problems

For time-harmonic acoustic problems, the governing equation is the Helmholtz equation which is expressed as

$$\nabla^2\phi(\mathbf{x}) + k^2\phi(\mathbf{x}) = 0 \tag{1}$$

where $\phi(\mathbf{x})$ is the acoustic pressure and k is the wavenumber defined as $k = \frac{\omega}{c}$ where ω is the angular frequency and c is the thermodynamic speed of sound. Several numerical methods can be used to solve Eq. (1) but many suffer from problems including dispersion error and difficulties in handling infinite domains (e.g. the finite element method). In contrast, the Boundary Element Method does not suffer from dispersion error and naturally handles infinite domains. A core feature of the BEM is the use of

fundamental solutions to arrive at a numerical solution, and in the case of 3D acoustic problems the fundamental solution is given by:

$$G(\mathbf{x}, \mathbf{y}) = \frac{e^{ikr}}{4\pi r} \tag{2}$$

where $\mathbf{x}$ is the source point, $\mathbf{y}$ is the field point and $r = |\mathbf{x} - \mathbf{y}|$. The corresponding normal derivative of this kernel can be expressed as:

$$\frac{\partial G(\mathbf{x}, \mathbf{y})}{\partial n} = \frac{e^{ikr}}{4\pi r^2}(ikr - 1)\frac{\partial r}{\partial n}. \tag{3}$$

The use of Eq. (2) and (3) allows a boundary integral equation to be formulated that relates acoustic pressure and its normal derivative as:

$$c(\mathbf{x})\phi(\mathbf{x}) + \int_s \frac{\partial G(\mathbf{x}, \mathbf{y})}{\partial n}\phi(\mathbf{y})\, \mathrm{d}S(\mathbf{y}) = \int_s G(\mathbf{x}, \mathbf{y})\frac{\partial \phi(\mathbf{y})}{\partial n}\, \mathrm{d}S(\mathbf{y}) + \phi_{inc}(\mathbf{x}) \tag{4}$$

where S represents the boundary surface, ϕ_{inc} denotes the acoustic pressure of a prescribed incident wave (only applicable in the case of scattering problems) and $c(\mathbf{x})$ is a coefficient that depends on the geometry of the surface at the source point. In the case of smooth boundaries, its value is given by $c(\mathbf{x}) = \frac{1}{2}$.

For computer implementation purposes, the acoustic pressure and normal derivative are discretised through an appropriate set of basis functions as:

$$\phi(\mathbf{x}) = \sum_{A=1}^{n} \phi_A N_A(\mathbf{x}) \qquad \frac{\partial \phi(\mathbf{x})}{\partial n} = \sum_{A=1}^{n} q_A N_A(\mathbf{x}) \tag{5}$$

where in the present study $\{N_A(\mathbf{x})\}_{A=1}^{n}$ is a global set of subdivision basis functions, $\{\phi_A(\mathbf{x})\}_{A=1}^{n}$ is a set of nodal acoustic pressure coefficients and $\{q_A(\mathbf{x})\}_{A=1}^{n}$ is a set of nodal acoustic velocity coefficients.

3. Subdivision Surfaces

There exist a variety of subdivision schemes, but all are based on the idea of generating a smooth surface from a coarse polygon mesh. Subdivision refinement schemes construct a smooth surface through a limiting procedure of repeated refinement starting from an initial control mesh. Subdivision refinement schemes can be classed as either an interpolating or approximation scheme where Figure 3 illustrates the commonly used Catmull-Clark approximation scheme.

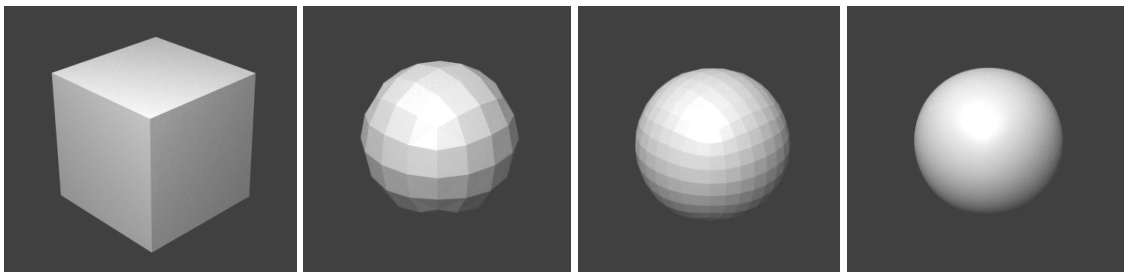

Figure 1: Successive levels of Catmull-Clark subdivision refinement applied to an initial cube control mesh.

Subdivision basis functions can be used as a basis for analysis [5] and have successfully been used in variety of applications including thin-shell finite element analysis [3]. We extend the work of [3] by adopting a Loop subdivision scheme and applying subdivision basis functions for acoustic boundary element analysis.

The Loop subdivision scheme is based on a triangular tessellation with a typical element and its one-ring neighbours shown in Figure 2 corresponding to a regular patch where each vertex has 6 connecting edges.

The shaded element in this patch contains 12 non-zero quartic basis functions as detailed in [5]. In the present study these basis functions are used to dicretise the acoustic pressure and acoustic velocity. In addition, we apply a collocation procedure whereby a set of global collocation points is generated through interpolation of the limit surface at vertex locations allowing a system of equations to be constructed.

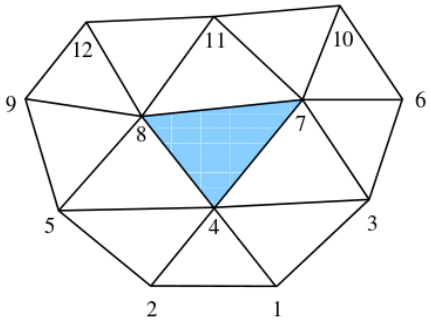

Figure 2: An element defined over a regular patch with 12 control points

4. Results

To validate the current subdivision BEM the approach was applied to the problem of a 'hard' sphere impinged by a plane-wave, as illustrated in Figure 3. In this problem a dimensionless wavenumber of $k/a = 8$ was chosen with the acoustic pressure sampled at a set of points surrounding the sphere.

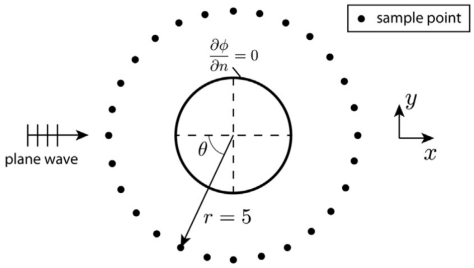

Figure 3: Problem of a plane wave impinged on a 'hard' sphere [4]

Two sets of boundary element analysis were performed for this problem: the first applied a conventional Lagrangian discretisation using quartic basis functions defined over triangular elements and the second applied quartic subdivision discretisations. In the study, a Lagrangian mesh with 1152 degrees of freedom (dof) and two subdivision meshes with 438 and 1746 dof were used.

The results for the three discretisations at each of the sampling points are shown in Figure 4 along with the analytical solution. A a closeup view of this plot illustrates that both subdivision discretisations deliver higher accuracies compared to the Lagrangian discretiation even with fewer degrees of freedom.

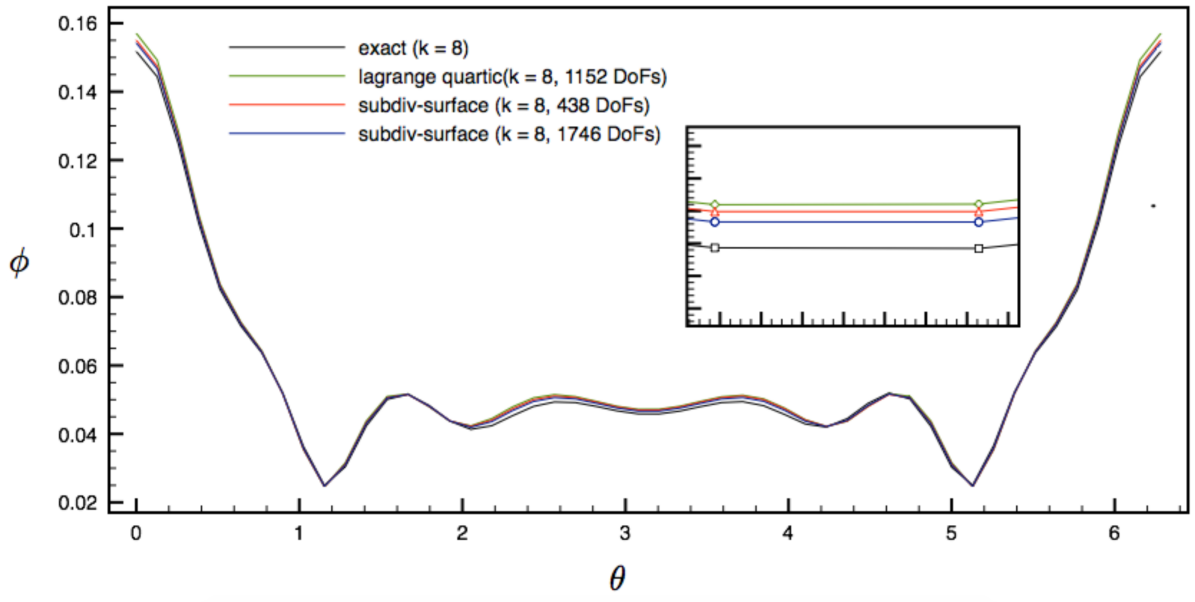

Figure 4: A comparison between Lagrangian discretisations and subdivision surfaces (k = 8)

5. Conclusions and Future Research

The present work develops a new isogeometric Boundary Element Method with subdivision surfaces for solving Helmholtz problems where it is found that higher accuracies are obtained over a Lagrangian discretisation of the same order. There are several future research directions for the present work:

- Coupling the Boundary Element Method and the Finite Element Method for structural-acoustic analysis
- Simulating electromagnetic scattering problems by developing suitable div- and curl-conforming discretisations

References

[1] T.J.R. Hughes, J.A. Cottrell, and Y. Bazilevs. Isogeometric analysis: CAD, finite elements, NURBS, exact geometry and mesh refinement. *Computer Methods in Applied Mechanics and Engineering*, 194(39):4135-4195, 2005.

[2] Y. Bazilevs, V.M. Calo, J.A. Cottrell, J.A. Evans, T.J.R. Hughes, S. Lipton, M.A. Scott, and T.W. Sederberg. Isogeometric analysis using T-splines. *Computer Methods in Applied Mechanics and Engineering*, 199(5-8):229-263, 2010.

[3] F. Cirak, M. Ortiz, and P. Schroder. Subdivision surfaces: a new paradigm for thin-shell finite-element analysis. *International Journal for Numerical Methods in Engineering*, 47(12):2039-2072, 2000.

[4] R.N. Simpson, M.A. Scott, M. Taus, D.C. Thomas, and H. Lian. Acoustic isogeometric boundary element analysis. *Computer Methods in Applied Mechanics and Engineering*, 269:265-290, 2014.

[5] J. Stam. Exact evaluation of Catmull-Clark subdivision surfaces at arbitrary parameter values. *Proceedings of the 25th annual conference on Computer graphics and interactive techniques*, 395–404, ACM, 1998.

Fluid mechanics and F/S interaction I

SIMULATION OF SELF-COMPACTING CONCRETE FLOW IN J-RING USING SMOOTHED PARTICLE HYDRODYNAMICS

***Mohammed S. Abo Dhaheer[1, 2], Bhushan L. Karihaloo[1] and Sivakumar Kulasegaram[1]**

[1]School of Engineering, Cardiff University, UK, CF24 3AA

*Abodhaheerms@cardiff.ac.uk

ABSTRACT

In this study, an incompressible mesh-less smoothed particle hydrodynamics (SPH) methodology has been implemented to simulate the flow of self-compacting concrete (SCC) mixes in the J-ring test. A suitable Bingham constitutive model has been coupled with the Lagrangian momentum and continuity equations to model the flow. The capabilities of the SPH methodology are validated by comparing the simulation results with the actual J-ring tests carried out in the laboratory. The comparison shows that this methodology is efficient to predict precisely the behaviour of SCC in the sense that the simulated mixes meet the passing ability criterion and the shapes and diameters of the flow spread are nearly the same as observed in the laboratory test.

Keywords: *Self-compacting concrete (SCC); Smoothed particle hydrodynamics (SPH); Non-Newtonian fluid; J-ring test; plastic viscosity.*

1. Introduction

With the recent tendency towards the use of computer modelling in concrete technology, its application in self-compacting concrete (SCC) is in demand and increasingly becoming an important issue. In this regard, one of the important approaches offering considerable potential is the smoothed particle hydrodynamics (SPH). It is able to simulate flows that contain particles of different sizes. SPH is a particle-based method (it does not require re-meshing) to represent with an acceptable level of accuracy the rheological behaviour of heterogeneous flow. This method has been examined and proved to be efficient and accurate in modelling the flow of SCC in the cone slump flow and L-box tests [1, 2]. The goal of this paper is to extend its application to simulating the flow of SCC in the J-ring test. This methodology will provide a thorough understanding of whether or not an SCC mix can satisfy the self-compatibility criteria. For this purpose, a series of SCC mixes differing in target plastic viscosity and compressive strength were prepared in the laboratory. These mixes were designed according to the rational mix design method proposed in [3].

2. Numerical modelling

Fresh SCC is a non–Newtonian fluid best described by a Bingham–type constitutive model. From a practical computational perspective, it is expedient to approximate the bi-linear Bingham constitutive model, which has a kink at zero shear strain rate, by a smooth continuous function in which *m* is a very large number (e.g. $m = 10^5$).

$$\tau = \eta\dot{\gamma} + \tau_y\left(1 - e^{-m\dot{\gamma}}\right) \tag{1}$$

Here, τ, η, $\dot{\gamma}$ and τ_y represent shear stress tensor, mix plastic viscosity, shear strain rate and mix yield stress, respectively. The Bingham constitutive model of the mix is coupled with the Lagrangian continuity equation (Eq.2) and momentum conservation equation (Eq.3) to model the flow of the SCC mix:

$$\frac{1}{\rho}\frac{D\rho}{Dt} + \nabla.\mathbf{v} = 0 \quad , \quad \frac{D\mathbf{v}}{Dt} = -\frac{1}{\rho}\nabla P + \frac{1}{\rho}\nabla.\boldsymbol{\tau} + \mathbf{g} \tag{2), (3}$$

[2] On leave from University of Al-Qadisiyah, Iraq

where ρ, t, **v**, P and g represent the fluid particle density, time, particle velocity, pressure and gravitational acceleration, respectively.

A projection method based on the predictor-corrector time stepping scheme has been adopted to track the Lagrangian non-Newtonian flow. The prediction step is an explicit integration of the momentum conservation equation (Eq.3) in time without enforcing incompressibility. Only the viscous stress and gravity terms are considered in Eq.3 and an intermediate particle velocity $\mathbf{v}^*_{n+1}$ is obtained as:

$$\mathbf{v}^*_{n+1} = \mathbf{v}_n + \left(\mathbf{g} + \frac{1}{\rho} \nabla . \boldsymbol{\tau} \right) \Delta t \tag{4}$$

Then the correction step is performed by considering the pressure term in Eq.3:

$$\frac{\mathbf{v}_{n+1} - \mathbf{v}^*_{n+1}}{\Delta t} = -\left(\frac{1}{\rho} \nabla P_{n+1} \right) \tag{5}$$

where $\mathbf{v}_{n+1}$ is the corrected particle velocity at the time step *n+1*. Computing Eq.5 requires the pressure P_{n+1}, which is obtained by enforcing the incompressibility condition from the continuity equation (Eq.2):

$$\nabla . \mathbf{v}_{n+1} = 0 \tag{6}$$

Hence the intermediate velocity can be projected on the divergence-free space by writing the divergence of Eq.5, using Eq.6, as:

$$\nabla . \left(\frac{1}{\rho} \nabla P_{n+1} \right) = \frac{\nabla . \mathbf{v}^*_{n+1}}{\Delta t} \tag{7}$$

As the density of particles remains constant in this simulations, Eq.7 can be rewritten as:

$$\nabla^2 P_{n+1} = \frac{\rho}{\Delta t} \nabla . \mathbf{v}^*_{n+1} \tag{8}$$

where ∇^2 is the Laplacian. Once the pressure is obtained from the Poisson equation (Eq.8), the particle velocity is updated by Eq.5. Finally, the instantaneous particle position is updated as:

$$\mathbf{x}_{n+1} = \mathbf{x}_n + \mathbf{v}_{n+1} \Delta t \tag{9}$$

3. Boundary conditions

Three types of boundary conditions need to be considered in the simulation of the J-ring test when solving the continuity and momentum conservation equations. These are: (1) a zero pressure condition on the free surface; (2) Dirichlet boundary condition at the wall of the cone, J-ring bars and the bottom plate, and (3) Neumann conditions on the pressure gradient (this zero pressure gradient is used only for solving the pressure Poisson equation), as shown in Figure 1A.

In this simulation, the technique based on arrays of rigid dummy particles was used to implement the cone wall, J-ring bars and base plate boundary conditions, as shown in Figure 1B. For realistic simulations, the friction between the SCC mix and the contacting surfaces should be taken into consideration. Here, the coefficient of kinematic friction (C_f) for the horizontal plate and J-ring bars is 0.55 and 0.48 N s/m, respectively. The former was determined previously by matching the t_{500} (the time when the mix spread reaches 500 mm) in slump cone test with the simulated results [2]. The latter was chosen by matching the t_{500J} in the J-ring test with the simulated results of Mix50 in the present study.

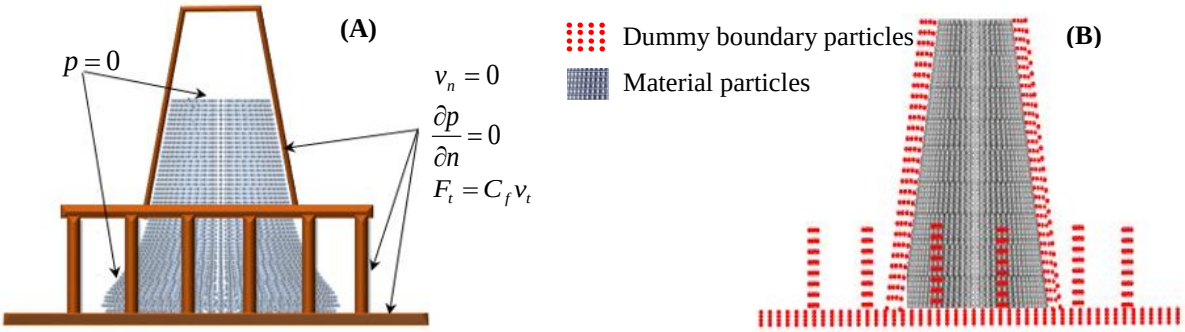

Figure 1: (A) boundary conditions, (B) Dummy particles for enforcing boundary conditions

4. Treatment of particles in the simulated mixes

In order to monitor the velocity vectors and positions of coarse aggregates of different representative sizes, as well as those of the fluid particles representing the mortar, the particles were represented by recognisable colours as shown in Figure 2. The volume of the mix in the cone was simulated by 23,581 particles. These particles were generated randomly in this simulation. Particles representing the mortar as well as the coarse aggregate form a homogeneous mass and possess the same continuum properties except for their assigned volumes. The masses of the SPH particles representing different coarse aggregate particles in the mix were calculated according to their respective volume fractions in the mix. Throughout the simulation, particles representing the coarse aggregates based on their assigned volumes were tagged (Figure 2) in order to monitor their velocity vectors and positions.

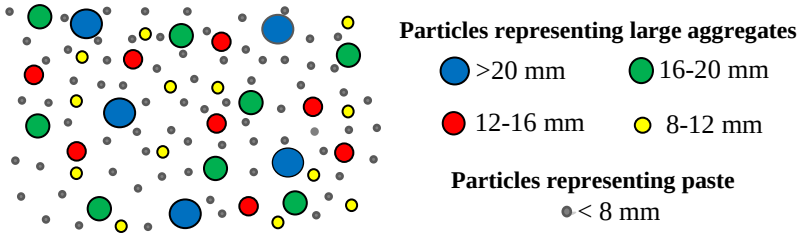

Figure 2: Schematic sketch of particle representation in the simulated mixes

5. Simulation results

To investigate how efficient the SPH is to predict the flow of SCC mixes through reinforcing bars, different SCC mixes were three-dimensionally simulated using the J-ring test. The fundamental parameters (plastic viscosity and yield stress) of these mixes have been determined to be used in the present simulation. The plastic viscosity was estimated by a micromechanical procedure from the known plastic viscosity of the paste and the SCC mix proportions [4] while the yield stress was predicted in an inverse manner using the SPH simulation of slump flow test [1].

The results of a typical SCC mix (Mix50) regarding its shape and spread as well as its blockage assessment are shown in Figures 3 and 4. From Figure 3A it can be noticed that the shape of the simulated spread looks smooth as a ‘pan cake’ identical to that in the laboratory test (Figure 3B). It can also be seen that the diameters of the flow spread of the simulated mix are nearly the same as that observed in the laboratory test.

With the reference to the passing ability criterion, SCC should have the ability to flow and pass through congested reinforcement and narrow openings while maintaining adequate suspension and distribution of coarse particles in the matrix. This means that arching near obstacles and blockage during flow have to be avoided. In this simulation, the SCC passing ability can be judged in terms of the height difference between the concrete inside and outside the steel bars of the J-ring using the following equation.

$$P_J = \frac{\Delta h_{x1} + \Delta h_{x2} + \Delta h_{y1} + \Delta h_{y2}}{4} - \Delta h_0 \qquad (10)$$

Here, P_J is the blocking step, Δh_0 is the height measurement at the centre of flow and Δhx_1, Δhx_2, Δhy_1, Δhy_2 are the four measurement heights at positions just outside the J-ring. Taking the acceptance criterion of SCC passing ability as the blocking step (P_J) is no more than 10 mm [5], the simulated mix did flow homogeneously without blockage, as it is clearly observed in Figure 4.

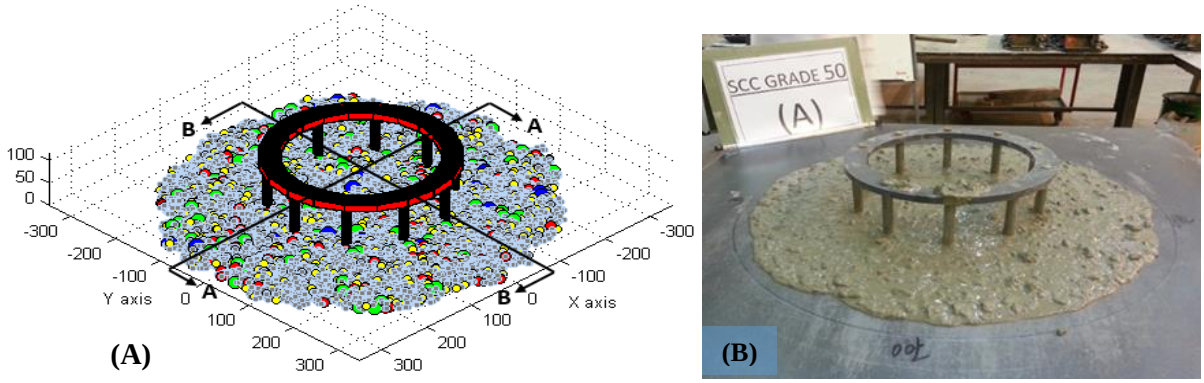

Figure 3: Flow pattern of SCC (Mix50) after final spread: (A) simulated mix, (B experimental mix

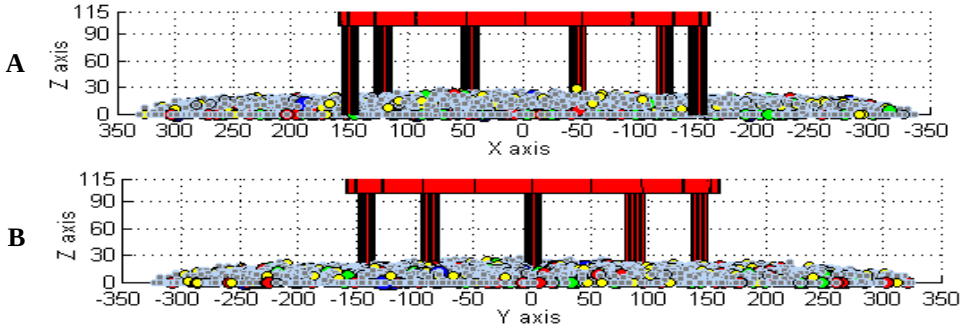

Figure 4: Diametrical cross-sections (A and B) of the simulated mix

6. Conclusions

This study reveals that the developed numerical methodology (SPH) is able to capture the flow behaviour of SCC mixes in the J-ring test. This has been validated by benchmarking the results of the numerical simulation against actual J-ring tests carried out in the laboratory. SPH simulation is therefore an indispensable and cost-effective tool for understanding the behaviour of fresh SCC replacing time-consuming laboratory tests, thereby saving time, effort and materials.

References

1. Badry F., Kulasegaram, S. and Karihaloo, B.L., Estimation of the yield stress and distribution of large aggregates from slump flow test of self-compacting concrete mixes using smooth particle hydrodynamics simulation. J Sustainable Cement-based Materials, doi:10.1080/21650373.2014.979266, 2016 (in press).
2. Deeb, R., Kulasegaram, S. and Karihaloo, B.L., 3D modelling of the flow of self-compacting concrete with or without steel fibres. Part II: L-box test and the assessment of fibre reorientation during the flow. Computational Particle Mechanics, 1, p. 391-408, 2014.
3. Abo Dhaheer, M.S., Al-Rubaya, M.M., Alyhya, W.S., Karihaloo, B.L. and Kulasegaram, S., Proportioning of self-compacting concrete mixes based on target plastic viscosity and compressive strength: mix design procedure. Journal of Sustainable Cement-Based Materials, doi: 10.1080/21650373.2015.1039625, 2016 (in press).
4. Ghanbari, A. and Karihaloo, B.L., Prediction of the plastic viscosity of self-compacting steel fibre reinforced concrete. Cement and Concrete Research, 39, p. 1209-1216, 2009.
5. BS EN 206-9, Concrete, Part 9: Additional rules for self-compacting concrete. British Standard Publications, 2010.

Proceedings of the 24th UK Conference of the
Association for Computational Mechanics in Engineering
31 March - 01 April 2016, Cardiff University, Cardiff

EFFICIENT IMPLEMENTATION OF VOLUME/SURFACE INTEGRATED AVERAGE BASED MULTI-MOMENT METHOD

***Mohammed Al-Mosallam[1], *Kensuke Yokoi[1]**

[1]School of Engineering, Cardiff University,The Parade, Cardiff, CF24 3AA, UK

*Al-MosallamMB@cardiff.ac.uk, YokoiK@cardiff.ac.uk

ABSTRACT

We investigate discretization strategies of the conservation equation in VSIAM3 (volume/surface integrated average based multi-moment method) which is a numerical framework for incompressible and compressible flows based on a multi-moment concept. We investigate these strategies through the droplet splashing on a superhydrophobic substrate. We find that the use of the CIP-CSLR (constrained interpolation profile-conservative semi-Lagrangian with rational function) method as the conservation equation solver is critically important for the robustness of incompressible flow simulations using VSIAM3 and that numerical results are sensitive to discretization techniques of the divergence term in the conservation equation.

Key Words: *multi-moment method; VSIAM3; CIP-CSL method; droplet splashing*

1. Introduction

VSIAM3 [1, 2] is a numerical framework to simulate fluid flows, and employs a CIP-CSL method [4, 3] as the conservation equation solver. VSIAM3 is a highly robust and efficient numerical framework [5]. However, a multi-moment framework which has been used in VSIAM3 (including the CIP-CSL method) have increased some complexities in the implementation. Although several CIP-CSL methods such as CSL2 (CSL with quadratic function) [4], and CSLR (CSL with rational function) [3] have been proposed, little attention has been given to the formulation of the divergence term in the CIP-CSL methods.

In this study, we propose efficient formulations for the divergence term in the CIP-CSL schemes and we identify reasons for robust implementation of VSIAM3.

2. The CIP-CSL and the Velocity Divergence Term

The CIP-CSL methods are used to solve the conservation equation

$$\frac{\partial}{\partial t}\int_{\Omega}\phi dV + \int_{\Gamma}\phi(\mathbf{u}\cdot\mathbf{n})dS = 0, \tag{1}$$

here ϕ is a scalar value. In the CIP-CSL, an interpolation function $\Phi_i(x)$ is constructed using different moments in one cell. For instance, in the CIP-CSL2 [4] method, a quadratic interpolation function $\Phi_i(x)$

$$\Phi_i(x) = a_i(x - x_{i-1/2})^2 + b_i(x - x_{i-1/2}) + \phi_{i-1/2}, \tag{2}$$

is used to interpolate between $x_{i-1/2}$ and $x_{i+1/2}$ as shown in Fig. 1. By using the following constraints

$$\Phi_i(x_{i+1/2}) = \phi_{i+1/2}, \tag{3}$$

$$\phi_i = \int_{x_{i-1/2}}^{x_{i+1/2}} \Phi_i(x)dx/\Delta x, \tag{4}$$

the coefficients, a_i and b_i, can be determined. In the CIP-CSLR [3] method which is characterised by less numerical oscillations, the following interpolation function

$$\Phi_i(x) = \frac{\alpha_i\beta_i(x - x_{i-1/2})^2 + 2\alpha_i(x - x_{i-1/2}) + \phi_{i-1/2}}{(1 + \beta_i(x - x_{i-1/2}))^2}, \tag{5}$$

with

$$\alpha_i = \beta_i \phi_i + (\phi_i - \phi_{i-1/2})/\Delta x, \tag{6}$$

$$\beta_i = \frac{1}{\Delta x}\left(\frac{|(\phi_{i-1/2} - \phi_i)| + \epsilon}{|(\phi_i - \phi_{i-1/2})| + \epsilon} + 1\right), \tag{7}$$

is used. Here ϵ is an infinitesimal number. Once the interpolation function $\Phi_i(x)$ is ready, the cell average ϕ_i is updated by a finite volume formulation

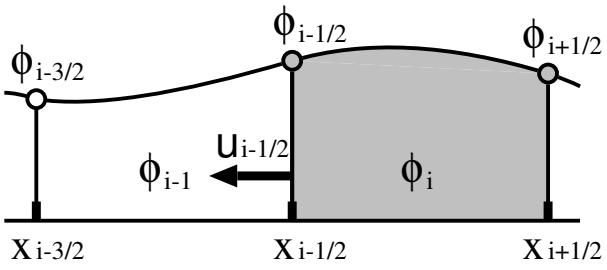

Figure 1: Schematic figure of the CIP-CSL2 method. $u_{i-1/2} < 0$ is assumed. The moments which are indicated by gray color ($\phi_{i-1/2}$, ϕ_i and $\phi_{i+1/2}$) are used to construct the quadratic interpolation function.

$$\frac{\partial}{\partial t}\int_{x_{i-1.2}}^{x_{i+1/2}} \phi dx = -\frac{1}{\Delta x}(F_{i+1/2} - F_{i-1/2}), \tag{8}$$

here $F_{i-1/2}$ is the flux

$$F_{i-1/2} = \begin{cases} -\int_{x_{i-1/2}}^{x_{i-1/2}-u_{i-1/2}\Delta t} \Phi_{i-1}(x)dx & \text{if} \quad u_{i-1/2} \geq 0 \\ -\int_{x_{i-1/2}}^{x_{i-1/2}-u_{i-1/2}\Delta t} \Phi_i(x)dx & \text{if} \quad u_{i-1/2} < 0. \end{cases} \tag{9}$$

The boundary value $\phi_{i-1/2}$ can be updated by the conservation equation of a differential form

$$\frac{\partial \phi}{\partial t} + u\frac{\partial \phi}{\partial x} = -\phi\frac{\partial u}{\partial x}. \tag{10}$$

(10) is solved using a splitting approach as follows

$$\frac{\partial \phi}{\partial t} + u\frac{\partial \phi}{\partial x} = 0, \tag{11}$$

$$\frac{\partial \phi}{\partial t} = -\phi\frac{\partial u}{\partial x}. \tag{12}$$

A semi-Lagrangian approach is used for the advection equation (11)

$$\phi^*_{i-1/2} = \begin{cases} \Phi_{i-1}(x_{i-1/2} - u_{i-1/2}\Delta t) & \text{if} \quad u_{i-1/2} \geq 0 \\ \Phi_i(x_{i-1/2} - u_{i-1/2}\Delta t) & \text{if} \quad u_{i-1/2} < 0. \end{cases} \tag{13}$$

(12) represents a correction due to the divergence term of the velocity and is solved by a finite difference method. We propose the following approximations of the velocity divergence term of the 1D conservation equation.

Simple upwind based on boundary value (UPW)

$$\phi\frac{\partial u}{\partial x} = \begin{cases} \phi^*_{i-1/2}(\frac{u^n_{i-1/2} - u^n_{i-3/2}}{\Delta x}) & \text{if} \quad u_{i-1/2} > 0 \\ \phi^*_{i-1/2}(\frac{u^n_{i+1/2} - u^n_{i-1/2}}{\Delta x}) & \text{if} \quad u_{i-1/2} \leq 0. \end{cases} \tag{14}$$

This is a simple upwind approximation based on the boundary values.

Central difference based cell centre value (CDcc)

$$\phi\frac{\partial u}{\partial x} = \phi^*_{i-1/2}\frac{\hat{u}^n_i - \hat{u}^n_{i-1}}{\Delta x} \tag{15}$$

This is a central difference approximation based on the cell center values ($\hat{u}_i$), where $\hat{u}_i$ is the velocity calculated at cell centre [2]

$$\hat{u}_i = \frac{3}{2}u_i - \frac{1}{4}\left(u_{i+1/2} + u_{i-1/2}\right). \tag{16}$$

Mixed formulation of the simple upwind and a central difference (UPW-CDcc)

$$\phi\frac{\partial u}{\partial x} = \begin{cases} \mathrm{D}_{UPW} & \text{if} \quad \mathrm{D}_{UPW}\cdot\mathrm{D}_{CDcc} < 0 \\ \mathrm{D}_{UPW} & \text{else if} \quad |\mathrm{D}_{UPW}| < |\mathrm{D}_{CDcc}| \\ \mathrm{D}_{CDcc} & \text{else,} \end{cases} \tag{17}$$

here D_{UPW} and D_{CDcc} represent $\phi\frac{\partial u}{\partial x}$ which are calculated by (14) and (15), respectively. The mixed formulation is introduced to take advantages of both upwind and central difference approximations.

3. Numerical results of the droplet splashing

We conducted numerical simulations of droplet splashing on a superhydrophobic substrate to study the effects of these discretization strategies of the conservation equation in VSIAM3 through a highly complicated free surface flow problem.For more detail see [5].

In the set of numerical simulations, quantitative parameters, the densities $\rho_{liquid} = 1000\,\mathrm{kg/m^3}$, $\rho_{air} = 1.25\,\mathrm{kg/m^3}$, viscosities $\mu_{liquid} = 1.0\times10^{-3}$ Pa·s, $\mu_{air} = 1.82\times10^{-5}$ Pa·s, surface tension $\sigma = 7.2\times10^{-2}$ N/m, gravity 9.8 m/s^2, initial droplet diameter $D = 1.86$ mm, impact speed 2.98 m/s and the equilibrium contact angle 163° are used. A regular Cartesian grid system of $192\times192\times48$ is used.

Fig. 2 shows the results. VSIAM3 with CSL2-UPW could not capture droplet splashing well as shown in Fig. 2a. CSL2-UPW also was not stable after around 1.1 ms. VSIAM3 with CSL2 with any central difference formulation was not stable for this problem. VSIAM3 with CSLR is stable when UPW was used for the divergence term as shown in Fig. 2b. However if we use any central difference formulation for the divergence term, VSIAM3 with CSLR was also unstable. If we use UPW-CDcc (mixed formulation), VSIAM3 with CSLR could conduct stable numerical simulation of droplet splashing and capture droplet splashing well as shown in Fig. 2c.

4. Conclusions

The numerical results showed that VSIAM3 with CSL2 is not robust enough and that VSIAM3 with CSLR is highly robust (if an appropriate formulation is used for the divergence term). We also found that the numerical results are sensitive depending on discretization formulations of the divergence term in the conservation equation. The numerical results of droplet splashing showed that VSIAM3 with any central difference formulation is not robust even though CSLR is used, while VSIAM3 with the simple upwind formulation was highly robust and captures the droplet splashing well. These results indicates that the use of the upwind formulation is suitable for robust numerical simulations, especially for highly complicated flows like droplet splashing.

We also proposed the mixed formulation using both a central difference and the simple upwind formulation for the divergence term. The mixed formulation can simulate the droplet splashing like the result using the simple upwind. The mixed formulation can take advantages of both central difference and upwind formulations.

In conclusion, employing the less oscillatory CSL scheme (i.e. CSLR) with an appropriate divergence term formulation is critically important for robust implementation of VSIAM3.

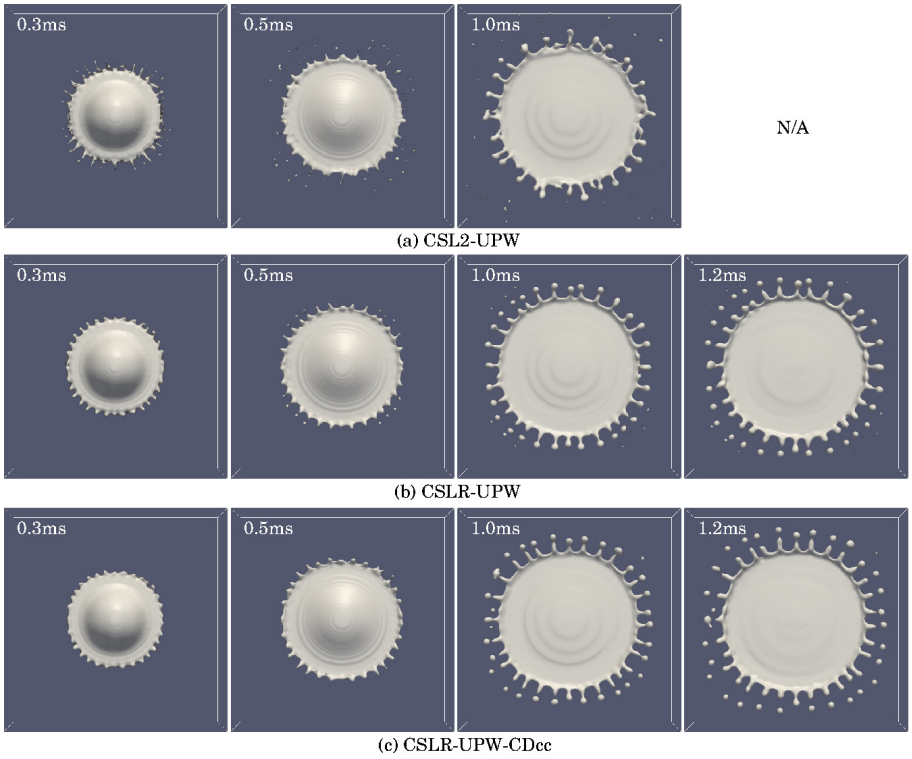

Figure 2: Numerical results of droplet splashing by CSL2-UPW (a), CSLR-UPW (b) and CSLR-UPW-CDcc (c). VSIAM3 with CSL2-UPW was not stable after around 1.1ms.

Acknowledgements

This work was partially supported by College of Engineering in University of Basrah. The numerical simulations were partially conducted on computers at Earth Simulator Center in JAMSTEC, at Yukawa Institute of Theoretical Physics in Kyoto University and at HPC Wales.

References

[1] F. Xiao, A. Ikebata, T. Hasegawa, Numerical simulations of free-interface fluids by a multi-integrated moment method, Computers and Structures, **83**, 409-423 (2005).

[2] F. Xiao, Unified formulation for compressible and incompressible flows by using multi-integrated moments I: one-dimensional inviscid compressible flow, J. Comput. Phys., **195**, 629-654 (2004) .

[3] F. Xiao, T. Yabe, X. Peng, H. Kobayashi, Conservative and oscillation-less atmospheric transport schemes based on rational functions, J. Geophys. Res., **107** (D22), 4609, doi:10.1029/2001JD001532, (2002).

[4] T. Yabe, R. Tanaka, T. Nakamura, F. Xiao, An Exactly Conservative Semi-Lagrangian Scheme (CIP-CSL) in One Dimension, Mon. Wea. Rev.,**129**, 332-344 (2001).

[5] K. Yokoi, A practical numerical framework for free surface flows based on CLSVOF method, multi-moment methods and density-scaled CSF model20: Numerical simulations of droplet splashing, J. Comput. Phys., **232**, 252-271 (2013).

SIMULATION OF THE FLOW OF SELF-COMPACTING CONCRETE IN THE L-BOX USING SMOOTHED PARTICLE HYDRODYNAMICS (SPH) METHOD

***Muna M Al-Rubaye[1, 2], Bhushan L Karihaloo[1] and Sivakumar Kulasegram[1]**

[1]School School of Engineering, Cardiff University, Queen's Buildings. The Parade, Cardiff, CF24 3AA

*AL-RubayeMM@cardiff.ac.uk

ABSTRACT

Self-compacting concrete (SCC) has been widely used in structures around the world because of its ability to flow without external intervention. The ability of passing around and between obstacles and the filling of the formwork are important properties of SCC; they determine how well the SCC mix can flow through confined and limited zones. For this reason, it is essential to devise numerical tools aimed at the simulation of how SCC fills formwork as a homogeneous mass without the segregation of mix components. The present study reports a numerical investigation of the flow and the distribution of large coarse aggregates of SCC mixes in the L-box using the three-dimensional Lagrangian particle based smooth particle hydrodynamics (SPH) method.

Keywords: *Self-compacting concrete; Smooth particle hydrodynamics; yield stress; plastic viscosity and L-box.*

1. Introduction

Self-compacting concrete is described in its fresh state by high flow-ability, filling ability of the formwork, passing ability through restricted reinforcement bars and resistance to segregation without requiring any external vibration for compaction. The durability of concrete structures is affected by many problems of compactness; these problems result from incomplete filling of formworks and segregation of aggregates inside the structure. This problem is getting more acute as SCC is used in structures with complex shape and denser reinforcements. It is therefore important to have a tool for predicting the flow, filling and passing ability in order to save time, effort and materials. Computational simulation of SCC flow can be a helpful tool for understanding the rheological behaviour of SCC and can allow to identify a lower workability of fresh concrete that could ensure proper filling of formwork [1]. For this purpose, the three-dimensional Lagrangian particle based smoothed particle hydrodynamics (SPH) method is employed to simulate the flow of SCC in the L-box configuration and to reveal the distribution of coarse aggregate particles larger than or equal to 8 mm in the mix and then to compare the numerical results with the corresponding experimental data.

2. Numerical implementations

SCC is treated as a non-Newtonian fluid best described by a Bingham-type model that contains two material properties: the yield stress (τ_y) and the plastic viscosity (η) [2]. From a practical computational point of view, it is expedient to approximate the bi-linear Bingham constitutive model with a kink at by a smooth continuous function, where *m* is a very large number (m=10^5) [3].

$$\boldsymbol{\tau} = \eta\dot{\boldsymbol{\gamma}} + \tau_y(1 - e^{-m\dot{\gamma}}) \qquad (1)$$

There are two basic equations solved in the SPH method together with the constitutive relation; the incompressible mass and momentum conservation equations

$$\frac{1}{\rho}\frac{D\rho}{Dt} + \nabla.\mathbf{v} = 0 \ , \quad \frac{D\mathbf{v}}{Dt} = -\frac{1}{\rho}\nabla P + \frac{1}{\rho}\nabla.\boldsymbol{\tau} + g \qquad (2), (3)$$

[2]On leave from University of Babylon, Iraq

where ρ, t, $\mathbf{v}$, P, $\mathbf{g}$ and $\boldsymbol{\tau}$ represent the fluid particle density, time, particle velocity, pressure, gravitational acceleration, and shear stress tensor, respectively. Below we shall consider flows in which the density is constant, so that the first term in Equation (2) vanishes.

The solution procedure uses prediction-correction fractional steps with the temporal velocity field integrated forward in time without enforcing incompressibility in the prediction step. Only the viscous stress and gravity terms are considered in the momentum Equation (3) and an intermediate particle velocity $\mathbf{v}^*_{n+1}$ is obtained as:

$$\mathbf{v}^*_{n+1} = \mathbf{v}_n + \left(g + \frac{1}{\rho} \nabla . \boldsymbol{\tau} \right) \Delta t \qquad (4)$$

Here, $\mathbf{v}_n$ and $\mathbf{v}^*_{n+1}$ are the particle velocity and intermediate particle velocity at time t_n and t_{n+1} respectively. Then the correction step is performed by considering the pressure term in Eq. (3):

$$\frac{\mathbf{v}_{n+1} - \mathbf{v}^*_{n+1}}{\Delta t} = -\left(\frac{1}{\rho} \nabla P_{n+1} \right) \qquad (5)$$

Rearranging Equation (5) gives,

$$\mathbf{v}_{n+1} = \mathbf{v}^*_{n+1} - \left(\frac{1}{\rho} \nabla P_{n+1} \right) \Delta t \qquad (6)$$

where $\mathbf{v}_{n+1}$ is the corrected particle velocity at the time step t_{n+1}. By imposing the incompressibility condition in the mass conservation Equation (2), the pressure P_{n+1} in equation (6) will be obtained. As the particle density remains constant during the flow, the velocity $\mathbf{v}_{n+1}$ is divergence-free. Enforcing the incompressibility condition as Equation (2) yields,

$$\nabla . \mathbf{v}_{n+1} = 0 \ , \ \nabla . \left(\frac{1}{\rho} \nabla P_{n+1} \right) = \frac{\nabla . \mathbf{v}^*_{n+1}}{\Delta t} \qquad (7), (8)$$

Since the density of particles remains constant in the present simulations, Equation (8) can be rewritten as:

$$\nabla^2 P_{n+1} = \frac{\rho}{\Delta t} \nabla . \mathbf{v}^*_{n+1} \qquad (9)$$

where ∇^2 is the Laplacian operator. Once the pressure is obtained from the Poisson Equation (9), the particle velocity is updated by the computed pressure gradient (see equation (6)). Finally, the instantaneous particle position is updated using the corrected velocity:

$$\mathbf{x}_{n+1} = \mathbf{x}_n + \mathbf{v}_{n+1} \Delta t \qquad (10)$$

where $\mathbf{x}_{n+1}$ and $\mathbf{x}_n$ is the particle position at t_{n+1} and t_n respectively.

3. Modelling of the flow of SCC mix and the boundary conditions

The modelling of the flow of the SCC mix in the L-box has been done previously [4]. In the present study, three additional aspects are taken into consideration. These aspects include; friction on the sides of L-box and on the steel bars, the effect of the time delay in the lifting of the L-box gate manually on the simulated flow times and the comparison between the simulated distribution of larger coarse aggregates with the distribution in tests performed in the laboratory using colour coded aggregates. The distribution of the aggregate particles equal or larger than 8 mm in size have been modelled as separate particles suspended in the viscous paste containing the particles less than 8 mm in size. Four ranges of size of the coarse aggregates have been used during the numerical simulation size as follows; $8 \leq g \leq 12$, $12 \leq g \leq 16$, $16 \leq g \leq 20$ and $g \geq 20$ mm with a total number of particles 59,568 and these particles were represented by distinct colours as shown in Figure 1(a). When solving the momentum and continuity equations, the boundary conditions need to be applied. Four arrays of rigid dummy particles placed outside the sides and the base of the L-box were used to implement the

boundary conditions as illustrated in Figure 1(b). Dirichlet and Neumann boundary conditions were imposed on the sides and the base of the L-box. Friction between the boundaries and the SCC mix was imposed on the L-box sides and the base with a dynamic coefficient of friction between the SCC mix and steel equal to 0.55 Ns/m.

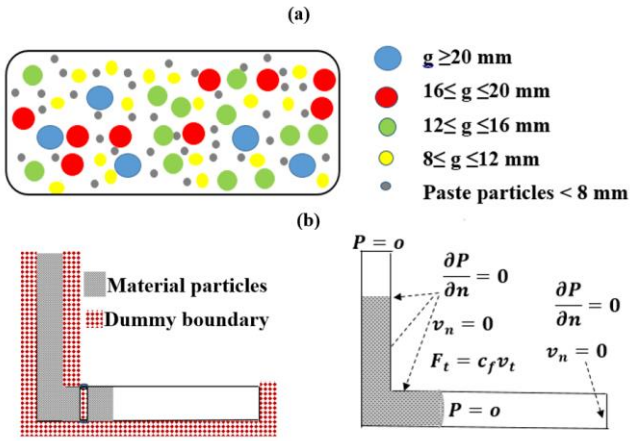

Figure 1 : (a) The aggregate particle representation (b) The boundary conditions of the L-box

4. Simulation results of the flow and the distribution of the coarse aggregates

The 3D simulation of the SCC flow and distribution of the large coarse aggregates has been performed on the mix of strength 60 MPa, which was developed according to the rational mix design method[5]. The results of the simulation when SCC mix reached 200 mm, 400 mm of horizontal section of the L-box are illustrated in Figure 2(a), (b). These flow times differ from the corresponding test results as a result to delay time in the lifting of the gate L-box manually. By cutting the simulated L-box specimen after the mix reached the end of horizontal section of the L-box and flow stopped by two longitudinal sections A-A and B-B Figure 2(c), it was found the modelled distribution patterns are agreed with the distribution of coarse aggregates in the experimental test results as illustrated in Figure 3.

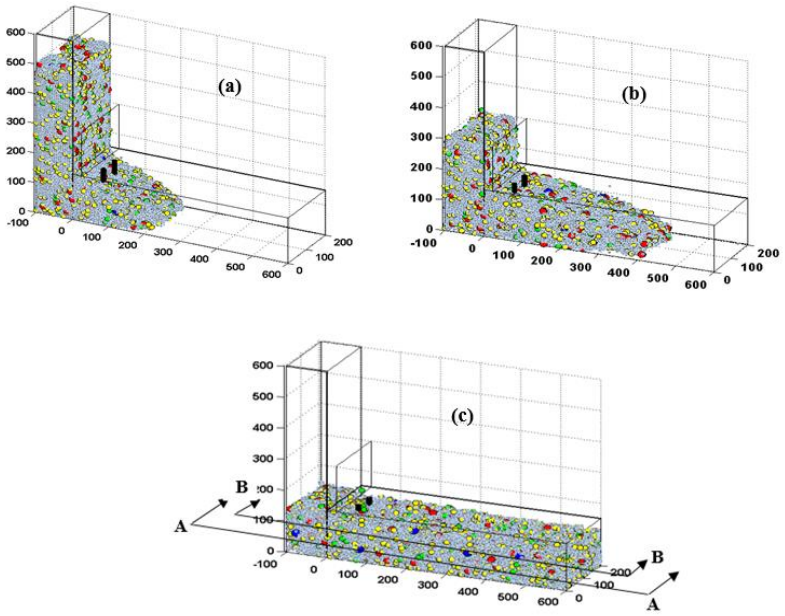

Figure 2 : The 3D simulation of the flow in the L-box after SCC mix reached (a) 200 mm (b) 400mm (c) the end of horizontal section of the L-box and the flow stopped

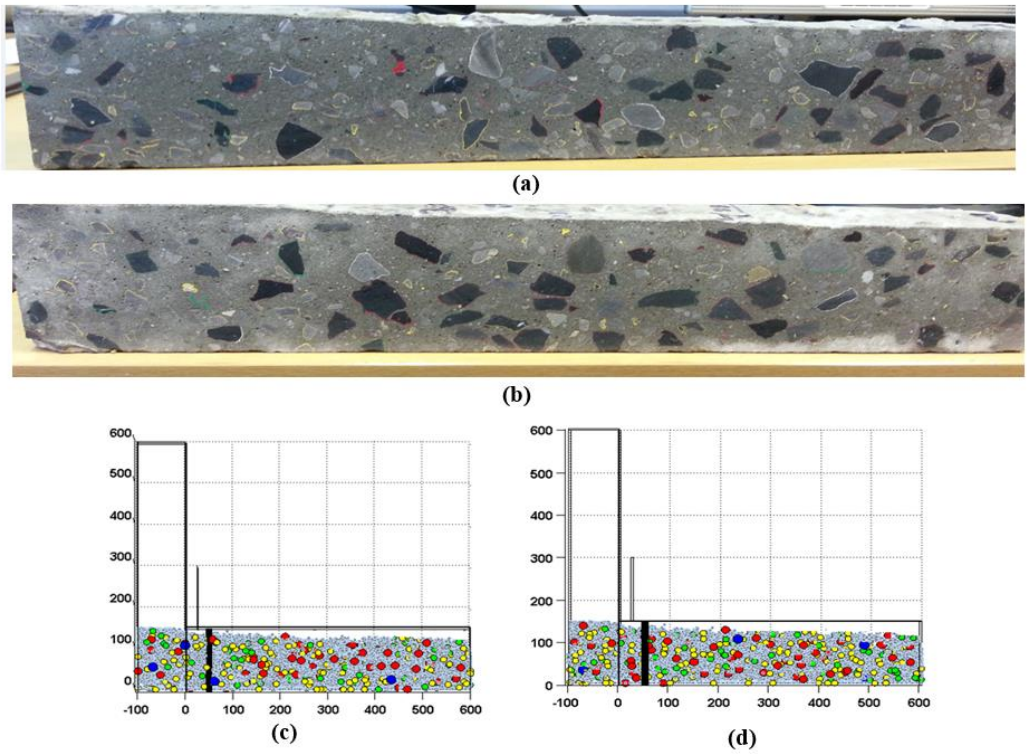

Figure 3: The distribution of the coarse aggregates in the experimental test (a) section A-A (b) section B-B and numerical simulation (c) section A-A (d) section B-B

5. Conclusions

The 3D simulation of the flow of the SCC mix in the L-box presents a prediction of the filling behaviour similar to that observed in the laboratory test. With regard to the flow times needed for the mix to reach 200 mm and 400 mm, there is a difference between the simulation flow times and that the corresponding experimental data due to the delay time in the lifting of the gate L-box manually. The 3D numerical simulations of the distribution of the coarse aggregates showed that the larger aggregates remained homogeneously distributed in the mix exactly as in the L-box test in the laboratory.

References

[1] N. Roussel, M.R. Geiker, F. Dufour, L.N. Thrane, P. Szabo, Computational modeling of concrete flow: General overview, Cem. Concr. Res. 37 (2007) 1298–1307.

[2] S. Kulasegaram, B.L. Karihaloo, A. Ghanbari, Modelling the flow of self-compacting concrete, Int. J. Numer. Anal. Methods Geomech. 35 (2011) 713–723.

[3] R. Deeb, S. Kulasegaram, B.L. Karihaloo, 3D modelling of the flow of self-compacting concrete with or without steel fibres. Part I: slump flow test, Comput. Part. Mech. 1 (2014) 373–389.

[4] R. Deeb, S. Kulasegaram, B.L. Karihaloo, 3D modelling of the flow of self-compacting concrete with or without steel fibres. Part II: L-box test and the assessment of fibre reorientation during the flow, Comput. Part. Mech. (2014) 391–408.

[5] M.S. Abo Dhaheer, M.M. Al-Rubaye, W.S. Alyhya, B.L. Karihaloo, S. Kulasegaram, Proportioning of self–compacting concrete mixes based on target plastic viscosity and compressive strength: mix design procedure, J. Sustain. Cem. Mater. (2016) doi:10.1080/21650373.2015.1039625.

SIMULATION OF SELF-COMPACTING CONCRETE IN V-FUNNEL TEST BY SPH

***Wajde S. Alyhya[1, 2], Bhushan L. Karihaloo[1] and Sivakumar Kulasegaram[1]**

[1]School of Engineering, Cardiff University

[*]Alyhyaws@Cardiff.ac.uk

ABSTRACT

Computational modelling of the flow for a viscous fluid such as self-compacting concrete (SCC) is a potential tool for understanding its rheological behaviour and for mix proportioning as well. The present paper describes a simple approach to simulate the flow of SCC mixes of different strengths and performances containing aggregate particles of various sizes in the V-funnel test using 3-dimensional mesh-less smooth particle hydrodynamics (SPH) computational technique. A comparison between the results of the numerical simulation with the corresponding experimental observations has revealed the flow characteristics of SCC mixes and confirmed the capability of SPH and the rheological model to predict SCC flow and mould filling behaviour.

Keywords: *Self-compacting concrete; V-funnel; SPH; Bingham parameters; plastic viscosity; yield stress.*

1. Introduction

In concrete construction, massive problems arise from the insufficient filling of formwork, inadequate de-airing and concrete segregation. The impact of such problems has increased year after year since the formwork is becoming continuously more complex and reinforcement is becoming denser. Self-compacting concrete (SCC) has been developed to solve these engineering issues. It is a concrete that flows under its own weight, without external vibration, while maintaining homogeneity. This ensures proper filling of formwork and produces high quality finish in restricted areas and heavily reinforced structural members. Various tests are implemented to evaluate the characteristics of SCC, including its filling ability, passing ability, and segregation resistance [1].These tests can be avoided by using the most cost-effective computational modelling to save time, effort and materials. Such modelling can also provide an understanding of the SCC flow behaviour, which is crucial to achieving high quality. Indeed, the employment of the modelling has brought insight into the significance of the rheology as a tool for the optimization of mix composition, and the processing techniques to fulfil the levels of engineering properties required for the intended civil applications.

The V-funnel test, which is one of the standard SCC tests, is designed to determine the filling ability of SCC in which shorter flow time indicates greater flowability. The V- shape restricts the flow, and prolonged flow times may give some indication of the susceptibility of the mix to blocking.The actual time ($t_{v\text{-}funnel}$) taken (the discharge time) when it is possible to see vertically through the V-funnel into the container below is measured. A time delay of 10 ± 2 s from filling the V-funnel to the release of the gate at the bottom of the V-funnel is permissible. In this paper, SCC flow during the V-funnel test of SCC mixes of various strengths and performances is modelled using the SPH method and the concrete discharge time is determined. This will provide a tool for simulating the discharge time and its comparison with the EFNARC guidelines.

2. Numerical simulation

Since SCC flow during the V-funnel test is typically a free surface flow with large deformations, the Lagrangian mesh-less SPH numerical method is preferred to solve the governing SCC flow equations. It is also able to treat naturally highly-varying density, deformable boundaries, propagation of discontinuities, multi-phase flows and other physically complex flow situations. The SPH is a mesh-less particle numerical approach based on an interpolation theory, in which the partial differential equations of motion of continuum fluid dynamics are transformed into integral equations by using an interpolation function.

[2] On leave from University of Karbala, Iraq

This interpolation is carried out by ‘‘kernel estimate’’ of the field variable at any point. The basic equations solved in the SPH are the incompressible mass and momentum conservation equations [2], together with the Bingham-type constitutive relation. In this approach, the flow continuum is discretized into a limited number of particles, *N*. The particles, which behave as Lagrangian fluid elements, carry all the necessary information needed about the flow variables; this feature is the principal strength of the method. The field variables and their gradients are approximately calculated and interpolated from values at a discrete set of particles in a domain of influence. All randomly generated particles, which represent the paste and the large aggregates, form a homogeneous mass with the same properties as the continuum except their assigned volumes.

3. Governing equations

Given its shear rate-dependent response, SCC can be regarded as a non-Newtonian incompressible fluid. Its rheology is best described by a Bingham-type model which contains two material properties, the yield stress, τ_y and the plastic viscosity, η. From a computational perspective, it is expedient to approximate the bi-linear Bingham constitutive model with a kink at $\dot{\gamma}$= 0 by a continuous function:

$$\tau = \eta\dot{\gamma} + \tau_y\left(1 - e^{-m\dot{\gamma}}\right) \qquad (1)$$

in which *m* is a very large number, $m = 10^5$. Suitable numerical schemes, which integrate the Lagrangian SPH approximations of the governing equations (i.e. mass and momentum conservation equations) with the rheological Bingham type model for SCC, have been developed. These schemes have been exploited to understand the flow behaviour of SCC containing coarse aggregate particles of various sizes. The isothermal, Lagrangian form of mass and momentum conservation equations are:

$$\frac{1}{\rho}\frac{D\rho}{Dt} + \nabla.v = 0 \qquad (2) \qquad \frac{Dv}{Dt} = -\frac{1}{\rho}\nabla P + \frac{1}{\rho}\nabla.\tau + \mathrm{g} \qquad (3)$$

where ρ, t, $\boldsymbol{v}$, P, $\boldsymbol{\tau}$ and g represent the fluid particle density, time, particle velocity, pressure, shear stress tensor and gravitational acceleration, respectively. The first term in Eq.(2) vanishes since the density is constant due to the incompressible flow assumption. A projection method based on the predictor-corrector time stepping scheme has been adopted to implement the incompressible SPH approach. The prediction step is an explicit integration in time without enforcing incompressibility. Only the viscous and gravity terms (second and third terms, respectively) in Eq. 3 are initially considered to obtain temporal velocity for particles (v^*_{n+1}). Then, the correction step is performed by considering the pressure term (first term) in Eq.3, which will be obtained by imposing the incompressibility condition using Eq.2. Once the pressure is obtained from Poisson’s Equation, the particle velocity and position are updated by the computed pressure gradient. Figure 1 illustrates the time stepping scheme [3].

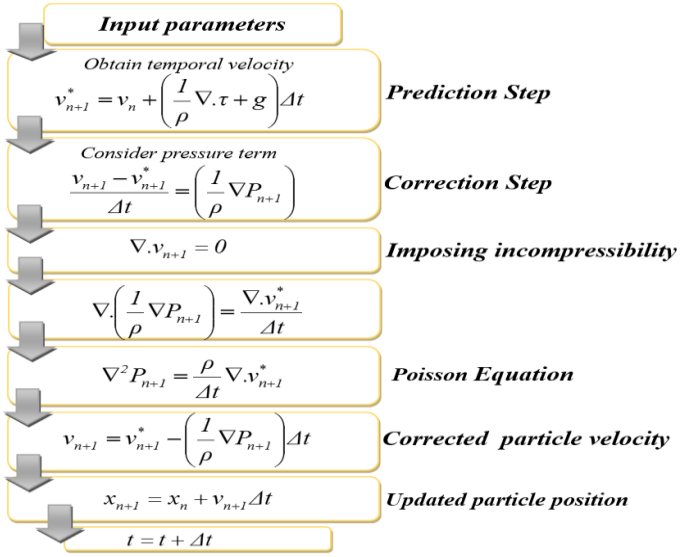

Figure 1: The predictor-corrector time stepping scheme of the incompressible SCC flow [3]

4. Initial configuration and treatment of large aggregates

It is necessary to impose appropriate initial boundary conditions to solve the mass and momentum conservation equations. Three sorts of boundary conditions have been applied in the modelling of the V-funnel test: zero pressure condition on the free surface (*P=0*), Dirichlet boundary condition at the walls of the V-funnel ($v_n = 0$), and Neumann conditions on the pressure gradient ($\partial P/\partial n = 0$) (zero pressure gradient is used only for solving the Poisson equation to find the pressure), as illustrated in Figure 2, where the geometry of the V-funnel apparatus is also shown. Rigid dummy particles of four arrays placed outside the walls of the V-funnel were used to implement the wall boundary conditions. To reveal the positions and velocity vectors of aggregates of various sizes, and those of the fluid particles representing the paste, the particles are represented by distinct colours and generated randomly. In order to get reliable simulation results, the kinematic coefficient of friction (c_f) between the V-funnel wall and the SCC mix has been altered to get the best fit between the experiment and simulated results for one mix. The same coefficient was then used for all other mixes.

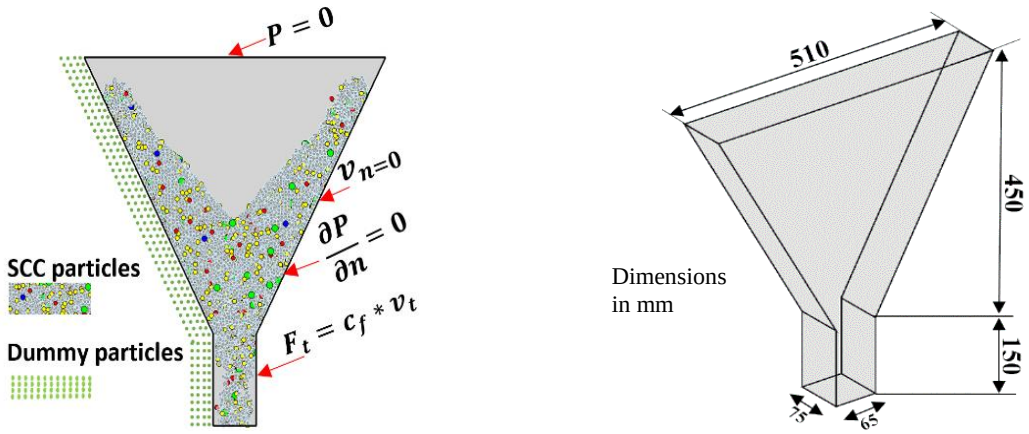

Figure 2: Boundary conditions and geometry of the V-funnel apparatus

5. Preliminary simulation results

A range of SCC mixes with 28-day cube compressive strength between 30 and 80 MPa has been developed following the rational mix design procedure described in [4].The plastic viscosities of these mixes were estimated following the micromechanical procedure described in [5]. This procedure is based on the rheology of concentrated suspensions, and it can predict accurately in a stepwise way the plastic viscosity of heterogeneous SCC mixtures beginning with the plastic viscosity of the homogeneous paste. On the other hand, the yield stress of a mix was estimated in an inverse manner from the measured time, t_{500} to reach 500 mm spread of the SCC mixes in a cone flow test using the three-dimensional SPH [6]. Details of the SCC mixes and their plastic viscosities are given in [7].The 3D numerical simulation of the V-funnel test for a typical SCC mix (Mix 50B) has been represented by 53,846 particles to investigate its flow characteristics and compare with the corresponding experimental results. The simulation has revealed the distribution of the large aggregates in the SCC mix (coarse aggregate size (g) ≥8 mm) to check whether these heavier aggregates remain homogenously distributed in the viscous mix during the flow.

It can be noticed from Figure 3 that the flow patterns obtained from the numerical simulation at various time step are very similar to those observed in the laboratory test. The slight difference in the discharge time, $t_{v\text{-}funnel}$ may be due to two possible reasons: firstly, the assumption that the SCC particles are spherical in shape and secondly, the slight time delay in opening the bottom gate. Importantly however, it can be observed from the simulated flow illustrated in Figure 3 that the larger aggregates (g) do indeed stay homogeneously distributed in the mix at various times during the flow.

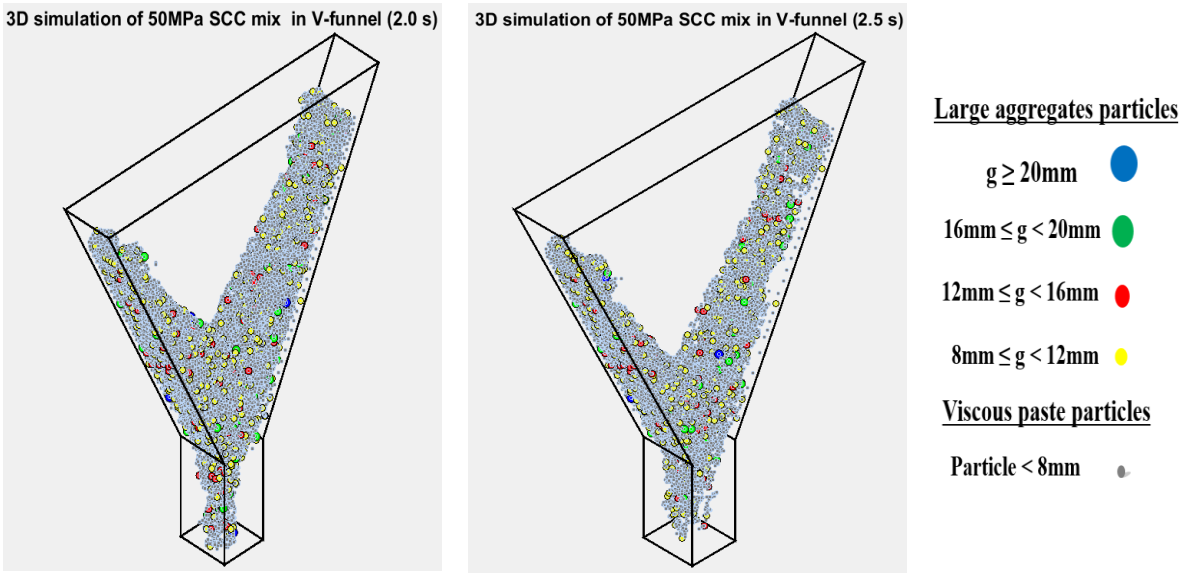

Figure 3: 3D simulation of 50MPa SCC mix in V-funnel after 2.0 s and 2.5 s showing the larger aggregates (g)

6. Conclusions

A 3D Lagrangian SPH numerical model has been developed to simulate the flow of SCC mixes of varying strengths and performances and to estimate the discharge time in the V-funnel test. Concrete is assumed as a heterogeneous, non-Newtonian fluid whose relation between shear stress and strain rate is of the Bingham type. This relation has been coupled with the Lagrangian mass and momentum conservation equations to simulate the SCC mixes of different viscosities and yield stresses in the V-funnel test after determining the proper number of particles for simulations. The predicted discharge time result is generally in good agreement with the test data. The numerical methodology also shows that it can conceptualise the flow behaviour of SCC mixes and provide insight into the distribution of larger aggregates during the flow. It can be concluded that without performing the V-funnel test, concrete discharge time, and consequently its suitability for application as SCC can be established when the plastic viscosity and yield stress are known.

References

[1] BS EN 206-9, Additional Rules for Self- Compacting Concrete (SCC), (2010).
[2] B.L. Karihaloo, S. Kulasegaram, Fibre-reinforced, self-compacting concrete flow modelled by smooth particle hydrodynamics, Proc. ICE - Eng. Comput. Mech. 166 (2013) 22–31.
[3] R. Deeb, Flow of Self-Compacting Flow of Self-Compacting, School of Engineering, Cardiff University, UK, 2013.
[4] M. Abo Dhaheer, M.M. Al-Rubaye, W.S. Alyhya, B.L. Karihaloo, S. Kulasegaram, Proportioning of self–compacting concrete mixes based on target plastic viscosity and compressive strength: mix design procedure, J. Sustain. Cem. Mater. (2016). doi:10.1080/21650373.2015.1039625.
[5] A. Ghanbari, B.L. Karihaloo, Prediction of the plastic viscosity of self-compacting steel fibre reinforced concrete, Cem. Concr. Res. 39 (2009) 1209–1216.
[6] F. Badry, S. Kulasegaram, B.L. Karihaloo, Estimation of the yield stress and distribution of large aggregates from slump flow test of self-compacting concrete mixes using smooth particle hydrodynamics simulation, J. Sustain. Cem. Mater. (2016). doi:10.1080/21650373.2014.979266.
[7] M. Abo Dhaheer, M.M. Al-Rubaye, W.S.S. Alyhya, B.L. Karihaloo, S. Kulasegaram, Proportioning of self-compacting concrete mixes based on target plastic viscosity and compressive strength: experimental validation, J. Sustain. Cem. Mater. (2016). doi:10.1080/21650373.2015.1036952.

Proceedings of the 24th UK Conference of the
Association for Computational Mechanics in Engineering
31 March - 01 April 2016, Cardiff University, Cardiff

A Novel Black-Box Massively Parallel Partitioned Approach to Fluid-Structure Interaction Problems

***Sam Hewitt [1], Alistair Revell[1] and Lee Margetts[1]**

[1] School of Mechanical, Aerospace and Civil Engineering, University of Manchester, Manchester, UK, M13 9PL

* Sam.Hewitt@postgrad.manchester.ac.uk

ABSTRACT

This paper describes new software based on a partitioned, black box approach for solving fluid structure interaction (FSI) problems. It couples the open source finite volume solver OpenFOAM, to the open source finite element solver ParaFEM [1]. This coupling is done using a conventional serially staggered scheme, that is first order accurate in time. The software has been tested using benchmark FSI problems, with long term goals to investigate the broad range of large scale FSI cases relevant to the wind energy industry. The aim is to demonstrate the potential benefits of such a tool, by delivering a unique capability to investigate novel concepts, to levels of physical realism not yet achieved.

Key Words: *Fluid-Structure Interaction; High Performance Computing; Computational Fluid Dynamics; Finite Element Analysis; Partitioned Coupling*

1. Introduction

Over the past thirty years the average size of offshore wind turbines has increased, with rotor diameters growing from 10m to 160m. It therefore becomes increasingly important to simulate the complex dynamics involved with unsteady and turbulent flow through rotating blades, and the large structural deformations of blades, in order to optimise their design.

The motivation is to produce software capable of solving coupled FSI problems to investigate the dynamics of wind turbines; both individually and ultimately in arrays relevant to farm configurations. The project will focus on coupling OpenFOAM to ParaFEM [1] in such a way as to minimise communication bottleneck and to maximise performance of the software.

The developed software uses a partitioned approach, with OpenFOAM and ParaFEM acting as blackbox fluid and structural solvers respectively. Using this approach makes use of already existing models and solution algorithms that have been previously validated, and the user has the versatility to select the type of CFD and FEM simulations independently from the coupling strategy. The coupling is achieved using a conventional serially staggered (CSS) scheme to solve the governing equations. The software will be highly parallel allowing large complex problems to be run with sufficient accuracy in a reasonable time on High Performance Computers.

FSI modelling offers the potential to accurately predict the deforming blade shape across a range of load conditions and thus improve the prediction of blade efficiency and noise production. FSI with ParaFEM not only provides fast stress analysis through parallel processing, but also the capability to incorporate more heavy weight structural integrity assessment through stochastic simulations [2], thermo-mechanical analysis [3] and multi-scale modelling of fracture [4].

2. Method

This section will give a brief description of the governing equations associated with the fluid and solid, and the interface conditions. Finally the system architecture and coupling algorithm between OpenFOAM and ParaFEM is described.

2.1. Fluid/OpenFOAM

The flow variables are described by the Navier-Stokes equations (1,2). The subscripts s and f represent the solid and fluid respectively.

$$\frac{\partial}{\partial t} + \nabla \cdot (\rho U_f) = 0 \tag{1}$$

$$\rho \frac{\partial U_f}{\partial t} + \rho U_f \cdot \nabla U_f - \nabla \cdot \sigma_f = f \tag{2}$$

Where U represents the velocity vector [u,v,w], ρ the density, t the time and σ the stress tensor. The governing equations are discretised using the finite volume method (FVM).

2.2. Solid/ParaFEM

The solid is solved using an element by element variant of the finite element method (FEM), through the linear equation:

$$\sum_{1}^{nels} \{f_e\} = [K_e]\{x_e\} \tag{3}$$

Where f_e and x_e are the elements nodal forces and displacements respectively, and K_e represents the element stiffness matrix which is computed from the material properties and shape functions. $nels$ is the total number of elements in the mesh.

2.3. Interface

The interface between the fluid and solid is described by kinematic (4) and dynamic (5) equilibrium. Where n represents the unit normal.

$$U_f = \frac{dU_s}{dt} \tag{4}$$

$$\sigma_f . n_f = -\sigma_s . n_s \tag{5}$$

The kinematic condition ensures the spatial variables, velocity and displacement, at the interface between the fluid and structure are in equilibrium. The dynamic condition states that the force/stress exerted by the fluid and solid at the interface are equal and opposite.

2.4. System Architecture

The software considers OpenFOAM and ParaFEM as two black box solvers. This partitioned approach means the numerical schemes and discretisation methods, for the structure and flow, can be chosen independently. The modular approach makes the software robust and flexible for different types of problems. However if a dynamic structural model is used, care must be taken with the choice of time step so as to avoid spurious oscillations in the acceleration and traction at the interface [5].

The algorithm used in solving the FSI problem is shown in Figure 1a. The algorithm currently used is the most basic coupling technique, the conventional serially staggered scheme, developed in [6]. The coupling between the two programs is in its most simplistic form, a transfer of data. The difficulty comes from two sources. Moving data from an object orientated language (C++) to a procedural language (Fortran) and from a FVM to FEM. The quasi standard coupling interface MpCCI has been used for a similar problem in [7]. OpenFOAM contains good interpolation libraries, making the use of external packages unnecessary. OpenFOAM acts as the master program with ParaFEM being called as a subroutine at runtime. Figure 1b shows the data coupling, interpolation and data transfer between the two programs. This is described more comprehensively below.

1. Geometry : The initial geometry data (nodal coordinates and connectivity matrix) of the solid mesh are passed to ParaFEM, before the time loop begins.

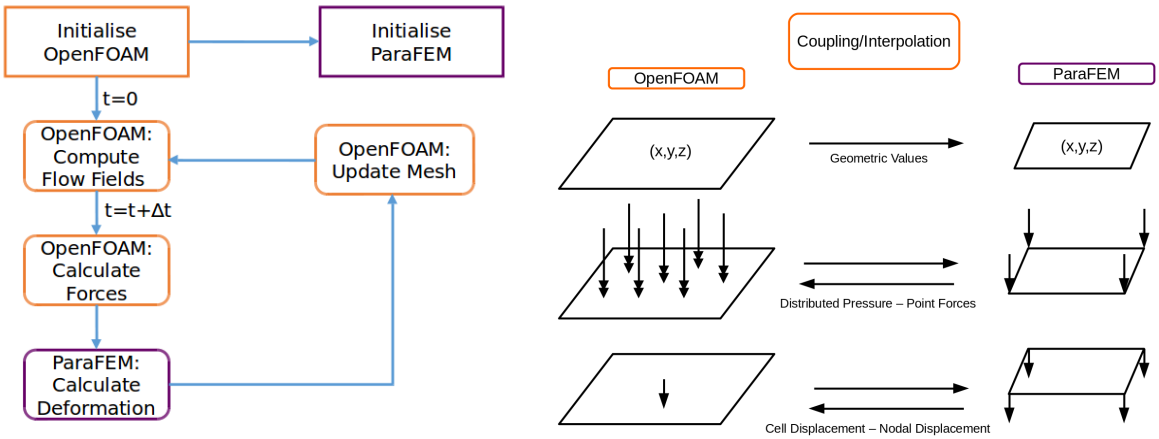

(a) Conventional Serially Staggered Scheme (b) Interpolation between FEM and FVM

Figure 1: High level diagrams of the 1a Solution Algorithm & 1b Data Transfer

2. Dynamics : The pressure on each face, at the interface, is interpolated to a point force and a direction vector. This force is then distributed over the nodes of the FE element according to [1].
3. Kinematics : The nodal displacements are passed back to OpenFOAM that interpolates the nodal values into patch/face displacements.

3. Test Problems and Results

The software has been checked using the FSI benchmark problem proposed by Stefan Turek and Jaroslav Hron in [8]. This test involves the 2D laminar flow of an incompressible, Newtonian fluid, through a channel and around an elastic object (Figure 2). The values for the geometric parameters are shown in Table 1. The test involves fixing the elastic solid until the flow is fully developed before allowing the solid to move under the force of the fluid. The displacement at position A, is compared to the benchmark results over one full cycle.

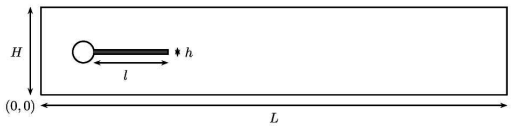

(a) Fluid Domain

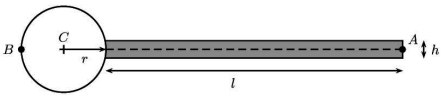

(b) Solid Domain

Figure 2: Schematic of the Hron and Turek benchmark case, taken from [8]

During the conference, the implementation of the software will be described before presenting the results and performance of the code for the FSI benchmark problem described earlier. Figure 3 shows an example of the problem run using the current FSI solver in OpenFOAM. This uses a finite volume solver for both the fluid and the solid.

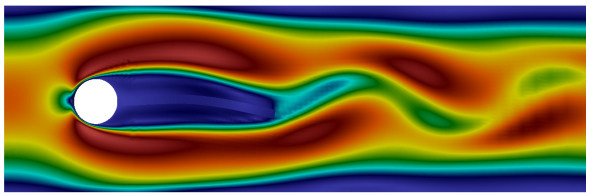

Figure 3: An example of Hron Turek Test case

Parameter	Value(m)
L	2.5
H	0.41
C	(0.2,0.2)
r	0.05
l	0.35
h	0.02
A	(0.6,0.2)
B	(0.2,0.2)

Table 1: Geometric Parameters from [8]

Scaling tests for both OpenFOAM and ParaFEM have been performed in the literature. Smith et al [1] has shown that ParaFEM scales well on up to 32,000 cores. while the HPC Advisory Council [9] have shown that OpenFOAM can scale well to 1024 cores.

4. Conclusions

This paper has described new software that couples the finite volume CFD solver, OpenFOAM with the finite element structural solver, ParaFEM. OpenFOAM has acted as the master, calling ParaFEM as a subroutine each time step.The modular set up of the software makes it flexible and robust. The code will be able to tackle larger and more complex problems, with good fidelity in the results, specifically to investigate physical phenomena that occur in wind turbines and ultimately arrays/farms.

Acknowledgements

The first author is supported by an Alstom/EPSRC PhD Studentship. The authors would like to express their gratitude to Prof. Hrvoje Jasak and Dr Stefano Rolfo for their help at the 3rd UK and Ireland OpenFOAM User Meeting at the Hartree Center.

References

[1] I. M. Smith, D. V. Griffiths, and L. Margetts. *Programming the Finite Element Method*. John Wiley & Sons, Ltd, 5th edition, 2014.

[2] Jose David Arregui-Mena, Lee Margetts, D. V. Griffiths, Louise Lever, Graham Hall, and Paul M. Mummery. Spatial variability in the coefficient of thermal expansion induces pre-service stresses in computer models of virgin Gilsocarbon bricks. *Journal of Nuclear Materials*, 465:793–804, 2015.

[3] Llion Evans, Lee Margetts, Valentina Casalegno, Louise Lever, Joe Bushell, Tristan Lowe, Andrew Wallwork, Philippe Young, Andre Lindemann, Marc Schmidt, and Paul Mummery. Transient thermal finite element analysis of CFC-Cu ITER monoblock using X-ray tomography data. *Fusion Engineering and Design*, 100:100–111, 2015.

[4] A Shterenlikht and L Margetts. Three-dimensional cellular automata modelling of cleavage propagation across crystal boundaries in polycrystalline microstructures. *Proceedings of the Royal Society of London A: Mathematical, Physical and Engineering Sciences*, 471(2177), 2015.

[5] Joris Degroote. Partitioned Simulation of Fluid- Structure Interaction. *State of the Art Reviews*, 20(3):185–238, 2013.

[6] M. Lesoinne and C. Farhat. Higher-Order Subiteration-Free Staggered Algorithm for Nonlinear Transient Aeroelastic Problems. *AIAA Journal*, 36(9):1754–1757, sep 1998.

[7] Michael Schäfer, Marcus Heck, and Saim Yigit. An implicit partitioned method for the numerical simulation of fluid-structure interaction. *Fluid-structure interaction*, pages 171–194, 2006.

[8] Stefan Turek and Jaroslav Hron. Proposal for numerical benchmarking of fluid- structure interaction between an elastic object and laminar incompressible flow. *Lecture Notes in Computational Science and Engineering*, 53:371–385, 2006.

[9] Scale Working Group. Computational Fluids Dynamics (CFD) Simulations at Scale OpenFOAM open source applications. Technical report, 2010. Available: http://www.hpcadvisorycouncil.com/best_practices.php.

Advanced Applications I

Proceedings of the 24th UK Conference of the
Association for Computational Mechanics in Engineering
31 March – 01 April 2016, Cardiff University, Cardiff

RESPONSES AND VULNERABILITY OF COMPOSITE RAILWAY TRACK SLAB TO TRAIN DERAILMENTS

***Sakdirat Kaewunruen[1], Olivia Mirza[2] and Daniel Thomson[3]**

[1]School of Engineering, University of Birmingham, Edgbaston, B15 2TT UK
[2]School of Computing, Engineering and Mathematics, Western Sydney University, Kingswood NSW, 2577 Australia
[3]Engineering Services, Sydney Trains, Sydney NSW 2000 Australia

*s.kaewunruen@bham.ac.uk

ABSTRACT

Modern replacement of deteriorated timber transom sleepers by steel-concrete composite slabs can significantly improve asset management strategy for railway bridges over their life cycle. Track engineers can take advantage of steel-concrete composite technology over traditional concrete slabs. The design of such steel-composite track slabs has shown 10-20% reduction in the component depth and thus the weight. These benefits enable the composite slabs to fit brown-field maintenance project where merely aging transoms can be renewed and the new composite slabs can be installed over existing girders and support systems. In practice, railway bridge structure is designed to embrace redundancy assuring public safety. The risk and consequences of train derailment over the bridge has prompted railway authority to investigate the vulnerability of railway bridge system. Therefore, the design and modelling of this composite slab has been verified by previous work of the authors. This paper presents the dynamic responses and vulnerability of the composite track slabs to train derailments. A nonlinear finite element model of integrated train-track-bridge has been developed and validated using field data. The impact analysis has then been carried out using ABAQUS Explicit to evaluate the dynamic responses of the composite railway track slabs, benchmarked with quasi-static code-based design method. This study enhances the insight into the dynamic behaviour of vulnerable track slabs so that track engineers can predict the damage arisen from a train derailment.

Keywords: *Railway bridge; steel-concrete composite; transom; railway bridge sleeper; track slab, train derailment; failure analysis; dynamic finite elements*

1. Introduction

Over 90% of Australia's railway bridges are using timber transoms. Similar percentages of aged railway bridges in the UK and Europe have also utilised timber transoms (or commonly known as 'railway bridge sleepers'). At present, railway infrastructure managers require to renew around 3.5 million of aging and failing timber transoms around the world in order to upgrade the railway lines and to maintain existing rail lines. Griffin et al. [1-2] found that timber transoms are generally replaced within 10 to 20 years' period of time, resulting in a shorter turnover period and additional costs for track maintenance [3-4]. This research was undertaken to explore the replacement of timber transoms based on a case study for the iconic Sydney Harbour Bridge using new composite materials. Composite transoms are a good alternative to timber transoms due to the production of greenhouse gas emission for timber transoms are 6 times higher than in the concrete and composite transom [5]. However, an alternative material for the replacement of timber transoms shall be compatible with the existing structural system. Furthermore, it should also be able to be replaced without much effort in order to enhance resilience and maintainability [6-7]. Therefore, composite precast concrete retrofitted on the existing steel girder would be a good alternative.

It is interesting to find that train derailments keep presenting challenges to the railways system around the world. Indeed, not only can the derailments occur on turnouts and curved tracks, but they could also occur on a straight rail viaduct such as those due to broken bogie axles [8]. The aim of this study is to investigate the complex and unprecedented behaviour of composite transoms acting as track

slabs caused by train derailments. Failure modes of the rail transoms due to train derailments need to be well understood for public safety protection and fail-safe design principle of critical infrastructures. This outcome of this study will improve a performance-based design methodology for railway bridge transoms using steel-precast concrete composite members. Possible failure modes can be identified by previous failure investigations of railway bridges. Grayrigg train derailment in the UK [9] is a good example for progressive failure of railway structures triggered by derailments. Therefore, train derailment is a scenario, which cannot be ignored in designing structural components that enable a fail-safe railway system.

The steel-concrete composite transoms are being tested using full-scale specimens in the laboratory at Western Sydney University. However, in order to carry out experimental investigations, numerical analysis is required for a better insight into its dynamic behaviour so that test setup arrangement could be safely managed. Also, experiments are generally very expensive and time consuming. Therefore, this study is aimed at using numerical analysis to investigate the failure modes and behaviour of composite transoms caused by train derailment. Based on critical literature review, Brabie and Andersson [10] have investigated high speed derailments through various computer models. This simulation has been done on the wheel – sleeper impact when derailments occurred. They have further enhanced the model to simulate a post derailment scenario. Gu and Franklin [11] then created a model to analyse dynamic impact loading accurately. They considered the response of the railway bridge over the travelling speed of the train. Ju [12] studied non-linear behaviour of the wheel rail interaction. Effects of the profile of the track on derailment failure were later studied [13]. Fang and Zhang [14] developed a model to investigate the feasibility of using fiber concrete in transoms. In his study, a detailed parametric study was carried out by changing selected material properties of the fiber concrete to simulate different test models. However, all the above literatures did not considered the newly retrofitting precast steel-concrete composite slab into existing steel girders. The paper here is the first to look at the behaviour and failure modes of composite track slabs subjected to train derailment loads.

2. Structural track system, design load actions and derailment

Transoms are simply supported on stringers and the walk-way has been designed as a cantilever, as shown in Figure 1. The designed composite transoms are connected to the existing steel stringers using headed shear stud connectors. Existing rails then be fastened to the composite transoms using rail pads installed on steel baseplates. Actions of the design loads on transoms shall either be considered in their serviceability and ultimate limit states. LC1, LC2, LC5 and LC10, which will be described later, are considered as the most unfavorable load combinations or the set of worst case scenarios for design according to precedent research [1-2, 13]. The maximum static axle load acting on a transom during a train derailment has been taken as 20 tons, and its derailment impact can be calculated as per the guide lines established by the transport for New South Wales [2].

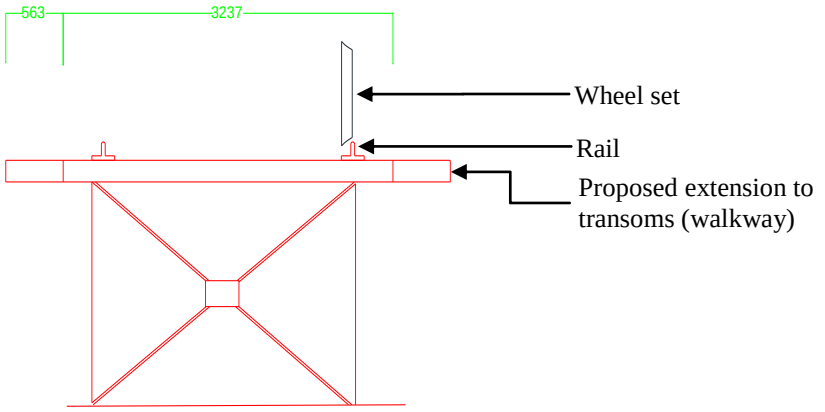

Figure 1: Structural system

3. Finite element model and its validation

Numerical model was developed using ABAQUS Explicit to simulate the impact of derailment loadings on the proposed steel-concrete composite panel [1-2]. For design purpose, the maximum influences on the composite transoms of single wheel derailment have been considered in the derailment model as is illustrated in Figure 2. Due to the nature of loading, which is applied on the stringer not being of importance, the model has been simplified using symmetry. The concrete slab and steel components were modelled using the eight-node linear hexahedral solid elements with reduced integration and hourglass control (C3D8R). Elements with reduced-integration have been adopted as they could reduce computing run time. These elements were incorporated in a reasonably fine mesh in order to improve the accuracy of these models. The mesh sizes were also verified by carrying out a sensitivity analysis to develop a convergence chart. The shear connectors were modelled using second order three-dimensional twenty-node quadratic brick elements with reduced integration (C3D20R). The connectors were modelled to represent the actual geometric size and shape within the limitations of the application. The reinforcing bars were modelled with two-node linear three-dimensional truss elements (T3D2). The track stiffness of 40 MPa (or rail displacement of 4.5mm specified by the rail authority) was used to validate the finite element model [2].

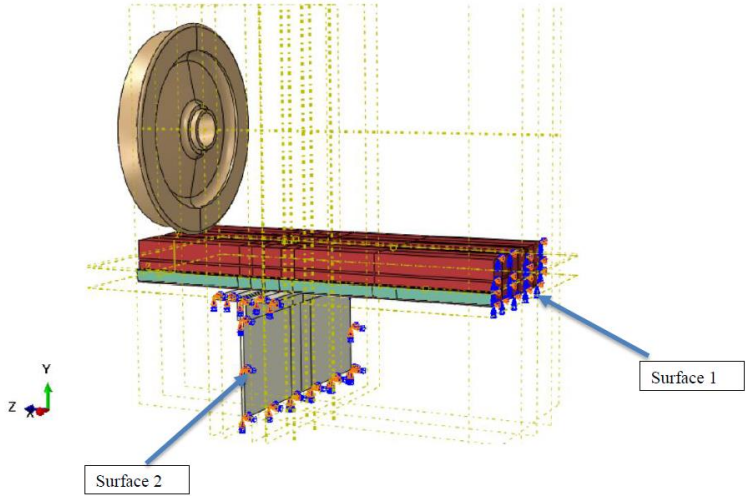

Figure 2: Finite element model

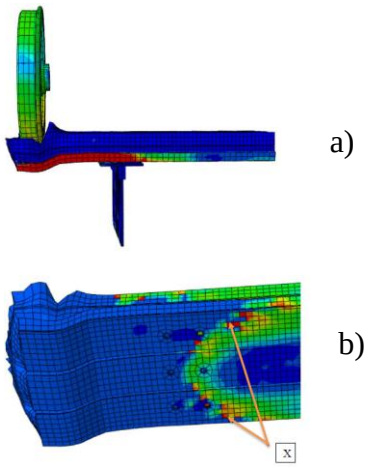

Figure 3: Finite element results

4. Results

The stress distribution in Figure 3(a) displays the resulting stress levels carried by the Bondek II at impact caused by derailment. The derailment relationship of the Bondek II is shown as stress versus time. From initial impact at time 0, the graph displays a linear curve up until about time 0.004, this is due to the combination of concrete and steel taking load. The maximum stress is reached at time 0.005 with a value of 550 MPa and fluctuates up until time 0.015. Beyond time 0.02 the stress level is reached and is maintained constant. Figure 3(b) displays the deformed model of the Bondek II caused at the impact once the wheel interacts with the panel. Figure 4 shows the parametric effects on the dynamic responses of the steel-composite composite track slab components.

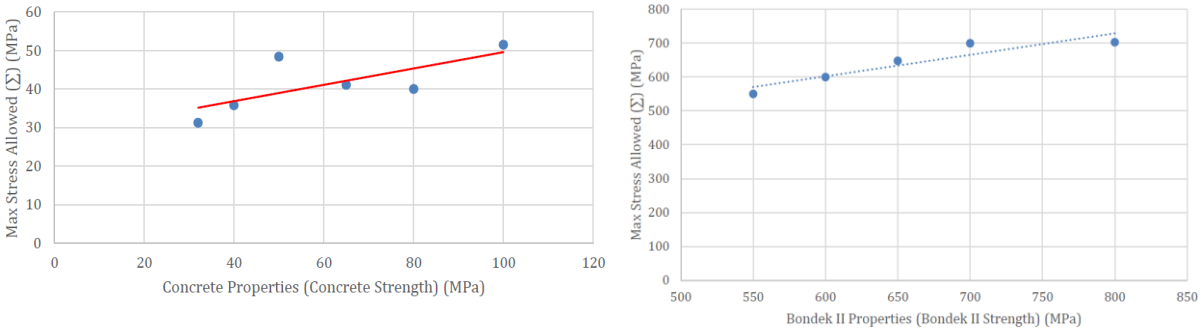

Figure 4: Parametric studies

5. Conclusions

Composite panels can be effectively used as a replacement of timber transoms in a railway bridge. In this study, the provisions given in the Australian standards was utilised for the composite steel-concrete transoms. A finite element model (FEM) was used to simulate the behavior of the composite transom under derailment loads. Impact loads were applied within a selected period of time. Allowable stresses in components of the composite transom could also be determined experimentally in the simulation. Stresses developed in various components were observed for deferent characteristic strength of the materials. The maximum allowable stress in concrete increased with increasing characteristic compressive strength of concrete. Defection control test simulation was done to find out the relationship between strength of Bondek sheet (yield strength) and the allowable stress. The allowable stress increased linearly until the yield strength of bondek sheet increased to 700MPa.

Acknowledgements

The first author wishes to gratefully acknowledge the Japan Society for Promotion of Science (JSPS) for his JSPS Invitation Research Fellowship (Long-term), Grant No L15701. The second author wishes to thank Western Sydney University for her Early Career Research Award. The authors are sincerely grateful to European Commission for the financial sponsorship of the H2020-RISE Project No. 691135 "RISEN: Rail Infrastructure Systems Engineering Network".

References

[1] Griffin, D., Mirza, O., Kwok, K., and Kaewunruen, S., 'Composite slabs for railway construction and maintenance: a mechanistic review', The IES Journal Part A: Civil & Structural Engineering, 7 (4), 243-262, 2014.

[2] Griffin, D., Mirza, O., Kwok, K., and Kaewunruen, S., 'Finite element modelling of modular precast composites for railway track support structure: A battle to save Sydney Harbour Bridge', Australian Journal of Structural Engineering, 16 (2), 150-168, 2015.

[3] Kaewunruen, S., Sussman, JM., and Einstein, H. H. 'Strategic framework to achieve carbon-efficient construction and maintenance of railway infrastructure systems'. Front. Environ. Sci. 3:6. 2015, doi:10.3389/fenvs.2015.00006.

[4] Kaewunruen S, Sussman JM and Matsumoto A. 'Grand challenges in transportation and transit systems'. Front. Built Environ. 2:4. 2016, doi: 10.3389/fbuil.2016.00004

[5] Krezo, S., Mirza, O., He, Y., Makim, P., and Kaewunruen, S. 'Field investigation and parametric study of greenhouse gas emissions from railway plain-line renewals'. Transp. Res. D Transp. Environ. 42, 77–90, 2016. doi:10.1016/j.trd.2015.10.021

[6] Kaewunruen, S., Griffin, DWP, Mirza, O, Kwok, K, 'Resilience-based design of precast steel-concrete composites for railway track slabs', Proceedings of the 13th International Railway Engineering Conference, Edinburgh, 30 June – 1 July, 2015.

[7] Kaewunruen, S., Meesit, R., 'Sensitivity of crumb rubber particle sizes on electrical resistance of rubberised concrete', Cogent Engineering, 3(1), 2016. doi:10.1080/23311916.2015.1126937

[8] Australian Transport Safety Bureau, 'Derailment of Sydney Trains Passenger Train 602M', ATSB Transport Safety Report Rail Occurrence Investigation RO-2014-001, Australian Capital Territory, Commonwealth of Australia, 2014.

[9] The Guardian, 'Grayrigg train crash', [Access Online URL http://www.theguardian.com/uk/grayrigg-train-crash], 2016.

[10] Brabie, D & Andersson, E, 'Dynamic simulation of derailments and its consequences', Vehicle System Dynamics, vol. 44, no. sup1, pp. 652-62. 2006.

[11] Gu, G & Franklin, FJ, 'Application of the structural articulation method to dynamic impact loading of railway bridges – a case study', Vehicle System Dynamics, vol. 48, no. 10, pp. 1097-113, 2010.

[12] Ju, SH, 'A simple finite element for nonlinear wheel/rail contact and separation simulations', Journal of Vibration and Control, vol. 20, no. 3, pp. 330-8. 2014.

[13] Remennikov A.M. and Kaewunruen, S., 'A review of loading conditions for railway track structures due to train and track vertical interaction', Structural Control and Health Monitoring, 15 (2), 207-234. 2008.

[14] Fang, Q and Zhang, J, 'Three-dimensional modelling of steel fiber reinforced concrete material under intense dynamic loading', Construction and Building Materials, vol. 44, no. 0, pp. 118-32. 2013.

DETERMINATION OF RELATIONSHIP BETWEEN UNIAXIAL COMPRESSIVE STRENGTH (UCS) AND ROCK DENSITIES USING FRACTAL MODELLING IN KAROUN-4 DAM, SW IRAN

Mahdi Mahdizadeh[1], Kaveh Ahangari[1], Akbar Javadi[2], Peyman Afzal[3, 4*], Amir Bijan Yasrebi[2, 4]
[1] Department of Mining Engineering, Science and Research Branch, Islamic Azad University, Tehran, Iran
[2] Computational Geomechanics Group, University of Exeter, Exeter, UK
[3] Department of Mining Engineering, South Tehran Branch, Islamic Azad University, Tehran, Iran
[4] Camborne School of Mines, University of Exeter, Penryn, UK

* peymanafzal@yahoo.com

ABSTRACT

The aim of this study is to identify different populations for rock characteristics based on uniaxial compressive strength (UCS) and density within limestones of Karoun-4 Dam, SW Iran. The results from a Number-Size (N-S) fractal model log-log plots for UCS and rocks' densities reveal that there are four populations for the studied variables. The last populations for UCS and density commence from 87 MPa and 2.65 t/m^3, respectively. Finally, a log-ratio matrix is applied to validate and determine the overlaps between the N-S fractal model for UCS and density values within the main rock type. The overall accuracy (OA) is 85% which shows that there are positive correlations between UCS and rock density in the Karoun-4 Dam.

Keywords: *number size fractal modelling; uniaxial compressive strength (UCS); logratio matrix; karoun-4*

1. Introduction

Outlining of host rock characterisation in terms of uniaxial compressive strength (UCS) and density is one of the fundamental aspects in a reservoir dam planning and design. Main host rocks of Iranian dams are carbonate rocks especially limestones and dolomites. Numerical models specifically based on geostatistics and fractal have been utilised to define various phenomena for better interpretation of the parameters' variability for rock mass characteristics in rock mechanics [1, 2, 3, 4].
Fractal/multifractal modelling, established by Mandelbrot (1983), has been used for delineation and classification of various parameters in mining engineering and geomechanical modelling such as ore grades, geophysical parameters and rock characteristics since the 1980s [5]. Consequently, several fractal models have been proposed and developed for a wide application from rock 1980s to mineral exploration [5, 6, 7, 8].
The purpose of this study is to recognise different populations for rock characteristics with respect to UCS and density within limestones as the main lithological unit of Karoun-4 dam, SW Iran according to the Number-Size (N-S) fractal modelling proposed by Mandelbrot (1983) [5]. Furthermore, a log-ratio matrix is used to determine the intersections between the N-S fractal model for UCS and density values within the limestones.

2. Studied area characteristics

The Karun 4 reservoir dam is an arch dam on the Karun River located in Charmahal and Bakhtyari Province, SW Iran (Fig. 1). Marginal part of Zagros orogeny has a high amounts of carbonate rocks especially limestones and dolomites. Main rock type of the studied area is limestones and minor lithological units are sandstones, marls and shales.

3. Methodology

In this study, 70 rock samples were collected from limestones in different situations within the dam

area and also, their UCS and density values were measured. Moreover, the main parts of the limestones were determined using N-S fractal modelling in terms of the above-mentioned variables. Finally, the main populations for these parameters were correlated and compared by the logratio matrix as proposed by Carranza (2011) [9].

Fig. 1: The location of Karoun-4 dam in Iran

4. N-S Fractal Modelling

The N–S fractal model can be utilised to describe the distribution of geomechanical populations without pre-processing of data. The N-S log–log plot describes the power law relationship according to the frequency distribution of size, which is UCS and density values in this study, and cumulative number of samples [5, 10]. This model is expressed by following equation [2, 5, 10]:

$$N(\geq\rho) = F\ \rho^{-D} \qquad (1)$$

Which in this equation ρ and N(≥ρ) denote elemental values (UCS and density) and samples cumulative number with values greater than or equal to ρ respectively, F is a constant and also, D is fractal dimension. The N-S log-log plots show straight lines segments, with different slopes (-D) corresponding to different intervals [10].

There are four populations based on the N-S log-log plot which indicate that the main UCS and density populations have the USC and density values higher than 87 MPa and 2.65 t/m^3, respectively (last populations: Fig. 2). The background parts for USC and density values are lower than 60 MPa and 2.45 t/m^3, respectively, as depicted in Table 1.

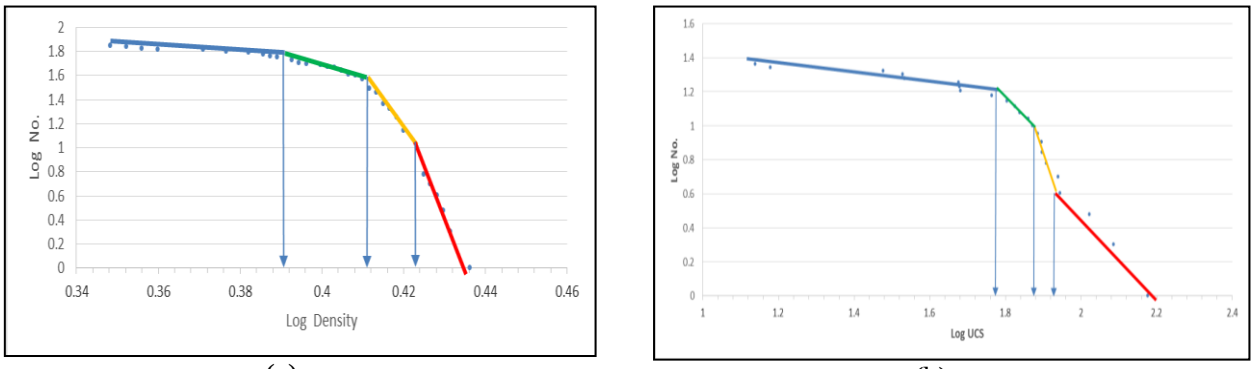

(a) (b)

Fig. 2: The N-S log-log plots for (a) Density for (b) UCS

Table 1: The UCS and density thresholds derived via the fractal modelling

UCS(MPa)	Density (g/cm3)
60	2.45
76	2.57
87	2.65

5. Correlation between the UCS and density

Based on the N-S fractal modelling, the main populations of UCS and density for limestones were compared and correlated by the logratio matrix proposed by Carranza (2011) [9]. An intersection operation between major parts of UCS and density derived via the fractal modelling was performed to obtain the number of samples according to each of the four classes, as indicated in Table 2. Overall accuracy (OA) of the populations was calculated which shows that the OA is 0.85. This reveals that there is a direct relationship between high intensity populations of UCS and density within limestones.

Table 2: The correlation between main UCS and density populations

		Main density population (> 2.65 t/m^3)	
		Inside zone	Outside zone
Main UCS population I(> 87 MPa)	Inside zone	True positive (A) = 2	False positive (B) = 8
	Outside zone	False negative (C) = 4	True negative (D) = 68
		Overall accuracy = (A+D)/(A+B+C+D) = 0.85	

6. Conclusions

Results obtained by the N-S fractal modelling show that there is a positive and direct relationship between two important parameters of rock characteristics including UCS and density in the Karoun-4 dam, SW Iran. The major populations of these characteristics obtained by fractal modelling have a good correlation based on the high value for OA resulted via the logratio matrix. As a result, the limestones contain high density with large values of UCS.

References

[1] A.B. Yasrebi, A. Wetherelt, P. Foster, J. Coggan, P. Afzal, F. Agterberg, D. Kaveh Ahangaran, Application of a density–volume fractal model for rock characterisation of the Kahang porphyry deposit. *International Journal of Rock Mechanics and Mining Sciences*, 66, 188-193, 2014.

[2] A.B. Yasrebi, A. Wetherelt, P. Foster, P. Afzal, J. Coggan and D. Kaveh Ahangaran. Application of RQD number and RQD-Volume multifractal modelling to delineate rock mass characterisation in Kahang Cu-Mo porphyry deposit, central Iran. *Arch. Min. Sci*, 58, 1023–1035, 2013.

[3] A. Rafiee and M. Vinches. Application of geostatistical characteristics of rock mass fracture systems in 3D model generation. International Journal of Rock Mechanics and Mining Sciences, 45, 644-652, 2008.

[4] A.B. Yasrebi, A. Wetherlet, P.J Foster, J. Coggan. APPLICATION OF A DENSITY-NUMBER (D-N) FRACTAL MODELLING TO CORRELATE MINERALISED ZONES IN KAHANG Cu-Mo PORPHYRY DEPOSIT. *22th UK Conference of the Association for Computational Mechanics in Engineering proceeding, Exeter, UK*, 9–12, 2014

[5] B.B. Mandelbrot, *The Fractal Geometry of Nature*, W.H. Freeman, Updated and Augmented Edition, San Francisco, 1983.

[6] F. P. Agterberg, Q. Cheng & D. F. Wright, Fractal modelling of mineral deposits. *In J. Elbrond, X. Tang (Eds.), 24th APCOM symposium proceeding, Montreal, Canada*, 43–53, 1993

[7] R. Zou, Q. Cheng, Q. Xia, Application of fractal models to characterization of vertical distribution of geochemical element concentration. *Journal of Geochemical Exploration*, 102(1), 37–43, 2009.

[8] P. Afzal, A. Y. Fadakar, A. Khakzad, P. Moarefvand, N. Rashidnejad Omran, H. Asadi Haroni, Application of power-spectrum-volume fractal method for detecting hypogene, supergene enrichment,

leached and barren zones in Kahang Cu porphyry deposit, Central Iran. *Journal of Geochemical Exploration*, 112,131–138, 2012.

[9] E. J. M. Carranza, Analysis and mapping of geochemical anomalies using log ratio transformed stream sediment data with censored values. *Journal of Geochemical Exploration*, 110, 167–185, 2011.

[10] Sh. Hassanpour, P. Afzal, Application of concentration-number (C-N) multifractal modelling for geochemical anomaly separation in Haftcheshmeh porphyry system, NW Iran. *Arabian Journal of Geosciences*, 6, 957–970, 2013.

Proceedings of the 24th UK Conference of the
Association for Computational Mechanics in Engineering
31 March – 01 April 2016, Cardiff University, Cardiff

DELAMINATION CHARACTERISTICS OF GLARE LAMINATES CONTAINING DOUBLER AND SPLICE FEATURES UNDER HIGH CYCLE FATIGUE LOADING

Ahmad S.M. Al-Azzawi [1,3]*, L.F. Kawashita [2], C.A. Featherston[1]

[1] Cardiff School of Engineering, Cardiff University, The Parade, Cardiff, CF24 3AA, UK
[2]Advanced Composites Centre for Innovation and Science, University of Bristol, Bristol, BS8 1TR, UK
[3] College of Engineering, University of Babylon, Babylon, Iraq

*Corresponding author: Email address. Al-AzzawiAS@cardiff.ac.uk

ABSTRACT

A modified cohesive zone model (CZM) has been developed to simulate damage initiation and evolution in Glare™ Fibre-Metal Laminate (FML) specimens containing both splice and doubler features under high-cycle fatigue loading. The model computes the cohesive stiffness degradation under mixed-mode loading based on user-defined crack growth rate data and is implemented in a VUMAT subroutine for the FEA software Abaqus/Explicit. To validate the model experimental data has been obtained for a number of Glare 4B specimens containing splice and doubler features monitored using digital image correlation (DIC) to provide full-field displacement and strain data and Acoustic Emission (AE) monitoring to detect damage initiation and propagation. The model was used to predict the initiation and growth of damage in splice joints under quasi-static loading. The results were verified against the cohesive zone model available in Abaqus and then validated against experimental data on Glare specimens. The codes are currently being extended to incorporate a mixed-mode fatigue damage evolution model based on input Paris laws, which have been extracted from high cycle fatigue experiments on Glare specimens containing both splice and doubler joints.

Keywords: *Fibre Metal Laminates, Fatigue, Cohesive Zone Model, DIC, AE*

1. Introduction

FMLs including Glare are manufactured from alternating metallic sheets bonded with fibre reinforced composite layers. Where large panels are required joints including splices (where metallic sheets are positioned side by side with a gap in between, with the gaps staggered to prevent loss of strength and the fibre layers providing load transfer) and doublers (additional external or internal layers introduced to reduce stresses) are used. One of the most common failure modes for FML structures is delamination in these joints [1]. Delamination in fibre composites has been modelled by researchers using a number of different approaches. These include the cohesive zone model (CZM) which incorporates both continuum damage and fracture mechanics concepts [2] and which has been used to model delamination initiation and propagation under high cycle fatigue [3-7]. This paper describes work done to extend this application to FMLs.

2. Experimental work

Fatigue tests were conducted on a series of Glare specimens containing splice and doubler features. Specimens had dimensions 153 mm × 13.5 mm and were manufactured from GLARE 4B which consists of 2024-T3 aluminium alloy sheets 0.4 mm thick and UD-S2 glass fibre reinforced epoxy (GFRP) layers each having 3 plies with the layup [$90^o/0^o/90^o$] and a cured ply thickness of 0.125 mm (Figure 1). They were tested in an MTS servo-Hydraulic (50 kN) machine using the setup shown in Figure 2 with a constant load ratio (trough/peak) of R= 0.1 and a frequency 5 Hz.

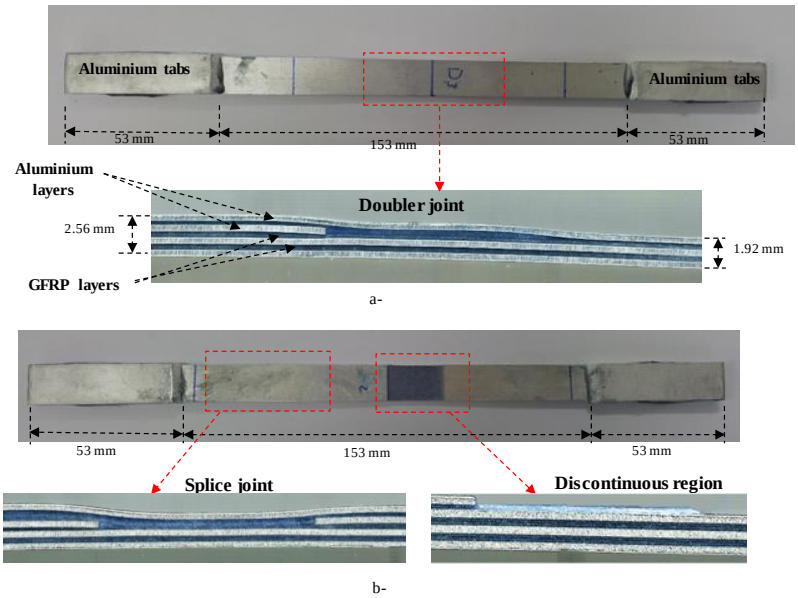

Figure 1. Specimen design for a) doubler b) splice

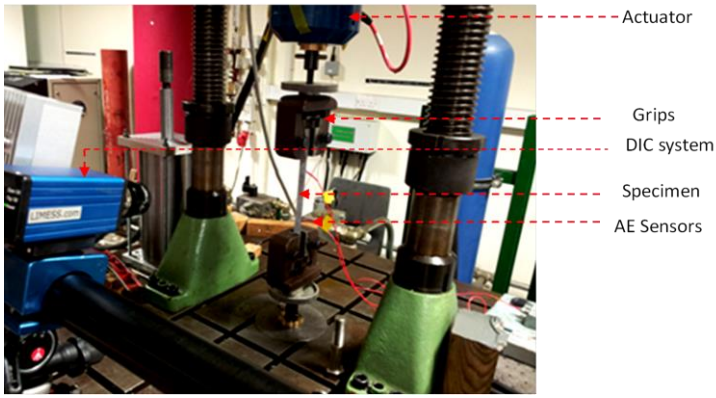

Figure 2. Experimental fatigue test setup

3. FE model

Two types of model were created to analyse the delamination behaviour of the joints. Initially a simplified model was generated as shown in Figure 3 in order to validate the cohesive zone approach for static loading. Following this a more accurate model of the specimens was created to explore the effect of fatigue loading. This involved extracting the geometry and thickness of each layer from scans of the actual specimens, as shown in Figure 4, and then meshing them using linear continuum elements (CPS4R). The interfaces were then meshed using two dimensional cohesive elements (COH2D4). In both cases a mixed mode cohesive zone model (CZM) (Figure 5) was assumed using a quadratic nominal stress criterion for damage initiation (equation 1) and a power law failure criterion (equation 2) for damage evolution. Strain energy release rates G_I and G_{II} where calculated using equations 3 and 4 and the power law parameter ϕ was determined by the best fit to mixed-mode delamination data from the literature [8]. Finally the model was implemented in the FEA software Abaqus/Explicit using a VUMAT subroutine.

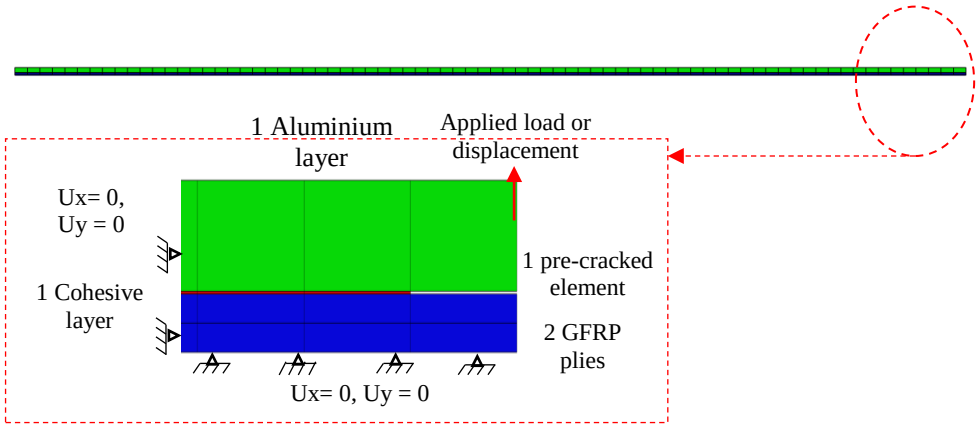

Figure 3. Simplified model

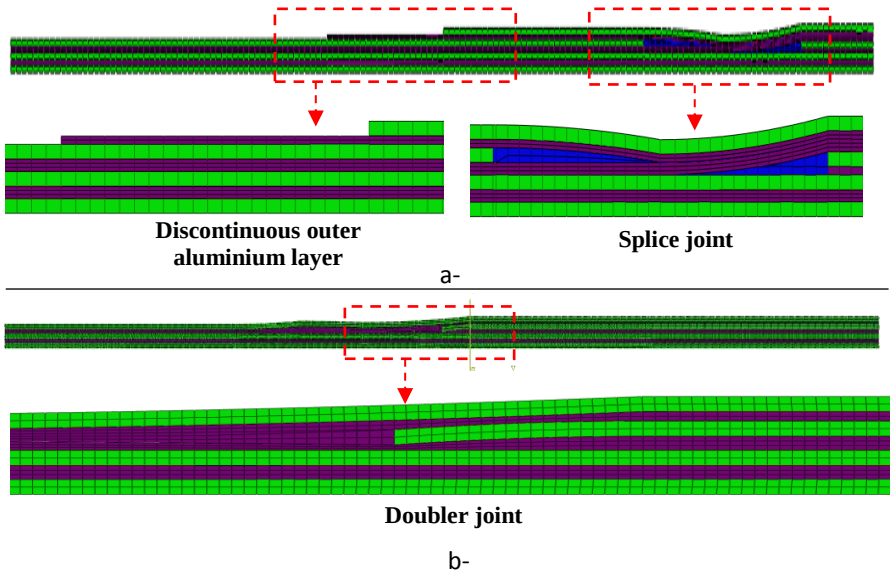

Figure4. 2D mesh for Glare4B specimens a) Splice b) Doubler

$$(\frac{\sigma_I}{\sigma_{Ic}})^2 + (\frac{\sigma_{II}}{\sigma_{IIc}})^2 = 1 \quad \text{... (1)}$$

$$(\frac{G_I}{G_{Ic}})^\phi + (\frac{G_{II}}{G_{IIc}})^\phi = 1 \quad \text{... (2)}$$

$$G_I = \int_0^u \sigma_I \, du_I \quad \text{... (3)}$$

$$G_{II} = \int_0^u \sigma_{II} \, du_{II} \quad \text{... (4)}$$

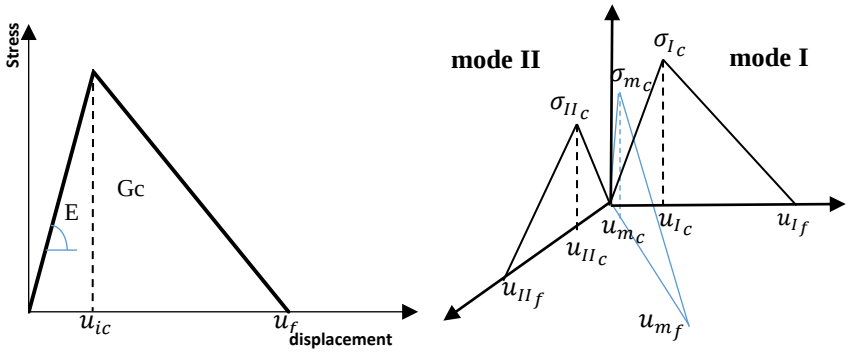

Figure5. Mixed mode cohesive law

The simplified model was loaded statically as shown in Figure 3. Fatigue loading on the other hand can be represented by a constant amplitude load equal to the maximum load level in the actual fatigue cycle. Only the envelopes of loads and displacements are then analysed following a 'cycle-jump' strategy [3-7] .As shown in Figure 6, the force applied to the model is increased gradually from zero to the peak load (F_{max}), and a fatigue degradation law is then activated to model fatigue crack growth and the corresponding reduction in overall stiffness and increase in axial displacement. Future results of fatigue tests will use this approach to calculate crack growth rate using a normalised Paris law:

$$\frac{da}{dN} = C\left(\frac{\Delta G}{G_c}\right)^m \quad \text{... (5)}$$

Where *da/dN* is the crack growth rate (increment in crack area with increasing number of cycles) and *C* and *m* are best fit coefficients to experimental data in a log-log plot.

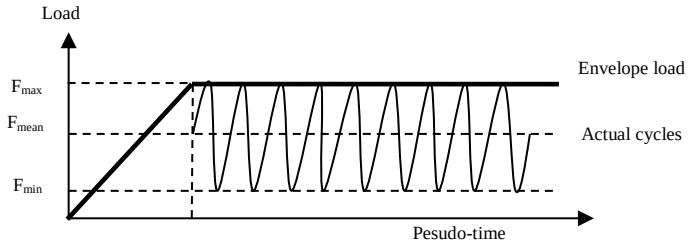

Figure 6. Schematic of fatigue modelling envelope load

4. Results and conclusions

The experimental results illustrated in Figure 7 show that the fatigue life for the doubler specimens was higher than for the splice specimens, as the doubler joint exhibited high fatigue damage tolerance compared with the splice joint. The results also showed that delamination onset and growth occured in the external discontinuous Aluminium/ GFRP interface for the splice specimens, while the doubler specimens did not show any delamination. The FE results for the simplified model in Figure 8 show good correlation with the ABAQUS cohesive zone model as expected. Although there is a small difference in simulation time (pseudo-time) for damage initiation, the damage evolution parameter is identical and the small differences are attributed to small oscillations in stresses in the VUMAT subroutine which is currently free of any viscous regularisation or damping. Ongoing work focuses on adding a Paris law-based fatigue damage evolution rule as described above.

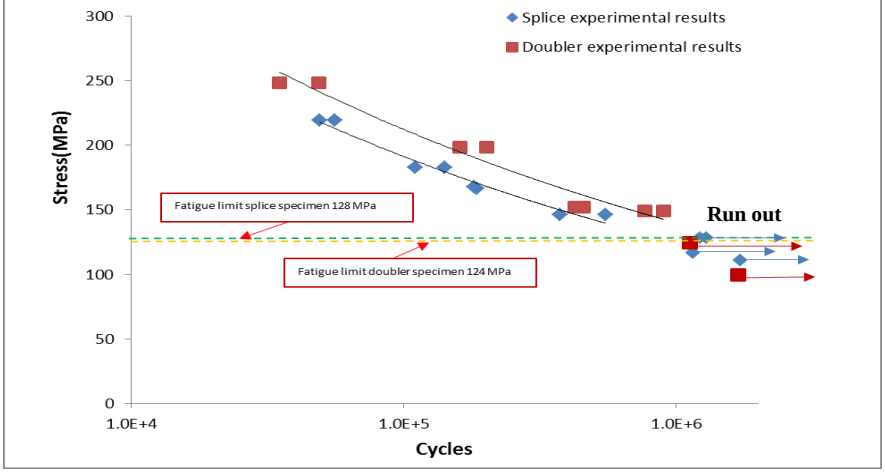

Figure 7. S-N curve comparison for doubler and splice specimens

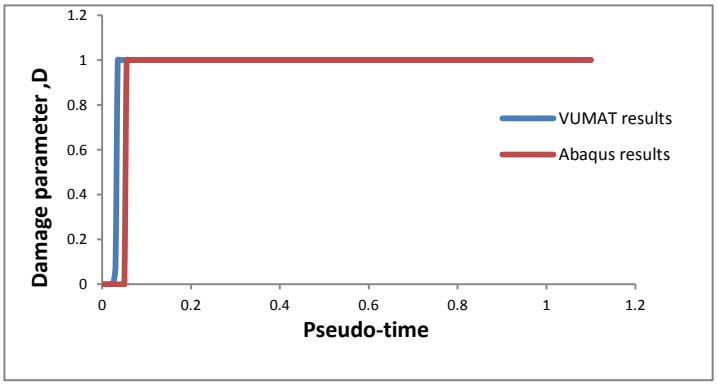

Figure 8. Comparison of evolution of static damage parameters

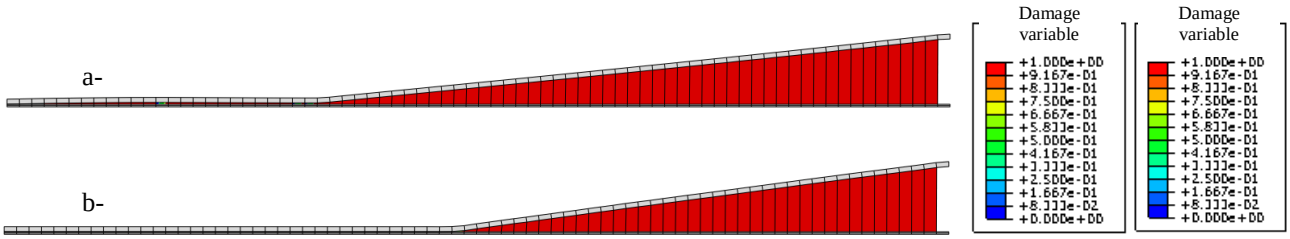

Figure 9. Comparison of evolution of static damage parameters, a- VUMAT results, b- Abaqus results

References

[1] J.W. Gunnink, A.D. Vlot, *Fibre Metal Laminates - An Introduction*. 2001, London: Kluwer Academic publishers.

[2] D.S. Dugdale, *Yielding of Steel Sheets Containing Slits.* Journal of the Mechanics and Physics of Solids, 1960. **8** p. 100-104.

[3] A. Turon, J. Costa, P.P. Camanho, C.G. Da´vila, *Simulation of delamination in composites under high-cycle fatigue.* Composites: Part A 2007. **38** p. 2270–2282.

[4] M.F.S.F. de Mouraa, J.P.M. Gonçalves, *Cohesive zone model for high-cycle fatigue of composite bonded joints under mixed-mode I+II loading*. Engineering Fracture Mechanics 2015. **140**: p. 31–42.

[5] Paul Robinson, U. Galvanetto, D. Tumino,G. Bellucci, D. Violeau, *Numerical simulation of fatigue-driven delamination using interface elements.* International Journal for Numerical methods in Engineering, 2005. **63**: p. 1824–1848.

[6] Paul W. Harper, S.R. Hallett, *A fatigue degradation law for cohesive interface elements – Development and application to composite materials.* International Journal of Fatigue 2010. **32**: p. 1774–1787.

[7] Luiz F. Kawashita, S.R. Hallett, *A crack tip tracking algorithm for cohesive interface element analysis of fatigue delamination propagation in composite materials.* International Journal of Solids and Structures 2012. **49** p. 2898–2913.

[8] Wen-Guang Jiang, S.R. Hallett, B.G. Green, M.R. Wisnom, *Aconcise interface constitutive lawfor analysis of delamination and splitting in composite materials and its application to scaled notched tensile specimens.* International Journal for Numerical methods in Engineering, 2007. **69**: p. 1982–1995.

Proceedings of the 24th UK Conference of the
Association for Computational Mechanics in Engineering
31 March – 01 April 2016, Cardiff University, Cardiff

Fast and Reliable Acoustic Emission Source Location Technique in Complex Structures

***Safaa Al-Jumaili[1,2], Matthew Pearson[1], Karen Holford[1], Mark Eaton[1] and Rhys Pullin[1]**

[1]Cardiff School of Engineering, Cardiff University, Queen's buildings, The Parade, Cardiff, CF24 3AA, UK
[2]University of Basrah, Basrah, Iraq

*Al-JumailiSK@cardiff.ac.uk

ABSTRACT

Acoustic emission (AE) provides engineers with a powerful tool by allowing the location of damage sources as they occur. Damage localisation using traditional time of arrival approaches is inadequate in complex structure components. Cardiff University presented a novel approach known as Delta T mapping which overcame these limitations but it was considered as time consuming and an operator dependent approach. This paper presents new full automatic Delta T mapping technique overcomes these remaining limitations.

Keywords: *acoustic emission; source location; complex structure; unsupervised clustering; Delta T technique*

1. Introduction

Damage localisation in complex structures, such as those found in aerospace applications, is a difficult problem in the field of structural health monitoring (SHM). The development of an easy to use, fast to apply, cost-effective and very accurate technique is key for the uptake of SHM. The use of Acoustic Emission (AE) [1] is important for SHM as it offers the potential for the real time monitoring of the health of a structure. Acoustic emission (AE) arising from damage mechanisms and propagating through the structure in the form of Lamb waves can be detected using piezoelectric sensors mounted on the surface of the structure. The ability to track the early onset of damage and hence determine the structure's integrity will enable the switch from periodic inspections to a more condition based approach, therefore enabling increased inspection intervals, reducing structure downtime and maintenance costs.

The time of arrival (TOA) technique is traditionally used to locate these sources, and relies on the assumption of constant wave speed within the material and uninterrupted wave propagation path between the damage and the sensor. In reality, structural complexities such as holes and thickness changes that may be present, which alter the wave propagation path and velocity. In order to overcome these limitations, Cardiff University developed a technique (called Delta T Mapping [2]) to locate damage in complex structures with high accuracy [3-5] by using artificial sources on an area of interest to create training maps. These maps are used to locate subsequent AE events arising from damage events. However, this technique needs high operator expertise to deal with the training map data (e.g. selecting the correct data) which can be a time consuming process as well as it requires the cluster diameter value to be identified in advance to be able to calculate the source location (only the convergence points inside a specific cluster diameter are used to calculate the probable AE source location). The most recent version of Delta T technique is known as the AIC Delta T Mapping technique and was developed by Pearson et al [6, 7] and overcame the limitation of arrival time calculation, another source of error in the traditional approach.

In this paper, a new and improved fully automatic Delta T Mapping technique is present. Here the correct data in the training maps were identified and selected automatically using a clustering algorithm and a new approach (Minimum Difference approach) is used to determine the damage location. This paper reports experimental validation of the advantages of the new techniques achievements. The results showed excellent reduction in running time (from 7 hours to only 11 seconds) as well as improved accuracy (location error improved from 4.96mm to 3.88mm in a complex geometry).

2. Automatic Delta T mapping technique Methodology

This approach can be divided into two parts; firstly, selecting the valid events (to be used for creating the initial maps) at each grid point using an unsupervised clustering technique and secondly, calculating the AE source location using the Minimum Difference approach [1].
In the first part, after collection of the training data by applying H-N sources [8] (an artificial AE source) on each node position in the grid the time of arrival to each sensor is obtained using the AIC approach [9]. The classification process is applied at each grid position to select AE events which are highly similar to each other, where the input data vector for the clustering process is the time difference between sensors pairs and will be used for the similarity criteria by following these steps:

- In each point of the Delta T grid, the recorded hits were separated automatically to create AE events using a time based approach. Simultaneously, the incorrect erroneous data were automatically removed.
- The AE hits from each point within the delta grid are correlated with the point coordinates (x, y) automatically, using time stamps placed by the operator within the collected data. Where the time stamps are placed in the data following acquisition from each grid node and are then used to automatically identify which hits are associated with each grid node.
- Each event is identified by the calculated difference in time of arrival for each sensor pair (e.g. the case of four sensors creates six sensor pairs 1-2, 1-3, 1-4, 2-3, 2-4 and 3-4).
- A complete link hierarchical clustering algorithm [10] is then used to group events based on their similarity, or correlation coefficient. In this work the 0.99 correlation coefficient level from the largest group was selected and all events in this group were used (correlation coefficient of 1 means total correlation).
- Delta T maps from the average values of the difference in time of arrival for each sensor pair are calculated for the selected highly correlated events at each grid point.
- Calculate location of real AE data: the Minimum Difference approach is a numerical approach, which is dependent on finding the point at which the difference between the source data and the training map data is minimised.

3. Experimental Procedure

An aerospace grade 2024-T3 aluminium plate, with dimensions of 370 x 200mm with a thickness of 3.18mm was used to assess the performance of the new technique. The specimen contained a series of differing diameter circular holes as shown in Figure 1a. A MISTRAS PCI-2 system was used to record all AE data at 40 dB threshold and 2MHz sampling rate. Four MISTRAS Nano-30s were adhered on the front face of the specimen (Figure 1a) using silicon RTV (Loctite 595). All transducers were connected to MISTRAS 0/2/4 pre-amps which had a frequency filter of 20 kHz to 1MHz. The Delta T Mapping grid on the specimen covered an area of interest of 200mm x160mm and had a resolution of 10mm (Figure 1a). Five H-N sources were used at each node position within the grid. In order to assess the performance of the new Delta T mapping technique in a more complex structure, six arbitrary positions were selected within the Delta T grid and three H-N sources were conducted at each position. The average wave speed was calculated as 5400 m/s. Source locations were calculated using all four sensors using the traditional approach, Time of Arrival (TOA), AIC Delta T and the new Automatic Delta T for comparison.

4. Results and Discussion

Source location calculations using the AIC Delta T were conducted using 20mm cluster diameter (calculated using a trial and error procedure) and the training maps were filtered manually. For the Automatic Delta T source location calculations, the training maps are constructed automatically using the unsupervised clustering procedure. The source locations are then calculated using the Minimum Difference approach. Finally, the TOA location results were exported directly from the MISTRAS AEwin software. Figure 1b shows the source locations on the specimen from the three location methods.

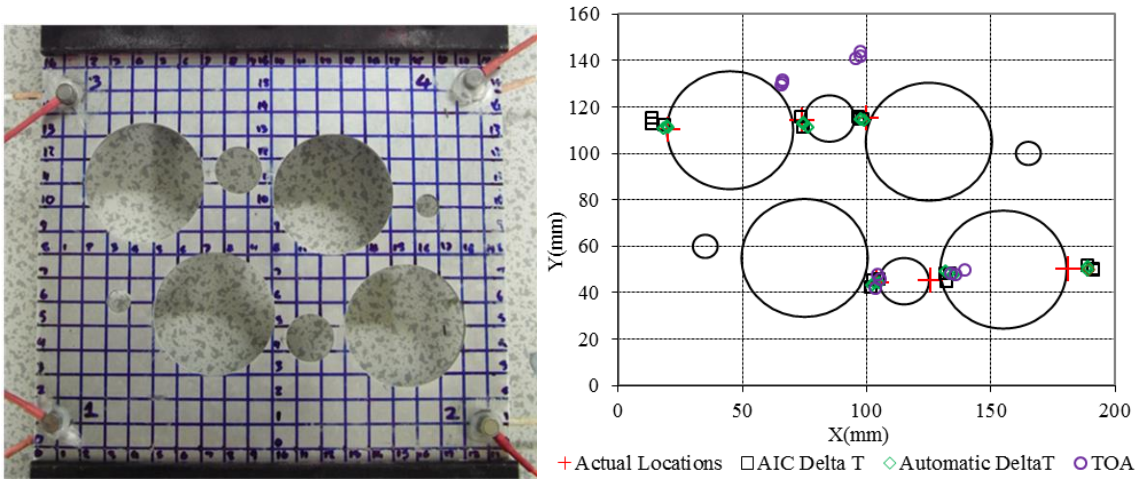

(a) (b)

Figure 1: (a) Specimen Configuration (b) Calculated source location by three techniques

A comparison between the three methods results are provided in Table 1. From the table it's clear that the average error of the Delta T techniques is considerably lower than the TOA and offers an improvement in accuracy from 222 mm to approximately 5mm. As well as the automatic Delta T shows an improvement in accuracy over the AIC Delta T results by reducing the error from 4.96mm to 3.88mm.

Furthermore, there is significantly reduces the time invested in implementing the technique. The most time consuming step in the AIC Delta T is represented by the selection and preparing of the AE data to construct the training maps which takes approximately 7 hours. On the other hand, the Automatic Delta T mapping is very fast and reduces the running time for constructing the training maps to approximately 11 seconds which is a significant improvement. Moreover, the new Delta T does not require the trial and error process of determining the optimal cluster diameter when compared with the AIC Delta T the cost is approximately 3.6 hours.

Table 1 Techniques performance comparison

	TOA	AIC Delta T	Automatic Delta T
Average location error	222.18mm	4.96mm	3.88mm
One standard deviation of the average	±177.75mm	±3.14mm	±3.19mm
Prepare the AE data to construct training maps	-	25200 sec (7 hours)	10.88 sec
Calculate the optimal Cluster size	-	13089	0

5. Conclusions

A new fully Automatic Delta T technique is introduced and verified experimentally using a complex structure. The results obtained are excellent and demonstrate the success of the adopted methodology. The AIC Delta T technique has been improved, with this approach, considerably and has increased in processing speed, increased reliability, efficiency, more accurate, increased simplicity and more capability to apply in large scale structures.

The results of this study highlight the potential for the use of AE monitoring as a tool of SHM for damage localisation tasks; a high simplicity, fast, reliable, cheap and accurate technique has been presented. If this technique is integrated with commercial AE monitoring systems, it will be a powerful tool to provide real time highly accurate source location within complex large-scale components.

Acknowledgements

The authors would like to thank the Iraqi Ministry of Higher Education and Scientific Research for supporting this research and the technical staff of Cardiff University School of Engineering for their kind assistance with the testing programme.

References

[1] K. R. Miller and E. K. Hill, *Non-Destructive Testing Handbook; Acoustic Emission Testing*, American Society for Non-Destructive Testing, VoL 6, 3rd Edition, 2005.

[2] M. G. Baxter, R. Pullin, K. M. Holford *et al.*, Delta T Source Location for Acoustic Emission, *Mechanical Systems and Signal Processing*, vol. 21, no. 3, pp. 1512-1520, 2007.

[3] S. K. Al-Jumaili, K. M. Holford, M. J. Eaton *et al.*, Classification of acoustic emission data from buckling test of carbon fibre panel using unsupervised clustering techniques, *Structural Health Monitoring*, vol. 14, no. 3, pp. 241-251, 2014.

[4] D. Crivelli, M. Guagliano, M. Eaton *et al.*, Localisation and identification of fatigue matrix cracking and delamination in a carbon fibre panel by acoustic emission, *Composites Part B: Engineering*, vol. 74, pp. 1-12, 2015.

[5] J. P. McCrory, S. K. Al-Jumaili, D. Crivelli *et al.*, Damage classification in carbon fibre composites using acoustic emission: A comparison of three techniques, *Composites Part B: Engineering*, vol. 68, pp. 424-430, 1, 2015.

[6] M. Pearson, Development of lightweight structural health monitoring systems for aerospace applications, *PhD Thesis*, Cardiff School of Engineering, Cardiff University, UK, 2013.

[7] M. R. Pearson, M. Eaton, C. A. Featherston *et al.*, Improved Acoustic Emission Damage Source Location During Fatigue Testing of Complex Structures, *Proceedings of the 34th Conference and the 28th Symposium of the International Committee on Aeronautical Fatigue and Structural Integrity (ICAF2015)*, vol. Helsinki, Finland, no. ISBN 978-951-38-7442-1, 1st – 5th June, 2015.

[8] N. N. Hsu, and F. R. Breckenridge, Characterization and Calibration of Acoustic Emission Sensors. *Materials Evaluation*, vol. 39, no. 1, pp. 60-68, 1981.

[9] H. Akaike, Markovian representation of stochastic processes and its application to the analysis of autoregressive moving average processes, *Annals of the Institute of Statistical Mathematics*, vol. 26, no. 1, pp. 363-387, 1974.

[10] M. R. Anderberg, *Cluster analysis for applications*, Academic Press, New York, 1973.

Proceedings of the 24th UK Conference of the
Association for Computational Mechanics in Engineering
31 March – 01 April 2016, Cardiff University, Cardiff

Experimental Model-Based Simulation for Health Monitoring of a Non-Linear Liquid Level System

***Ali A G Al-Khafaji[1, 2] and **Roger I Grosvenor[1]**

[1]School of Engineering, Cardiff University, Queen's Building, Cardiff, CF24 3AA
[2]Al-Nassiriya Technical Institute, Southern University, IRAQ

*al-khafajiaa@cardiff.ac.uk and **grosvenor@cardiff.ac.uk

ABSTRACT

Due to new technologies, the improvement of industrial systems is progressively complex. Accordingly, it has become difficult to manage and predict the behaviour of these systems, particularly when they will be exposed to failures. An identical dynamic model should reflect all characteristics of a planned integrated mechatronic system. Health monitoring of any system is essential in guaranteeing the safe, efficient, and correct operation of complex engineering systems. This paper presents a simulation of a non-linear, experimental based model of a coupled tank apparatus CE 105 by using LabVIEW 2014. In this study, a common modelling paradigm with several sources of fault was used to simulate both nominal and faulty behaviour. It is concluded that the liquid level, in the presence of a PID controller, will not be affected by the fault value until it reaches a certain threshold. Hence, the end of the useful life could be predicted by monitoring the PID voltage.

Keywords: *nonlinear system; health monitoring; liquid level system; model based simulation*

1. Introduction

Liquid level systems have an extensive variety of industrial process applications, such as petrochemical industries, papermaking, water treatment industries, and power plants. For example, controlling a liquid level in a tank and consequently the free outflow rate by using Proportional- Integral- Derivative (PID) controller is of crucial importance for mixing reactant processes [4]. A liquid level system is commonly controlled by using a conventional PID controller. This feedback controller minimises error through regulating the process-controlled inputs, the pump voltage for example [6]. Ogata [7] stated that a liquid level system can be considered linear if the liquid outflow is laminar; $Q = K\,h$, where Q is a steady-state liquid outflow rate, [m^3/sec], K is a coefficient [m^2/sec] and h is a steady-state head, [m]. If the flow through the outlet valve is turbulent, the steady-state outflow rate is: $Q = K\sqrt{h}$. Ogata [7] also stated that if the flow is turbulent, the system can be linearized when the change in the variables are kept small. The square root characteristic is widely used to model the flow through hydraulic orifices. This may cause numerical problems because the derivative of the flow with respect to the pressure drop tends to infinity when the pressure drop approaches zero. Furthermore, it is more reasonable to assume that the relationship between the free outflow rate and the pressure drop is linear for small values of pressure drop [2]. Non-linearity is the nature of all real systems [5].

PID controller is a widely recognisable type of feedback controller. A PID controller calculates an "error" value as a difference between the required demand and the measured process or plant variable. The purpose of the controller is to minimise the error through regulating the process-controlled inputs as each element of the PID controller assigns a specific activity taken on the error [6]. The liquid level system is commonly controlled by using a conventional PID. The main reason for using a PID controller is on account of its simple structure and application.

The contribution reported in this paper relates to the simulation and experimental validation of a CE 105 coupled-tank liquid level control system. The consideration of this system is extended via the inclusion of non-linear elements in the simulation created using a real-time control toolbox within LabVIEW 2014. The simulation is used to accelerate the timescales of monitoring in order to have a prior knowledge of the system behaviour and track different operational scenarios. Furthermore, faults

diagnosis and the remaining useful life prediction could be achieved in advance. Results are reported and discussed for a leakage and reduced pump performance faults.

2. Description of the coupled tank system

The coupled tank apparatus CE 105 was selected to study its nominal and faulty behaviour. In this set-up, a PC with NI USB– 6008 DAQ and LabVIEW 2014 programme serves to control and manage the system, as shown in Figure 1.

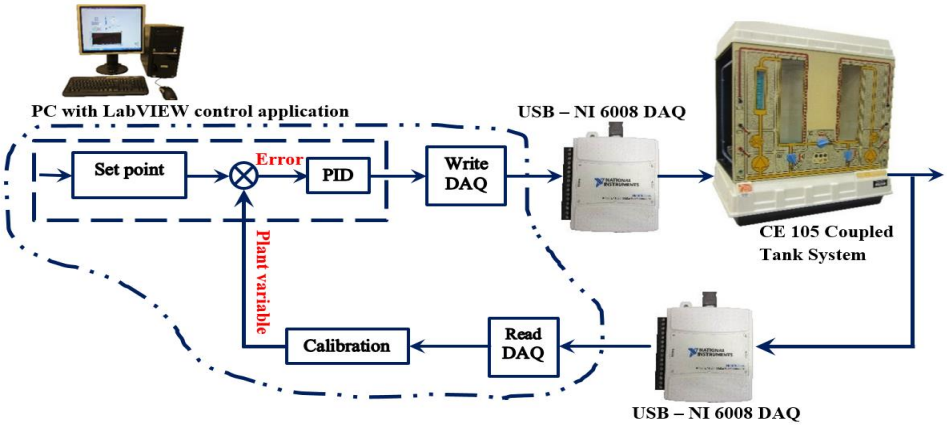

Figure 1: Schematic diagram of the system

3. Calibration equations

Open loop experimental tests were done on the CE105 apparatus in order to estimate the calibration equation of each single element of the system; the results are as shown in Figure 2.

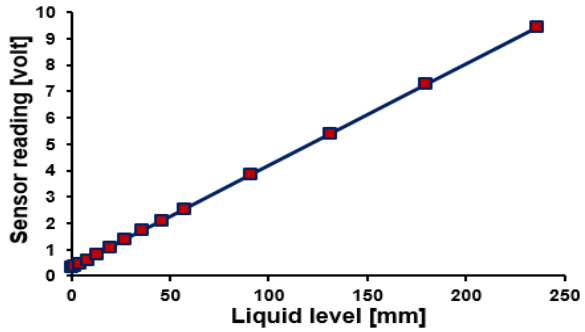

a. Calibration of the liquid level sensor [mm] to [volt]

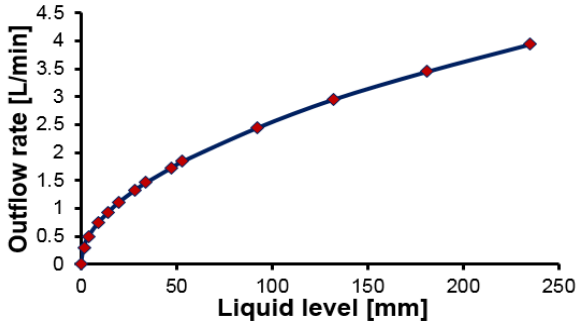

b. Steady state outflow rate [L/min] VS Liquid level [mm]

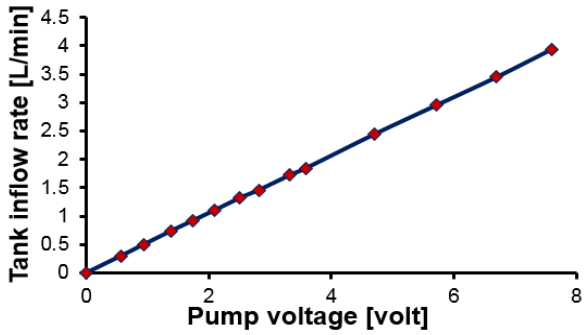

c. Tank inflow rate [L/min] VS Pump voltage [volt]

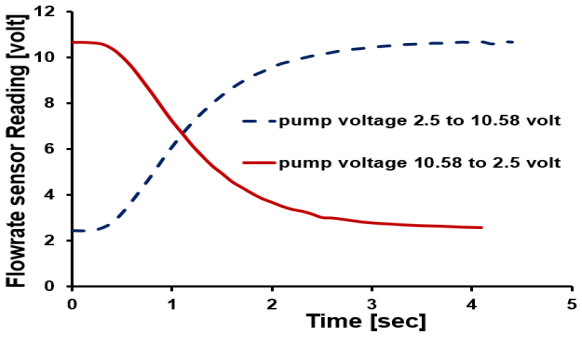

d. Dynamic response of the pump

Figure 2: Calibration equations of the system elements

Calibration equations of liquid level and flow rate sensors are linear functions companion an offset terms as shown in equations 1 and 2 respectively.

$$y = 0.0386\,x + 0.3231 \tag{1}$$

$$y = 2.0954\,x + 0.2377 \tag{2}$$

Laplace transformation of the liquid pump calibration equation is:

$$Q_p = \frac{0.515\,V_p + 0.0135}{1 + S + 0.29\,S^2} \tag{3}$$

Free outflow rate equation is a non-linear equation as shown below:

$$q_o = 0.2383\,h^{0.514} + 0.003 \tag{4}$$

These equations were used to build a closed loop simulation under LabVIEW 2014 environment in order to study the system behaviour when some faults may occur.

4. Case Study

In this study, a PID controller under LabVIEW 2014 environment was used to preserve the desired liquid height and hence the required discharge. Liquid level and outlet valve opening have a direct impact on the free outflow rate. The specifications of the coupled tank apparatus CE 105 were used to build a closed loop simulation incorporated with the system elements' calibration equations (1- 4) and the parameters shown in Table 1. This simulation shows a response as similar as the test rig does at the same system parameters.

Table 1: The parameters were used for the simulation purpose

The liquid level set point		125 mm
PID parameters	Proportional gain (K_c)	1
	Integral time (T_i, min)	0.01min
	Derivative time (T_i, min)	0 min
	Output high and low	10 volt and 0 volt respectively
Nominal pumping efficiency		100%
Nominal outflow rate		According to the free outflow rate Equation (4)

5. Fault Modelling

As a result of ageing or long-term use, the system behaviour could change due to one or more abrupt and/ or incipient faults in some parts. The liquid level system can be divided into two main sides, a high-pressure and a low-pressure side.

A. The high-pressure side contains the system pump and the tank inlet pipe. Faults in this portion can be divided into two categories. A leakage in the tank inlet pipe is assumed to be an abrupt fault, this is the first category while the second is incipient faults that progress slowly with time. The latter includes a pump internal leakage or impeller wear, represented as a progressive degradation in the impeller area [1]; [3]. Bearings wear fault can be considered as an incipient fault progression in any type of bearings have been used, e.g. radial bearing or thrust bearing [3]. Degradation in the mechanical and/ or electrical efficiency has been represented in this research as a percentage of the nominal pumping efficiency.
B. It is assumed that a fault in the low-pressure side, i.e. tank and drain line, occurs in two different ways. The first occurs when the outlet valve setting is abruptly changed to a new significant value and/ or a breakdown leads to massive leakage. Such fault usually settles at this value for a period of time. The second fault is assumed to be a time variant function and hence, the fault value has a

slow progression. For the purpose of this paper, this fault was represented as a percentage of the nominal outflow rate.

6. Results and Discussion

For the system parameters stated in the case study of a closed loop system and in presence of a PID controller, the liquid level will not be affected by a fault value if:

- The pumping efficiency reduces by up to 55.2%, as shown in Figure 3-a.
- The drainage from the tank increases by up to 81% from its designed value, as it can be seen in Figure 3-b.

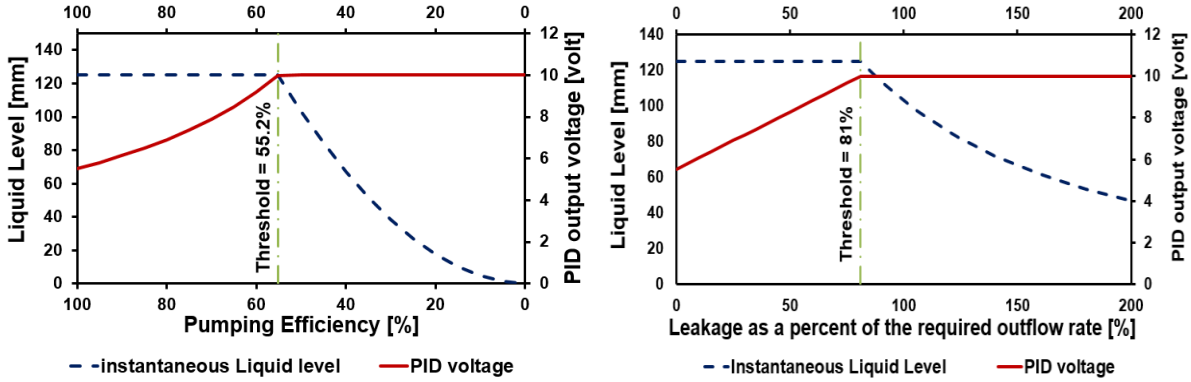

a. Pumping efficiency and its impact on the liquid level and PID output voltage

b. Liquid leakage and its impact on the liquid level and PID output voltage

Figure 3: Impact of the pumping efficiency and liquid leakage on the PID voltage and liquid level

7. Conclusions

The PID controller hastens an increase in the voltage supplied to the pump in order to boost the liquid pumping rate to mask any reduction, caused by faults, in the required liquid level. This is true until the controller reaches its saturated high value or the maximum permissible pumping rate. When the controller reaches this threshold, the liquid level will drop by reason of an incremental fault value as shown in Figures 3-a and b. Each liquid level has its own threshold as a result of each fault.

References

[1] Biswas, G. and Mahadevan, S. eds. 2007. A hierarchical model-based approach to systems health management. *Aerospace Conference, 2007 IEEE.*

[2] Borutzky, W. et al. 2002. An orifice flow model for laminar and turbulent conditions. *Simulation Modelling Practice and Theory 10(3), pp. 141-152.*

[3] Daigle, M. and Goebel, K. eds. 2011. Multiple damage progression paths in model-based prognostics. *Aerospace conference, 2011 IEEE.*

[4] Essahafi, M. 2014. Model Predictive Control (MPC) Applied to Coupled Tank Liquid Level System. *arXiv preprint arXiv:1404.1498.*

[5] Himanshu Gupta, O. P. V. April 2012. Intelligent Controller for Coupled Tank System. *International Journal of Advanced Research in Computer Science and Software Engineering 2(4).*

[6] Kumar, B. and Dhiman, R. 2011. Optimization of PID Controller for liquid level tank system using Intelligent Techniques. *Canadian Journal on Electrical and Electronics Engineering 2(11), pp. 531-535.*

[7] Ogata, K. 1997. *Modern control engineering*. Upper Saddle River, N.J. : Prentice-Hall

Biomechanics I

Proceedings of the 24th UK Conference of the
Association for Computational Mechanics in Engineering
31 March - 01 April 2016, Cardiff University, Cardiff

AN ITERATIVE LOCALLY CONSERVATIVE GALERKIN (LCG) METHOD FOR STUDYING FLOW IN A HUMAN ARTERIAL NETWORK

Hayder M. Hasan[1] and Perumal Nithiarasu[1]

[1]Zienkiewicz Centre for Computational Engineering, College of Engineering, Swansea University, Swansea SA2 8PP, United Kingdom

email: P.Nithiarasu@Swansea.ac.uk

ABSTRACT

In this study a robust iterative technique is developed for solving the one-dimensional human arterial blood flow problem by adopting Locally Conservative Galerkin method (LCG). Using Newton method with two different linear solvers (i.e. Gauss elimination and Jacobi methodologies), the non-linear governing equations are solved. Such strategies result in rapid convergence and fast solution without excessive memory cost for semi and full implicit LCG discretizations. In the proposed methods, the numerical strategies require computing a 4 x 4 matrix per element to determine blood flow characteristics. The novel methods developed are employed to study the blood flow through the major vessels of a complex human systemic circulation network. The validity and stability of the present methods are investigated by comparing the results against the available data in the literature.

Key Words: *Human Arterial Tree; One-dimensional Model; Locally Conservative Galerkin LCG; Finite Element Method; Newton-Gauss elimination and Newton-Jacobi.*

1. Introduction

Fundamental understanding of the blood flow behaviour is essential for predicting and treating common diseases in cardiovascular system such as aneurysm and atherosclerosis [1]. In order to achieve such comprehension in a complex geometry of human circulation, one-dimensional models have been used in most studies as they have been proven as efficient tools to give insight into quantities to interest [2, 3]. Among the schemes for solving the governing equations, explicit methodology in which the characteristic variables are employed to prescribe the boundary conditions is popular [2, 3]. Although such methods are more intuitive as the wave nature is considered and computationally efficient, time step restriction is the main drawback. Also, it leads to less stability especially at branching sites [4]. Alternatively, implicit treatment relaxes time step restriction but it is difficult to implement, especially in large scale problems due to large, complex and unsymmetric matrices which may lead to convergence issues. As the boundary conditions have to be prescribed in advance to allow a large time step, standard implicit schemes may affect the accuracy. Thus a combination of the advantages of steps from established explicit and implicit methods may lead to a better method. In the present work two such approaches , semi- and full- implicit Locally Conservative Galerkin (LCG) [5, 6] methods, are developed to relax the explicit LCG time step restriction and to enhance the stability. Basically, LCG method treats each element independently, this produces very small matrix of 4 x 4 per element and thus the solution is rapid. The standard Newton iteration is implemented here alongside a linear solver which is either Gauss elimination or Jacobi for the simultaneous solution. Such basic solvers are sufficient to achieve the rapid convergence since the matrices of LCG method are small unlike standard implicit methods. The results produced are compared against explicit methods to evaluate performance.

2. Governing Equations and Numerical Formulations

The governing equation (i.e. the conservation of mass and momentum equations) are numerically solved over 63 segments representing the major arteries in human systemic circulation as shown in Figure 1, also coronaries and ventricle valve are incorporated (All segments details can be found in [2, 3]). The compact form for the governing equation can be written as

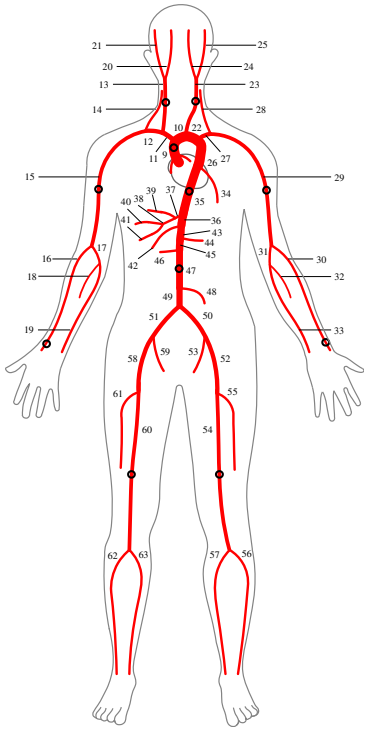

Figure 1: Configuration of the arterial tree for the current model [3].

$$\frac{\partial \mathbf{U}}{\partial t} + \frac{\partial \mathbf{F}}{\partial x} - \mathbf{S} = 0 \tag{1}$$

where

$$\mathbf{U}=\begin{bmatrix} A \\ u \end{bmatrix}, \ \mathbf{F}=\begin{bmatrix} Au \\ \frac{u^2}{2} + \frac{p}{\rho} \end{bmatrix} \text{ and } \mathbf{S}=\begin{bmatrix} 0 \\ -\frac{8\pi\mu}{\rho}\frac{u}{A} \end{bmatrix}$$

In above equation, A and u are the primitive variables (i.e. area and velocity respectively). The pressure p is linked to the cross sectional area through the non-linear relationship, $p = p_{ext} + \beta(\sqrt{A} - \sqrt{A_o})$. The parameters, ρ, μ, p_{ext} and A_o are fluid density, fluid viscosity, the pressure from the surrounding tissues and the area at zero transmural pressure respectively. And, β accounts for the material properties of the elastic vessel and given as $\beta = \frac{\sqrt{\pi}hE}{A_o(1-\sigma)}$, where h is the vessel wall thickness, E is Young's modulus and σ is the Poisson's ratio, assumed to be 0.5 (i.e. the vessel wall is incompressible) (see [2] for more details). The finite elements discretisation procedures are applied to the governing equation according to [7] by adopting linear shape functions, which results in fully discrete LCG form as

$$[\mathbf{M}]_e\{\Delta\ \mathbf{U}^n\} = \Delta t \left[[\mathbf{K}]\{\mathbf{F}^{n+1}\} + [\mathbf{L}]\{\mathbf{S}^{n+1}\} + \{\mathbf{f}_\Gamma\}^{n+\theta}\right]_e \tag{2}$$

where e refers to an element and all matrices details (i.e. $\mathbf{M}$,$\mathbf{K}$ and $\mathbf{L}$) can be found in [2]. The flux $\mathbf{f}_\Gamma$ is used to transfer information between elements. As stated before, we use both versions

of LCG method, i.e. semi- implicit in which $\mathbf{f}_\Gamma^n = \mathbf{F}^n$ at $\theta = 0$ and fully-implicit in which $\mathbf{f}_\Gamma^{n+1} = \mathbf{F}^{n+1}$ at $\theta = 1$. In both cases, the flux is rewritten in terms of implicit area and velocity at n or $n+1$ time level. After that, the primitive variables in Eq.2 are estimated according to Newton method [8, 9] along with Gaussian elimination or Jacobi for solving the simultaneous equations.

3. Results and Discussion

As stated before, the governing equations along with the boundary conditions are solved over the whole arterial tree. The input wave for the model is the pressure wave from left ventricle (see [2, 3] for more details). The pressure and flow rate are briefly discussed here as shown in Figure 2 at two monitoring positions along the aorta, i.e. ascending aorta (segment 9, denoted by A and B in the figure). The results are produced using Newton-Gauss elimination and semi- and full-implicit LCG method (legends Case 1 and Case 2 respectively). The Thoracic aorta II is also considered in Figure 2 (segment 35, denoted by C and D in the figure) in which Newton-Jacobi is adopted. We run three cardiac cycles where time step is chosen as $\Delta t = 0.0002s$, larger time step is possible but due to diffusive nature of Taylor-Galerkin method at larger time steps, this is not attempted here. For explicit LCG method used for comparison, time step was set in [3] as $\Delta t = 2$ x $10^{-5}s$. The figure clearly demonstrates that new methods proposed are close to the established explicit method. Between the two methods the semi-implicit method appears to be least accurate. This may be due to the flux being treated at n time level.

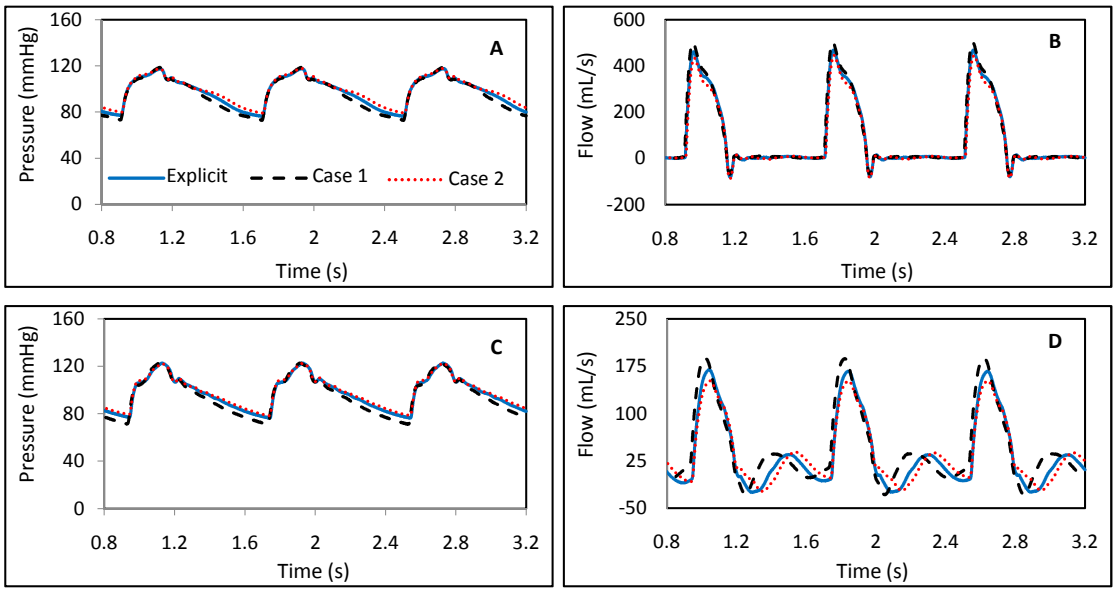

Figure 2: Comparisons for pressure and flow in various locations in the arterial tree.

In Table 1 the cost performance of the the three sachems are compared. As seen the fully-implicit method appears to be the fastest method among the methods compared and gives an accurate solution to the problem. The fully-implicit method also has the advantage of no time step restriction.

4. Conclusion

Two different time stepping schemes of LCG method, i.e. semi- and fully- implicit discretisations, have been developed for a human circulatory system. The solution is achieved by using the Newton iteration along with two linear solvers, Gauss elimination and Jacobi method. As LCG method generates only an element matrix (i.e. 4 x 4 size), this allows us to implement standard solvers. This enormously simplifies the computation. The comparisons between the proposed

Table 1: Computational speed comparison averaged over three cardiac cycles.

Method	Newton-Gauss, Semi-implicit	Newton-Gauss, Fully-implicit	Explicit
Time (s)	972.50	927.75	1017.00
Method	Newton-Jacobi, Semi-implicit	Newton-Jacobi, Fully-implicit	Explicit
Time (s)	942.00	896.25	1017.00

methods are established explicit method shows that the fully-implicit method is both fast and accurate. Thus the fully-implicit method proposed in this paper is recommended for future studies. Further investigation is essential to improve the fully-implicit method to enhance time step sizes, without compromising the accuracy.

ACKNOWLEDGEMENT

The authors acknowledge the financial support provided by the Iraqi Government and partial support provided by the Sêr Cymru National Research Network in Advanced Engineering and Materials.

References

[1] A. C. I. Malossi, P. J. Blanco, P. Crosetto, S. Deparis, and A. Quarteroni. Implicit coupling of one-dimensional and three-dimensional blood flow models with compliant vessel. *MULTISCALE MODEL. SIMUL*, 11:474–506, 2013.

[2] J.P. Mynard and P. Nithiarasu. A 1D arterial blood flow model incorporating ventricular pressure, aortic valve and regional coronary flow using locally conservative Galerkin (LCG) method. *Communications in Numerical Methods in Engineering*, 24:367–417, 2008.

[3] K. Low, R. van Loon, I. Sazonov, R. L. T. Bevan, and P. Nithiarasu. An improved baseline model for a human arterial network to study the impact of aneurysms on pressure-flow waveforms. *International Journal for Numerical Methods in Biomedical Engineering*, 28:1224–1246, 2012.

[4] A. C. I. Malossi, P. J. Blanco, and S. Deparis. A two-level time step technique for the partitioned solution of one-dimensional arterial networks. *Computer Methods in Applied Mechanics and Engineering*, 237-240:212–226, 2012.

[5] P. Nithiarasu. A simple locally conservative galerkin (LCG) finite-element method for transient conservation equations. *Numerical Heat Transfer Part B - Fundamentals*, 46(4):357–370, 2004.

[6] C. G. Thomas, P. Nithiarasu, and R. L. T. Bevan. The locally conservative galerkin (lcg) method for solving the incompressible navier-stokes equations. *International Journal for Numerical Methods in Fluids*, 57:1771–1792, 2008.

[7] P. Nithiarasu, R.W. Lewis, and K.N. Seetharamu. *Fundamentas of the finite element method for heat, mass and fluid flow.* Wiley, second edition, 2016.

[8] O. C. Zienkiewicz, R. L. Taylor, and P. Nithiarasu. *The Finite Element Method for Fluid Dynamics.* Elsevier, seventh edition, 2014.

[9] O.C. Zienkiewicz, R.L. Taylor, and D.D. Fox. *The finite element method for solid and structural mechanics.* Elsevier, seventh edition, 2014.

Proceedings of the 24th UK Conference of the
Association for Computational Mechanics in Engineering
31 March - 01 April 2016, Cardiff University, Cardiff

The Mechanical Underpinning of Tumour-induced Angiogenesis and Growth

***Vasileios Vavourakis[1], Peter Wijeratne[1], Rebecca Shipley[2], Triantafyllos Stylianopoulos[3] and David J. Hawkes[1]**

[1]Centre for Medical Image Computing, University College London, Gower Street, London, WC1E 6BT, UK
[2]Department of Mechanical Engineering, University College London, Gower Street, London, WC1E 6BT, UK
[3] Department of Mechanical & Manufacturing Engineering, University of Cyprus, Nicosia, 1678, Cyprus

*v.vavourakis@ucl.ac.uk

ABSTRACT

Angiongenic vessel growth is widely acknowledged to be a fundamental process that underpins cancer growth, invasion and metastasis, and it is highly instructive to construct and test reliable mechano-biological models of this process. Whereas previous studies have explored the chemical underpinning of both tumour growth and angiogenesis, here we extend these frameworks significantly to focus on the interplay between angiogenic network evolution and growth-induced solid stresses through a hapto- and mechanotactic stimulus for vessel sprouting, and a mechanics based remodelling process of the microvasculature. The proposed three-dimensional, multiscale *in silico* model for tumour-induced angiogenesis and growth is validated against *in vivo* data from murine mammary carcinomas, specifically focusing on the role of mechanical signals in recapitulating experimental evidence.

Key Words: *cancer mechanics; neo-vascularisation; tumour microenvironment; multiscale model; finite element method*

1. Introduction

Over the past two decades there has been a rapid development of deterministic mathematical and computational models describing cancer behaviour. These span from single scale to multiscale models, based either in continuum, discrete or hybrid methodology approaches. Cancer models that target simulating the dynamics of solid tumour biomechanics can be classified into avascular and vascular tumour growth models, with the reviews [4, 5] providing an exhaustive list of publications in the field. In this paper we propose a novel *in silico* model of tumour-induced angiogenesis and growth. This model is capable of producing high fidelity predictions of the morphology of the tumour microvasculature and its structural characteristics (e.g. endothelial lining, pore-size) and, importantly, it is has been validated against *in vivo* data from murine mammary carcinomas. The novelties of the model include: the introduction of mechano- and haptotaxis in capillary tip elongation; utilisation of a phenomenological description for the elongation speed of sprouts; and development of a constitutive model to describe vessel wall remodelling and structural integrity as a function of mechanical cues. Last but not least, an innovation of the proposed methodology is that it couples, in a partitioned manner, the tumour–host solid mechanics with the fluid mechanics of the capillary–interstitium interaction and the balance of biochemical factors regulating tumour growth and angiogenesis.

2. Methodology

The proposed *in silico* cancer modelling framework consists of four interconnected modules, as shown in Fig. 1: the solid mechanics (Box A), the biochemics (Box B), the microvasculature (Box C), and the fluid mechanics (Box D). This coupled model is solved using finite element (FE) methods using our in-house numerical analysis tool FEB3. Details of the novel aspects of the mathematical model and its computational implementation are summarised next.

We employ a continuum modelling approach to describe tissue solid and fluid mechanics, and biochemical transport. The domain of analysis consists of a spherical tumour (1 mm diameter) embedded in a cuboid (1.7 cm^3) of healthy tissue. The tumour region is initially avascular, with an initial spatially-uniform vascular network seeded in the healthy tissue. This 3D vasculature evolves temporally in response to

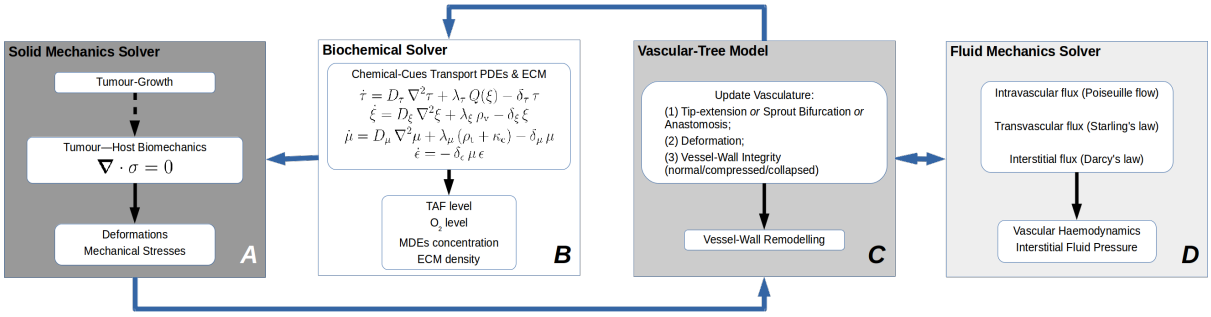

Figure 1: Flow diagram of the coupled multiscale solver illustrating the interaction between the different solvers.

both chemical and mechanical cues, and is described using a discrete description of individual vessel segments, connected via nodal junctions. Throughout, transient analysis is resolved using an explicit time-integration scheme. A set of three coupled equations are solved for the tumour angiogenic growth factor (TAF) concentration, τ, secreted by the cancer cells; the oxygen concentration, ξ, which diffuses from the blood vessels into the extracellular matrix (ECM) where it is metabolised by the cells; the concentration of matrix-degrading enzymes (MDE), μ, which is produced by endothelial cells in the sprouting vasculature, and the tumour cells, and diffuses through the ECM. The local composition of the ECM, ϵ, changes dynamically due to MDEs cleaving the proteins in the matrix. Tumour development is stimulated by the local increase of oxygen in the tissue using a physiologically representative growth expression and tissue biomechanical properties [9]. Boundary and initial conditions on the outer boundary of the tissue domain, and also healthy-tumour interface, are chosen to mimic *in vivo* conditions.

The initial vascular network, seeded within the healthy tissue, has properties (i.e. lumen size, thickness, pore size) obtained from *in vivo* data [6]. The vascular grid is non-conforming to the tissue FE-mesh. The meshes are coupled in the fluid mechanics solver (Box D of Fig. 1), where the steady-state fluid problem is solved [7], and the interstitial fluid pressure (IFP) and the fluid microvascular pressure (MVP) are evaluated. The vascular network evolves in response to both chemical and mechanical stimuli. First of all, the orientation of elongating vascular sprouts is described by the superposition of chemo-, hapto- and mechanotaxis stimuli: $\boldsymbol{e} = k_\tau \boldsymbol{\nabla}\tau - k_\epsilon \boldsymbol{\nabla}\epsilon - k_\mathrm{m}\,\boldsymbol{t}$, where k_τ, k_ϵ, k_m are scalar parameters, and $\boldsymbol{t}$ is the minimum eigenvector of the tissue mechanical stress tensor. Following recent *in vitro* experimental observations [10], we also impose that the tip elongation speed is inversely dependent to the vessel lumen size. Finally, the capillary lumen diameter and wall properties remodel in response to both the wall shear stress (WSS), and also compressions via the accumulated mechanical stresses in the tissue (a vessel collapses and its flow is occluded when the load exerted on its walls exceeds a critical value).

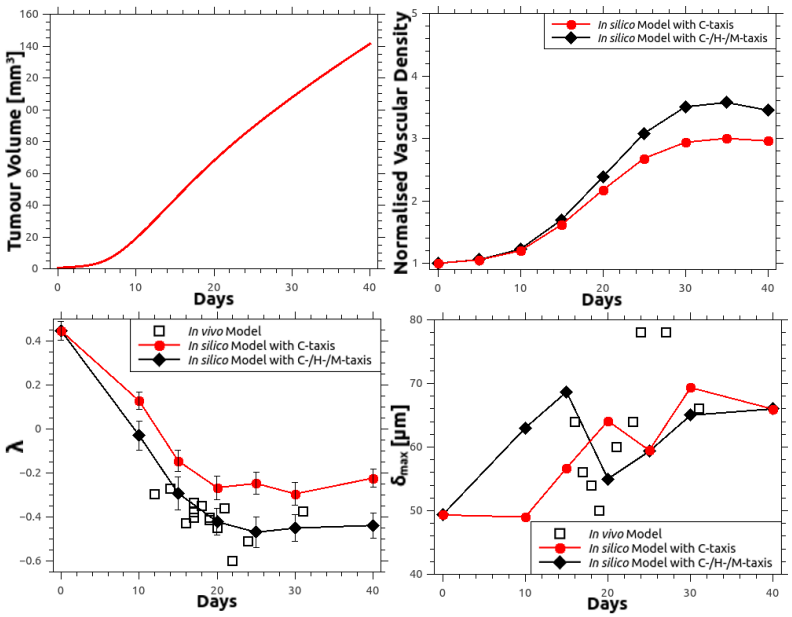

Figure 2: A. Predicted tumour volume as a function of time. B. Predicted vascular density (capillary lumen surface area to tissue volume ratio) normalised against the initial vascular density. C, D. Predictions of the tumour vasculature scaling parameters λ and $\delta_{\max}$ [1], compared with *in vivo* measurements [8].

Predictions of the *in silico* model (with and without mechanical stimuli switched on) are compared against both reported literature observations, and *in vivo* experimental data which characterises tumour growth, vascular extent and fluid flow characteristics in murine mammary carcinomas [8], providing a crucial validation step of these types of computational tumour frameworks.

3. Results

Fig. 2A shows the predicted bulk tumour growth (diameter increase from 1 to 6.5 mm in a month), with Fig. 3 illustrating tumour-induced angiogenesis and size at discrete time points (cancer mass shown as a transparent sphere); here the capillaries are shown as cylindrical tubes scaled to their lumen diameter. From left to right, Fig. 3 shows MVP, mean blood velocity, WSS, and radius respectively. In the rightmost panel, the concentration field of TAF (secreted by the tumour cells) is overlaid with the functional (red) and collapsed (blue) vessels; this collapse occurs due to the high solid stresses around the tumour-healthy tissue interface. The *in silico* cancer model predicts uniform IFP of around 8.5 mm-Hg in the tumour, with a steep decrease in the peri-tumoural region. This result is within the experimentally measured pressure range for tissue-isolated (7.8 ± 3.8 mm-Hg) and subcutaneous (9.1 ± 3.9 mm-Hg) small-size tumours [2]. The predicted maximum interstitial fluid velocity is approximately 0.15 μm/s, which is the correct order of magnitude with respect to experimentally measured values (0.6 ± 0.2 μm/s) [3]. In tumours, normalised vascular density (capillary lumen surface area to tissue volume ratio, normalised against the initial vascular density) is reported to range from 3.3 to 5 [11]. Fig. 2B depicts the temporal change of the normalised vascular density. We compare the model results when vascular sprouting is regulated by chemotaxis only, or in combination with mechano- and haptotaxis. Model predictions in each scenario are within physiological limits. We also adopt the method in [1], where two scaling parameters, λ and $\delta_{\max}$, were introduced to quantify key vascular features in 3D. Here λ is defined as a measure of the distribution of blood vessels in space, and $\delta_{\max}$ measures the distance between a point in the interstitium to the nearest blood vessel. A comparison between model predictions and the *in vivo* data from MCaIV carcinomas is presented in Figs. 2C and 2D. Whereas the simplified chemotaxis model (mechano- and haptotaxis switched off) overestimates λ at all time points, the agreement between model and experiments is excellent when the mechanical features are included. The impact of these features had a less significant effect on $\delta_{\max}$ because tumour growth in the model is not affected by the structure of the newly formed vasculature.

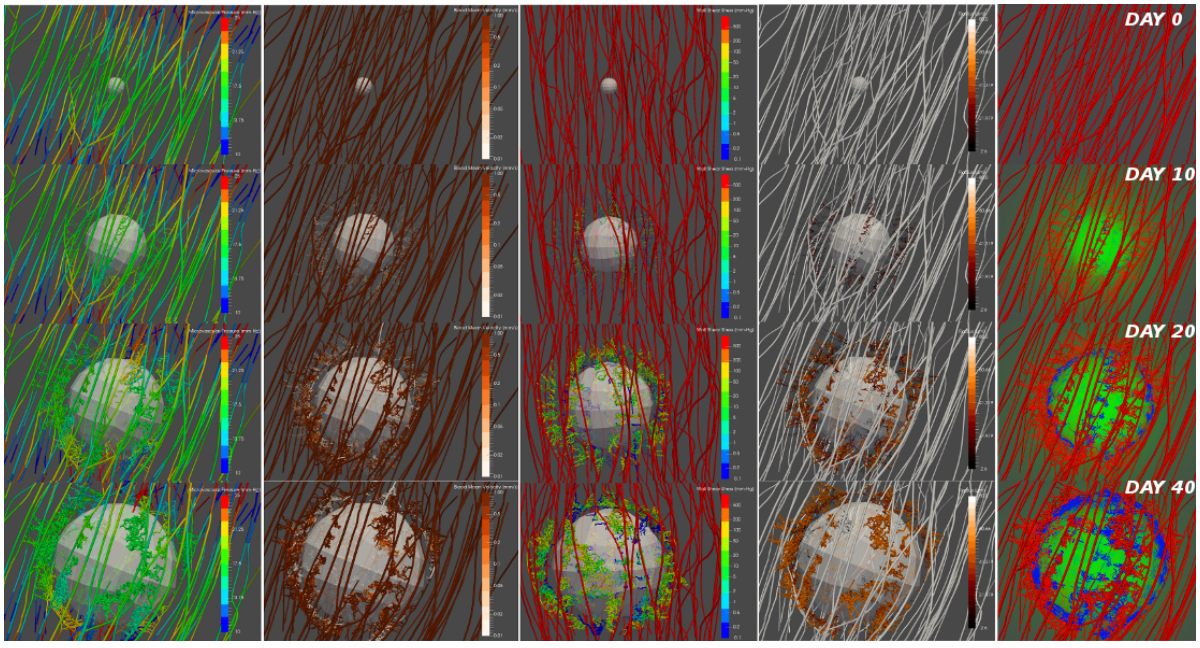

Figure 3: Snapshots of the *in silico* cancer model predictions, illustrating: MVP, velocity, WSS, capillary radius, and TAF distributions together with functional (red)/collapsed (blue) vessels.

4. Conclusions

This paper presents a validated 3D multiscale model of tumour-induced angiogenesis and growth, which incorporates a comprehensive description of the coupling between the tumour mechano-biology and capillary network fluid flows, functionality and growth. Model predictions are validated against experimental measurements of fluid pressures and velocities, and quantification of vascular parameters, and this agreement is strongest when angiogenic behaviours are driven by not only chemo-, but also hapto- and mechanotactic stimuli. Therefore, this study provides strong support for the importance of mechanical factors in influencing tumour vascularisation and development.

Acknowledgements

The authors would like to acknowledge the financial support of a Marie-Curie Fellowship (FP7-PEOPLE-2013-IEF, 627025), an ERC Starting Grant (336839-ReEngineeringCancer), an EPSRC Programme Grant "MIMIC" (EP/K020439/1), and an EU VPH Grant "VPH-PRISM" (FP7-ICT-2011-9, 601040).

References

[1] J.W. Baish, T. Stylianopoulos, R.M. Lanning, W.S. Kamoun, D. Fukumura, L.L. Munn, and R.K. Jain. Scaling rules for diffusive drug delivery in tumor and normal tissues. *Proceedings of the National Academy of Sciences of the United States of America*, 108(5):1799–1803, 2011.

[2] Y. Boucher, L.T. Baxter, and R.K. Jain. Interstitial Pressure Gradients in Tissue-isolated and Subcutaneous Tumors: Implications for Therapy. *Cancer Research*, 50(15):4478–4484, 1990.

[3] S.R. Chary and R.K. Jain. Direct measurement of interstitial convection and diffusion of albumin in normal and neoplastic tissues by fluorescence photobleaching. *Proceedings of the National Academy of Sciences of the United States of America*, 86:5385–5389, 1989.

[4] L.B. Edelman, J.A. Eddy, and N.D. Price. *In silico* models of cancer. *Wiley Interdisciplinary Reviews: Systems Biology and Medicine*, 2(4):438–459, 2010. doi: 10.1002/wsbm.75.

[5] A. Masoudi-Nejad, G. Bidkhori, S.H. Ashtiani, A. Najafi, J.H. Bozorgmehr, and E. Wang. Cancer systems biology and modeling: Microscopic scale and multiscale approaches. *Seminars in Cancer Biology*, 30:60–69, 2015.

[6] H. Sarin. Physiologic upper limits of pore size of different blood capillary types and another perspective on the dual pore theory of microvascular permeability. *Journal of Angiogenesis Research*, 2(1):1–19, 2010.

[7] T. Stylianopoulos, K. Soteriou, D. Fukumura, and R.K. Jain. Cationic Nanoparticles Have Superior Transvascular Flux into Solid Tumors: Insights from a Mathematical Model. *Annals of Biomedical Engineering*, 41(1):68–77, 2012.

[8] B.J. Vakoc, R.M. Lanning, J.A. Tyrrell, T.P. Padera, L.A. Bartlett, T. Stylianopoulos, L.L. Munn, G.J. Tearney, D. Fukumura, R.K. Jain, and B.E. Bouma. Three-dimensional microscopy of the tumor microenvironment in vivo using optical frequency domain imaging. *Nature medicine*, 15 (10):1219–1223, 2009.

[9] P.A. Wijeratne, V. Vavourakis, J.H. Hipwell, C. Voutouri, P. Papageorgis, T. Stylianopoulos, A. Evans, and D.J. Hawkes. Multiscale modelling of solid tumour growth: the effect of collagen micromechanics. *Biomechanics and Modeling in Mechanobiology*, pages 1–12, 2015.

[10] L.B. Wood, R. Ge, R.D. Kamm, and H.H. Asada. Nascent vessel elongation rate is inversely related to diameter in in vitro angiogenesis. *Integrative Biology*, 4(9):1081–1089, 2012.

[11] F. Yuan, Y. Chen, M. Dellian, N. Safabakhsh, N. Ferrara, and R.K. Jain. Time-dependent vascular regression and permeability changes in established human tumor xenografts induced by an anti-vascular endothelial growth factor/vascular permeability factor antibody. *Cancer Research*, 93(25): 14765–14770, 1996.

Proceedings of the 24th UK Conference of the
Association for Computational Mechanics in Engineering
31March – 01 April 2016, Cardiff University, Cardiff

BLOOD FLOW SIMULATION USING SMOOTHED PARTICLE HYDRODYNAMICS

***Mohammed AL-SAAD, Sivakumar Kulasegaram** and **Stephane P.A. Bordas**
School of Engineering, Cardiff University

*Al-SaadMK@Cardiff.ac.uk

ABSTRACT

To understand the characteristics of blood flow, it is important to identify the key parameters that influence the flow of blood. The characterisation of blood flow will also enable us to understand the flow parameters associated with physiological conditions such as atherosclerosis. Thrombosis plays a crucial role in atherosclerosis and it also helps to stop bleeding when a blood vessel is injured. This article focuses on using a meshless particle-based Lagrangian numerical technique, named the smoothed particles hydrodynamic (SPH) method, to study the flow behaviour of blood and to explore the flow conditions that induces the formation of thrombus in a blood vessel. Due to its simplicity and effectiveness, the SPH method is employed here to simulate the process of thrombogenesis for various blood flow parameters. In the present SPH simulation, blood is modelled by particles that have the characteristics of plasma and of platelets. To simulate the coagulation of platelets which forms thrombus, the adhesion and aggregation processes of the platelets are modelled by an effective inter-particle attraction force model. With these models, the motion of platelets in flowing blood, and their adhesion and aggregation are effectively coupled with viscous blood flow. In this study, the adhesion and aggregation of blood particles are analysed on a (straight vessel) under various low Reynolds number scenarios. The results are compared with the experimental results, and a good agreement is found between the simulated and experimental results.

Keywords: *smooth particle hydrodynamics (SPH); blood flow; thrombus; arteries*

1.Introduction

A thrombus is considered to be one of the most important causes of many diseases in human body. On the other hand, A blood clot anchored to a damaged vascular wall can stop bleeding or it can prevent atherosclerosis in arteries. The danger is that a thrombus can affect the blood flow in the vessels and this can cause potentially deadly accidents, such as cardiac infarction (or heart attack) or ischemic stroke when the damage occurs in the coronary or the carotid arteries, respectively. The formation of a thrombus depends on platelet flow; for example, the transport to denuded subendothelium, formation of membrane tethers, adhesion to the subendothelium, and aggregation. Many experimental studies have provided information on the biochemical effects of fluid forces on thrombogenesis. In recent years, due to the availability of vast computational power, research on computer simulation of thrombosis has become a field of deep interest. Although fluids can be simulated in either the Eulerian or Lagrangian method, the Lagrangian method is considered to be more suitable for this type of simulation due to their obvious advantages in tracking movement of particles similar to platelets[1]. The purpose of this study is to analyse flow parameters that influence the formation of thrombosis inside arteries. A Lagrangian smoothed particles hydrodynamics (SPH) is used for numerical simulations of the blood flow consisting plasma and platelets.

2. Numerical Methodology

The governing equations for solving incompressible or weakly compressible isothermal fluid flow using SPH are mass and momentum conservation equations given by,

$$\frac{1}{\rho}\frac{D\rho}{Dt} + \nabla.\mathbf{v} = 0; \qquad \frac{D\mathbf{v}}{Dt} = -\frac{1}{\rho}\nabla \mathrm{p} + v\nabla^2\mathbf{v} + \mathbf{F}. \qquad (1),(2)$$

Where ρ, t, v, $\mathbf{v}$, and p represent the density, time, kinematic viscosity, velocity and pressure of the fluid particles and, **F** represents the external force acting on fluid particles. The fluid pressure for weakly compressible SPH formulation is obtained by an equation of state as presented in [2]**.** The numerical procedure to calculate fluid velocity is derived from the momentum equation (2) as,

$$\mathbf{v}^{n+1} = \mathbf{v}^n + \left(-\frac{1}{\rho}\nabla P + v\nabla^2\mathbf{v}^n + \mathbf{F}\right)\Delta t \qquad (3)$$

Where superscript n and $n+1$ refer to current and next time steps, respectively, and Δt is the numerical time step. The position and density of the fluid can be updated respectively at every time step by,

$$\mathbf{x}^{n+1} = \mathbf{x} + \mathbf{v}^{n+1}\Delta t, \qquad (4)$$

and (from the continuity equation (1)),

$$\rho^{n+1} = \rho^n - \rho^n(\nabla.\mathbf{v}^{n+1})\Delta t. \qquad (5)$$

The pressure is then estimated from the updated density.

3. Modelling Platelet Motion

The platelets tend to adhere and aggregate when the blood vessel is damaged. This can lead to formation of a primary thrombus. Inside the primary thrombus the neighbour platelets link together, which are then bound by vWF fibrinogen in plasma and collagen in the sub-endothelial tissue [3]. This process takes place by making a link between neighbouring platelets and bound by vWF fibrinogen in plasma and collagen in the sub-endothelial tissue. To numerically model such platelet motion, an algorithm based on a penalty or spring force mechanism [4] is adopted. This model dictates the interactions between platelets and plasma inside the blood vessel. When the platelets are within a distance d_{ad} from the damaged area, the platelets are attracted towards the damaged wall by an adhesive force given by eq. (6). The platelets adhering to the wall are then activated and attract other platelets which are within a distance of d_{ag} from them. This attractive force is called an aggregation force which is given by eq. (7). The aggregation force takes the same form as that of the adhesive force but has a different spring constant.

$$\boldsymbol{F}_{ad} = \begin{cases} K_{ad}(|\boldsymbol{r}_{ij}| - r_o)\boldsymbol{n}_{ij} & (|\boldsymbol{r}_{ij}| \le d_{ad}) \\ 0 & (|\boldsymbol{r}_{ij}| > d_{ad}) \end{cases}; \boldsymbol{F}_{ag} = \begin{cases} K_{ag}(|\boldsymbol{r}_{ij}| - r_o)\boldsymbol{n}_{ij} & (|\boldsymbol{r}_{ij}| \le d_{ag}) \\ 0 & (|\boldsymbol{r}_{ij}| > d_{ag}) \end{cases} \qquad (6), (7)$$

In the above equations $\boldsymbol{F}_{ad}, \boldsymbol{F}_{ag}$ are the adhesive and aggregate forces and K_{ad}, K_{ag} are the corresponding spring constants. The $\boldsymbol{r}_{ij}$ here is distance between activated platelet and vessel wall (or other non-activated platelets), r_o is the original or natural length of the spring and $\boldsymbol{n}_{ij}$ is a unit vector linking platelet and damaged wall (or linking activated platelet and other surrounding platelets). These two forces are introduced in equation (2) for platelet particles which are influenced by adhesion and aggregation.

4. Blood Flow Model

In this work, the blood flow simulations were performed inside a straight blood vessel with flow Reynolds numbers 0.01, 0.02, and 0.03, which were defined at the inlet velocity. The total length of

the vessel (L) and the width between two walls (D) are respectively 130μm and 20μm. The dimensions of the damaged wall (L_i) is 30μm (refer to the length of the wall damage) and the distance from the inlet to the damaged wall (L_o) is 40μm (see Fig.1). The total number of particles used in the simulation was 5079. Four layers of boundary dummy particles were also used. The initial distance between particles is 1.0 μm. The density ρ and kinematic viscosity v of the plasma and platelets, were set as $\rho = 1\text{x}10^3 \text{kg/m}^3$ and $v = 1\text{x}10^{-6}\text{m}^2/\text{s}$. The boundary conditions were; a uniform velocity at the inlet, zero pressure at the outlet and, non-slip condition at the walls enforced by dummy boundary particles. The amount of the platelet particles used is approximately 8.8% of the plasma to resemble normal physiological condition. The time step was set to $5\text{x}10^{-7}\text{s}$ to ensure the stability of numerical integration scheme. In the reported numerical simulations, the spring constants K_{ad} and the K_{ag} are $9.0\text{x}10^9\ N/\text{m}$ and $4.5\text{x}10^9\ N/m$ respectively, while d_{ad}= 3.0μm = d_{ag}, and r_o = 2.0μm.

5. Results

The purpose of this study is to demonstrate the formation of thrombus and to investigate the applicability of SPH in modelling such process. The corrected SPH is used to improve the accuracy [5] of the simulation. Normally, a thrombus is formed by adhesion and aggregation of platelets which are transported by the blood flow in different geometries of arteries or vessels, where the growth rate of thrombus formation varies with the stenosis and the flow rate of blood. Figure 1 illustrates the formation of thrombus at two different stages of the flow. In these figures, for clarity, plasma and platelet particles are shown by two different the plasma and platelets are denoted by light and the dark grey respectively. The platelets are activated when they are within d_{ad} distance from the damaged region and form a primary thrombus. During the course of time, a primary thrombus is developed to cover the whole damage area by forming several layers of platelets. When thrombus grows to a certain volume, part of the thrombus is separated and transported downstream by the blood flow. Figures 1 and 2 depict the growth of thrombus at different times for Reynolds numbers 0.01 and 0.03 of the flow. From the figures below, various stages of thrombus growth on the damaged area of the wall are clearly evident. It can be noted from Fig. 1(b) and 2(b) that, part of the thrombus is separated from primary thrombus once the primary thrombus grows to a substantial volume. It is interesting to observe that the volume of the primary thrombus and the time at which separation of the thrombus takes place are affected by the flow rate. From these figures it can be concluded that the higher the flow rate the thinner the thrombus growth would be. Further, it can be noted that with higher flow rates the separation of thrombus takes place quicker.

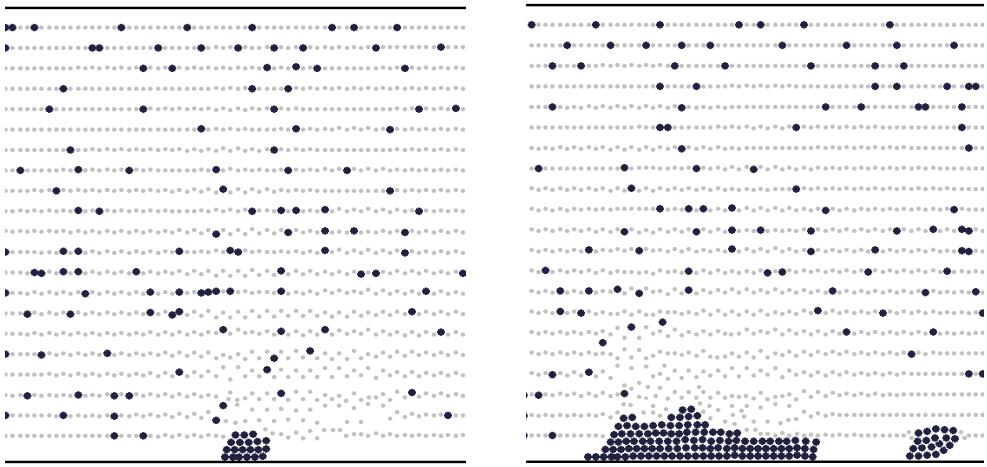

(a) (b)

Figure 1: The platelet aggregation in the flow Re=0.01 at (a) t=0.2s; (b) t=0.6s

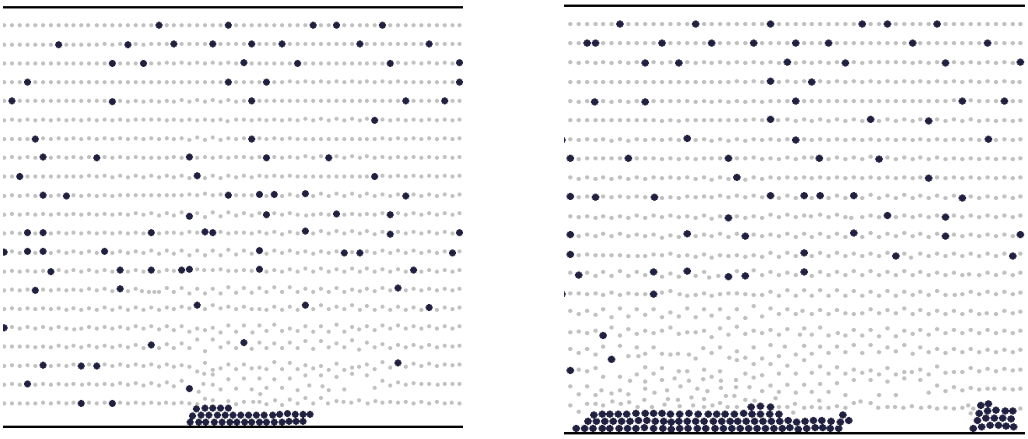

(a) (b)

Figure 2: The platelet aggregation in the flow Re=0.03 at (a) t=0.2s; (b) t=0.6s

6. Discussion

The influence of changing hemodynamics on the platelet transport and thrombus formation was investigated using SPH. The formation and subsequent behaviour of thrombus at various blood flow rates were analysed by numerical simulations. It is evident from the results above that the blood flow rate plays a crucial role in the build-up and separation of thrombus. The results show that the growth rate of the thrombus, its thickness, and formation/separation vary according to the blood flow rate. These results are consistent with the observations reported in [6].

7. Conclusions

This work has focused on the simulation of the thrombogenesis process using the SPH method by considering platelet aggregation and the influence of blood flow rates on thrombus growth. In the numerical simulations, blood inside a straight vessel is discretised by particles which are assumed to have the characteristics of blood constituents, such as plasma and platelets. The potential of SPH method to simulate thrombogenisis process is demonstrated via numerical examples. This study also demonstrates the ability and accuracy of the SPH method in modelling blood flow with low Reynolds numbers.

References

[1] Sulsky, D. and H.L. Schreyer, *Axisymmetric form of the material point method with applications to upsetting and Taylor impact problems.* Computer Methods in Applied Mechanics and Engineering, 1996. **139**(1): p. 409-429.

[2] Batchelor, G., *K. 1967 An Introduction to Fluid Dynamics*. 1970, Cambridge University Press.

[3] Savage, B., E. Saldívar, and Z.M. Ruggeri, *Initiation of platelet adhesion by arrest onto fibrinogen or translocation on von Willebrand factor.* Cell, 1996. **84**(2): p. 289-297.

[4] Kamada, H., et al., *A three-dimensional particle simulation of the formation and collapse of a primary thrombus.* International Journal for Numerical Methods in Biomedical Engineering, 2010. **26**(3-4): p. 488-500.

[5] Bonet, J. and S. Kulasegaram, *Correction and stabilization of smooth particle hydrodynamics methods with applications in metal forming simulations.* International journal for numerical methods in engineering, 2000. **47**(6): p. 1189-1214.

[6] Begent, N. and G. Born, *Growth rate in vivo of platelet thrombi, produced by iontophoresis of ADP, as a function of mean blood flow velocity.* Nature, 1970. **227**: p. 926-930.

Proceedings of the 24th UK Conference of the
Association for Computational Mechanics in Engineering
31 March – 01 April 2016, Cardiff University, Cardiff

Mechanical description and engineering analysis of cutting and (sterile) needle insertion into Human skin

***Kevin Bronik[1], Prof Sam L Evans[2] and Dr Pierre Kerfriden[3]**

[1]Mechanical engineering department, School of Engineering ,Cardiff University
[2] Director, School of Engineering, Cardiff University
[3]Mechanical engineering department, School of Engineering, Cardiff University

*BronikK@cardiff.ac.uk

ABSTRACT

Understanding the total complexity of biomechanical/mechanical properties of the human skin and developing an advance computational model (e.g. the Finite element skin models) that do not differ (or not so much differ!) from experimental data would provide information which could be very useful for surgical training and practical use (special in this project, the goal is to inform the development of optimized device which can be used for effective and reproducible skin penetration in the clinical setting. This project will also provide clear definition of underlying mechanisms of penetration and cutting and make it possible of generating a robust computational and physical model and an excellent technique for measuring skin deformation and in combination with advanced computational/mechanical methods it will offer many possibilities for in vivo measurements).
Difficulties and solutions related to the experience of developing this project beside the fundamental limitation of the finite element method for solving fracture mechanics problem, were dealing with the complicated multilayer structures and strong non-linearity in human skin which make the computational model difficult to create and analyse. However, to overcome the difficulties with fracture mechanical part the Theoretical and Computational Aspects of Cohesive Zone Modelling has been adapted to make it suitable for(Frictional and Thermodynamically coupled Frictional) modelling of cutting and needle insertion by using a modified version of Contact-Fracture formulation (a specific implementation of a mesh independence method for straightforward controlling of (non-linear) fracture mechanical processes using Mixed Mode Cohesive-Zone method). To successfully deal with the problem or difficulty with the modelling of human skin for fracture mechanical analysis, because of its complexity, the problem has been subdivided into simpler problems and analysed.

Keywords: *Fracture Mechanics; Cohesive Zone Method; Cutting; Needle insertion; Contact Mechanics*

1. Introduction

Various theoretical and numerical formulation of the Cutting and needle insertion have been widely studied and applied for the different problem classes using the (traditional) finite element methods.
Using a combination of digital image correlation and advanced Finite element modelling and explicitly taken into consideration the complexities of the algorithms due to the complexity of non-linear mechanical behaviour of human skin, after a series of Experimental Measurements on human skin and related computational modelling, S Evans and C A Holt [4] found evidence to suggest the application of stochastic optimization algorithms (due to the reduction of the errors).
In other study, in order to design optimised micro-needle device which completely depends on understanding of human skin biomechanics under small deformations, after doing a series of optimized laboratory developed tests and using much more precise model (considering the skin as a multilayer composite) by applying multilayer finite element model (with the results of which show a remarkable degree of success), R.B. Grovesa, S.A. Coulmanb, J.C. Birchallb and S.L. Evans[2,3] argue that, the problem with the precise approach and optimum development of numerical-experimental procedure and modelling of very complex mechanical behaviour of human skin would require first the perfect understanding of dependency and in-dependency of parts or elements of skin combined with mechanical description which can be used later for computational modelling.

At this point it is worth adding that, there were two main studies which aim to help us develop this project. The first one was the study by Oliver A.Shergold and Norman A. Fleck[1] about the development of the deep penetration of a soft solid by a flat-bottomed and by a sharp-tipped cylindrical punch with application of one term Ogden strain energy function and consideration the skin as an incompressible hyper-elastic isotropic solid. The second one was the study by Vincent Hayward and Mohsen Mahvash[5] about the development of the haptic-rendering of cutting with the clarification of the geometry and the mechanism of the interaction of the tools and the sample.

Without being affected by the complex nature of soft solid penetration, it is worth noting that the existing literature unfortunately provides little insight into Underlying Mechanisms of the penetration and cutting. Generally they indicate the deep penetration involves deformation and cracks and in most case without taking the existence of (sliding) friction into account. Therefore, this Project goals keep the focus on what is most important; namely mathematical and physical clarification of the mechanisms of the penetration and cutting processes following the related algorithms and computational implementation of the theory.

2. Methodology

In order to process the development of this project, the first step was the classification of computational and mechanical-mathematical problems related to modelling which were clearly separated into those with the implementation of the clarified underlying theory and those problems with optimization using advanced computational and mechanical optimization algorithms and methods. Then the accuracy of the implemented algorithms has been practically and experimentally verified.

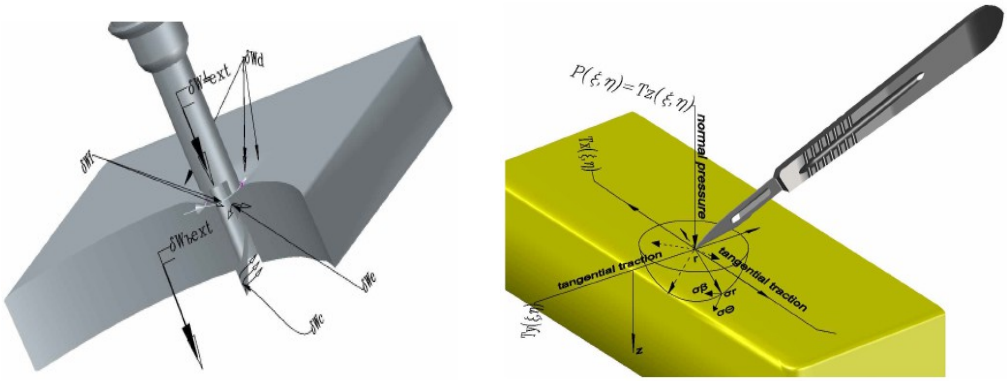

Figure 1: Geometrical description of cutting and needle insertion

Following Equation represents the underlying mathematical concepts(total energy functional-energy conservation law):

$$\frac{DE_{total}}{Dt} = \frac{D}{Dt}\{ \underbrace{\sum_{\forall i}(\int_{\Omega} U_i^t d_\Omega}_{Totalstrainenergy} \underbrace{- \int_{\Omega} b.u_i d_\Omega - \int_{\partial\Omega_\sigma} t_\sigma.u_i d_{\partial\Omega_\sigma})}_{Appliedenergy} -$$

$$- \underbrace{\sum_{\forall s,m} \int_{\partial\Omega_\Gamma} (q_c^s + q_c^m)_t d_{\partial\Omega_\Gamma}}_{FractureSurface-Thermodynamicenergy} + \underbrace{\sum_{\forall i,j,\beta} \int_{\partial\Omega_\Gamma} t_f^i.\tau^\beta(u_j^\beta - u_i^\beta) d_{\partial\Omega_\Gamma}}_{FractureSurface-Frictionenergy} +$$

$$\underbrace{\sum_{\forall\partial\Omega_\Gamma} \int_{\partial\Omega_\Gamma} G_c[G_{Ic} \mid G_{IIc}] d_{\partial\Omega_\Gamma}}_{Fractureenergy} + \underbrace{\sum_{\forall\Omega}(\int_{\Omega} C(T_{current} - T_{initial})\rho d_\Omega}_{Heatenergy}$$

$$\underbrace{-\sum_{\forall\partial\Omega_\Gamma}\Big(\int_{\partial\Omega_\Gamma} T_x\{u_i\}d_{\partial\Omega_\Gamma}+\int_{\partial\Omega_\Gamma} T_y\{u_i\}d_{\partial\Omega_\Gamma}+\int_{\partial\Omega_\Gamma}[P=T_z]\{u_i\}d_{\partial\Omega_\Gamma}\Big)+}_{\iint_s Tx(\xi,\eta)\phi d\xi d\eta+\iint_s Ty(\xi,\eta)\phi d\xi d\eta+\iint_s[P(\xi,\eta)=Tz(\xi,\eta)]\phi d\xi d\eta}$$

$$\underbrace{\int_\Omega \frac{1}{2}\rho(\frac{\partial u_i}{\partial t})(\frac{\partial u_i}{\partial t})d_\Omega}_{Kineticenergy}-\underbrace{\int_\Omega R^t d_\Omega+\int_{\partial\Omega} Q^t N d_{\partial\Omega}\Big)\Big\}=0}_{AppliedThermalenergy} \tag{1}$$

The algorithm proceed with the adaptation of the definition and the algorithm of the modified contact[additionally thermodynamically coupled friction concept](in the previous study has been practically and analytically verified), optimized with inequality constraints: the Kuhn-Tucker conditions which enforces the contact constrains within a strong Mixed Mode Cohesive Law formulation by clearly taking the place of the classical contact constrains formulation and in the case of the physical requirement of impenetrability and compressive interaction between two bodies, enforces the classical contact constrains.

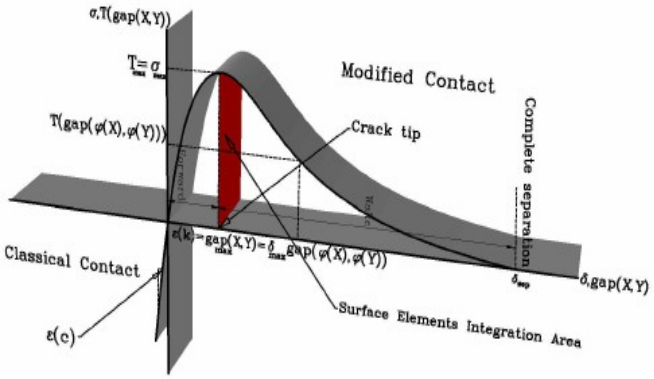

Figure 2: Definition of the Modified Contact combined with Classical Contact Mechanics

After applying this definition to the finite element discretisation of global variation equation(1), summarized, we obtain a non-linear ordinary differential equation (the Discrete Momentum Balance equation) expressed as (by using the residual vector concept and appropriated boundary conditions):

$$R(d_{n+1})=F_{ext}^{mech}(t_{n+1})+F_{ext}^{ther}(t_{n+1})-M[\frac{4d_{n+1}}{(t_{n+1}-t_n)^2}]$$

$$+M(a_n+\frac{4d_n}{(t_{n+1}-t_n)^2}+\frac{4v_n}{(t_{n+1}-t_n)})-\{C\dot{d}_{n+1}+F_{int}^{mech}[d_{n+1}]+$$

$$F_{int}^{ther}[d_{n+1}]+\underbrace{F_{Fst}[d_{n+1}]+F_{fric}[d_{n+1}]+F_{frac}[d_{n+1}]+F_{trac}[d_{n+1}]}_{F_{contact}[d_{n+1}]}\}=0 \tag{2}$$

$$(a_n,d_n,v_n,acceleration,displacement,velocity\ vectors)$$

Where commonly, $Given\ [\ddot{d}_n \mid a_n],d_n,v_n \quad \vec{Find} \quad [\ddot{d}_{n+1} \mid a_{n+1}],d_{n+1},v_{n+1}.$

Then the numerical implementation of the explained theories has been performed in the open source code FEBio (Non-linear finite element solver for biomechanical applications http://febio.org/febio/) by the modification of the existing contact algorithm.

3. Computational Model/Result/Discussion

Based on the collected experimental data[cutting test on silicon rubber type material (E=0.77 MPa,

v=0.48) by using Zwick universal testing machine] and practicing the advantage of FEBio package (PreView, PostView, FEBio) the computational model has been created and analysed. Beside issues related to computational model, an interesting issue had been examined was the sensitivity of the experimental result to the acceleration and velocity of the cutting tool during testing would have a direct effect on the under-resolving some local details.

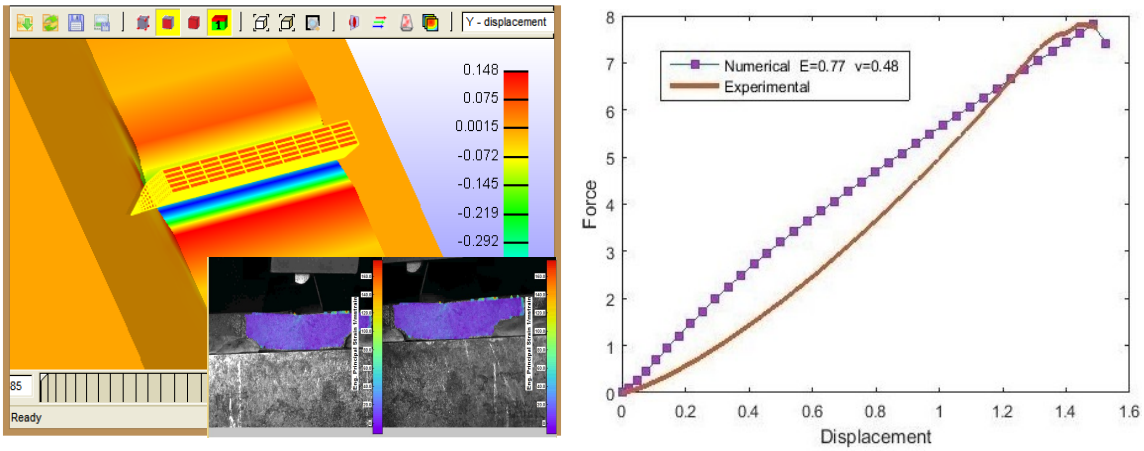

Figure 3: Computational versus Experimental results

However, comparison Computational with Experimental results reveals that using the modified contact algorithm in such a way can significantly increase the chances of success and will contribute to the achievement of desired results.

4. Conclusions

In this study it has been shown that the development of computation model, in this way, by using the Modified Contact fulfils the strong condition of the cohesive zone law and additionally supports the physical ideas and mathematical structures of the Classical Contact, allowing us a significant degree of flexibility and success in the deployment of robust models for engineering analysis.

Acknowledgements

The developer of this project would like to thank HPC Wales teams for setting up the facility supercomputing in order to perform high performance computing from which this study totally benefited. Additionally, he would like to extend his sincere gratitude and thankfulness to Fujitsu the Funder of the project.

References

[1] Oliver A.Shergold and Norman A. Fleck. Mechanisms of deep penetration of soft solids, with application to the injection and wounding of skin. 2004.

[2] R.B. Groves , S.A. Coulmanb, J.C. Birchallb and S.L. Evans. Quantifying the mechanical properties of human skin to optimise future microneedle device design. *Computational Methods Biomechanical Biomedical Engineering*, 15(1):73–82, 2012.

[3] R.B. Groves , S.A. Coulmanb, J.C. Birchallb and S.L. Evans. An anisotropic, hyperelastic model for skin: experimental measurements, finite element modelling and identification of parameters for human and murine skin. *Journal of Mechanical Biomechanical Engineering*, 2013.

[4] S Evans and C A Holt. Measuring the mechanical properties of human skin in vivo using digital image correlation and finite element modelling. *The Journal of Strain Analysis for Engineering Design*, 44(5):337–345, 2009.

[5] Vincent Hayward, Mohsen Mahvash. Haptic rendering of cutting: A fracture mechanics approach. 2001.

Proceedings of the 24th UK Conference of the
Association for Computational Mechanics in Engineering
31 March - 01 April 2016, Cardiff University, Cardiff

DEVELOPMENT OF A 1D CARDIOVASCULAR MODEL DURING PREGNANCY

***J. Carson[1], M. Lewis[1], D. Rassi[2] and R. Van Loon[1],**

[1]College of Engineering, Swansea University, Bay Campus, Fabian Way, Swansea, SA1 8EN
[2]College of Human and Health Sciences, Swansea University, Singleton Park, Swansea, SA2 8PP

*485621@swansea.ac.uk

ABSTRACT

The expectant mother undergoes many physiological changes over the course of pregnancy, many of which affect the cardiovascular system. An existing closed loop 1D cardiovascular network model has been modified, which includes the main systemic, pulmonary and cerebral arteries and veins. The enhanced trapezoidal rule method (ETM) is used to solved the 1D blood flow and lumped parameter system. Lagrange multipliers are use to constrain conservation of mass and conservation of total pressure at vessel junctions. The method is implicit and naturally incorporates coupling between 1D vessels and lumped models. The ETM has been compared with benchmark problems and results show excellent agreement with commonly used schemes. The aim of this research is to develop a cardiovascular model which describes various changes seen during pregnancy. A fully closed loop cardiovascular network is being developed which uses; a five element Windkessel model to connect arteries and veins; and 0D lumped models to describe the heart and valves.

Key Words: *Implicit Solver; 1D Blood Flow; Closed-Loop System; Cardiovascular Network; Pregnancy*

1. Introduction

During pregnancy the expectant mothers undergoes many physiological changes. The cardiovascular system needs to adapt to allow up to an additional 50% of maternal blood volume, and, increased stroke volume and heart rate. However, even with these effects it is common that the maternal blood pressure actually decreases. This is partly caused by the vascular resistance decreasing by around 20%, and, a number of maternal blood vessels increase in diameter, particularly those close to the womb, such as the ovarian and uterine arteries. This increase in blood volume also leads to lower blood viscosity. Moreover, as the foetus develops, external pressure on the maternal blood vessels will increase, particularly in the abdominal area.

1D blood flow models have been often used to study wave propagating in arteries, and have been extended to veins. Most so called closed loop models use lumped parameter models for the pulmonary circulation such as [3] rather than treating them as 1D vessels. Mynard and Smolich [4] have recently developed a fully closed loop 1D cardiovascular network which include 1D vessels in systemic arteries and veins and pulmonary arteries and veins, together with a heart model.

An improved version of the simplified trapezoidal rule method (STM) [2] has been developed for 1D blood flow which allows intuitive coupling of 1D vessels and lumped parameter models, such as valves, the heart and vascular beds. The method is applied to benchmark problems from [1] and compared with the results therein. The aim of this research is to develop a cardiovascular model which investigates the mechanisms involved during pregnancy.

2. Methodology

The system of equations that represent the linearised 1D blood flow are the conservation of mass and conservation of momentum

$$C_A^n \frac{\partial P}{\partial t} + \frac{\partial Q^{n+1}}{\partial x} = 0, \tag{1}$$

$$\frac{\rho}{A^n}\frac{\partial Q}{\partial t} + \frac{\rho}{A^n}\left(\frac{\partial \frac{Q^2}{A}}{\partial x}\right)^n + \frac{\partial P^{n+1}}{\partial x} + \left(\frac{8\mu\pi Q}{A^2}\right)^n = 0, \tag{2}$$

where C_A is the compliance; P and Q is the average pressure and average flow rate in the cross-section respectively; t is the time; A is the cross-sectional area; ρ is the density of blood; and μ is the blood viscosity. The system is closed by the constitutive law linking pressure and area $P(A)$.

The vascular beds are treated as lumped models using five element Windkessel models shown in figure 1(a), such as in [4, 5]. The model contains the characteristic impedance of an artery Z_{art}; the characteristic impedance of a vein Z_{ven}; a vascular bed resistance R_p and the arterial and venous compliances C_{art} and C_{ven} respectively.

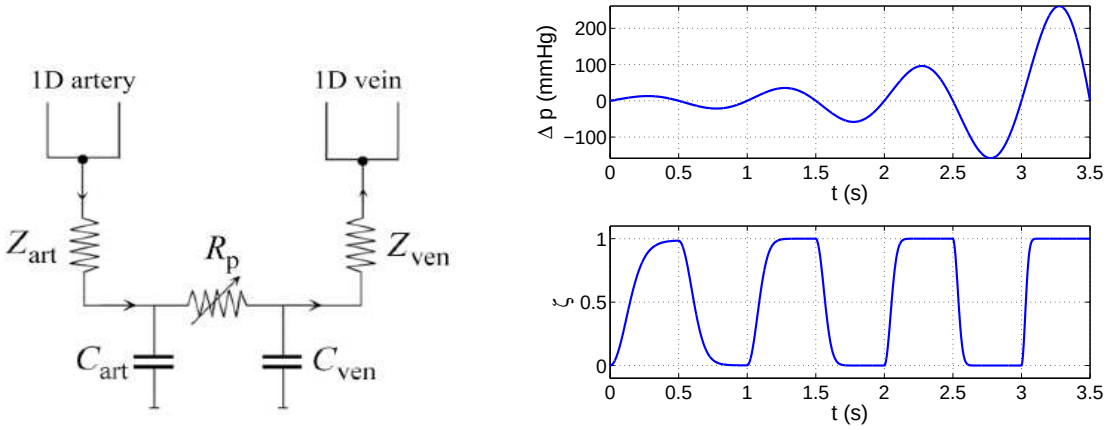

(a) Five element Windkessel model [5]

(b) Valve opening coefficient ζ for different values of ΔP

Figure 1: Peripheral circulation model and valve opening relationship with pressure difference across valve

The Windkessel model is treated by considering the following two noded resistance and compliance elements, which are coupled together by sharing a pressure node.

$$(P_1 - P_2)\frac{1}{R} = q_1 = -q_2, \qquad C\left(\frac{\partial P_2}{\partial t} - \frac{\partial P_3}{\partial t}\right) = q_3 = -q_4. \tag{3}$$

The heart and valve models are similar to those used in [5], which had been originally developed in [4]. The heart chambers are described using elastance curves E_{ch} built from two Hill functions. These elastance curves are used to construct the native E_{nat} and septal E_{sept} elastances. The pressure in a heart chamber is determined from

$$P_{ch} = E_{nat}\,(V_{ch} - V_{0,ch})\,[1 - K_{s,ch}Q_{ch}] + \frac{E_{nat}}{E_{sept}}P^*, \tag{4}$$

where V_{ch} is the volume of the chamber; $V_{0,ch}$ is the residual volume; $K_{s,ch}$ is a constant; Q_{ch} and P_{ch} is the flow rate and pressure in the heart chamber respectively; and P^* is the pressure in the contralateral chamber.

The valve model uses an opening coefficient $0 < \zeta < 1$ where

$$\frac{\partial \zeta}{\partial t} = K_o(1-\zeta)\Delta P, \qquad \frac{\partial \zeta}{\partial t} = K_c(\zeta)\Delta P. \tag{5}$$

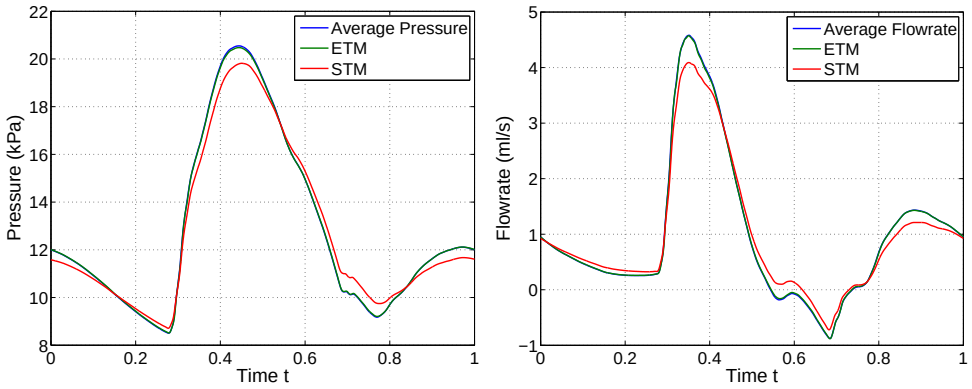

(a) Pressure in the right anterior tibial

(b) Flow Rate in the right anterior tibial

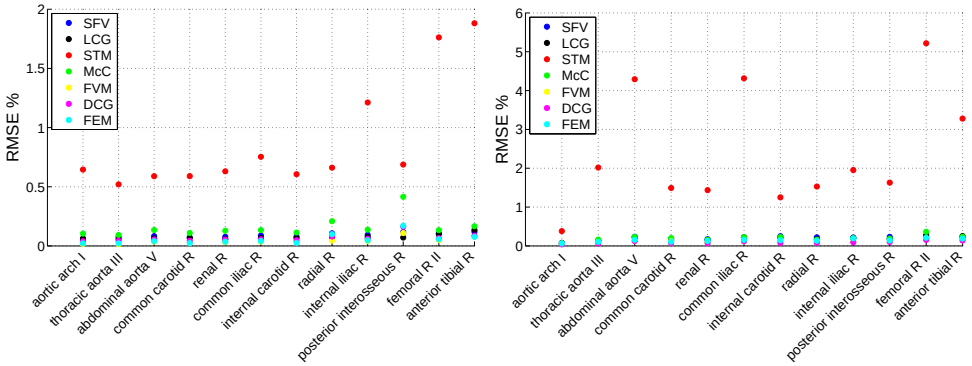

(c) RMSE of Pressure in various vessels

(d) RMSE of Flow Rate in various vessels

Figure 2: Pressure and flow rate waveforms and error comparison between ETM, STM and Averaged solution of methods from [1]

The relationship of this coefficient for varied pressure differences across the valves is shown in figure 1(b). This coefficient is used to determine an effective area, which, in turn is used to calculate the Bernoulli resistance B and inductance L. These are used to updated the flow rates using

$$\Delta P = BQ\,|Q| + L\frac{\partial Q}{\partial t}. \tag{6}$$

The implicit solver used is the enhanced trapezoidal method (ETM), which is a modified version of the simplified trapezoidal rule method (STM) [2]. The method relies on the ability to write the governing elemental equations in the form

$$\boldsymbol{F}_e\boldsymbol{P}_e^{n+1} + \boldsymbol{G}_e^c\boldsymbol{Q}_e^{c,n+1} = \boldsymbol{h}_e^n. \tag{7}$$

The method uses second order backward differences in time and the trapezoidal rule in space.

At vessel junctions the conservation of mass (8) is satisfied via the formulation, and, hence only conservation of total pressures (9) are held as system constraints. The constraints are held in place using using Lagrange multipliers. For example from a parent vessel (p) to N daughter vessels (d_i), constraint (9) will need to be satisfied, and hence N Lagrange multipliers will be needed.

$$g_1 = A_p u_p - \sum_{i=1}^{N} A_d^{(i)} u_d^{(i)} = Q_p - Q_{d1} - Q_{d2} = 0, \tag{8}$$

$$g_{i+1} = \frac{\rho}{2}\frac{Q_p^2}{A_p^2} + P_p - \frac{\rho}{2}\frac{Q_{di}^2}{A_{di}^2} - P_{di} = 0, \qquad i = 1, 2, \ldots, N. \tag{9}$$

The ETM scheme has been compared with benchmark problems from [1], and results are in agreement with other commonly used numerical methods.

3. Results

The enhanced trapezoidal rule method (ETM) has be applied to a cardiovascular network containing 56 one-dimensional vessels terminating in a three element Windkessel model, given in the benchmark paper [1]. For a time step of $\Delta t = 0.5$ ms and maximum element size of $\Delta x = 0.5$ mm the method gives expected results. Figure 2(a) shows the pressure in the right anterior tibial artery for the last cardiac cycle. The flow rate in the right anterior tibial artery is shown in 2(b). The root-mean-square error (RMSE) of pressure and flow rate waveforms for vessels which are monitored are shown in figures 2(c) and 2(d) respectively. The scheme was implemented in MATLAB Student R2013a (The MathWorks, Inc., Natick, MA, USA) on an Intel Core i5-3337U 1.8GHz. The code ran for 20 seconds per cardiac cycle and needed 8 cardiac cycles to converge to the desired tolerance.

4. Conclusions and Future Work

A 1D closed loop model using the ETM scheme is presented as an improvement to the STM [2]. The scheme has been compared with benchmark problems and gives excellent agreement with other commonly used schemes. Root mean square errors (RMSE) of the STM method vary up to 6.3% for flow rates and 2.3% for pressures. The new ETM method shows errors (whilst using the same time step and element size as the STM), that are less than 0.5% for flow rates and 0.25% for pressures.

The ETM scheme is being applied to a modified version of the model by [4], which is a closed loop system consisting of 396 1D vessels. The closed loop model is to be the basis for future research which involves investigating changes in the cardiovascular system during pregnancy. This will include the addition of ovarian and uterine arteries/veins, which increase significantly in diameter. The effects of a growing foetus will also investigated. Experimental data will be provided in order to aid the development and fine tuning of the model.

Acknowledgements

This work is funded by Swansea University and the College of Engineering.

References

[1] E. Boileau, P. Nithiarasu, P.J. Blanco, L.O. Müller, F.E. Fossan, L.R. Hellevik, W.P. Donders, W. Huberts, M. Willemet, J.Alastruey. A benchmark study of numerical schemes for one-dimensional arterial blood flow modelling. *International Journal For Numerical Methods In Biomedical Engineering*, e02732, 2015, DOI: 10.1002/cnm.2732.

[2] W. Kroon, W. Huberts, M. Bosboom, F. van de Vosse. A numerical method of reduced complexity for simulating vascular hemodynamics using coupled 0D lumped and 1D wave propagation models. *Computational and Mathematical Methods in Medicine*, (Article ID:156094), 2012, DOI: 10.1155/2012/156094.

[3] L.O. Müller, E.F. Toro. A global multiscale mathematical model for human circulation with emphasis on the venous system. *International Journal For Numerical Methods In Biomedical Engineering*, 30, 681-725, 2014, DOI: 10.1002/cnm.2622.

[4] J.P. Mynard, J.J. Smolich. One-Dimensional Haemodynamic Modeling and Wave Dynamics in the Entire Adult Circulation. *Annals of Biomedical Engineering*, Vol 43, No 6, 1443-1460, 2015, DOI: 10.1007/s10439-015-1313-8.

[5] J.P. Mynard, M.R.Davidson, D.J.Penny, J.J. Smolich. A simple, versatile valve model for use in lumped parameter and one-dimensional cardiovascular models . *International Journal For Numerical Methods In Biomedical Engineering*, 28, 626-641, 2012. DOI: 10.1002/cnm.1466

Solids and Structures I

Proceedings of the 24th UK Conference of the
Association for Computational Mechanics in Engineering
31 March - 01 April 2016, Cardiff University, Cardiff

GRADIENT ELASTICITY WITH THE MATERIAL POINT METHOD

***T.J. Charlton, W.M. Coombs and C.E. Augarde**

Mechanics Research Group, School of Engineering and Computing Sciences,
Durham University, Durham, DH1 3LE

*t.j.charlton@durham.ac.uk

ABSTRACT

The Material Point Method (MPM) is a method that allows solid mechanics problems with large deformation and non-linearity to be modelled using particles at which state variables are stored and tracked. Calculations are then carried out on a regular background grid to which state variables are mapped from the particles. There have been a selection of extensions to the MPM, for example, a problem in the original method that arises when a material point crosses the boundary between one background grid cell and another is addressed by the Generalised Interpolation Material Point (GIMP) method [2]. An area yet to be studied in as much depth in MPM is that conventional analysis techniques constructed in terms of stress and strain are unable to resolve structural instabilities such as necking or shear banding. This is due to the fact that they do not contain any measure of the length of the microstructure of the material analysed such as molecule size of grain structure. Gradient elasticity theories provide extensions of the classical equations of elasticity with additional higher-order terms [3]. This use of length scales makes it possible to model finite thickness shear bands that is not possible with traditional methods. Much work has been done on including the effect of microstructure on a linear elastic solid and has previously been combined with the Finite Element Method and with the Particle In Cell Method. In this work the MPM will be developed to include gradient effects.

Key Words: *Material Point Method; Gradient Elasticity*

1. The Material Point Method

The Material Point Method (MPM) was first developed by Sulsky *et al.* [1] as an extension for solid mechanics of the Particle in Cell (PIC) method used in fluid dynamics. The MPM can be referred to as a meshfree method as although a background grid of connected nodes is required to perform calculations, material properties are carried by a series of particles which are free to move independently of each other. In the MPM, material points, known as particles, store state variables and move through a background grid or mesh which can be changed or reset following each time step or load increment. This can be seen in Figure 1 where a material has been deformed and the mesh has been reset with particles in updated positions.

Initially a material domain is split into a number of elements similar to the Finite Element Method (FEM). Each of these elements are then populated with a number of material points, with each material point being assigned a weight based on the volume of material that the particle represents. In addition to the mesh covering the material's initial position, the mesh must extend to where the material is expected to deform as the particles move through the mesh during deformation.

In each element containing particles, the state variables must be mapped from the particles to the grid nodes. This mapping process is carried out within each element using shape functions similar to those used in the FEM. For instance the external force at a grid node, $\{f_g^{ext}\}$, (shown in 2D) given by

$$\{f_g^{ext}\} = \sum_{i=1}^{n_p} \{N(\xi_i, \eta_i)\} f_{p_i}^{ext} \tag{1}$$

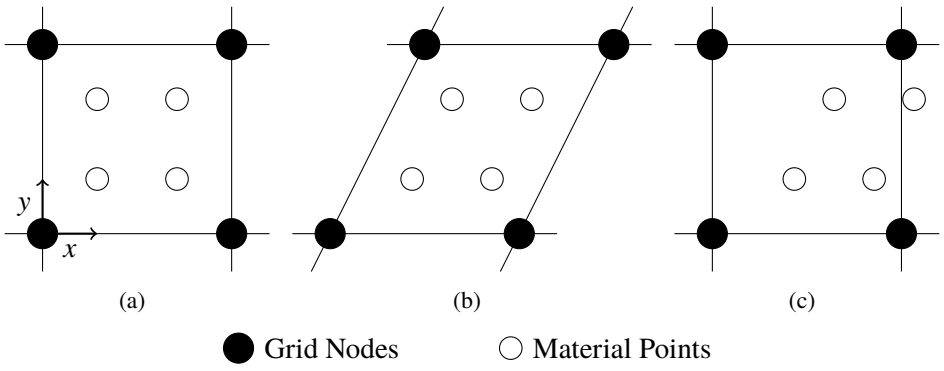

Figure 1: Material Point Method. Initial position of particles (a), deformed mesh and particles (b) and reset mesh with updated particles (c).

where f_p^{ext} is the particle external force, $\{N(\xi_i, \eta_i)\}$ are the nodal shape functions for the element containing the particle with local coordinates ξ and η and n_p refers to the number of material points in the grid element.

To be able to map to the correct grid nodes it is necessary to know in which element each material point located at a point in time. Although trivial initially, after particles have moved this problem can become more complex, especially if the mesh is not uniform. To simplify this process it is common to reset the background mesh to a uniform grid after each load step.

The stiffness of each element is determined from the contributions from each of the particles currently inside. A global stiffness matrix is assembled and the grid node displacements determined in a similar manner to FEM. At the end of a load step the grid node displacements $\{d_g\}$ are then mapped back to particles to get particle displacements for that loadstep $\{d_p\}$ through

$$\{d_p\} = \sum_{i=1}^{n_g} N_i \{d_{g_i}\}, \tag{2}$$

where n_g is the number of element nodes. The particle positions are then updated. The grid node displacements are not used to update the position of nodes in the mesh; the original undeformed mesh is used. An important aspect that should be noted is that even for linear MPM the simulation is done over multiple load steps, that is the MPM is an incrementally linear method.

2. Overview of gradient elasticity

Gradient elasticity theories are an extension of classical elasticity equations to account for microstructure of a material with extra higher order derivatives, the term gradient elasticity comes from higher order terms being proportional to the laplacian of lower order terms. An overview introducing gradient elasticity can be found in [3] by Askes and Aifantis.

Theories relating to enriching elasticity equations by capturing effects of microstructure using higher order gradients can be seen as far back as the 19th century. Theories were based on modelling particular physical phenomenon rather than mathematical completeness. More interest in the area developed in the 1960s when many studies began to extend this into elaborate full gradient theories, a landmark paper being Mindlin [5]. In modern times there has been another shift of interest towards simplified theories. This simplification allows for easier implementation with the popular FEM an example of this is the Ru-Aifantis theorem [6].

The majority of the gradient elasticity publications in the literature show how it can be used to eliminate strains singularities from dislocation lines and crack tips. However one of the current problems is the perceived drawback of identifying coefficients needed for implementing the method. It is clear that these

are somehow connected to the microstructure of a material however it is not clear what physically they represent. To be able to apply gradient elasticity to MPM it was necessary to choose a suitable method which should allow variables to be stored only at material points and not require any storage on the background grid. Due to the particles in the MPM being used as integration points the chosen method should not be too sensitive to slight errors in integration.

Mindilin's Theory of elasticity with microstructure [5] allows the deformation energy density U to be expressed as

$$U = \frac{1}{2}C_{ijkl}\varepsilon_{ij}\varepsilon_{kl} + \frac{1}{2}B_{ijkl}\gamma_{ij}\gamma_{kl} + \frac{1}{2}A_{ijklmn}\kappa_{ijk}\kappa_{lmn} + D_{ijklm}\gamma_{ij}\kappa_{klm} + F_{ijklm}\kappa_{ijk}\varepsilon_{lm} + G_{ijkl}\gamma_{ij}\varepsilon_{kl} \quad (3)$$

where the macroscopic strain ε_{ij} is defined from macroscopic displacements u_i, $\varepsilon_{ij} = \frac{1}{2}(u_{j,i} + u_{i,j})$. The microscopic deformation ψ_{ij} is used to calculate the micro-deformation gradient, $\kappa_{ijk} = \psi_{jk,i}$, and the relative deformation $\gamma_{ij} = u_{j,i} - \psi_{ij}$. However this is quite complicated, the constitutive tensors C_{ijkl}, B_{ijkl}, A_{ijklmn}, D_{ijklm}, F_{ijklm} and G_{ijkl} contain 1764 coefficients of which 903 are independent. It can shown that this can be reduced to 18 for isotropic materials however this is still an unworkably large number. As such there have been numerous simplifications to the theory to allow practical use in Engineering applications.

A simpler version was formulated by Mindlin using different relationships between macroscopic displacement u_i and microscopic deformation gradient κ_{ijk}. One example being that $\kappa_{ijk} = \varepsilon_{jk,i} = \frac{1}{2}(u_{k,ij} + u_{j,ik})$, here the micro deformation coincides with the gradient of macro deformation.

Based on work from the 1980s on plasticity [4] an extension of linear elasticity which can be shown to be a simplification of Mindlin theory using the Laplacian of the strain in the constitutive relationship.

$$\sigma_{ij} = C_{ijkl}(\varepsilon_{kl} - \ell^2\varepsilon_{kl,mm}) \quad (4)$$

where ℓ is a length scale parameter and C_{ijkl} is the classical constitutive tensor. Substituting this into the standard equilibrium equation gives

$$C_{ijkl}(u_{k,jl} - \ell^2 u_{k,jlmm}) + b_i = 0 \quad (5)$$

In [6] Ru and Aifantis show that this approach can be implemented in two steps with an uncoupled sequence of equations using an operator split.

To achieve this, first displacements u_i^c are are used obeying classical elasticity,

$$C_{ijkl}u^c_{k,jl} + b_i = 0, \quad (6)$$

this is then followed

$$u^g_k - \ell^2 u^g_{k,mm} = u^c_k, \quad (7)$$

where u_i^g are the gradient enriched displacements. This separation makes numerical solutions possible where they were not before with Mindlin's general theory. This split approach has the potential to be a good method to use with the MPM. Although this method doesn't remove all singularities at tips of sharp cracks this is not a major goal of the current MPM code as we are more interested in being able to model a shear band with a finite thickness.

In [7] this displacement based approach is compared with approaches where the displacements are replaced with strains and stresses. It is shown that all singularities are removed when the gradient enrichment is evaluated in terms of strains where this is not the case for the displacement approach. Both of these approaches will be considered when developing the MPM.

The Ru and Aifantis approach has been implemented in FEM in 1D to test the method before applying it to MPM. A bar with a young's modulus in one half 5 times greater than the other half (as shown in [7]), with original length of $10mm$, is extended by $0.1mm$. The axial strain is calculated using a classic FEM approach and a displacement based Ru and Aifantis gradient approach (u-RA) with $\ell = 2mm$. The results of this can be seen in figure 2 with the gradient approach eliminating the jump in strain.

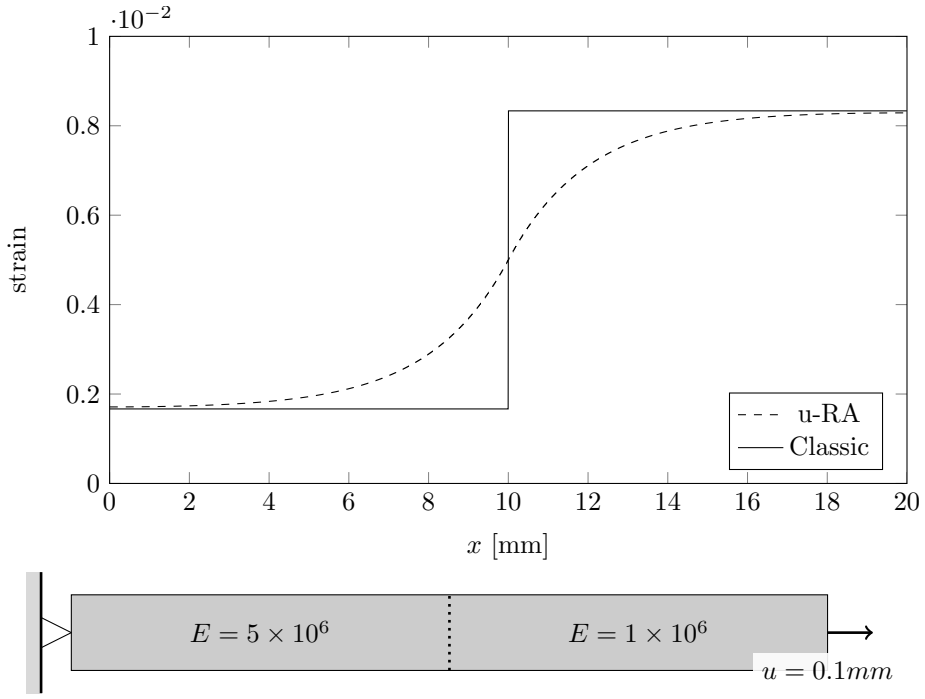

Figure 2: Strain along an extended bar using the FEM with and without gradient elasticity.

3. Current development and intended progress

As the operator split technique outlined above can be added as a post processing step it is possible to directly apply this to the MPM however due to the multiple steps in MPM it needs to be thought about whether gradient effects should be applied at the end of each loadstep or just at the end of the whole simulation. A further related question is will gradient dependent deformations map between grid and material points or are they only related to the grid? This work so far outlines the very basics of applying gradient effects to the MPM, for more interesting geomechanics problems it is likely that it will be necessary to implement plasticity and look at gradient plasticity methods.

References

[1] D. Sulsky, Z. Chen, and H. Schreyer, A particle method for history-dependent materials, *Computer Methods in Applied Mechanics and Engineering*, vol. 118, pp. 179 − 196, 1994.

[2] S. Bardenhagen and E. Kober, The generalized interpolation material point method, *Computer Modeling in Engineering and Sciences*, vol. 5, no. 6, pp. 477−496, 2004.

[3] H. Askes, E. C. Aifantis, Gradient elasticity in statics and dynamics: an overview of formulations, length scale identification procedures, finite element implementations and new results, *International Journal of Solids and Structures* 48 (13) (2011) 1962−1990.

[4] E. C. Aifantis, The physics of plastic deformation, *International Journal of Plasticity* 3 (3) (1987) 211−247.

[5] R. D. Mindlin, Micro-structure in linear elasticity, *Archive for Rational Mechanics and Analysis* 16 (1) (1964) 51−78.

[6] C. Ru, E. Aifantis, A simple approach to solve boundary-value problems in gradient elasticity, *Acta Mechanica* 101 (1−4) (1993) 59−68.

[7] H. Askes, I. Morata, E. C. Aifantis, Finite element analysis with staggered gradient elasticity, *Computers and Structures* 86 (11) (2008) 1266−1279.

Proceedings of the 24th UK Conference of the
Association for Computational Mechanics in Engineering
31 March - 01 April 2016, Cardiff University, Cardiff

Implicit essential boundaries in the Material Point Method

***Michael Cortis[1], William Coombs[1] and Charles Augarde[1]**

[1]School of Engineering and Computing Sciences, Durham University, South Road, Durham, DH1 3LE

*michael.cortis@durham.ac.uk

ABSTRACT

The Material Point Method (MPM) is a numerical boundary value problem (BVP) solver developed from particle-in-cell (PIC) methods that discretises the continuum into a set of material points. Information at these material points is mapped to a background Eulerian grid which is used to solve the governing equations. Once solved information is updated at the material points and these points are convected through the grid. The background grid is then reset, allowing the method to easily handle problems involving large deformations without mesh distortion. However, imposition of essential boundary conditions in the (MPM) is challenging when the physical domain does not conform to the background grid. In this research, an implicit boundary method (IBM), based on the work of Kumar et al. [1], is proposed to ensure that essential boundary conditions are satisfied in elastostatic MPM problems.

Key Words: *material point method; particle method; implicit boundary method; boundary conditions*

1. Introduction

A new modelling framework is under development at Durham University for problems associated with the ploughing of the seabed, an activity required for installation of offshore energy infrastructure (e.g. wind, tidal and marine) [1]. EPSRC have funded this research project (grant refs EP/M000397/1 and EP/M000362/1) with experimental work at Dundee University to validate the computational models developed at Durham [2]. The computational framework is based around the Material Point Method, first proposed in the 1990s [3], chosen because it is capable of modelling problems in which very large deformations occur, without the need for expensive remeshing and mapping of history variables.

The MPM for solid mechanics is described in detail in a number of references, usually in an explicit format (e.g. see [4]) although it is also possible to work with a fully implicit formulation (e.g. [5, 6]). Rather than present a lengthy derivation of the method here, the MPM is explained by reference to Figure 1. A problem domain is discretised as a set of distributed material points. In each load step, information carried at the points is interpolated to a surrounding grid of finite elements, larger than the problem domain itself. The BVP is solved on this grid using standard finite elements and the solution mapped back to the material points, which are translated into their new positions. The grid is then discarded and a new one provided for the next load step. In this way (a mixture of Lagrangian and Eulerian approaches) the issue of mesh entanglement is entirely avoided, while the individual pieces of the formulation use standard and robust finite element technology.

2. The Implicit Boundary Method

A key issue in the use of the MPM, and one not covered adequately in the existing literature, is the imposition of essential boundary conditions. Only if the background grid edge is coincident with the location of an essential boundary condition is a trivial solution to this problem possible and in the majority of modelling situations this is not possible to ensure. Burla and Kumar [7] addressed a similar problem with standard finite elements and developed a method for imposing essential boundary conditions away from finite element edges, based on ideas proposed over 50 years ago [8], using a trial function for displacement $\boldsymbol{u}$ defined as

$$\boldsymbol{u} = \boldsymbol{D}\boldsymbol{u}^g + \boldsymbol{u}^a, \tag{1}$$

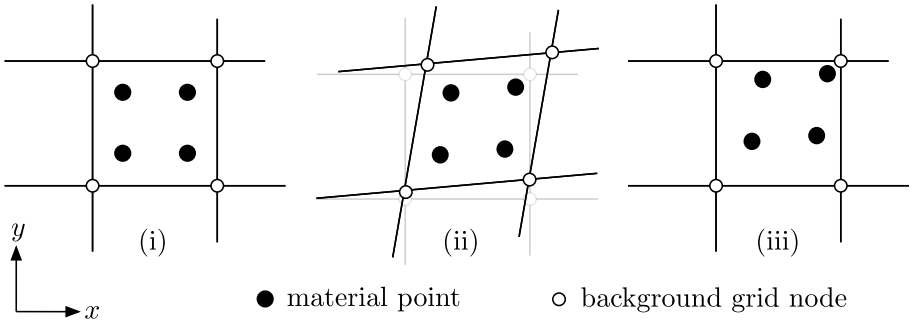

Figure 1: Steps in the Material Point Method

where $\boldsymbol{D}$ are Dirichlet functions, the components of which vanish on essential boundaries leading to the imposition of essential boundary conditions specified by $\boldsymbol{u}^a$, which could, of course, be homogeneous. The Dirichlet functions operate on the grid variable $\boldsymbol{u}^g$ which is defined in standard ways using finite element or other approaches. The same Dirichlet functions are used to construct test functions for substitution into a weak form of the PDE to be solved. The implicit boundary method for finite elements described in Burla and Kumar [7] is restricted to boundaries parallel to one or other of the coordinate axes. As part of the current project we have extended the implicit boundary method both to the MPM and also for the case of inclined boundaries and a few details and validation are presented here with a detailed description to appear in a forthcoming paper.

Figure 2 shows a straight inclined boundary in a 2D frame. For this boundary, a suitable expression for

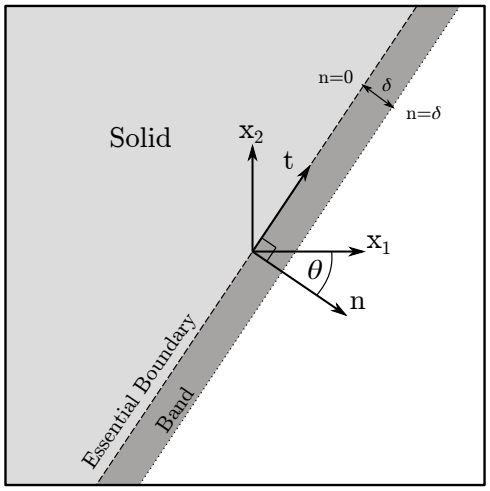

Figure 2: An implicit, inclined essential boundary showing the band width δ.

the Dirichlet function is

$$D = \frac{2n}{\delta} - \frac{n^2}{\delta^2}, \tag{2}$$

where δ defines the width of a narrow band adjacent to the boundary over which the Dirichlet function varies from zero to unity. In the implicit boundary MPM, the weak form leads to stiffness matrices associated with grid elements, which can be decomposed as follows

$$\boldsymbol{K}_e = \boldsymbol{K}_1 + (\boldsymbol{K}_2 + \boldsymbol{K}_2^T) + \boldsymbol{K}_3. \tag{3}$$

$\boldsymbol{K}_1$ is the standard local stiffness matrix of the part of the element within the solid region, while $\boldsymbol{K}_2$ and $\boldsymbol{K}_3$ are present only if an essential boundary crosses the element. These matrices are obtained from integration of matrix triple products similar to standard element stiffness matrices but with $\boldsymbol{B}$

matrices containing products of shape functions, Dirichlet functions and derivatives of both, and with transformations to fit inclined boundaries. Other approaches to dealing with this problem, e.g. non matching meshes and embedded boundary problems [9, 10], often requires the use of more complex techniques such as Lagrange multipliers, penalty methods or variations which do not have the advantage of being close to simple finite element formulations as here.

3. Validation

To demonstrate the implementation of this implicit boundary method in the MPM, results are presented for a very simple model problem. A 2D plane strain square domain of linear elastic material (100 units square) is subjected to uniaxial compression orthogonal to one side with “roller" boundary conditions on the other three sides. This problem was tested for various inclinations of the square domain while maintaining a structured background grid (Figures 3, 6 and 9). The problem domain was initially discretized by a set of material points each of which centred on a 10 unit square domain. Any void region was then truncated from material point domains lying on the border of the solid continua, and the associated material point was repositioned to the new centroid of the domain. The initial volume associated with every material point was then determined from the area of its domain. The background grid on which the elastic problem was solved consisted of a regular grid of bilinear quadrilateral elements (each 10 units square). The relative displacement and stress errors were computed and are plotted in Figures 4 & 5 (

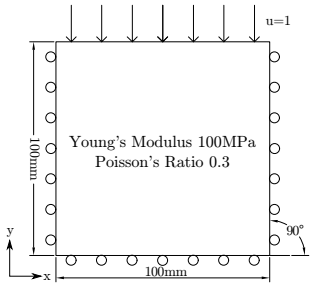

Figure 3: 90° Model

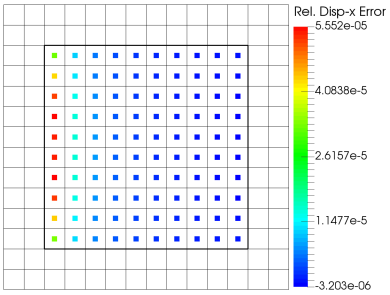

Figure 4: Relative Error in Displacement - 90° Model

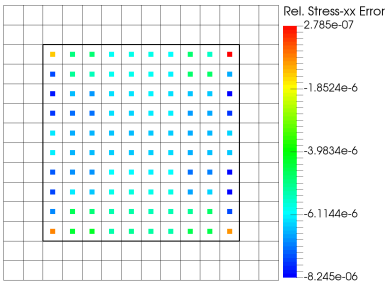

Figure 5: Relative Error in σ_{yy} - 90° Model

90° model), 7 & 8 (45° model), 10 & 11 (30° model) respectively. 5.55e-5 and 8.25e-6 relative errors in displacements and stress were obtained in the 90° model when compared to the analytical solution. The relative error in displacements and stresses reduced to 1.06e-3 and 9.9e-4 in the 45° model, and 3.14e-3 and 4.48e-3 in the 30° model respectively.

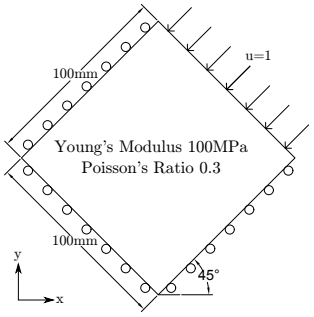

Figure 6: 45° Model

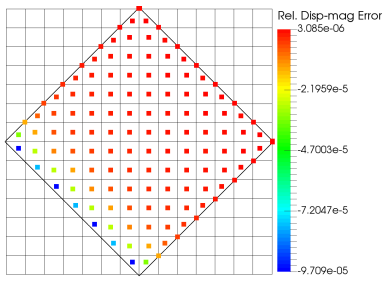

Figure 7: Relative Error in Displacement - 45° Model

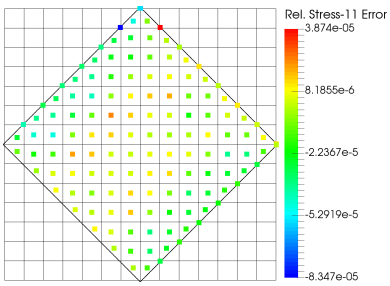

Figure 8: Relative Error in σ_1 - 45° Model

4. Conclusions

A method for imposing essential boundary conditions in the MPM without adjusting the grid or layout of material points is demonstrated in this paper. It takes a simple idea previously applied to coordinate-parallel boundaries crossing finite elements, and further develops it to model inclined essential boundaries (e.g. rollers) within an exciting new numerical methods. Ongoing work will take this into 3D.

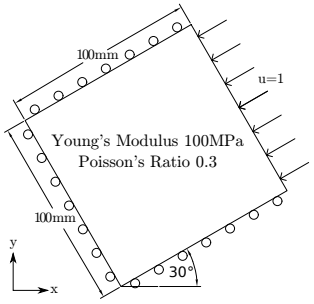

Figure 9: 30° Model

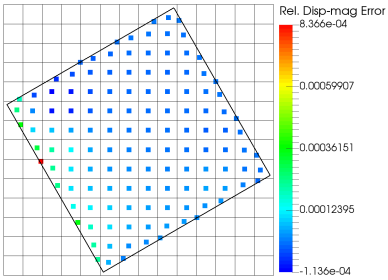

Figure 10: Relative Error in Displacement - 30° Model

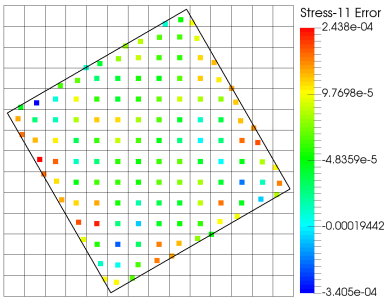

Figure 11: Relative Error in σ_1 - 30° Model

Acknowledgements

The research described in this paper is supported by the UK EPSRC in grants EP/M000397/1 and EP/M000362/1.

References

[1] K.D. Lauder, M.J. Brown, M.F. Bransby, and S. Boyes. The influence of incorporating a forecutter on the performance of offshore pipeline ploughs. *Applied Ocean Research*, 39:121 – 130, 2013.

[2] T Robinson, M.J. Brown, A.J. Brennan, M. Cortis, C.E. Augarde, and W.M. Coombs. Development of low cost 3d soil surface scanning for physical modelling. In *3rd European Conference on Physical Modelling in Geotechnics (Eurofuge 2016), Nantes, France. 1-3 June.*, 2016.

[3] D. Sulsky, Z. Chen, and H.L. Schreyer. A particle method for history-dependent materials. *Computer Methods in Applied Mechanics and Engineering*, 118:179–196, 1994.

[4] S.G. Bardenhagen and E.M. Kober. The generalized interpolation material point method. *CMES-Computer Modeling in Engineering and Sciences*, 5(6):477–495, JUN 2004.

[5] T.J. Charlton, W.M. Coombs, and C.E. Augarde. On the implicit implementation of the Generalised Interpolation Material Point method. In *Proc. 23rd ACME conference (Gil & Sevila, Eds), Swansea, April.*, 2015.

[6] J.E. Guilkey and J.A. Weiss. Implicit time integration for the material point method: Quantitative and algorithmic comparisons with the finite element method. *International Journal for Numerical Methods in Engineering*, 57:1323–1338, 2003.

[7] R. K. Burla and A.V. Kumar. Implicit boundary method for analysis using uniform B-spline basis and structured grid. *International Journal for Numerical Methods in Engineering*, 76(13):1993–2028, December 2008.

[8] L.V. Kantorovich and V.I. Krylov. *Approximate Methods of Higher Analysis*. Interscience Publishers, 1958.

[9] D. Schillinger, M. Ruess, N. Zander, Y. Bazilevs, A. Düster, and E. Rank. Small and large deformation analysis with the p- and b-spline versions of the finite cell method. *Computational Mechanics*, 50(4):445–478, 2012.

[10] M. Hautefeuille, C. Annavarapu, and J. E. Dolbow. Robust imposition of dirichlet boundary conditions on embedded surfaces. *International Journal for Numerical Methods in Engineering*, 90(1):40–64, 2012.

Proceedings of the 24th UK Conference of the
Association for Computational Mechanics in Engineering
31 March – 01 April 2016, Cardiff University, Cardiff

Effect of shear load direction in the critical buckling of anisotropic composite laminates under combined in plane loading

Muthana Sh. Al-Saymaree [1, 2], David Kennedy [1] and Carol Featherston [1]

[1]Cardiff School of Engineering, Queen's Buildings, The Parade, Cardiff CF24 3AA, United Kingdom
[2]Basrah University, Basrah, Iraq
Al-SaymareeMS@cardiff.ac.uk

ABSTRACT

This paper studies the buckling behaviour of anisotropic composite laminates under combined in-plane compression and shear loading using the exact strip analysis software VICONOPT to calculate the critical buckling load of a range of plates. Changes in critical buckling load are studied for both flat and stiffened composite plates and the results presented in the form of interaction curves. Different lay-ups are studied to illustrate the effect of different combinations of anisotropy and shear load direction on the critical load factor. Results are validated using the finite element software ABAQUS/Standard.

Key words: *Buckling, Anisotropic, Laminates, Combined loading, VICONOPT*

1. INTRODUCTION

Composite plates and panels are used in aerospace, marine structures, bridges and other structural applications, where they offer mass reductions over conventional materials, fulfilling a key commercial objective. When used for example in aircraft fuselage and wings, these structures are subject to in-plane compression, shear or a combination of both making them sensitive to buckling failure. The buckling of composite plates under combined loading can be described by buckling interaction curves. Many theoretical and experimental studies have investigated this buckling failure. Stowell and Schwartz [1] studied the behaviour of an infinitely flat plate under combined shear and direct stress, whilst Selyugin [2] studied flexural anisotropic plates under combined loading using a special Galerkin-type solution and compared it with a high accuracy numerical solution, for cases of combined in plane compression, shear and in plane bending.

In the case of an anisotropic composite laminate under pure compression the nodal lines (i.e. lines of zero out of plane displacement) are skewed. In the presence of shear loading the skewing of these nodal lines can be increased or decreased according to the shear load direction, with consequent decreases or increases in the critical buckling load. This study explores this effect using the exact strip analysis software VICONOPT [3] which has the capacity to carry out buckling, post buckling and vibration analysis and optimum design for prismatic composite plate assemblies to determine critical buckling loads for composite plates under different combinations of loads. Examples for flat plates and stiffened panels with different aspect ratios and stiffener sizes are studied, with results validated using the finite element software ABAQUS/Standard [4]. Composites are designed to minimize panel mass subject to critical buckling constraints involving specified loading combinations.

2. CASE STUDY

Results are first presented for two rectangular composite flat plates under combined in plane compression (N_x) and shear (N_{xy}). The plates are made of T300-carbon/5208 epoxy tape material, of thickness 0.125 mm with Young's moduli E_1=181 GPa, E_2= 10.3 GPa, shear modulus G_{12}=7.17 GPa and Poisson's ratio ν_{12}= 0.28. Plates 1 and 2 have the symmetric layups $[45,-45, 45, 90, 45,-45, 45, 0]_s$ and $[45, 45, -45, -45, 45, 45, -45, -45]_s$, respectively. Both plates have length a, width b=500 mm and total thickness 2 mm. Results are then presented for two stiffened panels made from the same material, each of length a and width b=400mm, and having four blade stiffeners of height 25mm, 100mm from each other and 50mm from the panel edges. In both panels the skin has the symmetric layup $[45, -45, 0, 90]_s$. The stiffeners also have this layup in panel 1, while in panel 2 they have the thicker layup $[45, -45, 0, 90, 45, -45]_s$. Each of the plates and panels has simply supported edges.

The results for flat plates and stiffened panels are denoted by FL i-j and ST i-j, respectively, where i (=1,2) indicates the different layups defined in this paragraph, and j (=1,2,3) indicates one of three aspect ratios considered: (1) a/b=1, (2) a/b=1.5, (3) a/b=2.

3. SOFTWARE USED

VICONOPT [3] incorporates the earlier programs VIPASA [5] and VICON [6]. VIPASA analysis uses exact flat plate theory and an algorithm that guarantees convergence on critical buckling loads or natural frequencies [7]. The buckling and vibration modes are assumed to vary sinusoidally in the longitudinal direction. However, when shear or anisotropy is present the nodal lines are skewed and the solution becomes excessively conservative because it cannot satisfy simply supported end conditions [5]. VICON analysis overcomes this limitation by coupling VIPASA responses using Lagrangian multipliers to satisfy point constraints representing the required end conditions. VICON and VIPASA results are compared with finite element results from ABAQUS/Standard 6.12 software. The flat plates and panels with aspect ratio a/b=1 were modelled, respectively, using 400 and 1280 shell elements of type S4R5 [2].

5. DISCUSSION OF NUMERICAL RESULTS

Fig. 1 shows interaction curves for plate FL 2-3. The VICON results show that under pure compression the buckling load N_x is 9.64 kN/m, which increases to 9.99 (10.00) kN/m when accompanied by a positive shear load N_{xy} of 2.00 (4.00) kN/m. These increases occur because of the anti-clockwise skewing of the mode due to anisotropy is negated by the clockwise skewing due to the shear load, so that eventually the nodal lines become normal to the longitudinal edges of the plate and then skew in the opposite direction. It can be seen that there is good agreement between the critical buckling loads obtained by VICONOPT and ABAQUS, and it was noted that there is also good agreement between the mode shapes with the ABAQUS results showing the same pattern. Both programs show that the composite laminate can carry greater loads when the shear load acts to reduce the skewing which then reduce as the skewing occurs in the other direction. Shear loading in the same direction of the skewing also cause a reduction in buckling load

The results for stiffened panel ST 1-1 are shown in Fig. 2. Although the buckling mode is different from that of the flat plates, the same effect is observed. The VICON compressive buckling load N_x increases from 33.5 kN/m to 34.3 (34.4) kN/m when accompanied by a positive shear load N_{xy} of 4.29 (8.60) kN/m, and similar results were obtained using ABAQUS.

Figs. 3 and 4 summarise the interactions for all the plates and panels. In all cases the addition of a small positive shear load (which in this case acts to reduce the skewing) increases the compressive buckling load. Buckling load factors under combined compression and positive shear exceed those under combined compression and negative shear by 2%-8% for flat plates and by 3%-12% for stiffened panels. Fig. 5 illustrates that the maximum compression can be carried when there is no skewing in the buckling mode.

6. CONCLUSIONS

- The critical compressive buckling load increases slightly and then decreases for both flat composite plates and stiffened composite panels when the skewing of the buckling mode due to an applied shear load acts in the opposite direction to the skewing due to anisotropy.
- Conversely the compressive buckling load decreases significantly when the shear and anisotropy effects act in the same direction to increase the skew in the buckling mode.
- Critical buckling loads under combined compression and positive shear are significantly higher than those under combined compression and negative shear.
- The increment in critical buckling load depends on the layup of the composite laminate, whose anisotropy can be optimised to carry a particular combination of compression and shear.

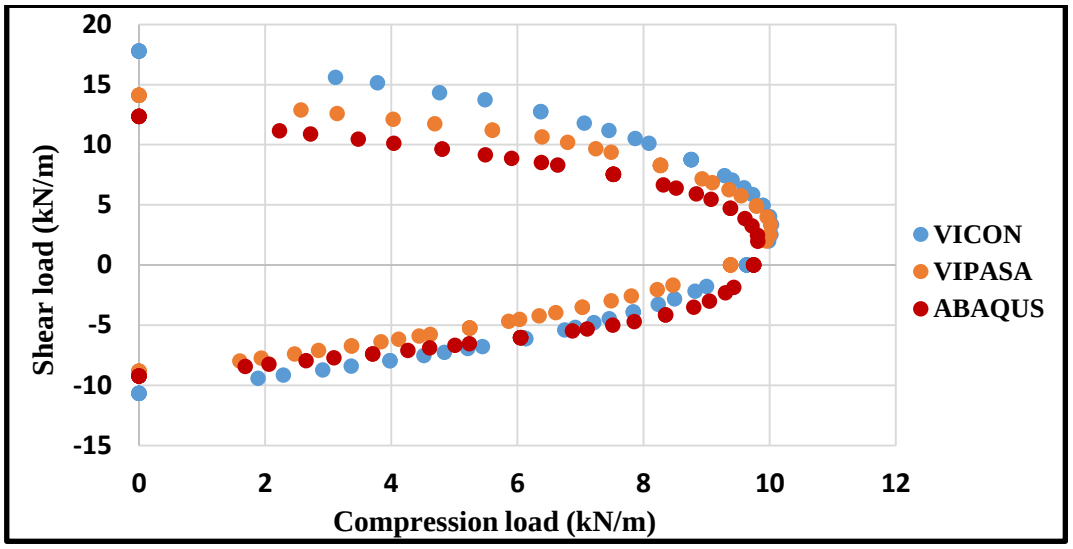

Fig. 1. Interaction curve for flat plate FL 2-3.

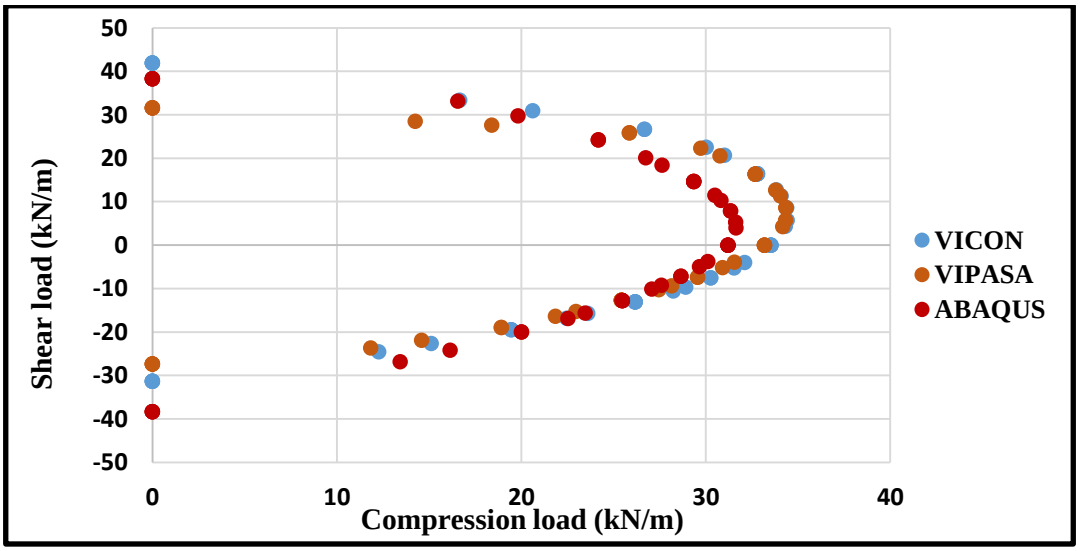

Fig. 2. Interaction curve for stiffened panel ST 1-1.

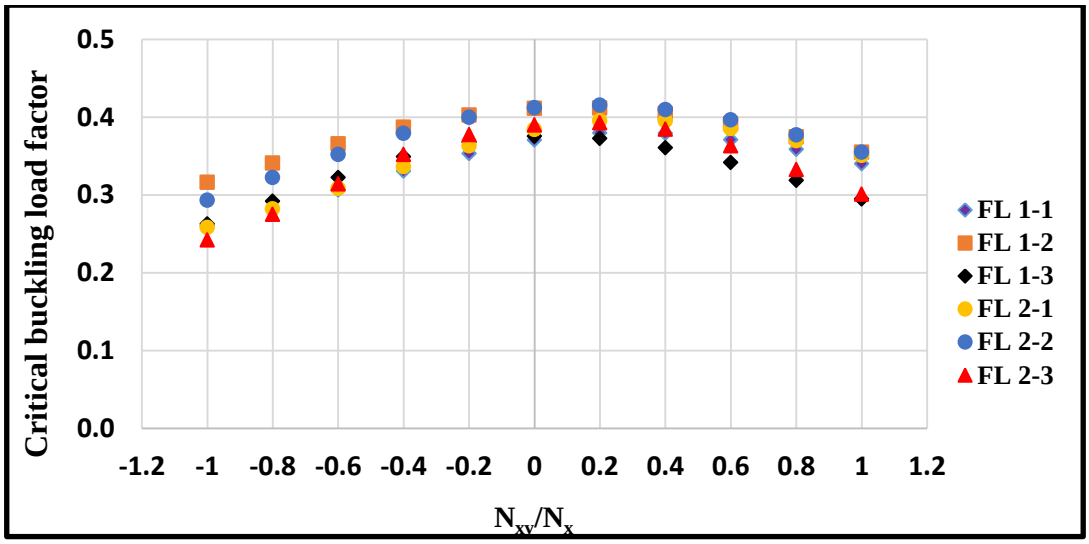

Fig. 3. Variation of ABAQUS buckling load factor with interaction ratio for all flat plates.

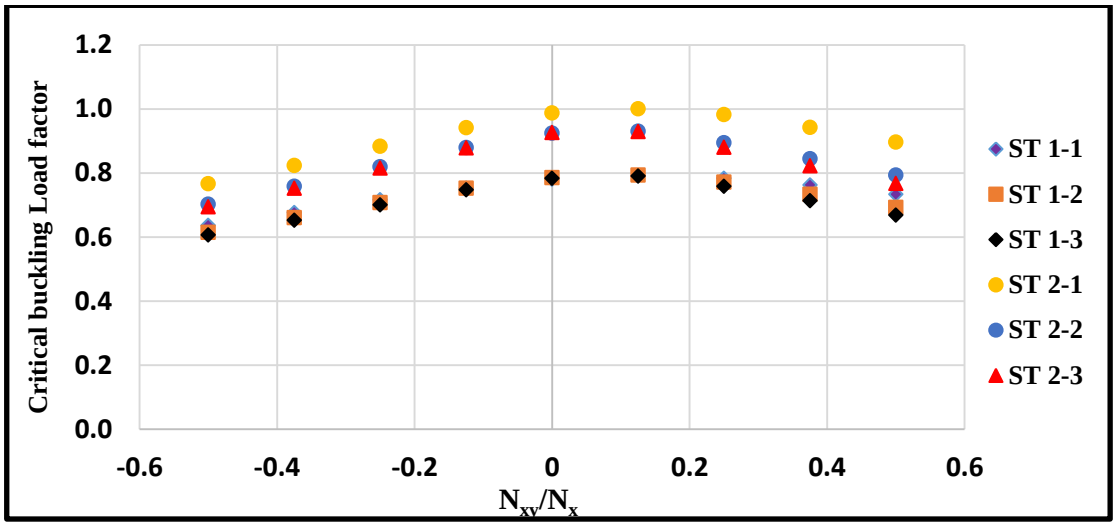

Fig. 4. Variation of ABAQUS buckling load factor with interaction ratio for all stiffened panels.

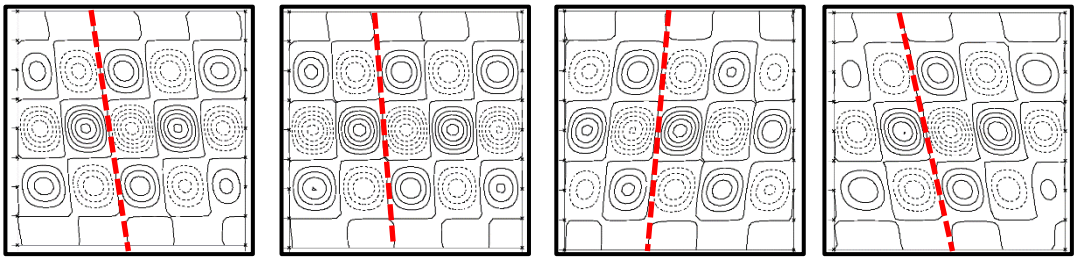

(a) $N_{xy}/N_x = 0$ (b) $N_{xy}/N_x = 0.125$ (c) $N_{xy}/N_x = 0.375$ (d) $N_{xy}/N_x = -0.125$

Fig. 5. VICON mode shapes of stiffened panel ST 2-1 for four different interaction ratios.

References

[1] Stowell, E. Z. and Schwartz, E. B., Critical stress for an infinitely long flat plate with elastically restrained edges under combined shear and direct stress. *NACA ARR 3K13*, 1943.

[2] Selyugin, S., Some approaches to buckling analysis of flexurally anisotropic composite plates subjected to combined in-plane loading. *Thin Walled Structures* **98**, 375-383, 2016.

[3] Kennedy, D. and Featherston, C.A., Exact strip analysis and optimum design of aerospace structures. *Aeronautical Journal*, **114**, 505-512, 2010.

[4] DS Simulia Inc. *ABAQUS Standard Manual* (version 6.10), 2012.

[5] Wittrick, W. H. and Williams, F.W., Buckling and vibration of anisotropic or isotropic plate assemblies under combined loadings. *International Journal of Mechanical Sciences*, **19**, 209-223, 1974.

[6] Anderson, M. S., Williams, F.W. and Wright, C.J., Buckling and vibration of any prismatic assembly of shear and compression loaded anisotropic plates with an arbitrary supporting structure. *International Journal of Mechanical Sciences*, **25**, 585-596, 1983.

[7] Wittrick, W.H. and Williams, F.W., A general algorithm for computing natural frequencies of elastic structures. *Quarterly Journal of Mechanics and Applied Mathematics*, **24**, 263-284, 1971.

Failure and Damage I

Proceedings of the 24th UK Conference of the
Association for Computational Mechanics in Engineering
31 March - 01 April 2016, Cardiff University, Cardiff

Branched crack modelling with the Cracking Particle Method

***Weilong Ai[1], Charles Augarde[1] and Jon Trevelyan[1]**

[1]School of Engineering and Computing Sciences, Durham University, South Road, Durham, DH1 3LE, UK

*weilong.ai@durham.ac.uk

ABSTRACT

Multiple crack simulation is of great importance in failure analysis since fracture in brittle materials in practice usually comprises multiple cracks. Traditional numerical methods such as the extended finite element and the element free Galerkin methods meet dilemmas when solving this kind of problem, as the computational expense increases with the number of level set functions used for crack descriptions. The cracking particle method (CPM) developed by Rabczuk, by which crack patterns are simplified and discretized through a set of cracking segments, has shown to be a promising alternative. The branched crack problem, as a representative of multiple crack problems, is studied here to demonstrate the advantages of the CPM. Cracking particles can be split multiply due to the use of bilinear cracking lines and then the discontinuity at the intersection is fulfilled easily. An adaptivity strategy is adopted to control the size of cracking segments and the number of degrees of freedom. Stress intensity factors at the crack tips are calculated and show good agreement with previous results.

Key Words: *branched cracks; cracking particle method; meshfree; adaptivity*

1. Introduction

Multiple-crack problems are common in natural brittle fracture, but are still challenging to model with current numerical methods, since crack propagation is a highly non-linear phenomenon. The finite element method (FEM) is the most common numerical method that has been tried on crack problems, however in its basic form requires that a crack edge propagates along element edges, otherwise there will be an overestimation of fracture energy [1]. The extended finite element method (XFEM) was proposed primarily to model cracks without reference to mesh arrangements but via enrichments [2]. A major issue, however, is that it requires an explicit description of crack surfaces which is usually through level set functions and this process becomes more complex with an increase in numbers of cracks [3]. Meshless methods only require nodal data to discretise a problem domain and can avoid many problems associated with element-based methods, such as mesh distortion and volumetric locking [4]. These methods have also been applied to crack simulation, combined in some cases with the level set method [5], then leading to the same issues with the XFEM as mentioned above. The numerical manifold method (NMM) has also been tried for multiple crack problems by separating the problem domain into “mathematical covers" and “physical covers", but it is still a bottleneck to generate these covers effectively [6]. The cracking particle method (CPM) was proposed to approximate a 2D crack path by the use of nodes with discontinuous lines representing crack paths [7, 8], a method in which it is relatively easy to update cracks through adding or deleting cracking particles, which makes it a promising way to handle cracks with complex patterns. In this work, the branched crack is studied as a representative of multiple-crack problems. A modified CPM is presented in which cracking particles can be split multiply. Numerical results are provided to demonstrate the performance of the proposed methodology.

2. Formulations

Consider a branched crack problem in two dimensions (2D) as shown in Fig. 1(a). The equilibrium equation in the domain Ω is

$$\nabla \cdot \boldsymbol{\sigma} = \mathbf{0} \qquad \text{in } \Omega \tag{1}$$

with boundary conditions

$$\boldsymbol{\sigma} \cdot \mathbf{n} = \bar{\mathbf{t}} \qquad \text{on } \Gamma_t, \tag{2}$$

$$\mathbf{u} = \bar{\mathbf{u}} \qquad \text{on } \Gamma_u, \tag{3}$$

where $\boldsymbol{\sigma}$ and $\mathbf{u}$ are the Cauchy stress tensor and displacement vector respectively, and body forces are not considered. $\mathbf{n}$ is the unit normal to the domain Ω, $\bar{\mathbf{t}}$ and $\bar{\mathbf{u}}$ are traction and displacement constraints on the boundary Γ with $\Gamma = \Gamma_t \bigcup \Gamma_u$.

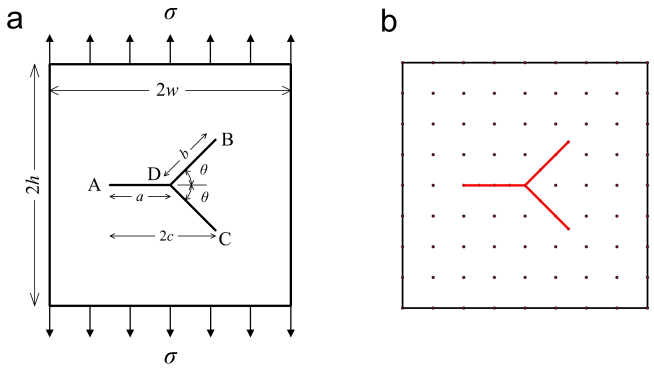

Figure 1: Problem statement: (a) sketch; (b) initial nodes.

In this work, the Element Free Galerkin method is used where Eqns 1 to 3 are discretised into a weak form and the essential boundary conditions are imposed with Lagrange multipliers. The approximate displacement at location $\mathbf{x}$ in Ω, $u^h(\mathbf{x})$ is given by a linear combination of shape functions $\Phi_i(\mathbf{x})$ and nodal displacements u_i as

$$u^h(\mathbf{x}) = \sum_{i=1}^{n} \Phi_i(\mathbf{x}) u_i = \boldsymbol{\Phi}^{\mathrm{T}} \mathbf{u}, \tag{4}$$

where i is the node index with coordinate $\mathbf{x}_i$ and n is the number of nodes. The shape functions $\Phi_i(\mathbf{x})$ are determined via a moving least squares (MLS) approximation and a quartic spline weight function is used, more details can be found in [4].

3. Crack description

In the CPM, crack surfaces are described by a set of cracking particles with discontinuous lines cutting the support. The discontinuity at cracks was firstly achieved through enrichments in the original CPM paper [7] and it has been shown that these enrichments can be removed by splitting cracking particles into two parts [8]. However, it is very hard to describe a branched crack in that way. Here a multiple split strategy is presented which is much simpler than approaches using level set functions,e.g. in [3, 5].

A point D at the branch point with a circular support as in Fig. 2 is split into three nodes D_1, D_2 and D_3 and the support of node D is cut by three crack branches. Point D_1 belongs to crack AD and DB, Point D_2 belongs to crack DB and DC and Point D_3 belongs to crack DC and DA. Nodes D_1, D_2 and D_3 are not connected to each other. The visibility method [4] is used to handle relationships among all nodes, through which discontinuity at crack surfaces is achieved.

4. Adaptivity

An *a posteriori* adaptivity strategy, as found in [10], is employed here to handle the contradiction between accuracy and calculating efficiency. Sound nodal arrangements with a high density of nodes around crack surfaces and fewer nodes away from cracks can be set up automatically. An error estimator for each cell (with subdomain Ω_i) is based on the difference between the "projected" stress $\boldsymbol{\sigma}$ (to approximate the unknown exact stresses [9]) and the calculated stress $\boldsymbol{\sigma}^h$ using the error energy norm

$$\|E_i\| = \left\{ \frac{1}{2} \int_{\Omega_i} (\boldsymbol{\sigma}^p - \boldsymbol{\sigma}^h)^{\mathrm{T}} \mathbf{D}^{-1} (\boldsymbol{\sigma}^p - \boldsymbol{\sigma}^h) \mathrm{d}\Omega_i \right\}^{1/2}, \tag{5}$$

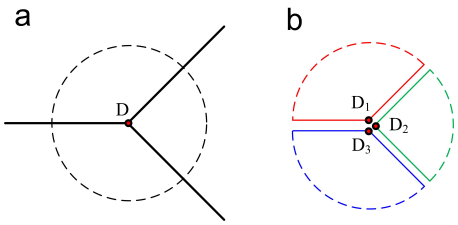

Figure 2: Multiply split cracking particle: (a) original support; (b) supports after being split.

with the elastic constitutive matrix being

$$\mathbf{D} = \frac{E}{1-\nu^2}\begin{bmatrix} 1 & \nu & 0 \\ \nu & 1 & 0 \\ 0 & 0 & (1-\nu)/2 \end{bmatrix} \quad \text{for plane stress .} \tag{6}$$

Cells with large errors are divided into four sub-cells by a quadtree structure and four sub-cells with small errors are combined together to recover an original cell.

5. Numerical results

The dimensions of the branched crack problem in Fig. 1 are $h = w = 50$mm, $\theta = 45°$ and $a = b = 25$mm with initial node arrangements in Fig. 1 (b). The material properties are Young's modulus $E = 200$GPa and the Poisson's ratio $\nu = 0.3$. A pair of uniform tensions are applied with $\sigma = 200$N/mm as shown under plane stress conditions.

The adaptive steps of the branched crack problem are shown in Fig. 3. During this process, three groups of nodes generate automatically around three crack tips, and the crack opening is achieved as in Fig. 3 (d). Global errors during the adaptive steps are shown in Fig. 4 (a) and the convergence rate achieved using the adaptive refinement is shown to be higher than that using uniform refinement. From Fig. 4 (b, c and d), it can be seen that calculated stress intensity factors around crack tips agree well with [3], and the difference with [5] is reasonable since those results were calculated without enrichments.

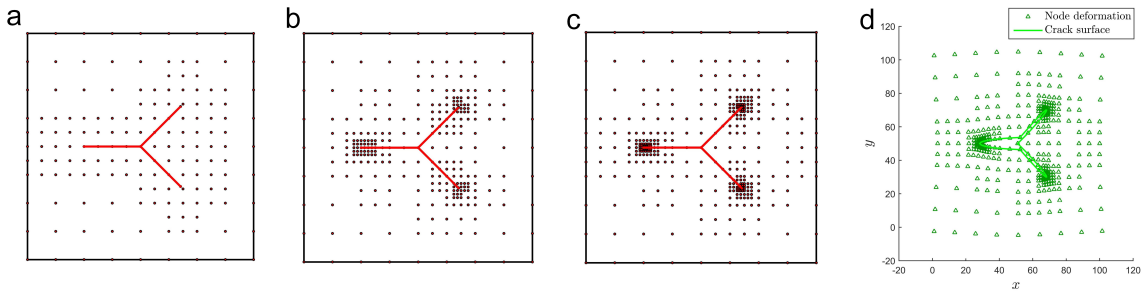

Figure 3: Adaptive steps of branched crack problem: (a) step 1; (b) step 3; (c) step 5; (d) final deformation enlarged by 100 times.

6. Conclusions

A new CPM is presented here which is able to handle multiple crack problems. A cracking particle belonging to more than one crack is split multiply and then the discontinuity at crack surfaces can be achieved through the visibility criterion, which is much simpler than through several groups of level set functions. An adaptivity strategy is introduced into the CPM to improve efficiency. A branched crack problem is studied here to demonstrate the performance of the new CPM and good agreement can be obtained compared with previous results.

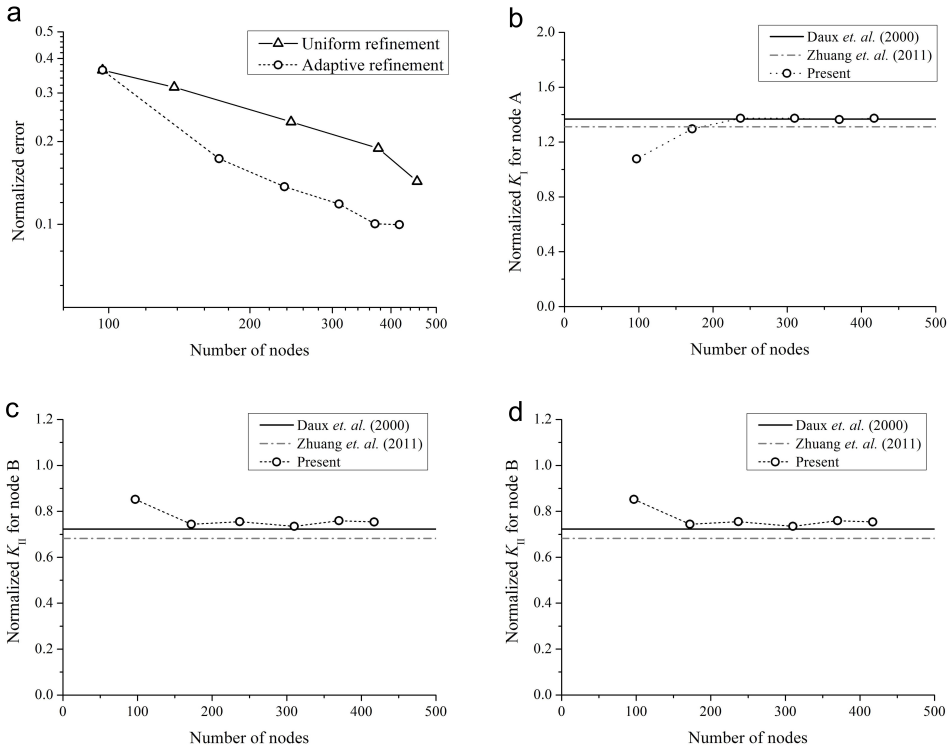

Figure 4: Verification of results: (a) global error; (b) K_{I} of node A; (c) K_{I} of node B; (d) K_{II} of node B.

Acknowledgements

The first author acknowledges the financial support from the China Scholarship Council (CSC) and the Faculty of Science, Durham University.

References

[1] X. Xu and A. Needleman. Numerical simulations of dynamic crack growth along an interface. *International Journal of Fracture*, 74(4), 289-324, 1995.

[2] J.O.H.N. Dolbow and T. Belytschko. A finite element method for crack growth without remeshing. *International journal for numerical methods in engineering*, 46(1), 131-150, 1999.

[3] N. Sukumar and T. Belytschko. Arbitrary branched and intersecting cracks with the extended finite element method. *International journal for numerical methods in engineering*, 48, 1741-1760, 2000.

[4] T. Belytschko, Y.Y. Lu and L. Gu. Element free Galerkin methods. *International journal for numerical methods in engineering*, 37(2), 229-256, 1994.

[5] X. Zhuang, C. Augarde and S. Bordas. Accurate fracture modelling using meshless methods, the visibility criterion and level sets: formulation and 2D modelling. *International Journal for Numerical Methods in Engineering*, 86(2), 249-268, 2011.

[6] Y.C. Cai, J. Wu and S.N. Atluri. A new implementation of the numerical manifold method (NMM) for the modeling of non-collinear and intersecting cracks. *Computer Modeling in Engineering and Sciences*, 92(1), 63, 2013.

[7] T. Rabczuk and T. Belytschko. Cracking particles: a simplified meshfree method for arbitrary evolving cracks. *International Journal for Numerical Methods in Engineering*, 61(13), 2316-2343, 2004.

[8] T. Rabczuk, G. Zi , S. Bordas and H. Nguyen-Xuan. A simple and robust three-dimensional cracking-particle method without enrichment. *Computer Methods in Applied Mechanics and Engineering*, 199(37), 2437-2455, 2010.

[9] H. J. Chung and T.Belytschko. An error estimate in the EFG method. *Computational Mechanics*, 21(2), 91-100, 1998.

[10] G.H. Lee, H.J. Chung and C.K. Choi. Adaptive crack propagation analysis with the element-free Galerkin method. *International Journal for Numerical Methods in Engineering*, 56(3), 331-350, 2003.

Fracture and fatigue of a self-compacting version of CARDIFRC mix II

Bakr S Al-azzawi * and Bhushan L Karihaloo

School of Engineering, Cardiff University
Cardiff University, UK
* Al-AzzawiBS@Cardiff.ac.uk

ABSTRACT

A self-compacting and industrially competitive version of CARDIFRC mix II has been developed. In this paper we describe the mechanical, fracture and fatigue performance of this ultra-high performance fibre reinforced concrete (UHPFRC).

Keywords: *UHPC; Self-compacting; Bi-linear stress-crack opening relation; fatigue life; endurance limit.*

1. Introduction

CARDIFRC is the trade name of two main groups of ultra-high performance fibre-reinforced concrete mixes – Mixes I and II – differing primarily in the maximum size of quartz sand used (0.6 mm in Mix I, and 2 mm in Mix II) [1,2].CARDIFRC Mix II has been converted to a self-compacting and industrially competitive ultra-high performance fibre-reinforced concrete (UHPFRC). Mix proportions are given in Table 1. In this paper, full mechanical, fracture and fatigue characterisation (i.e. size-independent fracture energy and the corresponding bi-linear stress-crack opening relationship, and endurance limit) of this UHPFRC is provided.

Table 1. Mix constituents of the self-compacting UHPFRC version of CARDIFRC Mix II (kg/m3)

Constituent	**Dosage (kg/m^3)**
Cement	450.3
Silica fume	169.5
GGBS	258.0
Quartz sand: 9-300μm 0.212-1 mm	 158.0 318.9
1-2 mm	639.7
Water	141.8
Superplasticizer (SP)	58.5
Fibres: 30 mm Dramix (Vol. 2.5%)	195.0
Water/cement	0.20
Water/binder	0.16
SP/water	0.41
Slump flow spread (mm)	705
t_{500} (s)	2.73

2. Mechanical properties

Compression tests were carried out on cube specimens according to BS EN 12390-3 (2009), whereas split tensile tests were performed on cylindrical specimens according to BS EN 12390-6 (2009). In addition, the modulus of elasticity was measured on a cylindrical specimen according to BS 1881-121 (1983) and the modulus of rupture of beam specimens was determined according to BS 1881-118 (1983). Table 2 shows the mechanical properties of the UHPFRC, together with the coefficient of variation (CoV in %).

Table 2. Mechanical properties of the self-compacting UHPFRC version of CARDIFRC Mix II

Compressive Strength (MPa)	Split cylinder Strength (MPa)	Modulus of Rupture (MPa)	Modulus of Elasticity (GPa)
148.0 (4.5%)	18.5 (6.0%)	20.0 (0.7%)	45.2 (0.2%)

3. Fracture properties

The fracture performance is characterised in terms of size-independent fracture energy obtained by the boundary effect model and the corresponding bilinear stress-crack opening relationship obtained by using the non-linear hinge. For this, six prisms 100 x 100 x 500 mm were casted with the self-compacting UHPFRC. After curing, three prisms were notched to a depth of 10 mm and the remaining three to a depth of 60 mm using a diamond saw (width approximately 2 mm). They were tested in three-point bending over a loaded span of 400 mm. The test was controlled first by a feedback signal from a crack mouth opening displacement (CMOD) gauge until the gauge reached its limit (around 3.5 mm), where after the control switched to mid-point displacement control. The load-CMOD was recorded until the gauge reached its limit, but the load-mid-point displacement continued to be recorded until the displacement reached 30 mm. The load had still not dropped to zero. The area under the load-deflection plot was therefore corrected to account for the unrecorded work-of-fracture using the procedure of Elices et al. [3]. The total work-of-fracture was divided by the projected fracture area (i.e. area of initially un-cracked ligament) of the notched specimen to calculate the specific fracture energy $G_f(a/W)$ corresponding to a/W = 0.1 and 0.6. Finally, the size-independent specific fracture energy G_F was determined using the appropriate relations of Hu and Wittmann [4] and the simplified boundary effect model of Abdalla and Karihaloo [5]. The values are reported in Table 3. The size-independent specific fracture energy is 36300 N/m compared to about 20000 N/m for the original Mix II measured in axial tension.

Table 3. Mean size-dependent fracture energies for a/W = 0.1 and 0.6 and size-independent specific fracture energy of UHPFRC version of CARDIFRC Mix II (bi-linear model)

Notch(mm)	Mean G_f (N/m)	a_l (mm)	G_F (N/m)
10	30190	30.3	36300
60	22600		

The unknown parameters of the bi-linear stress-crack opening diagram (the direct tensile strength, the critical crack opening and the co-ordinates of the knee in the bi-linear diagram) are identified in an inverse manner by minimizing the root mean square error between either the recorded and predicted load-CMOD or the load-deflection diagram at many values of the applied central load using the non-linear hinge model of Olesen [6]. The results are shown in Figure 1. The parameters of the tension softening curves obtained using the non-linear hinge model correspond to the measured G_f (0.1) and G_f (0.6), but not to G_F.

Abdalla and Karihaloo [7] proposed a simple method for the determination of the bi-linear softening diagram corresponding to the size-independent G_F of concrete mix by scaling the average parameters of the tension softening diagrams corresponding to the size-dependent fracture energies $G_f(0.1)$ and $G_f(0.6)$. This scaling procedure was followed in this work, giving the tension-softening diagram also shown in Figure 1.

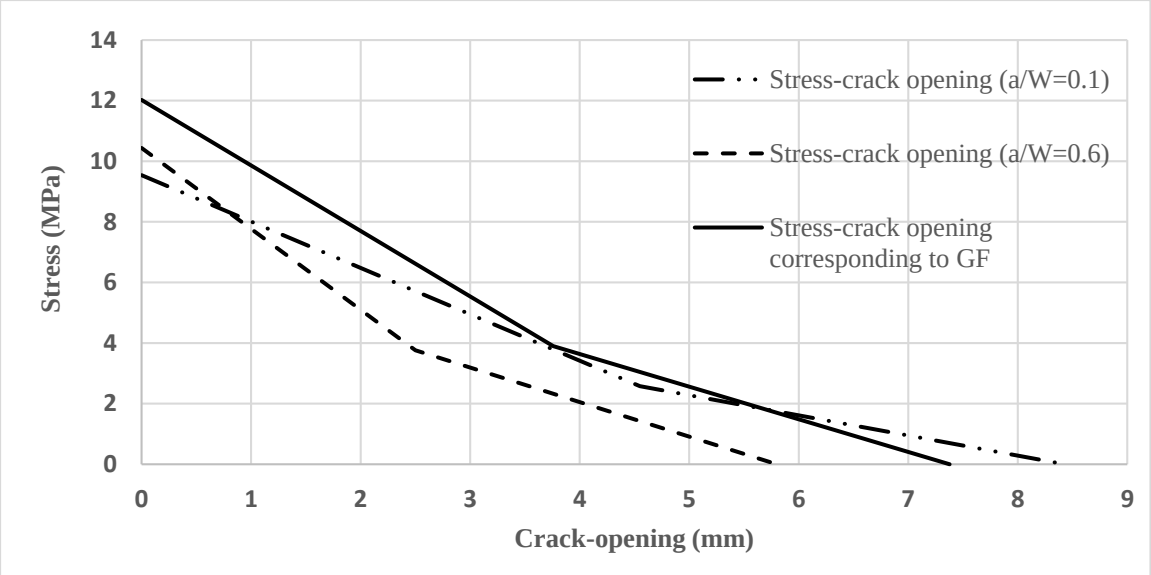

Figure 1. Bi-linear stress-crack opening relationships corresponding to a/W=0.6, 0.1 and G_F

4. Fatigue properties

Fatigue test under tensile cyclic loading was conducted on un-notched three point bend beams. Tests were performed in the sinusoidal load ranges between 0.6 – 4.0 kN, 0.6- 4.5 kN, and 0.6 – 5.5 kN, corresponding to 9.69 - 64.62%, 9.69 - 72.70% and 9.69 - 88.85% of the static three-point flexural strength. This meant that the mean stress level on the specimens during cyclic loading increased with the increase in the upper load limit (Table 4). This has a marked effect on reducing the fatigue life. The cyclic load-central deflection traces of the specimens were recorded every minute, i.e. every 300 cycles. From these the change in compliance of the specimens could be calculated. It was found that the endurance limit of the UHPFRC is around 64% of its static three point flexural strength at a mean stress level of 37.1% of this strength (Figure 2). This corresponds to an endurance limit close to 80% of the static three point flexural strength at zero mean stress.

Table 4. Increase in the mean stress level with increasing upper limit load

Upper Stress limit (%)	Mean Stress (MPa)
64.62	8.18
72.70	9.07
88.85	10.85

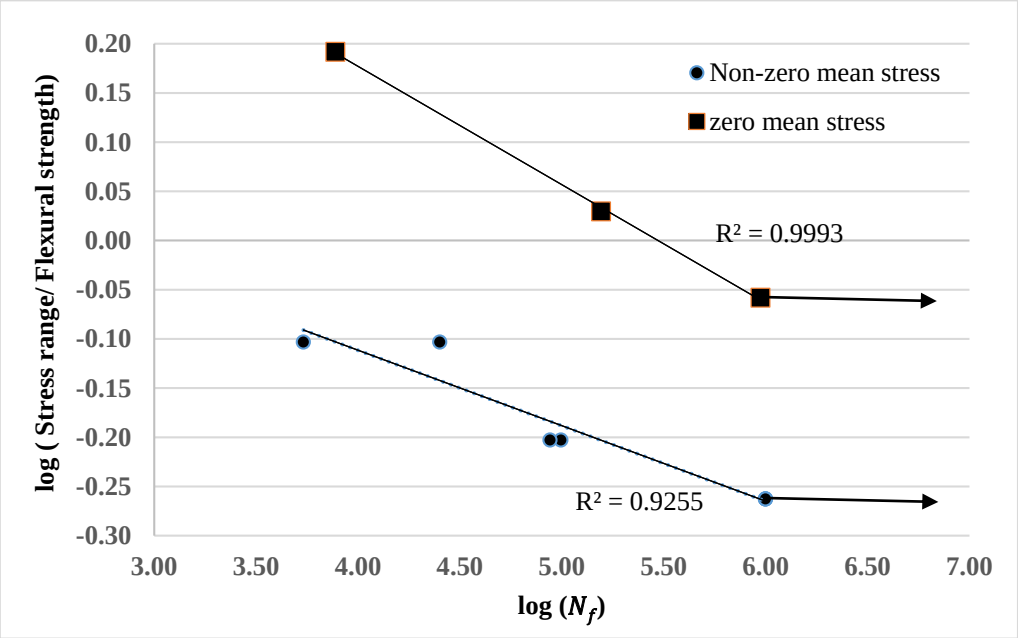

Figure 2. Fatigue life against stress range (logarithmic scale)

5. Conclusions

1. A self-compacting UHPFRC based on CARDIFRC Mix II was developed and fully characterised from both the mechanical and fracture points of view. As expected, the resulting UHPFRC has inferior compressive, tensile and flexural strengths than the original CARDIFRC Mix II. This is due to the absence of thin small brass-coated steel fibres (4.5% by volume; 6 mm long) in the UHPFRC. The UHPFRC is however much tougher thanks to the use of a larger volume fraction (2.5% against 1.5%) of longer steel fibres (30 mm against 13 mm).
2. An inverse approach based on the non-linear hinge model for crack growth from a pre-existing notch was used to identify the parameters of the bi-linear stress-crack opening relation of the UHPFRC.
3. The endurance limit of the test material is around 64% of its static three point flexural strength (Figure 2) at a mean stress level of 37.1% of this strength. This corresponds to an endurance limit close to 80% of the static three point flexural strength at zero mean stress.

References

[1] S.D.P. Benson and B.L. Karihaloo, CARDIFRC - development and mechanical properties. Part 1: development and workability. *Magazine of Concrete Research*, 57(6), 347-352, 2005a.

[2] S.D.P. Benson and B.L. Karihaloo, CARDIRFC - development and mechanical properties. Part III: uniaxial tensile response and other mechanical properties. *Magazine of Concrete Research* ,57(8), 433-443,(2005b).

[3] M. Elices, G.V. Guinea and J. Planas, Measurement of the fracture energy using three-point bend tests: Part 3 - Influence of cutting the *P-d* tail, Material and Structure, 25,327-334, 1992.

[4] X. Hu and F.H. Wittmann, Fracture energy and fracture process zone. Material and Structure 25(6), 319-326, 1992.

[5] H.M. Abdalla and B.L. Karihaloo, Determination of size-independent specific fracture energy of concrete from three-point bend and wedge splitting tests. *Magazine of Concrete Research*, 55(2), 133–141, 2003.

[6] J.F. Olesen, Fictitious crack propagation in fiber-reinforced concrete beams. ASCE Journal of Engineering Mechanics, 127(3), 272–280, 2001.

[7] H.M. Abdalla and B.L. Karihaloo, A method for constructing the bilinear tension-softening diagram of concrete corresponding to its true fracture energy. *Magazine of Concrete Research*, 56(10), 597–604. 2004.

Proceedings of the 24th UK Conference of the
Association for Computational Mechanics in Engineering
31 March – 01 April 2016, Cardiff University, Cardiff

Acceleration techniques for nonlinear finite element analysis of quasi-brittle materials

W. Alnaas[1] and A. Jefferson[1]

[1]School of Engineering, University of Cardiff, Queen's Buildings, Cardiff, CF24 3AA

AlnaasWF1@Cardiff.ac.uk

ABSTRACT

The nonlinear systems of equations resulting from the finite element modelling of quasi-brittle material are most-frequently solved using Newton-based incremental-iterative schemes. However, the poor convergence characteristics and frequent numerical breakdowns of those solutions schemes, when solving problems involving quasi-brittle materials, make the nonlinear finite element analysis of such materials a truly challenging undertaking. Recently, Alnaas and Jefferson [1] proposed an algorithm, named the smooth unloading-reloading (SUR) method, which circumvents these problems by employing a tangent matrix that is always positive definite but which is exact with respect to the nonlinear UR function. The present paper describes a further development of this method in which an acceleration technique is introduced into the solution algorithm. The performance of three alternative acceleration methods is reported in this paper. The main conclusion from the work is that all three acceleration methods result in a reduction in solution time for a range of problems.

Keywords: *Nonlinear FE analysis; quasi-brittle materials; damage, robustness, incremental-iterative*

1. Introduction

Numerical difficulties often arise in the finite element simulation of quasi-brittle materials. Such problems are associated with material softening behaviour and the loss of positive definitiveness of the tangent stiffness matrix. These difficulties often manifest as breakdown of the nonlinear incremental-iterative solution process [2].

As a response to these stability and convergence difficulties, researchers have developed solution algorithms that avoid multiple iterations. These methods include the 'Sequentially Linear Approach' (SLA), which was introduced by Rots [3] and improved later by others. The SLA method uses a 'saw-tooth' function to replace the post-peak softening function. Another approach, which avoids using multiple iterations, is the implicit-explicit "IMPL-EX" approach of Oliver et al [4]. In the IMPL-EX method, a projected state variable (e.g. a damage parameter) is used to determine a predicted consistent tangent matrix that is exact for the current increment but for which a correction is made in the subsequent stress-recovery phase.

Recently, Alnaas and Jefferson [1] developed a new approach called smooth unloading-reloading 'SUR' approach to work with an incremental iterative nonlinear FE solution scheme. This approach circumvents stability and convergence problems by employing a tangent matrix that is based on a smoothed unloading-reloading function. This function has a small positive gradient at its intersection with the principal softening evolution function. A key feature of this method is that it always uses a positive definite stiffness matrix. The authors have shown the approach to be numerically robust, reasonably efficient and accurate.

This paper describes three accelerations techniques to improve the convergence properties of the recently developed SUR approach for a finite element damage model, when applied to quasi-brittle fracture problems.

2. Smooth unloading-reloading (SUR) method

The SUR approach uses a target function material $f_s(r_p)$ and a smooth unloading-reloading (SUR) function $\sigma_p(r_p, r_{eff})$, as illustrated in Figure 1. As can be seen, the smooth unloading-reloading function has two parts: I) when $r_{eff} < a_p r_p$, for which linear unloading reloading with a slope $(1-\omega_{pf})E$ is assumed: and II) when $r_{eff} \geq a_p r_p$, for which nonlinear unloading-reloading is a assumed. The SUR depends on the damage evolution parameter (r_p).

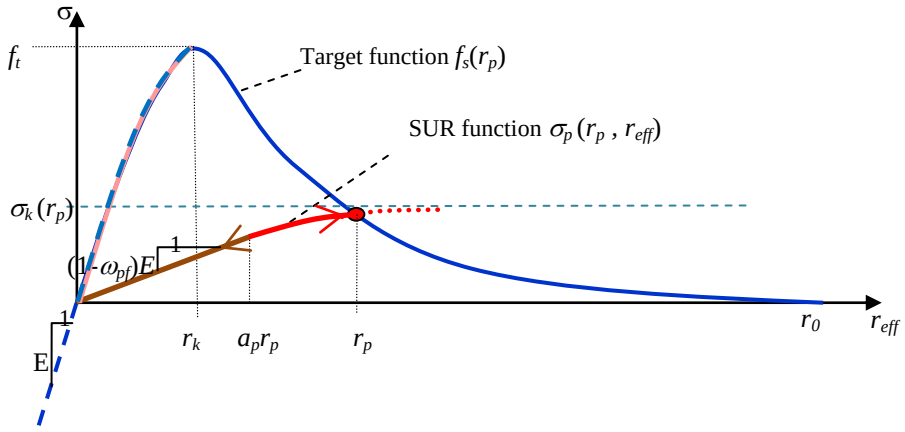

Figure 1: Target and unloading-reloading damage functions.

The target and smooth unloading-reloading functions are given in equations (1) and (2), respectively.

$$f_s(r_p) = \begin{cases} f_t & \forall \quad r_p < r_k \\ f_t \cdot e^{-c_1 \cdot \left(\frac{r_p - r_k}{r_0 - r_k} \right)} & \forall \quad r_p \geq r_k \end{cases} \tag{1}$$

$$\sigma_p(r_p, r_{eff}) = \sigma_k(r_p) \cdot \left[1 - (1 - \frac{a_p}{v}) \cdot e^{-\left[\frac{r_{eff} - a_p r_p}{(v - a_p) r_p} \right]} \right] \tag{2}$$

where r_{eff} is the effective damage parameter, E is Young's modulus, f_t is the tensile strength, r_0 is the effective end of the softening curve, r_k is the damage evolution parameter at the peak of the uniaxial stress curve. c_1=5, $a_p = 0.70$ and $v = 0.75$. See Ref [1] for more details of the SUR method.

3. Acceleration techniques for the SUR method

In this paper, three acceleration techniques are described for improving the convergence performance of the SUR solution procedure. These acceleration techniques are described below.

3.1 Predictive-SUR technique

The concept of the predictive-SUR algorithm relies on two parameters, namely the damage evolution parameter (r_p) and the number of iterations (*it*). The predictive function is based on two assumptions: I) The relationship between the number of iterations (*it*) within a time step and the iterative change in the damage evolution parameter ($\Delta r_{p_i} = r_{p_{it}} - r_{p_{it-1}}$) decays in semi-log space and approaches 0, once stable convergence has been achieved: II) when the slope of (it vs log (Δr_{p_i})) curve starts decreasing, a trial prediction of the damage evolution parameter (r_{pp}) can be computed using equation (3). Once the normalised difference between two consecutive predictions e.g. (r_{pp_i}) and ($r_{pp_{i-1}}$) is less than 5%, then r_p is set to the most recently computed trial value, i.e. $r_p = r_{pp}$.

$$r_{pp} = r_{p_{it}} + \frac{\Delta r_{p_i}{}^2}{\Delta r_{p_{i-1}} - \Delta r_{p_i}} \tag{3}$$

3.2 Fixing approach

The second acceleration technique named 'fixing' is based on a two stage algorithm, in which a damage evolution parameter is updated from the last converged increment in Stage-1 iterations, and then it is fixed in Stage-2 iterations within a step. In this acceleration approach, 3 and 5 iterations in Stage-1 were investigated.

3.3 Slack tolerance technique

This technique uses a slightly slacker convergence tolerance at key stages in a computation. The slacker tolerance (1% for the L2 norm of out of balance residual forces) is temporarily triggered when the number of iterations within an increment exceeds a certain limit (e.g. 5 iterations). Subsequently, the convergence tolerance reverts to the standard tighter tolerance of 0.001%.

4.1 One-dimensional example

The one-dimensional bar shown in Figure 2 was used. The bar was divided to three linear elements of equal length, with the middle element being assigned a small amount of initial damage such that damage only occurred in this central element. A prescribed displacement 0.2 was applied evenly over 40 and 100 increments in the analysis. The material properties of the bar are: E=20GPa, Poisson's ratio (υ=0.2), f_t=2.5 MPa, fracture energy (G_f=0.10 N/mm) and tolerance value for out-of balance force and displacement norms is $\Psi = 0.0001\%$.

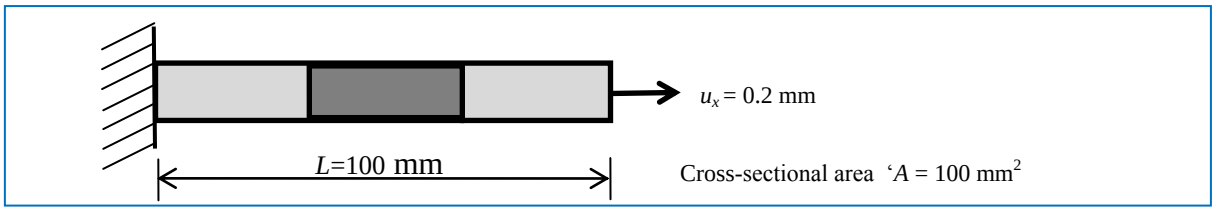

Figure 2: 1-D bar example

The resulting stress-displacement responses from the various analyses are indistinguishable from each other, as can be seen in Figure 3a.

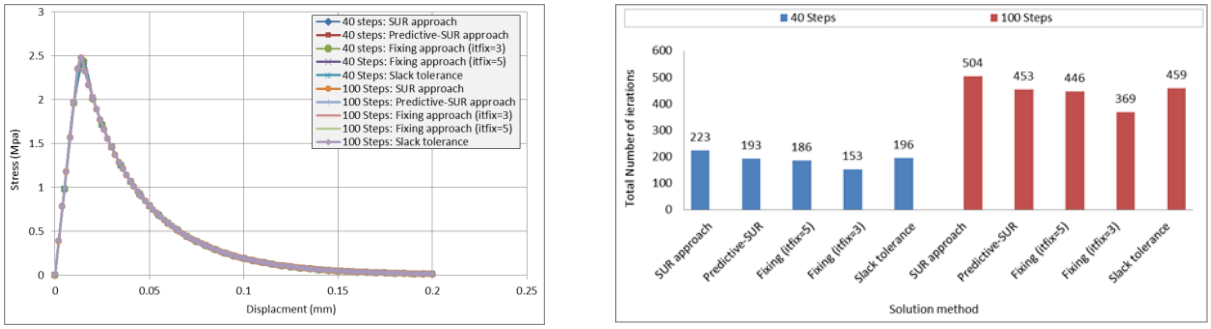

a b

Figure 3: (a) Stress-displacement response, (b) total number of iterations that needed for each solution.

In all sets of analyses, results showed that the three acceleration techniques achieved converged solutions in fewer iterations than the standard SUR solution, see Figure 3b. Furthermore, the 'fixing algorithm', with 3 iterations in Stage-1, was on average a little more efficient than the others, as can be noticed in Figure 3b.

4.2 Two-dimensional double notched example

The second example is a 2-D double notched specimen subjected to mixed mode loadings by prescribed displacement, as shown in Figure 4a. The analysis was undertaken using 40 and 100 prescribed displacement increments. The material properties of the specimen are: E=20 GPa, υ=0.2, f_t =2.5 MPa, G_f =0.10 N/mm and $\Psi = 0.001$.

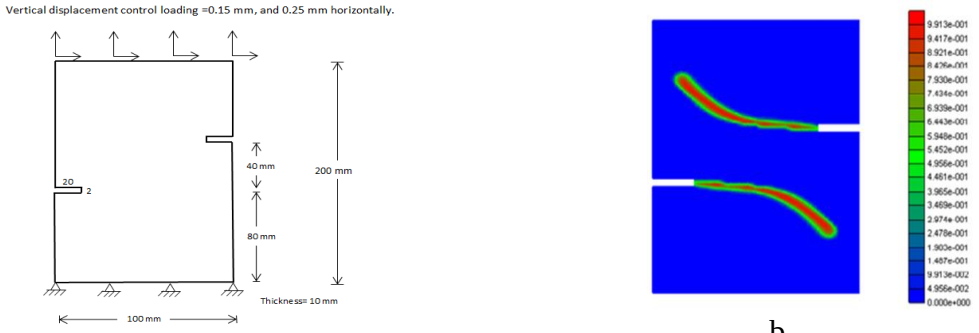

Figure 4: (a) Dimensions of the 2D-double notched specimen, (b) Damage contour plot

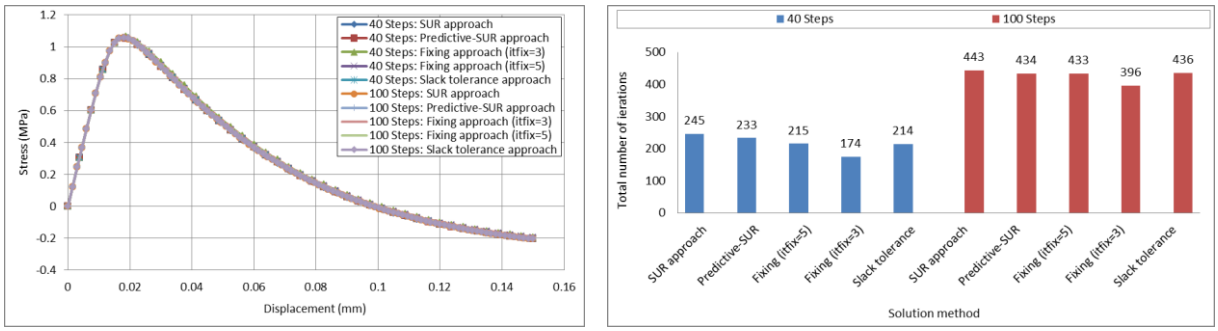

Figure 5: (a) Stress-displacement response, (b) total number of iterations that needed for each solution.

As you can see in Figure 5b, the three acceleration approaches require fewer iterations to achieve convergence, relative to the standard SUR method. Also, stress-displacement curves for all solutions are indistinguishable from each other, see Figure 5a.

Conclusion

The principle finding of this paper is that all three methods require less computer time than the standard SUR method, with no appreciable effect on the accuracy of simulations.

References

[1] Alnaas, W.F. and A.D. Jefferson, *A smooth unloading–reloading approach for the nonlinear finite element analysis of quasi-brittle materials.* Engineering Fracture Mechanics, 2015. **152**: p. 105-125.

[2] De Borst, R., Crisfield, M.A., Remmers, J.J.C. and Verhoosel, C.V., *Nonlinear Finite Element Analysis of Solids and Structures*. 2012: Wiley.

[3] Rots, J.G., *Sequentially linear continuum model for concrete fracture. In: de Borst R, Mazars J, Pijaudier-Cabot G, van Mier, JGM, Balkema AA, editors*. Fracture Mechanics of concrete Structures. The Netherlands: Liss. 2001: p. 831-839.

[4] Oliver, J., Linero, D.L., Huespe, A.E. and Manzoli, O.L., *Two-dimensional modeling of material failure in reinforced concrete by means of a continuum strong discontinuity approach.* Computer Methods in Applied Mechanics and Engineering, 2008. **197**(5): p. 332-348.

Proceedings of the 24th UK Conference of the
Association for Computational Mechanics in Engineering
31 March - 01 April 2016, Cardiff University, Cardiff

Two dimensional configurational-force-driven crack propagation using the discontinuous Galerkin method with rp-adaptivity

***Robert Bird[1], William M. Coombs[1] and Stefano Giani[1]**

[1]School of Engineering and Computing Sciences, Durham University, South Road, Durham, DH1 3LE

*robert.e.bird@durham.ac.uk

ABSTRACT

This paper presents a quasi-static configurational force (CF) brittle fracture propagation method, [1], using the discontinuous Galerkin (dG) symmetric interior penalty (SIP) method, [2]. The method is derived from the first law of thermodynamics with consideration of the Griffith fracture criterion [1]. The criterion is evaluated by finding the difference between the power applied to the domain and the rate of internal energy change at every point in the domain. If a node within the element mesh satisfies the criterion, a crack will propagate in the CF direction. Around the crack tip the advantage of element specific degrees of freedom in dG methods enables simple p-adaptivity to determine the CF in the spatial domain. In the material domain r-adaptivity is implemented, where the CF direction is used to align element edges, which are then split to propagate the crack.

Key Words: *Crack propagation; configurational force; discontinuous Galerkin; symmetric interior penalty; rp-adaptation*

1. Introduction

Fracture propagation is the generation of new surfaces in a domain through crack growth. Numerical implementations of brittle fracture propagation is relatively rare and remains to be one of the most significant challenges in solid mechanics. Numerical frameworks must be able to predict the initiation of a crack and the subsequent path. A promising technique, known as r-adaptivity, which mitigates influence from the mesh on the direction of the crack path has been presented by Miehe *et al.*, [1, 3, 4]. The method is based on the concept of material configuration force, [5, 6, 7], with the use of a Griffith brittle fracture failure criterion to determine crack growth. The unique aspect of the method is the realignment of an element face with the direction of the configurational force vector at the crack tip. The face is then split to propagate the crack.

In this paper the SIP dG finite element (FE) scheme, [8], is used to apply the r-adaptivity method in conjunction with hierarchical shape functions for p-adaptivity [9]. The connectivity between elements in the dG space is generated through dG face stiffness terms, not shared degrees of freedom. The implication is that new surfaces can be generated by removing dG face terms between elements, in the global element stiffness matrix. The second implication is adjacent elements can have varying degrees of freedom without concern over hanging nodes. Moreover, it is simple to incorporate new higher order elements into an already existing data structure as it is only necessary to ensure the new degrees of freedom are unique to a single element and that new dG face stiffness terms are calculated for the higher order element's connectivity to its adjacent elements.

In this paper the SIP dG method is initially defined as the scheme to model the CF crack growth. This is then followed by a definition of the CF, the growth rate and the corresponding consistency conditions. Next the method for applying rp-adaptivity within a SIP dG framework is outlined. Lastly results are represented to validate CF values and the crack propagation path against analytical solutions.

2. Discontinuous Galerkin method for linear elasticity

Here we introduce SIP dG for the linear elasticity problem,

$$-\boldsymbol{\nabla}\cdot\boldsymbol{\sigma}(\boldsymbol{u}) = \boldsymbol{f} \quad \text{in} \quad \Omega, \quad \boldsymbol{n}\cdot\boldsymbol{\sigma}(\boldsymbol{u}) = \boldsymbol{g}_N \quad \text{on} \quad \partial\Omega_N \quad \text{and} \quad \boldsymbol{u} = \boldsymbol{g}_D \quad \text{on} \quad \partial\Omega_D. \tag{1}$$

Ω is a polygonal domain and $\boldsymbol{f}$ is a force vector in $[\boldsymbol{L}^2(\Omega)]^2$. Ω is divided into elements K. We set $W_h = \{\boldsymbol{w} \in [L^2(\Omega)]^2 : \forall K, \boldsymbol{w}|_K \in \mathscr{P}_{p_K}(K)\}$ where $\mathscr{P}_{p_K}(K)$ is the space of polynomial functions of degree at most $p_K \geqslant 1$ on K. The elementwise approximation of $\boldsymbol{u}$ is defined $\boldsymbol{u_h} \in W_h$. (1) is weakly satisfied by $\boldsymbol{u_h}$ such that $\boldsymbol{a}(\boldsymbol{u_h}, \boldsymbol{v}) = \boldsymbol{l}(\boldsymbol{v})$. Here, $\boldsymbol{a}(\boldsymbol{u_h}, \boldsymbol{v}) = \sum_{K\in\Omega} \boldsymbol{a}_K(\boldsymbol{u_h}, \boldsymbol{v})$ and $\boldsymbol{l}(\boldsymbol{v}) = \sum_{K\in\Omega} \boldsymbol{l}_K(\boldsymbol{v})$ where,

$$\boldsymbol{a}_K(\boldsymbol{u_h}, \boldsymbol{v}) = (\boldsymbol{\sigma}(\boldsymbol{u_h}), \boldsymbol{\epsilon}(\boldsymbol{v}))_K - \langle\{\boldsymbol{\sigma}(\boldsymbol{u_h})\}, [\![\boldsymbol{v}]\!]\rangle_{\partial K\setminus\partial\Omega} - \langle [\![\boldsymbol{u_h}]\!], \{\boldsymbol{\sigma}(\boldsymbol{v})\}\rangle_{\partial k\setminus\partial\Omega} + \beta\langle h^{-1}[\![\boldsymbol{u_h}]\!], [\![\boldsymbol{v}]\!]\rangle_{\partial K\setminus\partial\Omega}, \tag{2}$$

and

$$\boldsymbol{l}_K(\boldsymbol{v}) = (\boldsymbol{f}, \boldsymbol{v})_K. \tag{3}$$

β is a penalty term for linear elastic SIP dG defined by [10], h is the element face length, and $\{\cdot\}$, $[\![\cdot]\!]$, $(\cdot,\cdot)$ and $\langle\cdot,\cdot\rangle$ are defined in [2]. The displacement boundary conditions are applied in the strong form.

3. Evaluation of the configurational force for fracture mechanics

Miehe *et al.*, [1], provide a robust derivation based on the work on the configuration force by Eshelby [5, 6, 11], to determine the configurational force as,

$$\boldsymbol{G_I} = \lim_{|C|\to 0} \int_C \boldsymbol{\Sigma}\cdot\boldsymbol{n}\mathrm{d}S, \tag{4}$$

where $\boldsymbol{\sigma} = \partial_{\boldsymbol{\epsilon}}\hat{\psi}(\boldsymbol{\epsilon})$ and $\boldsymbol{\Sigma} = \hat{\psi}(\boldsymbol{\epsilon})\mathbf{1} - \boldsymbol{h_d}^\top\boldsymbol{\sigma}$ are the symmetric Cauchy stress tensor and non-symmetric Eshelby stress tensor, $\boldsymbol{n}$ is an inward normal to the crack, $\hat{\psi}(\boldsymbol{\epsilon})$ is the free energy function, C is a surface around the crack tip and $\boldsymbol{h_d}$ is the displacement gradient. The method is cast within an arbitrary Lagrangian-Eulerian description of motion requiring a reference material domain and spacial domain. The velocity of the crack, $\Delta\boldsymbol{a_I}$, is controlled by the isotropic Griffith failure criterion function $\hat{\phi}(\boldsymbol{G_I}) = |\boldsymbol{G_I}| - g_c \leq 0$ where g_c is the material parameter specifying the critical energy release pre unit length. Propagation of the crack tip is controlled by the following consistency conditions,

$$\Delta\boldsymbol{a_I} = \Delta\gamma_I \frac{\boldsymbol{G}_I}{|\boldsymbol{G}_I|}, \quad \text{where} \quad \Delta\gamma_I \geq 0, \quad \hat{\phi}(\boldsymbol{G_I}) \leq 0, \quad \text{and} \quad \Delta\gamma_I\hat{\phi}(\boldsymbol{G_I}) = 0. \tag{5}$$

If the Griffith failure criterion is satisfied then $\Delta\gamma_I = H_c$, where H_c is the length of the face to be split.

4. RP-adaptivity

For our simulations hierarchical shape functions are employed for both the material and spacial domain. All elements are triangular and have a shape function order of 1 except those at the crack tip with an order p. The configurational force is evaluated at the crack tip using the domain method presented by Denzer *et al.*, [12]. If $|\boldsymbol{G_I}| \geq g_c$ is true then the crack will propagate in the direction $\boldsymbol{G_I}/|\boldsymbol{G_I}|$ and the rp-adaptivity method will be applied, see Figure 1.

The r-adaptivity step occurs in two stages. First, the face in the material domain most aligned to the CF direction is rotated about the crack node to be exactly parallel with the CF direction, [1]. Secondly, the crack surface is propagated by removing dG face stiffness terms from all future stiffness calculations for the manoeuvred face.

To initiate p-adaptivity all components of (2) for elements 1-6, and all external elements sharing faces with elements 1-6, are recalculated and steered back into the global stiffness matrix. This is necessary to accommodate changes in element topology, crack surfaces and element order. Management of the data structure is relatively simple, the only consideration being degrees of freedom must be unique to a single element.

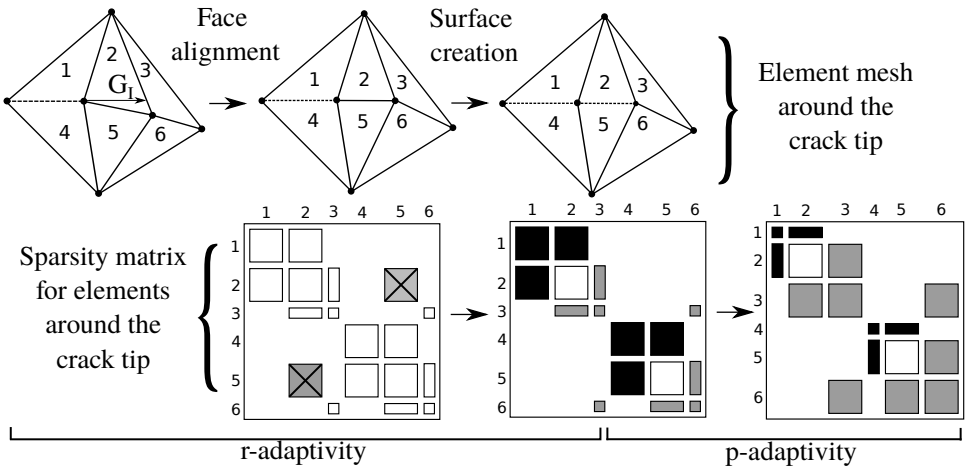

Figure 1: The rp-adaptivity for the element mesh at the crack tip with its corresponding sparsity matrix. Sparsity components with a grey box and X are removed dG face stiffness terms to increase the crack length. Black components are elements which undergo a reduction in polynomial order, white no change, and grey an increase.

5. Experimental results

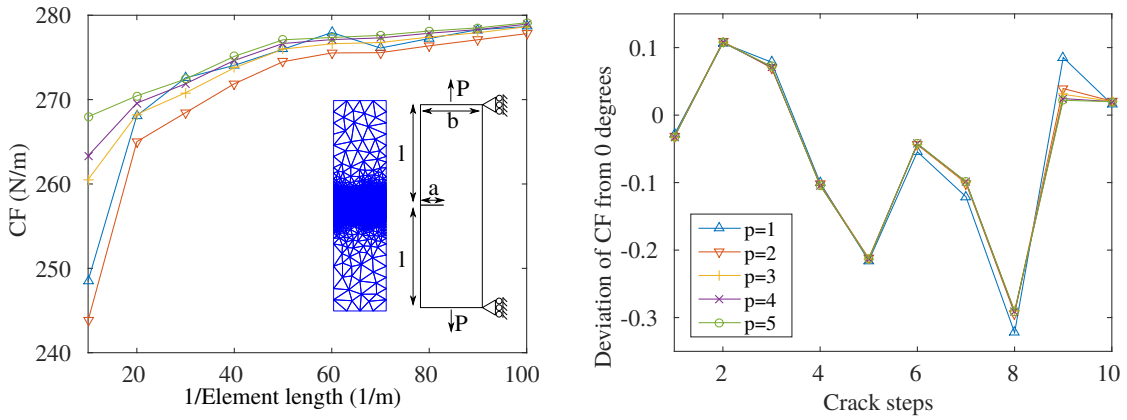

(a) CF value for varying element length and local p-adaptivity at crack tip.

(b) CF angle deviation from 0 degrees for a developing crack.

Figure 2: **a)** CF values for a force applied to a static crack, inset the experimental setup and mesh. **b)** CF angle for a propagating crack with a displacement boundary condition. CF values were calculated using the method presented by Denzer *et al.* [12], with a radius of 0.05 m.

A plane stress experiment using the SIP dG method was performed to validate CF values at the crack tip of a stationary crack against a known solution provided by [13]. The experimental setup is described in Figure 2a, the geometric parameters a b and l have values 0.1 m, 0.5 m and 1 m respectively. The plate has a Young's modulus of 208 GPa and Poisson's ratio of 0.3. The tensile stress, P, was 10 Mpa.

The unstructured mesh consists of triangular element generated using Triangle, [14]. The element face length is varied around the crack tip. The element polynomial order of elements that share a node at the crack tip is defined p, all other elements have an order 1. The CF force values for varying element length and polynomial order is displayed in Figure 2a.

In comparison to the analytical solution of 256.65 N/m, the results converge to a value with an error $\approx 8\%$. The error value similar to those expressed by [1] for the same experiment. Faster convergence is

achieved for meshes with higher element order around the crack tip.

A second experiment was performed to test how varying polynomial order of elements on the advancing crack tip effected the validity of the CF angle against the expected value of 0^o, as shown in Figure 2b. The problem was set up with the same geometric and material parameters as before, however an axial load in the form of a 0.1 m displacement boundary condition on either end of the plate is applied instead of P. All elements other than those at the crack tip have a polynomial order 1. The element length at the crack tip was 0.01m.

6. Conclusion

This paper has presented an rp-adaptivity method to model small strain quasi-static configurational-force-driven crack propagation. Problems are restricted to two-dimensions with linear geometric and material properties. A comparison of the CF values between analytical solutions and those calculated from surface integrals is presented. The application and results of applying the SIP dG method with hierarchical shape functions for a propagating and stationary crack have been presented.

References

[1] C. Miehe and E. Gürses, "A robust algorithm for configurational-force-driven brittle crack propagation with r-adaptive mesh alignment," *INT J NUMER METH ENG*, vol. 72, no. 2, pp. 127–155, 2007.

[2] D. N. Arnold, F. Brezzi, B. Cockburn, and L. D. Marini, "Unified analysis of discontinuous Galerkin methods for elliptic problems," *SIAM J NUMER ANAL*, vol. 39, no. 5, pp. 1749–1779, 2002.

[3] C. Miehe, E. Gürses, and M. Birkle, "A computational framework of configurational-force-driven brittle fracture based on incremental energy minimization," *INT J FRACTURE*, vol. 145, no. 4, pp. 245–259, 2007.

[4] E. Gürses and C. Miehe, "A computational framework of three-dimensional configurational-force-driven brittle crack propagation," *COMPUT METHOD APPL M*, vol. 198, no. 15, pp. 1413–1428, 2009.

[5] J. D. Eshelby, "The force on an elastic singularity," *PHILOS T ROY SOC A*, vol. 244, no. 877, pp. 87–112, 1951.

[6] J. D. Eshelby, "Energy relations and the energy-momentum tensor in continuum mechanics," in *Fundamental Contributions to the Continuum Theory of Evolving Phase Interfaces in Solids*, pp. 82–119, Springer, 1999.

[7] J. R. Rice, "A path independent integral and the approximate analysis of strain concentration by notches and cracks," *J APPL MECH*, vol. 35, no. 2, pp. 379–386, 1968.

[8] J. Douglas and T. Dupont, "Interior penalty procedures for elliptic and parabolic Galerkin methods," in *Lecture notes in Phys. 58*, Springer-Verlag, 1976.

[9] P. Solin, K. Segeth, and I. Dolezel, *Higher-order finite element methods*. CRC Press, 2003.

[10] P. Hansbo and M. G. Larson, "Energy norm a posteriori error estimates for discontinuous Galerkin approximations of the linear elasticity problem," *COMPUT METHOD APPL M*, vol. 200, no. 45, pp. 3026–3030, 2011.

[11] J. D. Eshelby, "The determination of the elastic field of an ellipsoidal inclusion, and related problems," in *PHILOS T ROY SOC A*, vol. 241, pp. 376–396, The Royal Society, 1957.

[12] R. Denzer, F. J. Barth, and P. Steinmann, "Studies in elastic fracture mechanics based on the material force method," *INT J NUMER ANAL MET*, vol. 58, no. 12, pp. 1817–1835, 2003.

[13] D. P. Rooke and D. J. Cartwright, "Compendium of stress intensity factors," *Procurement Executive, Ministry of Defence. H. M. S. O. 1976, 330 p(Book).*, 1976.

[14] J. R. Shewchuk, "Triangle: Engineering a 2D Quality Mesh Generator and Delaunay Triangulator," in *Applied Computational Geometry: Towards Geometric Engineering* (M. C. Lin and D. Manocha, eds.), vol. 1148 of *Lecture Notes in Computer Science*, pp. 203–222, Springer-Verlag, May 1996. From the First ACM Workshop on Applied Computational Geometry.

Geomechanics I

AN EVOLUTIONARY APPROACH TO MODELLING EFFECTS OF CHEMCALS ON SOILS

*** Alireza Ahangar Asr[1], Akbar A. Javadi[2]**

[1]School of Computing Science and Engineering, University of Salford, Manchester, M5 4WT
[2]College of Engineering, Mathematics and Physical Sciences, University of Exeter, Devon, EX4 4QF

*a.ahangarasr@salford.ac.uk

ABSTRACT

As part of a study undertaken to assess the impact of high-pH fluid circulation on the shear strength behaviour of a compacted soil with different additives and due to the complexity of the existing constitutive theories, a new approach was used, based on an evolutionary polynomial regression, for modelling the processes. EPR is an evolutionary-based data mining technique with the capability of generating transparent and structured representation of behaviour of materials and systems from measured data without any need for the data to be processed. EPR model developed and assessed using data from a set of triaxial tests. The outcome from developed model was compared to the experimental results expressing good consistency.

Keywords: *mechanical behaviour of soils; chemicals; evolutionary data mining*

1. Introduction

Cuisinier et al [1, 2] conducted a study to investigate the influence of circulation of high-pH water on the hydromechanical behaviour of compacted materials to be used for backfilling. During the study the geomechanical behaviour and the microstructure of the considered materials were followed over a period of alkaline water circulation of 12 months. The influence of the alkaline fluid on the geomechanical characteristics of the materials as a result was seen to directly relate to the nature of the additives. The geomechanical behaviour of the sand – argillite mixture has, for instance, remained almost stable during the period of alkaline water circulation while, over the same period, dramatic modification of the lime – argillite mixture was observed. The next stage in the study was to identify the coupling parameter(s) between the chemical stress induced by the circulation of alkaline water and changes in the hydromechanical behaviour of the tested mixtures, however, the large number of tests on various mixes proved the process to be complex [3].
Therefore, a new approach was implemented, based on evolutionary polynomial regression (EPR) to model the complex hydromechanical behaviour of the soil during circulation of the alkaline fluid. EPR is a data mining technique, based on evolutionary computing, aimed to search for polynomial structures representing a system [our paper]. The key idea behind the EPR is to use evolutionary search for exponents of polynomial expressions by means of a genetic algorithm (GA) engine [4]. The main advantage of EPR over other data mining techniques such as neural networks is that it provides a transparent and structured representation of the behaviour of the system in the form of a clear mathematical expression that is readily accessible to the user. EPR has shown its potential in application in modelling of complex behaviour of soils [5-9].

2. Evolutionary Polynomial Regression (EPR)

EPR is a data-driven method based on evolutionary computing, aimed to search for polynomial structures representing a system. A general EPR expression can be presented as [4]:

$$y = \sum_{j=1}^{n} F(X, f(X), a_j) + a_0 \quad (1)$$

where y is the estimated vector of output of the process; a_j is a constant; F is a function constructed by the process; X is the matrix of input variables; f is a function defined by the user; and n is the number of terms of the target expression. The general functional structure represented by F(X, f(X), a_i) is constructed from elementary functions by EPR using a Genetic Algorithm (GA) strategy. The GA is employed to select the useful input vectors from X to be combined. The building blocks (elements) of the structure of F are defined by the user based on understanding of the physical process. While the selection of feasible structures to be combined is done through an evolutionary process, the parameters a_j are estimated by the least square method. This technique uses a combination of the genetic algorithm to find feasible structures and the least square method to find the appropriate constants for those structures. In particular, the GA allows a global exploration of the error surface relevant to specifically defined objective functions. By using such objective (cost) functions some criteria can be selected to avoid the overfitting of models, push the models towards simpler structures and avoid unnecessary terms representative of the noise in the data. An interesting feature of EPR is in the possibility of getting more than one model for a complex phenomenon. A further feature of EPR is the high level of interactivity between the user and the methodology. The user physical insight can be used to make hypotheses on the elements of the target function and on its structure. Selecting an appropriate objective function, assuming pre-selected elements based on engineering judgment, and working with dimensional information enable refinement of final models. The level of accuracy at each stage is evaluated based on the coefficient of determination (COD) i.e., the fitness function as:

$$\mathbf{COD} = 1 - \frac{\sum_{N} (\mathbf{Y}_a - \mathbf{Y}_p)^2}{\sum_{N} \left(\mathbf{Y}_a - \frac{1}{N} \sum_{N} \mathbf{Y}_a \right)^2} \quad (2)$$

where Y_a is the actual output value; Y_p is the EPR predicted value and N is the number of data on which COD is computed. If the model fitness is not acceptable or the other termination criteria (in terms of maximum number of generations and maximum number of terms) are not satisfied, the current model goes through another evolution in order to obtain a new model. Detailed explanation of the method can be found in [4, 5].

3. Database used in developing the EPR model and model outcomes

Results obtained from 33 consolidated undrained triaxial tests on samples of argillite (MA), lime-MA, sand-MA, bentonite-MA mixtures, subjected to different periods of circulation of alkaline water, were considered in developing and validating of the EPR model. Of the total of 33 cases, 29 cases related to different circulation times (i.e. 0, 3, 6, 12 months) were used for training of the EPR model. Of these 29 cases, 11, 5, 2 and 11 cases were related to no circulation, 3 months, 6 months and 12 months of circulation of the alkaline water through the samples, respectively. The remaining cases relating to different soil and circulation times were kept unseen during the model development process and were used in the validation stage of the developed model. Parameters involved in the model development which were used as input for the EPR model were dry density, alkaline water circulation time, axial strain, pore pressure, effective confining pressure, porosity of macro-pores, porosity of micro-pores, and the specific surface of the soil particles. The only output was considered to be the deviatoric stress [3].

Figures 1 shows typical prediction results from the EPR model for lime-argillite mixture at confining pressure of 141 kPa after 6 months of circulation for training data. The results are compared with actual measurements. It can be seen that the EPR model has been able to capture the behaviour of the mixtures with a good accuracy. Figure 2 also presents results predicted by the developed EPR model

for a testing data series that was kept unseen to EPR in training stage for lime-argillite at confining pressure of 274kPa after 6 months of circulation of alkaline water.

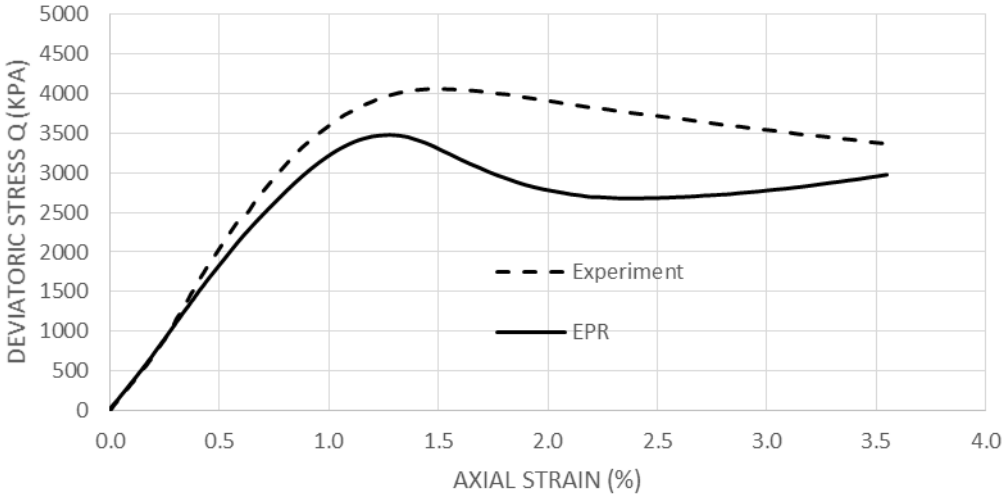

Figure 1: Results from the EPR model – lime-argillite, confining pressure =142kPa (training data)

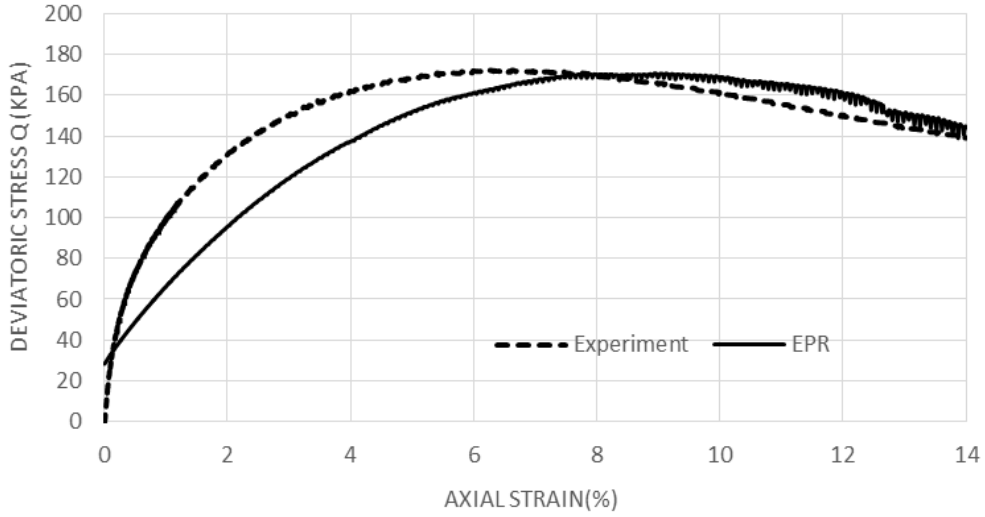

Figure 2: Results from the EPR model – lime-argillite, confining pressure =274kPa (testing data)

It can be seen that the developed model has presented high capabilities in generalising the training stage of the model development to conditions that were not introduced to the EPR during the stage that the training process took place.

4. Discussion and conclusions

The research was conducted to model the impact of alkaline fluid circulation on the mechanical behaviour of argillite mixes with different additives because of lack of sufficient constitutive relationships able to describe the behaviour of different mixtures in a unified framework. The work

aimed at developing a model based on an evolutionary-based data mining technique, evolutionary polynomial regression (EPR), to represent and predict complex hydromechanical behaviour of soils during circulation of an alkaline fluid.

The presented predictions from the developed EPR model showed that the model, which was trained from pure experimental data (with no pre-processing), was capable of capturing and representing many physical characteristics of the behaviour of the different mixtures considered in the study and the effect of the alkaline fluid circulation correctly, and with a high accuracy for training data. In order to validate the generalization capabilities of the developed model, unseen cases of data which were not presented to the EPR at the training stage was presented to the model. The predicted outcomes showed strong capabilities of the model in providing predictions for cases that were not previously known to the model.

An interesting feature of EPR is in the possibility of getting more than one model for complex phenomena. The best model is then chosen on the basis of its performances on a test set of unseen data. In general, EPR based modelling has several advantages including it provides a simple and straightforward framework for modelling of all materials. It does not require any arbitrary choice of the constitutive (mathematical) model, yield function, plastic potential function, flow rule etc. As EPR learns the material behaviour directly from raw experimental data, it is the shortest route from experimental research (data) to numerical modelling. Additional advantage of EPR model is that as more data becomes available, the material model can be improved by re-training the EPR.

References

[1] O. Cuisinier, F. Masrouri, M. Pelletier, F. Villieras and R. Mosser-Ruck. Microstructure of a compacted soil submitted to an alkaline plume. *Appl Clay Sci*, 40, 159–70, 2008a.

[2] O. Cuisinier, D. Deneele and F. Masrouri. Shear strength behaviour of compacted clayey soils submitted to an alkaline plume. *Eng Geol*,108, 177–88, 2008b.

[3] O. Cuisinier, A. A. Javadi, A. Ahangar-Asr and F. Masrouri. Identification of coupling parameters between shear strength behaviour of compacted soils and chemical's effects with an evolutionary-based data mining technique. *Computers and Geotechnics*, 48, 107-116, 2013.

[4] O. Giustolisi, D. A. Savic. A symbolic data-driven technique based on evolutionary polynomial regression. *J Hydroinform*, 8, 207-22, 2006.

[5] A. A. Javadi and M. Rezania. Applications of artificial intelligence and data mining techniques in soil modelling. *Geomech Eng*,1, 53-74, 2009.

[6] M. Rezania, A. A. Javadi and O. Giustolisi. An evolutionary-based data mining technique for assessment of civil engineering systems. *J Eng Comput*, 25, 500-17, 2008.

[7] A. Ahangar-Asr, A. A. Javadi and N. Khalili. An evolutionary approach to modelling the thermo-mechanical behaviour of unsaturated soils. *International Journal for Numerical and Analytical Methods in Geomechanics*, 39, 539-557, 2015.

[8] A. A. Javadi, M. Hussain, A. Ahangar-Asr and R. Farmani. A surrogate model for simulation-optimization of aquifer systems subjected to seawater intrusion. *Journal of Hydrology*, 532, 542-554, 2015.

[9] A. Ahangar-Asr, A. A. Javadi, A. Johari and Y. Chen. Lateral load bearing capacity modelling of piles in cohesive soils in undrained conditions; an intelligent evolutionary approach. *Applied Soft Computing; an international journal*, 24, 822-828, 2014.

Proceedings of the 24th UK Conference of the
Association for Computational Mechanics in Engineering
31 March - 01 April 2016, Cardiff University, Cardiff

A MICRO-MECHANICS BASED SOIL-FIBRE COMPOSITE MODEL FOR USE WITH FINITE ELEMENT ANALYSIS

***Thomas Bower[1], Anthony Jefferson[1], Peter Cleall[1] and Paul Lyons[2]**

[1]School of Engineering, Cardiff University, Queen's buildings, The Parade, Cardiff, CF24 3AA
[2]LUSAS, Forge House, 66 High Street, Kingston Upon Thames, Surrey, KT1 1HN

*BowerTA@cardiff.ac.uk

ABSTRACT

Inclusion of manufactured fibres into a soil has been shown to significantly increase its shear strength and modify its dilative behaviour. The primary mechanism for strength increase is due to the frictional interaction between individual fibres and soil particles. Each fibre resists the movement of soil around it and this has an overall effect of increasing the shear strength. This paper presents the initial development of a micro-mechanics based soil-fibre model which uses concepts from the well-known shear lag model and is extended to include fibre de-bonding. The distribution of fibre orientations is taken into account by use of a distribution function which can be modified according to different soil-fibre preparation techniques. The micro-mechanical model is homogenised using a spherical integration technique and inserted into a single point constitutive driver using the rule of mixtures. The hardening soil model was chosen as a matrix material for this study as it captures the non-linear stress-strain response and failure limit observed in triaxial compression tests. The proposed soil-fibre model is then compared against triaxial compression test data of a well graded sand with differing fibre contents of Loksand fibres and different confining stresses. Preliminary simulations of the experimental tests show promising results.

Key Words: *soil fibre composite; debonding; orientation distribution; constitutive model; triaxial tests*

1. Introduction

Adding fibres to a soil can significantly improve some of its properties. Several studies have shown to increase ultimate shear strength in sands in triaxial compression tests , and a decrease in dilatancy [6, 4, 12]. The strength of the composite is also heavily dependent on the distribution fibre orientations [11] such that the fibres aligned with the direction of the largest extension have the largest effect on the strength, hence the sample preparation method can have some effect on the composite strength [9].

Several soil-fibre models have been developed in recent years; namely by Maher and Gray [10] who used a statistical distribution function to model the variation of fibre orientations. Diambra et al. [6] used a similar basis for their model which also included an empirical debonding function. Diambra and Ibraim [7] improved this model by using shear lag theory [5] as a basis for debonding.

2. Behaviour of a single fibre

The matrix strain ε_{ma} surrounding the fibre drives the composite analysis (Figure 1). Balancing the interface shear forces and the internal tensile forces on an infinitesimal length of fibre gives the well known shear lag equation [5]. Manipulation of the shear lag equation and substitution of the fibre boundary conditions leads to a relationship for the fibre slip.

$$S(x, \varepsilon_{ma}) = \frac{\varepsilon_{ma}}{\beta \cosh(\beta l_f / 2)} \sinh(\beta x) \tag{1}$$

Where β is a material constant relating to the geometry and stiffness of the fibre and soil; it also includes a constant k_s relating the interface slip to the interface shear stress.

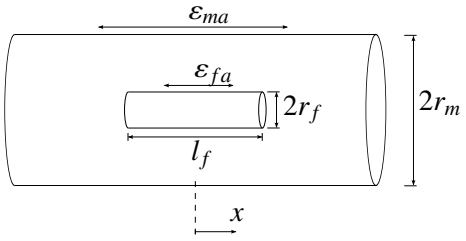

Figure 1: Soil-fibre composite cylinder

$$\sigma_{fa}(x, \varepsilon_{ma}) = \frac{-2k_s\varepsilon_{ma}}{r_f\beta^2 \cosh(\beta l_f/2)}(\cosh(\beta x) - 1) \tag{2}$$

After extensive loading, the interface will reach a shear stress limit τ_b (Figure 2), this is the debonding shear stress which can be found from the peak tensile load during a fibre pullout test. As the shear stress is always maximum at the fibre ends, debonding occurs first at the ends of the fibre and moves towards the centre with additional loading. The total length of this debonded region is $2l_b$.

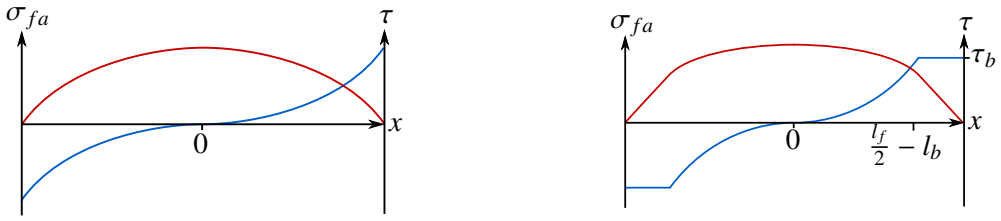

(a) Fully bonded

(b) Partially debonded

Figure 2: Tensile fibre stress σ_{fa} (—) and interface shear stress τ (—) distributions for bonded and partially debonded fibre along the length of the fibre.

Using a similar approach to the fully bonded case, the partially debonded slip relationship is given in Equation (3).

$$S = \begin{cases} \dfrac{\tau_b}{k_s}\dfrac{\sinh(\beta x)}{\sinh(\beta(l_f/2 - l_b))} & \text{if } 0 < x \leq l_f/2 - l_b \\ \dfrac{\tau_b}{k_s} & \text{if } l_f/2 - l_b < x \leq l_f/2 \end{cases} \tag{3}$$

Again, the fibre tensile stress σ_{fa} for the debonding case can be found by substituting the slip relationship in (3) into the shear lag equation and integrating. The stress distribution within the fibre for full and partial bonding can be found in Figure 2.

3. Continuum homogenisation

To analyse the global effect of fibre inclusion, the effects of a single fibre are averaged; taking into account the distribution of orientations and the volume fraction v_f. The distribution of fibres on the horizontal plane is uniform, and the vertical directions are assumed to follow the distribution (4) [11] where θ is the angle from horizontal. The constants $A = 0$, $B = 0.57$, $n = 7$ were determined by comparing with an experimental distribution study [14] for the sand and fibres used in this investigation .

$$\rho_\theta = A + B|\cos^n\theta| \tag{4}$$

The fibre stress relation is then integrated over its length, and over the surface of a sphere using the numerical approach by Bažant and Oh [1] with $n_d = 21$ sampling directions. $\chi(\theta_{id})$ is a transformation vector and w_{id} is a sampling weight.

$$\sigma_f = v_f \sum_{i_d=1}^{n_d} \rho(\theta_{id}) \cdot \chi(\theta_{id})^T \int_0^{l_f/2} \frac{2}{l_f} \sigma_{fa}(x, \varepsilon_{ma})\, \mathrm{d}x \cdot w_{id} \tag{5}$$

4. The hardening soil model

The soil model chosen to be used alongside the fibre model is the hardening soil model [2, 13]. The model extends the hyperbolic soil model from a hypo-elastic one to an elasto-plastic one. The hardening soil model makes use of multiple yield surfaces, however, this study uses only a modified version of the hardening shear surface. The original yield surface is shown in Equation (6), its modification (which is to be presented in future work) focusses on the robustness of the model, as well as developing a total strain formulation suitable for use in commercial finite element analysis software.

$$f = \frac{q_a}{E_{50}} \frac{q}{q_a - q} - \frac{2q}{E_{ur}} - \gamma_p \tag{6}$$

An explanation of the terms used here may be found in [2]. The plastic potential function is the Drucker-Prager cone [8] with a constant dilatancy angle.

5. Comparison with experimental results and discussion

The unreinforced sand exhibits a non-linear stress / strain relationship during triaxial loading with an upper limit to the available shear stress. This is reflected well in the predicted results whereby soil failure is reached at approximately 5% axial strain (Figure 3a). The strength is under-predicted by 10% and is most likely due to the chosen material parameters. The soil undergoes an initial compression then dilates from 2.2% axial strain. The predicted model also follows this trend but to a different dilating gradient. This is almost certainly due to the simplified dilatancy rule used in the hardening soil model and the lack of a cap surface.

Adding fibres to the soil appears to increase the shear strength indefinitely. The predictions capture the rate of strength increase well. Increased fibre content also reduces dilatancy in the experimental results; this is reflected in the prediction however the limitation with the dilatancy rule does not allow the model to give accurate results here. Also, none of the experimental results presented so far show and significant debonding characteristics, therefore it is not possible to determine the effectiveness of the debonding relationship described in Equation (3).

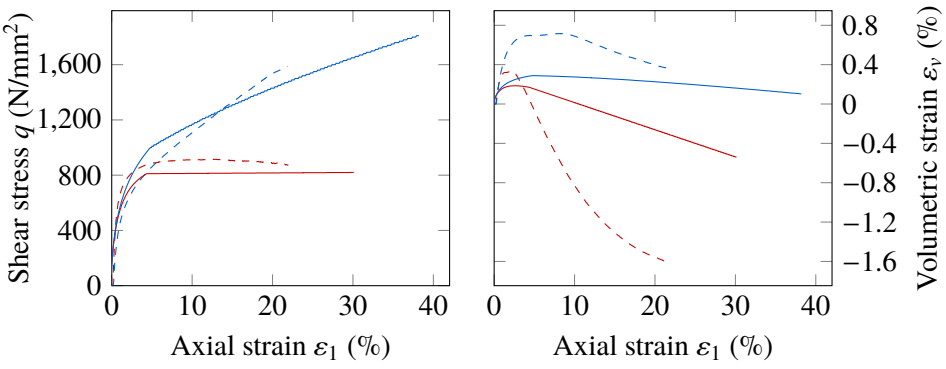

(a) Shear stress response

(b) Volumetric response

Figure 3: Triaxial test experimental results (dashed) and predicted (solid); for unreinforced sand (red) and with 0.3% fibre content by volume (blue); experimental results by Chatzopoulos [3]

6. Conclusions

The soil-fibre composite model described here performs to some degree as expected from experimental results. However, limitations in the underlying soil model may be dominating over any shortcomings in the fibre model. Therefore, further work will focus on completing the re-formulation of the hardening soil model and testing of the soil-fibre model under different conditions.

Acknowledgements

The work presented here was supported by LUSAS / Finite Element Analysis ltd. and Innovate UK / TSB as part of KTP project number 9082. I would also like to thank Drake Extrusion Inc. for supplying the fibres used in the experimental testing.

References

[1] Z. P. Bažant and B. H Oh. Efficient numerical integration on the surface of a sphere. *ZAMM - Journal of Applied Mathematics and Mechanics*, 66(1), 37-49, 1986.

[2] T. Benz. Small-strain stiffness of soils and its numerical consequences, PhD. Thesis, Univ. Stuttgart, Inst. f. Geotechnik, 2007.

[3] S. Chatzopoulos. Soil reinforced with discrete polypropylene fibers, MSc. Thesis, Cardiff University, 2015.

[4] N. C. Consoli, P. D. M. Prietto, and L. A. Ulbrich. Influence of fiber and cement addition on behaviour of sandy soil. *Journal of Geotechnical and Geoenvironmental Engineering*, 124(12), 1211-1214, 1998.

[5] H. L. Cox. The elasticity and strength of paper and other fibrous materials. *British Journal of Applied Physics*, 3, 72-79, 1952.

[6] A. Diambra E. Ibraim, D. Muir Wood and A. R. Russel. Fibre-reinforced sands: Experiments and modelling. *Geotextiles and geomembranes*, 28(3), 238-250, 2010.

[7] A. Diambra and E. Ibraim. Fibre-reinforced sand: interaction at the fibre and grain scale. *Géotechnique*, 65, 296-308, 2015.

[8] D. C. Drucker, W. Prager and H. T. Greenberg. Extended limit design theorems for coninuous media, *Quarterly of applied mathematics*, 1952.

[9] E. Ibraim, A. Diambra, A.R. Russel and D. Muir Wood. Assessment of laboratory sample preparation for fibre reinforced sands. *Geotextiles and Geomembranes*, 34, 69-79, 2012.

[10] M. H. Maher, and D. H. Gray. Static response of sands reinforced with randomly distributed fibres. *Journal of Geotechnical Engineering*, 116(11), 1661-1677, 2012.

[11] R. L. Michalowski and J. Čermák. Strength anisotropy of fibre-reinforced sand. *Computers and Geotechnics*, 29(4), 279-299, 2002.

[12] R. L. Michalowski and J. Čermák. Triaxial compression of sand reinforced with fibers. *Journal of Geotechnical and Geoenvironmental Engineering*, 129(2), 125-136, 2003.

[13] T. Schanz, P. A Vermeer and P. G. Bonnier. The hardening soil model: formulation and verification. *Beyond 2000 in computational geotechnics*, 281-296, 1999.

[14] Z. Wang. Fibre reinforced sand: from sample preparation to triaxial tests and orientation investigation, MSc. Thesis, Cardiff University, 2015.

Proceedings of the 24th UK Conference of the
Association for Computational Mechanics in Engineering
31 March – 01 April 2016, Cardiff University, Cardiff

MODELLING THE SEEPAGE FLOW DURING CAISSON INSTALLATION IN A NATURAL SEABED

***Asaad Faramarzi[1], Koohyar Faizi[1], Samir Dirar[1], Moura Mehravar[2] and Ouahid Harireche[3]**

[1]Department of Civil Engineering, School of Engineering, University of Birmingham, Birmingham, B15 2TT
[2]Wolfson School of Mechanical and Manufacturing Engineering, Loughborough University, LE11 3TU
[3]Department of Civil Engineering, Faculty of Engineering, Islamic University in Madinah, KSA

*A.Faramarzi@bham.ac.uk

ABSTRACT

Seepage plays a crucial role in the installation of suction caisson foundations and this has been considered by several researchers via experimental, numerical and analytical studies. In most of the available numerical and analytical studies, the actual seabed profile has been modelled using a number of assumptions and considering a limited number of idealised conditions to simplify the problem. However, it is well established that the behaviour of seabed, and soil in general, is a complex and nonhomogeneous one and that these assumptions can affect the reliability of the results. This paper examines the installation of suction caisson foundation into a realistic and natural seabed profile. It identifies the changes in seepage flow at different stages of installation and the role of crucial parameters such as permeability on the installation process is discussed. The results show that a significant increase in resistance to penetration occurs at the interface layers.

Keywords: *suction caisson; installation; natural seabed soil; permeability*

1. Introduction

Suction caissons are relatively new types of foundations which have applications in offshore oil and gas industry as well as offshore wind farms. They are upturned buckets of cylindrical shape made from steel. Installation of these foundations in seabed soil is achieved by pumping out water trapped in the caisson hollow space which enables their penetration into the seabed after initial penetration under self-weight. Seepage occurs in permeable soils during suction caisson installation, as discussed by Hogervorst [3], leading to a reduction in the soil effective stress and hence its resistance to penetration [8]. However, in soils with low permeability, installation is mainly achieved by the difference between pressure inside and outside the caisson, caused by pumping out the trapped water in the caisson cavity, and the effect of seepage is limited [8, 1]. Installation in multi-layered soil profiles, e.g. very low permeable soil overlaid by sand, is expected to be more challenging since the reduction in resistance to the caisson tip penetration is restrained by restrictions of flow in the lower less permeable layer. It is unclear to what extent the lower less permeable layer impacts the seepage flow and thus the resistance to the suction caisson tip penetration. Installation aspects of suction caissons in homogeneous clay [2] or granular materials [4] are extensively studied by many researchers. However, limited documentation, references or guidelines are available for installation in stratified soils [5, 6]. In the present paper, a finite element (FE) model is developed to study the effect of a multi-layered seabed on the installation process of suction caisson foundations. The results are compared with those obtained from installation in a single layer soil and the differences are highlighted.

2. Formulation of the Normalised Seepage Problem

In order to draw conclusions regardless of specific dimensions, an FE model of a suction caisson normalised with respect to the caisson radius (R) is developed. The caisson height and penetration depth into seabed are denoted as L, and h respectively. The first case represents caisson installation in homogeneous soil with permeability k and saturated unit weight γ_{sat}. For the second case of a two-layer soil profile, the depths of the upper and lower layers are taken as 2m and 4m respectively. The permeability of the upper layer is taken as 10 times higher than that of the second layer. Figure 1, shows a vertical section through the meridian plane of the caisson-soil system where a cylindrical system of coordinates $z^* = z/R$, and $r^* = r/R$ is used. For the caisson penetration depth, the dimensionless parameter $h^* = h/R$, is adopted [7].

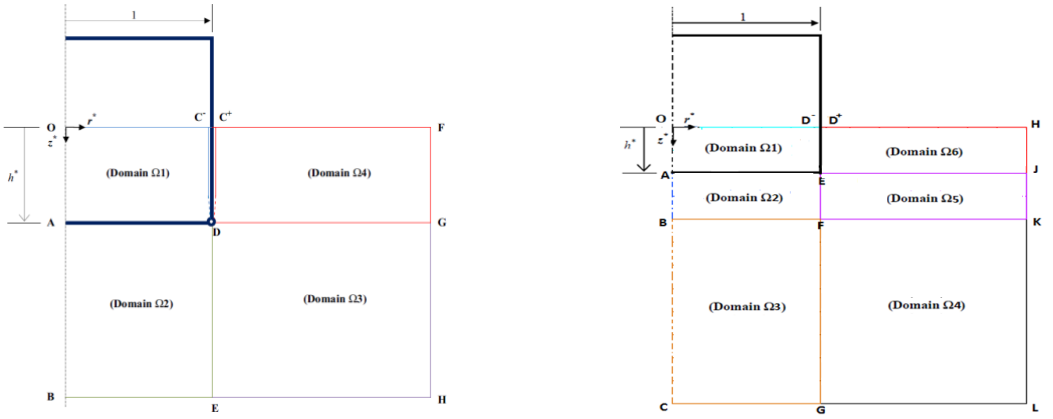

Figure1: Normalised Geometry and Finite Element Model; Homogeneous (left) and Layered (right)

To study the effect of porewater seepage on soil resistance to caisson penetration, lateral pressures on inside and outside caisson wall caused by seepage is investigated. Under seepage conditions produced by an applied suction, the lateral effective pressure (σ'_h) acting on the caisson wall at depth z, inside and outside the caisson is respectively given by:

$$\sigma'_{hi}(R,z) = K(\gamma' z - \int_0^z g_i(R,\zeta)d\zeta + \tilde{\sigma}_i(R,z)) \tag{1}$$

$$\sigma'_{ho}(R,z) = K(\gamma' z - \int_0^z g_o(R,\zeta)d\zeta + \tilde{\sigma}_o(R,z)) \tag{2}$$

where K is the coefficient of lateral earth pressure, γ' is the effective unit weight of the soil, $\tilde{\sigma}$ is the enhanced effective stress caused by the effect of shear resistance that develops on the soil-caisson interface and $g_i(R,\zeta)$,and $g_o(R,\zeta)$ denote the vertical component of the pressure gradient on the inner and the outer sides of the caisson wall respectively. Seepage causes the frictional resisting force acting on the caisson wall to decrease by a magnitude ΔF_s given as a function of the normalised penetration depth $h*$ by the expression:

$$\frac{\Delta F_s}{2\pi R^2 K\bar{s}\tan\delta} = \int_0^{h^*} \left| L_i^*(Z^*) + L_o^*(Z^*) \right| dz^* \tag{3}$$

$$\Delta F^*_s = \frac{\Delta F_s}{(2\pi R^2 K\bar{s}\tan\delta)} \tag{4}$$

Where:

$$L_i^*(Z^*) = \int_0^{z^*} g_i^*(1,\zeta^*)d\zeta^* \tag{5}$$

$$L_o^*(Z^*) = \int_0^{z^*} g_o^*(1,\zeta^*)d\zeta^* \tag{6}$$

and δ denotes the angle of friction at the interface soil-caisson. Suction magnitude at mudline level inside the caisson cavity are denoted by $\bar{s}$. In the next section, the normalised decrease of frictional resistance (ΔF_s^*) is calculated using the results of the FE models and the above relationships.

3. Results and Discussion

Figures 2a and 2b, show the distribution of normalised excess pore water pressure $P*$ around the caisson for the normalised penetration depth $h*$ =1 and 3 in a homogeneous seabed.

Water seepage cause by suction produces a hydraulic gradient which on both faces of the caisson wall varies with depth. Figures 2c, and 2d show the distribution of P^* for the seabed with layered soil profile at the same depths. From these figures it can be seen that the contours of excess pore water pressure have been affected due to the presence of a less permeable layer. This will accordingly have an impact on the penetration resistance as it can be seen in the next section. Figure 3a, and b depicts the contours of vertical component of the scaled pressure gradient $g^* = \partial p^* / \partial z^*$ for normalised penetration depth h^* = 1, and 3, corresponds to a homogeneous seabed. It can be observed that the highest gradient magnitudes are concentrated around the caisson tip. At shallow penetration depths, high gradients around the caisson wall affect the whole penetration depth. As the penetration depth increases, these gradients tend to localise around the caisson tip. For comparison, Figure 3c, and 3d shows similar contours for a seabed layered profile. From these figures, it can be seen that discontinuity in the permeability profile at the interface between the two layers is reflected in the profile of the pore pressure gradient. This in turn affects the magnitude of frictional soil resistance as a function of normalised depth as will be shown later.

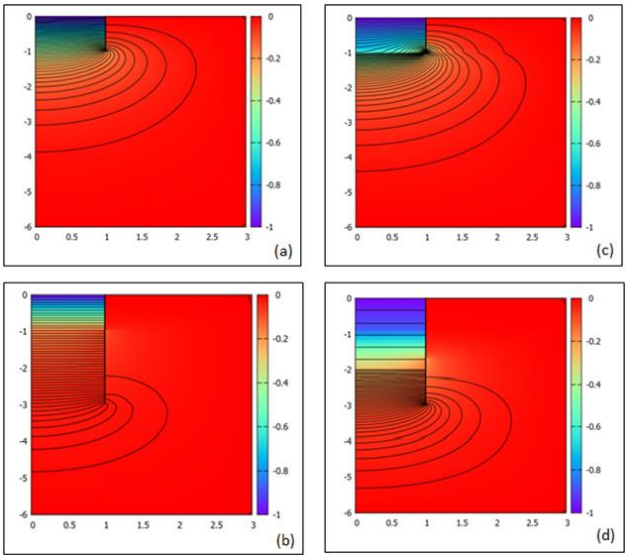

Figure 2: Excess pore water pressure for h*=1, 3; (a, b): homogeneous; (c, d): layered soil.

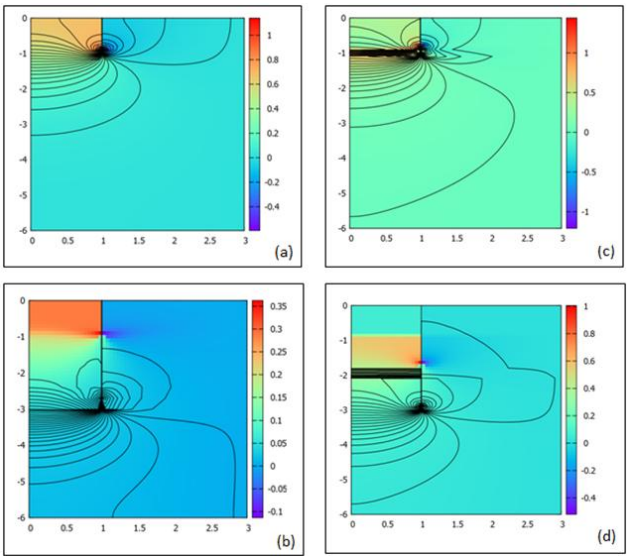

Figure 3: Normalised pressure gradient for h^*=1, 3; (a, b): homogeneous; (c, d): layered soil.

Figure 4 shows clearly that the reduction in the magnitude of lateral friction resistance (ΔF_s^*) increases as the caisson passes through the layer with higher permeability. An increase (i.e. 50%) in resistance to penetration occurs at the interface between the soil layers. This result shows clearly that the suction pressure required could be affected by sudden changes in permeability in layered soils.

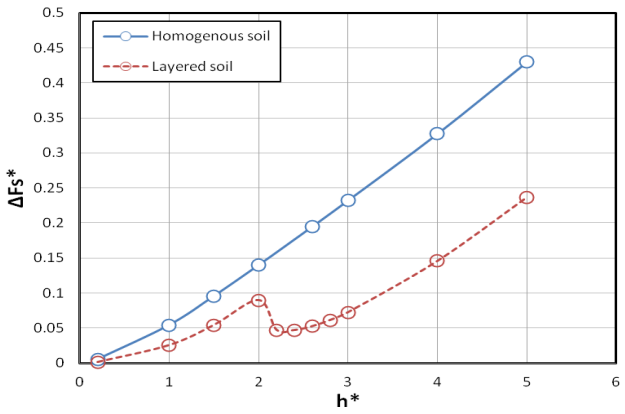

Figure 4: Effect of Suction-Induced Seepage on Soil Resistance at Caisson Wall

4. Conclusions

This study considered the effect of soil profile permeability on the prediction of soil resistance to caisson penetration. Two soil profiles were considered, namely homogeneous soil with constant permeability and a layered soil profile where low permeable soil is overlaid by a 2-meter thick layer of high permeable soil. The effect of suction-induced seepage on soil resistance to caisson penetration was investigated using the normalised solution of seepage around the caisson wall. It has been observed that taking into account the actual variation of permeability in layered soils may lead to a more accurate estimation of the critical suction.

References

[1] B. Zhu, D. Q. Kong, R. P. Chen, L. G. Kongand, Y. M. Chen. Installation and lateral loading tests of suction caissons in silt. *Canadian Geotechnical Journal*, Vol.48, pp.1070-1084, 2011.

[2] G. T. Houlsby and B. W. Byrne. Design procedures for installation of suction caissons in clay and other materials. *Geotechnical Engineering*, 2005, 158, 2: 75–82, 2005.

[3] J. R. Hogervorst. Field trials with large diameter suction piles, *Proceedings of the Offshore Technology Conference*, Houston, Paper OTC 3817, 1980.

[4] K. H. Andersen, H. P. Jostad, R. Dyvik. Penetration resistance of offshore skirted foundations and anchors in dense sand. *American Society of Civil Engineers*, Volume 134, pp. 106.116. 2008.

[5] M. Senders, M. F. Randolph. Theory for the installation of suction caissons in sand overlaid by clay. *Offshore Site Investigation and Geotechnics*, Proc. 6th Int. Conf. London, 2007.

[6] O. Cotter. Installation of Suction Caissons for Offshore Renewable Energy Structures, *A thesis submitted for the degree of Doctor of Philosophy*. Magdalen College, Oxford, 2009.

[7] O. Harireche, M. Mehravar, M.A. Alani. Suction caisson installation in sand with isotropic permeability varying with depth. *Applied Ocean Research*, Vol 43, pp 256- 263, 2013.

[8] R. Romp. Installation-effects of suction caissons in non-standard soil conditions, *Master Thesis, Delft University of Technology*, 2013.

Proceedings of the 24th UK Conference of the
Association for Computational Mechanics in Engineering
31 March – 01 April 2016, Cardiff University, Cardiff

An Investigation of Different Borehole Layouts for Carbon Sequestration in Coalbeds

***Lee J. Hosking[1] and Hywel R. Thomas[1]**

[1]Geoenvironmental Research Centre, Cardiff School of Engineering, Cardiff University, Queen's Buildings, The Parade, Newport Road, Cardiff, CF24 3AA

*HoskingL@cardiff.ac.uk

ABSTRACT

This paper investigates how the layout of injection boreholes can influence the effectiveness of carbon sequestration and enhanced methane recovery in a coalbed. A numerical model for high pressure gas transport with kinetically-controlled adsorption and desorption is used to predict the carbon dioxide storage and methane displacement behaviour in two simulation scenarios. In the first scenario, carbon dioxide is injected using a single borehole located at the centre of the domain, whereas the second scenario considers a four-spot layout for the injection boreholes. Both simulations consider the same arrangement of boreholes for the recovery of the displaced methane. It is demonstrated that the four-spot layout increases the amounts of carbon dioxide stored and methane recovered in the simulation period, although the increase in carbon dioxide storage is somewhat offset by interference between the injection boreholes.

Keywords: *carbon sequestration; coalbed methane recovery; borehole layout; coupled modelling*

1. Introduction

Geological carbon sequestration is set to play an integral role in the transition to the low carbon future by preventing the atmospheric emission of carbon dioxide generated in the energy and industry sectors. Coalbeds are among the candidate storage reservoirs since coal typically has a strong preference to retain substantial amounts of gas in the adsorbed phase [1]. Moreover, the injection of carbon dioxide into a coalbed may also serve to enhance the displacement and recovery of in situ methane to provide a supply of unconventional gas.

Gas transport, storage and displacement in coal involves seepage flows through the network of naturally-occurring fractures as well as diffusive transport, adsorption and desorption in the porous rock matrix [1,2]. The injection and recovery of gas changes the effective stress and subsequently causes physico-mechanical coal deformation [2]. In addition, chemo-mechanical deformation caused by the adsorption-induced swelling or desorption-induced shrinking of the coal solids can have a considerable feedback on the gas transport behaviour. The coal-gas interactions described play an important role in governing carbon dioxide storage and methane displacement in coalbeds. However, it is also important to understand how the application of the technology is influenced by some of the key engineering factors involved. The present work therefore investigates the role of the injection borehole layout in determining the performance of carbon sequestration in coal with enhanced methane recovery.

The investigation is carried out by applying the reactive gas transport module of the coupled thermo-hydro-chemo-mechanical (THCM) model COMPASS. An overview of the theoretical formulation for reactive gas transport and its numerical implementation is provided below, followed by a description and discussion of the numerical simulations conducted as part of this work.

2. Theoretical formulation

The coupled THCM model, developed by Thomas and co-workers [e.g. 3], forms the basis for the numerical simulations presented in this work. The model applies a mechanistic approach to solving for heat transfer, moisture and chemical/gas transport, and mechanical behaviour and has been applied to

simulate the reactive transport of multicomponent chemicals and gas in a range of geoenvironmental applications. The application of the gas transport module in this work has been based on the assumption that: i) the coalbed is completely dry, ii) coal is a homogenous, isotropic and elastic material, iii) a single continuum, equivalent continuum approach is valid, and iv) the coalbed is isothermal.

The governing equation describing the reactive transport of the i^{th} gas component can be expressed as:

$$\frac{\partial n c_g^i}{\partial t} + \rho_s \frac{\partial s_g^i}{\partial t} = -\nabla \cdot \left[c_g^i \mathbf{v_g}\right] - \nabla \cdot \left[n \tau_g D_g^i \nabla c_g^i\right] \tag{1}$$

where n is the porosity, c_g^i and s_g^i are the concentrations in the free and adsorbed phases, respectively, t is time, ρ_s is the density of the solid phase, ∇ is the gradient operator, τ_g is the gas tortuosity factor, and D_g^i is the diffusion coefficient. Darcy's law is employed to calculate the bulk gas velocity, $\mathbf{v_g}$, which in combination with the real gas law gives:

$$\mathbf{v_g} = -\frac{K}{\mu_g} \nabla u_g = -\frac{KZRT}{\mu_g} \sum_{j=1}^{n_g} \nabla c_g^j \tag{2}$$

where K is the intrinsic permeability, μ_g is the bulk gas viscosity, u_g is the bulk gas pressure, R is the universal gas constant, and T is the temperature. The compressibility factor, Z, is the ratio of the real and ideal molar volumes and expresses deviations of gas compressibility from the ideal gas law.

Gas retention behaviour at the coal surface is included as a kinetically controlled reaction formulated using a first-order kinetics model, giving [4]:

$$\frac{\partial s_g^i}{\partial t} = k_r^i \left(s_{g,\infty}^i - s_g^i\right) \tag{3}$$

where k_r^i is the sorption rate. $s_{g,\infty}^i$ is the adsorbed amount at equilibrium with the free gas phase obtained using the extended Langmuir isotherm model, given by:

$$s_{g,\infty}^i = \frac{n_L^i b_L^i ZRT c_g^i}{1 + ZRT \sum_{j=1}^{n_g} b_L^j c_g^j} \tag{4}$$

where n_L^i is the Langmuir adsorption capacity and b_L^i is the reciprocal of the Langmuir pressure.

Appropriate constitutive relationships have been employed in the model to accurately describe the real gas compressibility and viscosity. The former is included using the Peng and Robinson [5] equation of state (EoS). The gas viscosity is calculated via the dense gas model of Chung et al. [6]. Coal deformation due to effective stress changes and adsorption/desorption-induced matrix swelling/shrinking has been described using the following model by Palmer and Mansoori [7]:

$$\begin{aligned} \frac{K}{K_0} = \left(\frac{n}{n_0}\right)^3 = \Bigg[1 + \frac{1}{n_0 M} \sum_{j=1}^{n_g} \left(u_g - u_{g,0}\right) \\ + \frac{1}{n_0}\left(\frac{K}{M} - 1\right) \sum_{j=1}^{n_g} \left(\frac{\varepsilon_L^j b_L^j X_g^j u_g}{1 + u_g \sum_{k=1}^{n_g} X_g^k b_L^k} - \frac{\varepsilon_L^j b_L^j X_{g,0}^j u_{g,0}}{1 + u_{g,0} \sum_{k=1}^{n_g} X_{g,0}^k b_L^k} \right) \Bigg]^3 \end{aligned} \tag{5}$$

where the subscript 0 refers to the initial condition, M is the axial modulus, K is the bulk modulus, ε_L^i is the Langmuir volumetric strain, and X_g^i is the free gas mole fraction.

A numerical solution of the governing gas transport equations is achieved by applying the finite element method with Galerkin weighted residuals for spatial discretisation and a mid-interval backward-difference scheme for temporal discretisation. The sequential non-iterative approach (SNIA) is adopted to couple the gas transport and kinetically-controlled adsorption/desorption terms.

3. Problem setup

The simulations have been performed for carbon dioxide injection and methane recovery from a 500 m deep, hypothetically isolated coalbed of 200 m long by 200 m wide and 1 m thick. Two arrangements were considered for the injection of carbon dioxide, namely: i) a single injection borehole (Test A), and ii) a four-spot layout with a spacing of 50 m (Test B). The 0.1 m radius injection boreholes were located symmetrically at the centre of the coalbed. The recovery of methane was considered in both Tests with a borehole in each corner of the coalbed. Owing to the symmetry of the problem, the simulation domain represented one of the four 100 m by 100 m quadrants of the coalbed. The domain was discretised using around 500 triangular elements in Test A and around 600 elements in Test B, with elements concentrated around the boreholes. The initial condition in both Tests was pure methane at a uniform pore gas pressure of 5 MPa and an isothermal temperature of 298 K. The injection of carbon dioxide at 5 MPa was prescribed at the injection boundary (borehole) with the gas recovery boundary (borehole) fixed at 1 MPa. Since the coalbed was assumed to be isolated, all other boundaries were closed. A 3 year simulation period was considered. The set of material parameters applied, presented in Table 1, was formed through a combination of laboratory characterisation [8] and literature survey [e.g. 2,9].

Table 1 Summary of material parameters used in the numerical simulations.

Parameter	**Value**		**Source**
Initial porosity, n_0 (-)	0.1		[9]
Initial permeability, K_0 (m^2)	1.0×10^{-16}		[8]
Coal density, ρ_s (kg)	1495.9		[8]
Axial modulus, M (Pa)	4.16×10^9		[2]
Bulk modulus, K (Pa)	2.81×10^9		[2]
	CO_2	**CH_4**	
Sorption rate, k_r^i (s^{-1})	3.60×10^{-4}	5.00×10^{-5}	[8]
Langmuir constant, b_L^i (Pa^{-1})	0.20×10^6	0.45×10^6	[8]
Langmuir capacity, n_L^i (mol kg^{-1})	1.26	1.09	[8]
Langmuir volumetric strain, ε_L^i (-)	0.021	0.009	[8]

4. Numerical results

Figure 1 presents the results of the numerical simulations in terms of the distributions of carbon dioxide and methane in the gas phase at the end of the 3 year simulation period. The results are given for a cross section of the domain taken along the diagonal passing through the gas injection and recovery boreholes. The steep decline in the concentration of carbon dioxide in the vicinity of the gas injection boreholes, predicted in both Tests, is attributed to the dissipation of the injected gas away from the borehole boundary. Similarly, it can be seen that a steep decline in the methane concentration developed in the vicinity of the gas recovery boreholes. As expected, the displacement of methane by carbon dioxide followed a similar trend in both Tests due to the seepage-driven displacement of free gas in the pores and the preferential adsorption of carbon dioxide ahead of methane. As the carbon dioxide advanced into the coalbed, the kinetically-controlled displacement of the adsorbed phase resulted in the mixing front of the gases gradually widening.

By the end of the simulation period, 8.44×10^6 mol of carbon dioxide had been stored in Test B compared to 3.52×10^6 mol in Test A. Likewise, 6.96×10^6 mol of methane had been recovered in Test B compared to 3.57×10^6 mol in Test A. The respective amounts of carbon dioxide stored and methane recovered were therefore 140% and 95% higher for four injection boreholes compared to a single borehole. Interference between the injection boreholes can be seen towards $x = 0$ m in Figure 1b and restricted the carbon dioxide storage to considerably less than a four-time increase (i.e. an increase of 300%). Moreover, Figure 1 shows that an earlier breakthrough of carbon dioxide in the recovered gas would occur in Test B. This would necessitate an earlier termination of methane recovery and may result in a lower overall displacement, or 'sweep', efficiency compared to that at the time of breakthrough in Test A. This premise will be studied in future work.

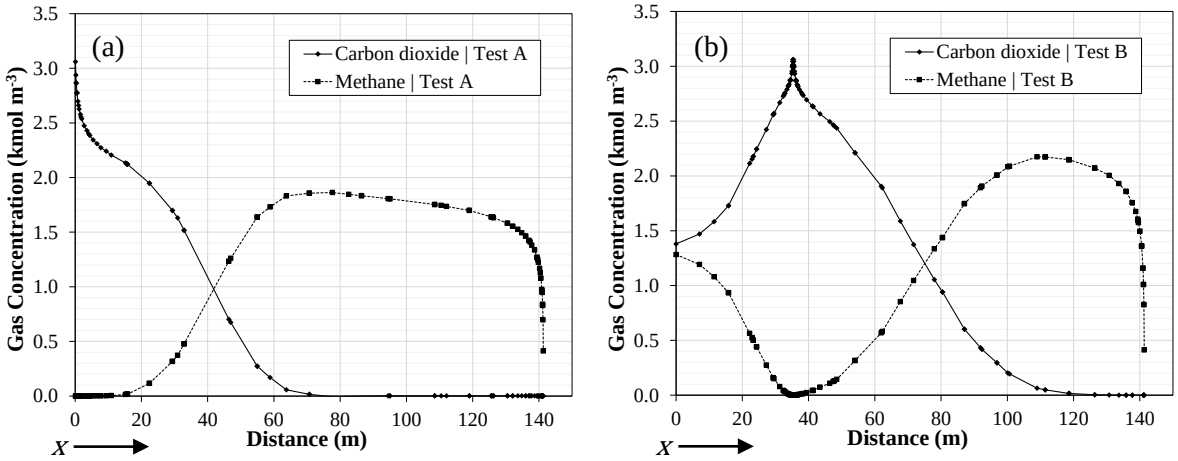

Figure 1 Distributions of carbon dioxide and methane taken along the diagonal of the domain passing through the gas injection and recovery boreholes after 3 years for: (a) Test A, and (b) Test B.

5. Conclusion

This paper has presented a numerical investigation of carbon sequestration in coal using different injection borehole layouts. In addition, some of the main physical and chemical phenomena responsible for the observed gas storage and displacement behaviour have been discussed. Based on the observations made, it can be concluded that the layout of the injection boreholes is a key engineering factor influencing the performance of carbon sequestration in coal with enhanced methane recovery. The four-spot layout delivered significant increases in the amounts of carbon dioxide stored and methane recovered, although the increase in carbon dioxide storage was somewhat offset by interference between the injection boreholes. The next step will be to expand the study to consider a number of different borehole spacings and different reservoir conditions.

Acknowledgements

The work described here has been carried out as part of the GRC's Seren project, which is funded by the Welsh European Funding Office (WEFO). The financial support is gratefully acknowledged.

References

[1] White, C. M., et al. Sequestration of carbon dioxide in coal with enhanced coalbed methane recovery - a review. *Energy & Fuels*, 19(3), 659-724, 2005.

[2] Zhang, H., Liu, J. and Elsworth, D. How sorption-induced matrix deformation affects gas flow in coal seams: a new FE model. *International Journal of Rock Mechanics and Mining Sciences*, 45, 1226-1236, 2008.

[3] Thomas, H.R. and He, Y. Modelling the behaviour of unsaturated soil using an elastoplastic constitutive relationship. *Géotechnique*, 48, 589-603, 1998.

[4] King, G.R., Ertekin, T. and Schwerer, F.C. Numerical simulation of the transient behavior of coal-seam degasification wells. *Society of Petroleum Engineers Formation Evaluation*, 1, 165-183, 1996.

[5] Peng, D-Y., Robinson, D.B. A new two-constant equation of state. *Ind. Eng. Chem. Fund.*, 15, 59-64, 1976.

[6] Chung, T-H., Ajlan, M., Lee, L.L. and Starling, K.E. Generalized multiparameter correlation for nonpolar and polar fluid transport properties. *Industrial and Engineering Chemistry Research*, 27, 671-679, 1988.

[7] Palmer, I. and Mansoori, J. How permeability depends on stress and pore pressure in coalbeds: A new model, *Society of Petroleum Engineers Reservoir Evaluation and Engineering*, 1 , 539-544, 1998.

[8] Hadi Mosleh, M. An experimental investigation of flow and reaction processes during gas storage and displacement in coal. PhD Thesis, Cardiff University, 2014.

[9] Rodrigues, C.F. and Lemos de Sousa, L. The measurement of coal porosity with different gases. *International Journal of Coal Geology*, 48, 245-251, 2002.

Material Modelling I

Proceedings of the 24th UK Conference of the
Association for Computational Mechanics in Engineering
31 March - 01 April 2016, Cardiff University, Cardiff

A MULTI-SCALE GRADIENT ELASTICITY MODEL WITH DISPERSION CORRECTION

***Harm Askes[1] and Dario De Domenico[2]**

[1]Department of Civil and Structural Engineering, University of Sheffield, Mappin Street, Sheffield S1 3JD, UK
[2]Department of PAU, Università Mediterranea Reggio Calabria, Via Melissari, Reggio Calabria 89124, Italy

*h.askes@sheffield.ac.uk

ABSTRACT

We postulate a new gradient elasticity formulation with three higher-order terms and, thus, three independent length scale constants. The formulation has one higher-order stiffness term and two higher-order inertia terms. It is shown that this formulation is better able to capture the wave disperion characteristics as seen in nano-scale experiments or layered composites. We derive a C^0 finite element implementation based on a newly developed operator split, which allows the governing fourth-order partial differential equations to be rewritten in a set of fully coupled second-order partial differential equations. The fundamental unknowns of these coupled equations are the micro-scale and macro-scale displacement; thus, this is intrisically a fully coupled multi-scale formulation. With the reduction of the order of the equations, finite element implementation becomes straightforward.

Key Words: *gradient elasticity; wave propagation; length scale; wave dispersion; multi-scale*

1. Introduction

Wave propagation through heterogeneous media is characterised by the occurrence of dispersion, meaning that the different harmonic wave components travel with different velocities. If this is to be captured with computer simulations, classical elasticity theory is only effective if every individual micro-structural constituent is modelled separately — but such an approach is usually deemed prohibitive in terms of associated computer costs. As an alternative, gradient elasticity theory can be used. Compared to classical elasticity theory, additional spatial derivatives of relevant state variables (such as stresses, strains and/or accelerations) are included in the field equations. These additional terms are accompanied by material length scales that represent the micro-structure of the material. An overview of various gradient elasticity formulations is given in [1].

A popular gradient elasticity theory was formulated by Aifantis in the 1990s and can be written, using index notation, as

$$C_{ijkl}\left(u_{k,jl} - \ell^2 u_{k,jlmm}\right) + b_i = 0 \tag{1}$$

where u_i are the displacements and b_i are the body forces. Furthermore, C_{ijkl} contains the usual elastic constants and ℓ is a micro-structural length parameter. The Aifantis model has been shown to be effective in removing singularities from stress and strain fields such as occur at the tips of sharp cracks or dislocation cores. However, its use in dynamics is not recommended due to the appearance of unbounded phase velocities [1]. Instead, in [3] it was argued that in a dynamics context gradient enrichment should be applied simultaneously to the stiffness terms and the inertia terms. Thus, a model is obtained according to

$$\rho\left(\ddot{u}_i - \alpha\ell^2\ddot{u}_{i,mm}\right) = C_{ijkl}\left(u_{k,jl} - \gamma\ell^2 u_{k,jlmm}\right) + b_i \tag{2}$$

where ρ is the mass density of the material. Dimensionless constants α and γ have been added so that different weights can be assigned to the two higher-order terms. It was shown that the latter model provides a reasonable approximation of the dispersive behaviour of discrete lattice model [3], however further improvement is possible as will be explored below.

2. A gradient elasticity model with two acceleration gradient terms

An effective and simple improvement of the dispersive behaviour of gradient elasticity models can be achieved by adding one more acceleration gradient term. We postulate

$$\rho\left(\ddot{u}_i - \alpha\ell^2\ddot{u}_{i,mm} + \beta\ell^4\ddot{u}_{i,mmnn}\right) = C_{ijkl}\left(u_{k,jl} - \gamma\ell^2 u_{k,jlmm}\right) + b_i \tag{3}$$

where β is yet another dimensionless weighting constant.

To assess the behaviour of the above models in dynamics, a dispersion analysis is carried out by substituting a trial solution $u(x,t) = U\exp\left(\mathrm{i}\left(kx + \omega t\right)\right)$ into the one-dimensional equation of motion. Here, k and ω are the wave number and angular frequency, respectively, whereas U is the amplitude. After some straightforward algebra, we obtain the following dimensionless expression:

$$\left(\frac{\omega\ell}{c_e}\right)^2 = \frac{\chi^2\left(1+\gamma\chi^2\right)}{1+\alpha\chi^2+\beta\chi^4} \tag{4}$$

where $c_e \equiv \sqrt{E/\rho}$ is the one-dimensional wave velocity of classical elasticity and $\chi \equiv k\ell$ is the wave number normalised with respect to the material length scale.

In Figure 1 we have plotted the dispersion curves for a range of parameter values. Firstly, the case $\alpha \neq 0$ with $\beta = \gamma = 0$ corresponds to a model with only one higher-order inertia term and leads to a horizontal asymptote for the dimensionless frequency. Next, the case $\alpha \neq 0$ and $\gamma \neq 0$ but $\beta = 0$ leads to a model with one higher-order stiffness term and one higher-order inertia term; in case $\alpha \neq \gamma$ the model is dispersive with a slant asymptote. Taking $\beta \neq 0$ alongside $\alpha \neq 0$ and $\gamma \neq 0$ leads again a horizontal asymptote, but there may also be an inflection point in case $\beta > \alpha\gamma$. Figure 1 includes the case where $\beta < \alpha\gamma$ which leads to a monotonically increasing curve, as well as the case $\beta > \alpha\gamma$ which predicts a curve that is concave for lower wave numbers and convex for larger wave numbers — the latter is in line with certain experimental results [4].

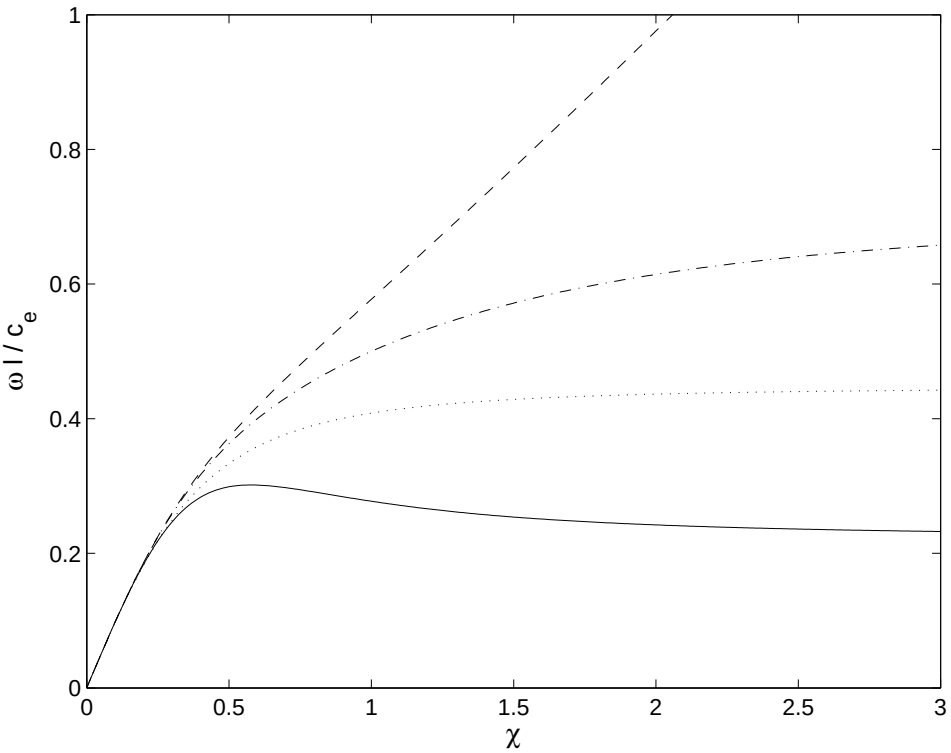

Figure 1: Dispersion curves — normalised frequency against normalised wave number for $\alpha = 5$, $\beta = 0$ and $\gamma = 0$ (dotted); $\alpha = 5$, $\beta = 0$ and $\gamma = 1$ (dashed); $\alpha = 5$, $\beta = 2$ and $\gamma = 1$ (dash-dotted); $\alpha = 5$, $\beta = 20$ and $\gamma = 1$ (solid)

3. Symmetric multi-scale formulation

The equations of motion given in expression (3) contain fourth-order spatial derivatives. This can be problematic for subsequent finite element implementations, which are usually based on C^0-continuous interpolations. Whilst it is certainly possible to formulate C^1 finite elements for gradient elasticity [5], here we will follow another approach. An operator split has been developed by which the fourth-order spatial derivatives are rewritten in terms of second-order spatial derivatives; this leads to auxiliary equations which, as we will show, can be symmetrised.

First, the right-hand-side of Eq. (3) is rewritten according to

$$\rho\left(\ddot{u}_i^{\mathrm{M}} - \alpha\ell^2\ddot{u}_{i,mm}^{\mathrm{M}} + \beta\ell^4\ddot{u}_{i,mmnn}^{\mathrm{M}}\right) = C_{ijkl}u_{k,jl}^{\mathrm{m}} + b_i \tag{5a}$$

$$u_k^{\mathrm{M}} - \gamma\ell^2 u_{k,mm}^{\mathrm{M}} = u_k^{\mathrm{m}} \tag{5b}$$

Superscripts M and m have been used to indicate macro-scale and micro-scale displacements, respectively; this nomenclature is motivated in [2]. Substituting Eq. (5b) back into Eq. (5a) would of course lead to Eq. (3), but instead we will take the double time derivative of Eq. (5b):

$$\ddot{u}_k^{\mathrm{M}} - \gamma\ell^2\ddot{u}_{k,mm}^{\mathrm{M}} = \ddot{u}_k^{\mathrm{m}} \tag{6}$$

This acceleration format can then be used to rewrite various terms in Eq. (5a), namely

$$\alpha\ell^2\ddot{u}_{i,mm}^{\mathrm{M}} = \frac{\alpha}{\gamma}\left(\ddot{u}_i^{\mathrm{M}} - \ddot{u}_i^{\mathrm{m}}\right) \tag{7}$$

and, in multiple stages,

$$\beta\ell^4\ddot{u}_{i,mmnn}^{\mathrm{M}} = \frac{\beta\ell^2}{\gamma}\left(\ddot{u}_{i,mm}^{\mathrm{M}} - \ddot{u}_{i,mm}^{\mathrm{m}}\right) = \frac{\beta}{\gamma^2}\left(\ddot{u}_i^{\mathrm{M}} - \ddot{u}_i^{\mathrm{m}}\right) - \frac{\beta\ell^2}{\gamma}\ddot{u}_{i,mm}^{\mathrm{m}} \tag{8}$$

Substituting Eqns. (7) and (8) into Eq. (5a) and multiplying Eq. (6) with $\rho\left(\alpha/\gamma - \beta/\gamma^2 - 1\right)$ leads to

$$\rho\left(\frac{\alpha\gamma-\beta}{\gamma^2}\ddot{u}_i^{\mathrm{m}} - \frac{\beta\ell^2}{\gamma}\ddot{u}_{i,mm}^{\mathrm{m}} - \frac{\alpha\gamma-\beta-\gamma^2}{\gamma^2}\ddot{u}_i^{\mathrm{M}}\right) = C_{ijkl}u_{k,jl}^{\mathrm{m}} + b_i \tag{9a}$$

$$\rho\left(-\frac{\alpha\gamma-\beta-\gamma^2}{\gamma^2}\ddot{u}_i^{\mathrm{m}} + \frac{\alpha\gamma-\beta-\gamma^2}{\gamma^2}\ddot{u}_i^{\mathrm{M}} - \frac{\left(\alpha\gamma-\beta-\gamma^2\right)\ell^2}{\gamma}\ddot{u}_{i,mm}^{\mathrm{M}}\right) = 0 \tag{9b}$$

4. Spatial and temporal discretisation

The advantages of Eqns. (9) are that they contain at most second-order spatial derivatives (so that C^0 finite element interpolations can be used) and that they are symmetric: the coefficient of $\ddot{u}_i^{\mathrm{M}}$ in Eq. (9a) is equal to the coefficient of $\ddot{u}_i^{\mathrm{m}}$ in Eq. (9b). The latter means that symmetric system matrices can be formulated, which facilitates computer storage.

On the other hand, with the various mathematical manipulations explained above, it is no longer possible to retrieve Eq. (3) because the displacement format of Eq. (5b) has been replaced by the acceleration format of Eq. (6). However, this also means that the inf-sup condition does not apply to Eqns. (9) since the equations are no longer "reducible". This implies that there are no constraints on the shape functions used for the two displacement fields.

Using the same shape functions $\mathbf{N}$ for u_i^{M} as well as u_i^{m} leads to a system of semi-discretised equations as

$$\begin{bmatrix} \frac{\alpha\gamma-\beta}{\gamma^2}\mathbf{M} + \beta\ell^2\mathbf{D} & -\frac{\alpha\gamma-\beta-\gamma^2}{\gamma^2}\mathbf{M} \\ -\frac{\alpha\gamma-\beta-\gamma^2}{\gamma^2}\mathbf{M}^T & \frac{\alpha\gamma-\beta-\gamma^2}{\gamma^2}\mathbf{M} + \frac{(\alpha\gamma-\beta-\gamma^2)\ell^2}{\gamma}\mathbf{D} \end{bmatrix} \begin{bmatrix} \ddot{\mathbf{d}}^{\mathrm{m}} \\ \ddot{\mathbf{d}}^{\mathrm{M}} \end{bmatrix} + \begin{bmatrix} \mathbf{K} & \mathbf{0} \\ \mathbf{0} & \mathbf{0} \end{bmatrix} \begin{bmatrix} \mathbf{d}^{\mathrm{m}} \\ \mathbf{d}^{\mathrm{M}} \end{bmatrix} = \begin{bmatrix} \mathbf{f} \\ \mathbf{0} \end{bmatrix} \tag{10}$$

with the usual definitions of the mass matrix $\mathbf{M}$ and stiffness matrix $\mathbf{K}$, i.e.

$$\mathbf{M} = \int_{\Omega} \mathbf{N}^T \rho \mathbf{N} \, \mathrm{d}V \tag{11}$$

and

$$\mathbf{K} = \int_{\Omega} \mathbf{B}^T \mathbf{C} \mathbf{B} \, \mathrm{d}V \tag{12}$$

where $\mathbf{B}$ is the usual strain-displacement matrix containing shape function derivatives and $\mathbf{C}$ is the matrix equivalent of the tensor C_{ijkl}. Furthermore, matrix $\mathbf{D}$ has the structure of a diffusivity matrix and is defined by

$$\mathbf{D} = \int_{\Omega} \sum_{i=1}^{3} \frac{\partial \mathbf{N}^T}{\partial x_i} \rho \frac{\partial \mathbf{N}}{\partial x_i} \, \mathrm{d}V \tag{13}$$

Finally, the force vector $\mathbf{f}$ contains the effects of all externally applied forces.

Inspection of Eq. (10) shows that lumping of the mass matrix leads to cancellation of all gradient effects. As a consequence, lumping is not an option and there is therefore little value in using an explicit time integrator that is only conditionally stable. Instead, the use of an implicit time integrator is recommended.

5. Conclusions

In this short paper we have reported the formulation of an enhanced gradient elasticity model with one higher-order stiffness term and two higher-order inertia terms. The model is capable of capturing a range of dispersion characteristics. Despite the presence of two terms that contain fourth-order spatial derivatives, it is possible to reformulate the model such that no higher than second-order spatial derivatives are included. This turns out to be a multi-scale formulation whereby micro and macro-scale displacements are the primary unknowns.

We have also carried out a number of parameter identification studies to relate the new constitutive parameters to the properties of a discrete lattice and those of a laminate. Furthermore, variationally consistent boundary conditions have been derived, and numerical results for a number of initial-boundary value problems have been obtained. These results will be presented in a forthcoming journal publication.

References

[1] H. Askes and E.C. Aifantis. Gradient elasticity in statics and dynamics: an overview of formulations, length scale identification procedures, finite element implementations and new results. *International Journal of Solids and Structures* **48**, pp. 1962–1990 (2011).

[2] T. Bennett, I.M. Gitman and H. Askes. Elasticity theories with higher-order gradients of inertia and stiffness for the modelling of wave dispersion in laminates. *International Journal of Fracture* **148**, pp. 185–193 (2007).

[3] A.V. Metrikine and H. Askes. One-dimensional dynamically consistent gradient models derived from a discrete microstructure. Part 1: Generic formulation. *European Journal of Mechanics A/Solids* **21**, pp. 555–572 (2002).

[4] J. Yarnell, J. Warren, R. Wenzel and S. Koenig. Phonon dispersion curves in bismuth. *IBM Journal of Research and Development* **8**, pp. 234–240 (1964).

[5] S.-A. Papanicolopulos, A. Zervos and I. Vardoulakis. A three-dimensional C^1 finite element for gradient elasticity. *International Journal for Numerical Methods in Engineering* **77**, pp. 1396–1415 (2009).

Proceedings of the 24th UK Conference of the
Association for Computational Mechanics in Engineering
31 March – 01 April 2016, Cardiff University, Cardiff

MICROMECHANICAL SOLUTION FOR SIMULATING AUTOGENOUS HEALING IN CEMENTITIOUS MATERIALS (ACME 2016)

***Robert Davies[1] and Anthony Jefferson[1]**

[1]School of Engineering, Cardiff University, Queens Buildings, Cardiff, CF24 3AA

*DaviesRE11@Cardiff.ac.uk

ABSTRACT

Self-healing cementitious materials could greatly improve the durability properties of concrete structures relative to those constructed with conventional cementitious composites. However, there is a need to understand better the healing processes, to predict accurately experimental behaviour and to determine the impact on mechanical properties. Micromechanical modelling, with a two-phase Eshelby inclusion solution, is chosen as a suitable framework within which to explore such a response in cementitious materials. A constitutive material model is described, consideration is given to a self-healing model framework and how the mechanical strength recovery of a micro-cracked material can be simulated with a simplified volumetric micromechanical model.

Keywords: *micromechanics; micro-cracking; healing; cementitious*

1. Introduction

Micromechanics is a technique are used to describe engineering material properties based on basic continuum mechanic concepts; conservation of mass and balance of momentum and energy. Micromechanical models allow the individual material properties, damage and inelastic response to be modelled at the same length scale whilst also linking to the macroscale. This paper simulates a two-phase composite material which has a matrix phase and inclusions. The particular focus is on building a framework for simulating healing in a cracked material.

In recent years much research has been undertaken on the subject of self-healing in cementitious materials [1], [2]. A number of models have been developed for simulating self-healing behaviour [3]–[6]. The majority of the mechanical healing models developed to date are phenomenological in nature and have been applied in finite element codes using the smeared crack concept. However, the present authors favour more mechanistic approach. In cementitious materials, the development of material properties and recovery can be linked to the hydration process, particularly for early age crack healing. Hydration processes and damage have been considered in a coupled model [7] where the evolution of healing was linked to both the degree of hydration and to the value of the damage parameter at time of healing.

A micro-scale model naturally captures the early stages of micro-cracking and the extent of damage in the fracture process zone around a macro-crack by considering the behaviour of the composite components. A model which can represent micro-cracks is ideally suited for including self-healing behaviour by healing these explicit cracks.

2. Essential components of the micro-mechanical model

A cementitious material with aggregate particles and cement paste is represented using a two phase composite with inclusions (Ω) and a matrix (M) phase. A detailed description of the basic micromechanical model can be found in [8], [9]and [10]. The essential components of the micro-mechanical model are shown in the following constitutive equation and are taken forward to establish a framework for instructing healing:

$$\bar{\boldsymbol{\sigma}} = \mathbf{D}_{M\Omega} : (\bar{\boldsymbol{\varepsilon}} - \boldsymbol{\varepsilon}_{\mathbf{a}}) \tag{1}$$

$\bar{\boldsymbol{\sigma}}$ is the average stress and $\bar{\boldsymbol{\varepsilon}}$ is the total strain in the composite. $\mathbf{D}_{M\Omega}$ is the composite elastic tensor whose properties are computed using the classical Eshelby [11] solution and the Mori-Tanaka homogenization scheme for non-dilute inclusions [12]. $\boldsymbol{\varepsilon}_{\mathbf{a}}$ is the total additional strain resulting from anisotropic micro-cracking using the approach of Budiansky and O'Connell [13]. A local stress-strain relationship for the micromechanical model is defined in equation (2), in which the added strain is taken to be the equivalent of a micro-cracked band in the material.

$$\mathbf{s}_L = (1-\omega)\mathbf{D}_L\boldsymbol{\varepsilon}_L \tag{2}$$

$\mathbf{s}_L$ is the equivalent local stress tensor and $\boldsymbol{\varepsilon}_L$ is the equivalent local strain tensor, both of which are expressed in a reduced vector form that considers only those components that are non-zero. $\mathbf{D}_L$ is a 3x3 matrix containing the non-zero components the local stiffness tensor. The local compliance tensor is defined as $\mathbf{C}_L = \mathbf{D}_L^{-1}$. ω is the micro-crack variable for each direction, taking the values between 0 for uncracked and 1 for the fully micro-cracked state. The elastic local strain can be subtracted from the local strain within the micro-crack band $(\boldsymbol{\varepsilon}_{\mathbf{L}})$ to give the additional strain resulting from the crack in one direction.

3. Self-healing model framework

The local constitutive relationship presents itself as a convenient form for including healing. The healing restores the stiffness of a proportion of the damaged component of material. An offset or 'solidification' strain is included to ensure that the healing material solidifies in a stress free state. The healed local stress is given in equation (3).

$$\mathbf{s}_{Lh} = (1-\omega)\mathbf{D}_L\boldsymbol{\varepsilon}_{Lh} + (1-\omega_h)h\omega_{th}\mathbf{D}_{Lh}(\boldsymbol{\varepsilon}_{Lh} - \boldsymbol{\varepsilon}_s) \tag{3}$$

The healing proportion is defined by the parameter *h*, which takes the values between 0 for no healing and 1 for fully healed. A subscript *h* is added to the terms to show the healing equivalent terms. $\mathbf{s}_{Lh}$ is the equivalent local stress tensor after healing, $\boldsymbol{\varepsilon}_{Lh}$ is the local equivalent strain tensor after healing and ω_{th} is the micro-cracking parameter at the time of healing. $\mathbf{D}_{Lh}$ is the local stiffness of the healed material and $\boldsymbol{\varepsilon}_s$ is the 'solidification' strain. Since this newly healed material can also undergo micro-cracking, a term is also included to simulate this further micro-cracking, where ω_h is the healed micro-cracking variable.

4. Self-healing model volumetric example

A volumetric isotropic model is used here to give an insight into how the model responds to a strain path. The single phase volumetric constitutive relationship is shown in equation (4), which has the same basic form as that given in equation (3).

$$\sigma = (1-\omega)K_M\varepsilon + (1-\omega_h)h\omega_{th}K_{Mh}(\varepsilon - \varepsilon_s) \tag{4}$$

K_M and K_{Mh} are the bulk modulus of the material before and after healing. All other terms remain as previously defined. The material properties used are shown in Table 1. The original and healed micro-crack initiation and evolution criteria are based on the form adopted by Mihai & Jefferson [8] and are

based on; ε_{tv} which is the volumetric strain at first uniaxial micro-cracking and ε_{0v} which is the volumetric uniaxial local strain in the effectively fully micro-cracked state. This model is subjected to a volumetric strain increment where both micro-cracking parameters are calculated directly.

Table 1: Material properties for volumetric model response

K_M (N/mm^2)	K_{Mh} (N/mm^2)	ε_{tv}	ε_{tvh}	ε_{0v}	ε_{0v}	h
11429	5714	4.17×10^{-5}	8.33×10^{-5}	6.67×10^{-3}	6.67×10^{-5}	0.5

The volumetric strain is incremented until the original material reaches a point on the load-displacement (stress-strain) softening curve equal to half the peak stress, after which the strain is returned to zero. This strain response is shown in Figure 1. The healing here is assumed to take place when the sample is unloaded which occurs when there is zero stress and zero strain. For the time strain plot shown in Figure 1, this unloading point occurs at a pseudo-time t = 1000(s). At this point the ε_s is zero and the ω_{th} is fixed. The new material incorporating the healing is then subjected to further strain increments up to and beyond the initial peak strain, until the strain is four times the original unloading strain. Figure 2 shows the stress strain response of the volumetric healed model. The first loading phase, up to t = 1000(s), can be seen where the stress returns along a linear line to zero. The second loading phase shows a bi-linear line returning to the softening curve (in stress-time space) of the healed material. This increase in stress directly relates to the healed material. The first steep gradient is due to the elastic response of the healed material and the second flatter gradient is the sum of stresses in both materials. The peak stress after healing is reached at the same strain at which the model was first unloaded, this being t = 1500(s).

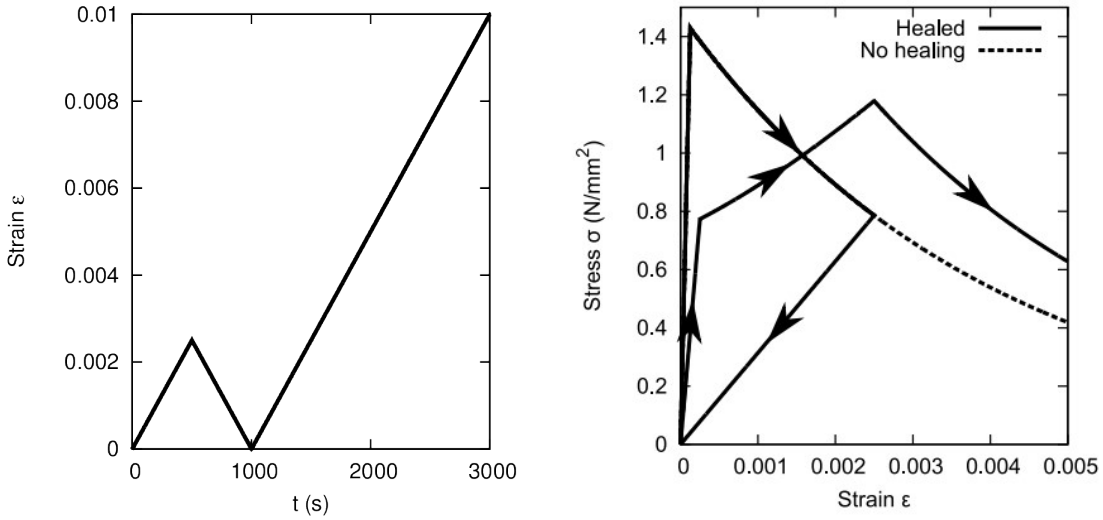

Figure 1: a) Volumetric strain driver b) Typical volumetric stress strain healing response

5. Conclusions

A two phase composite micro-mechanical constitutive model, that includes anisotropic micro-cracking, provides an excellent basis for the development of a model for cementitious materials that includes self-healing behaviour. The relative simplicity of this micromechanical healing model combined with the fact that it requires a small number of physically meaningful parameters shows that it is suitable for simulating a wide range of two-phase cementitious materials. The volumetric example shown is useful to illustrate the mechanisms that occur during the micro-cracking and healing processes.

Acknowledgements

Thank you must go to EPSRC for their funding of the Materials for Life (M4L) project (EP/K026631/1) which has allowed the continuation of the modelling work in the area of self-healing.

References

[1] M. R. de Rooij, K. Van Tittelboom, N. De Belie, and E. Schlangen, Self-Healing Phenomena in Cement-Based Materials: State-of-the-Art Report of RILEM Technical Committee 221-SHC: Self-Healing Phenomena in Cement-Based Materials. Bagneux, France: Springer, 2013.

[2] K. Van Tittelboom and N. De Belie, 'Self-Healing in Cementitious Materials—A Review', Materials, vol. 6, no. 6, pp. 2182–2217, May 2013.

[3] E. Schlangen, N. Ter Heide, and K. Van Breugel, 'Crack healing of early age cracks in concrete', in ECF16, Alexandroupolis, Greece, 2006.

[4] G. Ye and K. van Breugel, 'Potential use of HYMOSTRUC cement hydration model for self-healing of microcracks in cementitious materials', in Proceedings of the First International Conference on Self Healing Materials, Noordwijk aan Zee, The Netherlands, 2007.

[5] J. J. Remmers and R. de Borst, 'Numerical Modelling of Self Healing Mechanisms', in Self Healing Materials, Springer, 2008, pp. 365–380.

[6] M. K. Darabi, R. K. Abu Al-Rub, and D. N. Little, 'A continuum damage mechanics framework for modeling micro-damage healing', Int. J. Solids Struct., vol. 49, no. 3–4, pp. 492–513, Feb. 2012.

[7] S. Granger, G. Pijaudier-Cabot, and A. Loukili, 'Mechanical behavior of self-healed Ultra High Performance Concrete: from experimental evidence to modeling', Proc Fram., vol. 6, 2007.

[8] I. C. Mihai and A. D. Jefferson, 'A material model for cementitious composite materials with an exterior point Eshelby microcrack initiation criterion', Int. J. Solids Struct., vol. 48, no. 24, pp. 3312–3325, Dec. 2011.

[9] I. C. Mihai and A. D. Jefferson, 'Smoothed contact in a micromechanical model for cement bound materials', Comput. Struct., vol. 118, pp. 115–125, Mar. 2013.

[10] R. Davies and A. Jefferson, 'The simulation of inelastic matrix strains in cementitious materials using micromechanical solutions', Eng. Fract. Mech., 2014.

[11] J. D. Eshelby, 'The determination of the elastic field of an ellipsoidal inclusion, and related problems', Proc. R. Soc. Lond. Ser. Math. Phys. Sci., vol. 241, no. 1226, pp. 376–396, 1957.

[12] T. Mori and K. Tanaka, 'Average stress in matrix and average elastic energy of materials with misfitting inclusions', Acta Metall., vol. 21, no. 5, pp. 571–574, 1973.

[13] B. Budiansky and R. O'Connell, 'Elastic-moduli of a cracked solid', Int. J. Solids Struct., vol. 12, no. 2, pp. 81–97, 1976.

Biomechanics II

Proceedings of the 24th UK Conference of the
Association for Computational Mechanics in Engineering
31 March - 01 April 2016, Cardiff University, Cardiff

A MONOLITHIC APPROACH TO CELL CONTRACTILITY

***Pradeep Keshavanarayana[1], René de Borst[2] and Martin Ruess[1]**

[1]School of Engineering, University of Glasgow, Glasgow G12 8LT, UK
[2]Faculty of Engineering, University of Sheffield, Sheffield A1 3JD, UK

*p.keshavanarayana.1@research.gla.ac.uk

ABSTRACT

Contraction of cells leads to stress fibre formation in the cytoplasm. They extend along the length of the cell, terminating at focal adhesions. Modelling the growth of stress fibres coupled with focal adhesions, assumed to be made up of high and low affinity integrins, results in a bio-chemo-mechanical problem. Solving the coupled system of equations in a staggered manner restricts the time step used. In this contribution, we present a monolithic approach which relaxes this restriction. The stress fibre is assumed to obey the Hill type growth, where the stress depends on the strain rate, even in non-muscle cells, which we approximate through a non-linear model. We have also implemented the feedback within the system, which is a fundamental nature of all living organisms.

Key Words: *Focal Adhesion, Staggered, Monolithic, Non-linear Hill Model, Feedback*

1. Introduction

Cells are the fundamental units of all cellular organisms. Response of cells to external stimuli is a topic which has been dealt thoroughly, yet not understood completely. The role of mechanics in cellular behaviour has been established almost half a century ago [8]. The advancements in experimental techniques have been successful in quantifying such a role [6]. Bolstering the experimental progress with numerical modelling is the recent trend in various disciplines, including bio-mechanics. With studies emphasising the understanding of the functioning of cells in a mechanical perspective, numerical models are being developed. Such models involve a coupled system of equations, to be solved with boundary conditions matching the experimental observations. The solution schemes used to solve the governing equations play a prominent role in the overall analysis. In this contribution, we consider the continuum model [13] as a base and solve the system of equations with different numerical schemes.

2. Cell motility, contractility and focal adhesion

Cell motility is mainly responsible for processes such as wound healing and growth. Assuming cells to crawl and not swim [12], the process involves continuous reorganisation of the cellular shape and internal skeletal structure [9]. The cellular integrity is maintained by a special structure called the cytoskeleton. Apart from its scaffolding and cell shaping properties, it acts as a dynamic structure which resists, generates and transmits cellular forces. The forces in the cytoskeleton results in contractility of the cell. This in turn decides the connectivity of the cell membrane to the extracellular matrix (ECM), at focal adhesions (FA) [4]. The tension dependent assembly of actin and myosin, forming stress fibres, extend along the length of the cell. The formation of stress fibres involves a series of biochemical activities [11], for which the concentration of calcium ions in the cytoplasm is of utmost importance [10]. At FA, the forces are transferred from and to the cell, resulting in a continuous reorientation of the cytoskeleton. The proteins present at FAs, called integrins, are responsible for sensing the properties of the ECM. Thus, the formation of FAs along with stress fibre growth decides the direction and magnitude of the movement of cells.

3. A bio-chemo-mechanical model

In the recent past, there have been many mathematical models developed to explain the experimental observations of cell contractility. Each of these models could simulate a few set of experiments. Some of the models were developed by assuming the cell as a continuum, while some other modelled it in a discrete sense. Tensegrity models of cells [5], chemo-mechanical models with and without focal adhesions [13] [1] [7] or the modelling of focal adhesions alone [2] are some of the important types of models considered in the past. In this contribution, the mathematical model developed in [13] is considered and the resulting system of equations and its solution scheme is studied.

Noting the importance of calcium in the formation of stress fibres, an ad-hoc signal representing the concentration of calcium activates the system. The stress fibres ending on the cell membrane result in the formation of focal adhesions satisfying the mechanical equilibrium. Focal adhesions are assumed to be made up of high affinity integrins ξ_H and low affinity integrins ξ_L, where only the high affinity integrins form bonds with the ECM, while the low affinity integrins are allowed to diffuse. The integrins are governed by thermodynamic equilibrium, and hence they are interconvertible. The active stress is assumed to follow Hill type growth and passive stress follows from the elastic contribution. In [13] the active stress σ is estimated using a linear piecewise continuous equation:

$$\frac{\sigma}{\sigma_0} = \begin{cases} 0 & \frac{\dot{\varepsilon}}{\dot{\varepsilon}_0} < -\frac{\eta}{\bar{k}_v} \\ 1 + \frac{\bar{k}_v}{\eta}\left(\frac{\dot{\varepsilon}}{\dot{\varepsilon}_0}\right) & -\frac{\eta}{\bar{k}_v} \leq \frac{\dot{\varepsilon}}{\dot{\varepsilon}_0} \leq 0 \\ 1 & \frac{\dot{\varepsilon}}{\dot{\varepsilon}_0} > 0 \end{cases} \tag{1}$$

where, $\dot{\varepsilon}$ is the strain rate, η is the stress fibre concentration, σ_0 is the isometric tension in the stress fibres and $\bar{k}_v$ is a parameter representing the fractional reduction in stress when the strain rate is increased by $\dot{\varepsilon}_0$. Thus, the bio-chemical behaviour is converted to a mathematical problem, where, the mechanical equilibrium and the diffusion equations are solved in a coupled setting. In [13], a staggered solution scheme is used for the solution of the system of equations. It was found that the staggered scheme restricts the time step that can be used. Hence, a monolithic solution approach has been developed which is discussed in the next section.

4. Monolithic solution approach

In the staggered approach, the mechanical equilibrium equation is solved assuming the concentration of high affinity integrins to be constant. Then, the diffusion equation is solved to update the integrin concentration. In the monolithic approach, the equations are coupled to form a larger stiffness matrix. The advantages of the monolithic approach are that the solution involves only one matrix decomposition and the time step being used can be increased without affecting the result.

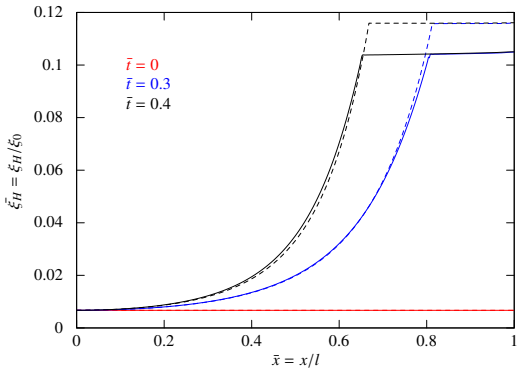

Figure 1: $\Delta_t = 1.0s$

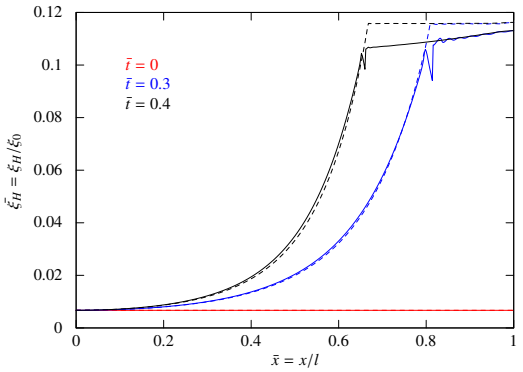

Figure 2: $\Delta_t = 6.0s$

Analysis results according to the monolithic and the staggered solution approach for different time steps Δ_t (— staggered, - - - monolithic).

It can be seen from Fig. 1 and Fig. 2 that, as the time step is increased, the solution of the monolithic approach remains more stable compared to the solution from staggered approach. The values of the reference integrin concentration ξ_0, length of the cell l and other parameters used are taken from [13].

5. Hill model

The Hill model used in [13] provides piecewise continuity, Eq. (1). The computational experiments revealed numerical instabilities when the strain rate conditions changed its regime. Hence in this contribution, we changed to the following non-linear Hill model for the active stress growth :

$$\frac{\sigma}{\sigma_0} = 1 + \frac{\bar{k}_v}{\eta}\left(\frac{\dot{\varepsilon}}{\sqrt{\dot{\varepsilon}^2 + \dot{\varepsilon}_0^2}}\right) \tag{2}$$

which has proven full stability throughout the computations performed. In [13], it has been assumed that the low affinity integrins diffuse along the cell membrane, while high affinity integrins are fixed. In our computations, we found that the growth of focal adhesions shows a similar response even when the diffusion is neglected. In addition, in order to enforce the condition of thermodynamic equilibrium by the interconversion of these integrins and keeping in view the bio-chemical simplifications made in the model, the diffusion of low affinity integrins becomes obsolete. Hence, we have neglected the diffusion of low affinity integrins in further calculations.

6. Feedback cycle

When an external signal acts upon the cell, a series of biochemical reactions results in the release of calcium to the cytoplasm which forms stress fibres. The stress fibres further result in the growth of FAs. The growth of FAs is also a type of stimulus which releases calcium again. Hence, the process becomes cyclic, due to which, there is a need for a feedback loop within the system of equations. This problem of providing feedback has been solved in [3], where the calcium growth is put in a feedback loop. We use this feedback mechanism in combination with the non-linear Hill model to solve the 1-D cell problem as provided in [3].

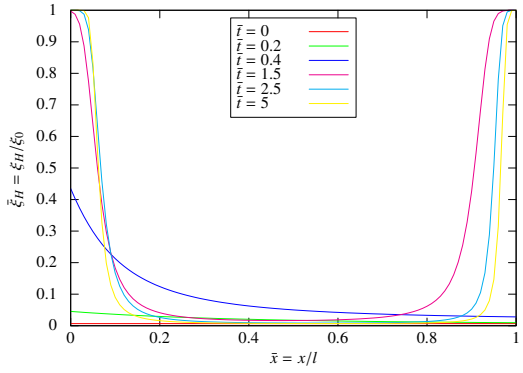

Figure 3: Without feedback

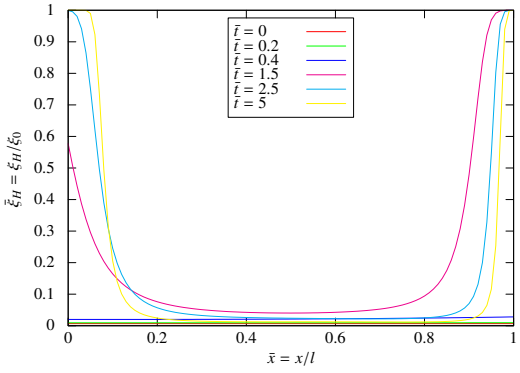

Figure 4: With feedback

A 1-D cell is placed on a substrate and a prescribed displacement is applied to the right end of the cell. Sensing the external stimulus, the focal adhesions start forming near the right end. It can be seen from Fig. 3 that the high affinity integrins are formed on the left end prior to the right end, which do not match the physical observations. In contrast, the results including the feedback mechanism match very well with the experiments, Fig 4. Hence, a feedback mechanism becomes essential for a reliable analysis result.

7. Summary and future work

Most of the models that have been developed to explain the cellular processes are phenomenological models. The solution schemes used to solve the governing system of equations plays a very important role in obtaining the right solution. In this contribution, we have demonstrated that the monolithic solution scheme provides a stable result irrespective of the time step chosen. A continuous non-linear Hill type model has been used for the active stress growth. A Feedback mechanism within the cell was implemented and compared with the system without feedback. In future, the model has to be extended to 2D and different solution schemes are to be compared. Motivated from [11], spiking in calcium signals has to be considered and the effect on the formation of stress fibres will be studied. The current model has to be further developed in order to make it suitable to explain cell motility.

References

[1] A. Besser and U.S.Schwarz. Coupling biochemistry and mechanics in cell adhesion: a model for inhomogeneous stress fiber contraction. *New Journal of Physics*, pp.425, 2007.

[2] A. Besser and Samuel A Safran. Force-Induced Adsorption and Anisotropic Growth of Focal Adhesions. *Biophysical Journal*, 90, 3469-3484, 2006.

[3] A. Pathak, R. M. McMeeking, A. G. Evans and V. S. Deshpande. An Analysis of the Cooperative Mechano-Sensitive Feedback Between Intracellular Signaling, Focal Adhesion Development, and Stress Fiber Contractility. *Journal of Applied Mechanics*, 78, 2011.

[4] B. Geiger, A. Bershadsky, R. Pankov and K. M. Yamada. Transmembrane crosstalk between the extracellular matrixcytoskeleton crosstalk. *Nature Reviews. Molecular Cell Biology*, 2, 793-805, 2001.

[5] D. E. Ingber. Tensegrity I. Cell structure and hierarchical systems biology. *Journal of Cell Science*, 116, 1157-1173, 2003.

[6] G. Bao and S Suresh. Cell and molecular mechanics of biological materials. *Nature materials*, 2, 715-725, 2003.

[7] I. L. Novak, B. M. Slepchenko, A. Mogilner and L. M Loew. Cooperativity between Cell Contractility and Adhesion. *Physical Review Letters*, 93, 2004.

[8] Paul Weiss and Beatrice Garber. Shape and Movement of Mesenchyme Cells as Functions of the Physical Structure of the Medium. *Proceedings of the National Academy of Sciences of the United States of America*, 38, 264–280, 1952.

[9] R. Ananthakrishnan and A. Ehrlicher. The forces behind cell movement. *International journal of biological sciences*, 3, 303-317, 2007

[10] S. Pellegrin and H. Mellor.Actin stress fibres. *Journal of Cell Science*, 120, 3491-3499, 2007.

[11] T. Meyer and L. Stryer. Molecular model for receptor-stimulated calcium spiking. *Proceedings of the National Academy of Sciences*, 85, 5051-5055, 1988.

[12] T. Risler. Cytoskeleton and Cell Motility. *in Encyclopedia of Complexity and System Science*, pp.1738-1774, 2011.

[13] V. Deshpande, M. Mrksich, R. Mcmeeking and A. Evans. A bio-mechanical model for coupling cell contractility with focal adhesion formation. *Journal of the Mechanics and Physics of Solids*, 56, 1484–1510, 2008.

Proceedings of the 24th UK Conference of the
Association for Computational Mechanics in Engineering
31 March – 01 April 2016, Cardiff University, Cardiff

Preliminary Numerical Simulations to Investigate the kinematics of Infant Head Impact.

*** Ghaidaa A Khalid [1], R. Prabhu [2], Allan Mason-Jones[1], Peter S Theobald[1], Shwe P Soe[1], Michael D Jones[1].**

[1]School of Engineering, Cardiff University, Cardiff, UK

[2] Centre for Advanced Vehicle Systems, Mississippi State University, Mississippi, USA

*****KhaidGA@cardiff.ac.uk

ABSTRACT

Presented is the development of a simulation that allows for preliminary investigation of impact to a 10 day old infant head. A computer-aided drafting (CAD) model is reconstructed from high resolution computerised tomography (CT) scan images and meshed for finite element analysis (FEA); soft tissue responses were defined using recently derived material properties. It is anticipated that the FE model will be used to investigate the paediatric head response during impact conditions, to provide a better understanding/prediction of injury biomechanics.

Keywords: *Finite element analysis; 3D rendering; image extraction; impact simulation; injury prediction*

1. Introduction

Traumatic brain injury (TBI) is the leading cause of death and disability among the paediatric population [5]. Most TBI is a result of either a fall, or motor vehicle interaction [4]. Injury biomechanics research plays a vital role in providing guide lines that can inform design engineers and reduce head injuries by developing preventions strategies. Additionally, an understanding of the head impact response and injury mechanisms can help clinicians distinguish between accidental and inflicted TBI. Computational models of the head, associated with injury biomechanics, represent a powerful tool that can be used to achieve all these goals.
Many researchers have focused on the biomechanics of adult head injury, using finite element models (FEMs). In paediatric impact biomechanics, however, FE paediatric head models are few due to several limitations the limited availability of material property data, quantitative age-dependent anatomical data, and paediatric impact response data.

2. Methodology

2.1 Geometrical Acquisition and Meshing Generation

Axial head CT scans of a 10 days old infant were selected and construct cranial geometry using Mimics Software (Materialise; Leuven, Belgium). Mimics softweare uses gray scale image values from CT scans to segment the model into regions by defining a threshold value. All pixels within the upper and lower threshold of grayscale were defined into the region of interest, and regarded as the cross - section of three dimensional (3D) geometry. Certain tissues have a distinguished threshold, such as the cranial bones (parietal, occipital, and frontal bones) and skull base that has a particularly intricate geometry, including the multiple foramina, processes, internal cavities and branching structures, which were segmented using the threshold filter. The cervical vertebrae and mandible were removed. Other tissues displayed similar gray value intervals making their segmentation, based on threshold values, difficult. In this case an interactive segmentation method was applied to isolate single tissues from surrounding tissues, such as the brain. Fontanelle and sutures, which consist of fibrous connective tissues, filled the gap between skull plates. Possessing gray scale values very close to the cranial bones made segmentation, using the segmentation tools, problematic. They were created and developed by using wrapped, Boolean operations and manual editing tools. A detailed 3D

representation of major tissues within the head was developed, including cranial bones, skull base, sutures, fontanelle and brain as shown in Figure 1. Subsequently, the autoremesh function was applied by the Mimics Remesher (3-matic v10) with different quality parameters and element mesh size, to optimise the mesh quality and reduce the number of elements, to achieve more accurate results with a reduced computational time.

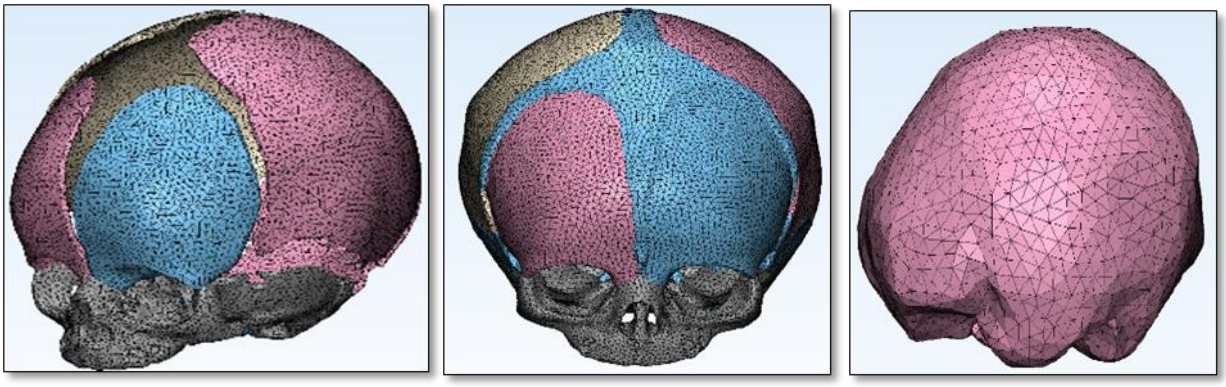

Figure1: Finite element (FE) mesh of the cranial bone, and sutures of a 10 day old infant through an (a) front oblique view, (b) front boss view, and (c) front oblique view of 10 day old infant brain.

2.2 Material Properties

Previous attempts at producing validated infant head models have represented the material properties of the cranial bone as homogeneous and isotropic [6 &8]. At birth, however, paediatric cranial bone has a visible fibre orientation due to the bone trabecula, supported by the orthotropic response in foetal cranial bone reported by McPherson & Kriewall [7]. High-rate testing of infant bone conducted by Coats & Margulies [1] also revealed that infant bone is inhomogeneous, with the parietal and occipital bone having different stiffness properties. These differences in the elastic modulus between the parallel and perpendicular specimens confirm the significant anisotropic material proprieties in the immature cranial bone. Thus, infant cranial bones were modelled as orthotropic- elastic, with different elastic moduli parallel and perpendicular to fiber orientation. The suture was modelled as elastic - isotropic, whilst a gelatin substance was used for the brain [3].

2.3 FE Simulation

The environment in the FE solver (Abaqus/ Explicit^{TM} 6.12) was established, following development of the FE model. A frictional contact coefficient of 0.2 was used to model the interaction between the FE head and a rigid plate [2]. A tie constraint was applied, for the interaction between the skull-sutures, and skull-brain. General contact sliding was used to model the interaction between the head model and rigid plate. The model was rotated and translated (Figure 2), so its position corresponded with the rigid surface for a specific impact location on the head. The model was dropped from 30cm onto the occipital region with an impact velocity of 2.4 m/s, as shown in Figure 2, to provide a comparison with Coats & Margulies [2], who investigated an impulse force-time response for a 1.5 month old infant head model. It is anticipated that the FE model will be validated with additional experimental response data, to provide an effective tool for quantifying nature and magnitude of skull and brain deformation and subsequent prediction of the risk of injury during a traumatic event.

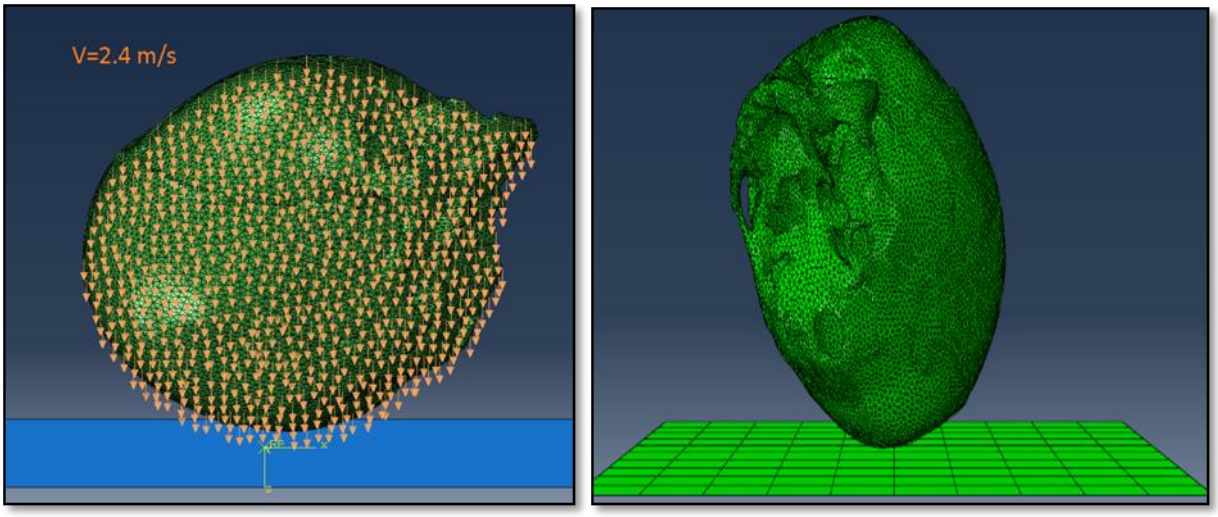

Figure 2: Illustration of (a) the boundary value problem of an occipital impact to a 10 day old infant head (with skull, sutures, and brain), and (b) Finite element (FE) simulation of the same.

3. Results and Discussion

Impact to the occipital region was simulated for a fall of 30 cm height, resulting in a velocity equal to 2.4 m/s (Figure 2). The results, presented in Figure 3, represent the energy dissipation of the model during a 20 ms FE simulation. The total energy is relatively constant throughout the simulation. Energy output can be used to evaluate whether an Abaqus/Explicit simulation is predicting an appropriate response. Evaluating the energy curve, at the beginning of the simulation the components of the head are in free fall, meaning relatively high kinetic energy (ALLKE). The initial impact deforms the head, reducing the kinetic energy; thereafter, the continuing head deformation causes transfer of kinetic energy to internal energy (ALLIE) within the head i.e. the internal energy increases as the kinetic energy decreases. Another important energy output variable is the total artificial energy (ALLAE), which is a substantial fraction of the internal energy. Artificial strain energy should not be a substantial percentage of the overall internal energy of the system. In this case, it is a very small percentage of the overall internal energy and thus, the model is considered to be valid, at least from the perspective of element behaviour and possibility of error due to meshing. The peak impact force from our model (a 10-day old child), is similar to the impact force reported by Coats & Margulies (1.5 month old child), as described in Figure 4 [2]. Both of these models show very similar material responses, though there is a difference in impulse force response that is perhaps related to subtle variations in anatomy, age and non linear geometrical differences. The mass of 1.5 month old model was 0.87 kg, while the head model of 10 day old equated to 0.46 kg; thus, higher impact forces and shorter durations appeared in the impulse force – time responses, which was 3.54 Ns for 1.5 month old child and 1.82 Ns from our simulation.

4. Conclusions

High resolution CT scan images were used to construct a finite element model of a 10 day old infant head, consisting of accurate geometries for the skull, sutures, fontaneelles and brain. Obtaining the sutures from CT images was shown to be possible by using thresholding and manual editing. The HU range for the sutures is relatively large and further studies need to be conducted to obtain a more precise and accurate HU range. Preliminary results are presented to show how the paedatric head tissue boundaries were segmented to build a detailed, accurate anatomical model. We have successfully meshed our existing model and, in combination with low strain rate material response data, provide relatively accurate results versus reduced computational time.

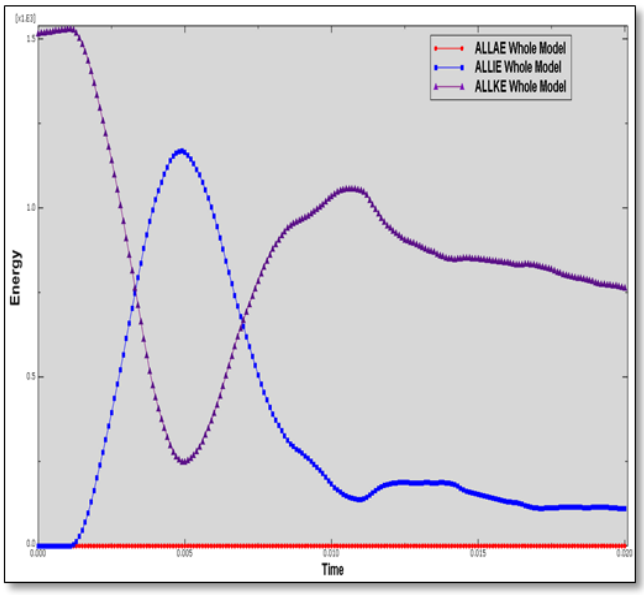

Figure 3: Energy - time curves for an occipital impact from a 30cm height drop.

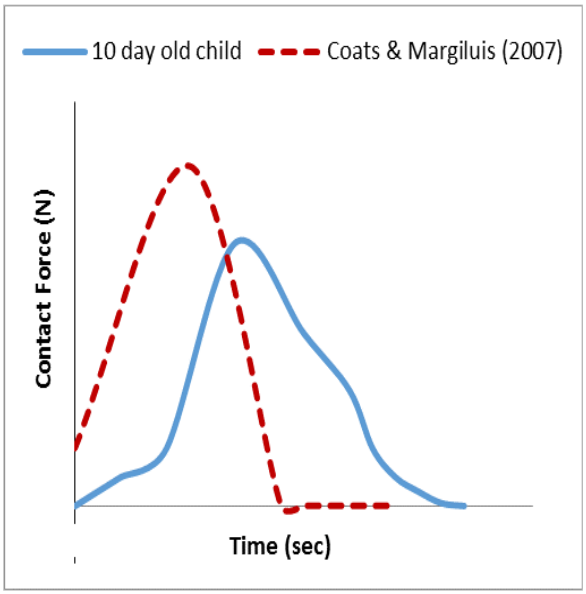

Figure 4: Force-time contact curve for the occipital area from a 30 cm height drop.

References

[1] Coats, B. & Margulies, S.S. (2006) Material properties of human infant skull and suture at high rates. *Journal of Neurotrauma*, 23(8), 1222–1232.

[2] Coats, B. Margulies, SS. Ji, S. (2007) Parametric study of head impact in the Infant, *Proceedings of Stapp Car Crash Journal* 51, 1–15.

[3] Cheng, J., Howard, I.C. & Rennison, M. (2010) Study of an infant brain subjected to periodic motion via a custom experimental apparatus design and finite element modelling. *Journal of Biomechanics*, 43(15), 2887–2896.

[4] Greenes D. S. and Schutzman S. A. (1999) Clinical indicators of intracranial injury in head-injured infants *Pediatrics*, 104, 861-7

[5] Langlois J, Rutland –Brown W et al (2004) Traumatic Brain Injury in the United States: Emergency department visits, hospitalizations, and deaths. CDC, NCIPC. Atlanta, GA.

[6] Li, Z., Luo, X. & Zhang, J., (2013). Development/global validation of a 6-month-old pediatric head finite element model and application in investigation of drop-induced infant head injury. *Computer Methods and Programs in Biomedicine*, 112(3), 309–319.

[7] McPherson, G.K. & Kriewall, T.J., 1980. Fetal head molding: an investigation utilizing a finite element model of the fetal parietal bone. *Journal of biomechanics*, 13(1), 17–26.

[8] Roth, S., Raul, J.-S. & Willinger, R., (2010). Finite element modelling of paediatric head impact: global validation against experimental data. *Computer methods and programs in biomedicine*, 99(1), 25–33.

Proceedings of the 24th UK Conference of the
Association for Computational Mechanics in Engineering
31 March – 01 April 2016, Cardiff University, Cardiff

Finite Element Analysis on Knee joint for Knee OA Patients

*** K. Thienkarochanakul, D. Hiscocks and A.A. Javadi**

Department of Engineering, University of Exeter, Harrison Building, North Park Road, Exeter, EX4 4QF
kt301@exeter.ac.uk,

ABSTRACT

Understanding the mechanical behaviour of the knee joint is essential in the design of treatment for patients with knee OA or people with knee injuries. Previous research has often overlooked the stresses and strains in the cartilage soft tissue that causes pain, while walking or bending legs, as a result of the rubbing between the upper leg bone (Femur) and the lower leg bone (Tibia). Simulating a human knee joint using the Finite Element Method can show not only how much stress the knee joint cartilage takes due to human bodyweight, but the distribution of stress throughout the cartilage as well. This paper presents a 3D FE model of a knee joint, created from geometry obtained from a human CT scan. The effect of OA has been modelled by halving the Young's Modulus of OA cartilage, whilst maintaining the same boundary conditions. A comparison of OA knee & healthy knee has been completed, and results show that the stress in the cartilage increases by 1Mpa as a result of OA. Good agreement was found in both results, and the location thereof, between presented and other published work.

Keywords: *knee osteoarthritis (knee OA); cartilage; orthosis; FEA*

1. Introduction

Knee anatomy and functions

Human walking is the result of a complex process involving the brain, spinal cord, peripheral nerves, muscles, bones and joints [9]. Human walking requires the coordination of multiple muscles and joints to simultaneously move the legs in a periodic pattern, support body weight and maintain dynamic stability. Coordination may be simplified by taking advantage of the passive dynamics of the legs which can perform all of these functions automatically [9].

Knee diseases –OA

Osteoarthritis (OA) is a disease which influences the body joints. The most common affected joints are in the hands, spine, knees and hips. Knee OA is a degenerative, painful disease that if left untreated it can have crippling effects on those affected. Unfortunately, nearly every aging person develops knee OA to some extent [5]. OA causes damage to the articular cartilage (protective surface of the knee bone) and mild swelling of the tissues in and around the joints. OA is one of the most common causes of disability in the world. It is regarded as a whole joint disease with a multifactorial aetiology, including increased mechanical stress, ligament derangements, cartilage degradation, subchondral bone changes and muscular impairments [10]. However, not all knee pains are associated with OA, there are other diseases e.g. patella tendonitis, chrondromalacia, Osgood-Schlatter disease or gout that can also cause pain to the knee, either acute or chronic [6]. In addition, obesity and lower limb misalignment have also been associated with increased risk for knee OA [8]. In OA patients, the cartilage (connective tissue) between the bones gradually degrades leading to painful rubbing of bone on bone in the joints. Sitting between the upper and lower leg bones at the knee joint are rubbery pads of tissue called menisci. These cushion the bones, acting as shock absorbers. The menisci can become worn as one gets older, and are commonly the reason for knee pain in middle-aged people. A meniscus can also be torn after suddenly twisting the knee joint, resulting in pain, swelling and occasionally the locking of the knee. The illness is caused by muscle weakness, ligaments, nerves, degenerative bone disease or cerebrovascular disease. Current treatments include medical procedures or surgical treatment including physiotherapy. The damage of these symptoms may cause tearing in the cartilage soft tissue due to the force of body weight, resulting in activities such as walking,

running or squatting causing great pain to the patient. In some cases, rehabilitation may be impossible and some older patients with OA, not fit for surgery, will continually suffer in pain.
A number of devices exist that assist walking and provide knee pain relief, ranging from staff to robotic devices. Several knee braces are currently available on the market that not only deal with OA but also with other diseases or injuries. Some braces may not be comfortable to wear or slim enough to put under dress. Furthermore, as the complexity of the devices increase, so too does their cost to the extent that some are unaffordable to some patients. The main focus of the research undertaken is towards the design of a new knee bracing system, which allows effective control of the transfer of forces through the knee joint. This can reduces the amount of force that is transferred through the joint and hence reduce the pain and improve mobility. The study of knee anatomy and the mechanical behaviour of knee is an important part of this research.

This paper presents the study of mechanical behaviour of knee joint, in order to better understand the function and behaviour of human knee joint and its load bearing mechanism. This will allow the distribution of stresses in the cartilage to be determined, and in turn, the effects of OA on the stress distribution throughout the cartalage to be assessed.

A finite element model of a knee joint is developed and analysed. The model of a genuine human knee joint is constructed from a CT scan, using a digital imaging suit, ScanIP software from Simpleware Ltd. Three masks are created to define the femur, cartilage and tibia shown as yellow, purple and blue respectively, in Figure 1a. The constructed model is then analysed using the finite element code ABAQUS 6.13-1.

Boundary conditions and material properties are both applied based on published information [1, 3]. By way of boundary conditions, both displacements and rotations at the bottom surface of the tibia are fixed in all directions. The displacement is fixed for the femur and tibia in Y direction, shown in Figure 1b. Different material properties are considered for bone and cartilage, however they are both assumed to be linear elastic. The Young's moduli of bone and cartilage are considered as E_{Bone} = 18.6 GPa, and $E_{Cartilage}$= 12 MPa with Poisson's ratios of v_{Bone} = 0.3 $v_{Cartilage}$= 0.46 respectively. The property of the OA cartilage was redefined with a reduction of 50% of $E_{Cartilage}$, $E_{OACartilage}$ = 6 MPA and Poisson's ratio $v_{OACartilage}$= 0.49, as used in [10]. The geometry of the model, loading and boundary conditions are shown in Figure 1b. Contact elements are used in the model to tie the cartilage to the femur and tibia. Quadrilateral (8-noded) elements and structured meshing are used in the discretisation of the domain. The system is subjected to a vertical load of 392 N, (pressure of 0.3 MPa), representing the weight of an average person going through a leg.

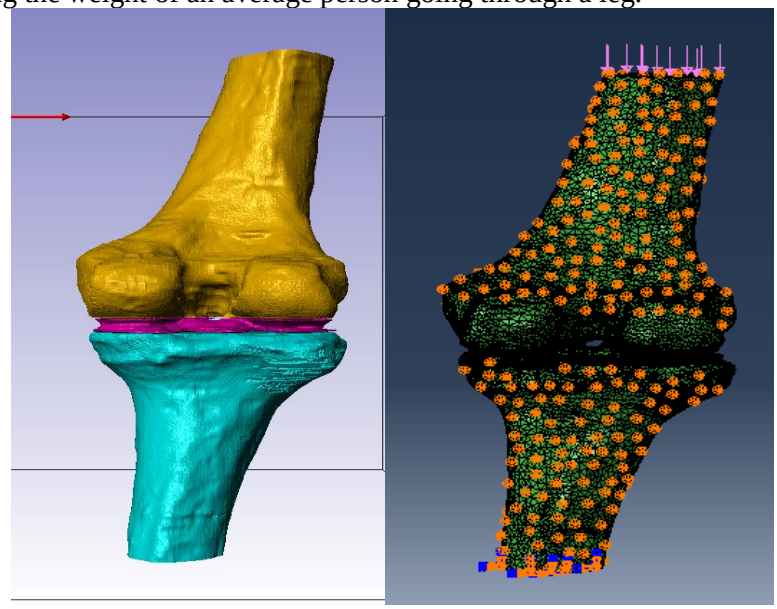

(a) **(b)**

Figure 1 (a) 3 Masks created with ScanIP, (b) Geometry, loading and boundary conditions

2. Result and Discussion

Figure 2 shows the geometry before and after loading, in the healthy knee model. The model is not perfectly aligned, instead it is skewed (shown in Figure 2a), and hence it is deflected by the loading.

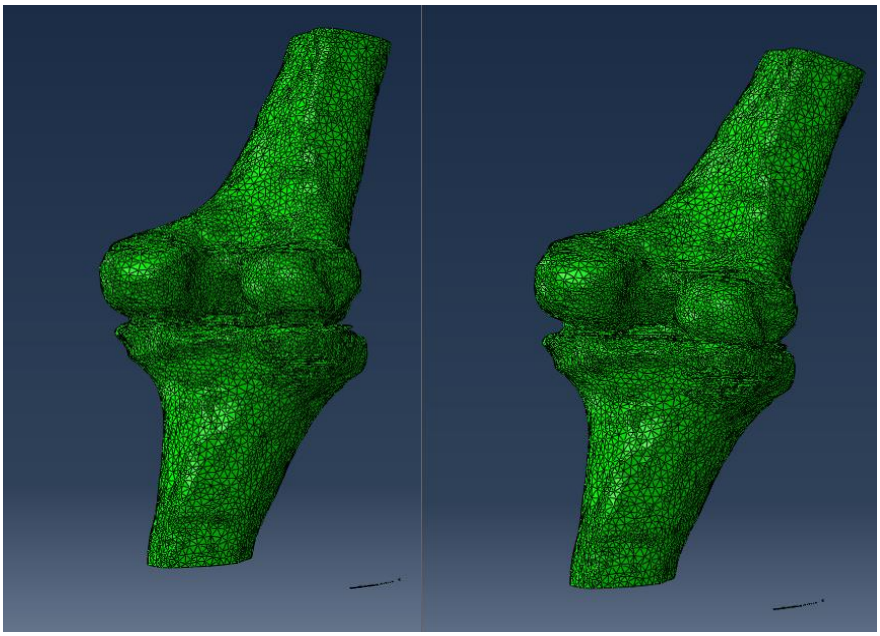

Figure 2 (a) unloaded geometry, (b) deformed geometry

The results of the healthy and OA knees are shown in Figures 3a and 3b respectively. A similar stress distribution is found in both cases; however a difference in the maximum stress of 1 MPa is recorded in the OA case. This is due to the weakened cartilage collapsing between the two bones.

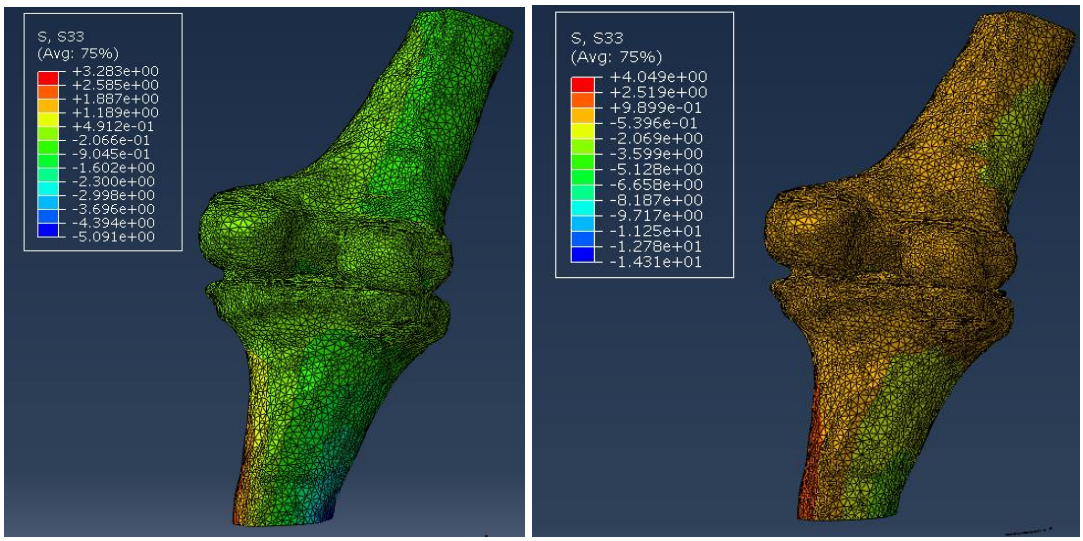

(a) **(b)**

Figure 3 (a) Deformed Healthy knee, (b) Deformed OA knee

Figure 4 shows the distributions of vertical stresses and deformations in the cartilage, for both healthy (4a) and OA knee joints (4b). In both cases, there is an area of high stress in the right hand section, as a result of the off – cantered model. This is a result of the femur and tibia colliding and compressing the cartilage located between the bones.

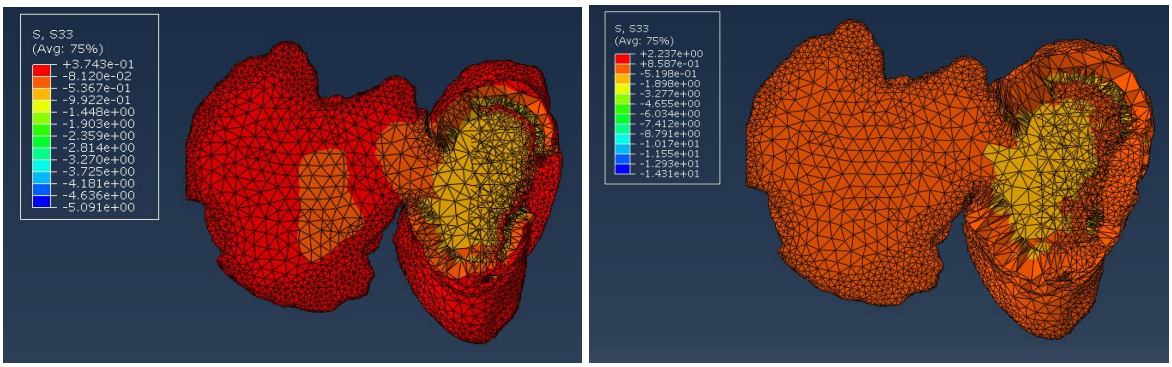

(a) **(b)**

Figure 4 (a) Deformed Healthy cartilage, (b) Deformed OA cartilage

Strong agreement is found between the increase in stress (due to the onset of OA), and the location of the maximum stress, between these results and those published in [10]. Discrepancies can be assigned to differing material properties, boundary conditions and geometry. Moreover, the location of the maximum stress, and the stress distribution found in the OA cartilage matched that of [10]. Further work will aim to refine the model, and in particular the boundary conditions. The use of a 'slip' boundary condition will be investigated, to better simulate the knee joint, and a dynamic model will be developed, in order to study the effect of the gait cycle on the knee joint.

References

[1] Bogatay, W., 2009. Finite Element Analysis of Knee Cartilage with an Osteochondral Graft.

[2] Brouwer RW, van Raaij TM, Verhaar JA and Bierma-Zeinstra, S.M.A., 2009. Brace treatment for osteoarthritis of the knee: a prospective randomized multi-centre trial. Osteoarthritis Cartilage 2006; 14(8):777-83.

[3] Cartana, M., Tarnita, D. and Tarnita, D., 2013. Modelling, Simulation and Optimization of a Human Knee Orthotic Device. Applied Mechanicas and Materials Vol. 371 (20143) pp549-553. Trans Tech Publication, Switzerland.

[4] Dean, JC and Kuo, AD., 2008. Elastic coupling of limb joints enables faster bipedal walking. Depts. Of Biomedical Engineering and Mechanical Engineering, University of Michigan

[5] Elliott, G.A., 2012 Design and Evaluation of a Quasi-Passive Robotic On the Effects of Parallel Elasticity Knee Brace: on Human Running

[6] Hutcheon, O. and Vhadra, R., 2013. Knee Pain Treatment. Patent application number: 20130012850

[7] Ibrahim, B.S.K., 2011. Modelling and Control of Paraplegic's Knee Joint (Fes-Swinging). Thesis

[8] Kirane, Y., Orth, D., Zifchock, R. and Hillstrom, H., 2010. Offloading strategies for knee osteoarthritis. Available at: https://lowerextremityreview.com/article/offloading-strategies-for-knee-osteoarthritis

[9] Lee,G. and Pollo, F.E. 2001. Peer review: Technology Overview: The Gait Analysis Laboratory. Journal of Clinical Engineering.

[10] Cartana, M., Tarnita, D. and Tarnita, D., 2013. Nonlinear Analysis of Osteoarthritis Process in Virtual Human Knee Joint. Conference Paper: November 2013

[11] Popa, D., Tarnita, D., Tarnita, D. and Lordachita, L., 2012. About the Simulation of the Human Knee Joint for Walking Locomotion.

[12] Van Raaij TM, Reijman M, Brouwer RW et al. Medial Knee Osteoarthritis Treated by Insoles or Braces: A Randomized Trial. Clin Orthop Relat Res 2010.

Proceedings of the 24th UK Conference of the
Association for Computational Mechanics in Engineering
31 March – 01 April 2016, Cardiff University, Cardiff

COMPUTER MODELLING OF CELLULAR STRUCTURES UNDER UNIAXIAL LOADING

***Hayley Wyatt[1], Khulud Alayyash[1], Muhammad Rahman[2], Sam L. Evans[2] and L. Angela Mihai[1]**
[1]School of Mathematics, Cardiff University, Senghennydd Road, Cardiff, CF24 4AG
[2]School of Engineering, Cardiff University, The Parade, Cardiff, CF24 3AA

*wyatthl@cardiff.ac.uk

ABSTRACT

For structures with uniform cell size, wall thickness, and shape, the fundamental question arises whether the same volume of cell wall material has the same effect when arranged as many small cells or as fewer large cells. A combination of finite element modelling (FEM) and experimental work was conducted to investigate the effect of the number of cells for a fixed volume of nonlinear hyperelastic material subject to large uniaxial tension. Three different structural geometries were analysed using FEM, with all models created within the FEBio software suite. For all structures analysed, the computer results show that the stiffness of the cell walls increases as the number of cells increases while the total volume of solid material is fixed, suggesting that the stiffness of the overall structure also increases. Experimentally, digital image correlation (DIC) was employed to investigate the behaviour of silicone structures of neo-Hookean material under tensile loading. This allowed displacement and strain maps to be created over the surface of the specimen whilst observing also the mechanical behaviour of the overall structure. The experimental results were compared to the FEM results to validate the computer models and to show the influence of the local finite deformation effects in the cell walls on the global mechanical performance of the structures.

Keywords: *cellular bodies; constitutive behaviour; hyperelastic material; finite elastic deformation.*

1. Introduction

In many natural load-bearing structures, support requirements are typically met through a combination of increase in cell number or size and sustained sclerification (thickening and lignification) of the cell walls [1]. For example, dicotyledon stems (e.g. magnolias, sycamores) increase their diameter primarily by cell division which ultimately form the characteristic annual rings, while monocotyledon stems (e.g. lilies, palms) prevent mechanical failure through a combination of initiation of growth with a stem that is sufficiently wide for future supply and support demands, and increase in stem diameter and strength by sustained cell wall expansion and lignification, predominantly toward the stem periphery and base (Figure 1). Even though some monocot plants attain tree stature comparable with arborescent dicotyledons and conifers their stems are relatively slender. By contrast, tall dicot trees have bigger stem diameters relative to their height than small trees, although the wood density representing the relative quantity of the cell wall in a given volume of wood made up of cells and lumens does not vary significantly among wood species [2].

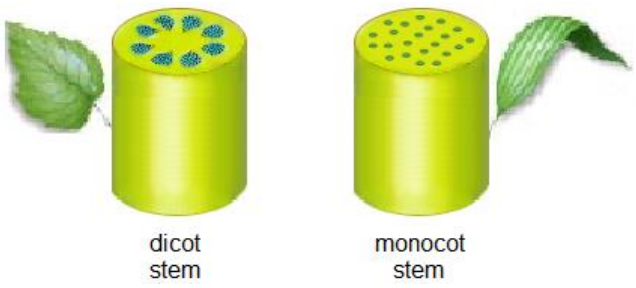

Figure 1. Schematic of cross-section of dicotyledon and monocotyledon stem.

For living cellular structures, there are many physiological and ecological factors that determine their material properties and influence their mechanical support system. Nevertheless, for structures with uniform cell size, wall thickness, and shape, the fundamental question arises whether the same volume of cell wall material has the same effect when arranged as many small cells or as fewer large cells. In the case of small strain deformations, thresholds on stiffness or strength can be set as constraints in the mechanical design or development process [1, 2]. However, when large strains and stresses occur during functional or physiological changes, finding a suitable criterion that accounts for the nonlinear properties of the deforming cell wall is needed [3,4].

2. Finite Element Modelling

Finite element modelling (FEM) was used to investigate the effect of varying the number of cells in periodic cellular structures made from a fixed volume of elastic material. Model structures with three different cell geometries, namely stacked, staggered, and diamond cells, respectively, were designed, as illustrated in Figure 2. The structures were created in SolidWorks, meshed in Gmsh, and imported into the FEBio software suite [5], and a mesh refinement study was performed for each structure.

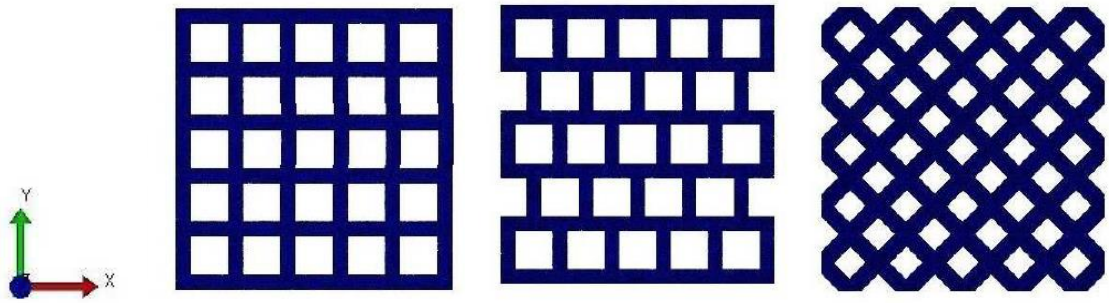

Figure 2. Examples of model structures with (a) stacked, (b) staggered, and (c) diamond cells investigated using FEM.

Every structure was made from a single piece of elastic material which occupied a thin square domain of (dimensionless) side one in the X- and Y- directions, and 0.1 in the Z-direction. Cells were equal in size throughout the structure. Both Mooney-Rivlin and neo-Hookean hyperelastic models were used for the cell wall material. The lower external horizontal face was free to slide in the X- and Z-direction, and fixed in the Y-directions. The upper external horizontal face was subject to a prescribed vertical stretch of 50% in the Y-direction, was free to slide in the X- and Z-direction. The remaining external and internal cell faces were allowed to deform freely.

For these cellular structures of hyperelastic material subject to large strain deformations, a nonlinear elastic modulus representing the mean ratio between the Cauchy stress and logarithmic strain (the sum of all the small strain increments) in a principal direction associated with the largest change of curvature was identified. For all structures analysed, the computational results show that the stiffness of the elastic cell walls as measured by this apparent elastic modulus increases as the number of cells increases while the total volume of solid material is fixed, suggesting that the stiffness of the overall structure may also increase. The results for structures with staggered cells of neo-Hookean material are shown in Figure 3. Due to its behaviour, this nonlinear elastic modulus can provide a viable criterion for finding the optimum wall thickness or number of cells in periodic structures of nonlinear elastic material.

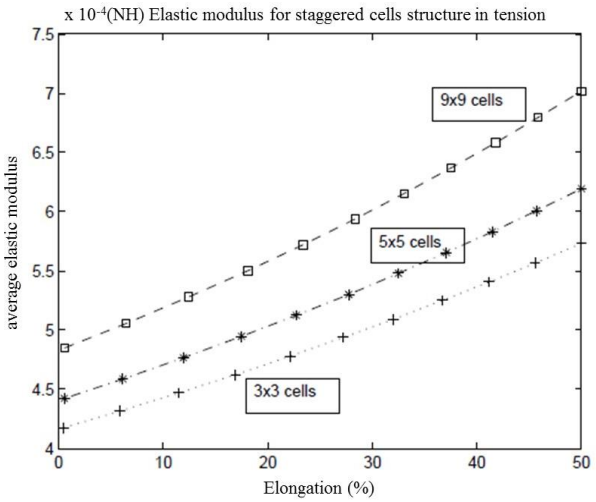

Figure 3. The mean elastic modulus for staggered cells of neo-Hookean material, with the results corresponding to structures with different number of cells while the total volume of material is fixed.

3. Tensile Testing

Seamless periodic cellular structures of silicone rubber were moulded with the moulds manufactured by 3D printing. The silicone used was a neo-Hookean material with defined properties of 0.74 MPa for Young's modulus and 0.48 for Poisson's ratio. The structures were mounted into a Zwick testing machine using specially made specimen holders, as shown in Figure 4 (a), and tested up to a maximum tensile load of 70N, at a rate of 1mm/min. To accurately measure the overall displacement of the structure, optical images were taken at every 5N load increments, and the displacement was measured using ImageJ, an open source image processing software.

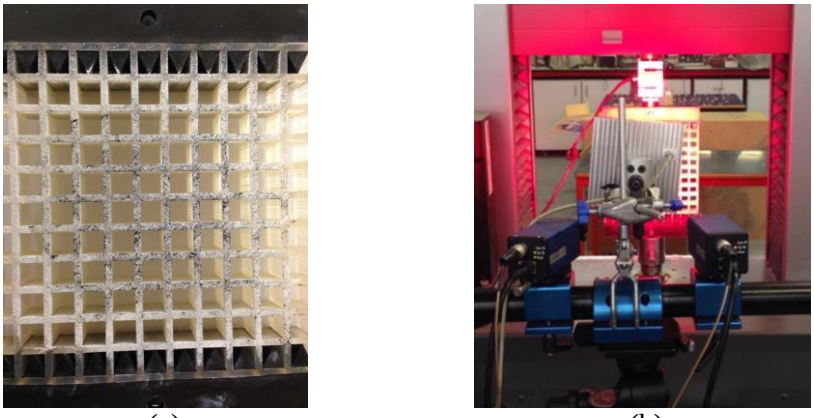

(a) (b)

Figure 4. (a) Stacked cellular structure of neo-Hookean material with the random speckle pattern applied and the structure held within the test fixtures used for tensile testing. (b) The DIC set-up, with a two camera system used to capture 3D images and a light source providing homogeneous light to the specimen.

Digital image correlation (DIC) was employed to map the displacement across the surface of the specimen. DIC is an optical technique that maps the displacement field across the surface of a specimen and can thus be used to compute strains. In order to measure the displacement across the specimen, a high contrast speckle pattern is required. For this study, the speckle pattern was created on the surface of the silicone structure by applying a base layer of white face paint followed by the application of a random black pattern using black face paint. A two camera DIC system was used to enable three dimensional (3D) data to be captured for the uniaxial tensile test [6] (see Figure 4 (b)), and local displacements and strains in the cell walls were recorded at every 5N load increments.

The results from the DIC data showed similar displacement and strain maps when compared to the FEM data. In particular, for staggered cellular structures, areas of low strain were found along the cell walls at the centre of the cell, while areas of high strain were obtained diagonally between the corners of the cell (see Figure 5). Further experimental work is on-going to provide a thorough quantitative validation of the FEM models for structures with different geometries as shown in Figure 2.

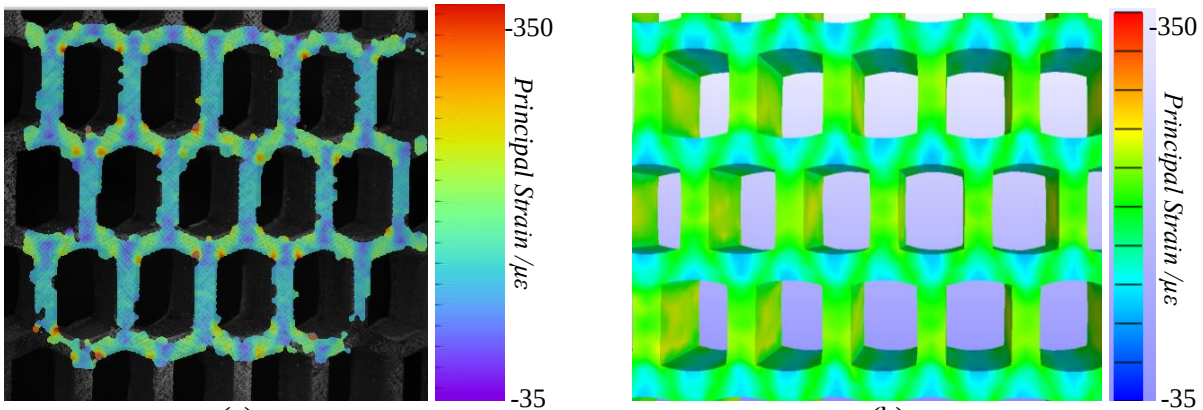

(a) (b)

Figure 5. Example of (a) DIC and (b) FEM data for structure with staggered cells, with images showing results at 18% elongation in the vertical direction.

4. Conclusion

In order to derive important insights into the mechanical behaviour of cellular structures of nonlinear elastic material subject to large strain deformations, the numerical performance of a nonlinear elastic modulus for periodic structures of hyperelastic material was examined. Computationally, this apparent modulus suggests that the cell walls in structures with many small cells are stiffer than in those with fewer large cells if the total volume of material remains unchanged. The mechanical behaviour of structures made from a neo-Hookean material and subject to uniaxial loading was also studied experimentally using DIC, and the experimental data showed similar displacement and strain maps as for the computed FEM models. The influence of the local finite deformation effects on the global stiffness behaviour of these structures remains to be established.

Acknowledgements

The support for L.A.M. and H.W. by the Engineering and Physical Sciences Research Council of Great Britain under research grant EP/M011992/1 is gratefully acknowledged. The authors would like to thank Richard Thomas for his help with conducting the experimental testing. The authors would also like to thank the undergraduate project students who have contributed to this work.

References

[1] Gibson L.J., Ashby M.F., Harley B.A.: Cellular Materials in Nature and Medicine, Cambridge University Press, 2010.
[2] Fournier M., Dlouhá J., Jaouen G., Almeras T.: Integrative biomechanics for tree ecology: beyond wood density and strength, Journal of Experimental Botany, doi:10.1093/jxb/ert279, 2013.
[3] Mihai L.A., Goriely A.: Finite deformation effects in cellular structures with hyperelastic cell walls, International Journal of Solids and Structures 53, 107-128, 2015.
[4] Mihai L.A., Alayyash K., Goriely A.: Paws, pads and plants: The enhanced elasticity of cell-filled load-bearing structures. Proceeding of the Royal Society A 471, 20150107, 2015.
[5] Maas SA, Ellis BJ, Ateshian GA, Weiss J.: FEBio: Finite Elements for Biomechanics, Journal of Biomechanical Engineering 134, 2012.
[6] Evans S.L., Holt C.A.: Measuring the mechanical properties of human skin *in vivo* using digital image correlation and finite element modelling. The Journal of Strain Analysis for Engineering Design 44, 337-345, 2009.

Solids and Structures II

Proceedings of the 24th UK Conference of the
Association for Computational Mechanics in Engineering
31 March - 01 April 2016, Cardiff University, Cardiff

Prism solid-shell with heterogonous and hierarchical approximation basis

***Lukasz Kaczmarczyk[1], Zahur Ullah[1] and Chris Pearce[1]**

[1]School of Engineering, University of Glasgow

*Lukasz.Kaczmarczyk@glasgow.ac.uk

ABSTRACT

A solid-shell element which does not possess rotational degrees of freedom (DOFs) and which is applicable to thin plate/shell problems is considered. The element approximation is constructed in prisms, where displacements on the upper and lower surfaces are approximated in the global coordinate system. In addition, two other fields are defined in the shell natural (local) coordinate system that represent the components of the displacement vector in both the current shell normal direction and the current shell tangent plane. To each field, an arbitrary order of approximation can be defined, and all fields reproduce a complete and conforming polynomial approximation basis for the solid prism element. It is not necessary to augment the formulation with an assumed natural strain (ANS) field or enhanced assumed strain (EAS) field or to use reduced integration, making the element ideally suited for geometrically and physically nonlinear problems.

Key Words: *solid shell, large deformations, hierarchical approximation*

1. Introduction

In standard thin shell formulations, the approximation through the thickness is assumed to be linear or higher order, i.e. the normals to the mid-surface in the initial configuration remain straight but not normal during the deformation. In the proposed formulation the thickness of the element is not constant and the normal stress in through-thickness direction is considered. For this reason, the kinematics of this solid-shell element is richer than the kinematic assumed in Kirchhoff - Love plate theory. In formulating this element, we do not aim to reproduce classical shell kinematic, thereby avoiding the problem of element locking. This work builds on a substantial body of published work by a number of different authors, most notably [4]. However this implementation proposes a new formulation exploiting hierarchical, heterogeneous and anisotropic approximation spaces.

2. Hierarchical approximation in prism

In constructing the approximation space in a prism we apply a similar procedure to that shown in [2] for tetrahedra. Nodal basis functions using barycentric coordinates are given by

$$\phi^v = \lambda_v, \quad {}_L\phi^v = \phi^v\zeta, \quad {}_U\phi^v = \phi^v(1-\zeta) \tag{1}$$

where right subscript ${}_L\phi^v$ and ${}_U\phi^v$ indicates shape functions on lower and upper triangles respectively and λ_v denotes the barycentric coordinates. Convective coordinate $\zeta \in [0,1]$ is the coordinate through the prism thickness. $\zeta = 0$ defines the lower prism triangle and $\zeta = 1$ the upper prism triangle.

The edge hierarchical approximation basis is constructed as follows

$$\beta_{0i} = \lambda_0\lambda_i, \quad \phi_l^{e_t} = \beta_{0i}L_l(\lambda_i - \lambda_j), \quad {}_L\phi_l^{e_t} = \phi_l^e\zeta, \quad {}_U\phi_l^{e_t} = \phi_l^e(1-\zeta), \tag{2}$$

where i and j are nodal indices on a triangle. L_l is the Legendre polynomial of order l. If p is the order of the polynomial for the triangle, then $0 \geq l \geq p-2$ and the number of DOFs on an edge is $p-1$. The triangle approximation basis is constructed by

$$\beta_{0ij} = \lambda_0\lambda_i\lambda_j, \quad \phi_{l,m}^t = \beta_{0ij}L_l(\lambda_0-\lambda_i)L_m(\lambda_0-\lambda_j)\zeta, \quad {}_L\phi_{l,m}^t = \phi_{l,m}^t\zeta, \quad {}_U\phi_{l,m}^t = \phi_{l,m}^t(1-\zeta) \tag{3}$$

If p is the order of the polynomial on a triangle, then $0 \geq l, m, l+m \geq p-2$ and number of DOFs on triangle is $(p-1)(p-2)/2$.

The edge through-thickness basis function is given by

$$\beta_{00} = \lambda_0 \lambda_0, \quad \phi_l^{e_q} = \beta_{00}\zeta(1-\zeta)L_l(2\zeta-1) \tag{4}$$

where λ_0 is the barycentric coordinate for the node of the triangle to which the edge through thickness is adjacent. If p is the order of the polynomial in the prism, then $0 \geq l \geq p-2$ and the number of DOFs on edge is $p-1$. The quadrilateral through thickness basis function is

$$\beta_{0i} = \lambda_0 \lambda_i, \quad \phi_{l,m}^{q} = \beta_{0i}\zeta(1-\zeta)L_l(\lambda_0-\lambda_i)L_m(2\zeta-1) \tag{5}$$

where 0 and i indicate nodes on opposite corner nodes of a quadrilateral with its own canonical numbering. If p is the order of the polynomial in the prism, then $0 \geq l, m, l+m \geq p-4$ and the number of DOFs on the quadrilateral is $(p-3)(p-2)/2$. The bubble prism basis functions are given by

$$\beta_{0i} = \lambda_0 \lambda_i \lambda_j, \quad \phi_{l,m,k}^{p} = \beta_{0ij}\zeta(1-\zeta)L_l(\lambda_0-\lambda_i)L_m(\lambda_0-\lambda_j)L_k(2\zeta-1) \tag{6}$$

where $0, i, j$ are indices of nodes on the triangle. If p is polynomials order in prism, then $0 \geq l, m, k, l+m+k \geq p-5$ and number of DOFs of the prism is $(P-5)(P-4)(P-3)/6$.

3. Geometry approximation in reference configuration

A pragmatic approach is to generate the input mesh surface using a standard mesh generator. In case of non-planar surfaces, the geometry can be defined by 6-noded or higher-order triangles. The geometry defined by the surface mesh is then projected using a hierarchical basis onto the prism. Thus all approximations for the shell geometry using a hierarchal basis shown below is directly inferred from the input triangular mesh. The only additional information required is the shell thickness.

The reference position of points on the shell mid-surface, in the global Cartesian coordinate system, is given on the triangular mesh by

$${}^{M}\mathbf{Z}(\xi,\eta) = {}^{3}\boldsymbol{\phi}^{v}(\xi,\eta)\underline{\mathbf{Z}}^{v} + {}^{3}\boldsymbol{\phi}^{e_t}(\xi,\eta)\underline{\mathbf{Z}}^{e_t} + {}^{3}\boldsymbol{\phi}^{t}(\xi,\eta)\underline{\mathbf{Z}}^{t} = \sum_{g=v,e_t,t} {}^{3}\boldsymbol{\phi}^{g}(\xi,\eta)\underline{\mathbf{Z}}^{g} \tag{7}$$

where $\underline{\mathbf{Z}}^{v,e_t,t}$ are DOFs on vertices, edges and triangles. Left upper-script ${}^{3}\boldsymbol{\phi}$ indicate that it is matrix of base approximation functions for vector field, where size of vector is three. In addition we define on the surface mesh a field of unit length director vectors [6], as follows

$${}^{M}\mathbf{V}(\xi,\eta) = \sum_{g=v,e_t,t} {}^{3}\boldsymbol{\phi}^{g}(\xi,\eta)\underline{\mathbf{V}}^{g} \tag{8}$$

Finally reference position vector in prism element is given by in global Cartesian coordinate system

$$\mathbf{Z}(\xi,\eta,\zeta) = {}^{M}\mathbf{Z}(\xi,\eta) + a\,{}^{M}\mathbf{V}(\xi,\eta)(\zeta-\frac{1}{2}) = \sum_{s=L,U}\sum_{g=v,e_t,t} {}^{3}\boldsymbol{\phi}_s^{g}(\xi,\eta,\zeta)\underline{\mathbf{Z}}_s^{g} \tag{9}$$

where a is the shell thickness, which may not necessarily be constant.

4. Curvilinear systems in reference and current configuration

The vector coefficients in the Cartesian coordinate system are Z^I and z^i for the current and reference configuration, respectively. For simplicity, we use both coordinate systems with the same base vectors and origin. In addition we use local curvilinear coordinate base for reference configuration, where vectors of the base are $\mathbf{E}_\alpha$ and vector of covariant coefficients in that base are X^A. The field of $\mathbf{E}_\alpha$ is consequently approximated using hierarchical approximation as follows

$${}^{M}\mathbf{E}_{0,1}(\xi,\eta) = \left\{ \sum_{g=v,e_t,t} {}^{3}\boldsymbol{\phi}^{g}(\xi,\eta)\underline{\mathbf{E}}_{0,1}^{g}, \right\}\mathbf{I}^{I} \quad {}^{M}\mathbf{E}_2(\xi,\eta) = \left\{\mathrm{Spin}[{}^{M}\mathbf{E}_0(\xi,\eta)]\,{}^{M}\mathbf{E}_1(\xi,\eta)\right\}\mathbf{I}^{I} \tag{10}$$

where Spin[·] is a spin operator acting as a vector product and $\underline{\mathbf{E}}^{g}_{0,1}$ are coefficients of the approximation functions.

The local curvilinear coordinate base in the current configuration, convected by the motion of the shell mid-surface is given by

$$\mathbf{e}_a = e^a_i \mathbf{i}_i = {}^M F^i_I \, {}^M E^{AI} \delta^a_A \mathbf{i}_i \tag{11}$$

where ${}^M\mathbf{F}^i_I(\xi, \eta, \zeta)$ is component of the gradient of deformation, i.e. for the discretized system, the gradient of deformation is additively decomposed into a part resulting from through-thickness DOFs and a part resulting from DOFs on the triangles. The latter part is used to push the base vectors.

5. Displacements and physical equations

In the following approach, for convenience, we use the local shell coordinate system to evaluate the physical equations. The Cartesian global coordinate system is used to express coefficients of DOFs on entities adjacent to the upper and lower triangles. For DOFs on entities through the shell thickness, i.e. edges through the thickness, quads and the prism itself, the current curvilinear (convected) shell coordinate system is used to express coefficients of the displacement vector.

The position of a material point in the current configuration is given by

$$z^a \mathbf{i}_a = Z^J \mathbf{I}_J + u^J \mathbf{I}_J + v e^J_2 \mathbf{I}_J \tag{12}$$

where displacements are additively decomposed into a global and through thickness component. The displacement $\mathbf{u}$ is approximated in the global coordinate system as

$$u^J(\boldsymbol{\xi}) = \sum_{s=L,U} \sum_{g=v,e_t,t} {}^3\boldsymbol{\phi}^g_s(\boldsymbol{\xi}) \underline{\mathbf{u}}^{g,J}_s = \left[{}^3\overline{\boldsymbol{\phi}}(\boldsymbol{\xi}) \right] \underline{\mathbf{u}}^J. \tag{13}$$

Note that displacement DOFs in vector $\underline{\mathbf{u}}$ are in global Cartesian coordinate system, thus this solid shell element could be assembled with other tetrahedral elements without the need for any linking/transfer elements. The displacement $\mathbf{v} = v e^J_2 \mathbf{I}_J$ is approximated in the local conservative system following global mid-surface deformation. The vector of displacements through the thickness is given by

$$v(\boldsymbol{\xi}) = \sum_{g=e_q,p} {}^1\boldsymbol{\phi}^g(\boldsymbol{\xi}) \underline{\mathbf{v}}^{g,a} = \left[{}^1\overline{\boldsymbol{\phi}}(\boldsymbol{\xi}) \right] \underline{\mathbf{v}}. \tag{14}$$

Note that the vector of values of DOFs $\underline{\mathbf{v}}$ is in the local, curvilinear current (conservative) coordinate system. Those degrees of freedom are associated with edges, quads and volume of prism itself, thus are inside volume of shell structure and are not adjacent to any other DOFs except those of the considered shell.

Consequently the vector of internal forces is

$$\mathbf{f}^{\text{int}}_{\text{u}}(\underline{\mathbf{u}}, \underline{\mathbf{v}}) = \int_\Omega \left[\nabla_{Z^I} {}^3\overline{\boldsymbol{\phi}} \right] P^I_i(\underline{\mathbf{u}}, \underline{\mathbf{v}}) \mathrm{d}\Omega \quad \text{and} \quad \mathbf{f}^{\text{int}}_{\text{v}}(\underline{\mathbf{u}}, \underline{\mathbf{v}}) = \int_\Omega \left[\nabla_{X^A} {}^1\overline{\boldsymbol{\phi}} \right] P^A_2(\underline{\mathbf{u}}, \underline{\mathbf{v}}) \mathrm{d}\Omega, \tag{15}$$

where P^I_i and P^A_a are Piola - Kirchhoff tensors in the Cartesian and local convected curvilinear system. Consequently $\mathbf{f}^{\text{int}}_{\text{u}}$ and $\mathbf{f}^{\text{int}}_{\text{v}}$ are internal force vectors associated with DOFs adjacent to triangles (upper and lower) in a global cartesian system and DOFs adjacent to edges through the thickness, quads and prism itself in a local curvilinear coordinate system.

In the formulation presented here, the current curvilinear system follows the shell deformation given by DOFs on upper and lower triangle. This, in some sense, leads to a co-rotational like formulation [3]. As result it is noted that the tangent stiffness is non-symmetric. This observation is consistent with that made by Crisfield [3], who adapted the co-rotational formulation whereby the coordinate systems is rotated when shell is deformed. However, numerical experiments have shown that for the problems addressed here, like for the co-rotational formulation, the tangent stiffness matrix becomes symmetric as the iterative procedure reaches equilibrium, thus the matrix can be symmetrized without deteriorating the rate of convergence.

6. Example

In the following examples we present two classical tests of a pinched cylinder. The reference solutions provided by [5] are reproduced. However, exploring the flexibility of the method, increasing the approximation order in the shell plane or shell thickness, we are able to find a softer, converged solution, see Figure 1.

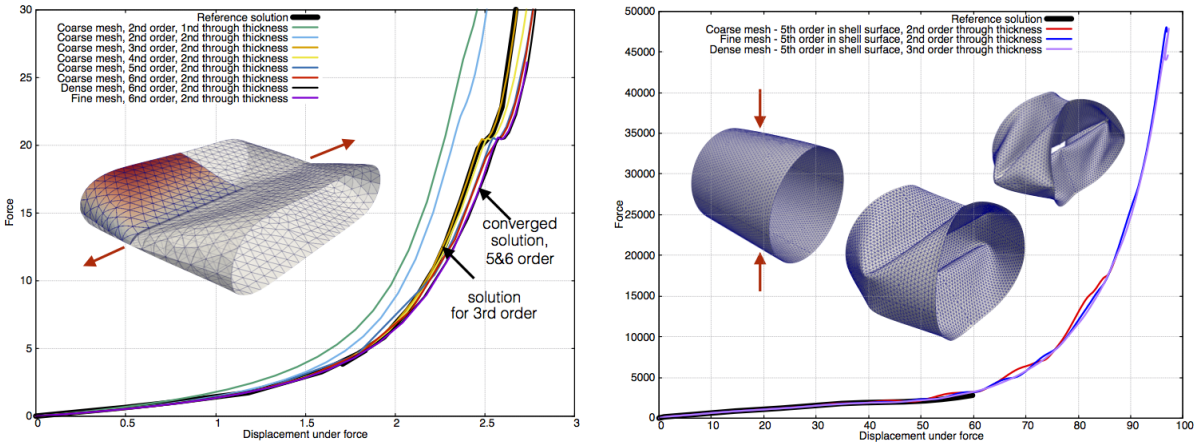

Figure 1: Pinched cylinder without diaphragm tension on the left and with diaphragm compression on the right. See [5] for more information about geometry, material parameters and reference solution. Analysed meshes are available from [1].

7. Conclusions

The solid-shell element presented here has a number of properties. First, element DOFs do not posses rotations, such that element could be used in conjunction with classical solid elements without the need for any additional transfer elements. Second, the approximation basis is hierarchical. Such an approximation allows for efficient construction of iterative solvers tailored for hp-adative code. Third, the approximation basis is heterogenous, that is an arbitrary approximation order can be set independently for each geometrical entity, i.e. edge, triangle, quad or prism. Fourth, local approximation of membrane displacements and normal displacements through the thickness are independent from each other. Finally, the physical equation for 3d solid can be used in the local shall coordinate system.

References

[1] MoFEM finte element code. http://userweb.eng.gla.ac.uk/lukasz.kaczmarczyk/MoFem/html/index.html.

[2] Mark Ainsworth and Joe Coyle. Hierarchic finite element bases on unstructured tetrahedral meshes. *International Journal for Numerical Methods in Engineering*, 58(14):2103–2130, 2003.

[3] Michael A Crisfield. A consistent co-rotational formulation for non-linear, three-dimensional, beam-elements. *Computer methods in applied mechanics and engineering*, 81(2):131–150, 1990.

[4] R Hauptmann and K Schweizerhof. A systematic development of solid shell element formulations for linear and non linear analyses employing only displacement degrees of freedom. *International Journal for Numerical Methods in Engineering*, 42(1):49–69, 1998.

[5] Saman Hosseini, Joris JC Remmers, Clemens V Verhoosel, and René Borst. An isogeometric solid-like shell element for nonlinear analysis. *International Journal for Numerical Methods in Engineering*, 95(3):238–256, 2013.

[6] Theodore Sussman and Klaus Jurgen Bathe. 3d-shell elements for structures in large strains. *Computers and Structures*, 122:2 – 12, 2013. Computational Fluid and Solid Mechanics 2013Proceedings Seventh {MIT} Conference on Computational Fluid and Solid Mechanics.

Proceedings of the 24th UK Conference of the
Association for Computational Mechanics in Engineering
31 March - 1 April 2016, Cardiff University, Cardiff

A first order hyperbolic framework for large strain computational solid dynamics: A vertex-centred Updated Lagrangian scheme

***Osama Ibrahim [1], Antonio J. Gil [1], Chun Hean Lee [1], Javier Bonet [2]**

[1] Zienkiewicz Centre for Computational Engineering, College of Engineering
Swansea University, Bay Campus, SA1 8EN, United Kingdom
[2] University of Greenwich, London, SE10 9LS, United Kingdom

* o.i.i.hassan@swansea.ac.uk

ABSTRACT

Current industrial codes (e.g. PAM-CRASH, ANSYS, LS-DYNA) for the simulation of large-scale solid dynamics are typically based on the use of traditional displacement-based finite element formulations. However, these formulations present a number of shortcomings, namely, (1) reduced order of convergence for strains and stresses, (2) poor performance in bending and shock dominated scenarios and (3) appearance of numerical instabilities associated with volumetric locking and pressure fluctuations.

To circumvent these drawbacks, a system of first order hyperbolic conservation laws for large strain solid dynamics was introduced [1–3]. Essentially, the formulation was established in terms of the linear momentum and the deformation gradient tensor [3]. This paper builds on recent Total Lagrangian based work [1] developed by the authors, by introducing a vertex centred Finite Volume Method on a mixed Updated Lagrangian formalism, with the aim of further enhancing the robustness of the algorithm. In the case of extremely high nonlinear deformations, the Updated Lagrangian framework provides extra flexibility into the formulation, thus extending the range of applications to near incompressibility. For computational efficiency, an adapted artificial compressibility approach is also introduced for truly and nearly incompressible materials [2].

A series of numerical examples are presented in order to assess the robustness and the applicability of the proposed framework, benchmarking it against alternative numerical strategies developed by the authors in recent publications [1–3]. The overall scheme shows excellent behaviour in shock and bending dominated nearly incompressible scenarios without spurious pressure oscillations, yielding second order of convergence for both velocities and stresses.

Key Words: *Fast solid dynamics ; Updated Lagrangian ; Finite volume ; Locking; Incompressibility*

1. Introduction

Over the last few years, the authors have introduced a new mixed Total Lagrangian conservation-based methodology, where the linear momentum $\boldsymbol{p}$ and the deformation gradient $\boldsymbol{F}$ are treated as primary variables of a system of first order conservation laws. Both velocities, deviatoric stresses and volumetric stresses display the same rate of convergence, which proves ideal in the case of linear finite elements. This approach has been thoroughly analysed by the authors using a wide variety of spatial second order discretisation techniques, namely cell centred upwind Finite Volume Method (FVM), vertex centred Jameson-Schmidt-Turkel (JST) and upwind FVM, two step Taylor Galerkin and Petrov Galerkin Finite Element Method (FEM). Moreover, the two-field $\boldsymbol{p}$-$\boldsymbol{F}$ formulation was then augmented by incorporating a new conservation law for the Jacobian of the deformation J to effectively solve nearly incompressible deformations. The $\boldsymbol{p}$-$\boldsymbol{F}$-J formulation was also extended to account for truly incompressible materials utilising a tailor-made fractional step Petrov Galerkin approach.

In this paper, the conservation-based $\boldsymbol{p}$-$\boldsymbol{F}$-J system through the use of either upwind or JST stabilisation is revisited, but this time established in terms of Updated Lagrangian formalism. This framework leads to a simpler expression for Jacobian evolution and, more importantly, further enhances the robustness of the algorithm. For nearly and truly incompressible materials, an adapted artificial compressibility approach is also introduced, with the aim of increasing computational efficiency.

2. Governing equations

The motion of a continuum, which occupies a volume Ω_0 in the reference configuration and a volume Ω in the deformed configuration, expressed in Updated Lagrangian formalism is described through the following ***p*-*F*-*J*** first order conservation laws:

$$\frac{d}{dt}\int_{\Omega_0} \boldsymbol{p}\, d\Omega_0 = \int_{\partial\Omega} \boldsymbol{t}\, da + \int_{\Omega} \boldsymbol{f}\, d\Omega; \tag{1a}$$

$$\frac{d}{dt}\int_{\Omega_0} \boldsymbol{F}\, d\Omega_0 = \int_{\partial\Omega} \left(\frac{\boldsymbol{p}}{\rho_0} \otimes \boldsymbol{H}^{-1}\right)\boldsymbol{n}\, da; \tag{1b}$$

$$\frac{d}{dt}\int_{\Omega_0} J\, d\Omega_0 = \int_{\partial\Omega} \frac{\boldsymbol{p}}{\rho_0} \cdot \boldsymbol{n}\, da; \tag{1c}$$

$$\frac{d}{dt}\int_{\Omega_0} E\, d\Omega_0 = \int_{\partial\Omega} \frac{\boldsymbol{p}}{\rho_0} \cdot \boldsymbol{t}\, da + \int_{\Omega} \frac{1}{\rho_0}\boldsymbol{f} \cdot \boldsymbol{p}\, d\Omega. \tag{1d}$$

where $\boldsymbol{p} := \rho_0 \boldsymbol{v}$ is the linear momentum, ρ_0 is the material density, $\boldsymbol{v}$ is the velocity field, $\boldsymbol{\sigma}$ is the Cauchy stress tensor, $\boldsymbol{f}$ is the body force per unit current volume, $\boldsymbol{F}$ is the deformation gradient (or fibre map), $\boldsymbol{H} := J\boldsymbol{F}^{-T}$ is the cofactor of the deformation gradient (or area map), J is the Jacobian of the deformation (or volume map), E is the total energy per unit undeformed volume and $\boldsymbol{t}$ represents the nominal traction related through the Cauchy stress tensor $\boldsymbol{\sigma}$ and the spatial unit outward normal vector $\boldsymbol{n}$. Crucially, the fibre map evolution (1b) needs to satisfy an additional set of compatibility conditions (also known as involutions), namely $CURL\boldsymbol{F} = \boldsymbol{0}$. In the context of isothermal process, the energy equation (1d) is redundant and is decoupled from the ***p*-*F*-*J*** system (1a-1c). However, equation (1d) can still be employed when measuring the amount of numerical dissipation introduced into the system.

For closure of the above system (1), appropriate initial and boundary conditions, as well as a constitutive model, are supplemented. For simplicity, a nearly incompressible neo-Hookean material is used by relating Cauchy stress $\boldsymbol{\sigma}$ with the geometrical measures $\{\boldsymbol{F}, J\}$:

$$\boldsymbol{\sigma} = \boldsymbol{\sigma}_{dev}(\boldsymbol{F}) + p(J)\boldsymbol{I}; \quad \boldsymbol{\sigma}_{dev} = \mu J_{\boldsymbol{F}}^{-5/3}\left[\boldsymbol{b} - \frac{1}{3}(\boldsymbol{F} : \boldsymbol{F})\boldsymbol{I}\right]; \quad p = \kappa(J-1), \tag{2}$$

where p is the pressure, $J_{\boldsymbol{F}} := \det \boldsymbol{F}$ is the Jacobian evaluated directly from the deformation gradient, $\boldsymbol{b} := \boldsymbol{F}\boldsymbol{F}^T$ is the left Cauchy-Green strain tensor, μ and κ are the shear and bulk moduli.

3. Finite volume spatial discretisation

From the spatial discretisation viewpoint, the above set of hyperbolic conservation laws (1) is semi-discretised using the vertex centred finite volume method widely accepted in fluid dynamics applications. The introduction of appropriate numerical viscosity is of paramount importance due to the hyperbolic nature of the system. In the following section, two variants of the numerical dissipative mechanisms are discussed, namely a nodally conservative JST stabilisation (see Section 3.1) and an Upwind Riemann solver stabilisation (see Section 3.2).

3.1. Jameson-Schmidt-Turkel (JST) nodally conservative stabilisation

Following Reference [3], one of the most effective options is to incorporate a nodally conservative numerical viscosity (e.g. second order and fourth order stabilisations) into the system without amending the flux computations. The fourth order term $\mathcal{D}_4$ (biharmonic) provides stabilisation against odd-even decoupling phenomena, whilst the second order term $\mathcal{D}_2$ (harmonic) is activated with steep gradients, capturing any discontinuity in the solution. For simplicity, we restrict ourselves to problems where no physical shocks occur. For this reason, there is no need to consider harmonic stabilisations in our system:

$$\Omega_0^a \frac{d\boldsymbol{p}_a}{dt} = \sum_{b\in\Lambda_a} \frac{1}{2}(\boldsymbol{\sigma}_a + \boldsymbol{\sigma}_b)\boldsymbol{c}_{ab} + \sum_{\gamma\in\Gamma_a^B} \boldsymbol{t}_a^\gamma \frac{a^\gamma}{3} + \mathcal{D}_4(\boldsymbol{p}_a); \tag{3a}$$

$$\Omega_0^a \frac{d\boldsymbol{F}_a}{dt} = \sum_{b\in\Lambda_a} \frac{1}{2\rho_0}(\boldsymbol{p}_a + \boldsymbol{p}_b) \otimes \boldsymbol{C}_{ab} + \sum_{\gamma\in\Gamma_a^B} \frac{1}{\rho_0}\left(\boldsymbol{p}_a^\gamma \otimes \boldsymbol{N}^\gamma\right)\frac{A^\gamma}{3}; \tag{3b}$$

$$\Omega_0^a \frac{dJ_a}{dt} = \sum_{b\in\Lambda_a} \frac{1}{\rho_0}\boldsymbol{p} \cdot \boldsymbol{c}_{ab} + \sum_{\gamma\in\Gamma_a^B} \frac{1}{\rho_0}\boldsymbol{p}_a^\gamma \cdot \boldsymbol{n}^\gamma \frac{a^\gamma}{3} + \mathcal{D}_4(J_a), \tag{3c}$$

where $\boldsymbol{C}_{ab}$ and $\boldsymbol{c}_{ab}$ are the initial and current area vectors and $\mathcal{D}_4(\boldsymbol{\beta}_a)$ represents the fourth order JST dissipation defined as:

$$\mathcal{D}_4(\boldsymbol{\beta}_a) = -k^{(4)} \sum_{b\in\Lambda_a} \Psi_{ab}(c_p)\theta_{ab}(\boldsymbol{L}(\boldsymbol{\beta}_b) - \boldsymbol{L}(\boldsymbol{\beta}_a)); \quad \boldsymbol{L}(\boldsymbol{\beta}_a) = \sum_{b\in\Lambda_a} \theta_{ab}(\boldsymbol{\beta}_b - \boldsymbol{\beta}_a); \quad \boldsymbol{\beta}_a = \{\boldsymbol{p}_a, J_a\}. \tag{4}$$

Here, $k^{(4)}$ is a user-defined parameter, $\Psi_{ab}(c_p)$ is the spectral radius depending only on the volumetric wave c_p and θ_{ab} is a geometrical weight used to preserve second order accuracy in unstructured meshes. For the satisfaction of involutions, it is crucial to ensure that no dissipation is introduced in the fibre map evolution (3b) by approximating the corresponding fluxes via central difference method [3].

3.2. Upwind stabilisation: Acoustic Riemann solver

In contrast to the JST stabilisations described above, a more refined approach by adding appropriate conservative numerical viscosity through fluxes is introduced [1]. Naturally, discontinuity of the conservation variables across control volume interfaces leads to a Riemann problem. A suitable numerical interface (acoustic) flux can be obtained by making use of the Rankine-Hugoniot jump conditions, of standard use within the field of fluid dynamics:

$$\Omega_0^a \frac{d\boldsymbol{p}_a}{dt} = \sum_{b\in\Lambda_a} \boldsymbol{t}^C \|\boldsymbol{c}_{ab}\| + \sum_{\gamma\in\Gamma_a^B} \boldsymbol{t}_a^\gamma \frac{a^\gamma}{3}; \tag{5a}$$

$$\Omega_0^a \frac{d\boldsymbol{F}_a}{dt} = \sum_{b\in\Lambda_a} \frac{1}{2\rho_0}(\boldsymbol{p}_a + \boldsymbol{p}_b) \otimes \boldsymbol{C}_{ab} + \sum_{\gamma\in\Gamma_a^B} \frac{1}{\rho_0}\left(\boldsymbol{p}_a^\gamma \otimes \boldsymbol{N}^\gamma\right) \frac{A^\gamma}{3}; \tag{5b}$$

$$\Omega_0^a \frac{dJ_a}{dt} = \sum_{b\in\Lambda_a} \frac{1}{\rho_0}\boldsymbol{p}^C \cdot \boldsymbol{c}_{ab} + \sum_{\gamma\in\Gamma_a^B} \frac{1}{\rho_0}\boldsymbol{p}_a^\gamma \cdot \boldsymbol{n}^\gamma \frac{a^\gamma}{3}, \tag{5c}$$

where

$$\boldsymbol{t}^C = \frac{1}{2}(\boldsymbol{\sigma}^- + \boldsymbol{\sigma}^+)\,\boldsymbol{n} + \frac{1}{2}\left[\frac{1}{c_p}(\boldsymbol{n}\otimes\boldsymbol{n})(\boldsymbol{\sigma}^+ - \boldsymbol{\sigma}^-)\boldsymbol{n} + \frac{1}{c_s}(\boldsymbol{I} - \boldsymbol{n}\otimes\boldsymbol{n})(\boldsymbol{\sigma}^+ - \boldsymbol{\sigma}^-)\boldsymbol{n}\right]; \tag{6a}$$

$$\boldsymbol{p}^C = \frac{1}{2}(\boldsymbol{p}^+ + \boldsymbol{p}^-) + \frac{1}{2c_p}(\boldsymbol{\sigma}^+ - \boldsymbol{\sigma}^-)\boldsymbol{n}; \quad \boldsymbol{\sigma}^{-,+} = \boldsymbol{\sigma}_{dev}^{-,+} + \kappa(J^{-,+} - 1)\boldsymbol{I}. \tag{6b}$$

Notice that this type of upwinding stabilisations (which depends on both volumetric wave c_p and shear wave c_s) is derived with the consideration of wave directional character, being more accurate in comparison to JST stabilisation [1].

Finally, the set of stabilised semidiscrete equations (see (3) and (5)) can then be explicitly integrated from time step t^n to t^{n+1}. In this case, the explicit one-step two-stage Total Variation Diminishing Runge Kutta (TVD-RK) time integrator [2] is preferred due to its excellent TVD properties. The geometry is also advanced in time using the exact same time integrator in a monolithic manner. As described in [1, 3], the scheme is suitably modified to guarantee the conservation of angular momentum. In the case of nearly and truly incompressible materials, the volumetric wave speed c_p can reach very high values leading to prohibitively small time steps. This can have a very negative effect in the computational efficiency of the algorithm. Taking inspiration from Reference [2], a tailor-made artificial compressibility algorithm is also introduced for the three-field ***p*-*F*-*J*** mixed formulation.

4. Numerical examples

A column with a unit square cross section is subject to different loading conditions; a prescribed sinusoidal angular velocity (see Figure 1) and a linearly varying velocity along its height (see Figures 2 and 3). The examples show the applicability and robustness of the scheme in truly and nearly incompressible bending dominated scenarios.

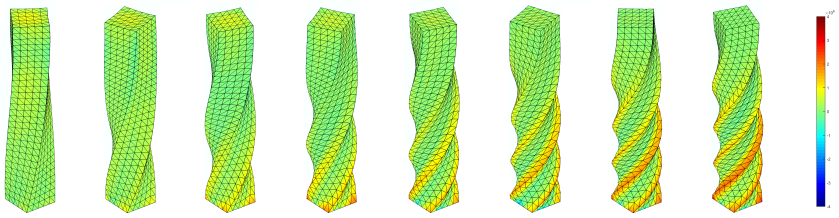

(a) Explicit Updated Lagrangian ***p*-*F*-*J*** Upwind algorithm

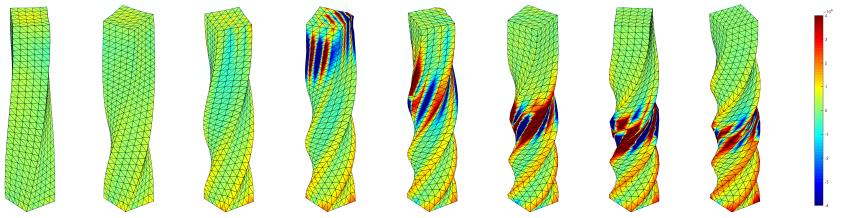

(b) Explicit Total Lagrangian ***p*-*F*-*J*** Upwind algorithm

Figure 1: Illustrate the robustness of Updated Lagrangian formalism over Total Lagrangian formalism.

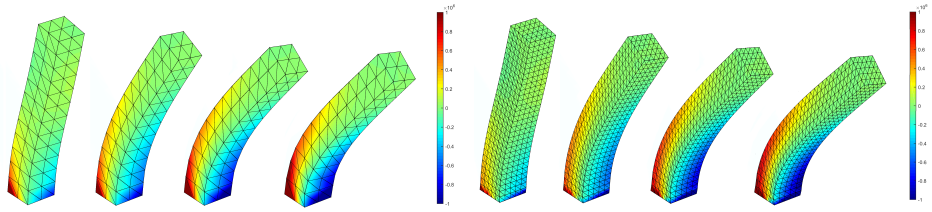

(a) Explicit Updated Lagrangian ***p*-*F*-*J*** Upwind (b) Explicit Updated Lagrangian ***p*-*F*-*J*** JST

Figure 2: Demonstrate the accuracy of the stabilisations: Upwind is less dissipative than JST.

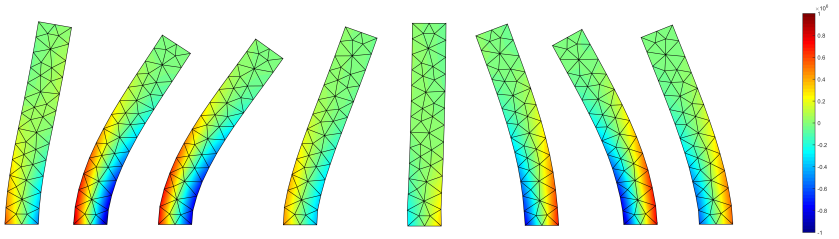

Figure 3: Robustness of ***p*-*F*-*J*** Upwind artificial compressibility in truly incompressible material.

5. Conclusion

This paper introduces a second order Updated Lagrangian vertex centred finite volume algorithm in the numerical simulation of large strain solid dynamics. A mixed formulation written in the form of a system of first order hyperbolic equations is employed. The linear momentum $\boldsymbol{p}$, the deformation gradient $\boldsymbol{F}$ and the Jacobian J are regarded as primary conservation variables. The overall scheme shows excellent behaviour in truly and nearly incompressible bending dominated scenarios without spurious pressure oscillations, yielding second order of convergence for velocities and stresses.

Acknowledgement

The first author gratefully acknowledge the financial support provided by the Erasmus Mundus Program (SEED). The second and third authors acknowledge the financial support provided by the Sêr Cymru National Research Network for Advanced Engineering and Materials, United Kingdom.

References

[1] M. Aguirre, A. J. Gil, J. Bonet and C. H. Lee. An upwind vertex centred finite volume solver for Lagrangian solid dynamics. *JCP*, 300, 387–422, 2015.

[2] A. J. Gil, C. H. Lee, J. Bonet and M. Aguirre. A stabilised Petrov-Galerkin formulation for linear tetrahedral elements in compressible, nearly incompressible and truly incompressible fast dynamics. *CMAME*, 276, 659–690, 2014.

[3] M. Aguirre, A. J. Gil, J. Bonet and A. A. Carreño. A vertex centred finite volume Jameson–Schmidt–Turkel (JST) algorithm for a mixed conservation formulation in solid dynamics. *JCP*, 259, 672–699, 2014.

Proceedings of the 24th UK Conference of the
Association for Computational Mechanics in Engineering
31 March - 01 April 2016, Cardiff University, Cardiff

Solution of three dimensional transient heat diffusion problems using an enriched finite element method

***M. Iqbal[1], M.S. Mohamed[1], O. Laghrouche[1], H. Gimperlein[2,3], M. Seaid[4], J. Trevelyan[4]**

[1]Institute for Infrastructure and Environment, Heriot Watt University, Edinburgh, EH14 4AS
[2]Maxwell Institute for Mathematical Sciences and Department of Mathematics, Heriot Watt University, Edinburgh, EH14 4AS
[3]Department of Mathematics, University of Paderborn, Warburger Str. 100, 33098 Paderborn, Germany
[4]School of Engineering and Computing Sciences, Durham University, Durham, DH1 3LE

*mi130@hw.ac.uk

ABSTRACT

We propose an enriched finite element method for the solution of three dimensional transient heat diffusion problems. The steep gradient of the solution is captured by a suitable enrichment of the finite element space. We use multiple exponential functions to enrich the solution space. This results in an efficient method, as is illustrated in an example problem with known analytical solution. In this problem we compare the proposed scheme with a standard FEM discretization. It is shown that the enriched FEM strongly reduces the necessary number of degrees of freedom to achieve a prescribed accuracy.

Key Words: *partition of unity method; 3D heat diffusion problems; enrichment functions*

1. Introduction

For decades FEM has been used for solving complex problems in many engineering and scientific applications. This method has shown significant accuracy and robustness for complex problems governed by steady-state PDEs. Solving time-dependent PDEs on complex geometries is still a substantial task for FEM especially for 3D problems. To overcome these difficulties various generalized and meshless numerical methods have been introduced in the recent decades. Partition of unity method PUFEM is one of the important subclass of these methods which was introduced by Melenk and Babuska [1].

The Partition of Unity Method is used for a wide variety of engineering and scientific applications. Shadi *et al* [2] solved two dimension transient heat diffusion problem using FEM and PUFEM. The authors compared results for both the methods and showed the efficiency of PUFEM compared to FEM. A full description of the use of PUFEM for different heat transfer applications can be found in their work. In the current work we exploit the PUFEM to solve 3D transient diffusion problem and show its efficiency as compared to FEM. In the proceeding section we present the formulation of the transient diffusion problem with selected initial and boundary conditions followed by its weak formulation. In Section 3, we present partition of unity method to solve the problem considered with some numerical results presented in Section 4. In Section 5 some concluding remarks are presented.

2. Weak formulation and numerical approximation

Given an open bounded domain $\Omega \subset \mathbb{R}^2$ with boundary Γ and a given time interval $]0,T]$, we consider the transient heat diffusion equation

$$\frac{\partial u}{\partial t} - \lambda \Delta u = f(t,\mathbf{x}), \qquad \text{in }]0,T] \times \Omega \tag{1}$$

where $\mathbf{x} = (x,y,z)^T$ are the spatial coordinates, t is the time variable, $\lambda > 0$ is the diffusion coefficient and $f(t,\mathbf{x})$ represents the effects of internal heat sources/sinks. We consider an initial condition

$$u(t=0,\mathbf{x}) = U_0(\mathbf{x}), \qquad \mathbf{x} \in \Omega \tag{2}$$

where $U_0(\mathbf{x})$ is a prescribed initial field. We impose Robin–type boundary condition

$$\frac{\partial u}{\partial n} + hu = g, \qquad \text{in }]0,T] \times \Gamma \tag{3}$$

Here $\mathbf{n}$ denotes the outward unit normal on the boundary Γ, and $h \geq 0$ is the heat convection coefficient on Γ, and g represents boundary sources.
To solve equation (1)-(3) numerically, the time interval is divided into N_t subintervals $[t_n, t_{n+1}]$ with duration $\Delta t = t_{n+1} - t_n$ for $n = 0, 1, ...N_t$ and then discretized it using an implicit scheme

$$\frac{u^{n+1} - u^n}{\delta t} - \lambda \nabla^2 u^{n+1} = f(t_{n+1}, \mathbf{x}) \tag{4}$$

This can be rearranged as

$$-\nabla^2 u^{n+1} + k u^{n+1} = F \tag{5}$$

where F and k are defined as

$$F = k\left(\delta t f(t_{n+1}, \mathbf{x}) + u^n\right), \qquad k = \frac{1}{\lambda \delta t}$$

To solve equation (5) with FEM we first multiply the equation with a weighting function, W, and then integrate over Ω

$$-\int_\Omega W \nabla^2 u^{n+1} d\Omega + \int_\Omega W k u^{n+1} d\Omega = \int_\Omega W F d\Omega \tag{6}$$

Applying the divergence theorem, substituting the initial and boundary conditions and taking g=0, the final weak form is given by

$$\int_\Omega (\nabla W \cdot \nabla u^{n+1} + W k^2 u^{n+1}) d\Omega + \int_\Gamma W h u^{n+1} d\Gamma = \int_\Omega W F d\Omega + \int_\Gamma W g \, d\Gamma \tag{7}$$

3. Solving the problem with FEM and PUFEM

To solve the weak form (7) with FEM, the domain Ω is approximated as a set of elements where the temperature over each element is approximated using the nodal values and polynomial shape functions

$$u = \sum_{i=1}^{n} N_i u_i \tag{8}$$

In the PUFEM these nodal values u_i are written as combination of enrichment functions. Here we propose using the following global exponential basis functions to enrich the solution space

$$G_q(\mathbf{x}) = \frac{e^{-\left(\frac{R_0}{C}\right)^q} - e^{-\left(\frac{R_c}{C}\right)^q}}{1 - e^{-\left(\frac{R_c}{C}\right)^q}}, \qquad q = 1, 2, ...Q \tag{9}$$

With $R_0 := | \mathbf{x} - \mathbf{x}_c |$ being the distance from the function control point x_c to the point x. The constants $R_c = \sqrt{\frac{14}{1.195}}$ and $C = \frac{1}{1.195}$ controls the shape of the exponential function G_q.
Considering the aforementioned enrichment, the nodal values might be rewritten as

$$u_i = \sum_{q=1}^{Q} A_j^q \frac{e^{-\left(\frac{R_0}{C}\right)^q} - e^{-\left(\frac{R_c}{C}\right)^q}}{1 - e^{-\left(\frac{R_c}{C}\right)^q}} \tag{10}$$

Using (10) to rewrite (8) we get

$$u = \sum_{j=1}^{M} \sum_{q=1}^{Q} A_j^q N_j \frac{e^{-\left(\frac{R_0}{C}\right)^q} - e^{-\left(\frac{R_c}{C}\right)^q}}{1 - e^{-\left(\frac{R_c}{C}\right)^q}} \tag{11}$$

Where FEM is now used to find the unknowns A_j^q instead of the nodal values, u_i.

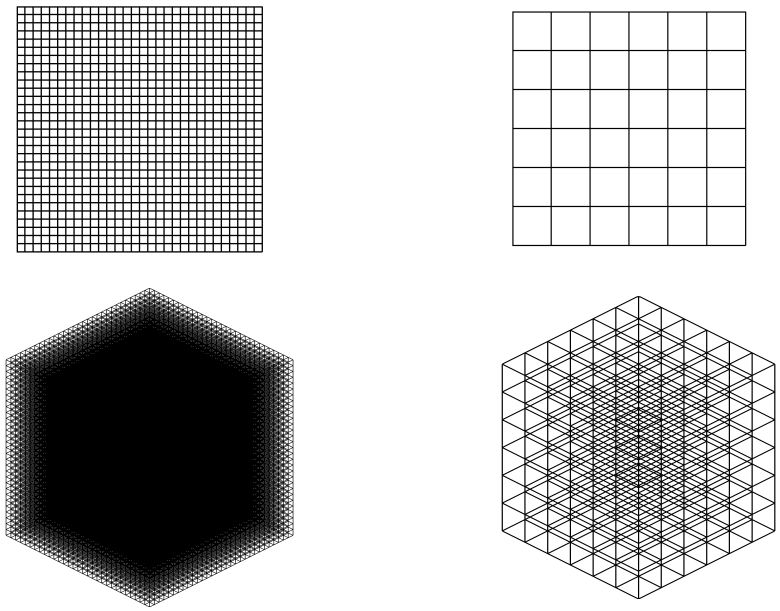

Figure 1: 3D mesh used for FEM (left) and PUFEM (right)

4. Numerical Results

In this section, we present results for the transient heat diffusion problem given by (1) - (3) using the classical FEM approach and the PUFEM approach. As a test example with consider a diffusion problem in 3D domain Ω defined by ($\mathbf{x} \in \Omega$; $0 \leq \mathbf{x} \leq 2$). For the proposed problem, reaction term $f(t,\mathbf{x})$, the boundary function g and the initial condition $u_0(\mathbf{x})$ are chosen such that the exact solution is given by

$$U(\mathbf{x},t) = x^{20}(2-x)^{20}y^{20}(2-y)^{20}z^{20}(2-z)^{20}(1-e^{-\lambda t}) \tag{12}$$

where t is the time variable and $\mathbf{x} = (x,y,z)^T$ are the spatial coordinates. To quantify the error in both FEM and PUFEM, we use the l_2 norm error defined as

$$l_2 = \frac{||u-U||_{L^2(\Omega)}}{||U||_{L^2(\Omega)}} \times 100 \tag{13}$$

where u and U are the numerical and exact solutions respectively. Our aim is to compare the results of the proposed problem using the standard FEM and the PUFEM. For both the FEM and PUFEM computations we use the parameter h=1, the heat diffusion coefficient λ=0.1 and the time step value Δt =0.001. All integrals over Ω are evaluated numerically using Gaussian quadrature with 20 integration points in each direction for PUFEM and 2 integration points for FEM. A direct solver is used to solve the resulting system of equations. For convergence of solution, we considered h-refinement for FEM and Q refinement for PUFEM. In case of FEM, we started with a coarse mesh of 1000 elements having total 1331 degrees of freedoms (DoFs) with which we get l_2 error of 8.7 % at t=0.05. We refined the mesh gradually until we get l_2 error of 0.62 % with 27000 elements having total 29791 DoFs. For the PUFEM we used a fixed mesh of 216 elements and four different number of enrichment functions Q = 3,4,5 and 6 having total 1029, 1372, 1715 and 2058 DoFs respectively. In case of PUFEM we get a comparable l_2 error of 0.69 % with only 1715 DoFs. Figure 1 shows the meshes used to get a comparable error for both FEM and PUFEM.

Figure 2 compares the convergence of FEM and PUFEM at different time intervals. On graph the log of DoFs is plotted on the abscissa while on ordinate l_2 error is plotted on logarithmic scale. It is clear from the graphs that PUFEM converges much faster than FEM and gives better l_2 error with lesser DoFs.

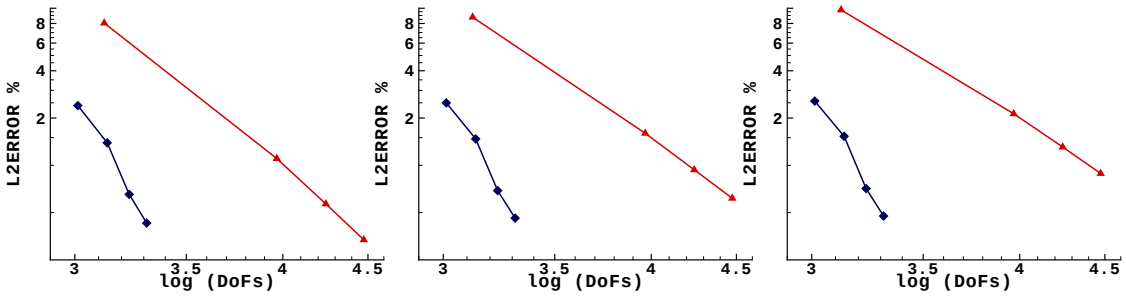

(a) t =0.01 (b) t =0.05 (c) t =0.1

Figure 2: L2 error for FEM and PUFEM with increasing no of DoFs

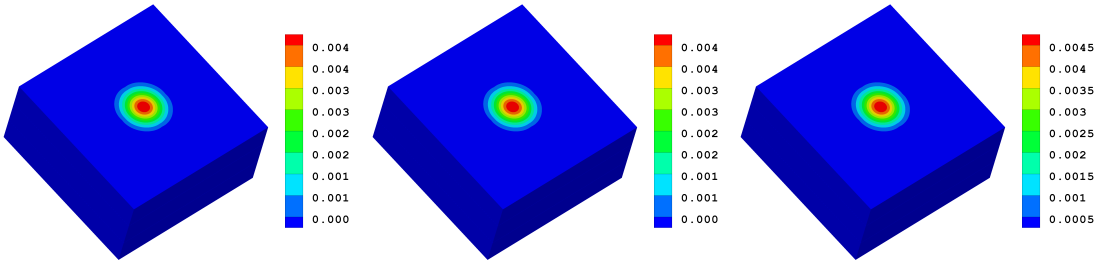

(a) exact solution (b) FEM (c) PUFEM

Figure 3: Temperature distribution in the middle of domain at t =0.05

Figure 3 shows the temperature distribution at t=0.05 for the exact, FEM and PUFEM solution with 4 enrichment functions. For both FEM and PUFEM we are getting the same temperature trends as that of the exact solution but in case of PUFEM the total DoFs used to get the solution is only a small fractions of that used to obtained the solution with FEM.

5. Conclusions

We used FEM and PUFEM to solve time-dependent heat diffusion problem in 3D domain. The solution space was enriched with an approximate solution describing the heat diffusion decay. For a specified no of DoFs, we calculated l_2 error for both the methods. We concluded that for a comparable accuracy PUFEM requires less DoFs than FEM. Numerical results show that with PUFEM the total DoFs are less than 10 % of that used with FEM. Due to its higher accuracy and requiring less computational resources, the PUFEM can be used as an attractive alternative for the solution of heat diffusion problems.

Acknowledgements

H. G. acknowledges support by ERC Advanced Grant HARG 268105.
M. Iqbal acknowledges support of Heriot Watt University for providing the James Watt Scholarship.

References

[1] J.M. Melenk and I. Babuska. The partition of unity finite element method: basic theory and applications. *Computer methods in applied mechanics and engineering*, 139(1): 289-314, 1996.

[2] M.S. Mohamed, M. Seaid, J. Trevelyan and O. Laghrouche. A partition of unity FEM for time-dependent diffusion problems using multiple enrichment functions. *International Journal for Numerical Methods in Engineering*, 93(3): 245-265, 2013a.

Proceedings of the 24th UK Conference of the
Association for Computational Mechanics in Engineering
31 March - 01 April 2016, Cardiff University, Cardiff

A stabilised Total Lagrangian Corrected Smooth Particle Hydrodynamics (CSPH) in large strain explicit solid dynamics

***G. Greto[1], S. Kulasegaram[1], C. H. Lee[2], A. J. Gil[2], and J. Bonet[3]**

[1]Cardiff University, The Parade, Cardiff, CF24 3AA
[2]Swansea University, Bay Campus, Swansea, SA1 8EN
[3]University of Greenwich, London, SE10 9LS

*GretoG@cardiff.ac.uk

ABSTRACT

An explicit Total Lagrangian mixed momentum/strains formulation [2], in the form of a system of first order conservation laws, has been recently proposed to overcome the shortcomings posed by the traditional second order displacement-based formulation, namely: (1) bending and volumetric locking difficulties; (2) hydrostatic pressure fluctuations; and (3) reduced order of convergence for derived variables. Following the work of Bonet and Kulasegaram [4, 5], the main objective of this paper is the adaptation of Corrected Smooth Particle Hydrodynamics (CSPH) in the context of Total Lagrangian mixed formulation. Appropriate nodally conservative Jameson-Schmidt-Turkel (JST) stabilisation is introduced taking advantage of the conservation laws. A mixed linear momentum/deformation gradient technique performs extremely well in nearly incompressible bending dominated scenarios [1, 2] without the appearance of spurious pressure oscillations. As both linear momentum and deformation gradient are used as primary variables of the system, equal order of approximation is achieved in both fields. A series of numerical examples are carried out to assess the applicability and robustness of the proposed algorithm.

Keywords: *Conservation laws; SPH; Locking; Incompressibility; Fast dynamics; JST*

1. Introduction

Dynamic explicit displacement-based finite element codes, based on low order finite element technology, are commonly used for the simulation of large strain impact problems by aerospace, automotive, biomedical, defence and manufacturing industries. In these codes, the 8-noded underintegrated hexahedral element is the preferred option to model solid components. Many practical applications (i.e. crashworthiness and drop-impact modelling), however, experience extremely large solid deformations accompanied by severe mesh distortion. This may lead to poorly shaped elements unless some form of adaptive remeshing is applied.

From the viewpoint of spatial discretisation, the standard displacement-based formulation for low order elements is known to experience locking difficulties in nearly-incompressible, bending dominated scenarios. It is also known that the use of linear interpolation within a finite element leads to second order convergence for the primary variables, but one order less for derived variables. From the time discretisation point of view, the Newmark method has a tendency to introduce high frequency noise in the solution field, especially in the vicinity of sharp spatial gradients.

To overcome the shortcomings mentioned above, a mixed methodology [1, 2] is presented in the form of a system of first order conservation laws, where the linear momentum and the deformation gradient tensor are regarded as the two main conservation variables. In addition, this approach enables the deviatoric and volumetric stresses (or strains) to converge at the same rate as the velocities (or displacements).

The main goal of this paper is the introduction of a stabilised Corrected Smooth Particle Hydrodynamics (CSPH) methodology, tailor-made for this mixed formulation. The adoption of a system of first order conservation laws allows CFD techniques to be introduced for the very first time within the context of particle methods, in the form of an adapted nodally conservative JST stabilisation [2]. JST will be used to provide artificial (numerical) dissipation and shock-capturing capabilities. In particular, the second order (harmonic) and fourth order (biharmonic) operators employed in the JST stabilisation can be readily obtained by closed-form differentiation of the interpolating kernel functions. A quintic kernel approximation [4, 5] is suitably used, due to the presence of the biharmonic JST operator.

2. Reversible elastodynamics

The motion of a deformable continuum body from an initial (or undeformed) configuration $\boldsymbol{X} \in V \subset \mathbb{R}^3$ to a current (or deformed) configuration $\boldsymbol{x} \in v(t) \subset \mathbb{R}^3$ can be described by the relation $\boldsymbol{x} = \boldsymbol{\phi}(\boldsymbol{X}, t)$, where $\boldsymbol{\phi}$ links each material particle in $\boldsymbol{X}$ to its current position $\boldsymbol{x}$ at time t during the motion. In the case of isothermal process, a mixed formulation in the form of a system of first order conservation laws for elastodynamics can be cast as [1, 2]:

$$\frac{\partial \boldsymbol{p}}{\partial t} - \boldsymbol{\nabla}_0 \cdot \boldsymbol{P}(\boldsymbol{F}) = \rho_0 \boldsymbol{b}\,; \qquad \frac{\partial \boldsymbol{F}}{\partial t} - \boldsymbol{\nabla}_0 \cdot \left(\frac{1}{\rho_0} \boldsymbol{p} \otimes \boldsymbol{I}\right) = \boldsymbol{0}. \tag{1}$$

Here, $\boldsymbol{p} = \rho_0 \boldsymbol{v}$ is the linear momentum per unit of undeformed volume, ρ_0 is the material density, $\boldsymbol{v}$ represents the velocity field, $\boldsymbol{P}$ is the first Piola-Kirchhoff stress tensor, $\boldsymbol{b}$ is the body force per unit mass, $\boldsymbol{F}$ is the deformation gradient and $\boldsymbol{I}$ is the identity matrix. The notation $\boldsymbol{\nabla}_0$ denotes the material gradient operator in undeformed space, where $[\boldsymbol{\nabla}_0]_I \equiv \frac{\partial}{\partial X_I}$. In a more compact form, system (1) reads:

$$\frac{\partial \boldsymbol{\mathcal{U}}}{\partial t} + \frac{\partial \boldsymbol{\mathcal{F}}_I}{\partial X_I} = \boldsymbol{\mathcal{S}}; \qquad \forall I = 1, 2, 3; \tag{2}$$

where $\boldsymbol{\mathcal{U}}$ is the vector of conservation variables, $\boldsymbol{\mathcal{F}}_I$ is the flux vector in the material direction I and $\boldsymbol{\mathcal{S}}$ is the source term described by:

$$\boldsymbol{\mathcal{U}} = \begin{bmatrix} \boldsymbol{p} \\ \boldsymbol{F} \end{bmatrix}; \qquad \boldsymbol{\mathcal{F}}_{\boldsymbol{N}} = \boldsymbol{\mathcal{F}}_I N_I = \begin{bmatrix} -\boldsymbol{P}\boldsymbol{N} \\ -\frac{1}{\rho_0}\, \boldsymbol{p} \otimes \boldsymbol{N} \end{bmatrix}; \qquad \boldsymbol{\mathcal{S}} = \begin{bmatrix} \rho_0 \boldsymbol{b} \\ \boldsymbol{0} \end{bmatrix}. \tag{3}$$

For closure of the above system (1), it is necessary to introduce an appropriate constitutive law by relating $\boldsymbol{P}$ with $\boldsymbol{F}$. For simplicity, a standard hyperelastic neo-Hookean model is used, whereby the first Piola $\boldsymbol{P}$ can be decomposed into the summation of deviatoric, $\boldsymbol{P}_{dev}$, and volumetric, $\boldsymbol{P}_{vol}$, contributions:

$$\boldsymbol{P} = \boldsymbol{P}_{dev} + \boldsymbol{P}_{vol}; \quad \boldsymbol{P}_{dev} = \mu J^{-2/3} \left(\boldsymbol{F} - \frac{1}{3}(\boldsymbol{F} : \boldsymbol{F})\, \boldsymbol{F}^{-T}\right); \quad \boldsymbol{P}_{vol} = p\boldsymbol{H}; \quad p = \kappa(J-1); \quad J = \det \boldsymbol{F}; \quad \boldsymbol{H} = J\boldsymbol{F}^{-T}. \tag{4}$$

3. Numerical methodology

In this section, the mixed $\boldsymbol{p}$-$\boldsymbol{F}$ system described by equation (1) will be discretised in space using the CSPH particle method with added dissipation from the JST technique ($\boldsymbol{p}$-$\boldsymbol{F}$ *JST-CSPH* scheme). To achieve this, and following the work of Bonet and co-authors [4, 5], the weak statement for the linear momentum evolution (1a) must be obtained through the use of work-conjugate principles [1] and integration by parts:

$$\int_V \delta \boldsymbol{v} \cdot \frac{\partial \boldsymbol{p}}{\partial t} dV = \int_V \delta \boldsymbol{v} \cdot \rho_0 \boldsymbol{b} dV + \int_{\partial V} \delta \boldsymbol{v} \cdot \boldsymbol{t}^B dA - \int_V \boldsymbol{P} : \boldsymbol{\nabla}_0 \delta \boldsymbol{v}\, dV. \tag{5}$$

Upon application of the particle integration on the above expression (5), and using the kernel approximation $\boldsymbol{\nabla}_0 \delta \boldsymbol{v}(\boldsymbol{X}) = \sum_{b \in \Lambda_X^b} V_b\, \delta \boldsymbol{v}_b \otimes \boldsymbol{\nabla}_0 W_b(\boldsymbol{X})$ to express the arbitrary virtual velocity field $\delta \boldsymbol{v}$, one obtains:

$$\frac{d\boldsymbol{p}_a}{dt} = \rho_0 \boldsymbol{b}_a + \frac{A_a}{V_a} \boldsymbol{t}_a^B + \sum_{b \in \Lambda_a^b} V_b\, (\boldsymbol{P}_b + \boldsymbol{P}_a)\, \tilde{\boldsymbol{\nabla}}_0 W_b(\boldsymbol{X}_a). \tag{6}$$

where V_b is the volume fraction assigned to the particle in $\boldsymbol{x}_b$ and $W_b(\boldsymbol{X})$ is the kernel function value there. Following References [3–6], the first Piola-Kirchhoff stress tensors $\{\boldsymbol{P}_a, \boldsymbol{P}_b\}$ are further approximated by using the coefficients directly from the particles. In (6), corrections are introduced on the kernel gradient to yield $\tilde{\boldsymbol{\nabla}}_0 W_b(\boldsymbol{X}_a)$, ensuring the correct evaluation of a gradient of a general linear function [4]. However, the above semi-discrete formulation still suffers from the appearance of accumulated numerical instabilities over a long term response. To put a remedy to this, in contrast to the dissipative mechanism introduced by Monaghan [4] through viscous fluxes, here an adapted nodally conservative JST stabilisation $\boldsymbol{\mathcal{D}}(\boldsymbol{p}_a)$ will be incorporated into (6), mirroring CFD techniques [2]:

$$\frac{d\boldsymbol{p}_a}{dt} = \rho_0 \boldsymbol{b}_a + \frac{A_a}{V_a} \boldsymbol{t}_a^B + \sum_{b \in \Lambda_a^b} V_b\, (\boldsymbol{P}_b + \boldsymbol{P}_a)\, \tilde{\boldsymbol{\nabla}}_0 W_b(\boldsymbol{X}_a) + \boldsymbol{\mathcal{D}}(\boldsymbol{p}_a). \tag{7}$$

The nodally conservative JST stabilisation is additively decomposed into a second order (harmonic) operator $\mathcal{D}_2(\boldsymbol{p}_a)$ and a fourth order (biharmonic) operator $\mathcal{D}_4(\boldsymbol{p}_a)$:

$$\mathcal{D}(\boldsymbol{p}_a) = \mathcal{D}_2(\boldsymbol{p}_a)+\mathcal{D}_4(\boldsymbol{p}_a) = \kappa^{(2)} c_p\, h_{\min} \sum_{b\in\Lambda_a^b} V_b\,(\boldsymbol{p}_b - \boldsymbol{p}_a)\,\tilde{\Delta}_0 W_b(\boldsymbol{X}_a) - \kappa^{(4)} c_p\, h_{\min}^3 \sum_{b\in\Lambda_a^b} V_b\,(\Delta_0\boldsymbol{p}_b - \Delta_0\boldsymbol{p}_a)\,\tilde{\Delta}_0 W_b(\boldsymbol{X}_a), \tag{8}$$

where c_p is the pressure wave speed, h_{min} is the particle spacing, $\kappa^{(2)}$ and $\kappa^{(4)}$ are user-defined parameters and $\tilde{\Delta}_0$ represents the corrected Laplacian operator [6]. In regard to the fibre map evolution (1b), the application of particle collocation method [4] directly on (1b), along with the use of kernel approximation W, leads to:

$$\frac{d\boldsymbol{F}_a}{dt} = \boldsymbol{\nabla}_0 \boldsymbol{v}\Big|_a \approx \sum_{b\in\Lambda_a^b} \frac{V_b}{\rho_0}\,(\boldsymbol{p}_b - \boldsymbol{p}_a) \otimes \tilde{\boldsymbol{\nabla}}_0 W_b(\boldsymbol{X}_a). \tag{9}$$

Finally, the set of stabilised particle equations (7) and (9) can then be explicitly integrated from time step t^n to t^{n+1}. In this case, the explicit one-step two-stage Total Variation Diminishing Runge Kutta (TVD-RK) time integrator [1, 2] is preferred due to its excellent TVD properties. Along with $\boldsymbol{p}$ and $\boldsymbol{F}$, the geometry, $\boldsymbol{x}$, is also advanced in time using the exact same time integrator in a monolithic manner. As described in [1], the scheme is suitably modified to guarantee the conservation of angular momentum.

4. Applications

A series of benchmark examples are assessed in order to test the applicability and effectiveness of the ***p*-*F*** JST-CSPH mixed algorithm over the Total Lagrangian CSPH displacement based formulation [4, 5].

- Tension instability [5, 6]: a 1D bar is clamped on one end and left free at the other, where is given an initial velocity of $5\,m/s$. Fig. 1a shows the velocity history at the free tip. The bar is discretised in space using the ***p*-*F*** JST-CSPH method. The JST term here has a decisive effect towards the achievement of a more accurate solution. The Total Lagrangian setting ensures the simulation does not suffer from tensile instability, a recurring issue for solid mechanics SPH simulations.
- Bending scenario [1, 2]: a bottom end clamp is imposed at $t = 0\,s$ on a 3D column of length $6\,m$, with unit cross section, initially travelling at constant side velocity $v = 10\,m/s$. Fig. 1b testifies to the good performance of the model in a bending dominated scenario.
- Robustness [1, 2]: the column of the previous example is subjected to a sinusoidal angular velocity and its bottom is clamped. A comparison between fig. 1c (standard CSPH) and fig. 1d (***p*-*F*** JST-CSPH) illustrates the robustness of the mixed Total Lagrangian method [4, 5]: while the simulation in fig. 1c fails after a few time steps, the one in fig. 1d accurately captures the structure behaviour.
- Extremely large distortions [6]: a rectangular region of $3\,cm \times 1\,cm$ is punched with a constant vertical velocity of $-10\,m/s$ on one-third of the top surface. As reported in [6], the standard CSPH method [4, 5] is not capable of solving this problem, which involves extremely large distortions. This deficiency can be alleviated using the proposed algorithm (see fig. 1e).
- Pressure instabilities [1, 2]: a 3D rubber cube of unit side length is left free at the top face and is constrained with rollers on the other sides. The right half of the domain experiences a prescribed punch velocity of $-100\,m/s$. As seen in fig. 1f, the ***p*-*F*** JST-CSPH algorithm eliminates the appearance of non-physical pressure fluctuations in near incompressibility.

5. Conclusions

In this paper, a stabilised Total Lagrangian mixed formulation ***p*-*F*** JST-CSPH algorithm is introduced for the numerical analysis of large strain solid dynamics. The methodology is based upon a system of first order conservation laws, where the linear momentum $\boldsymbol{p}$ and the deformation gradient $\boldsymbol{F}$ are regarded as the primary variables. A nodally conservative JST stabilisation is incorporated into the CSPH algorithm, taking advantange of the conservation laws. Finally, results from numerical simulations of benchmark problems are presented in order to demonstrate the applicability and robustness of the proposed methodology.

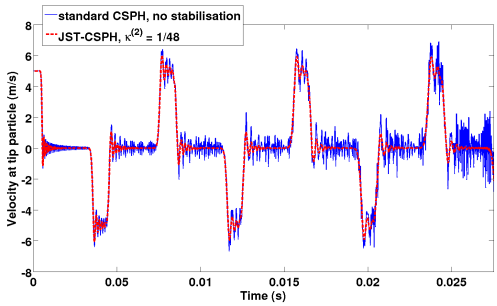

(a) 1d tensile test, ***p*-*F*** JST-CSPH based model

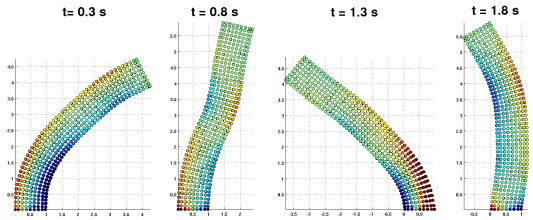

(b) Bending simulation, ***p*-*F*** JST-CSPH based model [1, 2]

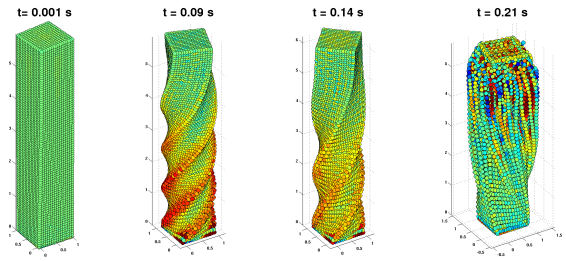

(c) Robustness: Standard CSPH based model [4, 5]

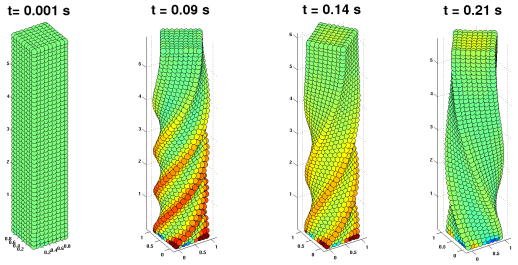

(d) Robustness: ***p*-*F*** JST-CSPH based model [1, 2]

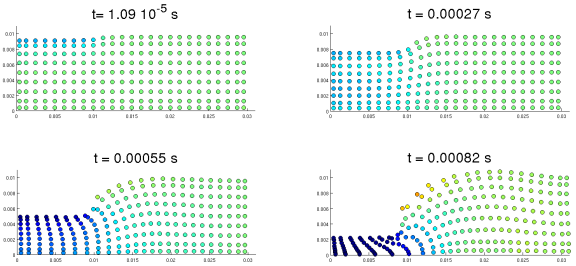

(e) Large distortions: ***p*-*F*** JST-CSPH [1, 2]

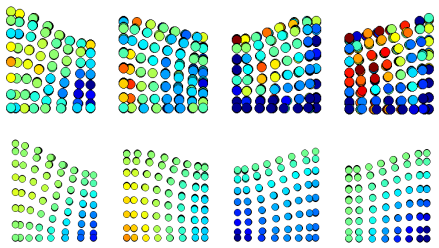

(f) Pressure instabilities: [Top] Standard CSPH [4, 5]; [Bottom] ***p*-*F*** JST-CSPH [1, 2]

Acknowledgements

The authors gratefully acknowledge the financial support provided by the Sêr Cymru National Research Network for Advanced Engineering and Materials, United Kingdom.

References

[1] M. Aguirre, A. J. Gil, J. Bonet, A. A. Carreño. A vertex centred Finite Volume Jameson-Schmidt-Turkel algorithm for a mixed conservation formulation in solid dynamics. *JCP*, 259, 672–699, 2014.

[2] A. J. Gil, C. H. Lee, J. Bonet and R. Ortigosa. A first order hyperbolic framework for large strain computational solid dynamics. Part II: Total Lagrangian compressible, nearly incompressible and truly incompressible elasticity. *CMAME*, 300, 146–181, 2016.

[3] J. J. Monaghan. Smoothed particle hydrodynamics. *ARA&A*, 30, 543–574, 1992.

[4] J. Bonet, S. Kulasegaram. Correction and stabilization of smooth particle hydrodynamics methods with applications in metal forming simulations. *IJNME*, 47, 1189–1214, 2000.

[5] J. Bonet, S. Kulasegaram. Remarks on tension instability of Eulerian and Lagrangian Corrected Smooth Particle Hydrodynamics (CSPH) methods. *IJNME*, 52, 1203–1220, 2001.

[6] Y. Vidal, J. Bonet and A. Huerta. Stabilized updated Lagrangian corrected SPH for explicit dynamic problems. *IJNME*, 69, 2687–2710, 2007.

Proceedings of the 24th UK Conference of the
Association for Computational Mechanics in Engineering
31 March– 01 April 2016, Cardiff University, Cardiff

Two level layup optimization of composite plate using lamination parameters

*** X. Liu, H. Patel, C.A. Featherston and D. Kennedy**

[1]School of Engineering, Cardiff University, Queens Buildings, The Parade, Cardiff, CF24 3AA

* LiuX72@cardiff.ac.uk

ABSTRACT

This paper presents a technique for the global layup optimization of laminated composite plates with initial buckling constraints based on lamination parameters. The method is computationally more efficient than previous solutions. The optimization problem is divided into two stages with continuous optimization followed by discrete optimization, in order to achieve the final optimum layup effectively using 0, 90, 45 and -45 plies. During the first stage, the optimal plate thickness and lamination parameters are obtained using VICONOPT, an exact finite strip software for the optimisation of prismatic plates and stiffened panels. In the second stage, a Matlab program based on the branch and bound method incorporating a layerwise technique is used to find the optimal stacking sequences to achieve the required lamination parameters obtained from stage 1. Moreover, the Matlab program is able to ensure the layup to be symmetric, balanced or both.

Keywords: *layup optimization, lamination parameter, branch and bound, buckling, composite*

1. Introduction

Composite material is increasingly used in aerospace structures because of its improved specific properties and ability to be optimized for particular application. Currently, the industry is substituting laminated composites for more conventional aircraft materials, but their optimization is still a challenging task. Miki and Sugiyama [1] used lamination parameters to optimize orthotropic and symmetric composite plates, significantly reducing the number of design variables but the stacking sequence obtained was unable to satisfy the discrete constraint. Yamazaki [2] first solved this obstacle by using a two-step optimization method in which gradient-based optimization was used in the first step, with genetic algorithms (GAs) then used to implement discrete optimization in the second. Herencia et al [3] developed a finite element method with a closed form (CF) solution and an energy method (Rayleigh-Ritz) used to compute buckling constraints in the first step, and then a GA for the second step. In Liu and Butler's work [4], GAs were also applied during the second stage, with VICONOPT (a buckling program based on the exact strip method and Wittrick-Williams algorithm [5]) used to minimise the panel's weight at the first stage. Kennedy [6] used a branch and bound method which combined with a layerwise technique in the second step was able to match the optimal values of lamination parameters found by VICONOPT in the first step.

2. Methodology

In this paper, an alternative two stage process is implemented. During the first stage, lamination parameters are used as the design variables in VICONOPT. A linear optimizer which assumes local linear approximations to the buckling constraints is used in combination with a penalty function [6] to direct infeasible solutions towards feasible ones without violating any of the constraints. Thus the optimal lamination parameters $\{\xi_j^k\}$ $(j = 1,2,3; k = A, B, D)$ and the laminate thickness h for the continuous problem are found.

In the second stage, these lamination parameters are used as targets in a Matlab program which then finds the stacking sequences which give lamination parameters closest to these optimum values. The angles of each of the plies are restricted to four choices (i.e. 0° 90° 45° -45°), resulting in constraints

on the lamination parameters [7] described in Equation (1).

$$2\left|\xi_1^k\right| - \xi_2^k - 1 \leq 0, \quad 2\left|\xi_3^k\right| + \xi_2^k - 1 \leq 0, \quad k = \text{A, D} \tag{1}$$

Therefore the feasible region for $\left\{\xi_j^k\right\}\ (j = 1,2,3; k = A, D)$ is triangular as shown in Figure 1.

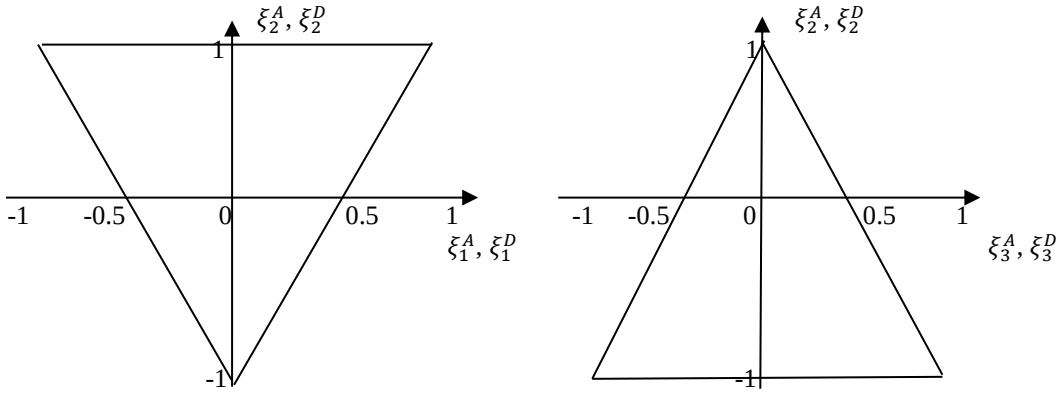

Figure 1: Feasible region for $\left\{\xi_j^k\right\}\ (j = 1,2,3; k = A, D)$

The Matlab program used can be used to constrain the layers to be symmetric, balanced or both. This programme which uses the branch and bound method calculates the contributions to the lamination parameter for each branch in different layers, as obtained from equation (2).

$$\begin{bmatrix} \xi_1^k \\ \xi_2^k \\ \xi_3^k \end{bmatrix} = \int_{-h/2}^{h/2} Z^k \begin{bmatrix} \cos 2\theta \\ \cos 4\theta \\ \sin 2\theta \end{bmatrix} dz \tag{2}$$

where $k = A, B, D, Z^A = \frac{1}{h}, Z^B = \frac{4z}{h^2}, Z^D = \frac{12z^2}{h^3}$, θ is the orientation of the fibres in laminas and z is the depth below the mid-plane.

From the lamination parameters, objective function contributions (Γ) are obtained by calculating the difference between the actual lamination parameter $\left(\xi_{0°,\pm 45°,90°}\right)$ and the required lamination parameter ($\xi_{required}$). Then from the summation of the objective function, the route to proceed with for the next branch (i.e. next layer) can be predicted, with the aim being to opt for a branch that is closest to the required lamination parameters.

The layerwise technique employed in this program enhances the optimization process. The ply orientations are successively altered, working inwards from the outer plies which make the most important contributions to the flexural lamination parameters. Initially only two plies are altered at once, then four at once, and so on until in the final cycle all of them can be altered. Thus the branch-and-bound method initially searches the stacking sequences by considering a small number of plies, so that good results can be obtained quickly by solving small problems. Subsequently, when considering larger numbers of plies, the previously found solutions give an upper bound on the objective function enabling many branches to be discarded without being explored. This layerwise approach helps to obtain the optimum layup efficiently whilst achieving a reduction in computational cost.

3. Examples and Results

A simply supported laminated composite plate of width 100mm and length 150mm is subject to longitudinal compression with a compressive load P_d of 10 kN and a shear load P_s of 0.011 kN/mm. The initial buckling load P_c for this plate is 10 kN. The ply thickness h_p is 0.1 mm and the initial laminate thickness is h_i 1.6 mm. The initial ply orientations chosen for this example are arbitrary, the initial lamination parameters corresponding to this initial layup are: $\xi_{1,}^{A}$= 0.0625, $\xi_{2,}^{A}$= -0.125, $\xi_{3,}^{A}$= 0.0625, $\xi_{1,}^{D}$= 0.0127, $\xi_{2,}^{D}$= -0.0723, $\xi_{3,}^{D}$= 0.0947, $\xi_{1,}^{B}$= -0.0078, $\xi_{2,}^{B}$= 0.1406, $\xi_{3,}^{B}$= 0.0859.

For the normal case, the results are illustrated in Table 1. After the first stage, the required lamination parameters are obtained by VICONOPT. Due to the initial buckling load P_c which is equal to the design load P_d, the reduction in laminate thickness is slight, and after rounding the optimized thickness h_0 to the nearest integer number of laminate thickness, the thickness of the optimized plate is 1.6 mm. The optimal sequences are listed at the bottom of the table, the value Γ - the difference between the lamination parameters of this sequences and the required lamination parameters being only 0.1379. The initial buckling load after optimization is 10.21 kN and the Matlab solution time is 141 seconds on a 4.00 GHz PC.

Table 1: Results for normal case

	ξ_1^A	ξ_2^A	ξ_3^A	ξ_1^D	ξ_2^D	ξ_3^D	ξ_1^B	ξ_2^B	ξ_3^B	h_0/h_i
After stage 1										
	0.0918	-0.1280	0.0334	-0.2372	-0.3766	-0.0930	-0.0095	0.0429	-0.0093	0.991
After stage 2										
	0.0625	-0.125	0.0625	-0.2158	-0.3887	0.1006	0.0078	0.0469	-0.0234	1

Ply	1	2	3	4	5	6	7	8	9	10	11	12	13	14	15	16	Γ	P_e, *kN*	Time, s
	90	-45	45	45	45	0	-45	0	-45	0	0	90	90	45	45	-45	0.1379	10.21	141

Table 2 demonstrates the results for the symmetric case, in which the three lamination parameters $\xi_{1,2,3}^{B}$ were forced to be zero to guarantee symmetric stacking sequences. In this case the final value of Γ is 0.2696 and the solution time is 0.4 second.

Table 2: Results for symmetric case

	ξ_1^A	ξ_2^A	ξ_3^A	ξ_1^D	ξ_2^D	ξ_3^D	ξ_1^B	ξ_2^B	ξ_3^B	h_0/h_i
After stage 1										
	0.0431	-0.1143	0.0431	-0.2334	-0.3466	0.075	0	0	0	0.992
After stage 2										
	0	0	0	-0.1875	-0.3281	0.0703	0	0	0	1

Ply	1	2	3	4	5	6	7	8	9	10	11	12	13	14	15	16	Γ	P_e, *kN*	Time, s
	45	90	-45	-45	0	45	90	0	0	90	45	0	-45	-45	90	45	0.2696	10.02	0.4

The balanced case is shown in Table 3. The lamination parameter ξ_3^A is forced to be zero to achieve the balanced layup. The final value of Γ is 0.367, solution time is 10 seconds.

Table 3: Results for balanced case

	ξ_1^A	ξ_2^A	ξ_3^A	ξ_1^D	ξ_2^D	ξ_3^D	ξ_1^B	ξ_2^B	ξ_3^B	h_0/h_i
After stage 1										
	0.0349	-0.1526	0	-0.2458	-0.3199	0.1188	0.0152	0.0805	0.0552	0.994
After stage 2										
	0	-0.25	0	-0.2344	-0.3086	0.0586	0.0156	-0.0625	0.0469	1

Ply	1	2	3	4	5	6	7	8	9	10	11	12	13	14	15	16	Γ	P_e, *kN*	Time, s
	90	-45	45	45	0	-45	-45	90	0	45	0	45	-45	-45	90	45	0.367	10.13	10

When the stacking sequence is required to be symmetric and balanced, the four lamination parameters ξ_3^A, $\xi_{1,2,3}^B$, must be zero during the two-stages of the optimization. Table 4 illustrates the results of this case in which $\Gamma = 0.244$ and the solution time for the second stage is 0.15 seconds.

Table 4: Results for symmetric and balanced case

	ξ_1^A	ξ_2^A	ξ_3^A	ξ_1^D	ξ_2^D	ξ_3^D	ξ_1^B	ξ_2^B	ξ_3^B	h_0/h_i
After stage 1										
	0.0383	-0.1099	0	-0.2422	-0.3512	0.0842	0	0	0	0.991
After stage 2										
	0	0	0	-0.2813	-0.375	0.1172	0	0	0	1

Ply	1	2	3	4	5	6	7	8	9	10	11	12	13	14	15	16	Γ	P_e, *kN*	Time, s
	45	-45	90	90	45	-45	0	0	0	0	-45	45	90	90	-45	45	0.244	10	0.15

The values of Γ in these four different cases are all close to zero illustrating the excellent performance of the Matlab program. All of the final sequences given by the second stage can carry the design load. The time to complete the optimization for these examples is short, especially when the layup is forced to be symmetric and balanced, showing the ability of the method to reduce the search time.

4. Conclusions

A new two-stage method to perform global layup optimization of laminated composite plates with initial buckling constraints has been presented. In the first stage, lamination parameters are used as design variables in VICONOPT to find the optimal plate thickness and required lamination parameters for stage two. The Matlab program used in the second stage employs the branch and bound method and a layerwise technique to find the optimal stacking sequences which can be forced to be symmetric, balanced or both. The results of four examples with different requirements presented in this paper show the versatility of this two-stage method, with the time taken for this global optimization illustrating its efficiency.

References

[1] M. Miki and Y. Sugiyama. Optimum design of laminated composite plates using lamination parameters. *AIAA Journal*, 31 (5), pp. 921-922. 1993.

[2] K. Yamazaki. Two-level optimization technique of composite laminate panels by genetic algorithms. *Proceedings of the 37th AIAA/ASME/ASCE/AHS/ASC*, pp. 1882-1887. 1996.

[3] J. E. Herencia, P. M. Weaver, M. I. Friswell. Initial sizing optimization of anisotropic composite panels with T-shaped stiffeners. *AIAA Journal* 46 (4), pp. 399-412. 2008.

[4] W. Liu, R. Butler, H. A. Kim. Optimization of composite stiffened panels subject to compression and lateral pressure using a bi-level approach. *Struct. Mult. Opt. DOI 10.1007/s00158-007-0156-9*. pp. 235-245. 2008.

[5] W, H, Wittrick and F. W. Williams. An algorithm for computing critical buckling loads of elastic structures. *Journal of Mechanical Sciences* 1 (4), pp. 497-518. 1973.

[6] D. Kennedy, B. Park, M. D. Unsworth. Towards global layup optimization of composite panels with initial buckling constraints. *Proceeding of 8th ASMO UK/ISSMO Conference*. London, pp. 221-231. 2010.

[7] C. G. Diaconu, M. Sato, H. Sekine. Feasible region in general design space of lamination parameters for laminated composites. *AIAA Journal* 40 (3), pp. 559-565. 2002.

Failure and Damage II

Proceedings of the 24th UK Conference of the
Association for Computational Mechanics in Engineering
31 March - 01 April 2016, Cardiff University, Cardiff

Fracture processes in quasi-brittle materials: Linking heterogeneity to crack roughness

Peter Grassl

School of Engineering, University of Glasgow, Rankine Building, Glasgow, G128LT

ABSTRACT

The roughness of crack surfaces of heterogeneous quasi-brittle materials such as concrete, bones, rock and wood is linked to the spatial extension of the fracture process zone. Modelling of this zone is required to predict the influence of size on the nominal strength of geometrical similar structures made of quasi-brittle materials or crack spacing in reinforced structures. The aim of this study is to further investigate the link between the heterogeneity of the material and the roughness of crack surface by means of discrete network analyses of the failure process of heterogeneous quasi-brittle materials. In the present study, a 3D periodic unit cell of a irregular structural network representing a heterogeneous material is subjected to direct tension. The material meso-structure is modelled by a random field of the material strength mapped on the irregular network of discrete elements. The influence of the standard deviation of the random fields on the crack roughness is investigated.

Key Words: *Fracture; roughness; discrete; dissipation; heterogeneous material*

1. Introduction

The fracture process in specimens made of heterogeneous quasi-brittle materials such as concrete, bones, rock and wood, subjected to direct tension is characterised by a transition from distributed micro-cracking to a localised stress-free macroscopic crack separating the specimen, whereby the final stress-free crack surface is rough. In [1], it was aimed to developed a procedure to link this roughness of the stress-free crack surface to the width of the fracture process zone, which could then be used to calibrate the interaction radius of nonlocal constitutive models for predicting the failure process of structures made of these heterogeneous materials (Figure 1). The key of this approach was to determine a measure from the roughness, which could be linked to the distribution of dissipated energy obtained from models to be calibrated. This measure is the standard deviation of the height of the crack surface from the mean crack plane. One of the assumptions of this approach was that the large majority of fracture energy was dissipated by the localised crack and not the distributed micro-cracking. This was supported by 2D numerical structural network analyses of specimens with random material strength properties subjected to direct tension, and experimental results reported in the literature [2]. In [1], the new calibration approach was applied to the fracture of a concrete beam subjected to three-point bending, which contained low strength aggregates. The roughness of the crack surface measured in these experiments was small, which was explained by low strength inclusions, which fractured during the tests. In the present study, the roughness of crack surfaces obtained from direct tensile tests is further investigated by means of a numerical approach based on a structural network model. The new contribution is the extension of the previous 2D modelling approach to 3D and an investigation of the influence of the standard deviation of the random material strength on the roughness.

2. Method

The method to computationally determine the roughness of crack surfaces of direct tensile tests is presented here by describing the discretisation approach, constitutive model, random field and roughness determination.

The spatial discretisation of the direct tensile specimens is performed using a 3D structural network model described in [3], combined with a 3D periodic cell proposed in [4] (Figure 2). The structural

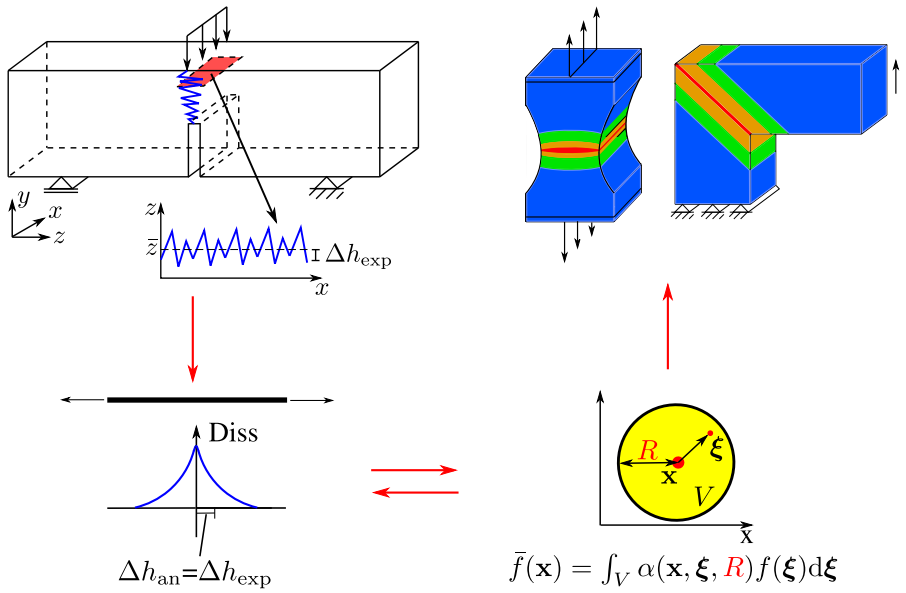

Figure 1: Schematic overview of the calibration strategy of the interaction radius of nonlocal constitutive models: Roughness measurements from experiments or analyses (left top) are used to determine the distribution of dissipated energy (left bottom). This distribution is used to calibrate the nonlocal constitutive model (right bottom) which is then used in structural analysis. Adapted from [1].

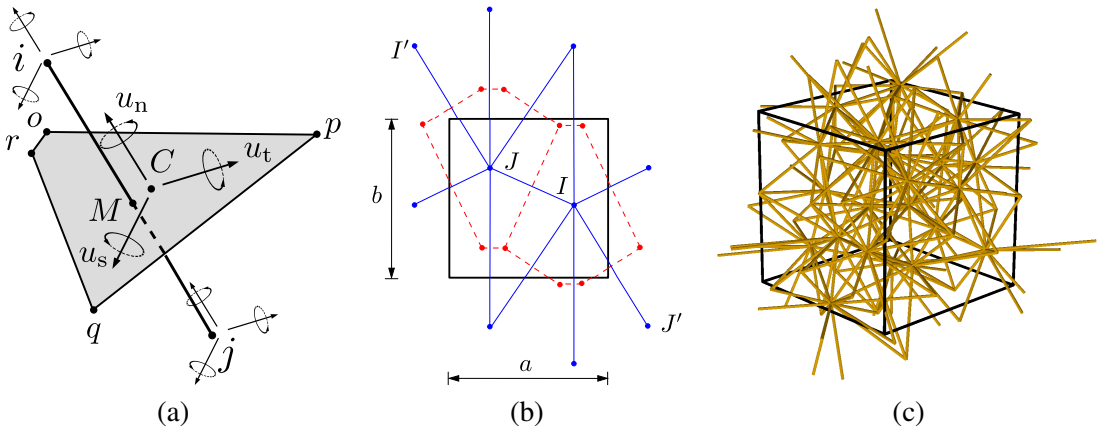

Figure 2: 3D discrete network model: (a) 3D network element, (b) schematic periodic network in the cell with elements crossing the boundary, and (c) 3D periodic cell of discrete elements.

network element in Figure 2a has three translational and three rotational degrees of freedom at each node. The spatial arrangement of the network is based on a Delaunay and Voronoi tessellation of a periodically arranged set of random points following the approach described in [4]. The vertices of the Delaunay tetrahedra are used as nodes for the structural network elements, which are placed on the edges of the tetrahedra. The mid cross-sections of the network elements are the facets of the Voronoi polyhedra associated with edges of the Delaunay tetrahedra [3]. The average element length is controlled by the minimum spacing $d_{\min}$ of the randomly placed points used for the tessellations.

The degrees of freedom of the nodes of an element are linked by kinematic relationships to displacement jumps at point C in Figure 2a, which enters the scalar damage model. The input parameters are the modulus of elasticity E, the strain at tensile strength $\varepsilon_0 = f_t/E$ and the displacement threshold w_f controlling the softening described by the damage model [1]. The strength envelope is an ellipsoid determined by the tensile strength f_t, the compressive strength $f_c = c f_t$ and the shear strength $f_q = q f_t$.

The heterogeneity of the material is represented by an autocorrelated Gaussian random field of the strain threshold ε_0. The input parameters of the random field are the autocorrelation length l_a and the mean $\bar{\varepsilon}_0$ and a coefficient of variation c_v of the Gaussian distribution. The values of the random field are mapped onto the structural network. The autocorrelation length l_a is chosen to be greater than the spacing $d_{\min}$ used for the network generation.

The roughness of crack surfaces from the analyses is determined from the weighted average and standard deviation of the dissipated energy as described in [1]. Firstly, the dissipated energy and the heights (in the direction of loading) of mid-cross-sections are determined. Then, the weighted mean $\bar{z}$ and the standard deviation Δh of all heights is calculated.

3. Analyses and Results

The influence of the coefficient of variation of the random field of strength used for the direct tensile specimen on the surface roughness was investigated. The structural network for a periodic cell of edge length $h = 0.1$ m was discretised using $d_{\min} = 3$ mm. For the random field, five coefficient of variation values $c_v = 0.05, 0.1, 0.2, 0.4$ and 0.6 were selected. Furthermore, the autocorrelation length was chosen as $l_a = 4$ mm. The mean values of the input parameters are $E = 30$ MPa, $\bar{\varepsilon}_0 = 0.0001$ and $w_f = 0.00004$, $c = 10$ and $q = 2$. For each c_v, 20 analyses with different networks and random fields were performed. The periodic cell was subjected to an incrementally applied axial displacement of 0.2 mm, while keeping the average lateral stresses equal to zero. The axial stress-displacement curve and crack patterns at different stages are shown in Figure 3 for one random analysis with $c_v = 0.2$. The crack patterns are visualised in the form of orange mid-cross-section at which energy is dissipated at this stage of analysis.

Initially, energy is dissipated throughout the specimen. However, very soon after the peak, the zone in which energy is dissipated shrinks and the fracture process zone is mainly formed by one rough crack, which dissipates the majority of energy. This evolution of the fracture process zone is very similar to the 2D results in [1]. According to the present simulations, the width of the fracture process zone is mainly controlled by the roughness of the crack. It should be noted that because of the use of a periodic cell, the location of this crack plane within the specimen depends only on the specific realisation of the random field, and not the specimen boundaries.

The influence of the coefficient of variation c_v on the roughness of the crack was investigate by evaluation the weighted standard deviation Δh of the mid-cross-sections. The preliminary analyses so far, show that an increase of c_v results in an increase of the roughness Δh. The preliminary results indicate that stronger inclusions represented by larger standard deviations result in rougher cracks.

4. Conclusions

3D structural network analyses of direct tension of a heterogeneous quasi-brittle material have shown that the energy during the fracture process was mainly dissipated in a localised rough crack plane. Therefore, the width of the fracture process was determined by the roughness of the crack plane. An increase of the

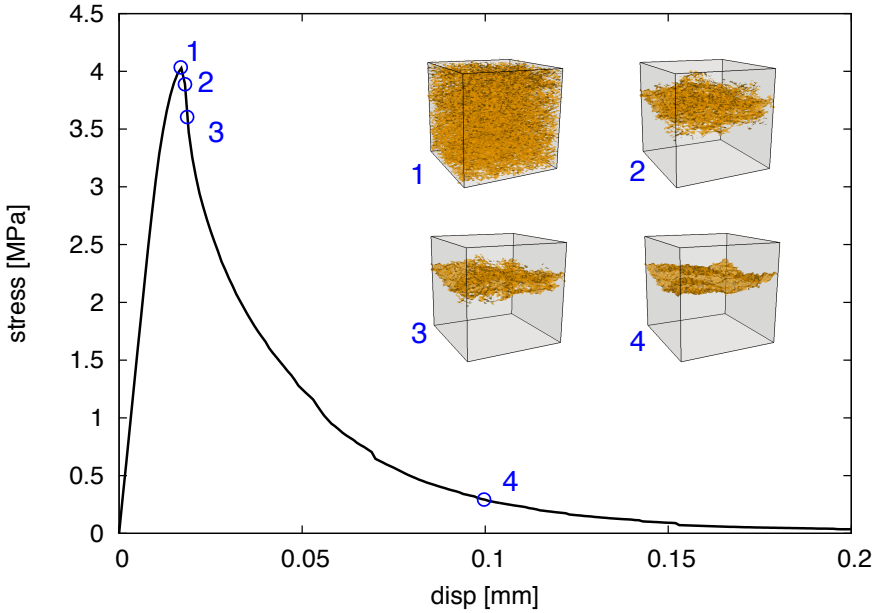

Figure 3: Periodic cell subjected to direct tension: Stress versus displacement and crack patterns (orange mid-cross-sections) at four stages of analysis.

coefficient of variation of the random field of tensile strength resulted in an increase of the roughness of the crack plane.

Acknowledgements

The numerical analyses were performed with the nonlinear analyses program OOFEM [5] extended by the present authors.

References

[1] D. Xenos and D. Grégoire and S. Morel and P. Grassl. Calibration of Nonlocal Models for Tensile Fracture in Quasi-brittle Heterogeneous Materials. *Journal of the Mechanics and Physics of Solids*, 82, 48–60, 2015.

[2] L. Cedolin and S. D. Poli and I. Iori, Tensile Behavior of Concrete, *Journal of Engineering Mechanics*, 113, 431–449, 1987.

[3] M. Yip and J. Mohle and J. E. Bolander. Automated Modeling of Three-Dimensional Structural Components Using Irregular Lattices. *Computer-Aided Civil and Infrastructure Engineering*, 20, 393–407, 2005.

[4] P. Grassl and I. Athanasiadis. 3D modelling of the influence of microcracking on mass transport in concrete, in: *CONCREEP 10*, pp. 373–376, 2015.

[5] B. Patzák. OOFEM – an Object-Oriented Simulation Tool for Advanced Modeling of Materials and Structures. *Acta Polytechnica*, pp. 59-66, 2012.

PROGRESSIVE DAMAGE ANALYSIS ON YIELDING OF BONDED PATCH REPAIRED COMPOSITE LAMINATES UNDER COMPRESSIVE LOADING

Jian Deng [1, 2], *Guangming Zhou[1], Pierre Kerfriden[2], Stéphane Bordas[2, 3], Qiaozhi Yin [1]
[1] State Key Laboratory of Mechanics and Control of Mechanical Structures,
Nanjing University of Aeronautics and Astronautics, Nanjing 210016, China
[2] 1 Institute of Mechanics and Advanced Materials, Cardiff School of Engineering, Cardiff University, UK,
[3] Université du Luxembourg, Faculté des Sciences, de la Technologie et de la Communication, Research Unit in Engineering Science, Campus Kirchberg, 6, rue Richard Coudenhove-Kalergi, L-1359 Luxembourg

*zhougm@nuaa.edu.cn

ABSTRACT

In this paper, a progressive damage model for single-side bonded repaired composites laminates under compressive loading is introduced. Continuum damage model and cohesive zone model including stiffness degradation schemes are employed in the nonlinear FEM to predict the initiation and evolution of damage in the repaired structures. In proposed model, solid elements are applied for composite layers and cohesive elements for the adhesive. The numerical results of failure loads under compression shows consistency with experimental ones. The damage evolution is studied with analysis of loading process and failure propagation in adhesive. It indicates buckling deformation initiates the damage in plate and finally make the repaired structure crush.

Keywords: *bonded repair; composite laminates; compression; buckling; progressive damage*

1. Introduction

Composite laminates are widely applied in high performance industries such as aerospace and other industries like automobile and civil construction due to its traits in weight loss, low energy cost and well developed mechanical behaviours. However, damage varying from production, appliance to maintenance cannot be totally removed, which could reduce the safety and reliability of structures. Considering the replacement costs of the damaged composite parts would be quite high, effective repair techniques have increasingly drew engineers' attention. Bonded patch repair, through removing the damaged material and adhesively bonding several patches on outfaces of damaged structures, surmount the shortcomings of mechanical repair (e.g. reverting and fastening). Specifically, it can be divided into single bond (SB) on one side and double bonds (DB) on both sides. Since the peel stress on the boundary of bonded patches is quite high, it is generally applied as temporary repair in highly loaded structures and a permanent method for lightly loaded and slightly damaged parts.

Considering composites structures are generally thin walled with modes of failure caused by compression, the compressive behaviour should not be ignored in designing process. This paper establishes a progressive damage model for SB repaired laminates under compressive loading. Continuum damage model and cohesive zone model are employed in the nonlinear FEM to predict the initiation and evolution of damage in the repaired structures. The finite element model is discretized by solid elements accounting for composite layers and cohesive elements for the adhesive. All the material softening laws and failure modes are implemented with ABAQUS UMAT code. The failure strengths are predicted comparing with experimental outcomes from Campilho [1]. Damage propagation of one typical specimen is also studied.

2. Damage Model

Fibre failure, matrix failure and delamination failure in composites are all considered here with Hashin criteria [2] for the damage initiation under a three-dimensional state of stress in composites. The relations between failure modes are illustrated in Table 1.

Table 1: Failure indexes corresponding to different failure modes

Fibre failure in tension ($\sigma_{11} \geq 0$)	$(\frac{\sigma_{11}}{X_T})^2 + (\frac{\sigma_{12}}{S_{12}})^2 + (\frac{\sigma_{13}}{S_{13}})^2 = e_1^2$
Fibere failure in compression ($\sigma_{11} < 0$)	$(\frac{\sigma_{11}}{X_C})^2 = e_1^2$
Matrix cracking in tension ($\sigma_{22} \geq 0$)	$(\frac{\sigma_{22}}{Y_T})^2 + (\frac{\sigma_{12}}{S_{12}})^2 + (\frac{\sigma_{23}}{S_{23}})^2 = e_2^2$
Matrix cracking in compression ($\sigma_{22} < 0$)	$(\frac{\sigma_{22}}{Y_C})^2 + (\frac{\sigma_{12}}{S_{12}})^2 + (\frac{\sigma_{23}}{S_{23}})^2 = e_2^2$
Delamination in tension ($\sigma_{33} \geq 0$)	$(\frac{\sigma_{33}}{Z_T})^2 + (\frac{\sigma_{13}}{S_{13}})^2 + (\frac{\sigma_{23}}{S_{23}})^2 = e_3^2$
Delamination in compression ($\sigma_{33} < 0$)	$(\frac{\sigma_{33}}{Z_C})^2 + (\frac{\sigma_{13}}{S_{13}})^2 + (\frac{\sigma_{23}}{S_{23}})^2 = e_3^2$

**Note:1- and 2- axis are parallel and transverse to the fibres, respectively, while the 3-axis represents the normal direction, σ_{ij} (i = 1, 2, 3; j=1,2,3) are the stress components in ij directions, X_T、Y_T、Z_T are relative material strengths in tension, X_C、Y_C、Z_C are strengths in compression and S_{ij} stand for shear strengths, and e_i^2(i = 1,2,3) are relative damage indexes.*

After the initiation of damage in composites, damage variables are introduced in the continuum damage model to simulate its decreasing load capacity.

$$d_i = \min\{1, \frac{\langle e_i^2 - \varepsilon \rangle}{1-\varepsilon}\},\ i = 1,\ 2,\ 3 \tag{1}$$

Where $\langle \cdot \rangle$ is the McCauley operator defined as $\langle a \rangle = (|a| + a)/2$, ε is the fitting parameter adjacent to 1, and e_i^2 are attained from equation in Table 1. Therefore, the reduced stiffness matrix in damaged configuration is expressed as follows.

$$\boldsymbol{C}^{\mathbf{d}} = \begin{bmatrix} (1-d_1)C_{11} & (1-d_1)(1-d_2)C_{12} & (1-d_1)(1-d_3)C_{13} & 0 & 0 & 0 \\ & (1-d_2)C_{22} & (1-d_2)(1-d_3)C_{23} & 0 & 0 & 0 \\ & & (1-d_3)C_{33} & 0 & 0 & 0 \\ & \text{sym} & & (1-d_1)(1-d_2)C_{44} & 0 & 0 \\ & & & & (1-d_1)(1-d_3)C_{55} & 0 \\ & & & & & (1-d_2)(1-d_3)C_{66} \end{bmatrix}$$

A bilinear cohesive zone model [3] is applied to model the mechanical behaviour in the adhesive between the plate and bonded patch. The damage initiation law is the following quadratic equation.

$$\left(\frac{\langle t_{\mathrm{n}} \rangle}{T_{\mathrm{n}}}\right)^2 + \left(\frac{t_{\mathrm{s}}}{T_{\mathrm{s}}}\right)^2 + \left(\frac{t_{\mathrm{t}}}{T_{\mathrm{t}}}\right)^2 = 1 \tag{2}$$

where t_i (i=n,s,t) are the normal and shear tractions, and T_i (i=n,s,t) are the corresponding strengths.

Damage evolution is modelled by quadratic fracture energetic criterion.

$$\left(\frac{G_{\mathrm{n}}}{G_{\mathrm{n}}^{\mathrm{C}}}\right)^2 + \left(\frac{G_{\mathrm{s}}}{G_{\mathrm{s}}^{\mathrm{C}}}\right)^2 + \left(\frac{G_{\mathrm{t}}}{G_{\mathrm{t}}^{\mathrm{C}}}\right)^2 = 1 \tag{3}$$

where G_i (i=n,s,t) are the current strain energy release rate and G_i^C are the corresponding critical energy release rate. When Eq.(3) satisfied, damage development occurs and stresses are released.

3. Numerical models based on FEM

To validate the efficiency of the proposed failure model, numerical studies based on FEM are established referring to the single bonded specimens tested by Campilho in experiments [1]. The geometrical dimension of the bonded repair laminates is shown in Figure 1(a). The stacking sequence of plate is $[0_2/90_2/0_2/90_2]_s$. The thickness of adhesive is 0.2mm.

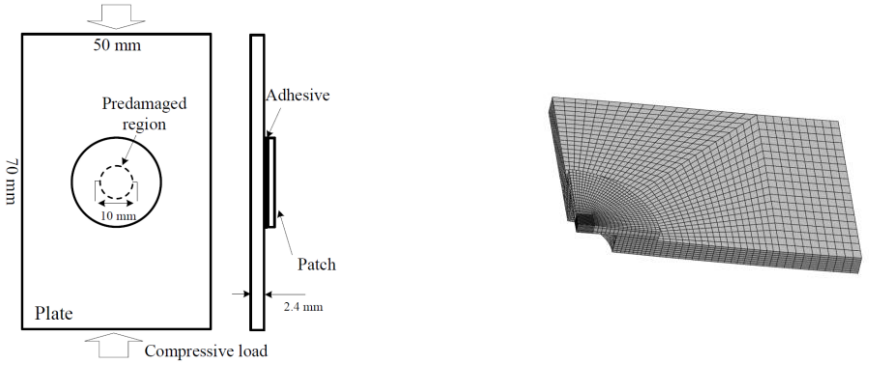

(a) Geometric dimension (b) Finite element model (quarter)

Figure 1: Dimension and finite element model of SB specimen

The material system of composites applied in simulation is TEXIPREG HS 160 RM, and the adhesive material is Araldite®2015. All the properties are given in Table 2.

Table 2: Mechanical Properties

TEXIPREG HS 160 RM										
E_{11}/GPa	$E_{22}=E_{33}$/GPa	$\nu_{12}=\nu_{13}$	ν_{23}	$G_{12}=G_{13}$/GPa	G_{23}/GPa	X_T/MPa	X_C/MPa	$Y_T=Z_T$/MPa	$Y_C=Z_C$/MPa	S/MPa
109	8.819	0.342	0.380	4.315	3.2	1401	1132	59	211	54

Araldite®2015						
E/GPa	ν	G/MPa	t_n/MPa	$t_s=t_t$/MPa	G_n/J mm-1	$G_s=G_t$/J mm-1
1.85	0.3	650	23	22.8	0.43	4.70

Composite materials in the plate and patch are simulated with C3D8R solid elements in ABAQUS while COH3D8 cohesive elements are employed for adhesive layer. All the material softening law and failure modes are implemented with ABAQUS UMAT code. A typical finite quarter model is shown in Figure 1(b) to illustrate the discretization scheme. To ensure the accuracy of simulation, the repair area in the center is refined with smaller element size, and the constraints as well as loading patterns are consistent with experiments from Campilho [1].

4. Results

Table 3 shows the comparison between the simulation results of failure loads under compression and experimental ones differing in patch parameters. It is noticed that the predictions of strengths agree well with experiments. It indicates the damage model proposed is effective. Comparing the failure loads of these specimens, it should be noted that the repair improves the mechanical performance of damaged structures.

A typical load-displacement curve and damage evolution for specimen C are demonstrated in Figure 2 and Figure 3, respectively. Damage firstly initiate in the adhesive layer along with the loading direction (Figure 3(a)). It is due to the stress concentration at the edge of the damaged hole and

stiffness difference between the plate and patch. Since the damage is developing in adhesive, its capacity of transferring loads from plate to patch is decreased. It indicates the patch support less for the loading and loads are distributed more on the plate. Then, the specimen is experiencing buckling as the displacement loading increased. It should be noted that stiffness reduction occurs when the structure start buckling in Figure 2. And as shown in Figure 3(c), the damage in adhesive develops perpendicular to the loading direction due to the buckling deformation. Afterwards, with continuously increased compressive loading, deformation caused by buckling of the structure becomes serious and the failure initiates in the plate. It is clearly seen significant stiffness reduction of the structure in Figure 2. The maximum load is taken at the point "Failure load" and then the repaired structure begins to collapse.

Table 3: Failure loads of single bonded specimens

	Diameter/mm	Thickness/mm	Stacking Sequence	Numerical Results / KN	Experimental Results / KN	Error / %
A		Without Repair		20.1	21.2	5.19%
B	20	1.2	$[0_2/90_2]s$	21.6	23.9	9.62%
C	30	1.2	$[0_2/90_2]s$	24.9	25.7	3.11%
D	20	0.6	[0/90]s	22.4	23.7	5.49%
E	30	1.8	$[0_2/90_2/0_2]s$	26.2	24.6	6.50%
F	20	2.4	$[0_2/90_2/0_2/90_2]s$	24.5	25.4	3.54%

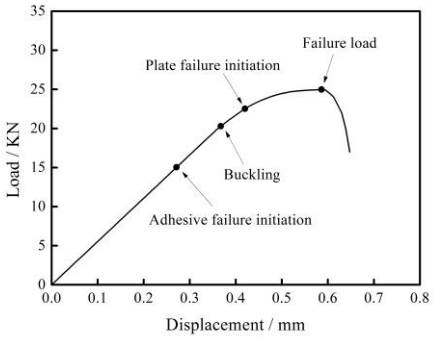

Figure 2: Load-Displacement curve

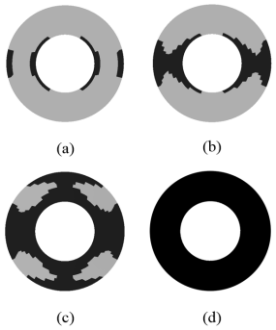

Figure 3: Adhesive failure propagation process

Acknowledgements

Jian Deng would like to acknowledge that this work was supported by Funding of Jiangsu Innovation Program for Graduate Education (KYLX15_0240, KYLX_0297) and the Fundamental Research Funds for the Central Universities.

References

[1] R. Campilho, M. de Moura, D. Ramantani, J. Morais and J. Domingues. Buckling strength of adhesively-bonded single and double-strap repairs on carbon-epoxy structures. *Composites Science and Technology*, 70(2), 371-379, 2010.

[2] Z. Hashin. Failure Criteria for Unidirectional Fiber Composites. *Journal of Applied Mechanics*. 47(2), 329-334, 1980.

[3] P. Maimí, P. Camanho, J. Mayugo and C. Dávila. A continuum damage model for composite laminates: Part I – Constitutive model. *Mechanics of Materials.* 39(10), 897-908, 2007.

Proceedings of the 24th UK Conference of the
Association for Computational Mechanics in Engineering
31 March - 01 April 2016, Cardiff University, Cardiff

An adaptive cross approximation (ACA) for the extended boundary element method (XBEM) in anisotropic materials

S. H. Kettle[1], *G. Hattori[1], L. Campos[2], J. Trevelyan[1] and E. L. Albuquerque[2]

[1]School of Engineering and Computing Sciences, Durham University, South Road, DH1 3LE, Durham, UK
[2] Department of Mechanical Engineering, University of Brasilia, 70910-900, Brasilia, Brazil

*gabriel.hattori@durham.ac.uk

ABSTRACT

The extended boundary element method (XBEM) is a modification from the standard BEM, where enrichment functions are embedded into the BEM formulation. The results obtained with this method were seen to be accurate and stable, being especially useful for fracture problems. However, the method suffers from the presence of a linear system containing unsymmetric and fully populated matrices which needs to be solved in order to get the solution of the boundary problem. This can be computationally expensive for problems dealing with multiple cracks for instance. Adaptive cross approximation (ACA) is used to reduce the number of operations necessary to solve the linear system of equations for a fracture problem with an anisotropic material.

Key Words: *Extended boundary element method; Adaptive Cross Approximation; Anisotropic materials, Fracture mechanics*

1. Introduction

The boundary element method (BEM) relies on a mathematical formulation that allows one to model a given domain considering only its boundaries. One of the advantages of this approach is to obtain a reduced mesh due to the boundary only discretisation. However, the linear system of equations is fully populated and non-symmetric. Large problems can become cumbersome to be solved numerically.

For this reason, adaptive cross approximation (ACA) has become a popular technique to accelerate the computational solution time. The idea of the method is to use the smoothness of the operator to approximate the so called admissible blocks, thus accelerating the evaluation of the matrix vector product that lies within each iteration of an iterative solver.

The extended boundary element method (XBEM) has been proposed by [1] for isotropic materials and extended to anisotropic materials by [2]. In this case the additional degrees of freedom correspond to the stress intensity factors (SIF), which are the key parameters in fracture mechanics problems. The advantage of this formulation is that the degrees of freedom do not depend on the number of enriched nodes, as they correspond to the SIF. Moreover, there is no need for post-processing (such as the J-integral) to obtain the SIF, since they are calculated as part of the displacement solution. In this work we tackle for the first time the use of ACA in an XBEM formulation for anisotropic 2D materials.

2. Extended boundary element method (XBEM)

A dual BEM formulation is modified with the enrichment as defined in [2]. Two boundary integral equations (BIE), are necessary to avoid the mathematical degeneration which arises from the coincidence of the crack faces. The displacement boundary integral equation (DBIE) and the traction boundary integral equation (TBIE) are given by [2]

$$c_{ij}(\boldsymbol{\xi})u_j(\boldsymbol{\xi}) + \int_\Gamma p^*_{ij}(\boldsymbol{x},\boldsymbol{\xi})u_j(\boldsymbol{x})d\Gamma(\boldsymbol{x}) + \int_{\Gamma_c} p^*_{ij}(\boldsymbol{x},\boldsymbol{\xi})\tilde{K}_{lj}F_{lj}(\boldsymbol{\xi})\mathbf{a}^\alpha_k d\Gamma(\boldsymbol{x}) = \int_\Gamma u^*_{ij}(\boldsymbol{x},\boldsymbol{\xi})p_j(\boldsymbol{x})d\Gamma(\boldsymbol{x}) \tag{1}$$

$$c_{ij}(\boldsymbol{\xi})p_j(\boldsymbol{\xi}) + N_r\int_\Gamma s^*_{rij}(\boldsymbol{x},\boldsymbol{\xi})u_j(\boldsymbol{x})d\Gamma(\boldsymbol{x}) + N_r\int_{\Gamma_c} s^*_{rij}(\boldsymbol{x},\boldsymbol{\xi})\tilde{K}_{lj}F_{lj}(\boldsymbol{\xi})d\Gamma(\boldsymbol{x}) = N_r\int_\Gamma d^*_{rij}(\boldsymbol{x},\boldsymbol{\xi})p_j(\boldsymbol{x})d\Gamma(\boldsymbol{x}) \tag{2}$$

where $\Gamma_c = \Gamma_+ \cup \Gamma_-$ stands for the crack surfaces Γ_+ and Γ_-, N_r is the normal at the observation point $\mathbf{x}$, F_{lj} is the enrichment function and $\tilde{K}_{lj}$ is the additional degree of freedom which stands for the SIF. Let us recall that strongly singular and hypersingular terms arise from the integration of the p^*_{ij}, d^*_{rij} and s^*_{rij} kernels and they have to regularised before numerical integration is possible. More details about the regularisation procedure and the XBEM formulation can be found in [1].

The enrichment function used in Eqs. (1) and (2) are the same as defined in [3] for anisotropic materials using the extended finite element method (XFEM).

3. Adaptive Cross Approximation (ACA)

In this paper the form of ACA used is fully pivoted ACA. While partially pivoted ACA allows for reductions in storage and generation of the system matrix, the subject of this paper is addressing reductions in computations in the solution. If the number of operations required for generation and storage are each proportional to the square of the dimension of the system matrix, the direct solution of the linear system requires a number of operations proportional to its cube. Iterative solvers such as GMRES reduce the complexity but involve an expensive matrix vector product within each iteration.

In order for ACA to produce an accurate low rank approximation, the matrix must be asymptotically smooth. In BEM, this smoothness is only found where the collocation nodes are well separated geometrically from the nodes upon which they are being integrated over. The admissibility of a matrix block is assessed based on geometric considerations, by performing hierarchical clustering [4], before ACA is applied. The whole matrix is recursively subdivided until it satisfies an admissibility criterion or a minimum block size has been reached.

Performing hierarchical clustering on a dual formulated BEM matrix requires separation of the boundary nodes and the crack nodes at all times [5]. Discontinuous elements are used on the crack, with one surface corresponding to the DBIE and the other corresponding to the TBIE. For this reason, when constructing the hierarchical cluster tree, the crack surfaces must be separated from the external boundaries, and both crack surfaces must be separated from each other in collocation, but can be considered as a whole when being integrated over by for a remote collocation point. Thus it is important to place nodes on opposing crack surfaces in different clusters row-wise, but unimportant column-wise in the matrix. This creates asymmetry in the structure of the hierarchical cluster tree.

Constraints other than the admissibility criterion must be put in place to assure that these conditions are met, as although the geometry of crack nodes are usually clearly distinguishable from those of the boundary, this is not always the case. Furthermore, coincident nodes on opposite crack surfaces will be clustered together unless the algorithm is instructed otherwise.

A detailed explanation about ACA applied to BEM can be found in [6].

4. Results

The results are presented for a two dimensional anisotropic plate containing 12 internal cracks. The problem is discretised with 2000 nodes for the external boundaries and 300 nodes per crack. Continuous elements are employed on the external boundaries and discontinuous elements are used on the crack faces. There are 9248 degrees of freedom (DOF) in total, of which 48 DOFs correspond to the SIFs of each crack (mode I and II). The material properties are given by: C_{11} = 117.97 GPa, C_{12} = 14.19 GPa, C_{16} = 35.43 GPa, C_{22} = 15.64 GPa, C_{26} = 7.49 GPa, C_{66} = 21.38 GPa. Figure 1 represents the matrix structure resulting from the hierarchical clustering of the problem.

Table 1 illustrates the savings of solving the linear system of equations using ACA. The solution error is defined as

$$\text{error} = \frac{||\mathbf{x}_{ACA} - \mathbf{x}||_F}{||\mathbf{x}||_F} \tag{3}$$

where $\mathbf{x}_{ACA}$ is the displacement solution when the linear system of equations was approximated with ACA, $\mathbf{x}$ is the displacement solution obtained by solving the full system using a direct solver and $||(.)||_F$

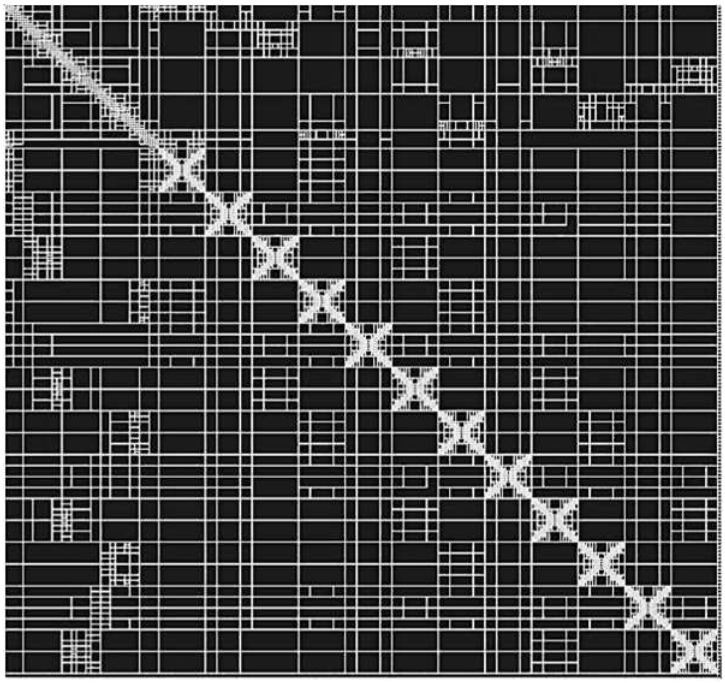

Figure 1: : ACA generated matrix partitioning.

stands for the Frobenius norm. The parameter ε_C is the threshold error of the ACA approximation using the Frobenius norm.

Table 1: Operational savings data

ε_C	Solution error		Operations	Saving(%)
	Total (%)	SIFs (%)		
1×10^{-4}	0.310	0.130	6.562×10^6	92.3
1×10^{-5}	0.022	0.018	7.499×10^6	91.2
1×10^{-6}	1.27×10^{-5}	1.26×10^{-5}	8.449×10^6	90.1

The data given as 'Operations' is the number of computations required to perform a matrix vector product using the approximated system matrix. This is the total sum of $O(r(N+M))$ for every low rank block combined with $O(NM)$ for every full rank block, where r represents the rank and N and M represent the rows and columns, respectively. 'Saving' stands for the gain in number of computations required to perform the full rank matrix-vector product.

The results show that reductions in ε_C, as expected, improves the accuracy of the eventual solution. ACA is successfully applied to all parts of the matrix, with exception of the last 48 rows and columns. For the latter, the columns are partitioned into 50×48 blocks and then approximated using ACA. For the former, these are extra rows necessary to balance the system of equations as shown in [1], and contain the so called tying equations. These rows are sparsely populated, therefore are not considered for ACA. Applying these configurations produces an accurate solution with computational savings in excess of 90% per iteration and low errors for both displacement field and SIFs.

In Table 1 the error for the Frobenius norm is the same for boundary displacements and the SIFs in the solution vector. However, it is known that the terms of the linear system of equations associated to the enriched terms can be of very different order of magnitude from the other terms. Moreover, it might be speculated that the accuracy of these terms is strongly influential over the accuracy of the computed SIFs. In this case, it is worthwhile, then, to consider lower error in the ACA approximation for the sub-blocks

containing terms related to the SIF and allowing a higher error in approximating all other sub-blocks. Table 2 analyses this issue considering two errors for the Frobenius norm, ε_C and ε_{SIF}. One can verify that the error in SIFs is strongly governed by ε_C, and less so by ε_{SIF} for the SIFs reduce slightly even for high accuracy, nevertheless the number of operations increases.

Table 2: Operational savings data for different levels of error

ε_C	ε_{SIF}	Solution error		Operations	Saving(%)
		Total (%)	SIFs (%)		
1×10^{-3}	1×10^{-4}	2.995	1.407	5.515×10^6	93.55
	1×10^{-8}	2.995	1.404	5.627×10^6	92.42
1×10^{-4}	1×10^{-4}	0.306	0.127	6.507×10^6	92.39
	1×10^{-8}	0.306	0.125	6.618×10^6	92.26
1×10^{-5}	1×10^{-4}	0.023	0.017	7.471×10^6	91.26
	1×10^{-8}	0.022	0.018	7.583×10^6	91.13

5. Conclusions

In this work we applied ACA with the XBEM for solving an anisotropic fracture problem for the first time in literature. ACA is employed as a method to accelerate the solution of the system of equations obtained from the XBEM formulation. The achieved saving times are more than 90% of efficiency compared to solving the system using regular Gauss elimination. We are looking forward to extend this formulation to deal with 3D problems.

Acknowledgements

The second author acknowledges the Faculty of Science, Durham University, for his Postdoctoral Research Associate funding.

References

[1] I. A. Alatawi and J. Trevelyan, "A direct evaluation of stress intensity factors using the extended dual boundary element method," *Engineering Analysis with Boundary Elements*, vol. 52, pp. 56–63, 2015.

[2] G. Hattori, I. A. Alatawi, and J. Trevelyan, "A direct SIF approach for anisotropic materials using the boundary element method," in *Proceedings of the 23rd UK Conference of the Association for Computational Mechanics in Engineering* (A. J. Gil and R. Sevilla, eds.), pp. 279–282, 2015.

[3] G. Hattori, R. Rojas-Díaz, A. Sáez, N. Sukumar, and F. García-Sánchez, "New anisotropic crack-tip enrichment functions for the extended finite element method," *Computational Mechanics*, vol. 50, no. 5, pp. 591–601, 2012.

[4] M. Bebendorf and S. Rjasanow, "Adaptive low-rank approximation of collocation matrices," *Computing*, vol. 70, no. 1, pp. 1–24, 2003.

[5] I. Benedetti, M. H. Aliabadi, and G. Davi, "A fast 3D dual boundary element method based on hierarchical matrices," *International journal of solids and structures*, vol. 45, no. 7, pp. 2355–2376, 2008.

[6] S. Rjasanow and O. Steinbach, *The fast solution of boundary integral equations*. Springer Science & Business Media, 2007.

Proceedings of the 24th UK Conference of the
Association for Computational Mechanics in Engineering
31 March – 01 April 2016, Cardiff University, Cardiff

Numerical investigation of hydraulic fracturing

*** D. Mahdavian[1], A.A. Javadi[2]**

[1] Department of Engineering, University of Exeter, North park Road, Exeter, EX4 4QF

*dm464@exeter.ac.uk

ABSTRACT

Hydraulic fracturing is a commonly used method for producing oil and gas from reservoirs. Analysis of hydraulic fracturing requires the study of fracture mechanics and fluids mechanics. The focus of this paper is to investigate the initiation and growth of cracks in a typical well. The finite element method is used to simulate the process of hydraulic fracturing, calculating the effective parameters in fracture analysis and studying the fracture characteristics under different conditions. According to the linear elastic fracture mechanics, if the stress intensity factor is equal to fracture toughness, the crack will propagate. The fracture parameters related to a semi-elliptical crack are studied using the finite element software ANSYS. The numerical results indicate that the stress intensity factor increases by increasing the crack length. The crack length increases by increasing the fluid leakage rate. The relationship between stress intensity factor, leakage rate and crack length (which represents crack growth in each step) is investigated.

Key words: hydraulic fracturing**;** stress intensity factor; crack; leakage; crack length, finite element

1-Introduction

Hydraulic fracturing is a fracturing processes initiated from a pressurized open borehole section into rock formations. The process is characterized by solid-fluid interaction. On the solid side, the rock formation deforms with the propagation of the fracture front and pressurization of the fracture face. On the other side, the fluid flows at high pressure into the narrow fracture cavity. At the same time, the fluid may also infiltrate into the porous rock. Even in the most basic form, hydraulic fracturing is a complex process, not just because of the heterogeneity of the earth structure, and indeterminate in-situ stresses or rock behaviour, but also because of the physical complexities of the problem. It involves coupling of three processes:

1- Mechanical deformation of the formation caused by the pressure inside the fracture,

2- Fluid flow within the fracture networks,

3- Fracture propagation.

2-Hydraulic fracturing mechanism

Hydraulic fracturing is a 3D phenomenon. Modelling of hydraulic fracturing involves determination of crack width, length and height and distribution of fluid pressure inside the crack as a function of time and location for a known flow rate or known fluid pressure in the borehole. But modelling of this 3 dimensional phenomenon is not easy because hydraulic fracturing includes coupling of at least three processes.

In order to model hydraulic fracturing, it is necessary to solve three governing equations:

1) Geo-mechanical behaviour of the reservoir,

2) Flow in the porous medium, and

3) Flow inside the crack.

The elasticity, fluid flow and fracture growth equations should ideally be fully coupled in order to solve the system of equations correctly and get the crack width, length, height and fluid pressure as a function of time and location. In general, the governing equations of a multiphase porous medium are as follow:

1) Momentum equilibrium equation for the whole multiphase medium,

2) Momentum equilibrium equation for each fluid phase,

3) Mass conservation equation for each porous medium phase.

Nevertheless, many research works on hydraulic fracturing, assuming elastic behaviour, have used single integral equation as:

$$p(x,y,t) - \sigma_c(x,y) = \int_{\Omega(t)} C(x,y;\xi,\eta)\, w(\xi,\eta,t)\, d\xi\, d\eta$$

or

$$w(x,y,t) = \int_{\Omega(t)} f(x-x', y-y')\{\, p(x',y') - \sigma_c(x',y')\,\}\, dx'dy'$$

In the above equations p is fluid pressure inside the crack, σ_c is the local minimum in-situ stress, w is crack width, C is non-local kernel function which contains all data about layered elastic medium, and f is elastic Influence Function [1,2]. It is assumed that the crack occupies the region denoted by $\Omega\,(t)$ at time t.

The governing equation of fluid flow inside the crack is as:

$$\partial w/\partial t = \nabla.\,[D(w)(\nabla p - \rho g)] + \delta(x,y)Q,$$

Where p is fluid pressure, ρ is the fluid density, g is the gravity vector, $\delta(.)$ is the Dirac delta function, $Q(x,y,t)$ is the source injection rate, $D(w)=w^3/12\mu$, w is the fracture width and μ is the Newtonian fluid viscosity.[1,2]

3-Numerical analysis

The finite element method was used to calculate the stress intensity factor due to the complexity of the geometry and boundary conditions. The FE model ANSYS was used to simulate the hydraulic fracture process.

In the ANSYS software, there are 3 main ways to evaluate fracture mechanic parameters:

1: Stress intensity factor (K) 2: J-integral JINT (J) 3: Energy release rate VCCT (G)

3.1-Stress Intensity Factors (SIF)

The stress-intensity factor, K, is a parameter to characterize "the stress field ahead of a sharp crack in a test specimen or a structural member". The parameter, K, is related to the nominal stress level (σ) in the structural member and the size of the crack, and has units of (MPa.mm$^{0.5}$). In general, the relationship is represented by:

$$K=\sigma \sqrt{a}\, p$$

where p is a geometrical parameter that depends on the structural member and crack, a is the crack length. All structural members or test samples that have flaws can be loaded to different levels of K. This is similar to the situation where unflawed structural can be loaded to different levels of stress (σ). [3]

3.2- *J*-integral JINT (*J*)

The *J*-Integral evaluation is based on the domain integral method proposed by Shih. The domain integration formulation applies area integration for 2-D problems and volume integration for 3-D problems. Area and volume integrals offer much better accuracy than contour integral and surface integrals, and are much easier to implement numerically [*4*].

3.3- Energy release rate VCCT (*G*)

Energy release rate is based on the assumption that the energy needed to separate a surface is the same as the energy needed to close the same surface. The approach for evaluating the energy-release rate is based on the virtual crack-closure technique (VCCT) [5].

4-Numerical simulation

The behaviour of a horizontal well with a crack initiated in its wall was studied under hydrostatic pressure. Figure 1 shows the stress intensity factor for the Modes I fracture versus the crack length. The results indicates that stress intensity factor increases by increasing the crack length. Figure 2 shows the variation of leakage rate with crack length. It can be seen that the leakage rate increases with increasing the crack length.

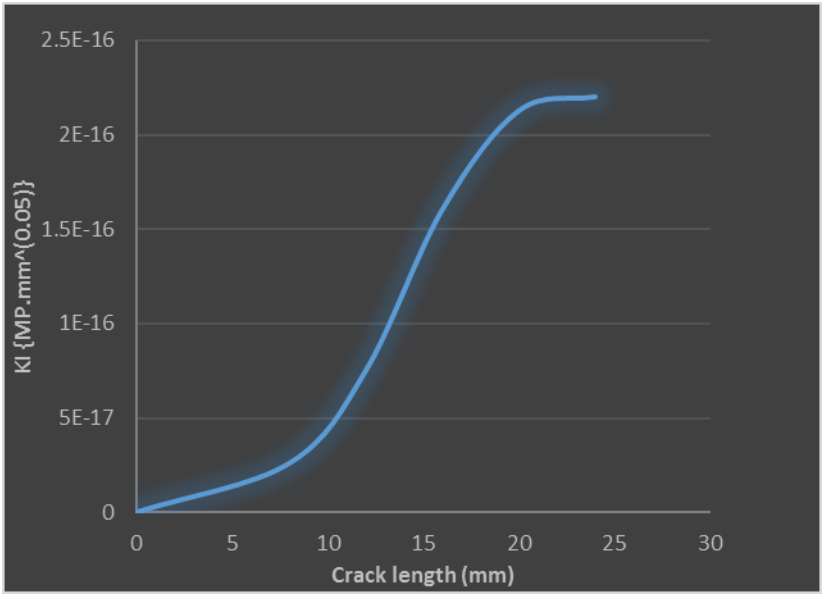

Figure1: Variation of stress intensity factor with crack length

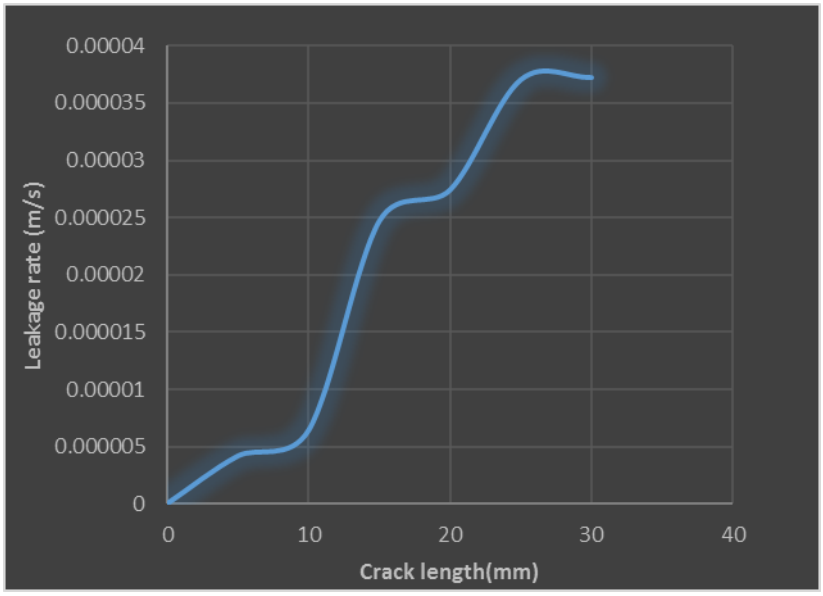

Figure2: Variation of leakage rate with crack length

5-Conclusion

The goal of this investigation was to better understand the link between crack lengths, leakage rate and stress intensity factor in a typical well.

The linear-elastic fracture toughness of a material with a thin crack was determined from the stress intensity factor (*K*).

The obtained results indicate that stress intensity factor increases by increase of crack length.

The numerical results indicate that the fluid leakage rate increases by increasing the crack length.

The leak rate analysis provided reasonable results when compared against the available research and test results.

It can be concluded that FE modelling is an efficient tool for the analysis of leakage and stress intensity factor in crack propagation.

Refrences

[1] Adachi J., Siebrits E., Peirce A., and Desroches J., Computer simulation of hydraulic fractures, Int. J. Rock Mech. Min. Sci., 44, pp. 739–757, 2007.

[2] Advani, S.H., Lee, T.S. and Lee, J.K., Three dimensional modelling of hydraulic fractures in layered media: Finite element formulations, J. Energy Res. Tech., 112, 1-18, 1990.

[3] Barsom, John M. and Rolfe, Stanley T., Fracture and Fatigue Control in Structures: Application of Fracture Mechanics, Philadelphia, 1999.

[4]Shih, C. F., B. Moran, and T. Nakamura, Energy Release Rate Along a Three-Dimensional Crack Front in a Thermally Stressed Body, International Journal of Fracture, 30, pp 79-102, 1986

[5] Delorenzi HG, On the energy release rate and the J-integral for 3-D crack configurations, Int. J. Fract. 19, 183–193, 1982.

Geomechanics II

Proceedings of the 24th UK Conference of the
Association for Computational Mechanics in Engineering
31 March - 01 April 2016, Cardiff University, Cardiff

A Contact Detection Code using Triangles for Non-Spherical Particle Simulations

***Konstantinos Krestenitis[1], Tobias Weinzierl[1] and Tomasz Koziara[1]**

[1]School of Engineering and Computing Sciences, University of Durham, DH1 3LE, Durham

*konstantinos.krestenitis@durham.ac.uk

ABSTRACT

We present a novel DEM (discrete element method) code with explicit time stepping. DEM codes simulate billions of small particles that interact with each other primarily through collisions. Different to state-of-the-art codes, we rely on triangulated non-spherical particles. This is computationally demanding, and we thus devise an asynchronous data exchange communication technique using MPI (Message Passing Interface) on manycore supercomputers, we discuss possible solutions to handle ghost particles that overlap multiple subdomains. At the compute node level, shared memory parallelism as well as vectorised SIMD executions are studied. On the algorithmic side, we explore a hybrid parallelisation approach and memory layouts that are suited to combine robust exact geometry checks with a fast penalty-based method.

Key Words: *SIMD; Contact Detection; MPI; Discrete Element Method*

1. Introduction

In contact mechanics, fluid-stucture interaction or other fields, it is an essential task to compute the distance between geometries to determine contact. We present a Discrete Element Method (DEM) code that simulates particles that interact through spring contact. DEM for example is used to study granular particles in environmental or medical engineering. Different to state-of-the-art codes, we do not use spheres to model the geometry [2] but rely on triangles to model meshed surfaces. Non-spherical particles promise to facilitate more accurate physics than sphere-based approaches [5]. The focus on triangles for rigid body contact dynamics rather than arbitrary polygons simplifies geometric checks and facilitates memory layouts allowing vectorised computation [5]. It is vital to obtain performance from current and upcoming architectures to enable engineers to simulate more realistic materials.

To achieve this we propose a hybrid method that combines the advantages of two triangle-to-triangle distance calculation methods. The method benefits from the performance of an iterative Newton-penalty convergence solver and the robustness of an all-to-all brute force geometric primitive comparison method [5]. We then make this method exploit multi-core and SIMD (Single Instruction Multiple Data) environments [4]. Finally we use the Message Passing Interface (MPI) and Recursive Coordinate Bisection (RCB) load balancing [1] to migrate particles over the HPC cluster nodes while we execute in parallel the contact detection stage of the simulation. The spatial domain decomposition and migration/movement of data requires a careful analysis of data alignment and data dependencies. We use asynchronous non-blocking communication such that there are no waiting delays during the data exchange.

2. Hybrid Vectorised Parallel Contact Detection

Contact detection for non-spherical particles requires us to find the distances between the triangles. Our implementation combines two methods, the brute force method and the iterative Newton-Raphson based on a penalty method for the inequality constraints. The brute force method computes the minimum distance between vertex-to-triangle, and segment-to-segment geometric combinations. Brute force always finds the correct solution but lacks performance as it involves many case distinctions. The penalty method parameterises the distance problem as $f\,(a,b,c,d)_{min} = \|x\,(a,b) - y\,(c,d)\|^2$ where x and y are the barycentric functions of two triangles and it creates a minimization problem to solve. The penalty method

also introduces the penalty parameter r for the steepness of the merit function outside from the feasible domain. In (1) c is the constraint function with six constraints.

$$P(x) = f(x) + r \sum_{i=1\ldots6} max(0, c(x_i))^2 \tag{1}$$

We propose a new hybrid algorithmic approach that combines iterative speed and the robustness of a brute force method. The hybrid 'Newton-Brute Force' solver first runs a penalty solver. If convergence is not achieved within a specified number of iterations (typically four) it falls back to the robust brute force. The decision to fall back is made when the difference between two Newton steps is not within a specified tolerance level.

We split the computational work into batches of fixed size. A batch is a set of triangle pairs that have to be checked against each other. Every batch passes through the penalty solver with SIMD. The handling of multiple triangle comparisons thus can be fused, which allows us to exploit wide vector registers. Convergence checks and fall-back to brute force is done on a per-batch basis. Using multiple cores/threads, it is possible to execute the batches in parallel.

Algorithm 1 DEM Simulation Pseudo code

1. Load balance triangles //assigment to subdomains
2. Migrate triangles to MPI network using blocking communication //balancing movement
3. Search overlapping ghost triangles to send
4. Initiate neighbors asynchronous MPI send/receive
5. Local all to all triangle contact detection
6. Retrieve required ghost triangles from neighbors
7. Local all to ghost triangle contact detection //data exchange
8. Wait for neighborhood asynchronous communication to terminate (No Real Wait)
9. Derive contact forces from contact points generated from contact detection
11. Explicit time integration

For many-node supercomputers we decompose the computational domain into subdomains. Alternative decomposition approaches in the literature such as force decomposition that are applied in molecular dynamics (MD) and smoothed particle hydrodynamics (SPH) simulations [2, 3] are not benchmarked. Our decomposition is based on the spatial position of triangle points using Recursive Coordinate Bisection (RCB) [1]. Each triangle thus is owned - and persistently stored-exclusively on one rank. Copies are exchanged per time step where triangles overlap into neighboring domains.

Algorithm 1 describes the whole DEM simulation and how MPI communication is realised. Data transfers between subdomain ranks on MPI use blocking synchronous and asynchronous non-blocking communication at different stages of the DEM simulation. During the data migration/movement stage blocking synchronous communication is used to move local triangles to neighboring processes to realise load re-balancing. Asynchronous communication is used to exchange ghost triangles between neighbors to maintain streamlined computation while minimizing communication waiting overhead.

3. Implementation

It is uncertain whether the penalty iterations converge for every batch in four iterations. This creates a couple of implementation challenges that affect performance. There are load balancing implications with OpenMP due to the non-deterministic nature of the algorithm. It is not possible to know a priori the balancing of such a non-deterministic algorithm. The uncertain runtime cost stems from the geometry of the problem. A solution is to rely on dynamic scheduling. Investigations however show that dynamic balancing does not show signs of performance improvement and this is subject to further investigation. It remains an open question whether static scheduling is sufficient.

Another tuning parameter is the batch/grain size. The grain size behavior affects the tolerance value and the SIMD work performed by both penalty and brute force methods. The bigger the more triangle

Algorithm 2 Hybrid Triangle Distance Computation Algorithm

```
1. FOR batches of grain size X loop through shared memory threads:
2.     run penalty-based Newton penalty solver
3.     IF batchError [i] > 1E-8 //fixed error value
4.       FOR batches of grain size X loop through shared memory threads:
5.         run brute force segment to segment, point to triangle comparison solver
6.       ENDFOR
7.     ENDIF
8. ENDFOR
```

comparisons can be fused into SIMD statements. However, if only one triangle fails to converge, the whole batch falls back to brute force. Tuning the grain size is nontrivial. Trial and error fine-tuning over a given set of random triangles worked best for static load balancing. The batch size for random triangles is optimal at size eight.

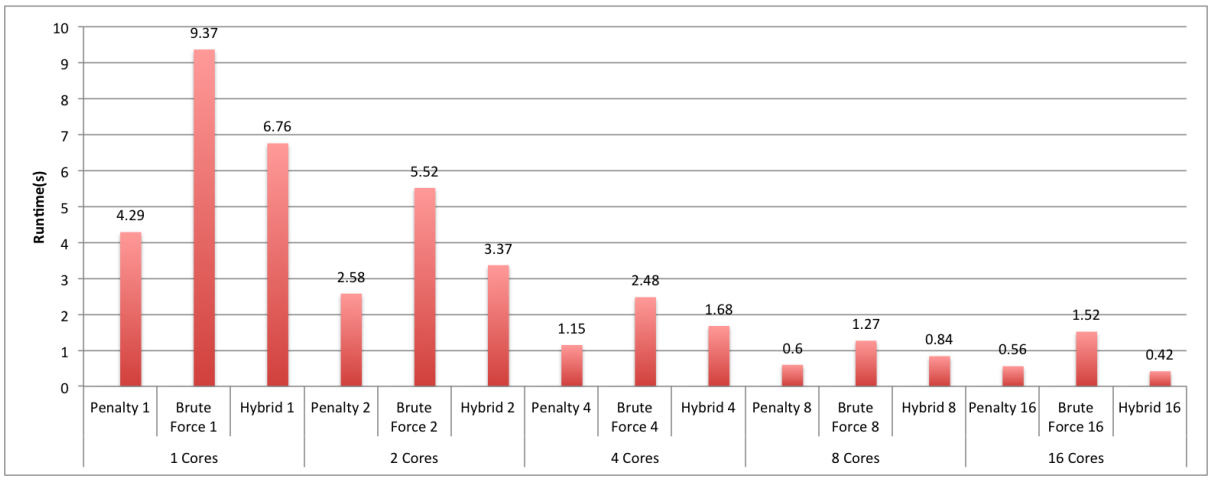

Figure 1: Run-time comparison of the penalty, brute force and the hybrid method over set of cores (OpenMP 4.0).

The hybrid approach performance is shown in Figure 1 where multi-core executions run on all cores. Its performance is settled between brute force and penalty. The hybrid method is slower than penalty because there are batches of triangle pairs that do not reach convergence tolerance. It is faster than brute force because if the batch size is optimal no significant number of batches fail the tolerance criterion. The hybrid algorithm scales over the second socket of the CPU. It is observed that brute force does not gain significantly between eight and sixteen cores because of bandwidth stagnation at the socket interconnect. Theoretically, performance can be tuned further by investigating the load balancing implications of the non-deterministic element of the algorithm.

A major challenge is sustaining a balanced workload while minimizing inter-node communication and maximizing intra-node vectorisation. Splitting the spatial domain and assigning subdomains to cores introduces data dependencies between neighboring ranks. Subdomains have to retrieve surface triangles that overlap into neighboring subdomains. We rely on the state-of-the-art load balancer Zoltan [1] and focus exclusively on the compute phase of the algorithm.

In Figure 2 we measure the total MPI waiting time of ranks for neighbor data exchange if no non-blocking MPI is used. We see an increase with the number of rank. This motivates our non-blocking scheme where neighbour data exchange is triggered before any local computation starts. Once all local computations terminate, the distance of local triangles against remote ghosts are computed to get the overall local domain contacts. The non-blocking communication strategy scales perfectly, if the local contact detection takes longer than the transmission of the ghost data exchange.

All performance tests in Figures 1 and 2 use the AVX instruction set on an Intel Sandy Bridge 2.0GHz i5

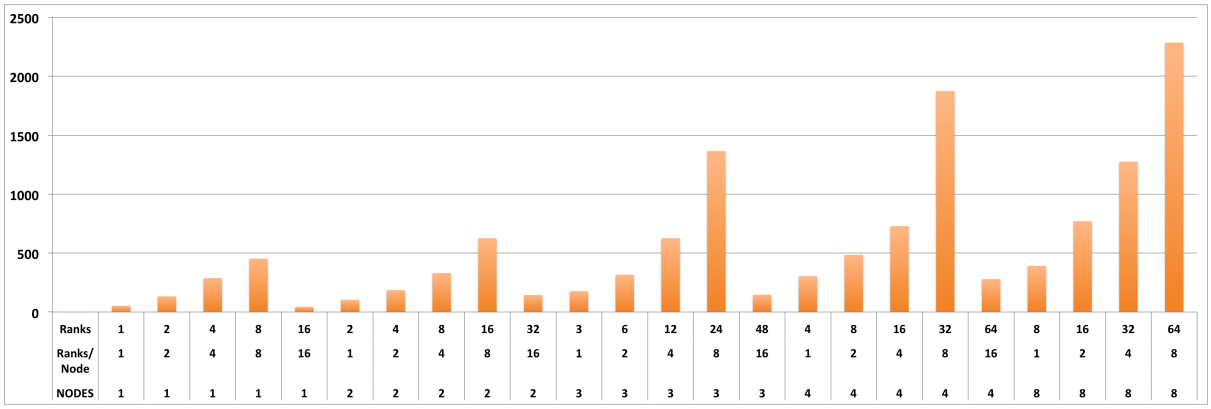

Figure 2: Waiting time [t]=s per MPI rank/node for all-to-all neighbor data exchange over 1000 timesteps (25 mil triangles, 10k non-spherical particles).

CPU with 600 MHz DDR3 RAM. The performance test comprises computing the distance of ten million pairs of multiple lengths.

4. Conclusion

The research provides insight to a hybrid solver that offers robustness and speed for triangle-based DEM algorithms. We study MPI communication patterns and the implications on data layouts using asynchronous non-blocking communication to avoid waiting delays during exchange of ghost triangles. We seem to obtain reasonable scalability and performance for triangle-based particle realisation but many important questions with respect to load balancing remain open.

5. Acknowledgments

This work has been sponsored by EPSRC (Engineering and Physical Sciences Research Council) and EDF Energy as part of an ICASE studentship. This work also made use of the facilities of N8 HPC provided and funded by the N8 consortium and EPSRC (Grant No. N8HPC_DUR_TW_PEANO). The Centre is co-ordinated by the Universities of Leeds and Manchester. We also thank University of Durham for the supercomputing resources and technical assistance. All underlying software is open source and available at [6].

References

[1] Erik G. Boman, Umit V. Catalyurek, Cedric Chevalier, and Karen D. Devine. The Zoltan and Isorropia parallel toolkits for combinatorial scientific computing: Partitioning, ordering and coloring. Sci. Program. 20, 2 (April 2012), 129-150. DOI=http://dx.doi.org/10.1155/2012/713587

[2] S. Plimpton, Fast Parallel Algorithms for Short-Range Molecular Dynamics, J Comp Phys, 117, 1-19 (1995).

[3] Shaw, D.E. A fast, scalable method for the parallel evaluation of distance-limited pairwise particle interactions. Journal of Computational Chemistry, 26(13):1318-1328, 2005.

[4] Shuo Li, Brian Rea, Jim Cownie. Extending Parallelism from Intel Xeon Processor to Intel Xeon Phi Coprocessor: A Structured, Stepwise Approach to Manycore Programming. Intel Corporation. 2014

[5] Krestenitis, K. Koziara, T. Calculating the minimum distance between triangles on SIMD Hardware. ACME. Swansea, United Kingdom. 2015

[6] Krestenitis, K. et al. Delta - A Contact Detection Framework for Non-Spherical Particle DEM Simulations. 2016. http://ikonstantinos.com/delta/.

Proceedings of the 24th UK Conference of the
Association for Computational Mechanics in Engineering
31 March - 01 April 2016, Cardiff University, Cardiff

ENERGY DISSIPATION IN GRANULAR MATERIAL UNDER 1D COMPRESSION

***R.A. Mukwiri[1], Y. Ghaffari Motlagh[1], W.M. Coombs[1] and C.E. Augarde[1]**

[1]School of Engineering & Computing Sciences, Durham University, South Road, Durham, DH1 3LE, UK

*r.a.mukwiri@durham.ac.uk

ABSTRACT

In recent years it has been shown that the micro-mechanics of one-dimensional normal compression of sands can be modelled in three-dimensions within the discrete element method [7]. The compression is displacement driven such that the top platen of the enclosing sample case is allowed to move at a constant or variable velocity. The test has been used to investigate sand behaviour such as compressibility and the evolution of the particle size distribution when particle crushing is permitted. This paper focuses on the findings related to energy dissipation under one-dimensional compression without particle crushing using the LIGGGHTS open source software. Energy tracing is done throughout the simulations by applying the energy conservation principle at every time step. This allows the evolution of energy dissipation to be determined. The relationship between energy dissipation and particle size distribution was investigated and is discussed in this paper. Understanding the relationship between grain scale properties and energy dissipation will help in the formulation of a constitutive relationship based on a hyperplasticity framework [8]. This could potentially lead to a shift in the way that continuum constitutive models are formulated, with numerical models truly being based on the constituents that they represent.

Key Words: *DEM; energy dissipation; compression; particle size distribution; hyperplasticity*

1. Introduction

The Discrete Element Method (DEM) has been used for numerical simulations of particle assemblies since its introduction in 1979 by Cundall and Strack [6]. More recently DEM has been used to model the one-dimensional normal compression of sands [7]. This work has aided in the study of sand behaviour such as compressibility and the evolution of the particle size distribution when particle crushing is permitted. However, in this paper particle crushing is not investigated.

Energy dissipation in granular media has been a subject of study in recent years using the DEM. Wang and Huang [13], for example, presented a DEM analysis of energy dissipation in crushable soils in which it was observed that crushability strongly affect energy dissipation. Zhang *et al.* [14] investigated the relationship between energy dissipation and shear band formation under rolling resistance. The effect of grain roughness on energy dissipation was investigated during a quasi-static homogeneous triaxial compression test on cohesionless sand under constant lateral pressure [10]. Shamy and Denissen [11] studied energy dissipation response due to seismic loading.

By obtaining an energy dissipation function for a material, a yield surface and plastic flow rule can be derived to describe the inelastic behaviour of a material based on the framework of hyperplasticity [8]. However, current dissipation functions are driven by obtaining better curve fits to experimental data rather than deep understanding of the underlying physics. Investigating the relationship of energy dissipation at a grain scale level will facilitate the transition from the convention by allowing the constituents of granular materials (sands here in particular) to dictate the form of the dissipation function. One of these constituents is the particle size distribution which is investigated in this paper. It was quantified by varying the coefficient of uniformity parameter, which is defined as

$$CU = \frac{D_{60}}{D_{10}} \tag{1}$$

where D_{60} grain diameter at 60% passing and D_{10} grain diameter at 10% passing. The grain diameter here defines the sieve sizes through which the particles of soils and sands pass during soil grading. Soil grading is a classification of soil based on its different particle sizes. If the soil or sand is predominantly of one grain size, it will be classed as poorly graded and will have a coefficient of uniformity close to one. A well graded soil will have a wide range of particle sizes in it with a CU value > 4 for gravels or CU ≥ 6 for sands.

2. Energy dissipation in DEM

To account for the dissipated energy, energy conservation is applied through either a simplified approach or a detailed consideration of the energy terms in the system. Houlsby *et al.* [9] for example, in the study of landslides take the dissipated energy to be the remainder of the total potential energy at the start of the simulation minus the sum of the potential energy and the kinetic energy at each stage of the simulation. Asmar *et al.* [5] explicitly worked out the dissipated energy from damping and friction. Other forms of energy: the elastic energy, potential energy, kinetic energy, and the input energy were also monitored. Wang and Yan [12] also included a bond energy between particles during particle breaking.

Wang and Yan [12] showed that at every stage of shearing (in the direct shear test of agglomerates), the conservation of energy equation is given by

$$dW + dW_g = dE_s + dE_b + dE_f + dE_k + dE_d \tag{2}$$

where the energy terms are: boundary work dW, potential energy dW_g, strain energy dE_s, bond energy dE_b, frictional dissipation dE_f, kinetic energy dE_k and damping dissipation dE_d. This is consistent with other literature (for example; [5]) when the effect of particle bonding is ignored. The energy loss due to damping is due to the need to dissipate excess kinetic energy.

3. Numerical simulations

There are a number of commercial and open source DEM software currently in use for the study of particulates (e.g EDEM, PFC, LIGGGHTS, etc. [1, 3, 2]). For the simulations in this paper, the open source LIGGGHTS software was used. Unlike many commercial codes, LIGGGHTS has no graphical user interface. The user drives the simulation using a text-based input script. This input script is read sequentially rendering the ordering of the statements important. The simulations for this paper consisted of four parts:

1. *Initialization:* parameters that need to be defined before the particles are created are set. The boundary was set to be non periodic and moving to allow for the one-dimensional compression. Other parameters such as the domain to run the simulation in and the style of particles specified.
2. *Setup:* material properties and geometry defined. The particle generation procedure was also detailed during the problem setup. The material properties are shown in Table 1 where μ is the friction coefficient between particles, E the particle Young's modulus, ν the Poisson's ratio, and ρ the particle density.
3. *Detailed settings:* settings that correspond to speed and memory utilisation were specified and the output options were also created.
4. *Execution:* actual run command that executes the simulation. The simulations were run in a number of stages. The first stage was to insert the particles into the simulation cylinder. These were then allowed to settle and then compressed at constant velocity by moving the top platen for a specified number of time steps at and then unloading by moving the platen upwards.

Table 1: 1D Compression test parameters

Sample size: $Dia \times H$ (mm)	μ	E (Mpa)	ν	ρ (Kg/m^3)
18×10	0.5	70	0.25	2650

There are two basic types of statements in a LIGGGHTS input deck - individual commands and fixes. The commands establish the settings of the simulations (e.g. the time step) while the fixes are used to set particular aspects of the simulation (e.g. material properties and meshes). For the simulations conducted in this paper, separate meshes were generated using the gmesh software and input as STereoLithography (STL) files via a fix statement in the input script.

Once the simulations were complete, the output files were run through the LIGGGHTS Post-Processing (LPP) software in which the Visualisation Toolkit (VTK) files were generated. They were then visualised using ParaView [4] and processed for energy dissipation using Matlab.

3.1. Results and discussion

Figure 1 shows the boundary energy input during the loading and unloading of sand samples of different coefficients of uniformity. The area enclosed between these two curves is proportional to the dissipated energy during the loading and unloading cycle. The top platens compressed the sand samples to 0.3 mm strains before unloading back to the same position. It was found that as the coefficient of uniformity was increased, the area between the loading and unloading curves also increased. More tests are currently being done to determine if the coefficient of uniformity is an accurate measure of the particle size distributions.

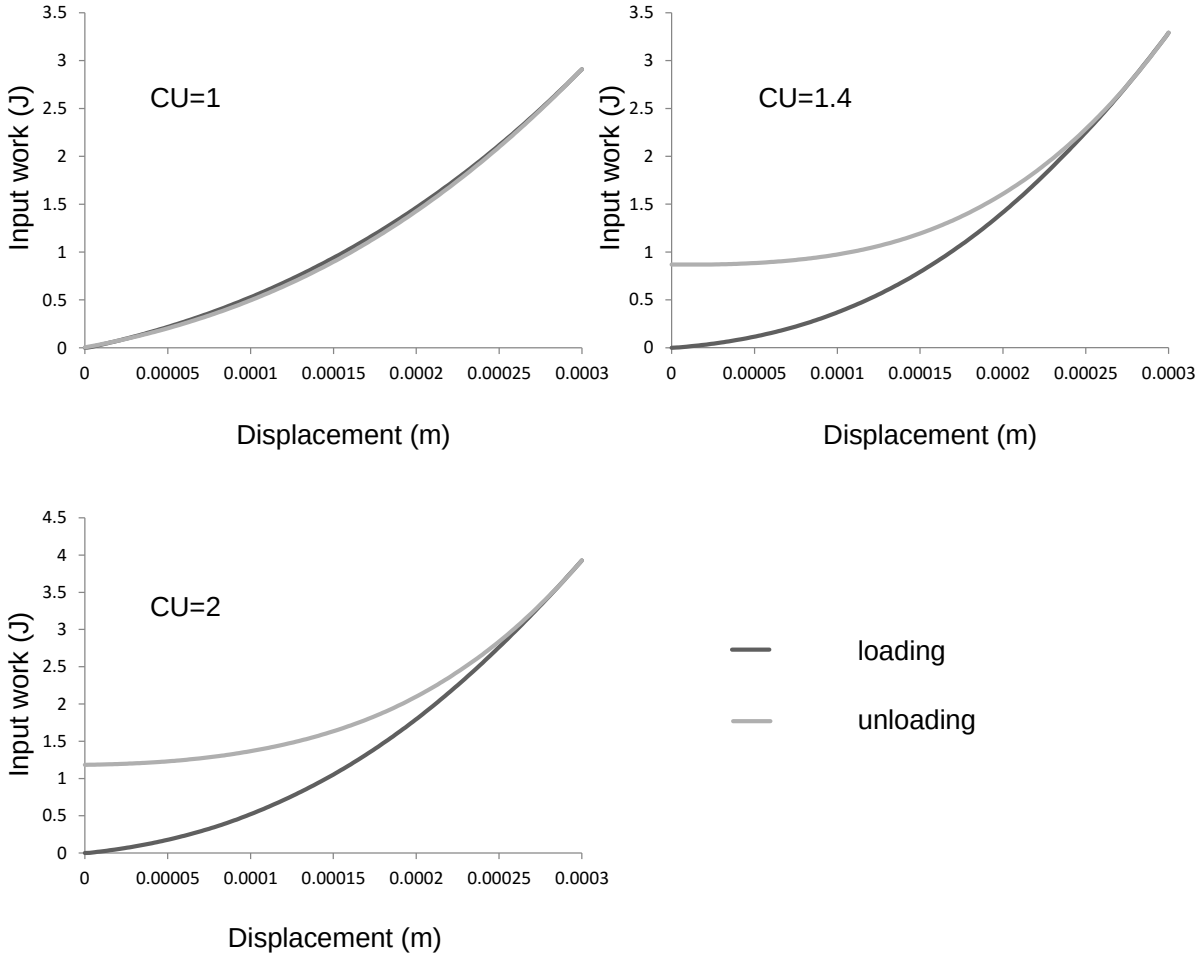

Figure 1: Energy input versus displacement for one dimensional compression tests with different CU values

4. Conclusions

One-dimension compression of sand has been carried out to study how energy is dissipated with a variety of particle size distributions using the DEM. The results suggest that more energy is dissipated as the coefficient of uniformity is increased. Further investigation is being done to determine if the particle size distribution is uniquely defined by the coefficient of uniformity for the purpose of the energy dissipation study. A parametric study is currently being carried out for other grain scale parameters such as coefficient of friction, particle density, voids ratio and compressibility and the results will be used to formulate a one dimensional dissipation function for sands. Experimental validations will then be carried out to ensure that the formulations made are consistent with the observed physical phenomena.

References

[1] *DEM-Solutions*, 2015. URL `http://www.dem-solutions.com/`. Last Accessed 20 Aug 2015.

[2] *LIGGGHTS Open Source Discrete Element Method particle simulation code*, 2015. URL `http://www.cfdem.com/`. Last Accessed 20 Aug 2015.

[3] *PFC*, 2015. URL `http://www.itascacg.com/software/pfc`. Last Accessed 20 Aug 2015.

[4] *ParaView*, 2015. URL `http://www.paraview.org/`. Last Accessed 20 Aug 2015.

[5] B.N. Asmar, P.A. Langston, A.J. Matchett, and J.K. Walters. Energy monitoring in distinct element models of particle systems. *Advanced Powder Technology*, 14(1):43–69, 2003.

[6] P.A. Cundall and O.D.L. Strack. A discrete numerical model for granular assemblies. *Géotechnique*, 29:47–65, 1979.

[7] J.P. de Bono and G.R. McDowell. On the micro mechanics of one-dimensional normal compression. *Géotechnique*, 3:166–172, 2013.

[8] G.T. Houlsby and A.M. Puzrin. *Principles of Hyperplasticity*. Springer, 2006.

[9] G.T. Houlsby, S. Utili, and T. Zhao. 3D DEM investigation of granular column collapse: Evaluation of debris motion and its destructive power. *Engineering Geology*, 186:3–16, February 2015.

[10] J. Kozicki, Z. Mróz, and J. Tejchman. Effect of grain roughness on strength, volume changes, elastic and dissipated energies during quasi-static homogeneous triaxial compression using dem. *Granular Matter*, 12:457–468, 2012.

[11] U. El Shamy and C. Denissen. Microscale characterization of energy dissipation mechanisms in liquefiable granular soils. *Computers and Geotechnics*, 37:846–857, 2010.

[12] J. Wang and H. Yan. DEM analysis of energy dissipation in crushable soils. *Soils and Foundations*, 52:644–657, 2012.

[13] J. F. Wang and R.Q. Huang. DEM study on energy allocation behavior in crushable soils. *Advanced Materials Research*, 871:119–123, 2013.

[14] W. Zhang, J. Wang, and M. Jiang. DEM-Aided discovery of the relationship between energy dissipation and shear band formation considering the effects of particle rolling resistance. *J. Geotech. Geoenviron. Eng.*, 139:1512–1527, 2013.

Impact of soil surface heat fluxes and weather conditions on the performance of near surface inter-seasonal ground energy collection and storage systems

***Jose J. Munoz-Criollo[1], Peter J. Cleall[1] and Stephen W. Rees[1]**

[1]School of engineering, Cardiff University, Queen's building The Parade, Cardiff, CF24 3AA

*munozcriollojj@cardiff.ac.uk

ABSTRACT

A numerical model based on the finite element method is applied to study the thermal performance of a near-surface inter-seasonal heat storage facility. The model is validated comparing 2D numerical results with experimental measurements from a case study project undertaken by others [Carder et al 2007]. The model is used to assess the impact that three alternative formulations of thermal fluxes at the soil surface have on the estimation of seasonal variations of temperature and stored thermal energy in the soil close to the surface. It is also shown that the choice of surface heat fluxes and initial conditions have an effect on the number of yearly cycles required to reach steady state conditions. The influence of weather conditions on the performance of the system is explored using weather data obtained from publicly available sources for three representative climates (hot, mild and cold).

Keywords: *Thermal Energy Storage ; Numerical modelling ; Soil surface heat flux ; Inter-seasonal Heat Transfer ; Inter-seasonal Thermal Storage*

1. Introduction

The process of inter-seasonal heat collection and storage imply taking thermal energy from a season with high availability to a season with high demand through the use of a suitable medium. A possible source of solar thermal energy for inter-seasonal heat storage systems are road surfaces [1]. In this case, the operation of the system is highly dependent on the interactions between the ground and pavement surfaces and the atmosphere since this determines the amount of energy available for the system. It is therefore necessary to correctly understand the processes of energy flux and heat balances at the surface of the ground. This is particularly true in near-surface systems. This paper presents selected results from a more comprehensive numerical investigation [2] of the processes affecting the performance of inter-seasonal heat storage systems. Numerical simulations are undertaken using a numerical model which is validated against an excellent dataset produced by others [3] in the course of a two year-long inter-seasonal heat storage system demonstration project. The results presented in this paper are selected with the purpose of exemplify the impact that different parameters have in the operation of these systems and the simulation of their behaviour, in particular the effect of: formulation of heat transfer coefficients at the soil surface, selection of bottom boundary conditions and initial conditions and weather influence in system performance are considered.

2. Theoretical and numerical model

The temperature variation in a soil domain is obtained by solving the transient heat transfer equation:

$$\frac{dT}{dt} = \alpha \nabla T \tag{1}$$

where T (˚C) and α (m^2/s) are the soil's temperature and thermal diffusivity. In this work equation (1) is solved by using a boundary condition of the third kind at the soil surface that takes into account heat transfer by solar and infrared radiation, convection and evaporation:

$$-k\frac{dT_{ss}}{dx}=(1-\alpha_S)R+\sigma\varepsilon_{ss}\left(\varepsilon_s T_{a,k}^4-T_{ss,k}^4\right)+h_E(q_a-q_{ss})+h_C\left(T_a-T_{ss}\right) \quad (2)$$

where T_{ss} (˚C), $T_{ss,k}$ (K), q_{ss}, k (W/mK), α_s and ε_{ss} are the soil's surface temperature, absolute surface temperature, surface specific moisture content, thermal conductivity, albedo and infrared emissivity respectively, R (W/m^2) is solar radiation, σ (W/m^{2}K^4) is the Steffan-Boltzmann constant, ε_s is the infrared emissivity of the sky, T_a (˚C) and $T_{a,k}$ (K) are the temperature and absolute temperature of air, q_a is the specific moisture content of air, h_E (W/m^2) and h_C (W/m^{2}K) are evaporative and convective heat transfer coefficients respectively.

Three approaches are used to investigate the impact that alternative theoretical formulations of the convective and evaporative heat transfer coefficients: i) a *turbulent* approach [4] that assumes turbulent conditions between the surface and the atmosphere; ii) a *non-turbulent* approach [5] that assumes the presence of natural convection and iii) an additional approach [6,7] that takes into account the presence of a canopy cover on top of the soil surface through a second heat balance equation additional to (2). A full description of the heat transfer coefficients and heat balance including a canopy cover as well as values for coefficients in equation (2) can be found in [2,8].

3. Case study

The experimental measurements used in this work have been provided by the Transport Research Laboratory (TRL) [3] from a two year-long demonstration project at Toddington, UK. The objective of that project was to assess the feasibility of recovering thermal energy in summer in order to be used for thermal maintenance of roads and/or building heating in winter. Approximate positions of two boreholes used in this paper and the position of the system are shown in Figure 1b. Full details regarding system operation, material properties, soil and meteorological data can be found in [2,3].

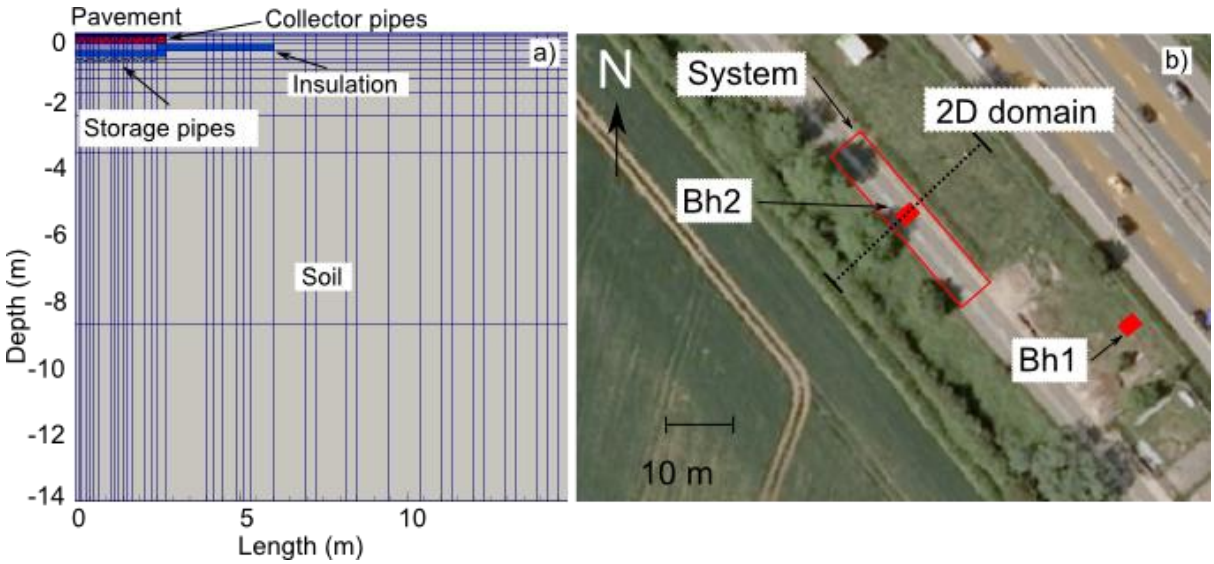

Figure 1 - a) Half of domain used in this work showing position of main elements. b) Position of experimental system and boreholes used in this work and approximate position of 2d domain.

4. Numerical study

The numerical model developed in this study is based on solving equation (1) using the finite element method. The boundary condition at the soil surface is assumed to be of the third type and given by equation (2). Far field boundary conditions are assumed to be adiabatic. The effect of the boundary condition at the bottom of the domain is part of the study of this work. Time discretization is performed using the Crank-Nicholson method using hourly time steps. Figure 1a shows a sub region of the domain considered in this work, full domain details, mesh refinement and representation of pipe system operation can be found in [2].

Figure 2 shows typical results from validation of the proposed model, comparing numerical results and recorded experimental measurements provided by Carder et al [3]. It can be seen that both are in good agreement. The validated model is further used to explore the effect of varying different parameters:

- *The effect of bottom boundary condition and initial temperature profile on the number of yearly cycles required to reach steady state conditions in the domain*. Two options are considered: a fixed value using experimental measurements; and adiabatic conditions allowing free variation at the bottom of the domain. Three initial temperature profiles are considered: homogeneous temperature profile, profile based on experimental measurements and a profile produced with analytical equations available in the literature [9].
- *The influence of using alternative formulations of heat transfer coefficients in the amount of thermal energy stored in the ground*. Two formulations are compared at the soil surface: non-turbulent formulation and a formulation considering the inclusion of a canopy layer.
- *The effect of different weather conditions in the collection performance of an inter-seasonal heat collection and storage system*. Three representative types of weather are explored: cold, mild and hot. Weather data is constructed using analytical functions available in the literature [9] based data obtained from publicly available meteorological sources from Iceland, UK and Mexico.

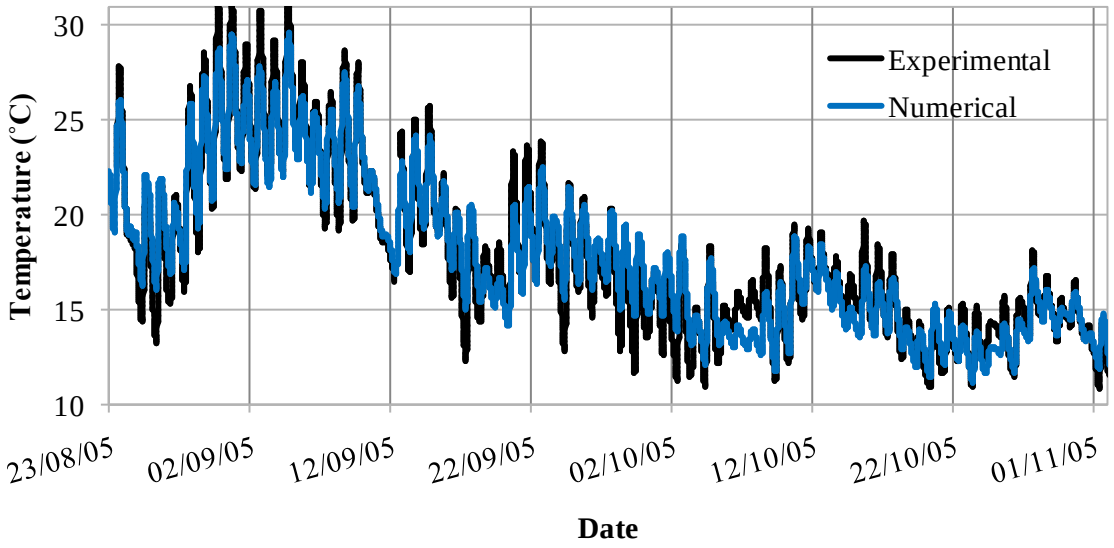

Figure 2 - Comparison between numerical results and experimental data at 0.1325 m depth (collector pipes depth) under the paved surface.

5. Discussion and conclusions

Analysis of the impact of initial and bottom boundary conditions in the number of yearly cycles necessary to reach a steady state near the bottom of the domain found that a fixed condition drastically reduces the number of cycles, however, it is dependent on suitable experimental measurements that might not always be available. On the other hand, an adiabatic condition requires a comparatively higher number of cycles and is dependent on the heat balance formulation assumed at the surface. However, it requires less information about the temperature in the domain. It was also found that the initial condition has a minimal impact in the number of cycles required.

Figure 3a presents the impact of the heat balance theoretical formulation assumed at the soil surface on the amount of thermal energy stored in a far field region of the ground. The thermal energy variation is compared from 23/08/05, it can be seen that as winter approaches, the soil energy content in the soil decreases as expected. However, a bare-soil formulation has a relatively higher loss of heat than a formulation that includes the presence of a canopy cover.

Figure 3b presents the influence of weather conditions on thermal energy collected by the system. It can be seen that hotter weathers have a comparatively higher energy potential than colder climates. However, the feasibility of the system needs to include also the potential demand for this thermal energy that is expected to be higher in colder regions than in hotter ones.

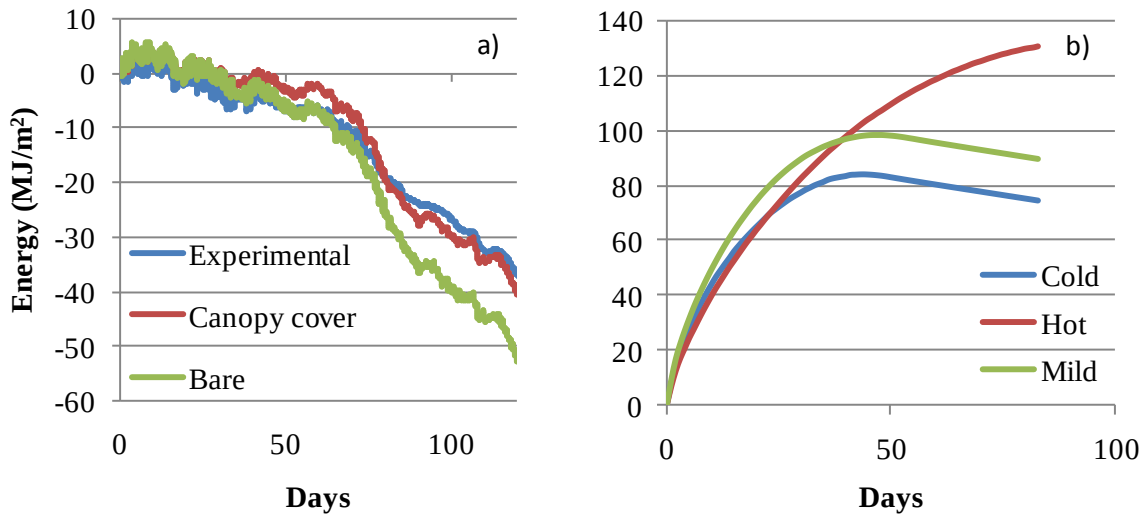

Figure 3 - a) Effect of theoretical formulation of heat balance at the soil surface on the amount of thermal energy stored in the far field ground. b) Influence of weather conditions on amount of estimated thermal energy collected by the system. Day 0 corresponds to 23/08/05.

Acknowledgements

The authors gratefully acknowledge the support given to the first author by CONACYT (the Mexican National Council of Science and Technology) and SEP (Mexican Secretariat of Public Education). Also we are grateful to TRL/HA for release of the source data published in (Carder et al., 2007).

References

[1] V. Bobes-Jesus, P. Pascual-Muñoz, D. Castro-Fresno, and J. Rodriguez-Hernandez, Asphalt solar collectors: A literature review, *Applied Energy*, vol. 102, pp. 962–970, 2013.

[2] J. J. Muñoz Criollo, *An investigation of inter-seasonal near-surface ground heat transfer and storage*, Ph.D. Thesis, Cardiff University, 2014.

[3] D. R. Carder, K. J. Barker, M. G. Hewitt, D. Ritter, and A. Kiff, *Performance of an interseasonal heat transfer facility for collection, storage and re-use of solar heat from the road surface*, Transport Research Laboratory, PPR302, 2007.

[4] J. E. Edinger and D. K. Brady, *Heat Exchange and Transport in the Environment*. John Hopkins University, 1974.

[5] W. R. Herb, B. Janke, O. Mohseni, and H. G. Stefan, Ground surface temperature simulation for different land covers, *Journal of Hydrology*, vol. 356, no. 3–4, pp. 327–343, 2008.

[6] M. J. Best, A Model to Predict Surface Temperatures, *Boundary-Layer Meteorology*, vol. 88, no. 2, pp. 279–306, 1998.

[7] J. Deardorff, Efficient Prediction of Ground Surface-Temperature and Moisture, with Inclusion of a Layer of Vegetation, *Journal of Geophysical Research-Oceans and Atmospheres*, vol. 83, no. NC4, pp. 1889–1903, 1978.

[8] J. J. Muñoz-Criollo, P. J. Cleall, and S. W. Rees, Analysis of Inter-seasonal Heat Fluxes in Soils, *Energy Procedia*, vol. 57, pp. 2315–2323, 2014.

[9] P. J. Cleall, J. J. Muñoz-Criollo, and S. W. Rees, Analytical Solutions for Ground Temperature Profiles and Stored Energy Using Meteorological Data, *Transp Porous Med*, vol. 106, no. 1, pp. 181–199, 2014.

Proceedings of the 24th UK Conference of the
Association for Computational Mechanics in Engineering
31 March - 01 April 2016, Cardiff University, Cardiff

The Effect of Particle Elongation on the Strength of Granular Materials

***M. Potticary[1], A. Zervos[1] and J. Harkness[1]**

[1]Faculty of Engineering and the Environment, University of Southampton, University Road, Southampton, SO17 1BJ

*m.potticary@soton.ac.uk

ABSTRACT

It has long been recognised that the macroscopic mechanical behaviour of a granular material depends on particle shape. However, a systematic investigation into particle shape is lacking. Particle shape is commonly split into the independent categories of form, angularity and roughness. The form of a particle can be quantified using the Longest (L), Intermediate (I) and Shortest (S) dimension of an equivalent scalene ellipsoid; two independent parameters of particle form are defined, termed platyness and elongation.

We use DEM simulations with the Potential Particle Method to investigate the effect of particle form on the friction angle of a granular material at critical state. It is found that deviation of particle form from that of a sphere leads to higher angles of friction at critical state. It is argued that, to some extent, the higher critical state strength exhibited by non-spherical particles is due to form suppressing particle rotation and leading to increased interparticle sliding, a mechanism that in comparison requires more energy to be expended.

Key Words: *Form ; Granular Materials ; DEM ; Ballast ; Shape*

1. Introduction

Particle shape is generally assumed to consist of 3 different independent properties: Form, Angularity and Roughness. Particle form describes the general shape, angularity describes the relative sharpness of angles on the surface and roughness describes the microscopic undulations on particles surface. Particle Form is normally quantified using the longest (L), intermediate (I) and shortest (S) dimensions of the particle, although there is no consensus as to which method is best [1]. Particle form can be characterised by two parameters, Elongation (ζ) and Platyness (α) presented in [4, 5]. Then we use DEM Models made up of particles of a single form and impose triaxial compression conditions to study the effect particle elongation has on the critical state strength. The particles were modelled in an in-house DEM code [2] that uses the concept of potential particles to model arbitrary ellipsoids.

2. Form

In this study we assume form is represented by the particle's longest (L), intermediate (I) and shortest (S) dimension. If we consider L, I and S to be coordinates in a three dimensional space, any particle can be represented by a vector $\mathbf{f}$ linking the origin of the axes to point (L, I, S). Clearly the shape (form) of the particle is represented by the direction of $\mathbf{f}$, whereas the magnitude of $\mathbf{f}$ merely quantifies the size of the particle. By considering the intersection F of $\mathbf{f}$ with the $L+I+S-1=0$ "deviatoric" plane, which is normal to the spherical axis $L=I=S$ (Figure 1), the form of each particle is uniquely defined by the two in-plane coordinates of F in a frame of reference centred at the intersection P of the spherical axis. In this way particle form is essentially quantified as the deviation of a particle's shape from that of a sphere. These two independent parameters of form are given by Equations 1 and are referred to as *platyness*

(α) and *elongation* (ζ) respectively. All possible scalene ellipsoids plot, on the α-ζ plane, within the triangle shown in Figure 1.

$$\alpha = \frac{2(I-S)}{L+I+S}, \qquad \zeta = \frac{L-I}{L+I+S} \tag{1}$$

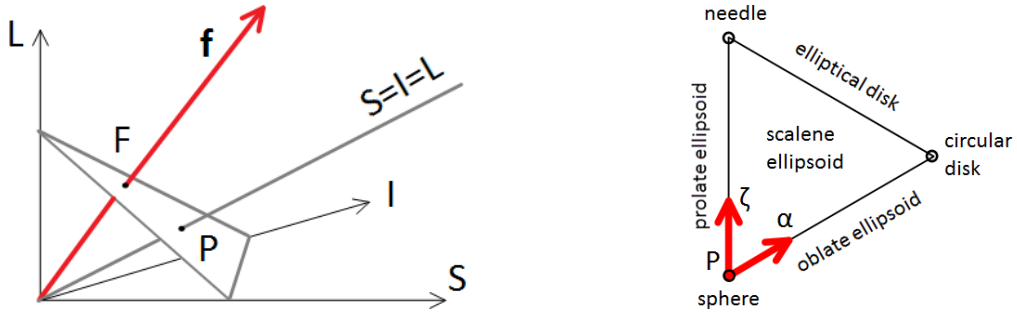

Figure 1: Left: L, I and S space; Right:Elongation and Platyness space with description of forms

Here we focus on the effect of particle elongation by systematically varying ζ, starting from a sphere and conidering increasingly prolate ellipsoid ($L \geqslant I = S$) by increasing the longest radius. Platyness α is kept at 0. The range of forms used is shown in table 1.

Form	Elongation	L : I : S
Form 1	0.000	1.00 : 1.00 : 1.00
Form 2	0.104	1.35 : 1.00 : 1.00
Form 3	0.200	1.75 : 1.00 : 1.00
Form 4	0.305	2.30 : 1.00 : 1.00
Form 5	0.400	3.00 : 1.00 : 1.00

Table 1: Range of forms tested

3. Method

Models were created using particles of a single form and a particle size distribution (PSD) representative of that of railway ballast. To determine the PSD, 5 different sizes between the maximum and minimum gradation curves for railway ballast, keeping I equal to the respective sieve size. To help constrain the models and ensure comparability of results, the total volume of solids contained within each model was kept as close to $0.2m^3$ as possible. Table 2 shows the different model parameters that where used, the material properties where that of a typical granite ballast.

Properties	Value
Particle Density	2700Kg/m^3
Interparticle Friction Angle	30 degrees
Particle Bulk Modulus	50 GPa
Particle Poison's Ratio	0.3

Table 2: Material Properties

To create a model, a number of particles were randomly dispersed within 3D space to a target initial void ratio of 2.0. The particles themselves were given random orientation to remove any bias in the initial conditions that could affect results. The model was then subjected to isotropic compression using periodic boundaries and zero gravity forces. Once a void ratio of 0.65 was reached, isotropic stress of $100kPa$ was applied to the boundaries and the model was

allowed to reach equilibrium. At that point triaxial compression conditions where applied, with stress controlled lateral boundaries at $100kPa$ and a strain controlled top boundary moving downwards at a constant velocity.

4. Results

The strength of a granular assembly is given by the mobilised angle of friction. When a model reaches a critical state the mobilised angle of friction is independent of its initial void ratio. Figure 2 shows how the strength changes as particle form becomes more elongated. It can be seen that spheres have the lowest strength and a linear relationship exists between between increases in elongation and increases in strength.

Quantifying rotations and rotation increments in 3D can be done using quaternions. Here we focus on differences of the amount of rotation between relatively closely spaced time-steps, so that the axis of rotation can be considered unchanged, and divide rotation by the corresponding vertical strain increment to produce a rate of rotation with strain.

Figure 2 plots the median rate of particle rotation against the proportion of sliding contacts for the different particle forms at critical state. Spherical particles rotate much more compared to elongated particles; the rate of rotation decreases with increased elongation. Also, as particle elongation increases there is a reduction in the proportion of sliding contacts at critical state. An inverse relationship is seen between rate of rotation and the proportion of sliding contacts at critical state. Therefore to some extent the higher critical state strength exhibited by elongated particles is due to elongation suppressing particle rotation and leading to increased interparticle sliding, a mechanism that in comparison requires more energy to be expended.

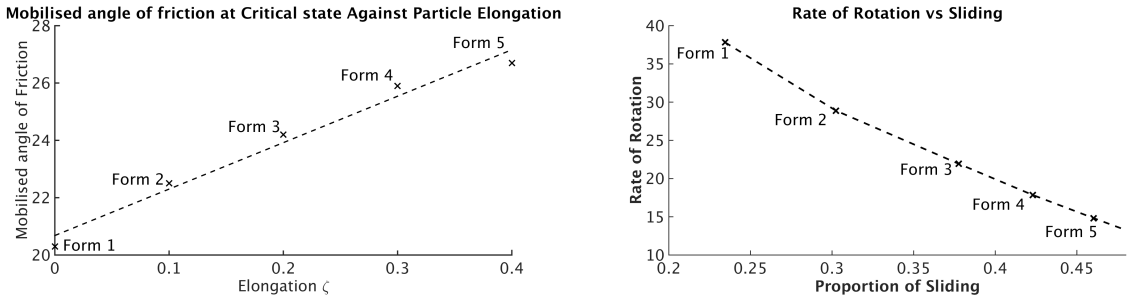

Figure 2: Left: Critical state angle of friction against particle elongation; Right: Median Rate of rotation at critical state against the proportion of contacts sliding

The orientation of elongated particle (prolate ellipsoid), due to symmetry, can be described by a single vector of the direction of the L axis. The average particle orientation with respect to the global model axes can be quantified by a fabric tensor given by Equation 2, [3]. This describes the average orientation of a set of n unit vectors V^k. For randomly oriented vectors the diagonal of G_{ij} will be equal to 0.33 and off-diagonal values will be zero, indicating lack of a preferential direction.

$$G_{ij} = \frac{1}{n}\sum_{k=1}^{n} V_i^k V_j^k \tag{2}$$

Figure 3 shows how the vertical component (G_{33}) of the fabric tensor, corresponding to the L axis of each particle varies with respect to vertical strain. This shows that whilst particles start off with a random orientation, for elongated particles as the model is strained there is a prevalence for the particles to orientate them selves with the L axis perpendicular to the major principal stress. As more particles orientate themselves "flat" there is a layering of particles, leading to a greater number of contacts in the vertical direction. This would provides an efficient skeleton that transfers vertical load, leading to an increase in strength.

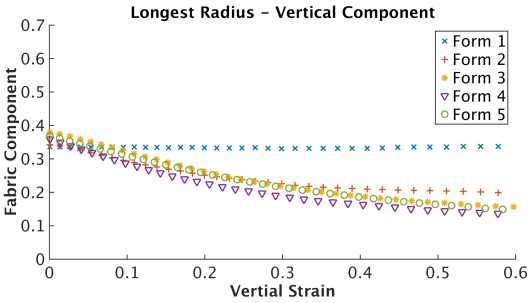

Figure 3: Vertical component of the fabric tensor of L axis

5. Conclusions

In this paper we present a method of characterising form using a scalene ellipsoid and used DEM to investigate the effect of changing particle elongation on critical state strength. It was found that as particle elongation increases there is a similar increase in critical state strength.

This increase in strength accompanied by a reduction in the amount of rotation and an increase in the proportion of sliding contacts. As the model is strained the preference for particles to orientate their longest axis perpendicular to the major principal stress allows for a more efficient way to transfer forces vertically, leading to a stronger assembly.

Acknowledgements

We gratefully acknowledge support from Network Rail (Strategic Partnership with the University of Southampton) and EPSRC Track21 Programme Grant, EP/H044949/1. Use of the IRIDIS High Performance Computing Facility and associated support services at Southampton are also acknowledged.

References

[1] SJ Blott and K Pye. Particle shape: a review and new methods of characterization and classification. *Sedimentology*, pages 31–63, September 2007.

[2] J Harkness. Potential particles for the modelling of interlocking media in three dimensions. *International Journal for Numerical Methods in Engineering*, 80:157315(June):1573–1594, 2009.

[3] Masanobu Oda. Initial fabrics and their relations to mechanical properties of granular material. *Soils and Foundations*, 12(1):17–36, February 1972.

[4] M Potticary, J Harkness, and A Zervos. An investigation in the effect of particle platyness on the strength of granular materials using the discrete element method. In E. Oñate, M., Bischoff, D.R.J. Owen, P. Wriggers, and T. Zohdi, editors, *Particle-based Methods IVFundamentals and Applications*, pages 767–778, Barcelona, 2015. International Center for N umerical Methods in Engineering.

[5] M Potticary, A Zervos, and J Harkness. A numerical investigation into the effect of particle form on the strength of granular materials. In *Proceedings of the 22nd UK Conference of the Association for Computational Mechanics in Engineering*, number April, 2014.

Material Modelling II

Proceedings of the 24th UK Conference of the
Association for Computational Mechanics in Engineering
31 March - 01 April 2016, Cardiff University, Cardiff

COMPUTATIONAL AND THEORETICAL ASPECTS OF A GRAIN-BOUNDARY MODEL THAT ACCOUNTS FOR GRAIN MISORIENTATION AND GRAIN-BOUNDARY ORIENTATION

***Andrew T. McBride[1], Daniel Gottschalk[2], B. Daya Reddy[3], Ali Javili[4] and Peter Wriggers[2]**

[1]School of Engineering, University of Glasgow, Glasgow, G12 8QQ
[2]Institute of Continuum Mechanics, Leibniz Universität Hannover, Hannover, 30167, Germany
[3]Centre for Research in Computational and Applied Mechanics, University of Cape Town, 7700, South Africa
[4]Institute of Mechanics, Technische Universität Dortmund, Dortmund, 44247, Germany

*andrew.mcbride@glasgow.ac.uk

ABSTRACT

A detailed theoretical and numerical investigation of the infinitesimal single-crystal gradient-plasticity and grain-boundary theory of Gurtin (2008) "A theory of grain boundaries that accounts automatically for grain misorientation and grain-boundary orientation". *Journal of the Mechanics and Physics of Solids* **56** (2), 640–662, is performed. The governing equations and flow laws are recast in variational form. The associated incremental problem is formulated in minimization form and provides the basis for the subsequent finite element formulation. Various choices of the kinematic measure used to characterize the ability of the grain boundary to impede the flow of dislocations are compared. A three-dimensional numerical example serves to elucidate the theory.

Key Words: *grain boundaries; crystal plasticity; finite elements; gradient plasticity*

1. Introduction

The miniaturisation of mechanical components composed of crystalline material requires a continuum theory that accounts for the role of the grain boundary and for size-dependent effects. The grain-boundary model should incorporate both the *misorientation in the crystal lattice* between adjacent grains, and the *orientation of the grain boundary* relative to the crystal lattice of the adjacent grains. Classical theories of plasticity are unable to describe the well-known size-dependent response exhibited by crystalline material at the micro- and nanometre scale. Numerous extended (gradient and non-local) continuum theories of single-crystal plasticity have been presented in the last two decades to circumvent these limitations. The thermodynamically consistent gradient theory of Gurtin and co-workers a [see e.g. 2] have received particular attention.

The gradient theory of [2] provides a basis to account for the role of the grain boundary [see 3]. Neumann and Dirichlet-type boundary conditions on the slip and the flux of the vectorial microforce respectively, can be prescribed and are often assumed homogeneous. The homogeneous Dirichlet condition, known as the micro-hard boundary condition, has been widely used to account for the grain boundary. Clearly this boundary condition ignores the complex geometric structures in the vicinity of the grain boundary.

Central to the theory of Gurtin [3] is the introduction of the *grain-boundary Burgers tensor* to parametrize the grain-boundary free energy. The grain-boundary Burgers tensor can be expressed in terms of the *intra-* and *inter-grain interaction moduli*. The inter-grain interaction moduli account for mismatch in the slip systems adjacent to the grain boundary and the orientation of the grain boundary.

The objective here is to investigate computational and theoretical aspects of the grain-boundary theory proposed by Gurtin [3]. For further details see [1], the finite-strain extension of this work is considered in [4].

Gurtin [3] proposes two thermodynamically admissible plastic flow relations for the grain boundary (denoted Gurtin I and II). The flow relations define the structure of the dissipative microscopic stress

in the grain boundary microscopic force balance. The flux of dislocations from the grains drives the microscopic force balance. In the first proposal, the grain boundary Burgers tensor is used to parametrize the flow relations, while in the second it is the slip. The first approach accounts for the interaction of slip systems adjacent to the grain boundary. This approach also allows for a recombination of the plastic distortion contributions from adjacent sides via the definition of the grain boundary Burgers tensor. The second approach does not directly account for the structure of the adjacent grains or the orientation of the grain boundary in the plastic flow relation. Both approaches account for the geometric structure of the adjacent grains and the grain boundary via the flux terms from the grains.

A series of three-dimensional numerical examples, performed using the finite element method, elucidate the grain-boundary theory.

2. Governing Relations

The governing relations in the grain and on the grain boundary are now summarised.

2.1. Grain

The relations governing the response of a grain $\mathcal{V}$ are obtained from a macroscopic and a microscopic force balance and are given given by

$$\operatorname{div}\boldsymbol{T} = \boldsymbol{0} \quad \text{in } \mathcal{V} \tag{1}$$

$$\operatorname{div}\boldsymbol{\xi}^\alpha + \tau^\alpha - \pi^\alpha = 0 \quad \text{in } \mathcal{V}\,. \tag{2}$$

The macroscopic Cauchy stress is defined by $\boldsymbol{T} = C[\boldsymbol{E} - \boldsymbol{E}^{\mathrm{p}}]$, where C is the tensor of elastic moduli, $\boldsymbol{E}$ is the strain tensor, and $\boldsymbol{E}^{\mathrm{p}}$ is the plastic strain tensor. The flow of dislocations through the crystal lattice is described kinematically via the assumption that the plastic strain tensor can be expressed in terms of the slip γ^α on the individual prescribed slip systems $\alpha = 1, 2, \ldots, N$ as

$$\boldsymbol{E}^{\mathrm{p}} = \sum_\alpha \gamma^\alpha \frac{1}{2}\left[\boldsymbol{s}^\alpha \otimes \boldsymbol{m}^\alpha + \boldsymbol{m}^\alpha \otimes \boldsymbol{s}^\alpha\right]\,. \tag{3}$$

The slip direction and slip plane normal of slip system α are denoted $\boldsymbol{s}^\alpha$ and $\boldsymbol{m}^\alpha$.

The resolved shear stress on slip system α is denoted by τ^α. The energetic contribution arising due to the gradient contribution is described by the vector microscopic force $\boldsymbol{\xi}^\alpha$. The flux of dislocations to the grain boundary is described by the term $\boldsymbol{\xi}^\alpha \cdot \overline{\boldsymbol{n}}$, where $\overline{\boldsymbol{n}}$ is the grain boundary normal. The (dissipative) scalar microforce is denoted by π^α. A viscoplastic flow relation for π^α is chosen.

2.2. Grain boundary

A balance of macroscopic and microscopic forces across the grain boundary $\mathcal{G}$ yields

$$[\![\boldsymbol{T}]\!]\overline{\boldsymbol{n}} = \boldsymbol{0} \quad \text{on } \mathcal{G} \tag{4}$$

$$[\![\boldsymbol{\xi}^\alpha]\!] \cdot \overline{\boldsymbol{n}} = \overline{\pi}^\alpha_A + \overline{\pi}^\alpha_B \quad \text{on } \mathcal{G}\,. \tag{5}$$

Eq. (4) is the standard traction continuity condition for an interface. The microforce balance (5) on the grain boundary states that the internal microforce $\overline{\pi}$ on either side of the grain boundary acts in response to the flux of the vectorial microforce from the grain. The gradient-plasticity formulation adopted in the bulk allows meaningful balance equations for the grain boundary to be constructed in a consistent manner. A micro-hard or micro-free boundary condition could be applied on the grain boundary. However all information about the geometry of neighbouring crystal structures and grain-boundary orientation would be lost.

A plastic flow relation for $\overline{\pi}^\alpha$ is required. Two options are considered and referred to as Gurtin I and II.

3. Numerical example

Consider a $100 \times 100 \times 100$ μm^3 polycrystal subject to tensile loading. The polycrystal is composed of 27 equal sized grains. The crystal lattice in each grain is that of a face-centered-cubic material.

The purpose of the polycrystal example is to explore the various choices of grain boundary models for reasonably complex, three-dimensional problems. A micro-free grain boundary model allows for a high flux of dislocations while the micro-hard model acts as an impenetrable barrier resulting in dislocation pile-up. The ability of the two Gurtin grain boundary models to impede dislocation flow is controlled, in part, by the slip resistance $\overline{S}$ of the grain boundary. The Gurtin I model also accounts for the slip system interaction at the grain boundary. The ability of the two Gurtin models to capture the spectrum of behaviour between the micro-hard and micro-free limits is investigated by examining a range of grain boundary resistances from a low $\overline{S} = 1 \times 10^{-4}$ to an extremely high value of $\overline{S} = 1 \times 10^{10}$.

The discretization of the domain and the boundary conditions are shown in Fig. 1. Each grain is discretized with 6^3 elements. A displacement of $u_y = 5$ μm is applied on the boundary with outward normal $\boldsymbol{n} = [0, 1, 0]$. The opposite boundary with outward normal $\boldsymbol{n} = [0, -1, 0]$ is prevented from displacing in the y-direction. The additional constraints to prevent rigid body motion are indicated in Fig. 1.

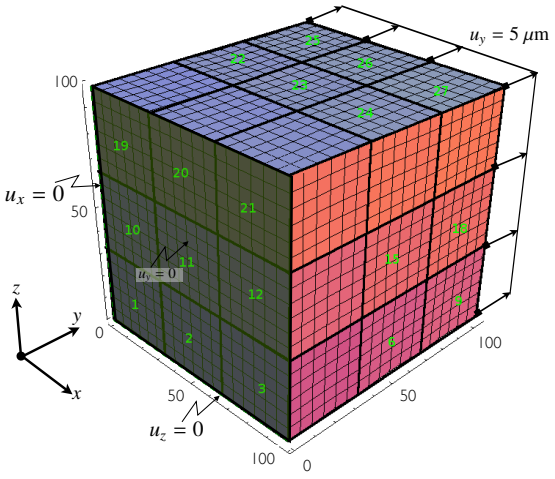

Figure 1: Discretization of the polycrsytal composed of 27 grains.

The y-component of the resultant traction on the right boundary for the Gurtin I, micro-hard and micro-free models is plotted against the prescribed displacement in Fig. 2 (a). As expected the micro-free condition provides a lower bound for the Gurtin models for very low values of $\overline{S}$. From the theory it is reasonable to expect the micro-hard condition to be an upper bound that is approached with increasing $\overline{S}$. It's important to note that the extremely high values of $\overline{S}$ chosen are not physically motivated, rather they penalize the response at the grain boundary. For the high-angle grain boundaries present in the current example it is physically reasonable that the models be capable of producing a response close to micro-hard. It is clear that this is not the case for the Gurtin I model.

The Gurtin II model can capture the range of responses from micro-free to micro-hard, as shown in Fig. 2 (b). A key observation is that the Gurtin II model can be tuned to account for the full range of interactions between micro-free and micro-hard. This observation motivates a possible extension of the current work where the value of the grain boundary slip resistance is chosen as a function of the mismatch at the grain boundary. The Gurtin II has the additional advantage that it is simpler to implement and is computationally more efficient.

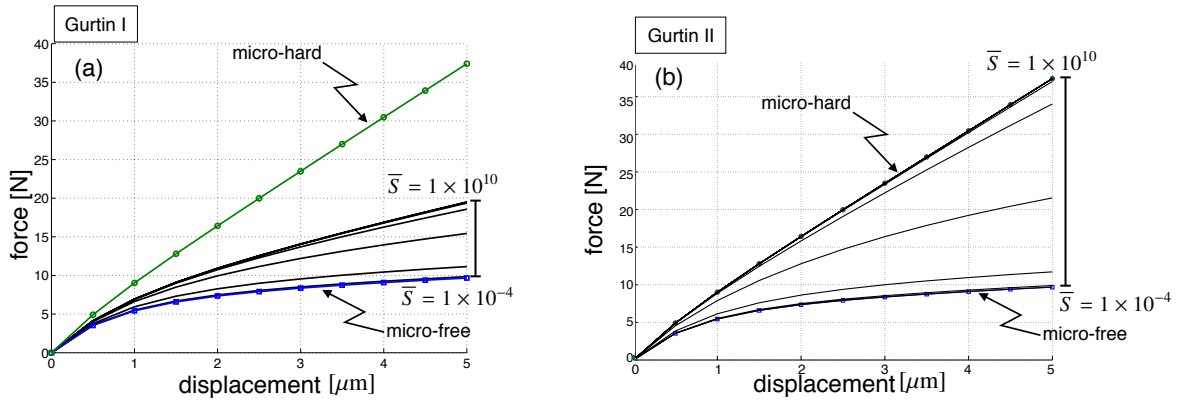

Figure 2: Applied displacement versus the y-component of resultant force on the right boundary for various grain-boundary models. The results of the Gurtin I model are shown in (a), and the Gurtin II model in (b).

4. Discussion and conclusion

Various features of the Gurtin grain-boundary models were illustrated for a polycrystal composed of grains with a face-centered-cubic structure. The Gurtin I model captures the geometric complexity of the grain boundary. A feature of the model is that it does not capture the full range of responses between micro-hard and micro-free. That is, it does not reproduce the widely used micro-hard limit when the grain-boundary slip resistance is used to penalize dislocation flow. The Gurtin II model does not contain the geometrical information concerning the grain boundary but can reproduce the micro-hard limit. The computational efficiency of the formulation is greatly impacted by the choice of the grain boundary flow relation.

The numerical simulations provide valuable insight into the models. They do not, however, allow one to judge the physical correctness of the model. A key challenge is therefore the validation and calibration of this and other grain-boundary models using well-devised experiments and microscopic modelling approaches (e.g. dislocation dynamics).

References

[1] Gottschalk, D., McBride, A., Reddy, B., Javili, A., Wriggers, P., Hirschberger, C., 2016. Computational and theoretical aspects of a grain-boundary model that accounts for grain misorientation and grain-boundary orientation. Computational Materials Science 111, 443 – 459.

[2] Gurtin, M., 2008. A finite-deformation, gradient theory of single-crystal plasticity with free energy dependent on densities of geometrically necessary dislocations. International Journal of Plasticity 24 (4), 702 – 725.

[3] Gurtin, M., 2008. A theory of grain boundaries that accounts automatically for grain misorientation and grain-boundary orientation. Journal of the Mechanics and Physics of Solids 56 (2), 640 – 662.

[4] McBride, A. T., Gottschalk, D., Reddy, B. D., Wriggers, P., Javili, A., 2016. Computational and theoretical aspects of a grain-boundary model at finite deformations. Technische Mechanik 36 (1-2), 92–109.

Proceedings of the 24th UK Conference of the
Association for Computational Mechanics in Engineering
31 March - 01 April 2016, Cardiff University, Cardiff

Modelling the Mechanics of Timber Cell Walls

***Euan Richardson[1], Lukasz Kaczmarczyk[1], Chris Pearce[1] and Karin de Borst[1]**

[1] University of Glasgow, School of Engineering, Rankine Building, Glasgow G12 8LT

*e.richardson.1@research.gla.ac.uk

ABSTRACT

Timber is a highly complex naturally occurring material, with properties adapted to its local environment. These properties, on its many length scales, determine its strength and stiffness and also how it interacts with moisture in the environment, causing dimensional instability both during drying and the lifetime of any building. Of particular importance is how the cell wall polymers interact with moisture in the environment and how this effects the properties, due to their strong dependence on intra-molecular hydrogen bonds. To model the dimensional behaviour of a wood cell under varying moisture conditions, the cell wall polymer matrix is modelled using a formulation of coupled deformation and moisture transport. These governing equations of mass and linear momentum conservation are strongly coupled and nonlinear and solved using the Finite Element Method. The associated constitutive equations are complex. The free energy is described through the deformation of the polymer matrix and the mixing with solvent (in this case, water). It is assumed that the polymer chains and water molecules are incompressible so that a change in volume of the polymer matrix corresponds to a change in the number of solvent molecules. The viscoelastic behaviour is resolved using a Zener spring-dashpot model, capturing both creep and relaxation phenomena, and the moisture transport is resolved using Fick's 2nd Law. The effects of wetting upon the stiffness and relaxation characteristics of the polymer matrix is taken into account through the chemical kinetics of hydrogen bond dissociation. Proper linearisation is achieved with automatic differentiation, using the library ADOL-C integrated with the group's FE code MOFEM.

Key Words: *Timber; Viscoelasticity; Finite Element Method; Coupled Problem*

1. Introduction

Timber is a highly complex multi-scale material, with properties of its many length scales. It is naturally occurring, with properties adapted to its local environment during growth, making timber an unpredictable material to work with. One particular problem is its dimensional instability when exposed to different environmental conditions, potentially causing issues during construction and the lifetime of a building. To enable prediction of dimensional changes in timber due to moisture sorption, the cell wall polymer matrix is modelled hygro-mechanically and the individual polymers are described chemically through the kinetics of hydrogen bond dissociation.

2. Timber Cell Wall

The wood cell wall is a multilayer composite structure, containing a primary cell wall and a 3 layer secondary cell wall. In the secondary cell wall, crystalline cellulose chains are arranged in a helical spiral. The chains are embedded within a polymer matrix consisting of amorphous cellulose, hemicelluloses and lignins. These polymers interact strongly with water, which binds to the hydroxyl groups contained within. This uptake of bound water within the cell wall replaces strong, intramolecular hydrogen bonds, leading to a corresponding loss of stiffness. Using an approach presented by Nissan [1], the Young's modulus of cellulose, at low moisture contents, can be related to the change in the number of intramolecular hydrogen bonds assuming each water molecule breaks one hydrogen bond. Considering the molecular weight of cellulose and water this yields:

$$\ln(N/N_0) = -1/3(w/W) \tag{1}$$

where N, denotes the number of effective hydrogen bonds at moisture content w, N_0 is the initial number of effective hydrogen bonds in the dry state, and W is the moisture content at which all hydroxyl groups carry one water molecule, which is close to 1/3 for cellulose. The number of hydrogen bonds can be related to the Young's modulus, E, as follows:

$$N = (E/k)^{1/3} \tag{2}$$

where the proportianality coefficient, k, describes the average force constant between the hydrogen bonds. By combining the equations we can formulate the change in Young's modulus, E/E_0, for low moisture contents,

$$\ln(E/E_0) = -w \tag{3}$$

where E_0 is the initial Young's modulus in the dry state. As the shear modulus is also dependent on the number of effective hydrogen bonds, the relationship can be adapted to incorportate shear modulus, G. The water content of each available sorption site can be described through the ratio of the number of moles of water and cellulose, and thus the mixture can be descibed in terms of its chemical potential, μ. By enforcing chemical equilibrium with the external environment, the conditions are present for diffusion to occur.

3. Model

Taking a similar approach to models on poroelastic gels [2], the cell wall polymer behaviour is modelled using a formulation of coupled deformation and moisture transport, described through linear momentum conservation Eq.(4) and the conservation of mass Eq.(5).

$$\mathrm{div}(\boldsymbol{\sigma}) = \boldsymbol{b} \tag{4}$$

$$\frac{\partial \varepsilon_{kk}}{\partial t} = -\frac{\kappa}{\eta\Omega}\mu_{,kk} \tag{5}$$

The volume change, $\varepsilon_{kk} = \Omega(C - C_0)$, where C is the concentration, assumes that the change of volume in the polymer network is due to the change in the number of bound water molecules. The volume of each water molecule, Ω, is constant, κ is the permeability and η is the viscosity of the polymer network. The moisture flux is given as $J_k = \mu_{,k}$.

The model is constitutively described using a Zener spring-dashpot configuration, shown in Figure 1. This arrangement allows both creep and relaxation phenomena to be captured. The model is formulated in terms of its external state variables (ε, σ) and (C, μ), representing the mechanical and chemical behaviour respectively, and the internal state variable, $\hat{\varepsilon}$, which represents the internal rearrangement of intramolecular hydrogen bonds under stress.

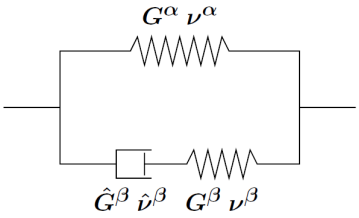

Figure 1: : Model representing a rheological Zener spring-dashpot arrangement. The spring α represents the instantaneous elasticity of the polymer network. The spring and dashpot in series arrangement, β, represents the viscoelastic relaxation.

The stress, σ, within the system Eq.(7) can be specified as the the sum of the stress within spring α, spring β and the hydrostatic pressure due to the concentration of solvent molecules, $\hat{\sigma}^{\beta}$, Eq.(6).

$$\hat{\sigma}^{\beta} = \frac{\Delta\mu}{\Omega}\,\mathrm{I} \tag{6}$$

$$\sigma = \sigma^{\alpha} + \sigma^{\beta} - \hat{\sigma}^{\beta} \tag{7}$$

The stresses within the individual springs, α and β, are specified in Eq.(8) and (9), where G^{α} and G^{β} are the shear moduli of each spring respectively and ν^{α} and ν^{β} are the Poisson's ratios.

$$\sigma^{\alpha}_{ij} = 2G^{\alpha}\left[\varepsilon_{ij} + \frac{\nu^{\alpha}}{1-2\nu^{\alpha}}\,\varepsilon_{kk}\,\delta_{ij}\right] \tag{8}$$

$$\sigma^{\beta}_{ij} = 2G^{\beta}\left[(\varepsilon_{ij} - \hat{\varepsilon_{ij}}) + \frac{\nu^{\beta}}{1-2\nu^{\beta}}\,(\varepsilon_{kk} - \hat{\varepsilon}_{kk})\,\delta_{ij}\right] \tag{9}$$

When stress is applied to the system, the viscous motion of the dashpot determines the rate at which spring β relaxes, Eq.(10). The viscous behaviour is determined by the rate of breakdown of intromolecular hydrogen bonds within the network, $\hat{G}^{\beta}$, and Poisson's ratio $\hat{\nu}^{\beta}$, which controls the time dependent deformation.

$$\frac{\partial\hat{\varepsilon_{ij}}}{\partial t} = \frac{1}{2\hat{G}^{\beta}}\left[\sigma^{\beta}_{ij} - \frac{\hat{\nu}^{\beta}}{1+\hat{\nu}^{\beta}}\,\sigma^{\beta}_{kk}\,\delta_{ij}\right] \tag{10}$$

4. Finite Element Implementation

The model is formulated in 3D using the Finite Element Method using MOFEM. The mesh consists of 10 node tetrahedral elements with a higher order of approximation applied to the displacement field to allow for the different orders of the two governing equations (Eq. (4) and (5)), ensuring stability. The tangent matrices are calculated using automatic differentiation (ADOL-C) to achieve proper linearisation.

$$\left(f_x{}^{internal}\right)_i = \int_V \frac{\partial N_i}{\partial X_j}\,\sigma_{ij}\,dV \tag{11}$$

$$\left(f_\mu{}^{v}\right)_j + \left(f_\mu{}^{J}\right)_j = \int_V N_j\,\frac{\partial V}{\partial t}\,dV + \int_V \frac{\partial N_j}{\partial X_k}\,J_k\,dV \tag{12}$$

$$(r_{\hat{\varepsilon}})_j = \int_V N_j\left(\frac{\partial\hat{\varepsilon}}{\partial X_j} - f(\sigma^{\beta})\right)dV \tag{13}$$

Equations (11) - (13) represent the internal force, the flux and the residual strain respectively, where N is a matrix of shape functions , $f\,(\boldsymbol{\sigma})$ is a function for a linear viscous material, and the volume is given by V. They are assembled in the system as follows:

$$\begin{bmatrix} K_{xx} & K_{x\mu} & K_{x\hat{\varepsilon}} \\ K_{\mu x} & K_{\mu\mu} & K_{\mu\hat{\varepsilon}} \\ K_{\hat{\varepsilon}x} & K_{\hat{\varepsilon}\mu} & K_{\hat{\varepsilon}\hat{\varepsilon}} \end{bmatrix}\begin{bmatrix} q_x \\ q_\mu \\ q_{\hat{\varepsilon}} \end{bmatrix} = \begin{bmatrix} f_x{}^{external} - f_x{}^{internal} \\ f_\mu{}^{v} + f_\mu{}^{J} \\ r_{\hat{\varepsilon}} \end{bmatrix}$$

The polymer network is described in terms of a rectangle, enforcing symmetry on the y axis, shown in figure 2. The Boundary condition μ, representing the external moisture conditions, is applied on all faces and held constant, with the exception of the symmetrical face where the flux is set to zero. A tensile force is applied in the y-direction and released once equilibrium has been reached.

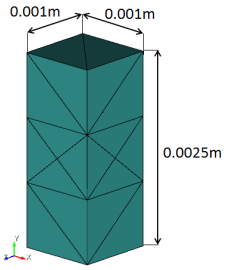

Figure 2: : Rectangular bar mesh consisting of 10 node tetrahedral elements, representing a 1/4 sample with symmetry on the x,y and z axis.

5. Numerical Example

A specimen, Figure 2, is loaded in tension. The load is held for 35 minutes and then released. The creep results shown in Figure 3 (right) demonstrate the coupling between the mechanical and hygral behaviour. The graph shows the displacement of the top face vs the chemical potential at the mid point of the specimen. Initially the applied force causes an elastic displacement, elongating the sample and causing a dip in the chemical load in the middle of the sample. The evolution of the chemical load through the sample is shown in Figure 3 (left). Over a longer length of time the sample then undergoes creep, increasing the displacement until it reaches equilibrium. At this point all the stress is taken by spring α. The load is then released, causing an increase in chemical load which reduces over time as the sample returns to its reference configuration.

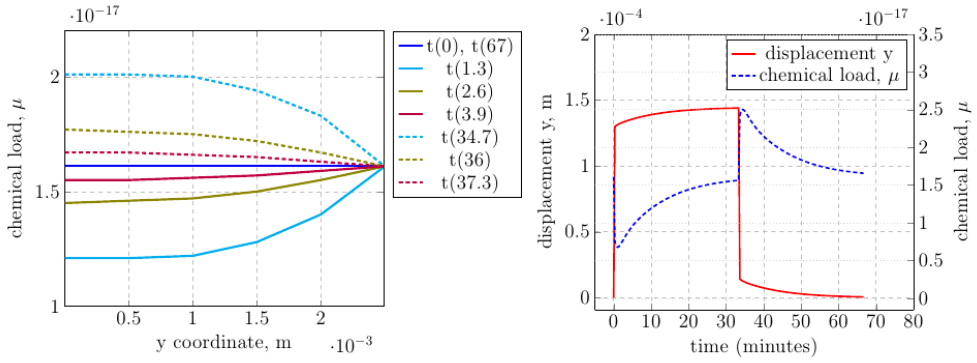

Figure 3: : Left: Evolution of the chemical load through the sample along the y-axis at given time steps, t(min), where the solid lines occur during the loading phase and the dashed lines occur post loading. Right: Demonstration of the coupling between the chemical load and the displacement due to an external force applied to the sample

6. Conclusions

The proposed model is currently formulated in small strains and as such can only be applied to small changes in deformation and cannot yet fully describe the mechano-soprtive behaviour in environmental conditions that exceed 50% relative humidity. All viscoelastic changes are fully reversible, and after a short time the sample with return its reference configuration if the conditions return to those at time zero. In the future the model will be formulated in large strains and take into account a larger degree of polymer softening at higher moisture contents.

References

[1] A. H. Nissan. H-bond dissociation in hydrogen bond dominated solids. *Macromolecules*, 9(5) 840-850, 1976.

[2] Y. Hu and Z. Suo. Viscoelasticity and poroelasticity in elastomeric gels. *Acta Mechanica Solida Sinica*, 25(5), 441-458, 2012

A Crystal Plasticity Finite Element Method (CPFEM) based study to investigate the effect of microvoids in single crystalline aluminium alloy

***M. Amir Siddiq[1], Umair Asim[1]**

[1]School of Engineering, University of Aberdeen, Fraser Noble Building, Aberdeen, AB24 3UE

*amir.siddiq@abdn.ac.uk

ABSTRACT

Aluminium alloys are typically used in a variety of applications, which require high strength, ductility and formability. In order to understand the formability of such alloys along with underlying mechanisms, a CPFEM based study has been performed using crystal plasticity theory. Crystal plasticity finite element methods [1]–[4] have been used to perform the simulations on representative volume elements (RVE's) of single crystal metal with different configurations, sizes and shapes of voids (defects). A part of the rigorous study will be presented in this work by taking into account the effect of void geometry, void fraction, void orientation, loading type (level of triaxiality), and crystallographic orientations. Using these large sets of simulations, analyses will be presented to better understand the underlying physical mechanisms which include interrelation among void growth, applied strain, void fraction, void size/shape, and plastic anisotropy effects under different types of loading.

Keywords: *Void Growth, Crystal Plasticity, Aluminium Alloys*

1. Introduction

A variety of applications require materials being light weight, high strength, corrosion resistant and formable which makes aluminium alloy as being one of the many best candidates. The behaviour of different types of aluminium alloys has been studied for a long time. Fractography of these alloys generally show that void growth and coalescence is one of the dominant fracture mechanisms.
The research on void nucleation, growth and coalescence during ductile damage in metal and alloys dates back to late 1950's. Studies have been performed to understand the basic physical phenomenon of void growth and numerical issues in solving such problems [5]–[11]. Most of the investigations are based on simplified assumptions, such as isotropic material, 2D plane strain, axisymmetric models, cylindrical/spherical voids or limited number of loading states and slip systems.
The presented work is an effort to advance the research in the field by performing a rigorous fully-validated 3D CPFEM based RVE study to better understand the relationship among void growth, initial porosity, initial void size, and plastic anisotropy effects.

2. Crystal Plasticity based Modelling

2.1 Crystal Plasticity Theory

General crystal plasticity framework is based on the assumption that plastic deformation is due to the crystalline slip in different slip systems [2], [12].
Plastic slip in α-th slip system is given by the conventional crystal plasticity based power law

$$\dot{\gamma}^{\alpha} = \dot{\gamma}_0 \left[\frac{|\tau^{\alpha}|}{g^{\alpha}}\right]^{1/m} sgn(\tau^{\alpha}) \qquad (1)$$

where τ^{α} is the resolved shear stress on slip system α, g^{α} is the strength of the slip system α, $\dot{\gamma}_0$ is a reference shear strain rate, and m is the rate sensitivity exponent.
The resolved shear stress τ^{α} in a specific slip system is computed through deviatoric stress tensor σ' and Schmidt factor based on slip system direction and normal, s^{α} and m^{α}

$$\tau^{\alpha} = \sigma' : (s^{\alpha} \otimes m^{\alpha}) \qquad (2)$$

The evolution of the strength of the slip system is based on the saturation hardening rule and is given by

$$\dot{g}^{\alpha} = h_0 \left(\frac{g_s(\dot{\gamma}) - g^{\alpha}}{g_s(\dot{\gamma}) - g_0} \right) \dot{\gamma}, \qquad (3)$$

where

$$g_s(\dot{\gamma}) = g_{s0} \left(\frac{\dot{\gamma}}{\dot{\gamma}_{s0}} \right)^{m'} \text{ and } \dot{\gamma} = \Sigma_{\alpha} |\dot{\gamma}^{\alpha}|$$

while h_0, g_{s0}, g_0, $\dot{\gamma}_{s0}$, and m' are material parameters to describe hardening behaviour for all slip systems.

2.2 Material Parameter Identification

Material parameters are identified through inverse modelling approach using uniaxial experimental stress strain data and are given in Table 1 while comparison between experimental and simulated response is given in Figure 1. Experimental data is from uniaxial test results obtained locally.

Table 1: Material Parameters for Aluminium Alloy AA-5xxx

m	$\dot{\gamma}_0$	h_0	g_0	g_{s0}	m'	$\dot{\gamma}_{s0}$
0.03	1.0 /sec	200.40 MPa	105 MPa	110 MPa	0.0	5e10 /sec

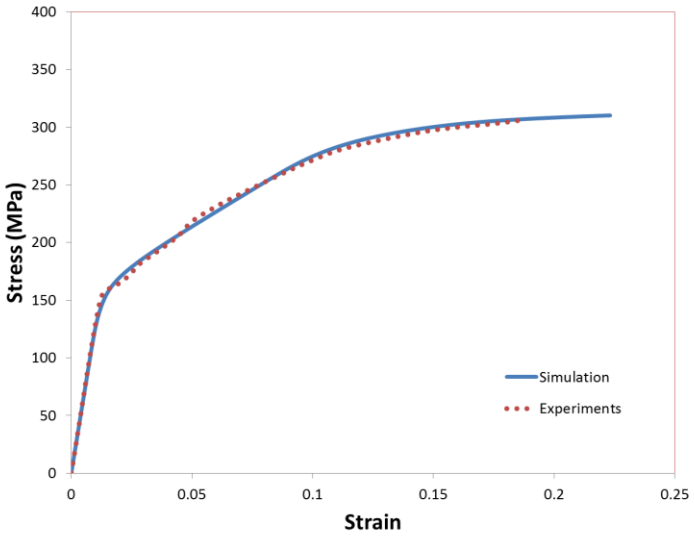

Figure 1: Comparison of Stress-Strain Curves after Material Parameter Identification

2.3 RVE Model

Finite element based 3D RVE model have been constructed for various void diameters (ranging from 310nm to 1.44mm); void fractions (0.001, 0.005, 0.01, 0.03, 0.05); loading types (triaxialities 1/3, 1, 2, 3) and crystal orientations (5 different orientations). A representative half sectioned model of two different porosities has been shown in Figure 2.

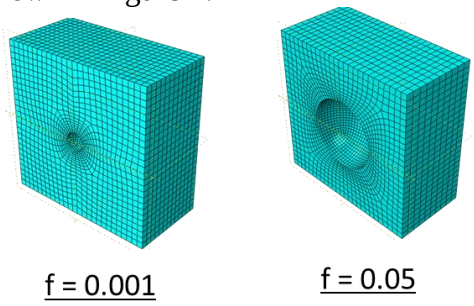

Figure 2: Half sectioned model of spherical void RVE

3. Results and Discussion

Four different loading types by varying the triaxiality were simulated for different porosities. Figure 3 shows the plot of void growth as a function of applied strain, and triaxiality for two different porosities with same crystal orientation. It can be inferred from the Figure 3 that as the applied strain is increased the void grows exponentially. It can also be inferred that the amount of void growth increases with the level of triaxiality. It is also found that larger voids (higher porosity) grow more, i.e. reaching to higher porosity value, than smaller voids at higher triaxialities. Lattice orientation evolution has been plotted in Figure 4 as {111} pole figures for initial porosity of 0.01. It can be inferred from figure that as the triaxiality increases the lattice rotation in the individual elements also increase. Uniaxial case shows very small amount of rotation due to the small amount of void growth. It can also be inferred from Figure 4 that larger the void growth higher is the lattice rotation. It was also found during the investigation that lattice rotation is higher for larger void growth and triaxiality. Also, most of the lattice rotation was found to occur in the vicinity of the defect.

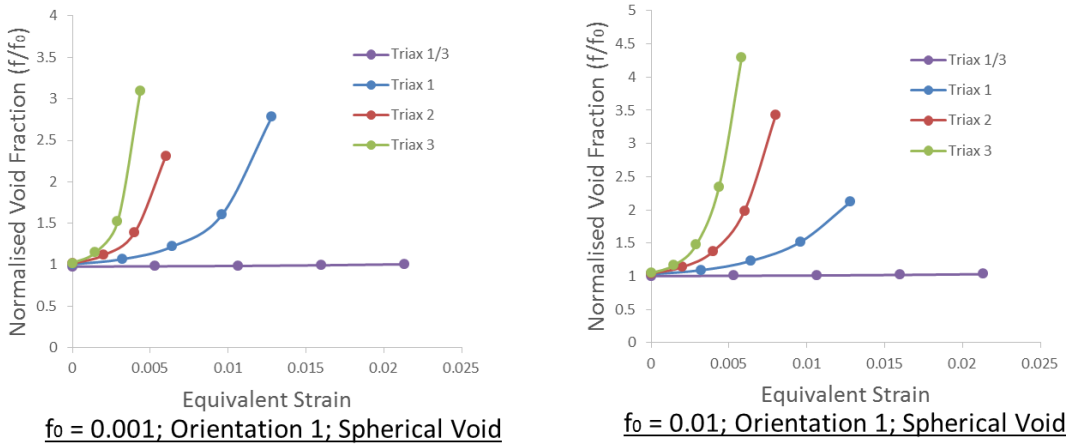

Figure 3: Void growth as a function of triaxiality and applied strain for two different porosities

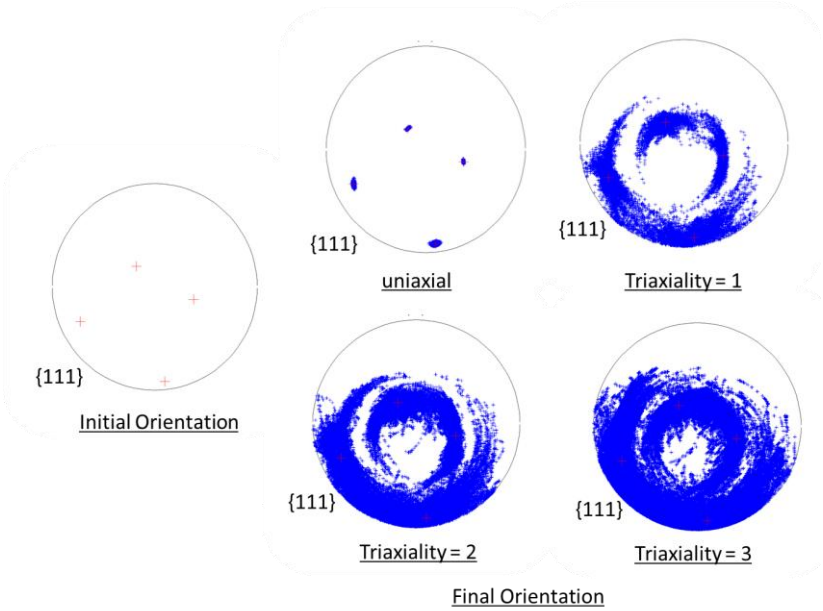

Figure 4: {111} pole figures showing initial (left) and final orientations for different loading types (f=0.01; Or1)

Figure 5 shows the plot of void evolution as a function of equivalent strain for five different orientations and three different triaxialities (1/3, 1, 2). It is found that void growth strongly depends on crystal orientation for uniaxial cases (Figure 5 (left)). The effect reduces as the triaxiality is increased and for higher triaxialities the effect of crystal orientation diminishes.

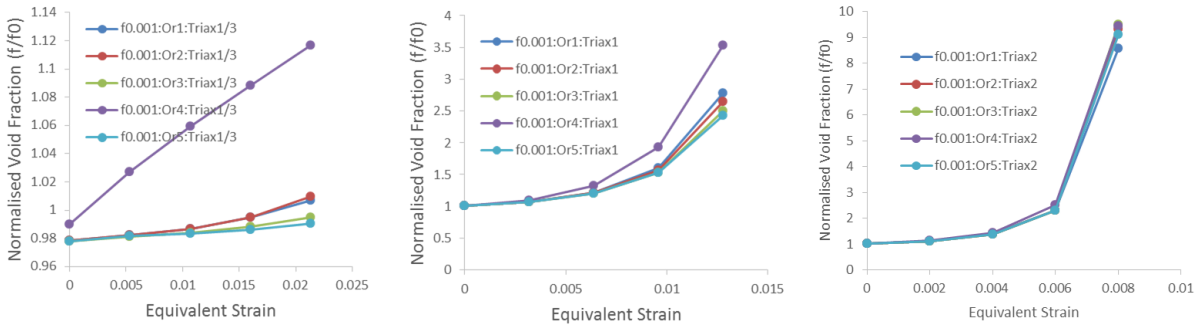

Figure 5: Void growth as a function of applied strain for different orientations and triaxialities

4. Conclusions

A three dimensional CPFEM based study has been presented to understand the formability of aluminium alloy single crystals. Material parameters were identified through inverse modelling approach using experimental data. The effect of applied strain, initial porosity, void size, initial crystal orientation, and triaxiality on void growth is presented. An effort was put to explain the void evolution behaviour by correlating with the lattice rotation. It is found that defects show exponential increase with respect to the applied strain. Larger voids grow more than smaller voids. Higher triaxiality cause higher amount of lattice rotation due to higher void growth. Plastic anisotropy has significant effect on the void growth and this effect diminshes as the triaxiality increases.

Acknowledgements

The author thankfully acknowledges the financial support of EPSRC funding (EP/L021714/1).

References

[1] A. Siddiq, S. Schmauder, and Y. Huang, "Fracture of bicrystal metal/ceramic interfaces: a study via the mechanism-based strain gradient crystal plasticity theory," *Int. J. Plast.*, vol. 23, no. 4, pp. 665–689, 2007.

[2] A. Siddiq and S. Schmauder, "Interface fracture analyses of a bicrystal niobium/alumina specimen using a cohesive modelling approach," *Model. Simul. Mater. Sci. Eng.*, vol. 14, no. 6, pp. 1015–1030, Sep. 2006.

[3] A. Siddiq and T. El Sayed, "Acoustic softening in metals during ultrasonic assisted deformation via CP-FEM," *Mater. Lett.*, vol. 65, no. 2, pp. 356–359, 2011.

[4] A. Siddiq and T. E. Sayed, "A thermomechanical crystal plasticity constitutive model for ultrasonic consolidation," *Comput. Mater. Sci.*, vol. 51, no. 1, pp. 241–251, 2012.

[5] K. E. Puttick, "Ductile fracture in metals," *Philos. Mag.*, vol. 4, no. 44, pp. 964–969, 1959.

[6] R. M. McMeeking, "Finite deformation analysis of crack-tip opening in elastic-plastic materials and implications for fracture," *J. Mech. Phys. Solids*, vol. 25, no. 5, pp. 357–381, 1977.

[7] R. Becker, R. E. Smelser, and O. Richmond, "The effect of void shape on the development of damage and fracture in plane-strain tension," *J. Mech. Phys. Solids*, vol. 37, no. 1, pp. 111–129, 1989.

[8] C. L. Hom and R. M. McMeeking, "Void growth in elastic-plastic materials," *ASME J. Appl. Mech.*, vol. 56, no. 2, pp. 309–317, 1989.

[9] Z. Li and P. Steinmann, "RVE-based studies on the coupled effects of void size and void shape on yield behavior and void growth at micron scales," *Int. J. Plast.*, vol. 22, no. 7, pp. 1195–1216, 2006.

[10] S. K. Yerra, C. Tekoğlu, F. Scheyvaerts, L. Delannay, P. Van Houtte, and T. Pardoen, "Void growth and coalescence in single crystals," *Int. J. Solids Struct.*, vol. 47, no. 7–8, pp. 1016–1029, 2010.

[11] W. Sun and S. Lu, "Void Shape Effects on Void Growth and Slip Systems Activity in Single Crystals," *Rare Met. Mater. Eng.*, vol. 43, no. 7, pp. 1571–1576, 2014.

[12] A. Siddiq and S. Schmauder, "Multiscale Simulation of Metal/Ceramic Interface Fracture," *IUTAM Symp. Multi-Functional Mater. Struct. Syst.*, pp. 343–355, 2010.

Proceedings of the 24th UK Conference of the
Association for Computational Mechanics in Engineering
31 March - 01 April 2016, Cardiff University, Cardiff

NONLINEAR MICRO-MECHANICAL RESPONSE OF THE FIBRE-REINFORCED POLYMER COMPOSITES INCLUDING MATRIX DAMAGE AND FIBRE-MATRIX DECOHESION

***Zahur Ullah[1], Łukasz Kaczmarczyk[1] and Chris J. Pearce[1]**

[1]School of Engineering, Rankine Building, The University of Glasgow, Glasgow, UK, G12 8LT

*Zahur.Ullah@glasgow.ac.uk

ABSTRACT

A three-dimensional multi-scale computational homogenisation framework was developed for the prediction of nonlinear micro-mechanical response of the fibre-reinforced polymer (FRP) composite. Two dominant damage mechanisms, i.e. matrix damage and fibre-matrix decohesion were considered and modelled using a non-associative pressure dependent thermodynamically consistent paraboloidal yield criterion and cohesive elements respectively. A linear-elastic transversely isotropic materials model was used to model yarns within the representative volume element (RVE), the principal directions for which were calculated using a potential flow analysis along these yarns. A unified approach was used to impose the RVE boundary conditions, which allows convenient switching between linear displacement, uniform traction and periodic boundary conditions. Furthermore, the flexibility of hierarchic basis functions and distributed memory parallel programming were fully utilised. The accuracy and performance of the developed computational framework were demonstrated using an RVE with randomly distributed but periodic and axially aligned unidirectional fibres subjected to transverse tension and shear. The macro-strain versus homogenised stress responses were validated against the reference results from the literature. Finally, effects of varying interfacial strength and fracture energy were studied on the homogenised stress versus macro-strain responses.

Key Words: *finite element analysis; fibre reinforced polymer; multi-scale computational homogenisation; cohesive zone models; computational plasticity*

1. Introduction

As compared to conventional materials, fibre-reinforced polymer (FRP) composites offer exceptional mechanical and chemical properties, making them ideal for a variety of engineering applications, including aerospace, marine, automotive industry, civil structures and prosthetics [1]. On the other hand, their computational modelling is more challenging due to their underlying complicated and heterogeneous microstructure and associated nonlinearities with the matrix damage and fibre-matrix decohesion. Therefore, multi-scale computational homogenisation (CH) provides an accurate modelling framework to simulate the behaviour of FRP composites and determine the macro-scale homogenised (or effective) properties, based on the physics of an underlying, microscopically heterogeneous, representative volume element (RVE). The homogenised properties calculated from the multi-scale CH are subsequently used in the numerical analysis of the macro-level structure.

This paper presents a generalised three-dimensional multi-scale CH framework for prediction of the nonlinear micro-mechanical response of FRP composites, including matrix damage and fibre-matrix decohesion. The pressure dependent thermodynamically consistent paraboloidal yield criterion and cohesive elements are used to model matrix damage and fibres-matrix interfacial decohesion respectively [2, 3], while yarns are considered as linear-elastic and transversely isotropic. The principal directions for the transversely isotropic material model are calculated using a potential flow along these yarns. A unified approach is used to impose the RVE boundary conditions, which allows convenient switching between displacement, traction and periodic boundary conditions [4]. The flexibility of the hierarchic finite element is fully utilised, which permits the use of arbitrary order of approximation leading to accurate results for relatively coarse meshes. Furthermore, the computational framework is designed to take advantage of distributed memory high-performance computing. The developed computational framework is implemented in our group's FE software, MoFEM (Mesh-Oriented Finite Element Method).

2. Model components

2.1. Material models

The RVE in the case of FRP composites consists of yarns embedded in an epoxy matrix. Epoxy matrix is modelled as an elasto-plastic material using a non-associative pressure dependent thermodynamically consistent paraboloidal yield criterion, the yield surface for which is shown in Figure 1(a) in the principal stress space and is mathematically written as

$$f\left(\boldsymbol{\sigma},\sigma_c,\sigma_t\right) = 6J_2 + 2I_1\left(\sigma_c - \sigma_t\right) - 2\sigma_c\sigma_t, \tag{1}$$

where $\boldsymbol{\sigma}$ is Cauchy stress tensor, $I_1 = \mathrm{tr}(\boldsymbol{\sigma})$ is the first invariant of Cauchy stress tensor, $J_2 = \frac{1}{2}\boldsymbol{\eta} : \boldsymbol{\eta}$ is the second invariant of deviatoric stress $\boldsymbol{\eta} = \boldsymbol{\sigma} - \frac{1}{3}I_1$ and σ_t and σ_c are yield strengths in tension and compression respectively. A non-associative flow rule is used, for which the plastic potential function is written as

$$g\left(\boldsymbol{\sigma},\sigma_c,\sigma_t\right) = 6J_2 + 2\alpha I_1\left(\sigma_c - \sigma_t\right) - 2\sigma_c\sigma_t, \qquad \alpha = \frac{1-2\nu_p}{1+\nu_p}, \tag{2}$$

where ν_p is a material parameter and is known as plastic Poisson's ratio. Furthermore, the Helmholtz free energy in the case of linear isotropic hardening is written as

$$\psi = \frac{1}{2}\lambda\mathrm{tr}[\boldsymbol{\varepsilon}]^2 + \mu\boldsymbol{\varepsilon} : \boldsymbol{\varepsilon} + \sigma_{t_0}\alpha_0 + \frac{1}{2}H_t\alpha_0^2 + \sigma_{c_0}\alpha_1 + \frac{1}{2}H_c\alpha_1^2, \tag{3}$$

where λ and μ are the Lame parameters, $\boldsymbol{\varepsilon}$ is the strain tensor, σ_{t_0} and σ_{c_0} are the initial yield strengths in tension and compression respectively, α_0 and α_1 are internal kinematic variables and H_t and H_c are hardening parameters in case of tension and compression respectively.

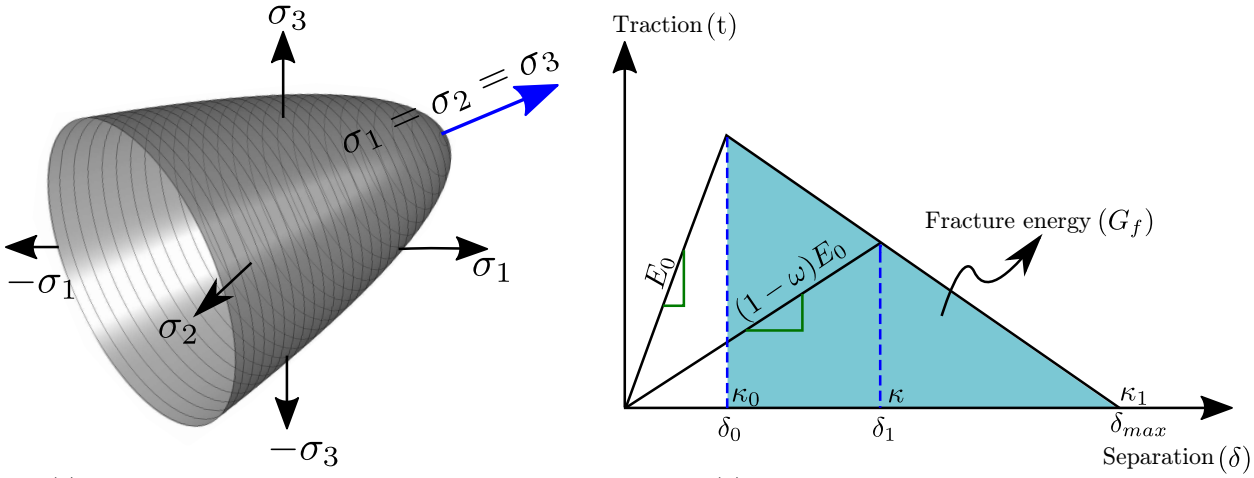

(a) Paraboloidal yield surface

(b) Traction-separation law

Figure 1: Material models for matrix and fibre-matrix decohesion

Fibre-matrix decohesion is modelled using the standard cohesive elements with a straightforward material model, i.e. linear traction-separation law (shown in Figure 1(b)), which requires only three material parameters including cohesive strength f_t, fracture energy G_f and material parameter β, which assign different weight to opening and shear displacements. Mathematically the material model for the cohesive element is written as

$$t = \begin{cases} E_0\delta & \text{if} \quad \delta < \delta_0, \\ (1-\omega)\,E_0\delta & \text{if} \quad \delta_0 \le \delta < \delta_{\max}, \\ 0 & \text{if} \quad \delta < \delta_{\max}, \end{cases} \tag{4}$$

where E_0 is the initial stiffness, $\delta = \sqrt{\delta_n^2 + \beta(\delta_{s1}^2 + \delta_{s2}^2)}$ is displacement jump with δ_n and δ_s as its normal and shear components and ω is damage parameter. Furthermore, κ is a history parameter and is equal to the highest value of displacement jump δ.

Finally, yarns are modelled as linear-elastic and transversely-isotropic material. The principal directions for the transversely isotropic material model are determined by solving a potential flow along each yarn [1].

2.2. Multi-scale computational homgenisaiton

In CH, a heterogeneous RVE is associated with each macroscopic Gauss point, the boundary conditions for which are implemented using the generalised procedure proposed in [1, 4]. A small strain formulation is assumed in this paper. For a global step $n+1$, the discretised system of equations in case of an iteration i of the Newton-Raphson algorithm is written as

$$\begin{bmatrix} \mathbf{K}^i_{n+1} & \mathbf{C}^T \\ \mathbf{C} & \mathbf{0} \end{bmatrix} \begin{Bmatrix} \triangle \mathbf{u}^i_{n+1} \\ \triangle \boldsymbol{\lambda}^i_{n+1} \end{Bmatrix} = \left\{ \mathbf{F}^i_{n+1} \right\}, \tag{5}$$

where $\mathbf{K}$ and $\mathbf{u}$ are the standard FE stiffness matrix and displacement vector respectively and $\boldsymbol{\lambda}$ is the unknown vector of Lagrange multipliers required to impose the RVE boundary conditions. Matrix $\mathbf{K}$ consists of contribution of elements from matrix, yarns and yarn-matrix interfaces. $\mathbf{F}^i_{n+1}$ is a vector of residuals and is written as

$$\mathbf{F}^i_{n+1} = \begin{bmatrix} \mathbf{C}^T \boldsymbol{\lambda}^i_{n+1} - \mathbf{F}^{\text{int}}_{n+1} \\ \mathbf{C}\ \mathbf{u}^i_{n+1} - \mathbf{D}\overline{\boldsymbol{\varepsilon}}_{n+1} \end{bmatrix}. \tag{6}$$

Matrices $\mathbf{C}$ and $\mathbf{D}$ in Equations (5) and (6) are calculated over the boundary Γ of the RVE and are constant throughout the calculations [1, 4]. At Newton-Raphson iteration i, variable $\boldsymbol{\phi} = \mathbf{u}, \boldsymbol{\lambda}$ is calculated using $\boldsymbol{\phi}^i_{n+1} = \boldsymbol{\phi}_n + \sum_{m=1}^{i} \boldsymbol{\phi}^m_{n+1}$. In Equation (6), $\mathbf{F}^{\text{int}}_{n+1}$ is a vector of internal forces consists of contribution of elements from matrix, yarns and yarn-matrix interfaces and $\overline{\boldsymbol{\varepsilon}}$ is the macro-strain associated with a Gauss point. Furthermore, vectors $\mathbf{C}\mathbf{u}^i_{n+1}$ and $\mathbf{C}^T\boldsymbol{\lambda}^i_{n+1}$ are associated with the RVE boundary conditions and are written as

$$\mathbf{C}\mathbf{u}^i_{n+1} = \int_{\Gamma} \mathbf{H}\mathbf{N}^T \mathbf{u}^{h\,i}_{n+1} d\Gamma, \qquad \mathbf{C}^T\boldsymbol{\lambda}^i_{n+1} = \int_{\Gamma} \mathbf{H}\mathbf{N}^T \boldsymbol{\lambda}^{h\,i}_{n+1} d\Gamma, \tag{7}$$

where $\mathbf{N}$ is the matrix of shape functions and $\mathbf{H}$ is a matrix that is specific to the type of boundary conditions used, each row of which represents an admissible distribution of nodal traction forces on the RVE boundary and $\mathbf{u}^h$ and $\boldsymbol{\lambda}^h$ are displacements and Lagrange multipliers calculated at a Gauss point, i.e. $\boldsymbol{\phi}^h = \mathbf{u}^h, \boldsymbol{\lambda}^h = \mathbf{N}\boldsymbol{\phi}^{e\,i}_{n+1}$, where $\boldsymbol{\phi}^e$ is a matrix of displacements or Lagrange multipliers associated with element e.

3. Numerical example

The correct implementation and performance of the computational framework is demonstrated with a polymer composite reinforced with unidirectional fibres subjected to transverse tension and shear. A periodic RVE, consisting of randomly distributed but axially aligned fibres is considered in this case and is shown in Figure 2(a). The RVE is generated using a statistically proven random distribution algorithm proposed in [5] and is consisting of fibres with 5μm diameter and volume fraction of 60%. For the elasto-plastic matrix material Young's modulus, Poisson's ratio, plastic Poisson ratio and initial yield strengths in tension and compression are 3.76 GPa, 0.39, 0.3, 29 MPa and 67 MPa respectively, while for the linear-elastic and isotropic glass fibres, Young's modulus and Poisson's ratio are 74 GPa and 0.2 respectively. For the cohesive elements interface strength and fracture energy are 50 MPa and 2 J/m^2 respectively. The RVE is discretised with tetrahedral elements including 8,436 and 12,136 elements for matrix and fibres respectively and is shown in Figure 2(b), while the fibres-matrix interfaces are discretised with 1652 zero-thickness cohesive elements. The macro-strain (applied to the RVE by using the periodic boundary conditions) versus the homogenised stress response for both transverse tension and shear cases are compared with the numerical results from [2] and are shown in Figure 2(c), which are in a very good agreement. The final damaged cross-section in the case of transverse-tension is shown in Figure 2(d), where a clear localisation region can be seen. Furthermore, the effect of varying interfacial strength and fracture energy for the transverse tension case is also illustrated in Figure 2(c), which illustrate a more distributed fracture throughout the RVE, e.g. as shown in Figure 2(e).

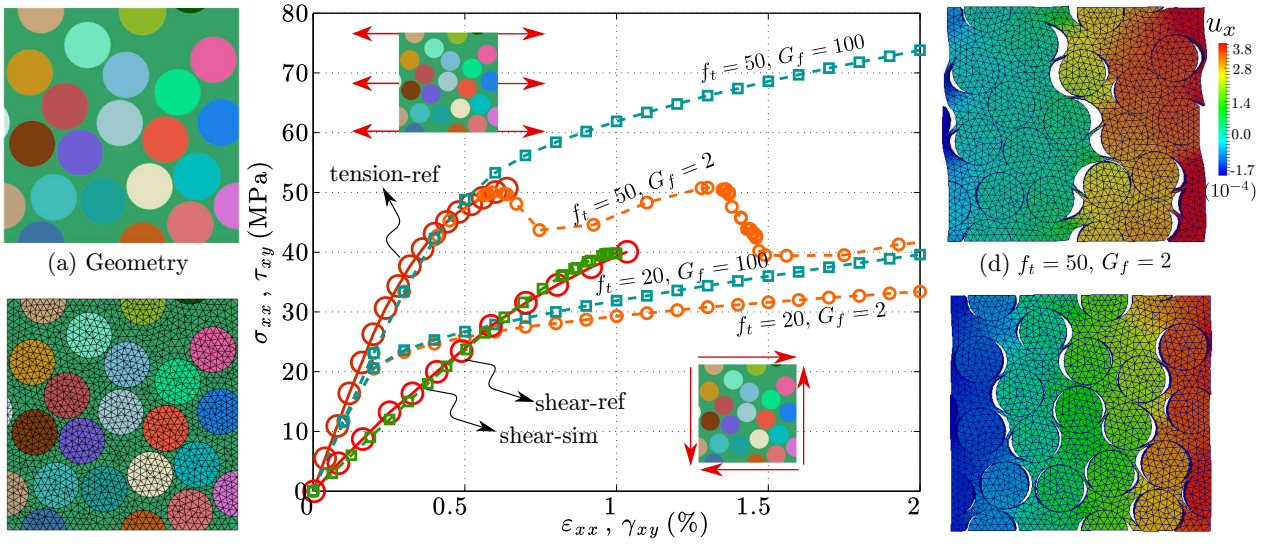

Figure 2: Geometry, mesh, damage and stress-strain plot for the numerical example

4. Conclusions

A three-dimensional, nonlinear micro-mechanical multi-scale computational homogenisation framework is developed for the FRP composites. Matrix and yarns-matrix interfaces are modelled using a paraboloidal yield criterion and cohesive elements respectively, while yarns are considered as linear-elastic and transversely isotropic. The computational framework is validated for FRP composites with unidirectional fibres subjected to transverse tension and shear, the RVE for which are generated using a statistically proven random distribution algorithm. Furthermore, the effect of varying interfacial strength and fracture energy on the homogenised stress versus macro-strain responses is also illustrated.

Acknowledgements

The authors gratefully acknowledge the support of the UK Engineering and Physical Sciences Research Council through the Providing Confidence in Durable Composites (DURACOMP) project (Grant Ref.: EP/K026925/1).

References

[1] Z. Ullah, Ł. Kaczmarczyk, S. A. Grammatikos, M. C. Evernden, and C. J. Pearce. Multi-scale computational homogenisation to predict the long-term durability of composite structures. *Computers and Structures (Under Review)*, 2016.

[2] A. R. Melro, P. P. Camanho, F. M. Andrade Pires, and S. T. Pinho. Micromechanical analysis of polymer composites reinforced by unidirectional fibres: Part II – micromechanical analyses. *International Journal of Solids and Structures*, 50(11–12):1906 – 1915, 2013.

[3] B. Stier, J. W. Simon, and S. Reese. Comparing experimental results to a numerical meso-scale approach for woven fiber reinforced plastics. *Composite Structures*, 122:553 – 560, 2015.

[4] Ł. Kaczmarczyk, C. J. Pearce, and N. Bićanić. Scale transition and enforcement of RVE boundary conditions in second-order computational homogenization. *International Journal for Numerical Methods in Engineering*, 74(3):506–522, 2008.

[5] A. R. Melro, P. P. Camanho, and S. T. Pinho. Generation of random distribution of fibres in long-fibre reinforced composites. *Composites Science and Technology*, 68(9):2092 – 2102, 2008.

Proceedings of the 24th UK Conference of the
Association for Computational Mechanics in Engineering
31 March – 01 April 2016, Cardiff University, Cardiff

Random Normal Contact Laws for Particles with Rough Surface in Discrete Element Modelling

*** T Zhao, J Kato and Y T Feng**

Zienkiewicz Centre for Computational Engineering, College of Engineering
Swansea University, Swansea, SA2 8PP

*842758@Swansea.ac.uk

ABSTRACT

Particles are assumed smooth in classical discrete element modelling, but real particles have random rough surfaces which may influence their mechanical properties. It is necessary therefore to quantitatively improve the conventional discrete element model by taking the surface roughness into consideration. In this work, a new normal contact law is established for particles that have random rough surfaces. The contact law, based on the classic Greenwood and Williamson (GW) model, is derived by both theoretical derivation and numerical calculations. Instead of a complicated integral expression involved in the GW model, the resulting empirical formula of the law retains the closed form and simplicity of the Hertz model, with only one added parameter, σ_S, the standard derivation of a surface roughness, and therefore can be readily incorporated into the current discrete element modelling framework.

Keywords: *Surface roughness; Contact law; Discrete element method, Stochastic DEM; Numerical model*

1. Introduction

The discrete element method (DEM) is a computational technique originally developed by Cundall and Strack [3] which is well suited to simulate the response of assembly systems of particles [9]. DEM has been widely accepted as an effective method to model engineering problems in granular and discontinuous materials, especially in granular flows, power mechanics and rock mechanics. The basic particles in DEM are regular geometric entities such as disk, sphere, ellipse and ellipsoid with smooth surface. However real particles contain geometric irregularities at both macroscopic and microscopic levels. The macroscopic irregularities of particles may be modelled by more complicated geometric shapes, while surface irregularities at the microscopic level, also called the surface roughness, are more difficult to be considered, although they may have strong influence on the phenomena of contact, friction, wear and lubrication [1]. Up to now, very few attempts have been reported to provide random interaction laws that can be readily applied in DEM to estimate the contact forces between rough particles. It is therefore necessary to quantitatively improve the classical DEM by taking the surface roughness into consideration. The main objective of this paper is to establish a new random interaction law which can be applied in DEM for particles having random rough surfaces.

There are several approaches that have been developed to understand the contact mechanism between rough surfaces, and can be classified into two categories: statistical and deterministic. The earliest and most recognized statistical treatment of rough surfaces is the work of Greenwood and Williamson [6]. This method can be viewed as a single scale method since statistical parameters used to represent rough surfaces are scale-dependent. Another statistical approach, where a fractal curve/surface is adopted to describe a rough surfaces together with a contact mechanism to resolve the contact, is introduced by Majumdar and bhushan [8]. This fractal based approach can be regarded as multiple scaled because of the inherent multi-scale invariant characteristics of most fractal curves/surfaces. On the other hand, the deterministic methods attempt to model rough surfaces precisely and the resulting contact problem is typically solved by the finite element method. Furthermore, the fast Fourier transformation is often used to treat the rough surface [10]. For the contact between two rough curved bodies, the first analytical study was conducted by Greenwood and Tripp [5] who employed the GW

asperity contact model together with the bulk surface deformation for circular point contact. More recent researches have extended the GW approach to the elasto-plastic deformation regime [2, 4, 7].

2. Numerical algorithms for the GW model

In the GW model, a rough flat surface is assumed to be an assembly of asperities whose properties are obtained from a given statistical height distribution of the surface and the Hertz contact law is then applied to these asperities which are also assumed to have the same radius of curvature. When this theory is applied to the contact problem of two rough spheres [6], the only difference from the rough flat contact problem is the geometrical aspect. Because of the spherical profile, the separation between two spheres will be a function of r, the distance from the centre of the contact area. The contact problem between two rough spheres is equivalent to the contact between a smooth sphere of radius R and a nominally rigid flat rough surface having a Gaussian distribution of asperities heights σ_s, where R and σ_s can be derived by the radii and roughness of the two spheres as

$$\frac{1}{R} = \frac{1}{R_1} + \frac{1}{R_2} \tag{1}$$

$$\sigma_s^2 = \sigma_{s1}^2 + \sigma_{s2}^2 \tag{2}$$

Then the contact pressure distribution is given by

$$p(r) = \frac{4}{3} E^* n \beta^{\frac{1}{2}} \int_{w(r)+\frac{r^2}{2R}}^{\infty} (z - \frac{r^2}{2R} - w(r))^{3/2} \frac{1}{\sigma\sqrt{2\pi}} e^{-\frac{(z-\delta)^2}{2\sigma^2}} dz \tag{3}$$

where w(r) is the deformation of the sphere and can be obtained from the solution for the axi-symmetric deformation of an elastic half-space as follows

$$w(r) = \frac{4}{\pi E^*} \int_0^a \frac{t}{t+r} p(t) \boldsymbol{K}(k) dt \tag{4}$$

$$w(0) = \frac{2}{E^*} \int_0^a p(t) dt \tag{5}$$

in which $\boldsymbol{K}(k)$ is the first kind complete elliptic integral of $k = 2(rt)^{\frac{1}{2}}/(r+t)$, and a is the radius of the contact area for the smooth surfaces under the same load. Then the total contact force can be obtained by the integration of the pressure distribution over the contact area.

Clearly, the $p(r)$ distribution in the GW model involves a complicated integral with n, β and σ as the statistical characteristic parameters of surface roughness. In order to obtain $p(r)$, the nonlinear equations (3) and (4) have to be solved simultaneously, with the later also including a non-integrable part. A numerical method based on the Newton-Raphson iterations is applied to solve this problem. First, introduce $N+1$ discrete points along the contact radius. Then equation (3) must be satisfied at each point i:

$$p_i = \mu g(w_i) \tag{6}$$

where

$$\mu = \frac{4}{3} E^* n \beta^{\frac{1}{2}} \tag{7}$$

$$g(w_i) = \int_{w_i+\frac{r_i^2}{2R}}^{\infty} (z - \frac{{r_i}^2}{2R} - w_i)^{3/2} \frac{1}{\sigma\sqrt{2\pi}} e^{-\frac{(z-\delta)^2}{2\sigma^2}} dz \tag{8}$$

or in a different form

$$F_i(p_0, p_1, \dots, p_N) = p_i - \mu g(w_i) = 0 \tag{9}$$

which leads to a nonlinear system of equations for all the points:

$$\mathbf{F}(\mathrm{p}) = \mathrm{p} - \mu \mathrm{g} = 0 \tag{10}$$

To solve this system of equations in terms of p, function **F** is expanded by the Taylor series in neighbourhood of p as

$$\mathbf{F}(\mathrm{p} + \delta\mathrm{p}) = \mathbf{F}(\mathrm{p}) + \mathbf{J} \cdot \delta\mathrm{p} + O(\delta\mathrm{p}^2) \tag{11}$$

where **J** is Jacobian matrix, which represents the gradient of the vector **F**. The value of **J** is obtained by a finite difference approximation. The increment δp is obtained by

$$\delta\mathrm{p} = -\mathbf{J}^{-1}\mathbf{F}(\mathrm{p}) \tag{12}$$

The solution p is achieved by the iterative process starting from a trial solution. Then the total contact force can be obtained by integrating the pressure $p(r)$ over the entire contact area. The $P \sim \delta$

relationships of two surfaces with different levels of roughness are shown in Fig. 1, in which the range of σ (normalised) is 0.0001~0.01 and δ (normalised) is 0~0.1. All the other parameters are set to be 1. The P~δ relationships of the Hertz law and the GW-model ($\sigma = 1.0e-4$) are shown in Fig. 2.

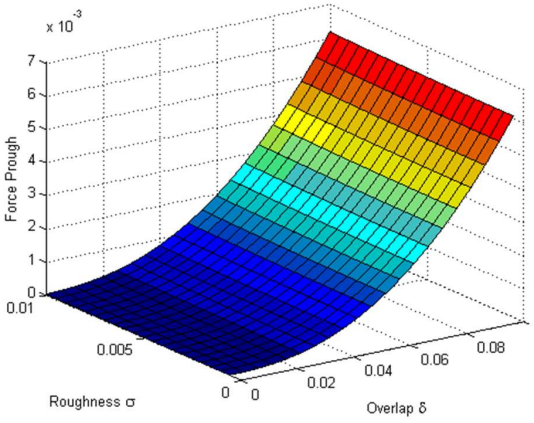

Figure 1: $P\sim\sigma\sim\delta$ relationships based on the numerical calculation

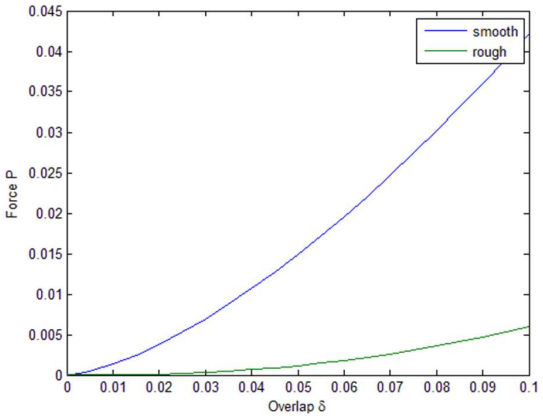

Figure 2: $P\sim\delta$ relationships of smooth surface and rough surface ($\sigma = 1.0e-4$)

3. Predictive formulas of the $P\sim\delta$ curve

In order to obtain the random normal interaction law that can be used in DEM, an explicit relationship between the total force P and the overlap δ needs to be defined from the numerical results via curve-fitting. It is of practical importance that the resulting relationship should have a simple closed form with the minimum number of added parameters. Equation (3) indicates that there are two added parameters, σ and $n\beta^{\frac{1}{2}}$, and that P is proportional to $n\beta^{\frac{1}{2}}$ (note that the numerical results obtained are for $n\beta^{\frac{1}{2}} = 1$).

It is obvious that the $P\sim\delta$ relationship should degenerate to the Hertz law when $\sigma = 0$. However, to treat $n\beta^{\frac{1}{2}}$ as an independent parameter from σ will violate this requirement as different values of $n\beta^{\frac{1}{2}}$ would lead to different $P\sim\delta$ curves at $\sigma = 0$. To resolve this issue, $n\beta^{\frac{1}{2}}$ is calibrated in the following way. When σ is sufficiently small, the rough surface should be regarded as a smooth surface and thus should have the same $P\sim\delta$ relationship as the Hertz law. However, Fig. 2 depicts a clear difference between P_{smo} and P_{rough} (with $n\beta^{\frac{1}{2}} = 1$, and assuming that $\sigma = 1.0e-4$ is sufficiently small). Our numerical calculation shows that the condition $P_{rou}\ (\sigma = 0) = P_{smooth}$ can be enforced if $n\beta^{\frac{1}{2}}$ takes the following value:

$$n\beta^{\frac{1}{2}} = \frac{P_{smooth}}{P_{rough}} = 0.62R^{-\frac{1}{2}}\delta^{-1} \tag{13}$$

Then σ now becomes the solely added parameter in the $P\sim\delta$ relationship, making the new interaction law much simpler. The correctness of this formula can be verified through the analysis of equation (3) at the special case $\sigma = 0$, based on the fact that the Gaussian distribution reduces to the Dirac Delta Function when $\sigma \to 0$:

$$\delta(t) = \lim_{\sigma\to 0} \frac{1}{\sqrt{2\pi}\sigma} e^{-t^2/2\sigma^2} \tag{14}$$

An important property of the delta function is that for a given function $f(x)$

$$\int f(t)\delta(t-t_0)dt = f(t_0) \tag{15}$$

Thus when $\sigma \to 0$, the pressure distribution $p(r)$ in equation (3) reduces to

$$p(r) = \frac{4}{3}E^* n\beta^{\frac{1}{2}}(\delta - \frac{r^2}{2R} - w(r))^{3/2} \tag{16}$$

An explicit expression for $p(r)$ is not possible because of the inter-dependence between $p(r)$ and $w(r)$ which is the deformation of the smooth sphere. However, we artificially set $w(r) = 0$, which leads to an explicit but approximate expression for $p(r)$

$$p(r) = \frac{4}{3}E^* n\beta^{\frac{1}{2}}(\delta - \frac{r^2}{2R})^{3/2} \quad (17)$$

The total contact force can be obtained by the integration of the pressure distribution over the contact area as

$$P_{rough} = \int_0^a 2\pi r p(r) dr = 2.76E^* n\beta^{\frac{1}{2}} R\delta^{\frac{5}{2}} \quad (18)$$

The nominally flat rough surface can be considered as smooth surface when σ→0. The contact force between the sphere and the smooth surface can be calculated by the Hertz law

$$P_{smoot} = \frac{4}{3}E^* R^{\frac{1}{2}}\delta^{\frac{3}{2}} \quad (19)$$

The condition $P_{rough} = P_{smoot}$ gives rise to

$$n\beta^{\frac{1}{2}} = 0.48R^{-\frac{1}{2}}\delta^{-1} \quad (20)$$

which is the same as formula (13) except for a smaller coefficient. This discrepancy can be explained: the assumption $w(r)$=0 increases the overlap between the sphere and the asperities, thereby leading to a larger $p(r)$, and thus a larger P_{rough}, and therefore a smaller coefficient.

Based on the above analysis and applying curve-fitting, the predictive formula for calculating the normal contact force between two rough spheres is derived as (with the $Rsqure = 0.98$)

$$P_{rough} = E^* R^{\frac{1}{2}}\left(\frac{4}{3} - 39.13\sigma\right)\delta^{\left(\frac{3}{2} - 9.57\right)} + 1.5\sigma^{2.5} \quad (21)$$

Cleary, when $\sigma = 0$, the formula recovers the Hertz law as required. Also, the total force is no longer zero when $\delta = 0$ for $\sigma > 0$ because some asperities of the two rough spheres may be in contact even there is no overlap between the two mean surfaces.

References

[1] Barber, J. R. and M. Ciavarella (2000), Contact mechanics, International Journal of Solids and Structures 37, 29–43.

[2] Cohen D, Kligerman Y, Etsion I. The effect of surface roughness on static friction and junction growth of an elastic-plastic spherical contact. Journal of Tribology. 2009 Apr 1;131(2):021404.

[3] Cundall, Peter A., and Otto DL Strack. A discrete numerical model for granular assemblies. Geotechnique 29.1 (1979): 47-65.

[4] Gelinck ER, Schipper DJ. Deformation of rough line contacts. Journal of tribology. 1999 Jul 1;121(3):449-54.

[5] Greenwood JA, Tripp JH. The elastic contact of rough spheres. Journal of Applied Mechanics. 1967 Mar 1;34(1):153-9.

[6] Greenwood, J.A. and J.B.P. Williamson (1966), Contact of nominally flat surfaces, Proceedings of the Royal Society, London 295(Series A), 300.

[7] Li L, Etsion I, Talke FE. Elastic–plastic spherical contact modeling including roughness effects. Tribology letters. 2010 Dec 1;40(3):357-63.

[8] Majumdar, A. and B. Bhushan (1990), Role of fractal geometry in roughness characterization and contact mechanics of surfaces, Journal of tribology (ASME) 112, 205–216.

[9] Owen, D. R. J., Y. T. Feng, M. G. Cottrel and J. Yu (2002), Discrete/finite element modelling of industrial applications with multi-fracturing and particulate phonomena, in '3rd Int. Conf. Discrete Element Methods', Santa Fe, New Mexico, USA, pp. 11–16.

[10] Stanley, M. and T. Kato (1997), An fft-based mothod for rough surface contact, Journal of tribology 119, 481–485.

Coupled Problems

Proceedings of the 24th UK Conference of the
Association for Computational Mechanics in Engineering
31 March - 01 April 2016, Cardiff University, Cardiff

FINITE ELEMENT MODELLING OF ELECTRO-OSMOTIC FLOW IN POROUS MEDIA

***Simona Di Fraia[1,2], Nicola Massarotti[1] and Perumal Nithiarasu[2]**

[1]Dipartimento di Ingegneria, Universitá degli Studi di Napoli "Parthenope", Napoli, 80143, Italy
[2]Zienkiewicz Centre for Computational Engineering, College of Engineering, Swansea University, Swansea, SA1 8EN, UK

*simona.difraia@uniparthenope.it

ABSTRACT

Electro-osmotic flow (EOF) in microchannels with and without porous media has been analysed in this work. The effect of the charge of solid particles on EOF has been taken into account by introducing an equivalent reference length into the equation that governs the static potential distribution. External electric field and internal potential have been determined by solving the Laplace and Poisson-Boltzmann equations, respectively. Their effect has been introduced into the Navier-Stokes equations to simulate fluid flow and heat transfer due to electro-osmosis. The set of equations that describes the problem has been solved using the finite element method combined with the characteristic-based split algorithm.

Key Words: *Electro-osmosis; Porous materials; Microscopic approach; CBS.*

1. Introduction

Electro-osmosis is important due to its applications in several fields of biology and engineering, mainly for pumping, cooling, mixing and separation processes. In Electro-Osmotic Flow (EOF) driven systems a solid surface, in contact with an electrolytic solution, becomes a charged surface. Consequently, the ions in the solution form of a high concentration region close to the solid surface, called Electrical Double Layer (EDL). When an external electric field is applied, the ions of the EDL move, dragging the nearby ions with them. In standard channel flow applications, the active surfaces are the channel walls. In channels filled with electrolyte saturated porous media, the boundaries of solid particles also contribute to electro-osmosis.
EOF in micro- and nano- fluidic systems has been widely investigated, experimentally and numerically. On the contrary, EOF in porous media is still not clearly analysed [1]. Experimental data are difficult to collect, due to the small scales, while for numerical modelling different approaches have been used and in most cases the results have not been validated against experimental results. In addition, several simplifying hypotheses have been considered in modelling EOF in porous media. To better understand EOF through porous media, a well defined porous medium is studied in the present work by using a microscopic approach. The flow results obtained for EOF through a of porous medium are compared against standard microchannel EOF without porous medium.

2. Mathematical model and solution procedure

The Laplace equation for the external applied potential and a non-linear Poisson-Boltzmann equation for the internal potential have been solved explicitly, by adding a pseudo time term. Their effect, responsible for EOF, has been implemented into the source term of the momentum equation of Navier-Stokes equations [3]. The Laplace and Poisson-Boltzmann equations are presented in non-dimensional form as

- *Laplace equation*

$$\frac{\partial^2 \phi^*}{\partial x_i^{*2}} = 0 \tag{1}$$

- *Poisson-Boltzmann equation*

$$\frac{\partial^2 \psi^*}{\partial x_i^{*2}} = -\left(\kappa L_{ref}\right)^2 \sinh\left(\frac{\psi^*}{T^*+1}\right) \tag{2}$$

where ϕ^* is the non dimensional applied external potential, ψ^* the non dimensional Electric Double Layer (EDL) potential (internal potential), κ is known as Debye-Huckel parameter, L_{ref} is the reference length and T^* is the non dimensional temperature. The Debye-Huckel parameter [2] is given as

$$\kappa = \left(\frac{2n_0 z^2 e^2}{k_B T \epsilon \epsilon_0}\right)^{1/2}$$

where n_0 is the ionic number concentration in the bulk solution, z the valance of the ions, e the elementary charge, k_B the Boltzmann's constant, T is the reference temperature measured in kelvin, ϵ the dielectric constant of the electrolyte and ϵ_0 the permittivity of vacuum.
The parameter κL_{ref} used in Equation (2) represents the thickness of the EDL: it largely affects the internal potential distribution and consequently the flow profile within the channel. It appears that in the literature, the equation that governs internal potential distribution has not been modified to include the effect of porous media. This approach tends to underestimate the contribution of the charge of solid particles in the porous medium. Therefore, in the present work the authors have considered an equivalent reference length, assumed equal to the ratio between the area the channel occupied by the fluid and the length of the channel:

- in case of fluid $L_{ref,eq}$ corresponds exactly to the channel width, consistent with the quantity commonly used in previous works concerning EOF;
- for porous media the use of $L_{ref,eq}$ into Equation (2) should allow flow enhancement due to the charge of solid particles. An equivalent length as discussed previously is employed in the present study.

Fluid flow and heat transfer in standard micro-channels and through porous media have been analysed through the Navier-Stokes equations. They are given in their non-dimensional form as

- *Continuity equation*

$$\frac{1}{\beta^{*2}} \frac{\partial P^*}{\partial t^*} = -\rho^* \frac{\partial u_i^*}{\partial x_i^*} \tag{3}$$

- *Momentum equation*

$$\rho^* \left(\frac{\partial u_i^*}{\partial t^*} + \frac{\partial \left(u_i^* u_j^*\right)}{\partial x_j^*}\right) = -\frac{\partial p^*}{\partial x_i^*} + \frac{1}{Re} \frac{\partial^2 u_i^*}{\partial x_i^{*2}} + J \sinh\left(\frac{\psi^*}{T^*+1}\right)\left(\frac{\partial \phi^*}{\partial x_i^*}\right) \tag{4}$$

- *Energy equation*

$$\frac{\partial T^*}{\partial t^*} + u_i^* \frac{\partial T^*}{\partial x_i^*} = \frac{\alpha^*}{RePr} \frac{\partial^2 T^*}{\partial x_i^{*2}} + Jo\left(\frac{\partial \phi^*}{\partial x_i^*}\right) \tag{5}$$

where

$$Re = \frac{\rho_{ref} u_{ref} L_{ref}}{\mu}; \qquad J = \frac{2n_0 k_B T}{u_{ref}^2 \rho_{ref}}; \qquad Jo = \frac{1}{RePr} \frac{\sigma_{ref}}{k_{ref}} \frac{k_B^2 T_{ref}}{z^2 e^2};$$

The other non-dimensional quantities used in the above non dimensional form of equations are

$$x_i^* = \frac{x_i}{L_{ref}}; \qquad \phi^* = \frac{ze\phi}{k_B T}; \qquad \psi^* = \frac{ze\psi}{k_B T}; \qquad T^* = \frac{T - T_{ref}}{T_{ref}}; \qquad \rho^* = \frac{\rho}{\rho_{ref}};$$

$$u_i^* = \frac{u_i}{u_{ref}}; \qquad u_{ref} = \frac{E_x \epsilon \epsilon_0 \zeta}{\mu} \qquad t^* = \frac{t u_{ref}}{L_{ref}}; \qquad p^* = \frac{p - p_{ref}}{\rho_{ref} u_{ref}^2}; \qquad \beta^* = \frac{\beta}{u_{ref}};$$

where β is an artificial compressibility parameter [4]. Fluid flow and heat transfer equations have been solved by using finite element method combined with a fully explicit artificial compressibility-based CBS (Characteristic Based Split) scheme [5] to overcome the instability caused by the pressure term of the momentum equation.
The walls and any solid boundary have been assumed to be active with a prescribed non-dimensional zeta potential and to obey no-slip velocity boundary conditions. An applied external potential difference between the inlet and outlet has been considered and the normal velocity gradients have been assumed to be zero at both inlet and outlet. The computation has been started with prescribed zero velocity components as initial condition. A 2D unstructured mesh refined near all solid boundaries to capture the rapid change in both internal potential and velocity has been used. A mesh sensitivity study has been carried out in order to find grid insensitive results.
In order to assess the effectiveness of using porous media to enhance EOF, a comparison with standard channel flow applications has been carried out. Fluid flow and heat transfer through porous media have been analysed through the so-called microscopic approach [6], that provides details of the fields for the quantities of interest at particle level. The analysis has been focused on the improvement in EOF due to the use of the equivalent reference length proposed in the present work.

3. Results and Discussions

A silicon micro-channel 30 μm in diameter characterized by an aspect ratio of 10, with deionized water as working fluid, has been considered. Porous media have been investigated at the pores level, with solid particles assumed to be circular in shape. Two cases have been considered:

- particles arranged in line, diameter equal to 50% of the channel diameter;
- staggered particles, diameter equal to 30% of the channel diameter.

A non-dimensional external potential difference of 2 000 was prescribed between the inlet and outlet of the channel. The non-dimensional zeta potential value of -3, corresponding to $-75mV$, has been considered for both the channel walls and the solid particles.
The distribution of the internal potential is shown in Figure 1, where only part of the whole domain is reported here to clearly view the details.

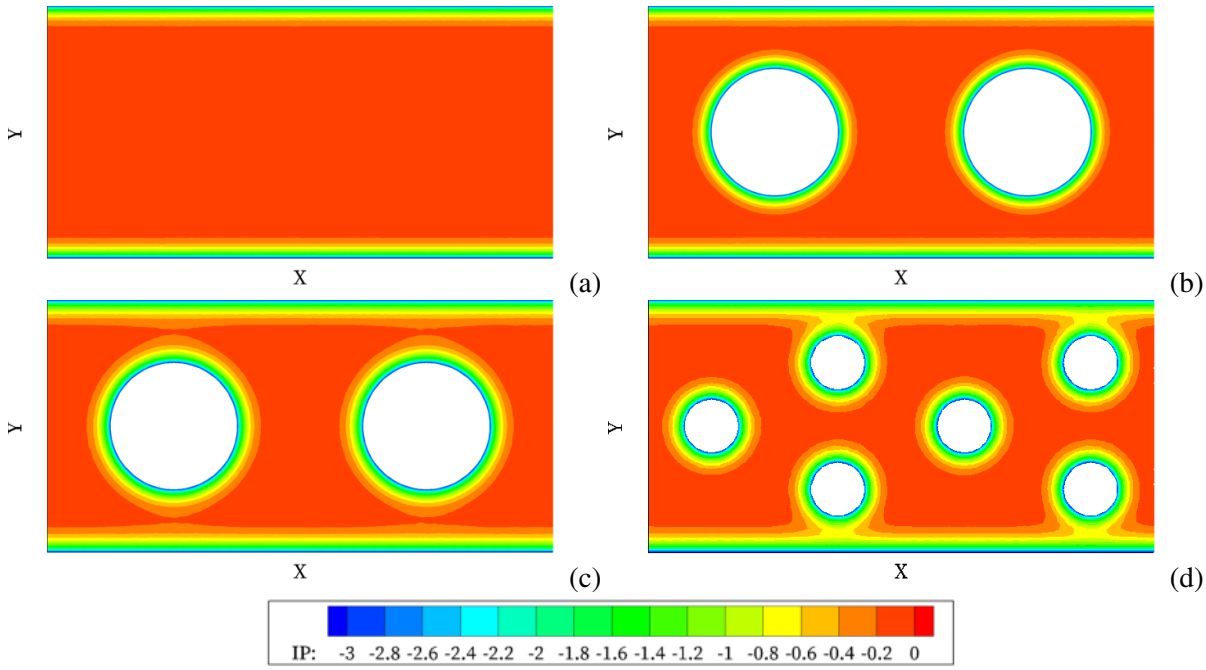

Figure 1: Internal potential (IP) distribution: standard fluid channel (a) and porous channel with in line particles with standard channel width (b) and with the proposed $L_{ref,eq}$ (c), staggered particles with the proposed $L_{ref,eq}$ (d).

For EOF in porous media with in line particles two cases have been considered: firstly, the equation that governs internal potential distribution has not been modified, and the width of the channel has been used (Figure 1 b), secondly the equivalent reference length proposed by the authors has been considered (Figure 1 c). The results obtained highlight that, by using $L_{ref,eq}$ instead of the whole width of the channel, the effect of the charge of solid material in the narrow region between the channel wall and the particle is taken into account. The internal potential distribution plays a fundamental role on the velocity distribution and consequently on the flowrate. The effect of using the proposed equivalent length on the outlet velocity profile is illustrated in Figure 2. As seen, the equivalent width used substantially increases the flow rate when porous media have been considered.

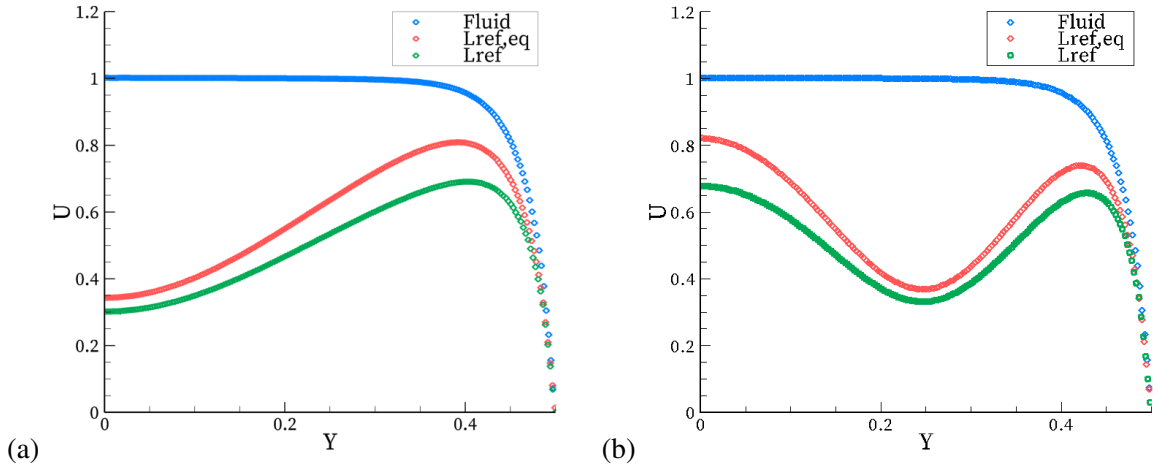

Figure 2: Outlet velocity profiles: comparison between fluid and in line particles (geometry b-c of Figure 1) (a), staggered particles (geometry d of Figure 1) (b).

4. Conclusions

Electro-osmotic flow through porous media has been studied and compared to the standard channel flow applications. For modelling porous media flow an equivalent reference length has been employed. The use of this parameter allows us to take into account the influence of the charge of solid particles on the internal potential distribution and capture the behaviour in the narrow regions between solid particles and channel walls. The results of this study will be used by the authors to define the parameters for modelling EOF in porous media by using a macroscopic approach.

References

[1] B. Li, W. N. Zhou, Y. Y. Yan, C. Tian. Evaluation of electro-osmotic pumping effect on microporous media flow. *Applied Thermal Engineering*, 60, 449–455, 2013.

[2] N. A. Patankar, H. H. Hu. Numerical simulation of electroosmotic flow. *Analytical Chemistry*, 70(9), 1870–1881, 1998.

[3] R. J. Yang, L. M. Fu, Y. C. Lin. Electroosmotic flow in microchannels. *Journal of colloid and interface science*, 239(1), 98–105, 2001.

[4] P. Nithiarasu. An efficient artificial compressibility (AC) scheme based on the characteristic based split (CBS) method for incompressible flows. *International Journal for Numerical Methods in Engineering*, 56(13), 1815–1845, 2003.

[5] P. Nithiarasu, R. W. Lewis, K. N. Seetharamu. *Fundamentals of the Finite Element Method for Heat and Mass Transfer*, John Wiley and Sons, 2016.

[6] N. Massarotti, P. Nithiarasu, A. Carotenuto. Microscopic and macroscopic approach for natural convection in enclosures filled with fluid saturated porous medium, *International Journal of Numerical Methods for Heat and Fluid Flow*, 13(7), 862–886, 2003.

Proceedings of the 24th UK Conference of the
Association for Computational Mechanics in Engineering
31 March – 01 April 2016, Cardiff University, Cardiff

NUMERICAL STUDY OF CONVECTIVE HEAT AND MASS TRANSFER THROUGH A SATURATED POROUS MEDIUM IN HORIZONTAL CYLINDRICAL ANNULUS

Hichem Boulechfar [1], *Mahfoud Djezzar [1]

[1]Physics and Energy Laboratory, Faculty of Exact Sciences, University of Constantine 1,
Aïn El Bey Street, 25000 Constantine, Algeria

* mdjezzar@umc.edu.dz

ABSTRACT

Two-dimensional heat and mass transfer of natural convection in an annular cylindrical space filled with fluid-saturated porous medium, is analyzed by solving numerically the mass balance, momentum, energy and concentration equations, using Darcy's law and Boussinesq approximation. Both walls delimiting the annular space are maintained at two uniform different temperatures and concentrations. The external parameter considered is Rayleigh-Darcy number. For the present work, the heat and mass transfer for natural convection is studied for the case of aiding equal buoyancies, where the flow is generated in a cooperative mode by both temperature and solutal gradients. The local Nusselt and Sherwood numbers are presented in term of the external parameter.

Keywords: *Heat and mass transfer; Natural convection; Porous media; cylindrical annulus.*

1. Introduction

The heat and mass transfer of natural convection confined into different annular enclosures was a subject of many theoretical, numerical and experimental studies. These annular spaces have different geometries and can be partly or completely filled with porous media. Interest in this phenomena is due to many potential applications in the engineering processes which involve the oil and gas industries, thermal recovery process, the underground spreading of chemical waste and other pollutants…etc.
F.M. Mahfouz [1] has investigated a buoyancy driven flow and associated heat convection in an elliptical enclosure. N. Allouache and al. [2] analyzed a solid adsorption refrigerator using activated carbon/methanol pair. It is a contribution to technology development of solar cooling systems. Edimilson J and al. [3] examined a numerical computation for laminar and turbulent natural convection within a horizontal cylindrical annulus filled with a fluid saturated porous medium. Leong and Lai [4] presented a natural convection in concentric cylinders with a porous sleeve, analytical solutions obtained through perturbation method and Fourier transform. Mota and al. [5] solved the two-dimensional Darcy-Boussinesq equations, governing natural convection heat transfer in a saturated porous medium, in generalized orthogonal coordinates, using high-order compact finites differences on a very fine grid.

2. Problem Formulation And Basic Equation

We consider a thermosolutale natural convection in an annular elliptical space filled with fluid-saturated porous medium. Figure 1(a) represents a cross section of the system. Both elliptic internal and external walls are isothermal and impermeable, kept at constant temperatures and concentrations T_1, C_1 and T_2, C_2 respectively with $T_1>T_2$ and $C_1>C_2$. The physical properties of the fluid are constant, apart from the density ρ whose variations are at the origin of the natural convection. Viscous dissipation and the radiation are neglected, Soret and Dufour effects are also neglected and we admit that the problem is bidimensional, permanent and laminar and the porous medium is considered isotropic and homogeneous. Dimensionless equations within the framework of the Boussinesq's approximation after the transformation from the Cartesian to the elliptic coordinates are:

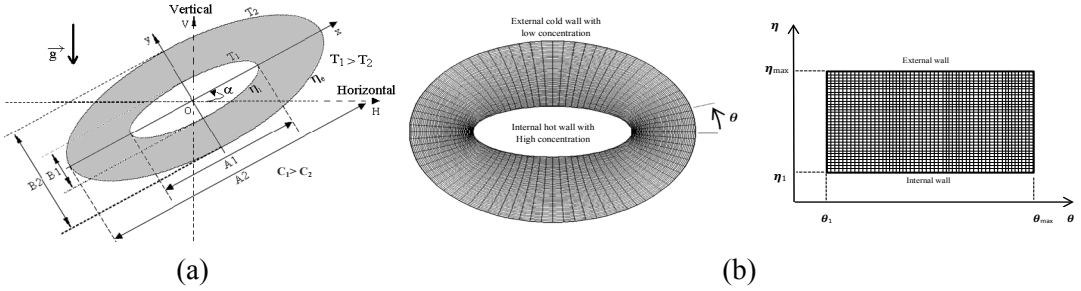

(a) (b)

Figure 1: (a) The cross section of the system, (b) Physical domain (left) and computational domain (right)

Continuity Equation:

$$\frac{\partial}{\partial \eta}\left(HV_{\eta}^{+}\right)+\frac{\partial}{\partial \theta}\left(HV_{\theta}^{+}\right)=0 \tag{1}$$

Momentum Equation:

$$\frac{1}{h}\left[\frac{\partial^2\psi^{+}}{\partial\eta^2}+\frac{\partial^2\psi^{+}}{\partial\theta^2}\right]=-Ra_m.H\left(\left[\cos(\alpha)F(\eta,\theta)-\sin(\alpha)G(\eta,\theta)\right]\left(\frac{\partial T^{+}}{\partial\eta}+N\frac{\partial C^{+}}{\partial\eta}\right)-\left[\sin(\alpha)F(\eta,\theta)+\cos(\alpha)G(\eta,\theta)\right]\left(\frac{\partial T^{+}}{\partial\theta}+N\frac{\partial C^{+}}{\partial\theta}\right)\right) \tag{2}$$

Heat Equation:

$$HV_{\eta}^{+}\frac{\partial T^{+}}{\partial\eta}+HV_{\theta}^{+}\frac{\partial T^{+}}{\partial\theta}=\left[\frac{\partial^2T^{+}}{\partial\eta^2}+\frac{\partial^2T^{+}}{\partial\theta^2}\right] \tag{3}$$

Concentration Equation:

$$HV_{\eta}^{+}\frac{\partial C^{+}}{\partial\eta}+HV_{\theta}^{+}\frac{\partial C^{+}}{\partial\theta}=\frac{1}{Le}\left[\frac{\partial^2C^{+}}{\partial\eta^2}+\frac{\partial^2C^{+}}{\partial\theta^2}\right] \tag{4}$$

V_η and V_θ are the velocity components in the directions η and θ, $F(\eta,\theta)$, $G(\eta,\theta)$ used in (2) are the coefficients resulting from the transformation and H represent the metric coefficients in the elliptic coordinates. Ra_m represents Rayleigh-Darcy number which is defined as: $Ra_m=Ra.Da$

The boundary conditions are expressed as following:

Hot inner wall with high concentration ($\eta=\eta_i$=cst):

$$V_{\eta}^{+}=V_{\theta}^{+}=\frac{\partial\psi^{+}}{\partial\eta}=\frac{\partial\psi^{+}}{\partial\theta}=0\ ,\ T_1{}^{+}=1,\ C_1{}^{+}=1$$

Cold outer wall with low concentration ($\eta=\eta_e$=cst):

$$V_{\eta}^{+}=V_{\theta}^{+}=\frac{\partial\psi^{+}}{\partial\eta}=\frac{\partial\psi^{+}}{\partial\theta}=0\ ,\ T_2{}^{+}=0,\ C_2{}^{+}=0$$

3. Numerical method

Figure 1 (b) shows the physical and computational domain and to solve (1), (3) and (4) with the associated boundary conditions; we consider a numerical solution by the finite volumes method, exposed by [6]. The power law scheme was used for the discretization. To solve (2), we consider a numerical solution by the centred differences method. The iterative method used for the numerical solution of algebraic system of equations is the Gauss-Seidel with an under-relaxation process. Local Nusselt and Sherwood numbers in the physical domain are defined as:

$$Nu=-\frac{1}{h}\frac{\partial T^{+}}{\partial\eta}\bigg|_{\eta=cst}\ ,\ Sh=-\frac{1}{h}\frac{\partial C^{+}}{\partial\eta}\bigg|_{\eta=cst}$$

4. Results and discussion

The objective is to analyze the effect of Rayleigh-Darcy number for the case of a cooperative mode of the heat and mass transfer. For this reason, we presented streamlines, isotherms and concentration contours for different values of Rayleigh-Darcy number for the case when the buoyancy ratio N=1 and for a determined value of Lewis number Le=0.1. The Nusselt and Sherwood numbers are presented for different values of Ra_m. The study was carried out for the case of the air and when the eccentricities of the internal and the external ellipses are respectively given by e_1=0.14 and e_2=0.07 in order to obtain a cylindrical configuration and the inclination of the system is α=0°. Figure 2 represent the streamlines (left), concentration contours (middle) isotherms (right), we note that these contours are symmetrical about the median fictitious vertical plane. The streamlines of figure 2 show that the flow is organized in two main cells that rotate in opposite directions. This is due to upward movement of the fluid particles under the aiding buoyancy effect related to temperature and solutal gradients, the fluid heat up along the hot wall and the downward movements of the fluid particles which cool along the cold wall under the gravity. Isotherms in figure 2(a) deform in the upper space where there is presence of two counter-rotating vortices. This configuration illustrates that the heat transfer is dominated by a convective mode in the upper space, in the lower space the heat transfer is dominated by a conduction mode with a slight contribution of the convection.

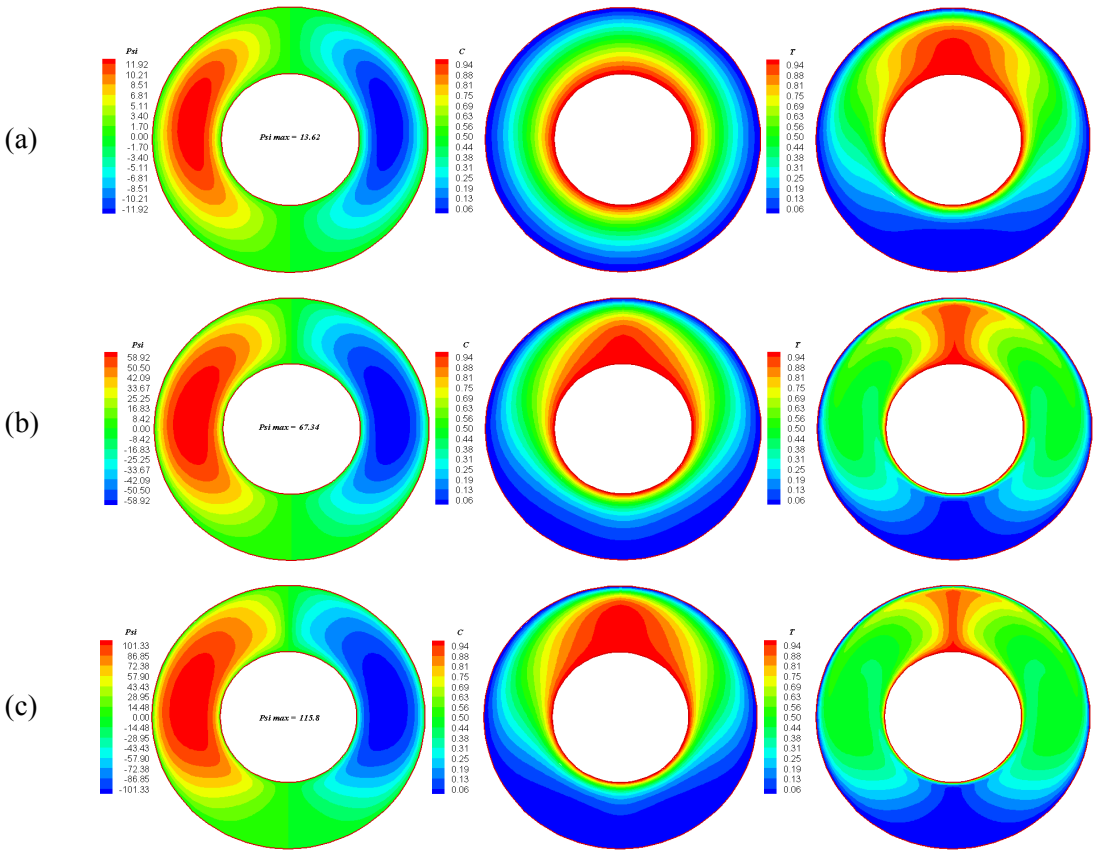

Figure 2: Streamlines, isotherms and concentration contours for N=1 and Le=0.1
(a) Ra_m=10, (b) Ra_m=100 and (c) Ra_m=250

The concentration contours in this figure are parallel and concentric closed curves which coincide perfectly with the walls profile in the annular space where the mass transfer is purely conducted by diffusion mode. In figure 2(b) we notice that with the increase isotherms show that the convective mode is gaining more space in the bottom section under the effect of the thermal gradient. The concentration contours show that the mass transfer is driven by a diffusive mode with a slight transition in the upper space due to the aiding buoyancies. Figure 2(c) shows that the streamlines from

both cells tend to become adjacent which decrease the gap between the cells in the upper annulus space, the flow remains organized in two main cells rotating in opposite directions with very high motion. In the same figure, isotherms have a significant change and are increasingly distorted at the top of the annular space due to the increase of the thermal gradient. The concentration contours illustrate a solutal stratification relatively decreasing in the upper section of the annular space.

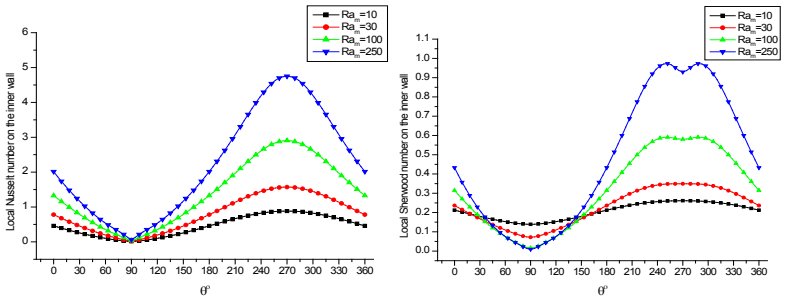

Figure 3: Variation of local Nusselt and Sherwood numbers on the inner wall for *Le*=0.1and *N*=1

Figure 3 illustrates the variation of local Nusselt and Sherwood numbers on the inner wall of the cylinder in term of Rayleigh-Darcy number. For the local Nusselt number this variation allows us to note that with the increase of Rayleigh-Darcy number, the value of local Nusselt number increase significantly due to the increase in the thermal gradient which is obvious. The local Sherwood number increases with increasing of Ra_m due to the aiding effect of thermal and solutal buoyancies.

5. Conclusion

Heat and mass transfer of natural convection in a porous cylindrical annulus saturated by a Newtonian fluid was studied by a numerical method using the method of finite volumes and the vorticity-streamline formulation. We examined, in particular, the influence of Rayleigh-Darcy number for the case when the thermal and the solutal buoyancies are equal and cooperating in the generation of the flow. The structures of bicellular convection take place according to the value of the Rayleigh-Darcy number. When increasing Ra_m the heat transfer is dominated by the convective mode in the entire annular space. The mass transfer remains dominated by a diffusive mode due to the high solutal diffusivity which is ten times higher than the thermal diffusivity for Le=0.1. With the increase of Ra_m the convection mode of the mass transfer rises in the upper space as consequence of the aiding effect of the thermal and the solutal buoyancies when the buoyancy ratio *N*=1.

References

[1] F.M. Mahfouz "Buoyancy driven flow within an inclined elliptic enclosure," International Journal of Thermal Sciences, 50 (2011), pp. 1887-1899

[2] N. Allouache, R. Bennacer, S. Chikh and A. Al Mers "Numerical Analysis of Heat and Mass Transfer in an Annular Porous Adsorber for Solar Cooling System" Defect and Diffusion Forum (2010), Vols. 297-301 pp.802-807.

[3] Edimilson J. Braga and Marcelo J.S. de Lemos "Simulation of turbulent natural convection in a porous cylindrical annulus using a macroscopic two-equation model," International Journal of Heat and Mass Transfer 49 (2006), pp. 4340–4351

[4] Leong, J.C. and Lai, F.C. "Natural convection in a concentric annulus with a porous sleeve," Int. J. Heat and Mass Transfer (2006), 49, pp. 3016-3027.

[5] J.P.B. Mota, I.A.A.C. Esteves, C.A.M. Portugal, J.M.S.S. Esperanca, E. Saatdjian "Natural convection heat transfer in horizontal eccentric elliptic annuli containing saturated porous media," Int. J. Heat and Mass Transfer (2000), 43, pp. 4367-4379.

[6] Patankar, S.V. (1980) "Numerical heat transfer and fluid flow," Hemisphere, Washington D.C.

Proceedings of the 24th UK Conference of the
Association for Computational Mechanics in Engineering
31 March – 01 April 2016, Cardiff University, Cardiff

A numerical model for simulating liquid flow in and around discrete concrete cracks (ACME 2016)

***Chuansan Ma[1], Tony Jefferson[1], Diane Gardner[1], Robert Lark[1]**

[1]School of Engineering, Cardiff University, Queens Buildings, Cardiff, CF24 3AA

*mac1@cardiff.ac.uk

ABSTRACT

A vascular self-healing system, which facilitates the storage, delivery, release, dissipation and curing of liquid self-healing agents, has been proved in the laboratory to be able to improve the durability of cementitious materials. To better understand the healing mechanisms associated with the system, and to optimise its design, a numerical model of the vascular system is proposed. In this study, the dissipation of the healing agent in and around discrete cracks after being released from the delivering flow network is simulated. This flow process comprises the flow of the liquid in the macro-crack space and the flow into the surrounding porous concrete matrix. The flow in the discrete crack is modelled by a modified Lucas-Washburn (L-W) equation, where an additional flow term Q has been introduced to take account of the mass being absorbed by the surrounding matrix. This flow term is determined by a 2D finite element continuum model of the surrounding matrix and is based on isothermal unsaturated flow theories. A mass balance equation is added to account for the interflow between the macro-crack and the matrix. This is achieved by treating the crack as an internal boundary within the matrix and computing the flow across this boundary. The simulation results suggest that imbibition has a significant influence on the flow in the macro-cracks and the degree of influence is related to the permeability as well as to the degree of saturation of the adjacent fracture process zone.

Keywords: *concrete, finite element model, moisture transportation, capillary movement, self-healing*

1. Introduction

Concrete structures are prone to cracking, and these cracks can lead to durability problems and increased maintenance costs. As a result, self-healing concrete has attracted much attention in recent years and has shown great potential to resolve some of these durability issues. Among the various existing self-healing techniques, the biomimetic vascular self-healing system is seen to be one of the most promising and versatile systems [1], and it has been applied to real structures at engineering scale [2]. It could also be easily combined with other self-healing techniques to form an integrated self-healing system [3]. Despite the huge efforts and vast advances in the development of vascular self-healing systems, there has been a lack of understanding, analysis, and simulation of the healing mechanisms and processes. This is, however, crucial to the further development of such systems. This study is to look at the crack filling process of the liquid self-healing agent after being released from the flow network in to the crack planes using a coupled numerical model.

Past experiments and previous literature have suggested that the movement of liquid in concrete cracks is primarily driven by capillary pressure [4,5]. This capillary flow in the crack comprises two distinct flow processes, i.e. the capillary flow in the macro-crack; and imbibition into the surrounding matrix. The flow in the macro-crack has been historically simulated by the modified Lucas Washburn (L-W) equation, which accounts for various factors such as dynamic contact angle and stick slip etc. [4]. However, the influence of the fluid absorbed (or expelled) from the adjacent porous matrix has not previously been included in the equation. For a typical self-healing flow problem, the influence of the matrix flow on the 'discrete' fluid flow in the macro-crack could be particularly important because the matrix around the macro-scale cracks has much higher permeability and porosity due to the developed fracture process zone.

In this study, the combined effect of these two flow processes is modelled by coupling the modified L-W equation with a finite element isothermal flow model of the surrounding matrix. The coupling is realised by adding a mass balance equation for the interflow between the discrete crack and the matrix through the crack faces. This is achieved by treating the crack as an internal boundary within the matrix and computing the flow across this boundary. The individual models for the crack and matrix flow, as well as the coupled flow model, were firstly calibrated and then validated using a range of experimental data. This paper describes a new way of coupling the 2D FE unsaturated flow model with the LW capillary flow equation, so that a better understanding of the movement of liquid healing agents in cementitious cracks can be achieved. The modelling scheme of a specific boundary condition is presented here, i.e. the liquid is freely available at the crack mouth and is not constrained by the delivery system.

2. The coupled model

The capillary flow in the discrete crack is described by a modified Lucas-Washburn Equation as shown in equation (1):

$$\mathrm{p_{c0}}(\mathrm{z})(1-\beta_\mathrm{s})-\frac{2\beta_\mathrm{m}\dot{\mathrm{z}}}{\mathrm{b(z)}}+\rho\mathrm{gz}\sin(\phi)-\int_0^{\mathrm{z}}\frac{\bar{\mathrm{v}}(\mathrm{x})}{\frac{\mathrm{k(x)}}{\mu}+\frac{\beta_\mathrm{w}\mathrm{b(x)}}{2}}\mathrm{dx}=0 \tag{1}$$

where $\mathrm{p_{c0}}$ is the surface tension at the meniscus; b(x) is the crack width for a planar water channel; z is the present rise height of the meniscus and ż is the velocity of the meniscus; μ is the viscosity of the flow agent and k(x) is the effective permeability term that accounts for the shape of the flow cross-section and may vary along the profile of the flow channel. A model that includes factors to account for stick-slip (β_s), friction dissipation at meniscus (β_m), and wall slip (β_w) has been proved to achieve better agreement with experiment results [4] than a model based on the standard L-W equation. Assuming a general expression for imbibition (flow) $q(x')$ along the crack faces. Based on the mass conservation law, the relationship between the moving velocity of the meniscus and the velocity at any point within the flow section is expressed in equation (2).

$$\bar{\mathrm{v}}(z)A(z)=\bar{\mathrm{v}}(x)A(x)-\int_x^z q(x')dx' \tag{2}$$

Substituting equation (2) into equation (1) and rearranging leads to the modified governing equation of the crack flow, which is as follows:

$$p_{c0}(z)(1-\beta_s)-\frac{2\beta_m\dot{z}}{b(z)}-\rho gz\sin(\phi)-\int_0^z\frac{\bar{v}(x)}{\frac{k(x)}{\mu}+\frac{\beta_w b(x)}{2}}dx-Q=0 \tag{3}$$

where:

$$Q=\int_0^z\frac{\left(\int_x^z q(x')\,dx'\right)}{A(x)\left(\frac{k(x)}{\mu}+\frac{\beta_w b(x)}{2}\right)}dx \tag{4}$$

The resulted additional double integration term Q accounts for the influence of the total imbibition. It may be seen that this height reduction term is an integral function of the flow field at the crack faces, which is then solved using an isothermal-hygral finite element model of the imbibition in the porous matrix continuum.

The governing equation for this microscopic flow is based on the mass balance equation of the water content in the domain [6, 7], as shown in equation 1.

$$\dot{\overline{\rho_v}}+\dot{\overline{\rho_l}}+\nabla\boldsymbol{q_v}+\nabla\boldsymbol{q_l}+\dot{\overline{\rho_{vl}}}+\dot{\overline{\rho_{lv}}}=0 \tag{5}$$

where $\dot{\overline{\rho_\mathrm{v}}}$ and $\dot{\overline{\rho_\mathrm{l}}}$ are the time differentiation of vapour mass and water mass in the domain; $\nabla\mathbf{q_v}$ and $\nabla\mathbf{q_l}$ are the mass flux of vapour and water out of the domain; because the mass balance equation of water content includes both liquid and vapour water, the phase change between the liquid water and

water vapour $\dot{\overline{\rho_{vl}}}$ and $\dot{\overline{\rho_{lv}}}$ may be cancelled. The movement of the water content is driven separately by the capillary pressure gradient and vapour concentration gradient. Darcy's law and Fick's law are used to determine the flow term due to capillary pressure and vapour diffusion respectively. Different flow properties have been applied to elements at different locations to account for the larger permeability in micro-cracked zones and surface zones. Capillary pressure p_c is the primary variable for the model and the van Genuchten equation is used to establish the relationship between saturation degree and capillary pressure. The relative permeability and vapour diffusion coefficient are functions of the water content; therefore the problem is nonlinear. Newton-Raphson iteration is adopted for solving the resulting nonlinear equations and the element averaged capillary pressure and the flow properties are updated within each iteration for a new cycle of calculation until the p_c converges for this time step.

A Dirichlet type of boundary condition is applied in the problem, prescribing a constant capillary pressure value which is equivalent to a constant saturated surface in contact of water. The oscillation of results near the sharp front has been eliminated by using mass lumped scheme for the formulation of mass matrix. The flux though the saturated nodes could then be calculated by substituting the known capillary pressure field into the left hand side of the finite element formulation. These resulting flux values are the equivalent nodal flux per unit width in $gs^{-1}m^{-1}$, which are then transformed into the equivalent distributed flux over the wetted surface in $gs^{-1}m^{-2}$ through the following operation:

$$\mathbf{f} = \mathbf{F} \cdot \mathrm{N}^{-1} \tag{6}$$

The flow rate profile over the saturated boundary is then obtained by susing equation (7):

$$q(x) = \begin{cases} f_j + (x - h_j)\frac{f_{j+1} - f_j}{he}; & x \in (h_j, h_{j+1}) \\ f_n + (x - h_j)\frac{f_{z_{i-1}} - f_n}{he}; & x \in (h_n, z_{i-1}) \end{cases} \quad j=1,2,\ldots,n-1 \tag{7}$$

where n is the total number of saturated nodes on one side the crack profile, f_j is the flux value at the j^{th} saturated node, and h_j is the elevation of the j^{th} saturated node. Equation (7) enables the construction of a continuous function for the flow rate profile over the wetted surface under the meniscus. This function is then used directly for the calculation of Q in equation (4) for the current time step.

3. Results and experimental validation

The finite element model for the imbibition in porous concrete matrix is validated by a series of experiments where both the mass of water being absorbed by the concrete as well the internal relative humidity level are monitored. The validated parameters are then used in the coupled flow model.

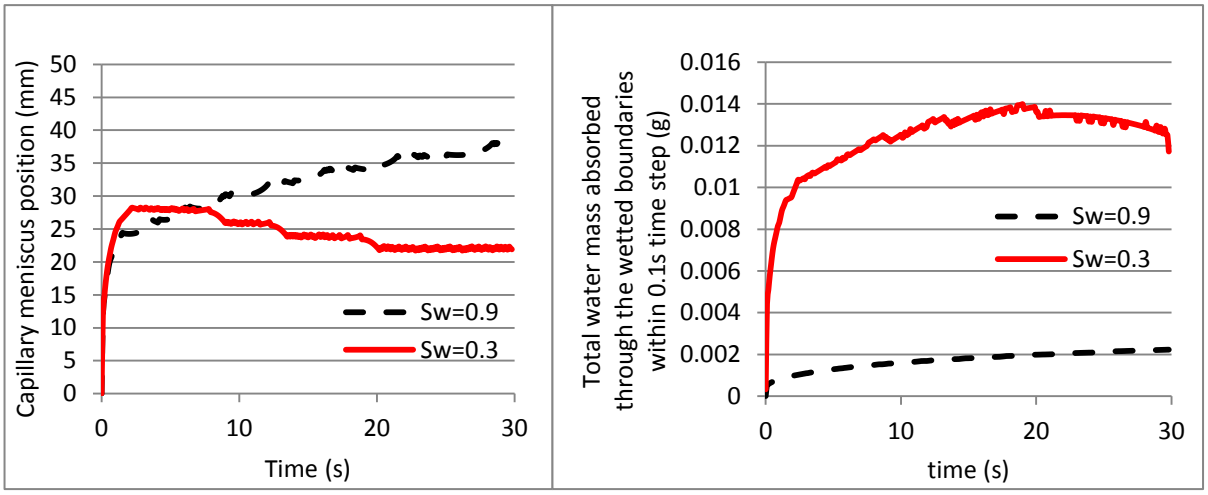

Fig
mo

Figure 1: Comparison of the capillary flow in a 0.05mm crack with different moisture condition in surrounding concrete matrix, with (a) Capillary rise height and (b) Total mass of water absorbed through crack faces.

no dramatic difference, the drier concrete with Sw=0.3 absorbs much more water and reduces the development of the capillary rise. The case with Sw=0.9 absorbs much less water and therefore has less influence on the capillary rise. It is also observed that the magnitude of the influence of the imbibition is also related to the crack width. The flow in wider cracks is less affected by the imbibition flow compared with narrower cracks.

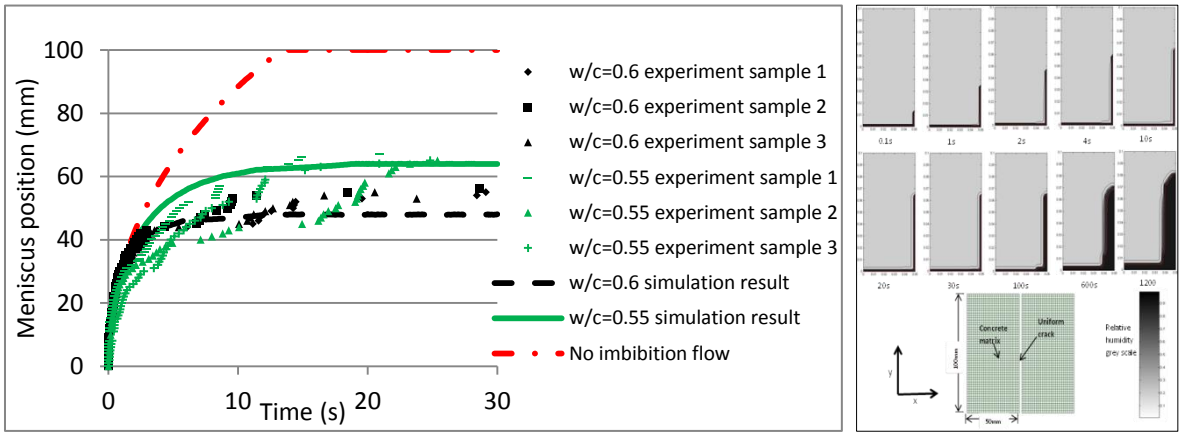

Figure 2: (a) Comparison between experiments and simulation for different concrete mix with 0.05mm crack width. (b) Contour plot of the moisture condition in one side of the concrete matrix during the capillary rise process

Experiments were carried out where the capillary rise in a discrete crack was recorded by a high speed camera. Figure 2 (a) shows that the coupled model is able to capture the capillary rise difference caused by the different permeabilities of different concrete mixes. Compared with the traditional L-W equation where no imbibition is considered, the couple model has shown more accurate simulation of the flow in the macro-crack. Figure 2(b) illustrates the development of the moisture conditions in the surrounding matrix, which has great implications on the design of vascular system to facilitate different self-healing techniques.

Acknowledgements

Financial support from EPSRC project Materials for Life (M4L) for this study is gratefully acknowledged by the author.

References

[1] Van Tittelboom, K., Adesanya, K., Dubruel, P., Van Puyvelde, P., De Belie, N. Methyl methacrylate as a healing agent for self-healing cementitious materials. Smart Materiales and Structures, 2011. 20

[2] Dry, C.M., "Repair of Highway Bridges by Internal Time-Release of Repair Chemicals," Proceedings of Engineering Mechanics: A Force for the 21st Century, La Jolla, California, May 17-20, 1998

[3] Kuang, Y., Ou, J., 2008. Passive smart self-repairing concrete beams by using shape memory alloy wires and fibers containing adhesives. J. Cent. South Univ. Technol. 15, 411–417.

[4] Gardner, D., A. Jefferson, and A. Hoffman, *Investigation of capillary flow in discrete cracks in cementitious materials.* Cement and Concrete Research, 2012. **42**(7): p. 972-981.

[5] Snoeck, D., Steuperaert, S., Van Tittelboom, K., Dubruel, P., De Belie, N. Visualization of water penetration in cementitious materials with superabsorbent polymers by means of neutron radiography.

[6] Schrefler, B.A., Mechanics and thermodynamics of saturated/unsaturated porous materials and quantitative solutions. 2002. 55(4): p. 351-388.

[7] Gawin, D., C. Majorana, and B. Schrefler, Numerical analysis of hygro-thermal behaviour and damage of concrete at high temperature. Mechanics of Cohesive-Frictional Materials, 1999. 4(1): p. 37-74.

Solids and Structures III

Proceedings of the 24th UK Conference of the
Association for Computational Mechanics in Engineering
31 March - 01 April 2016, Cardiff University, Cardiff

Evaluation of the Tangent Stiffness Matrix for Hyperelastic Fibres using Automatic Differentiation

***Euan Muir[1], Chris Pearce[1] and Lukasz Kaczmarczyk[1]**

[1] School of Engineering, University of Glasgow, G12 8QQ

*e.muir.1@research.gla.ac.uk

ABSTRACT

The numerical modelling of fibres undergoing finite deformations requires the implementation of a constitutive law and the solution of the governing PDE requires an accurate linearisation of the nonlinear response. In order to ensure a computationally efficient implementation and to simplify the implementation, automatic differentiation has been utilised.

Key Words: *finite element method; automatic differentiation; hyperelasticity; fibres*

1. Introduction

Fibres are present in many materials and serve to enhance the material performance in particular directions. In natural materials, this directional dependency is a result of optimisation whereby the increased strength and stiffness is only where it is needed. Synthetic materials such as fibre reinforced polymers (FRP) have been designed to deliberately exploit this benefit. This paper focuses on fibres in soft tissue but also has broader applicability. The implementation of a nonlinear material response in the finite element method requires linearisation of the constitutive relationship . This paper will describe this process for a hyperelastic fibre model subject to finite deformations using automatic differentiation.

2. Tangent Stiffness Matrix

The nonlinear system of equations are expressed simply as:

$$\mathbf{r}(x) = \mathbf{f}_{\text{ext}}(\mathbf{x}) - \mathbf{f}_{\text{int}}(\mathbf{x}) = \mathbf{0} \tag{1}$$

This is solved using a Newton-Raphson scheme. Equation 1 is expressed as a truncated Taylor series expansion, whereby the residual $\mathbf{r}$ at the next iteration is expressed as:

$$\mathbf{r}_{i+1} = \mathbf{r}_i + \frac{\partial \mathbf{r}_i}{\partial \mathbf{x}} d\mathbf{x} \tag{2}$$

where

$$\frac{\partial \mathbf{r}_i}{\partial \mathbf{x}} = -\frac{\partial \mathbf{f}_{\text{int}}(\mathbf{x})}{\partial \mathbf{x}} = -\mathbf{K}_t = -\int_V \boldsymbol{B}^T \frac{\partial \boldsymbol{P}}{\partial \boldsymbol{F}} \mathbf{B} \, dV \tag{3}$$

The derivative $\dfrac{\partial \boldsymbol{P}}{\partial \boldsymbol{F}}$ is the elasticity tensor $\mathbb{C}$, the computation of which is non-trivial. In this paper we demonstrate how to compute it using automatic differentiation.

3. Constitutive Models

Soft tissues are composed of an extracelluar matrix (ECM) with collagen fibres. The ECM is represented as a neo-Hookean material [1] and the fibres from the Eberlein model [2], both being hyperelastic materials. The two material models are combined in Equation 4. Equation 5 and Equation 7 are the strain energy functions (Ψ) for the neo-Hookean and fibre materials respectively and their corresponding Second-Piola Kirchoff stress ($\boldsymbol{S}$) are in Equation 6 and Equation 9.

$$\Psi = \Psi_n + \Psi_f \tag{4}$$

$$\Psi_n = \frac{\mu}{2}(I_C - 3) - \mu \ln J + \frac{\lambda}{2}(\ln J)^2 \tag{5}$$

where $\boldsymbol{F}$ is the gradient of deformation, J is the volumetric change, $\boldsymbol{C}$ is the right Cauchy-Green deformation tensor, $J = \det(\boldsymbol{F})$, $I_C = \operatorname{tr} \boldsymbol{C}$, and λ and μ are the Lamé coeficients.

$$\boldsymbol{S}_n = \mu(\boldsymbol{I} - \boldsymbol{C}^{-1}) + \lambda(\ln J)\boldsymbol{C}^{-1} \tag{6}$$

$$\Psi_f = \sum_{\alpha=1}^{2} \frac{k_1}{2k_2}\{[\exp[k_2(\bar{I}_\alpha^* - 1)^2] - 1]\} \tag{7}$$

$$\bar{I}_\alpha^* = \bar{\boldsymbol{C}} : \boldsymbol{A}_\alpha, \quad \alpha = 1, 2, \qquad \bar{\boldsymbol{C}} = J^{-2/3}\boldsymbol{C}, \qquad \boldsymbol{A}_\alpha = \boldsymbol{a}_\alpha \otimes \boldsymbol{a}_\alpha, \qquad \mathbb{P} = \boldsymbol{I} - \frac{1}{3}\boldsymbol{C}^{-1} \otimes \boldsymbol{C} \tag{8}$$

$$\boldsymbol{S}_f = J^{-2/3}\mathbb{P} : \hat{\boldsymbol{S}}_f \tag{9}$$

$$\hat{\boldsymbol{S}}_f = \sum_{\alpha=1}^{2} 2k_1\{\exp[k_2(\bar{I}_\alpha^* - 1)^2](\bar{I}_\alpha^* - 1)\boldsymbol{A}_\alpha\} \tag{10}$$

4. Elasticity Tensor

The constitutive equations are expressed in terms of the Second-Piola Kirchoff stress **S**; this can be pushed forward to obtain the First-Piola Kirchoff stress $\mathbf{P} = \mathbf{FS}$. Thus, the elasticity tensor can be calculated from $\dfrac{\partial \boldsymbol{P}}{\partial \boldsymbol{F}}$. To illustrate that this derivative is not trivial to obtain, the elasticity tensor for the fibre model is shown here: Equation 11 to Equation 13 [2].

$$\mathbb{C}_f = 2\frac{\partial \boldsymbol{S}_F}{\partial \boldsymbol{C}} = \mathbb{P} : \hat{\mathbb{C}}_f : \mathbb{P}^T + \frac{2}{3}\operatorname{tr}(J^{-2/3}\hat{\boldsymbol{S}}_f)\tilde{\mathbb{P}} - \frac{2}{3}(\boldsymbol{C}^{-1} \otimes \hat{\boldsymbol{S}}_f + \hat{\boldsymbol{S}}_f \otimes \boldsymbol{C}^{-1}), \tag{11}$$

$$\hat{\mathbb{C}}_f = 2J^{-4/3}\frac{\partial \hat{\boldsymbol{S}}_f}{\partial \hat{\boldsymbol{C}}} = \sum_{\alpha=1}^{2} \delta_\alpha \boldsymbol{A} \otimes \boldsymbol{A}, \tag{12}$$

$$\delta_\alpha = 4J^{-4/3}k_1[2k_2(\bar{I}_\alpha^* - 1)^2 + 1]\exp[k_2(\bar{I}_\alpha^* - 1)^2], \quad \alpha = 1, 2 \tag{13}$$

Alternatively, automatic differentiation can be used to calculate the elasticity tensor, thereby removing the need for it to be undertaken explicitly. In automatic differentiation the derivatives of a function can be evaluated numerically through the recursive application of the chain rule, exploiting the ability to express the function as basic arithmetic operators and functions.

5. Automatic Differentiation by OverLoading in C++ (ADOL-C)

ADOL-C is a open-source C++ library that applies the principles of automatic differentiation [3]. The independent variables subject to differentiation are defined using a special type *adouble* and all variables which depend on the independent variable must also be defined using this type. Constants are considered passive and can be defined using standard types such as *double*. The function description needs to be recorded to a tape for the differentiation process and so requires active sections to be set by `trace_on` and `trace_off`. To illustrate the process a piece of pseudo code is shown in Algorithm 1 that calculates the elasticity tensor for the Eberlein fibre model.

Algorithm 1 ADOL-C Fibres Constitutive Model

1: $double\ k_1, k_2$ ▷ passive variables
2: $adouble\ F, \bar{\boldsymbol{C}}, J, \boldsymbol{A}_\alpha, \boldsymbol{V}_{f1}, \boldsymbol{V}_{f2}$ ▷ active variables
3:
4: $double\ x$ = values
5: $double\ V_{f1i}, V_{f2i}$ = values ▷ local fibres direction
6:
7: TAPE(ON)
8: $\boldsymbol{F}$ <<= x ▷ independent variables
9: $\boldsymbol{V_{f1}}$ <<= V_{f1i} ▷ independent variables
10: $\boldsymbol{V_{f2}}$ <<= V_{f2i} ▷ independent variables
11:
12: calculate: $\boldsymbol{C}, J, \bar{\boldsymbol{C}}, \boldsymbol{A_\alpha}, \bar{I}_\alpha$
13: $\boldsymbol{S}$ = fibresFunction($\boldsymbol{C}, J, \bar{\boldsymbol{C}}, \boldsymbol{A_\alpha}, \bar{I}_\alpha$)
14:
15: $\boldsymbol{P} = \boldsymbol{FS}$
16: TAPE(OFF)
17:
18: $Jacobian(\boldsymbol{P}, \boldsymbol{F}, [x, V_{f1i}, V_{f2i}])$ ▷ $\dfrac{\partial \boldsymbol{P}}{\partial \boldsymbol{F}}$

6. FE Implementation Example

ADOL-C is integrated into our open source finite element software package MoFEM [4]. To demonstrate ADOL-C working it was used in the calculation of the elasticity tensor for the combined Eberlein Fibre and neo-Hookean material models; the fibre directions applied were not constant and so were considered active variables by ADOL-C. The physical problem was an uni-axially loaded cylinder with fibres wrapped around the circumference and the length as shown in Figure 1a. To demonstrate the influence of the fibres the analysis was repeated with no fibres, also shown in Figure 1b.

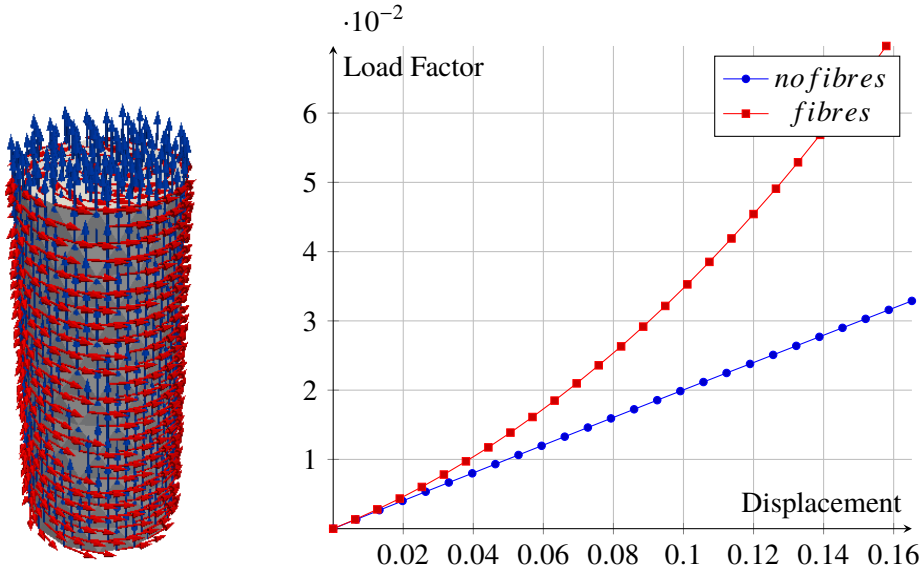

(a) Mesh and Fibres

(b) Load Displacement Graph

Figure 1: Uni-axial Load

7. Conclusion

Calculating the elasticity tensor to form the tangent stiffness matrix from the constitutive equations, can be a very involved process. The use of automatic differentiation can remove this step and thereby speeds up the implementation of constitutive models and removes errors.

References

[1] Bonet, J., Wood, R. Nonlinear Continuum Mechanics for Finite Element Analysis. Second. Cambridge Books Online. Cambridge University Press. ISBN: 9780511755446. 2008.

[2] Eberlein, R., Holzapfel, G., Schulze-Bauer, C. An Anisotropic Model for Annulus Tissue and Enhanced Finite Element Analyses of Intact Lumbar Disc Bodies. In: Computer Methods in Biomechanics and Biomedical Engineering 4.3, pp. 209-299, 2001.

[3] Walther, A., Griewank, A: Getting started with ADOL-C. In U. Naumann und O. Schenk, Combinatorial Scientific Computing, Chapman-Hall CRC Computational Science, pp. 181-202, 2012.

[4] MoFEM, Mesh Orientated Finite Element Method http://bitbucket.org/likask/mofem-joseph

Proceedings of the 24th UK Conference of the
Association for Computational Mechanics in Engineering
31 March - 01 April 2016, Cardiff University, Cardiff

BENDING AND BUCKLING ANALYSIS OF FUNCTIONALLY GRADED MICROPLATES USING ISOGEOMETRIC APPROACH

Hoang X. Nguyen[1], *Thuc P. Vo[1] and *Hung Nguyen-Xuan[2]

[1]Department of Mechanical and Construction Engineering, Northumbria University, Newcastle Upon Tyne NE1 8ST, United Kingdom
[2]Center for Interdisciplinary Research in Technology (CIRTech), Ho Chi Minh City University of Technology (HUTECH), Ho Chi Minh City 70000, Vietnam

*thuc.vo@northumbria.ac.uk, ngx.hung@hutech.edu.vn

ABSTRACT

This study aims at investigating size-dependent effects of functionally graded (FG) microplates for bending and buckling problems using isogeometric analysis (IGA). While displacement field of the microplates is established based on the refined plate theory (RPT) with four variables, the modified couple stress (MCS) theory is employed to capture small scale effects of the microplates. Bending and buckling analysis of rectangular and circular FG microplates based on these two theories are solved in the platform of isogeometric analysis. This recently developed method utilises the non-uniform rational B-splines (NURBS) functions to establish approximation functions and describe geometry domains. In addition, NURBS functions, by its nature, could satisfy high-order continuity which is required in RPT theory without any difficulty. A number of numerical examples conducting for rectangular and circular FG microplates reveal that the consideration of small scale effects is followed by the increase in plates' stiffness. Consequently, transverse deflection and buckling load of the FG microplates will be decreased and risen, respectively.

Key Words: *FG microplates; modified couple stress theory; refined plate theory; isogeometric analysis; bending and buckling analysis*

1. Introduction

Functionally graded materials (FGMs) are composite materials formed of two or more constituent phases in which material properties vary smoothly from one surface to the other. With the rapid development of technology, FGMs have been increasingly used in micro electromechanical systems (MEMS/NEMS), electrically-actuated MEMS devices, atomic force microscopes, etc. Mechanical properties of such small-scale structural devices including Young's modulus, flexural rigidity are size-dependent [6]. However, classical continuum elasticity which is scale-free theory fails to predict these size effects. Modified couple stress theory (MCST) [4, 6] appears to be one of the size-dependent theories in which only one material length scale parameter is employed. Based on the MCST, a couple of research works using various plate models have been carried out to investigate the size-dependent effects of micro FG plates, one of them is to use refined plate theory (RPT) [1]. However, RPT requires C^1-continuity of general displacements causing significant challenge to derive second derivative of deflection in the platform of finite element analysis (FEA) where C^0 elements are frequently used. Recently, a new numerical method so-called Isogeometric Analysis (IGA) which is able to deal with C^1-continuity problem without using any additional variables has been introduced by Hughes and his co-workers [2]. This method bridges the gap between Computer Aided Design (CAD) and FEA in which same basis functions generated by B-splines or non-uniform rational B-splines (NURBS) shape functions are employed to describe exact geometry and unknown variables. Since modelled geometry is exact and the number of unknown terms is not increased, it is expected that IGA would yield

more accurate results with lower computational cost for RPT problems in the comparison with regular FEA [3].

In this study, the size-dependent bending and buckling behaviours of FG microplates will be investigated. While the size effects are captured using the modified couple stress theory, the four-variable refined plate theory is employed to describe displacement field. The problems are solved in the platform of the isogeometric analysis.

2. Theoretical formulation of FG microplates

Assuming that the functionally graded microplates are made of metal and ceramic varying continuously through the plates' thickness, the effective material properties of the plates are obtain following the rule of mixture or Mori-Tanaka scheme. Detail of those expressions could be found from some research in the literature [3].

According to the modified couple stress theory, the strain energy is defined as a combination of strain tensor and curvature tensor [1]. The components of the deviatoric part of the symmetric couple stress tensor m_{ij} and symmetric curvature tensor χ_{ij} are given by

$$m_{ij} = 2Gl^2\chi_{ij}; \quad \chi_{ij} = \frac{1}{2}\left(\frac{\partial\theta_i}{\partial\chi_j} + \frac{\partial\theta_j}{\partial\chi_i}\right) \tag{1}$$

where G and l are shear modulus and material length scale parameter, respectively, and the rotation vector $\boldsymbol{\theta} = \frac{1}{2}curl(\mathbf{u})$ where $\mathbf{u}$ is the displacement vector.

In order to take into account the shear deformation effects, the plate displacement field is presented with respect to the refined plate theory as

$$u(x,y,z) = u_0(x,y) - zw_{b,x}(x,y) + g(z)\,w_{s,x}(x,y) \tag{2a}$$

$$v(x,y,z) = v_0(x,y) - zw_{b,y}(x,y) + g(z)\,w_{s,y}(x,y); \quad w(x,y,z) = w_b(x,y) + w_s(x,y) \tag{2b}$$

where u_0, v_0 are membrane displacements, w_b and w_s represent bending and shear components of transverse displacement, $g(z)$ is the distribution function which is taken as $g(z) = -4z^3/(3h^2)$ [5]. The rotation vector and curvature vector are obtained by substituting the above displacement expressions into Equation 1 [1].

3. NURBS-based formulation of FG microplates

By using the NURBS basis functions, the displacement field $\boldsymbol{u}$ of the FG microplates based on the RPT and MCST could be approximated as follow [2, 3]

$$\mathbf{u}^h(\xi,\eta) = \sum_{A}^{m\times n} R_A(\xi,\eta)\mathbf{q}_A \tag{3}$$

where $m \times n$ is the number of basis functions, R_A represents two-dimensional NURBS basis functions and $\mathbf{q}_A$ denotes the vector of degrees of freedom associated with the control point A. The isogeometric finite element formulation of the bending and buckling problems are defined as

$$\mathbf{Kq} = \mathbf{F}; \quad (\mathbf{K} - \lambda_{cr}\mathbf{K}_g)\,\mathbf{q} = \mathbf{0} \tag{4}$$

where λ_{cr} presents buckling parameter, and $\mathbf{F}$ and $\mathbf{K}_g$ are load vector and geometric stiffness matrix, respectively [3]. The global stiffness matrix $\mathbf{K}$ of the structures is a summation of two components corresponding to the classical term $\mathbf{K}_1$ and couple stress term $\mathbf{K}_2$. The full expression of classical term $\mathbf{K}_1$ in the global stiffness matrix could be found in the work of Nguyen *et al.* [3] while the couple stress counterpart is defined as

$$\mathbf{K}_2 = \int_\Omega \left[\begin{Bmatrix} \mathbf{B}^{b0}_{mA} \\ \mathbf{B}^{b1}_{mA} \end{Bmatrix}^T \begin{bmatrix} \mathbf{X}^c & \mathbf{Y}^c \\ \mathbf{Y}^c & \mathbf{Z}^c \end{bmatrix} \begin{Bmatrix} \mathbf{B}^{b0}_{mA} \\ \mathbf{B}^{b1}_{mA} \end{Bmatrix} + \begin{Bmatrix} \mathbf{B}^{s0}_{mA} \\ \mathbf{B}^{s2}_{mA} \end{Bmatrix}^T \begin{bmatrix} \mathbf{A}^c & \mathbf{B}^c \\ \mathbf{B}^c & \mathbf{D}^c \end{bmatrix} \begin{Bmatrix} \mathbf{B}^{s0}_{mA} \\ \mathbf{B}^{s2}_{mA} \end{Bmatrix} \right] d\Omega \tag{5}$$

where

$$\mathbf{B}_{mA}^{b0}=\frac{1}{4}\begin{bmatrix}0&0&4R_{A,xy}&2R_{A,xy}\\0&0&-4R_{A,xy}&-2R_{A,xy}\\0&0&2\left(-R_{A,xx}+R_{A,yy}\right)&-R_{A,xx}+R_{A,yy}\end{bmatrix},\quad \mathbf{B}_{mA}^{b1}=\frac{1}{4}\begin{bmatrix}0&0&0&-2R_{A,xy}\\0&0&0&2R_{A,xy}\\0&0&0&R_{A,xx}-R_{A,yy}\end{bmatrix} \tag{6a}$$

$$\mathbf{B}_{mA}^{s0}=\frac{1}{4}\begin{bmatrix}-R_{A,xy}&R_{A,xx}&0&0\\-R_{A,yy}&R_{A,xy}&0&0\end{bmatrix},\quad \mathbf{B}_{mA}^{s2}=\frac{1}{4}\begin{bmatrix}0&0&0&-R_{A,y}\\0&0&0&R_{A,x}\end{bmatrix} \tag{6b}$$

and material matrices are given by

$$\left(A_{ij}^{c},B_{ij}^{c},D_{ij}^{c}\right)=\int_{-h/2}^{h/2}\left(1,g'\left(z\right),\left[g'\left(z\right)\right]^{2}\right)G_{ij}dz;\left(X_{ij}^{c},Y_{ij}^{c},Z_{ij}^{c}\right)=\int_{-h/2}^{h/2}\left(1,g''\left(z\right),\left[g''\left(z\right)\right]^{2}\right)G_{ij}dz \tag{7}$$

4. Numerical examples

In this section, the bending and buckling analysis of the FG microplates will be conducted based on the RPT, modified couple stress, and the proposed IGA approach. While the square plates are used to investigate the bending behaviours, buckling analysis is conducted by considering circular ones. The Al/Al_2O_3 is chosen to be the metal-ceramic FG material whose properties are of $E_m = 70$ GPa, $E_c = 380$ GPa, $\rho_m = 2707$ kg/m^3, $\rho_c = 3800$ kg/m^3, and $\nu_m = \nu_c = 0.3$. For bending analysis, the fully simply-supported (SSSS) microplates subjected to sinusoidally

Table 1: Non-dimensional central deflection $\bar{w}$ and critical buckling load $\bar{P_{cr}}$ of Al/Al_2O_3 microplates

l/h	$\bar{w}$, square plates			$\bar{P_{cr}}$, circular plates		
	a/h	Present	Ref. [5]	h/R	Simple BC	Clamp BC
0	5	0.6688	0.6688	0.1	11.8496	38.3789
	100	0.5625	0.5625	0.2	11.4869	34.8238
0.2	5	0.5505	0.5468	0.1	12.2075	44.2232
	100	0.4689	0.4689	0.2	11.8392	40.3906
0.6	5	0.2288	0.2224	0.1	13.4377	90.9639
	100	0.2012	0.2011	0.2	12.9976	84.8716
1	5	0.1060	0.1017	0.1	14.1319	184.4163
	100	0.0939	0.0939	0.2	13.7383	173.7056

distributed load are analysed considering the aspect ratio a/h, material length scale ratio l/h, and material index $n = 1$. In order to verify the availability of the proposed theories and approach, the results are compared to analytical solutions reported by Thai and Kim [5]. As can be seen in the Table 1 showing the non-dimensional central deflection $\bar{w} = 10wE_ch^3/(q_0L^4)$, the present results, in general, are in good agreement with those of the previous authors [5]. For thick plates ($a/h = 5$), the solutions from both approaches which are very close to each other for $l/h = 0$ but they are discrepancy as l/h and n become larger. However, these discrepancies vanish as the thin plates become thinner, i.e. $a/h = 100$. It could also be observed that, for all cases, the increase in material length scale ratio l/h which rises the plate stiffness leads to the decrease of central deflection.

With regard to buckling analysis, non-dimensional biaxial critical buckling which is defined as $\bar{P_{cr}} = 12(1-\nu_m^2)P_{cr}R^2/(E_mh^3)$ of the Al/Al_2O_3 circular microplates for simple support and clamped boundary conditions are tabulated in Table 1. Similar to the case of bending analysis, due to the increase in the plates' stiffness, the critical buckling load grows up as the material parameter length scale l/h rises. Corresponding to $h/R = 0.2, l/h = 0.4$, and $n = 1$, the first

two buckling mode shapes along with their buckling load values of the clamped microplates are depicted in the Figure 1. The mode shapes are all scaled up for the illustration purposes.

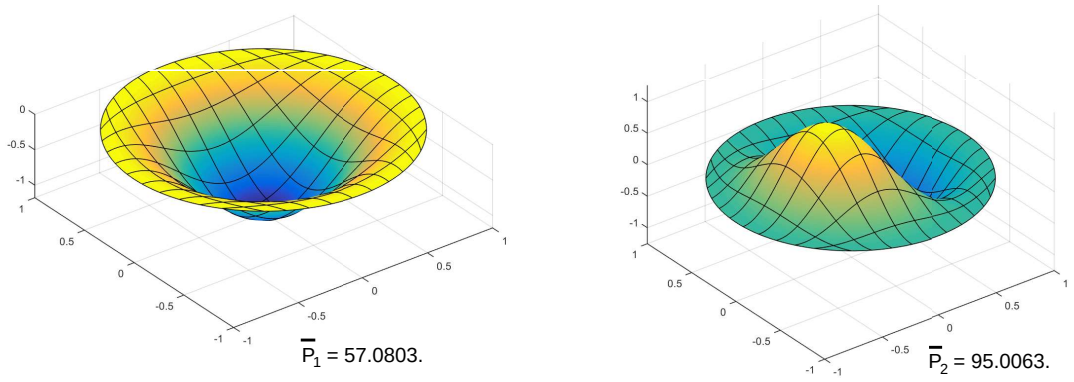

Figure 1: First two buckling mode shapes of clamped plates.

5. Concluding remarks

The size-dependent bending and buckling behaviours of the functionally graded microplates have been investigated. The size effects are considered by the modified couple stress theory. The four-variable refine plate theory is employed to describe the displacement field of the plates. The formulation of the square and circular microplates using the chosen theories which require C^1-continuity and exact geometry are then successfully integrated and solved in the platform of isogeometric analysis. The numerical results which are in good agreement with those exist in the literature reveal that the size-dependent investigation using modified couple stress theory result in an increase in the plates' stiffness. Consequently, the deflection and buckling load of the microplates decrease and increase, respectively.

Acknowledgements

The authors gratefully acknowledge research support fund from the Researcher Development Framework at Northumbria University.

References

[1] L. He, J. Lou, E. Zhang, Y. Wang, and Y. Bai. A size-dependent four variable refined plate model for functionally graded microplates based on modified couple stress theory. *Composite Structures*, 130, 107–115, 2015.

[2] T. J. R. Hughes, J. A. Cottrell, and Y. Bazilevs. Isogeometric analysis: CAD, finite elements, NURBS, exact geometry and mesh refinement. *Computer Methods in Applied Mechanics and Engineering*, 194, 4135–4195, 2005.

[3] H. Nguyen-Xuan, L. V. Tran, C. H. Thai, S. Kulasegaram, and S. P. A. Bordas. Isogeometric analysis of functionally graded plates using a refined plate theory. *Composites Part B: Engineering*, 64, 222–234, 2014.

[4] J. S. Stolken and A. G. Evans. A microbend test method for measuring the plasticity length scale. *Acta Materialia*, 46, 5109–5115, 1998.

[5] H.-T. Thai and S.-E. Kim. A size-dependent functionally graded Reddy plate model based on a modified couple stress theory. *Composites Part B: Engineering*, 45, 1636–1645, 2013.

[6] F. Yang, A. C. M. Chong, D. C. C. Lam, and P. Tong. Couple stress based strain gradient theory for elasticity. *International Journal of Solids and Structures*, 39, 2731–2743, 2002.

Proceedings of the 24th UK Conference of the
Association for Computational Mechanics in Engineering
31 March - 01 April 2016, Cardiff University, Cardiff

Guaranteed error bounds for the homogenisation of random materials

***D.A. Paladim[1], J.P.M. de Almeida[2], S.P.A. Bordas[1,3] and P. Kerfriden[1]**

[1] School of Engineering, Cardiff University, The Parade 14-17, Cardiff, CF24 3AA
[2] Instituto Superior Técnico, University of Lisbon, Av. Rovisco Pais 1, 1049-001 Lisboa, Portugal
[3] Faculté des Sciences, de la Technologies et de la Communication, Université du Luxembourg, Luxembourg, 1359

*alvesPaladimD@cardiff.ac.uk

ABSTRACT

The present paper aims to quantify the error due to homogenisation of highly heterogeneous diffusion fields in the solution of linear elliptic PDEs which are common in the modelling of packed particulate composites. This work takes as starting point the pioneering work Oden and Zohdi (1997) and extends it to bound the error in the expectation and second moment of quantities of interest without solving the intractable stochastic fine-scale problem. All the computations involved are deterministic, macroscopic and indepedent of the scale ratio. In the present work, the guaranteed error bounds are re-derived using the Prager-Synge hypercircle theorem. This enabled us to optimise and fully characterise the effectivity of the presented estimates. We also interpret our results in terms of the Reuss and Voigt approaches for the homogenisation of composites. Finally, an efficient procedure is presented to tighten the estimates through the local approximation of the fine-scale model.

Key Words: *error estimation; model error; homogenisation*

1. Overview

Composites play an increasing role in modern mechanical systems. This raises tremendous challenges for computational mechanics. Indeed, the direct modelling of such systems results in intractable problems due to the fast spatial variations of material properties. The analysis of realistic composite systems requires an additional modelling step, whereby the microscopic constituents are substituted by a single material in such a way that this resulting model captures the global behaviour of the system. This process is known as homogenisation (see for example [1, 2]). However, most composite systems used in engineering exhibit a weak scale separation. Worse still, the most interesting features of mechanical problems are located in regions where the scale separation is lost altogether, typically in regions of steep gradients (*e.g.* stress concentration in solid mechanics, localised limit-states such as damage, sharp geometrical irregularities, *etc.*). In such cases, the results provided by homogenised schemes may differ significantly from the results that would be obtained by solving the fine-scale problem directly. In this work, we aim to quantify this discrepancy.

Our work builds on the pioneering work [3]. In that paper, the authors introduced two problems, a fine-scale intractable problem ("true" model); and a homogenised tractable problem (surrogate model). Then, solving only the tractable, surrogate model and using ad hoc a posteriori error estimates, the authors were able to compare the solution of both problems. However, this modelling error bounding technique suffers from certain limitations, the most important of which is the fact that the bounds require the computation of terms involving the fine-scale description of the material properties. In practice, this means that the fine-scale heterogeneities need to be meshed, which becomes quickly intractable as the scale ratio increases. Secondly, the error is not strictly bounded, and a *sufficiently fine* macroscopic mesh needs to be used for the bounding properties to hold in practical applications. Finally, the various parameters that affect the quality of the error bounds, not the least of which is the type of homogenised model that is used to obtain an approximate solution to the fine-scale problem, are difficult to characterise and fully optimise.

In the present paper, we addressed the key limitations of this methods. Our fundamental suggestion is to allow for the position of the heterogeneities to be governed by a random process in the fine-scale problem. In this setting, we aim to estimate (a) the expectation of “energy-norm" and of “goal-oriented" measures of the error (*i.e.* statistical average) and (b) the moments of these measures (*i.e.* statistical dispersion, see fig. 1).

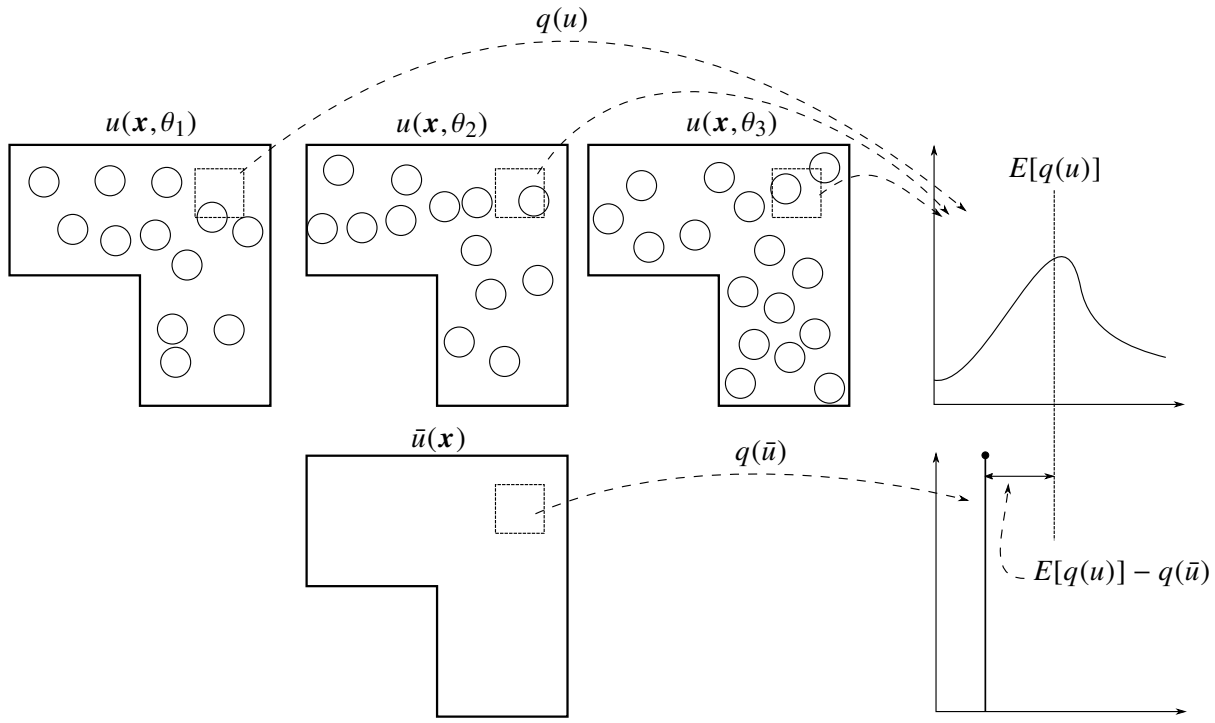

Figure 1: The quantity of interest of the “true model”, $q(u)$, is a probability density function, while it is a scalar in the surrogate model, $q(\bar{u})$. We aim to compare the expectation of both quantities.

In addition to being a realistic modelling setting for heterogeneous media, the direct consequence of this choice is that the computation of the error bounds only involves an integral of a function that, under weakly restrictive assumptions, varies slowly in space. This allows the application of upscaling error bounding without any restriction in terms of scale ratio.

Our second contribution is the development of a general error bounding framework in which the efficiency of the error estimates can be fully characterised and controlled. In order to achieve this difficult task, we propose to base our bounding approach on the Prager-Synge hypercircle theorem[4]. The resulting error bounds are strictly guaranteed and the “true” model is approximated by a pair of surrogates generated from different homogenisation schemes associated with complementary discretisation techniques (namely the compatible and the admissible FEM), instead of single field as proposed in [3]. This pair exhibits very strong similarities to those used to derive the classical Reuss-Voigt bounds for effective medium properties. Such an interesting property will give us a very strong background to characterise, both intuitively and mathematically, and to fully optimise the efficiency of the error estimates (*i.e.* minimise the remaining uncertainty on predicted quantities). One of the possible forms for the error bound is

$$R(\bar{\phi}^h) - \eta\eta_\phi \leq q(u) - q(\bar{u}^h) \leq R(\bar{\phi}^h) + \eta\eta_\phi \tag{1}$$

where R is the residue, $\bar{phi}^h$ is an homogenised approximation to the solution of the dual problem, and η and η_ϕ are upper bounds for the error in energy norm for the primal and dual problem.

Once this new framework has been established, we proceeded as in [5] and show that more accurate and guaranteed estimates can be obtained through locally replacing the homogenised surrogates by the “true”

microscopic model. We call *adaptive modelling* this dynamic, hybrid approximation with elements of the "true" and surrogate model working together towards the accurate bounding of engineering quantities of interest. New local error indicators will also be presented to guide this adaptive modelling process.

2. Numerical example

The methodology is applied to the cylinder head of an engine(fig. 2). At the bottom of the cylinder a temperature of $460K$ is prescribed. At the fins and the upper face it is assumed that a flux of $200W \cdot m^{-2}$ exits the body, while it is assumed that there is no heat exchange in the hole and lateral surfaces. The body is made of matrix enriched with particles. The thermal conductivity of the matrix is $460W/(m \cdot K)$, while the conductivity of the inclusions is $230W/(m \cdot K)$. The inclusions add up to 20% of the volume of the domain. We assume that the probability of being inside an inclusion is the same on every point of the domain and it coincides with the volume fraction. Hence, the expectation of the conductivity $E[k]$, is equal to $\nu k_p + (1-\nu)k_m$ and the expectation of its inverse $E[k^{-1}]$ is equal to $\nu/k_p + (1-\nu)/k_m$ on every point of the domain. An accurate description of those two functions $E[k]$ and $E[k^{-1}]$ is fundamental for the computation of the error bounds. The quantity of interest is the average temperature on the upper face. The domain was discretised with roughly 1.5 million linear tetrahedrons. The application of the Prager-Synge hypercircle theorem requires two approximate homogenised solutions, namely a kinematically admissible solution (KA) and a statically admissible solution. The KA approximations were obtained using rule of mixture, while the SA approximations were obtained using inverse rule of mixture. The resulting temperature field can be seen in fig. 2 while the bounds can be found in table 1.

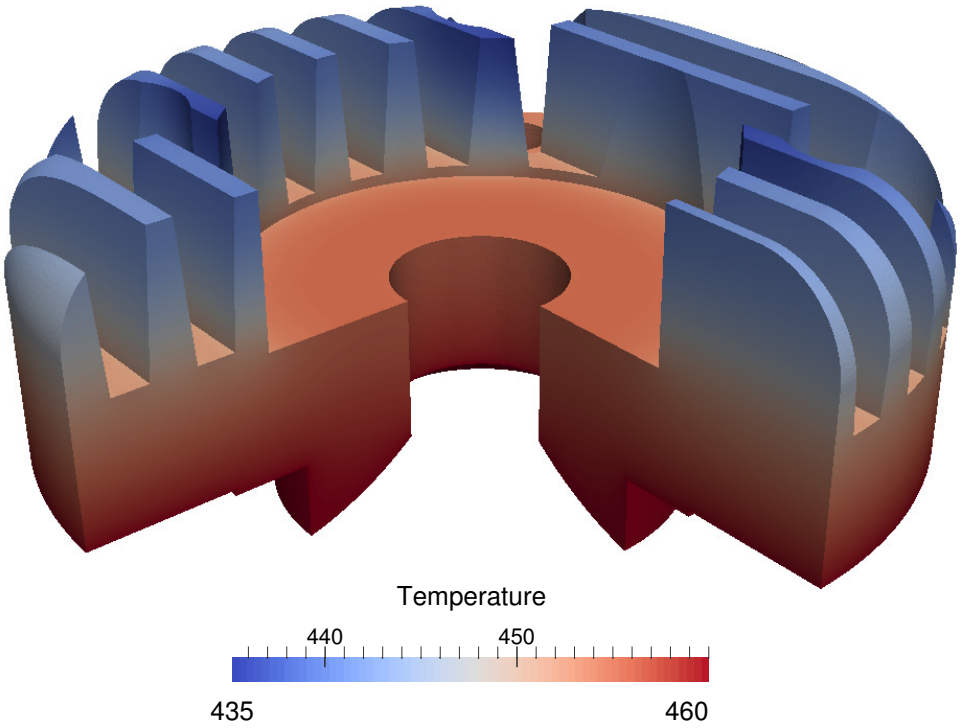

Figure 2: Temperature field of the cylinder head

$q(\bar{u}^h)$	$\zeta_l \leq$	$q(u) - q(\bar{u}^h)$	$\leq \zeta_u$	$\zeta_l + q(\bar{u}^h) \leq$	$q(u)$	$\leq \zeta_u + q(\bar{u}^h)$
445.8	-1.503	Intractable	0.002728	444.3	Intractable	445.8

Table 1: ζ_l and ζ_u represent both lower and upper bounds respectively for $q(u) - q(\bar{u})$, while $\zeta_l + q(\bar{u}^h)$ and $\zeta_u + q(\bar{u}^h)$ are lower and upper bounds for the quantity of interest itself. The direct computation of $q(u)$, the exact quantity of interest, is intractable.

Acknowledgements

The authors would like to acknowledge the financial support of the Framework Programme 7 Initial Training Network Funding under grant number 289361 "Integrating Numerical Simulation and Geometric Design Technology". The authors also acknowledge financial support of EPSRC under grant EP/J01947X/1: "Towards rationalised computational expense for simulating fracture over multiple scales (RationalMSFrac)", and thank Dr Claire Heaney for sharing the code that allowed us to generate realisations of random particulate composites.

References

[1] Nemat-Nasser, Sia and Hori, Muneo. Micromechanics: overall properties of heterogeneous materials

[2] Torquato, Salvatore. Random heterogeneous materials: microstructure and macroscopic properties

[3] Oden, J.Tinsley and Zohdi, Tarek I. Analysis and adaptive modeling of highly heterogeneous elastic structures *Computer Methods in Applied Mechanics and Engineering*

[4] Prager, William and Synge, John L. Approximations in elasticity based on the concept of function space *Quart. Appl. Math*

[5] Romkes, Albert and Oden, J. Tinsley and Vemaganti, Kumar. Multi-scale goal-oriented adaptive modeling of random heterogeneous materials *Mechanics of Materials*

Proceedings of the 24th UK Conference of the
Association for Computational Mechanics in Engineering
31 March – 1 April 2016, Cardiff (United Kingdom)

On the Small Scale Nonlinear Finite Element Analysis of Flexible Risers

***M.T. Rahmati, G. Alfano, H. Bahai**

Department of Mechanical, Aerospace and Civil Engineering

Brunel University London

Uxbridge, UK

*mt.rahmati@gmail.com

ABSTRACT

In this paper an efficient small-scale, detailed finite-element modelling method for flexible risers is presented. The method can be effectively implemented in a fully-nested (FE^2) multiscale analysis based on computational homogenization. To reduce the computational cost only a small fraction of a flexible pipe is used for a detailed nonlinear finite-element analysis at the small scale by exploiting the cyclic symmetry of the model and applying periodic boundary conditions. In this model, using three-dimensional elements, all layer components are individually modelled and a surface-to-surface frictional contact model is used to simulate their interaction. The approach is applied on a 5-layered pipe made of inner, outer and intermediate polymer layers and two intermediate armour layers, each made of 40 steel tendons. The capability of the method in capturing the detailed nonlinear effects and the great advantage in terms of significant CPU time saving are demonstrated by comparing the results obtained on elements of pipe of different lengths.

Keywords: *Periodic Boundaries, Fixed Boundaries, Flexible risers*

1. Introduction

Unbonded flexible risers have become the main means for transporting oil and gas between the seabed and surface in ultra-deep waters. They consist of several polymer and steel layers that can move internally relative to each other. Their ability of withstanding large displacements and rotations makes them ideal for floating platforms. In many problems of very significant industrial interest sufficient accuracy can only be obtained by the use of models that properly take into account contact and friction between layers and how these are related to internal and external pressure. Although FE models can account for the complex internal structure of flexible risers, their computational requirements limit their applicability to just a few meters in length at most. So, a more efficient methodology with lower computational cost is required to bridge the gap between nonlinear dynamic simulations at the large scale and detailed finite element models at the small scale.

One approach to reduce computational cost of the analysis of flexible risers is to develop constitutive laws for large-scale beam models, which link generalised stresses and strains to model the hysteresis loops occurring for flexible pipes subjected to cyclic loading, as shown by Tan et al. [1]. A model based on this approach is used by Alfano et al. [2], building on the analogy between frictional slipping between different layers of a flexible riser and frictional slipping between micro-planes of a continuum medium in non-associative elasto-plasticity. In this way, a linear elastic relationship was used for the initial response, in which no slip occurs, and a non-associative rule with linear kinematic hardening was then introduced to model the full-slip phase. One major challenge in using the constitutive law based on the non-associative elasto-plasticity analogy is the determination of the parameters of the constitutive law to bridge the small scale of the detailed FE simulations with the large scale of the model accurately. An alternative approach which does not have this limitation is a fully-nested multi-scale procedure [3], currently in widespread use for the modelling of composite materials. With this method, at each integration point (i.e. cross section) of the large-scale beam model, the stress resultants corresponding to assigned generalised strains are determined through the solution of the small-scale FE problem. Key to accurate solution of the small scale FE problem is the use of suitable boundary conditions. The

periodic boundary conditions are the most effective and accurate for most cases involving a periodic microstructure or when the microstructure is not periodic but the small scale model is sufficiently statistically representative [4, 5]. The motivation for this work is that previous models in the context of sequential multi-scale analysis [6] are too computationally expensive for a fully nested analysis. Hence, this paper describes an efficient modelling approach for the small-scale analysis, which exploits the cyclic symmetry of the riser detailed structure, and its implementation based on the introduction of periodic boundary conditions for detailed FE models in small scale simulations in a similar method used by [7]. The capability of the boundary condition treatment method in capturing the non-linear effects and the great advantage of significant CPU time saving by this method over using a larger model is shown.

2. Small scale model

A fully-nested computational homogenization scheme is essentially based on the construction of a micro-scale (or more generally small-scale) boundary-value problem (BVP) at each integration point of a macro (or large-scale) model. The small-scale model is solved numerically to determine the constitutive response of the material at each integration point [8]. If the FEM is used at both scales, the methods is also known as FE^2. If a displacement-based FE formulation and a Newton-Raphson incremental scheme are used at the large scale, 'tentative' strains resulting from an attempted displacement increment are calculated at each integration point for each iteration of each increment in the macro model. When a 3D continuum model is used at both scales, the tentative strains are imposed on a suitably defined representative volume element (RVE) of the micro scale (down-scaling procedure), each large-scale integration point corresponding to one and only RVE. For the flexible risers considered in this paper, a 3D continuum model is used at the small scale, which is to be linked to a large-scale beam model, where generalised strains and stress resultants are employed. A simplified 5-layer flexible pipe, made of three polymer layers and two armour layers, was considered. Both the inner and the outer armour layers are made of 40 steel tendons, with rectangular cross section, which are wound with the same pitch of length L_p equal should to 320mm. It is widely accepted that the use of periodic boundary conditions in multiscale computational homogenization provides the most accurate results, at least at sufficient distance from the real boundary of the structure. On the other hand, the solution for a segment of riser whose length is any multiple of L_p/N should be characterized by the same cyclic symmetry if periodic boundary conditions are applied and if such solution is unique. Figure 1 shows the the smallest model which has a length equal to $1/40$ of the pitch length of the tendons. For this small slice of pipe the position of each tendon on one end cross section is the same as the position of the adjacent tendon on the other end cross section. This makes this slice of $1/40$ of length the smallest repeating unit of the pipe. Furthermore, as typical in first-order computational homogenisation, the assumption is made that the variations of the internal stress resultant (i.e. large-scale stress) and of the generalised strain (i.e. large-scale strain) are small enough that, for the element of pipe under consideration, they can be neglected. Therefore, to within a rigid motion, the assumption of periodic kinematics is made, resulting in the enforcement of periodic boundary conditions. A set of linear constraint equations was generated relating the degrees of freedom of each pair of nodes on the boundaries having the same position on the cross-section [9].

3. Numerical results

The study in this paper focuses on cases in which the segments of pipes are subject to bending, as well as internal and external pressure, the latter being balanced to produce a relatively small and outward radial displacement of the inner surface of the inner polymer layer (inner liner). All components are modelled with fully-integrated 8-noded 3D solid elements with incompatible strains, with surface-to-surface frictional contact between all components. Details of the material, dimensions and arrangement of constituent layers are given in Table 1. A fully-implicit nonlinear static analysis based on the Newton-Raphson method is used to solve the models.

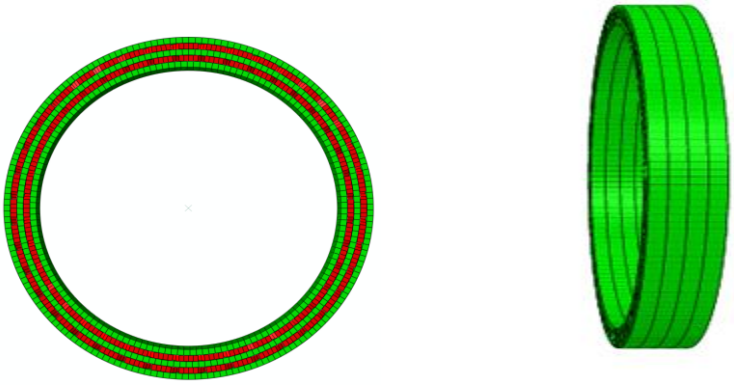

Figure 1: cross section of the FE model and FE models with lengths equal to $L_p/40$

Table 1: Dimensions and materials of components in the model.

Layer	r_0, r_1 (mm)	Material	E (MPa)	υ
1	48, 50	Polyethylene	0.35	0.4
2	50, 52	Carbon Steel	210	0.3
3	52, 54	Polyethylene	0.35	0.4
4	54, 56	Carbon Steel	210	0.3
5	56, 58	Polyethylene	0.35	0.4

The analyses were conducted by applying internal and external pressure in a first step, after which one symmetric cyclic history of bending curvature was prescribed, the maximum and minimum curvatures being 0.125 and -0.125 m^{-1}. The internal and external pressures were equal to 4 and 4.5 MPa, respectively. The curves in Figures 2 show the bending moment against the (prescribed) bending curvature for four models with length equal to L_p/N , with $N = 1, 5, 20, 40$. It can be appreciated that the difference in the results of the models with different lengths is practically negligible when periodic BC is used. These results confirm that use of the smallest repeating unit as the model to be used at the small scale of a multi-scale analysis is a valid choice. The analyses were carried out in parallel on a computer cluster with two dual-core 1.8 GHz processors (32 processors in total) using 8MB of RAM. The huge saving in CPU time, from 11 hours for the longest model of one pitch length to only few minutes, allows the smallest model to be effectively used in a nested multi-scale strategy.

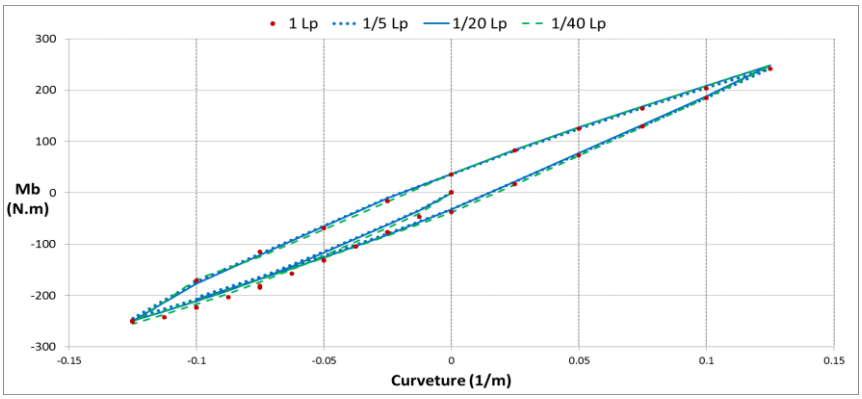

Figure 2: Bending moment vs prescribed bending curvature (internal pressure 4MPa, external pressure 4.5MPa).

4. Conclusions

An effective approach to minimize the computational cost of a detailed nonlinear FE analysis of a segment of flexible riser is presented in this paper. In this method frictional contact between all layers is taken into account. The key ideas behind the proposed approach are (a) the observation that flexible risers can be represented, with very good approximation, with a model having cyclic symmetry, (b) the use of such cyclic symmetry to reduce the length of the model to the smallest repeating unit and (c) the use of periodic boundary conditions. The enormous saving in computational cost entailed by the use of the smallest repeating unit makes this the optimal model to be used in a nested (FE^2) multiscale analysis.

Acknowledgements

The authors would like to acknowledge the financial support by EPSRC (grant EP/K034243/1).

References

[1] Tan, Z., Quiggin, P., Sheldrake, T. Time domain simulation of the 3D bending hysteresis behaviour of an unbonded flexible riser. Proceedings of the ASME 2007 26th International Conference on Ocean, Offshore and Arctic Engineering, OMAE2007-29315, 2007.

[2] Alfano, G., Bahtui, A., Bahai, H. Numerical derivation of constitutive models for unbonded flexible risers. International Journal of Mechanical Sciences, 51, 295-304, 2009.

[3] Geers, M.G.D., Kouznetsova, V., Brekelmans, W.A.M.Multi-scale computational homogenization: trends and challenges. Journal of Computational and Applied Mathematics 234(7), pp. 2175-2182, 2010.

[4] Hazanov, S., Amieur, M. On overall properties of elastic heterogeneous bodies smaller than the representative volume. Int. J. Engrg. Sci. 33, pp. 1289-1301, 1995.

[5] Amieur, M., Hazanov, S., Huet, C. Numerical and experimental assessment of the size and boundary conditions effects for the overall properties of granular composite bodies smaller than the representative volume. Parker, D., England, A. (Eds.), IAUTAM Symposium on Anisotropy, Inhomogeneity and Nonlinearity in Solid Mechanics, Kluwer Academic Publishers, Dordrecht. pp. 149-154, 1995.

[6] Bahtui, H. Bahai, G. Alfano . Numerical and analytical modeling of unbonded flexible risers. Journal of Offshore Mechanics and Arctic Engineering, 131(2), 2009.

[7] Leroy, J.M., Perdrizet, T., Le Corre, V., Estrier, P. Stress assessment in armour layers of flexible risers. Proceedings of the ASME 2010 29th International Conference on Ocean, Offshore and Arctic Engineering, OMAE2010-20932, 2010.

[8] Edmans, B.D., G. Alfano, H. Bahai. Nonlinear multi-scale homogenization with different structural models at different scales. International Journal for Numerical Methods in Engineering, 94(4): 355-373, 2013.

[9] Rahmati, M.T., H.Bahai, G. Alfano. Small-scale FE modelling for the analysis of flexible risers. OMAE2015-41825, St. John's, Canada, May 31- June 5, 2015.

Failure and Damage III

Proceedings of the 24th UK Conference of the
Association for Computational Mechanics in Engineering
31 March – 01 April 2016, Cardiff University, Cardiff

SMOOTH STATIC AND DYNAMIC CRACK PROPAGATION

***Chris J. Pearce[1], Lukasz Kaczmarczyk[1]**

[1]School of Engineering, University of Glasgow, G12 8QQ

*Chris.Pearce@glasgow.ac.uk

ABSTRACT

This paper presents both the theoretical basis for simulating unstable crack propagation in 3D hyperelastic continua within the context of configurational mechanics, and the associated numerical implementation. The approach taken is based on the principle of global maximum energy dissipation for elastic solids, with configurational forces determining the direction of crack propagation. The work builds on the developments made by the authors for static analysis, incorporating the influence of the kinetic energy. The nonlinear system of equations is solved in a monolithic manner using a Newton-Raphson scheme. Initial numerical results are presented.

Keywords: *Fracture; Finite element method; ALE; nuclear*

1. Introduction

The numerical simulation of unstable crack propagation in three-dimensional hyperelastic materials is studied within the context of linear elastic fracture mechanics (LEFM) and configurational mechanics [3]. Although quasi-static and dynamic fracture has been widely investigated in continuum mechanics, this remains a challenging topic. Our approach is to develop the physical and mathematical description to determine (a) when a crack will propagate, (b) the direction of propagation and (c) how far/fast the crack will propagate. Furthermore, we require a numerical setting to accurately resolve the evolving displacement discontinuity within the context of the Finite Element Method. In this study, we present a mathematical derivation and numerical implementation that can achieve these goals, solving for conservation of momentum in both the spatial and material domains. The spatial (or physical) domain can be considered as a description of what we physically observe and the material domain is the evolving reference domain due to crack evolution. The theory is an interpretation of linear elastic fracture mechanics and consistent with Griffith's fracture criterion. This paper represents a generalisation of the authors' previous work on static crack propagation, [3]. The approach taken is based on the principle of global maximum energy dissipation for elastic solids, with configurational forces determining the direction of crack propagation. This approach has been successfully adopted by a number of other authors in the context of quasi-static analysis, e.g. [3] and [2]. At present we restrict ourselves to the consideration of elastic bodies with energy dissipation limited to the creation of new crack surfaces.

In the context of the numerical setting, we have adopted the Arbitrary Lagrangian-Eulerian (ALE) method, which is a kinematic framework to describe movement of the nodes of the finite element mesh independently of the material. Thus, we are able to resolve the propagating crack without influence from the original finite element mesh, and maintain mesh quality. The efficient solution of 3D crack propagation, with a large numbers of degrees of freedom, requires the use of an iterative solver for solving the system of algebraic equations. In such cases, controlling element quality enables us to optimise matrix conditioning, thereby increasing the computational efficiency of the solver.

The resulting system of equations is highly nonlinear and requires a solution strategy that can trace the entire transient response. The application of this work is the predictive modelling of crack propagation in nuclear graphite bricks, which are used as the moderator in UK advanced gas-cooled nuclear reactors (AGRs).

2. Kinematics of Propagating Cracks

Differentiable mappings relate the reference material domain to both the current spatial and the current material domains. These mappings are utilized to independently observe the deformation of material in the physical space Ω_t and the evolution of the crack surface in the material space B_t, see Figure 1.

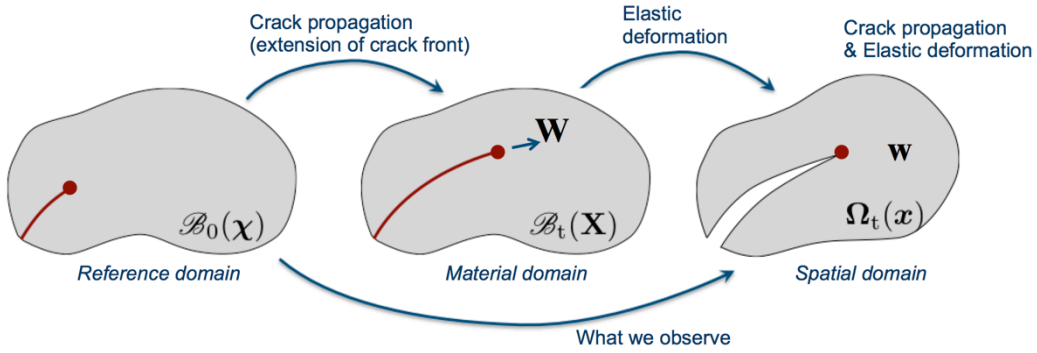

Figure 1: Deformation and configurational change of a body with a propagating crack

$$\mathbf{w} = \mathbf{x} - \boldsymbol{\chi}\,,\ \mathbf{W} = \mathbf{X} - \boldsymbol{\chi},\ \mathbf{u} = \mathbf{w} - \mathbf{W} \tag{1}$$

3. Numerical Implementation

The finite element approximation is applied to both the physical and material space. Three-dimensional domains are discretised with tetrahedral elements with hierarchical basis functions of arbitrary polynomial order, following the work of [1]. The higher-order approximations are only applied to displacements in the spatial configuration, whereas a linear approximation is used for displacements in the material space. The resulting residuals in the spatial and material domain, that represent the two primary, nonlinear equations that need to be solved, are expressed as:

$$\mathbf{r}_{\mathrm{s}} = \lambda(t)\mathbf{f}_{\mathrm{s,ext}} - \mathbf{f}_{\mathrm{s,int}}\,,\quad \mathbf{r}_{\mathrm{m}} = \mathbf{f}_{\mathrm{m,res}} - \mathbf{f}_{\mathrm{m,driv}} \tag{2}$$

where λ is the load factor that scales the external reference load, $\mathbf{f}_{\mathrm{s,ext}}$; $\mathbf{f}_{\mathrm{s,int}}$ is the internal force vector, $\mathbf{f}_{\mathrm{m,res}}$ is the material resistance and $\mathbf{f}_{\mathrm{m,driv}}$ is the driving force for crack propagation. These equations are linearised and solved using a Newton-Raphson procedure.

The spatial internal force vector is expressed as

$$\mathbf{f}_{\mathrm{s,int}} = \int \mathbf{B}_{\mathrm{X}}^{\mathrm{T}}\mathbf{P}\,\mathrm{dV} + \int \rho\mathbf{N}^{\mathrm{T}}\mathbf{a}\,\mathrm{dV} \tag{3}$$

and the material driving force is expressed as

$$\mathbf{f}_{\mathrm{m,driv}} = \int \mathbf{B}_{\mathrm{X}}^{\mathrm{T}}\boldsymbol{\Sigma}\,\mathrm{dV} - \int \rho_0\left(\mathbf{F}^{\mathrm{T}}\mathbf{a} + \dot{\mathbf{F}}^{\mathrm{T}}\mathbf{v}\right)\mathrm{dV} = \mathbf{G} - \int \rho_0\left(\mathbf{F}^{\mathrm{T}}\mathbf{a} + \dot{\mathbf{F}}^{\mathrm{T}}\mathbf{v}\right)\mathrm{dV} \tag{4}$$

where $\mathbf{P}$ is the first Piola Kirchoff stress tensor, $\boldsymbol{\Sigma}$ is the Eshelby stress, $\mathbf{a}$ is the spatial acceleration, $\mathbf{v} = \dot{\mathbf{u}} = \dot{\mathbf{w}} - \mathbf{F}\dot{\mathbf{W}}$ is the spatial velocity, $\mathbf{F}$ is the deformation gradient and $\mathbf{G}$ is the configurational force. The Eshelby stress is defined as:

$$\boldsymbol{\Sigma} = W\mathbf{I} - \mathbf{F}^{\mathrm{T}}\mathbf{P} \tag{5}$$

where W is the strain energy density.

In the restricted case of quasi-static analysis, the inertia and velocity terms in (3) and (4) vanish and the formulation reverts to that presented in [3]. Thus, equations (3) and (4) represent an important development in the modelling of dynamic crack propagation, generalising the configurational mechanics formulation. It is important to emphasise that, for fast crack propagation, whereby the inertia terms in equations (5) and (6) are included, the crack front velocities are calculated to satisfy

equilibrium of the crack front in the material space. Therefore, the crack front velocity is not a material or model parameter, as is the case in most models, but a natural result of a consistent mathematical derivation, starting from the first law of thermodynamics [3].

4. Mesh Quality

The continuous adaptation of the finite element mesh to resolve the propagating crack will result in a degeneration of the mesh quality. For large problems, where it is necessary to use iterative solvers, we need to control the quality of the elements to ensure good matrix conditioning. The key challenge is to enforce constraints to preserve element quality for each Newton-Raphson iteration, without influencing the physical response. Thus, we introduce a measure of element quality for tetrahedral elements in terms of their shape and use this to drive mesh improvement. Here we include both node movement and changes in element topology (face flipping). Thus, equations (4) and (5) are augmented by a third residual, $\mathbf{f}_q$, defined as

$$\mathbf{f}_q = \int \mathbf{B}_X^T \mathbf{Q} \, dV \tag{6}$$

where $\mathbf{Q}$ is a pseudo "stress" at the element level, as a counterpart to the first Piola Kirchhoff stress. Since the conditioning of the finite element stiffness matrix is controlled by the quality of the worst elements, we advocate that $\mathbf{Q}$ is a function of a log-barrier objective function as a means of evaluating the quality of an entire mesh (whilst punishing harshly the worst quality element), and the volume-length quality measure, [4].

5. Numerical Examples

To demonstrate the performance of the model for quasi-static loading, a numerical example is presented which considers a slice of a graphite brick under quasi-static loading of the keyway. Figure 3 shows a good comparison between the numerically simulated crack path and the experimentally observed crack. Figure 3(d) shows that the results are independent of the mesh size.

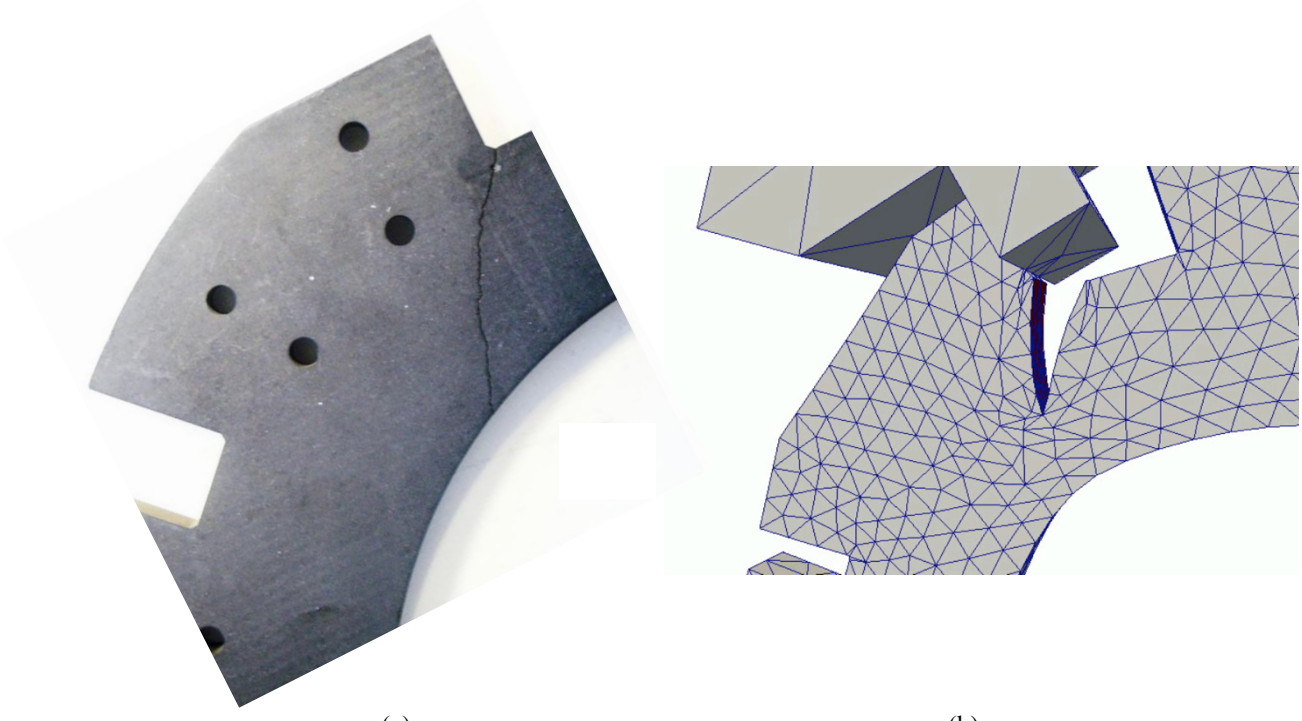

(a) (b)

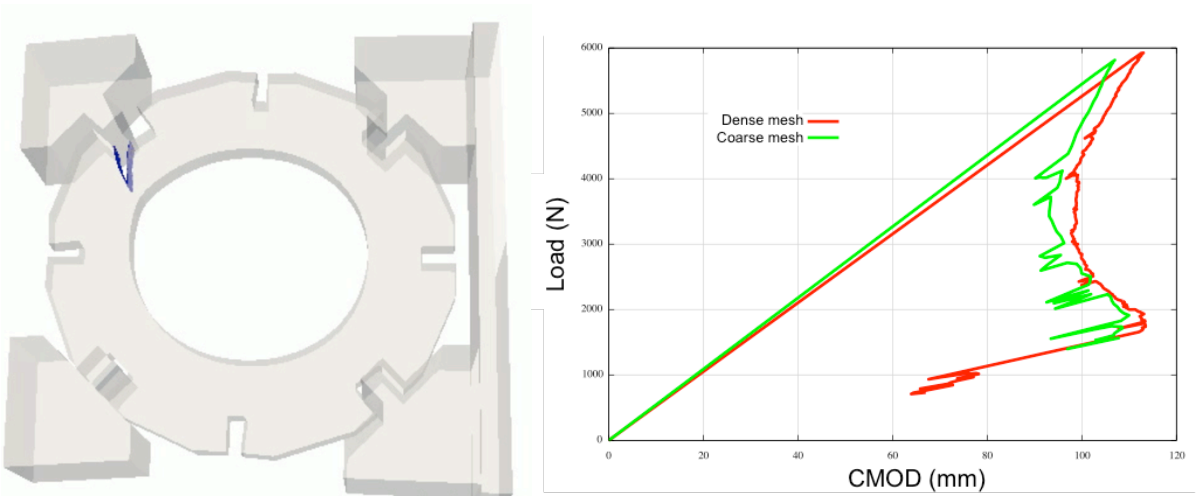

(c) (d)

Figure 3: Graphite brick slice. (a) Experimentally observed crack; (b) numerically predicted crack; (c) model geometry and predicted crack; (d) load-displacement response.

6. Conclusions

In this study, the basis for unstable crack propagation using configurational mechanics has been presented. The highly nonlinear system of equations are implemented in and solved using MoFEM, a finite element code for multi-physics problems which is developed at the University of Glasgow. Performance of the model is demonstrated on three numerical problems. The implementation has proved to be stable, robust and computationally efficient.

Acknowledgements

This work was supported by EDF Energy Nuclear Generation Ltd and the Royal Academy of Engineering (RAEng). The views expressed in this paper are those of the authors and not necessarily those of EDF Energy Nuclear Generation Ltd or RAEng.

References

[1] Ainsworth, M.A. and Coyle, J. Hierarchic finite element bases on unstructured tetrahedral meshes. International Journal for Numerical Methods in Engineering. 58, 2103–2130, 2003.

[2] Gurses, E. and Miehe, C. A computational framework of three-dimensional configurational-force-driven brittle crack propagation. Computer Methods in Applied Mechanics and Engineering, 198, 1413-1428, 2009.

[3] Kaczmarczyk, Ł., Mousavi, M. and Pearce, C.J. Three-dimensional brittle fracture: configurational-force-driven crack propagation. International Journal for Numerical Methods in Engineering, 7, 531–550, 2014.

[4] Pearce, C.J., MacKenzie, R. and Kaczmarczyk, Ł. Numerical approaches for brittle crack propagation, in B.H.V. Topping, (Eds), Computational Methods for Engineering Science, Saxe-Coburg Publications, Stirlingshire, UK, Chapter 6, pp 135-155, 2014.

Proceedings of the 24th UK Conference of the
Association for Computational Mechanics in Engineering
31 March - 01 April 2016, Cardiff University, Cardiff

An approach for dynamic analysis of stationary cracks using XFEM

***J. Navarro-Zafra[1], J. L. Curiel-Sosa[1], M. C. Serna Moreno[2], C. Pinna[1], J. L. Martínez Vicente [2], N. Rohaizat [1], B. Tafazzolimoghaddam[1]**

[1] Department of Mechanical Engineering, University of Sheffield. Sir Frederik Mappin Building, Mappin Street, Sheffield, S1 3JD, UK
[2] E.T.S. de Ingenieros Industriales de Ciudad Real, Universidad de Castilla La Mancha, Edificio Politécnico. Avda. Camilo José Cela s/n, Campus Universitario, 13071, Ciudad Real (Spain)

*jnavarrozafra1@sheffield.ac.uk

ABSTRACT

A numerical implementation of the eXtended Finite Element Method (XFEM) is presented. The proposed approach solves the system of discrete equations using an explicit integration scheme and it is capable of addressing dynamic and static fracture mechanics problems. Special attention to the mass matrix construction is required in order to avoid instability issues such a null stable time increment. Hence, different mass lumping strategies are adopted for enriched elements. The in-house implementation of this approach, so-called X^2FEM, is embedded in the main in-house FE platform called MULE. Numerical tests demonstrate that the proposed approach is able to provide an accurate calculation of static and dynamic stress intensity factors (SIFs) for different geometries and loading scenarios. Finally, in order to extend our point of view, an experimental analysis of a 10° off-axis carbon fibre laminate is carried out using Digital Image Correlation (DIC).

Key Words: *Extended finite element Method (XFEM); Explicit time integration; Stress intensity factors; Digital image correlation*

1. Introduction

During the last years, the XFEM [1] has been used successfully in the simulation of moving cracks throughout a structure such as [2, 3, 4]. Using this method for the simulation of fracture, the mesh is not updated at each time step in opposition to the Finite Element Method (FEM), where the mesh must be updated at each time step in order to conform with the moving discontinuity. Although, the FEM has solved many problems of interest such as [5, 6, 7], XFEM is computationally more efficient than the FEM while simulating the evolution of cracks.
Based on previous experience with XFEM [8] and FE modelling of damage [9] using commercial codes, the objective of this work is to present a numerical approach to analyze stationary cracks in the framework of XFEM. This approach will improve the flexibility during programming since an entire in-house code, so-called X^2FEM, is available. This in-house code is implemented in the main FE platform called MULE. The approach proposed considers an explicit time integration scheme. In this case, the well-known central difference method (CDM) is adopted for time discretisation. A diagonal mass matrix is used for solving the discrete momentum equation. Hence, the part of the mass matrix corresponding with the standard Degree Of Freedom (DOF) are lumped by direct mass lumping. However, for the lumping of the enriched DOF there is not straightforward way and a limitation exists. The limitation was found by Belytschko et al. [10]. Basically, they found out that the critical time step of the explicit XFEM decreases notably as a discontinuity gets closer to nodes. To alleviate this restriction, Belytschko et al. [10] used an implicit integrator for the enriched element and explicit integrator for standard elements. Recently, other possible solutions for solving this limitation are based on using mass lumping strategies. In this work, using specific lumping techniques for enriched elements the diagonalized mass matrix is obtained avoiding the possibility of having a null critical time step.

2. General problem

A two-dimensional dynamic problem is considered where a body Ω with boundary $\partial\Omega$ is defined. This boundary is divided into $\partial\Omega_u$, $\partial\Omega_F$ and Γ_c (see Figure 1). Hence, $\partial\Omega = \partial\Omega_u \cup \partial\Omega_F \cup \Gamma_c$, where $\partial\Omega_u$ represents the prescribed displacements in the body Ω, $\partial\Omega_F$ is the part of the body subjected to surface forces and Γ_c corresponds to the displacement discontinuity e.g. a crack. Note that crack 's faces are traction free. The motion of the body is defined by the displacement $\boldsymbol{u}(\boldsymbol{x}, t)$, which is a function of the location of the material point $\boldsymbol{x}$ and the time t. The material has a linear behaviour, it is isotropic and its mass density is ρ. The body presents applied displacements $\bar{\boldsymbol{u}}$ on the Dirichlet boundary $\partial\Omega_u$ and applied traction $\bar{\boldsymbol{t}}$ on the Neumann boundary $\partial\Omega_F$; $\partial\Omega_u \cap \partial\Omega_F = \emptyset$, $\partial\Omega_u \cap \Gamma_c = \emptyset$, $\partial\Omega_F \cap \Gamma_c = \emptyset$. The outward normal vector in the material boundary is defined as $\boldsymbol{n}^{\perp}$ and $\boldsymbol{b}$ is the body force per unit mass. Thus, the strong form of the problem is written as follows:

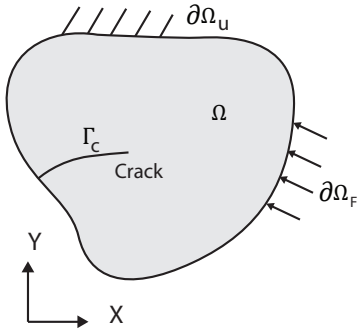

Figure 1: A two dimensional body cracked and its boundaries.

$$\nabla\boldsymbol{\sigma} + \rho\boldsymbol{b} - \rho\ddot{\boldsymbol{u}} = 0 \; in \; \Omega \tag{1}$$

subjected to the boundary conditions:

$$\boldsymbol{u} = \bar{\boldsymbol{u}} \; on \; \partial\Omega_u \tag{2}$$

$$\boldsymbol{\sigma} \cdot \boldsymbol{n}^{\perp} = \bar{\boldsymbol{t}} \; on \; \partial\Omega_F \tag{3}$$

$$\boldsymbol{\sigma} \cdot \boldsymbol{n}^{\perp} = 0 \; on \; \Gamma_c \tag{4}$$

The constitutive relation of the material is written:

$$\boldsymbol{\sigma}(\boldsymbol{x}, t) = \boldsymbol{C} \cdot \boldsymbol{\epsilon}(\boldsymbol{u}(\boldsymbol{x}, t)) \tag{5}$$

where $\boldsymbol{\sigma}$ is the Cauchy stress tensor, $\boldsymbol{C}$ the constitutive matrix and $\boldsymbol{\epsilon}$ the strain tensor.

3. Numerical framework

The displacement at a generic point $\boldsymbol{x}$, $\boldsymbol{u}(\boldsymbol{x}, t)$ is approximated by $\boldsymbol{u}^h$ using continuous and discontinuous terms as follows [11]:

$$\boldsymbol{u}^h(\boldsymbol{x}, t) = \boldsymbol{u}^{cont}(\boldsymbol{x}, t) + \boldsymbol{u}^{cut}(\boldsymbol{x}, t) + \boldsymbol{u}^{tip}(\boldsymbol{x}, t) \tag{6}$$

where $\boldsymbol{u}^{cont}$ corresponds to the continuous approximation of the displacement, $\boldsymbol{u}^{cut}$ corresponds to the discontinuous approximation for addressing the crack and $\boldsymbol{u}^{tip}$ denotes the discontinuous approximation corresponding to the crack tip.

For the implementation of approach presented, an in-house code developed in MATLAB is built. The element type considered in this code is a 4-node quadrilateral element. Each node for a standard element presents two DOF. The nodes of full cracked elements have two classical DOF and two additional DOF

addressing the strong displacement jump. The construction of the global mass matrix is not a trivial task. The mass lumping strategy adopted for the enriched part is critical for the stability of the CDM. Therefore, different mass lumping strategies are adopted depending on the type of enrichment. For standard elements, the calculation of the stiffness matrix considers four integration points. In the other hand, for elements containing the tip of the crack or cut by the crack, the integrals for the calculation of internal forces cannot be derived by standard quadrature methods since the integrand is defined as discontinuous. Therefore, the standard Gauss quadrature does not adequately considered the discontinuity and a subdivision of the elements into triangles is required. This subdivision of the elements has just integration purposes, hence, no additional DOF are added to the system.

4. Computational tests

In order to check the performance of the proposed approach, a semi-infinite stationary crack within an infinite plate is simulated. The plate is loaded in its vertical edge as depicted in Figure 2. The influence of the external loading on the Stress Intensity Factor (SIF) calculation is addressed. Hence, the load applied is introduced in three different manners: as a step, a ramp and a sinusoidal wave. The dynamic SIFs obtained from the code are compared with the analytical solution.

4.1. Analysis of a stationary crack: mode I

A schematic representation of the problem under consideration is depicted in Figure 2 where a tensile stress is applied perpendicular to the crack. The analytical solution of the SIF in mode I (denoted as K_I) for a linear elastic material was first proposed by Freund [12]. The analytical solution was obtained under the assumptions of an infinite plate with a semi-infinite crack. This solution is valid till the tensile wave stress is reflected in the bottom of the plate and reaches again the crack tip. The dimensions of the plate are L=10 m, h=2 m and the crack length is a=5 m. The material properties are presented on Table 1 where E is the elasticity modulus, ν the poisson ratio and ρ the density.

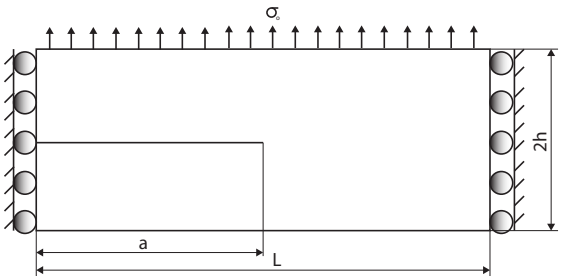

Figure 2: Geometry and loading for a infinite plate with a semi-infinite crack.

Table 1: Mechanical properties

$E[GPa]$	ν	$\rho[kg/m^3]$
210	0.3	8000

In Figure 4, the normalized mode I dynamic SIF $\frac{K_I}{\sigma_o\sqrt{h}}$ is depicted against the normalized time $\frac{t}{t_c}$ being $t_c = \frac{h}{c_d} = 3.36 \cdot 10^{-4} s$, where c_d is the dilatational wave speed. This graph serves to point out the mesh independence of the solution using two different discretisations with 92x39 and 140x59 elements. These discretisations were considered in order to have an aspect ratio of approximately one within the mesh. Note that the time step considered is $\Delta t_c^{XFEM} = 5\mu s$ (a simulation of 200 time steps). The tensile load applied $\sigma_0(t)$ is defined as $\sigma_0(t) = \sigma g^n(t)$, where $\sigma = 500MPa$ and $g^n(t)$ defines the way that the load is provided. Initially, a step load $g^1(t)$ is applied to the plate as follows:

$$g^1(t) = \begin{cases} 0 & \text{if} \quad t \leq 0 \\ \\ 1 & \text{otherwise} \end{cases} \tag{7}$$

Two more loading scenarios were considered: a ramp and a sinusoidal wave. The results depicted on Figure 4 while loading with $g^1(t)$ show a reasonable agreement between the analytical and the computational solution for the coarse and fine meshes. Consequently this proves the ability of the proposed code for the calculation of SIF considering different discretisations.

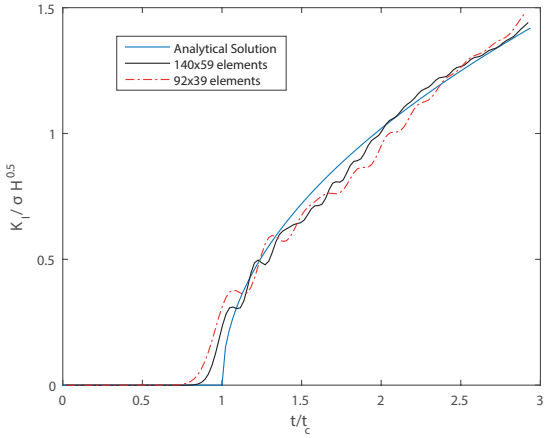

Figure 3: Normalized mode I stress intensity factor against normalized time for a stationary semi-infinite crack. The analytical solution is plotted as well as the computational solution considering two different discretizations: 92 by 39 and 140 by 59 elements .

5. Validation using Digital Image Correlation

Digital Image Correlation (DIC) [13][14] is an optical technique based on digital image processing and numerical computing. This technique provides the full-field displacements and strains for a surface by comparing a digital image reference (un-deformed) with a deformed image stage.

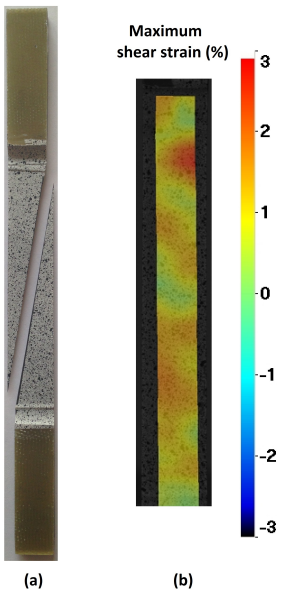

Figure 4: (a) Macro-crack observed during experimental tensile testing and (b) Map of maximum shear strain before failure.

In order to extend our point of view, a 2D experimental analysis of a 10° off-axis carbon fibre laminate is carried out using Digital Image Correlation (DIC). Therefore, the full-field of strains was obtained and those outcomes were compared with simulations. In Figure 5 (a), it is depicted the crack path for the 10° laminate once the specimen breaks. Additionally, in Figure 5 (b), it is presented a map of maximum shear strain before the macro-crack appears. Notice a peak of maximum shear strain in the zone where the crack is initiated.

6. Conclusions

A numerical approach for the simulation of stationary cracks in the context of XFEM is presented. This approach is numerically implemented in an in-house code programmed in MATLAB. By means of several tests, the performance of the in-house code is tested. The results obtained and its comparison with the analytical solutions proves the reliability of the approach. Additionally, in order to expand our point of view, an experimental analysis is carried out using DIC.

Acknowledgements

This work has been financially supported by the Engineering and Physical Sciences Research Council (EPSRC) through grant reference EP/K503149/1. Additionally, the first author would like to thank the University of Sheffield Learned Societies fund for covering all expenses related to this conference.

References

[1] Belytschko, T. and Black, T., Elastic crack growth in finite elements with minimal remeshing. *International journal for numerical methods in engineering*, 45(5), 601–620, 1999.

[2] Curiel-Sosa, J.L. and Karapurath, N., Delamination modelling of GLARE using the extended finite element method. *Composites Science and Technology*, 72(7), 788-791, 2012.

[3] Ibbett, J. , Tafazzolimoghaddam, B. , Hernandez Delgadillo, H. , Curiel-Sosa, J.L., What triggers a microcrack in printed engineering parts produced by selective laser sintering on the first place?. *Materials and Design*, 88, 588-597, 2015.

[4] Serna Moreno, M.C. , Curiel-Sosa, J.L. , Navarro-Zafra, J. , Martínez Vicente, J.L. and López Cela, J.J. , Crack propagation in a chopped glass-reinforced composite under biaxial testing by means of XFEM. *Composite Structures*, 119, 264-271, 2014.

[5] Curiel-Sosa, J.L. , de Souza Neto, E. , Owen, D.R.J. , A combined implicit-explicit algorithm in time for non-linear finite element analysis. *Communications in Numerical Methods in Engineering*, 22(1), 63-75, 2006.

[6] Curiel-Sosa, J.L. , Beg, O.A. , Murillo, J.M.L. , Finite element analysis of structural instability using an implicit/explicit switching technique. *International Journal of Computational Methods in Engineering Science and Mechanics*, 14(5), 452-464, 2013.

[7] Curiel-Sosa, J.L. and Gil, A.J., Analysis of a continuum-based beam element in the framework of explicit-FEM. *Finite Elements in Analysis and Design*, 45(8-9), 583-591, 2009.

[8] Navarro-Zafra, J. , Curiel-Sosa, J.L. , Serna Moreno, M.C. ,Three-Dimensional Static and Dynamic Analysis of a Composite Cruciform Structure Subjected to Biaxial Loading: A Discontinuum Approach. *Applied Composite Materials*, Article in Press, 2015.

[9] Navarro-Zafra, J. , Curiel-Sosa, J.L. and Serna Moreno, M.C. ,Mixed-mode damage into a CGRP cruciform subjected to biaxial loading. *Composite Structures*, 133, 1093-1100, 2015.

[10] Belytschko, T. , Chen, H. and Xu, J. and Zi, G. Dynamic crack propagation based on loss of hyperbolicity and a new discontinuous enrichment. *International Journal for Numerical Methods in Engineering*, 58(12), 1873-1905, 2003.

[11] Moes, N. , Dolbow, J. , Belytschko, T. .A finite element method for crack growth without remeshing. *International Journal for Numerical Methods in Engineering*, 46(1), 131-150, 1999.

[12] Freund, L. B. .Dynamic fracture mechanics. *Cambridge university press*, 1998.

[13] Chu, T.C. , Ranson, W.F. , Sutton, M.A. .Applications of digital-image-correlation techniques to experimental mechanics. *Experimental Mechanics*, 25(3), 232-244, 1985.

[14] Caminero, M.A. , Pavlopoulou, S. , Lopez-Pedrosa, M. , Nicolaisson, B.G. , Pinna, C. , Soutis, C., Sutton, M.A. .Analysis of adhesively bonded repairs in composites: Damage detection and prognosis. *Composite Structures*, 95, 500-517, 2013.

Proceedings of the 24th UK Conference of the
Association for Computational Mechanics in Engineering
31 March – 01 April 2016, Cardiff University, Cardiff

INDENTATION METHOD TO EVALUATE METAL-TO-METAL ADHESIVE BOND RESIDUAL STRENGTH

***Anil K. Prathuru, Nadimul H. Faisal, Sha Jihan, John A. Steel**

School of Engineering, Robert Gordon University, Garthdee Road, Aberdeen, UK, AB10 7GJ

*a.k.prathuru@rgu.ac.uk

ABSTRACT

The interface strength in an adhesive joint plays a major role in load transfer across bonded joints. However, the presence of defects hinders or deflects the load transmission. In this study, an attempt has been made using the cohesive zone method to study the effect of interfacial strength (or residual strength) on the interfacial crack propagation under indentation contact. Stable and unstable crack growth behaviour have been investigated and the effect of the presence of defects along one of the interfaces has been analysed. It has been concluded that higher interfacial strengths favour unstable crack propagation. The presence of defects does not affect the crack initiation but affects the crack initiation load because of the reduction in the apparent interface length.

Keywords: *adhesive joints; interface defects; finite element (FE); cohesive zone model (CZM); indentation*

1. Introduction

Adhesive joints are being widely implemented in a variety of applications such as aircraft structures, wind turbines and automotive body parts, etc. The failure prediction of adhesive joints has been studied and failure criteria have been established for various geometries and loading conditions. The previous research in this field is mostly based on analytical closed form solutions of stress and displacement fields in the adhesive and hence predict the failure based on stress or strain based criteria. However, these studies can only be used under the assumption that the interface between the adhesive layer and adherends is perfectly bonded and that there exist no defect within the adhesive layer. In the real world manufacturing of the adhesive joints, there exists a possibility of inclusion of defects in the form of air bubbles and foreign materials within the adhesive and improper bonding (Kissing bonds), the presence of oxide layers or the presence of interfacial defects because of improper surface cleaning methodologies. Investigation of the effect of these defects on the strength of the adhesive joint can be carried out either through experimentation or through numerical calculations based on finite element (FE) method. It is apparent that the interface between adhesive and adherends plays an important role in the load transmission through the adhesive joint. However, the isolation of the interface in terms of strength and fracture toughness is a difficult task as the crack propagation along the interface is always accompanied by plastic deformation either in the adhesive or the adherends.

The formation of a cohesive zone ahead of the crack tip and the size of this zone determines the steady state fracture toughness and the adhesive strength of the interface. The estimation of the interface toughness can be carried out through the calculation of the work of adhesion of the adhesive on the adherend material which is estimated to be around 0.1 J/m^2 [1] using the surface free energy of the adhesive and the contact angle of an adhesive droplet on the adherend surface. This estimate assumes a perfect interface without defects and 0^o contact angle. However, in the presence of defects or improper adhesion because of oxide layer formation on the metal surface this value can be lower than the estimated value. In the present study the different interfacial strengths have been represented by a cohesive zone model (CZM) embedded into an outer FE model of the adhesive and the adherends. The CZM models the interface as a series of springs whose stiffness is a function of the normal and tangential displacements. The principal advantage of the CZM is that the stress state at any node is independent of its distance from the crack tip. Moreover, the use of linear elastic fracture mechanics (LEFM) is limited to small-scale yielding conditions where the dissipation of work in the cohesive zone in front of the crack tip is negligible. LEFM breaks down where large scale yield conditions exist as in adhesive joints in front of an interfacial crack [2]. The importance of different CZM parameters has

been studied numerous times. The initial opening stiffness does not have a significant effect on the behaviour of the model. Increasing the critical traction (σ_c^m) increases the crack propagation load and increasing the steady-state toughness increases the overall load carrying capacity of the bonded joint.

In the present investigation, the toughness of the interface (i.e. area of the traction-separation curve) has been maintained constant and the critical traction (σ_c^m) has been varied as fractions of the adhesive material yield strength 'σ_y' (e.g. at 0.25σ_y, 0.5σ_y, 0.75σ_y, σ_y). In addition, interfacial defects were assumed to be along the lower interface. Three crack radii were considered (R = 200 µm, 400 µm, 600 µm) in addition to a joint with a perfectly bonded interface. The crack propagation with respect to indentation depth and the effect of varying the critical strength have been studied. It has been observed that the crack initiation load and depth varied with adhesive thickness and interfacial strength. Also, at lower adhesive thickness and lower interfacial strengths, cracks appeared at both the interfaces.

2. Indentation Simulations

The adherends (aluminium, *Al*) and adhesive have been modelled using an elastic-plastic bi-linear model in ANSYS APDL using PLANE 182 elements. The interfaces have been modelled using CONTACT 172 and TARGET 169 elements. The element size has been maintained at 5 µm in the adhesive to increase the accuracy of the model. A plane strain element formulation has been used along with a two-dimensional (2D) model. The simulation was displacement controlled with a 150 µm vertically downward displacement applied as boundary condition on the indenter (Rockwell B scale of 1.558 mm diameter). The material properties and geometry is shown in Fig. 1. The crack propagation has been analysed at various displacement levels. The lower edge of the lower adherend has been constrained in the Y-direction and the axis of symmetry is as shown in the above figure. The location of the crack along the lower interface is also shown in the Fig. 1.

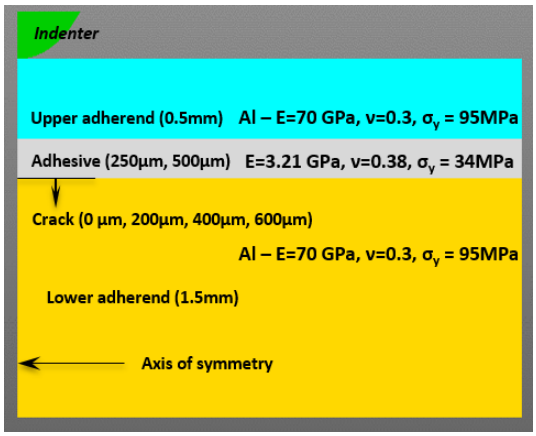

Figure 1: Representation of the model employed

2.1. Cohesive zone model (CZM) formulation

The CZM is governed by a traction-displacement law as shown in Fig. 2. The behaviour follows a triangular law (the area under which gives the steady-state fracture toughness). The behaviour is reversible below the critical stress and the elements retain the stiffness in this zone. After the critical stress is exceeded the behaviour is as indicated by the dotted line (shown in Fig. 2). Once the critical displacement (δ_c^m) has been exceeded, the surfaces become de-bonded and assume frictional contact. The mixed-mode displacement is calculated as a root-square value of the normal and tangential displacements. The initiation of a crack or delamination is tracked using a damage parameter and the stiffness is expressed as a function of this parameter so as to incorporate irreversible damage to the contact pair after the stress exceeds the corresponding critical value.

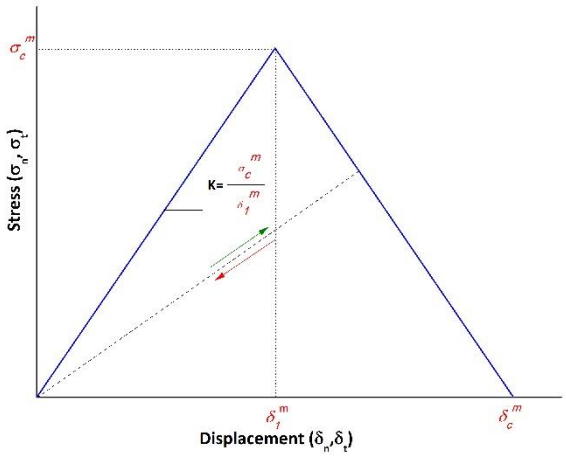

Figure 2: Traction-separation law of the CZM

The mixed-mode stress is given by Equation (1):

$$P_m = K_m U_m (1-d_m) \tag{1}$$

and the fracture criterion is given by Equation (2):

$$\frac{G_n}{G_{nc}} + \frac{G_t}{G_{tc}} = 1 \tag{2}$$

where 'd_m' is the damage parameter and varies between 0 and 1 between δ_1^m and δ_c^m respectively, 'K_m' is the initial stiffness of the interface, 'U_m' is the mixed mode displacement 'G_n', 'G_t' are the normal and tangential energy release rates and 'G_{nc}' and 'G_{tc}' are the critical values. As can be seen, the traction-displacement relation is represented by a triangle, the area of which is the steady-state toughness of the interface the value of which depends on the mode-mixity and the loading nature. Parameter δ_c^m represents the critical mixed-mode displacement beyond which the crack opens. Parameter σ_c^m represents the critical stress. The above parameters are for a mixed-mode cohesive law and are suitable for mixed-mode loading conditions. The Table 1 shows the CZM parameters employed for simulations.

Table 1: CZM parameters employed in the simulations

Parameter set no.	Mode-I critical stress (σ_n)	Mode-II critical stress (σ_t)	Mode-I critical displacement (δ_n)	Mode-II critical displacement (δ_t)
1	34	0.0005	34	0.0005
2	17	0.001	17	0.001
3	25.5	0.00067	25.5	0.00067
4	8.5	0.002	8.5	0.002

3. Results and Discussion

The variation of the crack initiation load with various interfacial strengths for an adhesive joint with no defect has been shown in Fig. 3(a). This critical initiation load increases with increasing interfacial strength and for the interface with no defect and interface with 200 µm long defect the critical initiation loads are very similar. However, for the interfaces with 400 µm and 600 µm long defects, the critical initiation loads are lower. This might be because of two reasons: (a) due to the appearance of crack tip stress concentration leading to premature failure, and/or (b) due to the reduction in overall interfacial load carrying capability because of the reduced interfacial bond length. In the present case the latter seems to be more applicable as there does not seem to be any stress concentration at the tip of the defect. This is because of the existence of the crack within the highly compressed zone underneath the indenter and so the initiation of the crack does not happen near the tip of the defect. The decrease in the critical load with the decreasing interfacial strength is also expected. The Fig. 3(b) shows the variation of the normalised (with respect to load-displacement data from joint with no interfacial bonding 'P_o') load with the normalised (with respect to total interface length 'L') crack length. The Fig. 3(b) shows that

the crack propagation behaviour changes from stable to unstable growth as the interface strength increases. As can be seen, the joint with interface strength of σ_y (yield strength of the adhesive) exhibits an unstable crack growth after a particular crack length where the load drops suddenly. Moreover, the crack initiation load is similar for interfaces with interfacial strengths $0.5\sigma_y$ and $0.75\sigma_y$. However, after the crack initiation, the crack extension in the latter case ($0.75\sigma_y$) takes place under an almost constant load where as for the former ($0.5\sigma_y$) the load increases. This observed behaviour at higher interface strengths is because of the accumulation of the energy within the adhesive layer and the interface with increasing indentation load and the sudden release of this energy beyond a critical load leading to crack extension under constant load. The area under the load-displacement curve can be used as a measure of the indentation energy. Also, the slope of the load-displacement curve (Fig. 3) after the crack initiation gives a fair idea of the crack propagation scheme. It has also been found that the joints with lower interfacial strengths exhibit a gentler slope of the load curve after crack initiation.

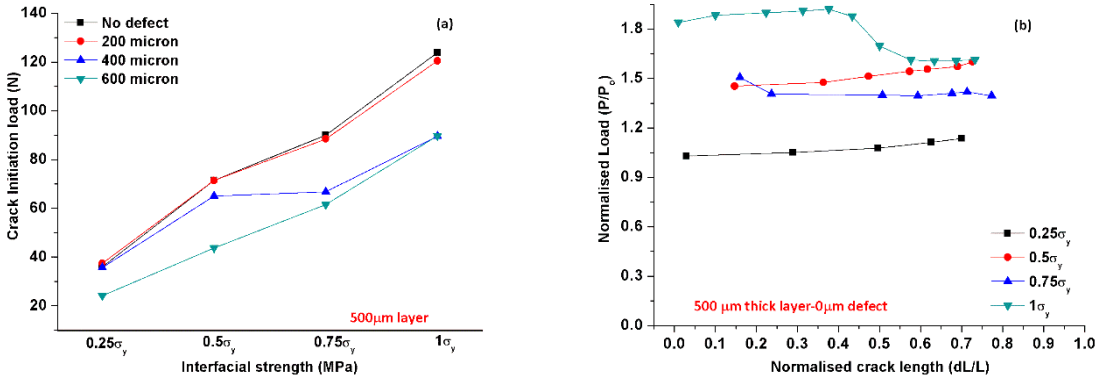

Figure 3: (a) Variation of crack initiation load with various interfacial strengths, and (b) various defects and variation of normalised load with normalised crack length

4. Conclusions and Future Work

a. Indentation based contact mechanics can be used as a testing method to evaluate the strengths (or residual strengths) of adhesively bonded joints of various adhesive layer thicknesses. The crack initiation load decreases with decreasing interfacial strength.
b. The effect of the presence defects (at the adhesive bond interface) on the load carrying capability can be seen as a reduction in the overall interfacial load carrying capability. This does not affect the crack initiation or propagation behaviour because of the presence of the crack within the high compressive stress zone (at indentation sub-surface zone). The effect of cracks situated away from this zone will be part of ongoing investigations.
c. The adhesive bond interfaces with higher bond strengths exhibit unstable crack growth behaviour and those with lower bond strengths exhibit stable crack growth. This is because of the higher crack length initiation loads at higher interfacial strengths leading to accumulation of strain energy in the bulk of the adhesive and adherends thus increasing the energy available for crack propagation.

References

[1] N. Badwe, R. Mahajan, K. Sieradzki. Interfacial fracture strength and toughness of copper/epoxy-resin interfaces. *Acta Materialia*, 103, 512-518, 2016.

[2] P. Feraren and H. M. Jensen, Cohesive zone modelling of interface fracture near flaws in adhesive joints. *Engineering Fracture Mechanics*, 71, 2125-2142, 2004.

Geomechanics III

Proceedings of the 24th UK Conference of the
Association for Computational Mechanics in Engineering
31 March – 01 April 2016, Cardiff University, Cardiff

MODELLING FLUID FLOWS THROUGH MULTIPLE DISCRETE FRACTURES USING FINITE ELEMENTS FOR GROUND ENERGY PROBLEMS

***Richard J. Sandford[1] and Hywel R. Thomas[1]**

[1]School of Engineering, Cardiff University, CF24 3AA

*SandfordR@Cardiff.ac.uk

ABSTRACT

Many geo-energy and geo-environmental problems require reliable and accurate predictions of fluid flow through fractured/faulted media. Examples of such problems include the extraction of methane from shale, the sequestration of carbon dioxide in coal beds and the circulation of water through faulted rock as part of an enhanced geothermal system (EGS). Computational modelling is important for the systematic assessment of the feasibility, reliability and performance of these technologies. Central to this computational modelling are the procedures used to account for the fluid flow through the fractures and its transfer in/out of the surrounding bulk material. In the following, a computational approach to modelling fluid flow through fractures is summarised, with an example simulation considered to demonstrate the influence of fracture aperture on the flow characteristics.

Keywords: *fracture; flow; discrete; finite elements; geo-energy*

1. Introduction

Based the work of Thomas and He [1], and following many subsequent developments, the computational code, COMPASS, has been developed at Cardiff University for the assessment of transport phenomena in deformable partially saturated media. COMPASS assumes C_0 continuity in the spatial domain via the use of finite elements and makes use of a finite difference scheme to discretise the underlying equations in time. While previous work has been undertaken using the code to model discretely fractured media [2, 3], this involved meshing both the interior of the fractures and the surrounding continuum. This approach is appropriate for problems involving a small number (<10) of large faults, but for more complex fracture networks it is impractical owing to the need to use a highly refined mesh for each fracture and the consequential high computational cost. Further, it does not lead naturally to an extension to consider fracture propagation.

An alternative approach is to consider the fractures as entities of one spatial dimension less than that of the overall continuum (i.e. as one-dimensional entities in a two-dimensional continuum and two-dimensional entities in a three-dimensional continuum), with the flow considered to be uniform across the aperture of the fracture. In the following, developments undertaken to implement such an approach to discrete fracture flow modelling in a finite element context are summarised.

2. Governing Equations, Fracture and Bulk Flow Coupling and Discretisation

The equations governing flow through the bulk material are those of continuity and Darcy's law, given respectively (using tensor notation) as:

$$\frac{\partial(\rho v_i)}{\partial x_i} + \rho q_{bulk} + \frac{\partial(\rho S n)}{\partial t} = 0 \tag{1}$$

$$v_i = -\frac{k_{ij}}{\mu}\frac{\partial p}{\partial x_j} \tag{2}$$

where ρ is the fluid density, v_i is the fluid velocity (in the global Cartesian coordinates, x_i), q_{bulk} is

the fluid flux per unit volume, S is the degree of saturation, n is the porosity, k_{ij} is the intrinsic permeability tensor, μ is the isotropic (scalar) viscosity and p is the fluid pressure. The fully saturated case is considered here; $S = 1$. Applying Galerkin's weighted residual method and introducing a finite element basis gives the following discrete form of the bulk transport equations:

$$\bar{F}_a = \bar{K}_{ab} P_b \tag{3}$$

where:

$$\bar{K}_{ab} = \int_{\Omega_\mathrm{b}} \frac{\partial N^b}{\partial x_j} \frac{\rho k_{ij}}{\mu} \frac{\partial N^a}{\partial x_i} d\Omega \tag{4}$$

$$\bar{F}_a = -\int_{\Gamma_{\mathrm{ext,b}}} \rho v_{ne} N_a \, d\Gamma + \int_{\Gamma_\mathrm{f}} \rho [\![v_n]\!] N_a \, d\Gamma - \int_{\Omega_b} \rho q_{bulk} N_a d\Omega - \int_{\Omega_\mathrm{b}} \frac{\partial (n\rho)}{\partial t} N_a d\Omega \tag{5}$$

Here, Ω_b is the spatial domain of the bulk material, $\Gamma_{\mathrm{ext,b}}$ is the external boundary of Ω_b, Γ_f is the boundary of a fracture within Ω_b, P_i are the nodal pressures, N_i are the shape functions, v_{ne} is the normal component of outflow on $\Gamma_{\mathrm{ext,b}}$ and $[\![v_n]\!]$ is the difference in the normal component of velocity across the fracture. Similar equations govern the flow through the fractures:

$$\frac{\partial (\rho \tilde{v}_i)}{\partial \tilde{x}_i} + \frac{\partial \rho}{\partial t} = 0 \tag{6}$$

$$\tilde{v}_i = -\tilde{k}_{ij} \frac{\partial p}{\partial \tilde{x}_j} \tag{7}$$

where $\tilde{v}_i$ is the fluid velocity in the local Cartesian coordinates, $\tilde{x}_i$, and $\tilde{k}_{ij}$ is the local permeability tensor. For a problem in two dimensions $(i, j = 1,2)$ with the $\tilde{x}_1$ axis tangential to the fracture, the restriction to one-dimensional flow through the fracture is succinctly made by setting the $\tilde{k}_{ij} = {b^2}/{12\mu}$ for $i = j = 1$, where b is the fracture aperture (in accordance with lubrication theory) and $\tilde{k}_{ij} = 0$ otherwise. Again, applying Galerkin's weighted residual method and introducing a finite element basis gives:

$$F^a = K_{ab} P^b \tag{8}$$

where:

$$K_{ab} = \int_{\Omega_\mathrm{f}} \frac{\partial N^a}{\partial \tilde{x}_i} \rho \tilde{k}_{ij} \frac{\partial N^b}{\partial \tilde{x}_j} d\Omega \tag{9}$$

$$F^a = -\int_{\Gamma_\mathrm{f}} \rho [\![v_n]\!] N_a \, d\Gamma - \int_{\Omega_\mathrm{f}} \frac{\partial \rho}{\partial t} N^a d\Omega \tag{10}$$

Here, Ω_f is the spatial domain of the fracture (an area in two-dimensions, a volume in three-dimensions). Owing the restriction placed on the form of $\tilde{k}_{ij}$, the integrals over the spatial domain of the fracture, Ω_f, reduce to integration over Γ_f, so that for a two-dimensional problem:

$$K_{ab} = \int_{\Gamma_\mathrm{f}} \frac{\partial N^a}{\partial \tilde{x}_1} \rho \tilde{k}_{11} \frac{\partial N^b}{\partial \tilde{x}_1} b d\Gamma \tag{11}$$

$$F^a = -\int_{\Gamma_\mathrm{f}} \rho [\![v_n]\!] N_a \, d\Gamma - \int_{\Gamma_\mathrm{f}} \frac{\partial \rho}{\partial t} b \, N^a d\Gamma \tag{12}$$

Elimination of the term: $\int_{\Gamma_\mathrm{f}} \rho [\![v_n]\!] N_a \, d\Gamma$, allows the bulk and fracture flows to be readily coupled together. For brevity in the above, flow through the fractures at their intersection with $\Gamma_{\mathrm{ext,b}}$ has been neglected.

3. Mesh Generation

The approach considered here does not involve enrichment of the finite element basis to allow fractures to bisect elements (as is the case in X-FEM, for example). Instead, the fractures are required

to align to element boundaries. It is often reported that generating meshes to align to internal fracture boundaries is problematic (*e.g.* [4]). As such, we elaborate briefly on our approach to mesh generation. Figure 1a displays an initial two-dimensional domain, the boundary of which is succinctly defined by the function $f_\alpha = 0$, where $f_\alpha = max(f_1 \dots f_N)$ and $f_1 = 0, \dots f_N = 0$ are functions defining the lines (in two dimensions) or planes (in three dimensions) that form the boundaries of the domain. The introduction of a fracture (Figure 1b), defined by the function $f_I = 0$, subdivides the initial domain into two subdomains. These two subdomains are succinctly defined by augmenting the definition of f_α to $max(f_1 \dots f_N, f_I) = 0$ and introducing the second function: $f_\beta = max(f_1 \dots f_N, -f_I) = 0$. Repeating this approach for all fractures gives M functions of the form $f_\alpha = 0, f_\beta = 0 \dots f_M = 0$, each defining one subdomain formed from the intersections of all the fractures cutting the domain. With the subdomains defined in this manner, it is a straightforward task to deduce the data needed to pass to third-party mesh generation software to obtain the mesh itself. For example, the software GiD [5] has been used here to obtain the mesh shown in Figure 1c. This approach can also readily be used in three-dimensions.

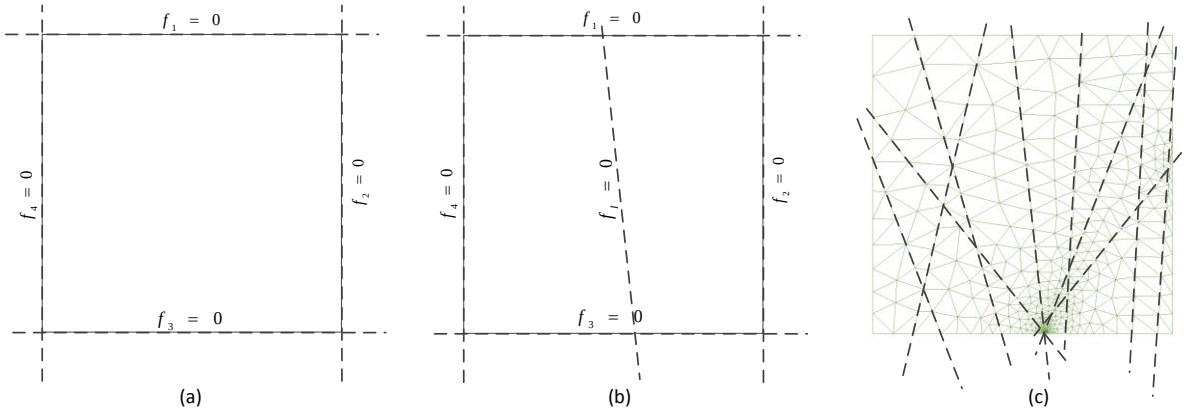

Figure 1: Mesh generation strategy

4. Simulation Results

The finite element formulation described in the previous sections has been implemented in a numerical code. Sample simulation results using this code are shown in Figure 2. The sample problem consists of a two-dimensional (plane strain) square domain of 1km side length. The mesh shown in Figure 1c was used for this simulation, together with the fracture network indicated by the dashed lines on this figure. The intrinsic permeability of the bulk material is 10^{-7}m^2 and the viscosity of the fluid is 10^{-3}Pas with four values for the fracture aperture considered (0.5mm, 1mm, 2mm and 5mm). Fluid is injected at a rate of $0.001\text{m}^2/\text{s}$ at the origin with outflow permitted at the point labelled, A. Velocity vectors obtained after 1 hour of flow through the domain are shown in the figure (the velocity scale of the plots is m/s). Comparison between the figures reveals that for the 0.5mm case (Figure 2a) the flow occurs principally through the bulk, with very minimal preferential flow through the fracture network. For the 1mm case (Figure 2b), the flow through the fracture is more pronounced, while flow through the fractures dominates for the 2mm case (Figure 2c). For the 5mm case (Figure 2d), the flow is almost exclusively through the fracture network with negligible flow through the bulk material. This sample simulation therefore provides an indication of the relative importance of fracture aperture on the flow characteristics of a given fractured rock mass.

5. Conclusions and further work

A finite element formulation for flow through a fractured body is described, accounting for the fluid exchange with the bulk material. Extensions are currently underway to account for the multi-component unsaturated case, and to analyse convective flows. These extensions build upon the modelling framework outlined here.

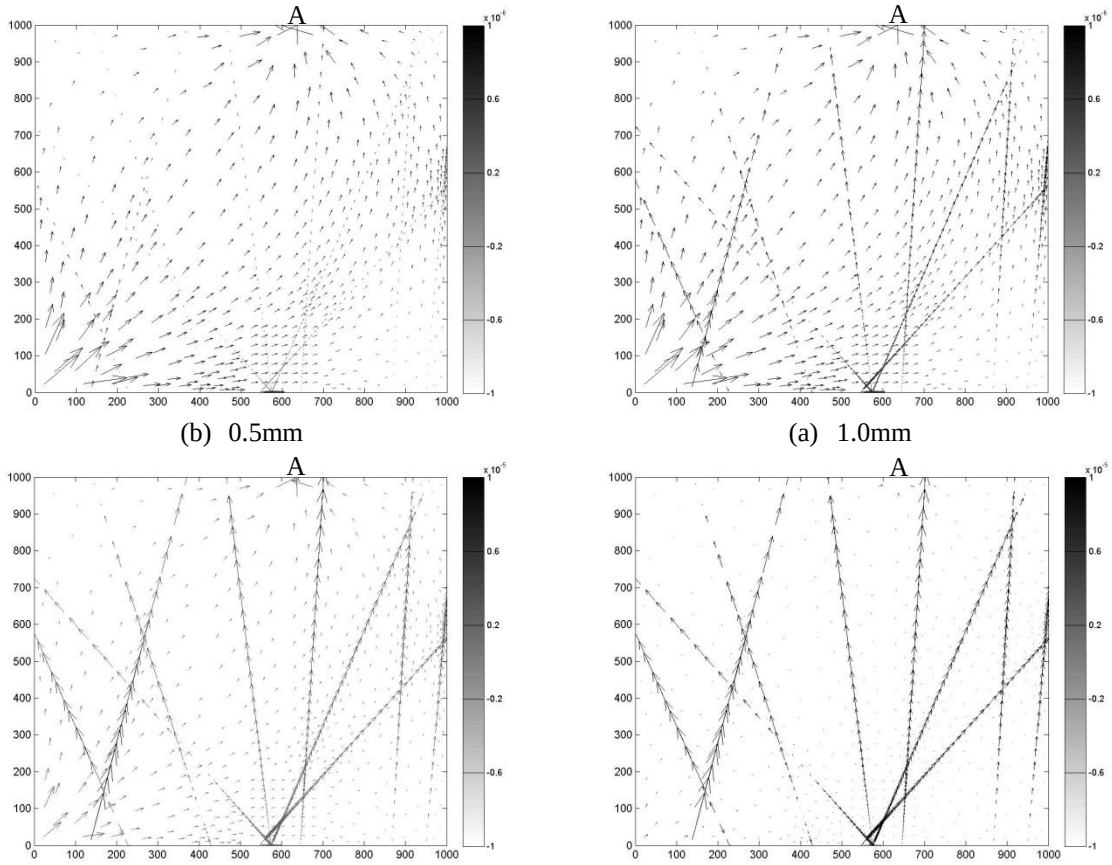

(b) 0.5mm (a) 1.0mm

(d) 2.0mm (c) 5.0mm

Figure 2: Velocity vectors for various fracture apertures

Acknowledgements

The work described here has been carried out as part of the GRC's Seren project, which is funded by the Welsh European Funding Office (WEFO). The financial support is gratefully acknowledged.

References

[1] H. R. Thomas and Y. He. Analysis of Coupled, Heat, Moisture and Air Transfer in a Deformable Unsaturated Soil. *Géotechnique*, 45:4, 677-689, 1995.

[2] P. J. Vardon, H. R. Thomas and P. J. Cleall. Three-dimensional behaviour of a prototype radioactive waste repository in fractured granite rock. *Can. Geotech. J.* 51, 246-259, 2014.

[3] P. J. Vardon. A three-dimensional numerical investigation of the thermo-hydro-mechanical behaviour of a large-scale prototype repository. *PhD thesis, Cardiff University*, 2009.

[4] A. Puoya. A Finite Element Method for Modeling Coupled Flow and Deformation in Porous Fractured Media. *Int. J. Numer. Anal. Meth. Geomech*. 39, 1836-1852, 2015.

[5] GiD The personal pre- and post- processor *URL: http://gid.cimne.upc.es/* [Accessed: 2016]

Development of a High Performance Computing Approach for Studying the Coupled Behaviour of Porous Media

***Manhui Wang [1], Lee Hosking [1], Shakil Masum [1] and Hywel Thomas [1]**

[1]Geoenvironmental Research Centre, School of Engineering, Cardiff University,
Queen's Buildings, The Parade, Cardiff CF24 3AA, United Kingdom

*wangm9@cardiff.ac.uk

ABSTRACT

High-performance computing (HPC) techniques, especially parallel computing, can be used to significantly reduce the computational time in very large scale simulations. In this work, the popular HPC hardware and parallel programming tools are reviewed and discussed. Then a hybrid Message Passing Interface/Open Multi-Processing (ie, MPI/OpenMP) model is proposed to parallelise the numerical code COMPASS, which adopts a coupled thermal/hydraulic/chemical/mechanical (THCM) approach to model the behaviour of saturated/unsaturated media. Various optimisation techniques have also been employed to achieve better performance. Together with code optimisation, the parallel COMPASS has shown significant performance improvement, which has been seen for an example application in carbon dioxide sequestration.

Keywords: *high performance computing; parallel computing; THCM; COMPASS*

1. Introduction

Geoenvironmental problems, such as contaminated land, landfills, waste disposal, and carbon dioxide sequestration, are generally based upon flow conditions through soils and/or chemical reactions. For example, the flow of carbon dioxide through rocks/soils and the associated chemical processes are important factors controlling the capacity and long term stability in carbon dioxide sequestration. These problems are often complex in respect to both the processes occurring and their geometry and scale. In recent years, a coupled thermal/hydraulic/chemical/mechanical (THCM) approach to model the behaviour of saturated/unsaturated media has been developed at the Geoenviromental Reseach Cenre (GRC) at Cardiff University [1-4]. The model has been implemented in the numerical computer code COMPASS (COde for Modelling PArtially Saturated Soils), and used to simulate a number of problems. The finite element method is employed for the spatial discretisation, and a finite difference time stepping scheme is implemented for temporal discretisation.

As the scale and complexity in geoenergy applications increases, the demands for computational resources increase dramatically and eventually become time-limiting for very large simulation problems. Recent developments of high-performance computing (HPC) provide great advantages to overcome these large computational demands and time-limiting issues. Parallel computing on HPC platforms can significantly reduce the computational time. It is worthwhile to invest time and efforts to develop numerical modelling code that run on a HPC system. In this paper, the authors briefly demonstrate the development of parallel version of the GRC's in-house numerical modelling code, COMPASS, with cutting-edge HPC technologies. It aims to enable the integrated parallel COMPASS code to run on supercomputers efficiently, reliably and quickly.

2. HPC hardware and parallel programming tools

The November 2015 Top 500 ranking of world supercomputers [5] shows that more than 80% of HPC machines are classified as having a cluster architecture. HPC clusters usually consist of a large number of distributed computer nodes linked through high performance networks. A well-known transport mechanism between nodes is message passing, which was adopted by many parallel

programming tools, such as Theoretical Chemistry Group Message Passing System (TCGMSG) [6], Parallel Virtual Machine (PVM) [7], and Message Passing Interface (MPI) [8]. With a number of features that provide both convenience and high performance communication, MPI is the most widely used model, and has become the de facto standard for incorporating parallelism into scientific and other application codes.

Table 1: Comparison of features between MPI and OpenMP

MPI	OpenMP
Shared or distributed memory architectures	Only shared memory architecture
Requires an MPI library(MPICH, Intel MPI etc)	Doesn't need other library
No specific requirements for compiler	Requires a compiler that supports OpenMP
Message based	Directive based
Both process and thread based approach	Only thread based parallelism
Overhead for creating process is one time	Threads can be created and joined for particular task which add overhead
There are overheads associated with transferring message between processes	No such overheads, as thread can share variables
Process in MPI has private variable only, no shared variable	Thread can have both private and shared variables
Requires more programming changes to go from serial to parallel version	Directives can be added incrementally, less changes from serial to parallel version
Rich functionality, flexible, harder to program	Easier to program, data racing bug

In a HPC cluster, each computer node itself is a symmetric multiprocessor (SMP) system, on which memory is shared across the processors. Open Multi-Processing (OpenMP) [9] has provided a very rich and flexible programming model for such shared memory systems. Now most computers, even desktops/laptops, have multi-core CPUs, which can have access to the common memory on the machine. This computer architecture provides great convenience for parallelism, and OpenMP becomes one of the most popular programming models as it is easy to implement. Table 1 lists the major features of MPI and OpenMP. In order to achieve scalable performance, many application programs typically maintain and manipulate global data structures that are distributed between the memory managed by individual processors. The application programming interfaces (API) that provide such functionality include the Global Arrays (GA) toolkit [10], Distributed Data Interface (DDI) [11], and Parallel Programming Interface for Distributed Data (PPIDD) [12].

With the development of new accelerator technologies, general-purpose graphical processing units (GPGPUs) now can be used for parallel computing [13]. CUDA and OpenCL are most widely used GPU parallel programming tools. The potential performance improvement is enormous if the algorithms can take advantage of the GPU's programming model and do most of their computation on the GPU. There are cases of over a 100X performance improvement for some codes running on GPUs relative to CPUs. But one of the critical limitations is that you have to rewrite the code for the GPU. It is particularly hard to port existing complex code for GPU parallel computing.

Basing on the above analysis and discussions, it is a good option to develop parallel implementation with both MPI and OpenMP for currently existing large packages, in order to take full advantage of modern HPC facilities available.

3. Parallel strategies for COMPASS

As the popular HPC clusters have the hybrid architecture, where memory is distributed across the computer nodes but shared within the node, a hybrid MPI/OpenMP model is proposed for parallel implementation for the numerical code COMPASS. The hybrid model can take advantage of the merits of both MPI and OpenMP. MPI facilitates efficient inter-node reductions and transferring of complex data structures, and it helps the application scale across multiple SMP nodes in the HPC cluster. OpenMP manages the workload on each SMP node, and makes more efficient use of the shared memory. By spawning several OpenMP threads for each MPI process, less replicated data and less memory are required due to the decrease of the total number of MPI processes. Within each SMP node where only one MPI process is allocated, the synchronization is implicit, which eliminates much of the overhead associated with message passing.

In COMPASS, the majority of the computation time is spent in two sections: *system matrix build* and *solver*. The *system matrix build* process is to form the matrices for each element, and then assemble them into global matrix. In this section, coarse-grained domain decomposition can be employed as there is no communication in the matrix forming process for each element. Only at the end are all element matrices synchronised and added together. The *solver* is to provide the solution for the equations involved. In general, there are two types of solvers, direct and iterative [14]. A direct solver, such as LU decomposition, is very robust and efficient, but for large and complex systems, the memory required may become a bottleneck. Iterative solvers require lower memory, which is crucial for large scale simulations. Among these iterative solvers, the conjugate gradient algorithm is one of the most effective iterative methods.

For LU decomposition, fine-grained parallelism is achieved during the forward and back substitution. In conjugate gradient algorithms, vector-vector and matrix-vector operations are heavily involved. For vector-vector operations, it is not suitable for MPI parallelism as the communication takes longer than the calculation itself [3]. However, OpenMP can take over them as there is no such communication. Matrix-vector multiplication is parallelised with MPI. In addition, substantial code optimisation is carried out to improve the performance further. For some frequently used code segments, memory and file input/output operations are carefully examined.

4. Application simulation and initial performance

The development of the parallel code is demonstrated by simulating the injection of carbon dioxide in a coal seam associated carbon capture and sequestration (CCS) technologies. The simulation considers carbon dioxide injection into a 500 m radius, two-dimensional, axisymmetric, hypothetically isolated coal bed. This example has a very large domain, which is discretised by about 20,000 triangle elements. Figure 1 shows the total wall time for system matrix build and solver. The

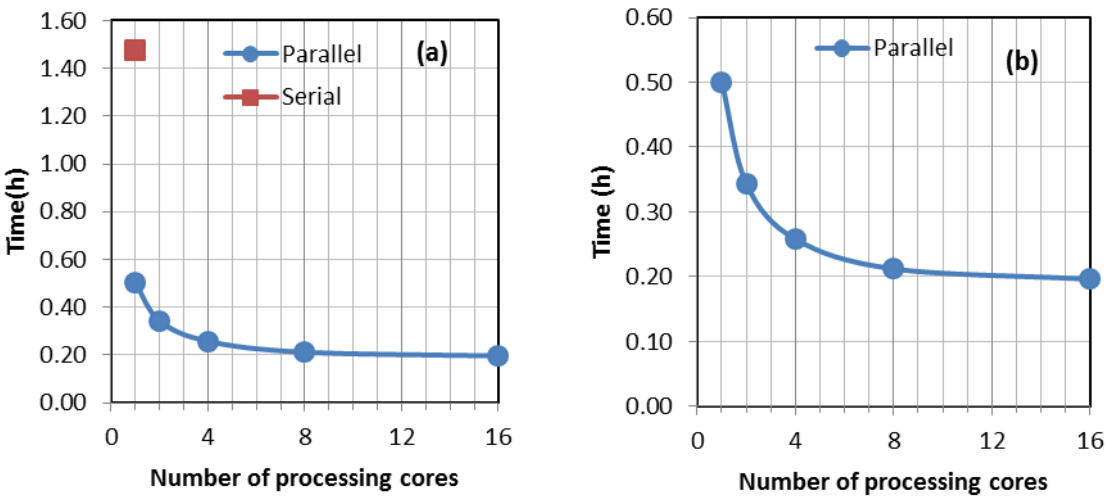

Figure 1: Total wall time of system matrix build and solver

wall time for parallel and serial modes is displayed in Figure 1(a), while the parallel results are displayed in a magnified mode in Figure 1(b). The serial code, which is not optimised, is three times slower compared with the parallel program with 1 core. Together with code optimisation, the parallel code has achieved a maximum 7.5 times speed-up compared to the non-optimised serial one.

5. Conclusions

This work here has reviewed and discussed the popular HPC hardware and parallel programming tools. Then a hybrid MPI/OpenMP model is proposed to parallelise the numerical code COMPASS. Together with code optimisation, a significant performance improvement has been seen for an example application in carbon dioxide sequestration. The developments presented in this paper will facilitate more efficient computational research in the study of carbon sequestration and other large scale geoenvironmental applications.

Acknowledgements

The work described here has been carried out as part of GRC's Seren project, which is funded by the Welsh European Funding Office (WEFO). The financial support is gratefully acknowledged. This work has been performed using the computational facilities of the Advanced Research Computing@Cardiff (ARCCA) Division, Cardiff University.

References

[1] H. R. Thomas and Y. He, A coupled heat-moisture transfer theory for deformable unsaturated soil and its algorithmic implementation, *International Journal for Numerical Methods in Engineering*, 40(18), 3421–3441, 1997.

[2] S. C. Seetharam, *An investigation of the thermro/hydro/chemical/mechanical behaviour of unsaturated soils*, Ph.D. Thesis, Cardiff University, Wales, UK, 2003.

[3] P. J. Vardon, *A three-dimensional numerical investigation of the thermo-hydro-mechanical behaviour of a large-scale prototype repository*, Ph.D. Thesis, Cardiff University, Wales, UK, 2009.

[4] S. A. Masum, *Modelling of reactive gas transport in unsaturated soil. A coupled thermo-hydro-chemical-mechanical approach*, PhD thesis, Cardiff University, Wales, UK, 2012.

[5] Top 500 supercomputer site, http://www.top500.org/.

[6] R. J. Harrison, Portable tools and applications for parallel computers, *International Journal of Quantum Chemistry*, 40, 847-863, 1991.

[7] PVM website, http://www.csm.ornl.gov/pvm/.

[8] Message Passing Interface (MPI), http://www.mpi-forum.org/.

[9] OpenMP Specifications, http://openmp.org/wp/openmp-specifications/.

[10] J. Nieplocha, B. Palmer, V. Tipparaju, M. Krishnan, H. Trease, E. Aprà, Advances, Applications and Performance of the Global Arrays Shared Memory Programming Toolkit, *International Journal of High Performance Computing Applications*, 20, 203-231, 2006.

[11] G. D. Fletcher, M. W. Schmidt, B. M. Bode, M. S. Gordon, The Distributed Data Interface in GAMESS, *Computer Physics Communications*, 128, 190-200, 2000.

[12] M. Wang, A. J. May and P. J. Knowles, Parallel programming interface for distributed data, *Computer Physics Communications*, 180(12), 2673-2679, 2009.

[13] S. Mittal and J. Vetter, A Survey of CPU-GPU Heterogeneous Computing Techniques, *ACM Computing Surveys*, 47(4), Article 69, 2015.

[14] R. Barrett, M. Berry, T. Chan, J. Demmel, J. Donato, L. Dongraa, V. Eijkhout, R. Pozo, C. Romine, H. Van derVorst, *Templates For the Solution of Linear Systems: Building Blocks For Iterative Methods*, John Wiley Press, New York, 1995.

Thermo-osmosis in saturated shale

***R. Zagorščak and H.R. Thomas**

Geoenvironmental Research Centre (GRC), School of Engineering, Cardiff University, The Queen's Buildings, The Parade, Cardiff, CF24 3AA

*ZagorscakR@Cardiff.ac.uk

ABSTRACT

An investigation of thermo-osmosis in a saturated and chemically active rock such as shale is presented. The model presented is based on an existing coupled thermal, hydraulic and mechanical model (THM) for unsaturated soils. A simplified form of a coupled THM model for saturated porous medium is developed which considers the effect of solid-fluid thermal expansion and the effects of thermal osmosis in hydraulic behaviour. An example problem dealing with pore water pressure development in saturated shale rock surrounding the bentonite buffer installed around high-level nuclear waste canister emitting heat is presented. It is demonstrated that the heat input from the waste canister can affect the pore water pressure evolution in the shale. In particular, under the conditions considered, it is shown that thermally driven liquid water flow due to thermal osmosis contributes to the convective transport of dissolved species.

Keywords: *saturated shale, hydraulic behaviour, thermal osmosis, coupled modelling*

1. Introduction

The safe storage of high-level radioactive waste is a subject of major strategic international importance. The disposal of such waste in geological repositories relies on a multi-barrier system consisting of the engineered materials placed within the repository and the natural barrier system which includes the repository rock and its surrounding subsurface environment. In the short term the heat generated by the waste will induce elevated temperatures in the engineered barrier system and the host rock [1].

During the very long lifespan of a geologic repository, the performance of the multi-barrier system is affected by a series of complex and coupled processes. Osmosis is one of the processes identified to affect the fluid pressure around the nuclear waste canisters [2]. While electro- and chemo-osmosis have been extensively identified and described in clay-rich media, a flow of water driven by temperature gradient, i.e. thermal osmosis has received less attention [2]. It is well known that an increase in temperature causes thermal expansion of mineral solids and pore water usually generating volume and effective stress changes in saturated soils [3]. The lower the hydraulic conductivity of the porous medium, the longer the time required for this pore water pressure to dissipate. However, it has been shown that in low porosity and chemically active porous media, inclusion of thermal osmosis provides further insights into pressure distribution and flow in shale layers [2].

In this work, the theoretical development of hydraulic behaviour with an emphasis on thermal osmosis is presented and implemented within an existing thermal, hydraulic and mechanical (THM) numerical model [4]. In order to assess the impact of temperature increase on pore water pressure evolution in the shale, a numerical investigation has been conducted with and without including thermo-osmotic effects.

2. Constitutive model

A constitutive model considering thermal expansion relationships, thermal osmosis and associated parameters of consolidation is implemented within an existing THM numerical model (COMPASS) developed at Cardiff University [5].

The governing equation of water flow is given by:

$$\frac{\partial}{\partial t}(\rho_l \theta_l \delta V) = -\delta V \nabla(\rho_l v_l) \tag{1}$$

where t, ρ, θ, δV and v are the time, density, volumetric water content, incremental volume of soil and the velocity of the liquid, respectively [5]. The subscript l stands for liquid. In this model, soil is deformable and the liquid phase is presented as a function of both temperature and pressure while the solid phase is presented solely as a function of temperature since the solid grains are assumed to be incompressible. Hydraulic, gravitational and thermo-osmosis potentials are considered as the mechanisms of water flow. Thermo-osmotic conductivity can be presented as a function of hydraulic conductivity:

$$k_T = k_l \frac{\Delta H}{\rho_l g T} \tag{2}$$

where ΔH is the mean value of excess enthalpy resulting from fluid-solid interactions, k_T and k_l are the thermo-osmotic conductivity and saturated hydraulic conductivity, respectively [2].

Expanding the equation 1 for a fully saturated soil with respect to its partial derivatives and using an incremental volume as a summation of the void volume and solid volume, yields:

$$\rho_l[n\beta_l + m_v]\frac{\partial u_l}{\partial t} + \rho_l[n(\beta_s^{'} - \beta_l^{'}) + \alpha]\frac{\partial T}{\partial t} = \nabla\left(\frac{k_l}{g}\nabla u_l\right) + \nabla(k_T \rho_l \nabla T) + \nabla(\rho_l \nabla z) \tag{3}$$

where n, β, β', m_v, u, α and T are the porosity, water compressibility, thermal expansion coefficient, compressibility of soil, pore water pressure, thermal expansion coefficient of the soil structure and temperature, respectively. The subscript s stands for solid.

The formulation for heat transfer is based upon the principle of conservation of energy where conduction is the primary mechanism of heat transfer [5]. The model described in this paper is a fully coupled THM model, which for the theoretical formulation presented has been tested against an analytical benchmark and a heating experiment [4].

3. Computational domain and material parameters

The properties and the stress state of the shale rock are assumed to be homogeneous for the considered area of investigation. The internal boundary of the modelled domain corresponds to the external radius of the engineered material, i.e. bentonite buffer which is placed 1.14 m from the axis of symmetry while the external boundary was placed to a sufficient distance of 200 m so the influence on the computation becomes minimal (Fig. 1). The domain was discretised into 400 quadrilateral elements with the mesh concentrated towards the heat source. A maximum time-step of 2 years was considered and the duration of the simulation was 10,000 years. The predicted temperature evolution over time at the bentonite buffer-shale interface, based on work of Lawrence Berkley International Laboratory – Earth Sciences Division [7], was prescribed at the internal boundary where the temperature slowly increases from initial ground temperature up to a temperature of 354 K over 65 years and then slowly and non-linearly decreases to 326 K by the end of the simulation. An axisymmetric analysis was performed.

Boundary Conditions	*Initial Conditions*	*Boundary Conditions*
$\partial u_l/\partial x = 0$ $T = T_{imposed}$	$u_l = 5$ *MPa* $T = 298$ *K*	$u_l = 5$ *MPa* $T = 298$ *K*

Figure 1: Schematic of the initial and boundary conditions

The parameters governing the thermal and hydraulic behaviour in shale were collected and established from a literature synthesis and are presented in Table 1 [2][3][6][8]. Gonçalvès et al. [2] reported that depending on the electro-chemical properties of the porous media, the thermo-osmotic conductivity for shale is between 10^{-10} and 10^{-15} m^2/sK. Hence, a value of $5x10^{-13}$ m^2/sK was adopted for this investigation.

Table 1: Material parameters

Material Parameter	**Value**
Porosity [2]	0.1
Solid density [2]	2600 kg/m^3
Thermo-osmotic conductivity [2]	$5x10^{-13}$ m^2/sK
Thermal conductivity [3]	1.5 W/mK
Hydraulic conductivity [6]	$1x10^{-13}$ m/s
Solid volumetric expansion coefficient [8]	$1.8x10^{-5}$ 1/K
Water volumetric expansion coefficient [8]	$3.0x10^{-4}$ 1/K
Water compressibility [8]	$3.0x10^{-10}$ 1/Pa
Soil compressibility [8]	$9x10^{-10}$ 1/Pa

4. Numerical results

The major heat-emitting phase from the radioactive nuclear waste is approximated to last about 10,000 years [5]. To investigate how osmotic flow modifies spatial and temporal pore water pressure field around a high-level waste, a case considering only thermal expansion of the shale constituents was compared with a case where thermo-osmotic phenomenon is included. The time evolution of the temperature can be seen in Figure 2a for different distances from the heat source. Due to the low thermal conductivity of the shale, slow heat propagation around the heat source leads to a maximum temperature difference of 15 °C between the studied locations within the domain, i.e. 2 m and 10 m from the buffer-shale interface. Hence, temperature gradient occurs in the shale around the heat source. In Figure 2b, pore water pressure evolution caused by heat emitted from the waste package is presented highlighting the thermo-osmotic and thermal expansion respective contributions. In case where only thermal expansion is considered, it can be observed that the pore water pressure in shale rock continuously increases up to the point where temperature becomes approximately constant and then the Darcian flux predominates due to pressure gradient established in the formation yielding slow pore water pressure dissipation. In case where thermo-osmosis is considered, when the temperature stabilises pore water pressure developed 2 m from the buffer-shale interface is less comparing to thermal expansion only case due to water flow induced by temperature gradient. Furthermore, due to thermo-osmotic water flow diverging from the heat source, an increase in pore water pressure is observed further in the domain, i.e. at the distance of 10 m from the buffer.

5. Conclusion

Based on observations from the current study, it can be concluded that thermo-osmosis modifies the pressure field in a natural environment subjected to heating. In the context of nuclear waste disposal and radionuclide release, thermal osmosis might contribute to the overall convective transport of water and radionuclides due to the low hydraulic permeability and low thermal conductivity of the shale rock. In this work, a value of $5x10^{-13}m^2/sK$ was chosen although higher values have been reported for shales. However, it can be concluded that for even relatively low value of thermo-osmotic conductivity, the thermal osmosis contributes to the water flow in such low permeability porous medium. This leads to a conclusion that in porous medium with higher thermo-osmotic properties, the effect of thermal-osmosis on pore water pressure evolution around the heat source could prevail over the Darcian flow.

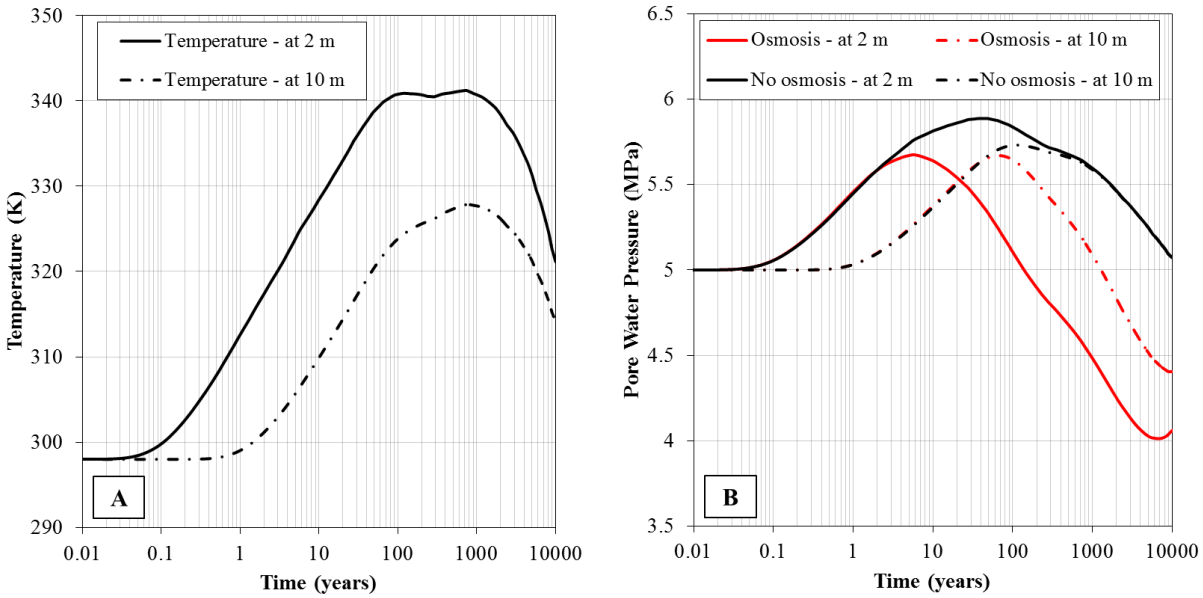

Figure 2: A) Temperature evolution with time at the distance equal to 2 m and 10 m from the buffer-rock interface, B) Pore water pressure evolution with and without the thermo-osmotic effect at the distance equal to 2 m and 10 m from the buffer-rock interface

Hence, inclusion of thermo-osmosis effect in chemically active rock such as shale for long-term numerical investigations of nuclear safety may be needed to understand the pressure distribution and flow in such porous medium.

Acknowledgements

The financial support from WEFO, for the first author, is gratefully acknowledged.

References

[1] Thomas, H.R., He, Y., Sansom, M.R. and Li, C.L.W. On the development of a model of the thermo-mechanical-hydraulic behaviour of unsaturated soils. *Engineering Geology*, 41, 197-218, 1996.

[2] Gonçalvès, J., De Marsily, G. and Trèmosa, J. Importance of thermo-osmosis for fluid flow and transport in clay formations hosting a nuclear waste repository. *Earth and Planetary Science Letters*, 339-340, 1-10, 2012.

[3] Mitchell, J. K. *Fundamentals of Soil Behavior*, 2nd Edition, John Wiley & Sons, Inc., 1993.

[4] Zagorščak, R., Sedighi. M. and Thomas, H.R. Effects of thermal osmosis on hydraulic behaviour of saturated clays. *International Journal of Geomechanics*, Accepted for publication.

[5] Thomas, H.R. and He, Y. A coupled heat-moisture transfer theory for deformable unsaturated soil and its algorithmic implementation. *International journal for numerical methods in engineering*, 40, 3421-3441, 1997.

[6] Trèmosa, J., Gonçalvès, J., Matray, J.M. and Violette, S. Estimating thermo-osmotic coefficients in clay-rocks: II. In situ experimental approach. *Journal of Colloid and Interface Science*, 342, 175-184, 2010.

[7] Lawrence Berkley National Laboratory, Earth Sciences Division. Available at: http:// http://esd.lbl.gov/used-fuel-disposition/engineered-barrier-research/, (Accessed: 9/2/16).

[8] Ghassemi, A., Tao, Q. and Diek, A. Influence of coupled chemo-poro-thermoelastic processes on pore pressure and stress distributions around a wellbore in swelling shale. *Journal of Petroleum Science and Engineering*, 67, 57-64, 2009.

Advanced Applications II

Proceedings of the 24th UK Conference of the
Association for Computational Mechanics in Engineering
31 March - 01 April 2016, Cardiff University, Cardiff

A reduced order model for criticality problems in reactor physics varying control rod settings

***Claire E. Heaney[1,2], Andrew G. Buchan[1], Christopher C. Pain[1] and Simon Jewer[2]**

[1]Applied Modelling and Computation Group, Imperial College, London SW7 2AZ
[2]Defence Academy, HMS Sultan, Gosport, UK

*c.heaney@imperial.ac.uk

ABSTRACT

In this paper we apply model order reduction to the criticality problem in reactor physics. Starting from the eigenvalue problem associated with the multigroup neutron diffusion equation we build a reduced order model from solutions for different control rod positions using proper orthogonal decomposition. The reduced system of equations can be solved at a fraction of the cost of the full system, yielding a solution for any given control rod height. We demonstrate this procedure for a section of a fuel assembly.

Key Words: *Reduced order modelling; proper orthogonal decomposition; multigroup neutron diffusion; eigenvalue problem; reactor criticality*

1. Introduction

Using reduced order models (ROMs) [1] when solving parameterised problems is known to be beneficial, as the problem size can be reduced by several orders of magnitude whilst retaining reasonable solution accuracy. In this paper, ROM is applied to the eigenvalue problem arising from the study of criticality in nuclear reactors. The method proposed is based on proper orthogonal decomposition (POD) [2] and the method of snapshots [3]. There has been a considerable amount of attention in POD from within the fluid dynamics community, having been successfully applied to a range of applications such as the mixing of fluid layers [4] and ocean models [5]. However, its application to solving reactor physics problems is less common. Notable exceptions are [6] which recasts the criticality eigenvalue problem as a time dependent problem, and [7] which develops a control-oriented model of nuclear reactor spatial kinetics.

The growth of the neutron population in a reactor is one of the most important characteristics of a nuclear system, knowledge of which determines the state of the reactor encapsulated in the effective multiplication factor k^{eff}. Ideally, for a particular reactor, k^{eff} needs to be calculated for any position of the control rods and any temperature distribution. As these change constantly, solving a demanding computation for each control rod height and temperature distribution is not practical. Reduced order modelling is ideally suited to such a problem.

The following section describes the multigroup diffusion equation and the formulation of the criticality problem. In section 3 the reduced order model is described. Section 4 presents some preliminary results, and the final section concludes and identifies future work.

2. Governing Equations

Under operating conditions in a reactor, the multigroup neutron diffusion equation can be used to model the neutron population. The multigroup discretisation splits up the energy into a number of so-called energy groups determined by a discrete set of values $E_G < E_{G-1} < \cdots < E_1 < E_0$. Each group has an associated scalar flux solution, ϕ_g, and a set of material parameters. The behaviour of the neutrons is described by the macroscopic cross-sections corresponding to fission, scattering and absorption, denoted Σ_g^f, $\Sigma_{g'\to g}^s$, Σ_g^a respectively, where the subscripts g and g' indicate a particular group. The cross-sections represent the probabilities that fission, scattering or absorption will occur. The parameter D_g

which controls how the neutrons diffuse through the domain, depends on the cross-sections according to $D_g(x) = \left(3(\Sigma_g^a(x) + \Sigma_g^s(x))\right)^{-1}$. Criticality is a measure of the growth or decay of the neutron population in a system over successive neutron generations in a fission chain reaction. In order to study criticality, the governing equation is cast in the form of an eigenvalue problem by introducing the effective multiplication factor, k^{eff}. If neutrons removed from the system exactly balance those created, the system is adjudged critical ($k^{\text{eff}} = 1$). If more neutrons are produced than removed then the system is super-critical ($k^{\text{eff}} > 1$). If fewer neutrons are produced than removed the system is sub-critical ($k^{\text{eff}} < 1$).

For group g, the criticality eigenvalue problem of the multigroup neutron diffusion equation is

$$-\nabla \cdot (D_g(x)\nabla\phi_g(x)) + \Sigma_g^a(x)\,\phi_g(x) - \sum_{\substack{g'=1 \\ g'\neq g}}^{G} \Sigma_{g'\to g}^s(x)\,\phi_{g'}(x) = \frac{\chi_g}{k^{\text{eff}}} \sum_{g'=1}^{G} \nu_{g'}\Sigma_{g'}^f(x)\,\phi_{g'}(x), \qquad (1)$$

where G is the total number of groups, χ_g is the probability that fission will result in a neutron being born in group g, ν_g is the average number of neutrons produced per fission event and k^{eff} is the effective multiplication factor. There are two types of boundary conditions considered here: reflective boundary conditions where $D_g\nabla\phi_g(x)\cdot n = 0$, and void boundary conditions $-\frac{1}{2}D_g\nabla\phi_g(x)\cdot n = \frac{1}{4}\phi_g(x)$.

Considering the case of two energy groups, we can make assumptions that (i) any neutrons created will be born into the higher energy group (ie. $\chi_1 = 1$ and $\chi_2 = 0$), (ii) upscatter from the low energy group to the fast energy group will not occur (ie. $\Sigma_{2\to1}^s = 0$) . For the full model, a Galerkin finite element discretisation is applied in space, so the solution is expanded in terms of piecewise polynomial functions (shape functions), $\phi_g(x) = N_j(x)\hat{\phi}_{g,j}$, the governing equation is weighted by the shape functions and integrated over the domain Ω. The divergence theorem is applied in order to impose boundary conditions, resulting in

$$A\,\phi \equiv \begin{bmatrix} A_{11} & A_{12} \\ A_{21} & A_{22} \end{bmatrix} \begin{Bmatrix} \phi_1 \\ \phi_2 \end{Bmatrix} = \frac{1}{k^{\text{eff}}} \begin{bmatrix} B_{11} & B_{12} \\ B_{21} & B_{22} \end{bmatrix} \begin{Bmatrix} \phi_1 \\ \phi_2 \end{Bmatrix} \equiv \frac{1}{k^{\text{eff}}} B\,\phi \qquad (2)$$

where

$$\left(A_{gg}\right)_{ij} = \int_V \left(-D_g\nabla N_i\cdot\nabla N_j + \Sigma_g^a N_i N_j\right) dV + \frac{1}{2}\int_{S^{\text{void}}} N_i N_j dS, \quad \text{for} \quad g = 1,2 \qquad (3)$$

$$(A_{21})_{ij} = \int_V -\Sigma_{1\to2}^s N_i N_j dV \qquad (4)$$

$$\left(B_{gg'}\right)_{ij} = \chi_g \int_V \nu_{g'}\Sigma_{g'}^f N_i N_j dV \quad \text{for} \quad g,g' = 1,2\,. \qquad (5)$$

The dependence of the shape functions on x is no longer indicated explicitly.

3. ROM

Reduced order modelling aims to solve a computationally costly problem in a cheaper way, by using information from a series of pre-calculated solutions. For a range of values of a parameter, high resolution solutions are sought, known as snapshots. A singular value decomposition (SVD) is then applied to the matrix of snapshots which results in a set of orthogonal basis functions and a set of singular values. The magnitudes of the singular values indicate the importance of each basis function therefore not all need be retained in the POD basis if their contribution is deemed sufficiently small relative to a predefined tolerance. Once the POD basis has been found the discretised governing equation is projected onto the reduced order space where it is then solved for desired values of the parameter. The parameter varied in this paper is the control rod height, which takes a set of values from h_1 (fully inserted) to h_n (fully withdrawn), yielding n snapshots. The fraction of energy of the original information which is contained by m POD basis functions is determined by the singular values σ_k:

$$\text{energy of the first } m \text{ modes} = \frac{\sum_{k=1}^{m}\sigma_k^2}{\sum_{k=1}^{n}\sigma_k^2}\,. \qquad (6)$$

For each control rod height, the matrices A and B are projected by the m POD basis functions from finite element (FE) space to the reduced space by the following

$$A_k^{\mathrm{POD}} = R^{\mathrm{T}} A_{h_k} R \tag{7}$$

where the POD basis functions make up the columns of R and A_{h_k} is given by equation (2) evaluated for a control rod height of h_k. In order to solve a problem in the reduced order space, for a control rod height of $\tilde{h} \in [h_i, h_{i+1}]$, a linear interpolation is performed between A_i^{POD} and A_{i+1}^{POD} such that

$$A^{\mathrm{POD}} = \omega A_i^{\mathrm{POD}} + (1-\omega) A_{i+1}^{\mathrm{POD}} \qquad \text{where} \quad \omega = \frac{h_{i+1} - \tilde{h}}{h_{i+1} - h_i} \,. \tag{8}$$

B^{POD} is constructed similarly. Now we are able to assemble and solve the reduced order system

$$A^{\mathrm{POD}} \phi^{\mathrm{POD}} = \lambda^{\mathrm{POD}} B^{\mathrm{POD}} \phi^{\mathrm{POD}} \,. \tag{9}$$

Finally we project the flux solution from the reduced space into the FE space by calculating $R\,\phi^{\mathrm{POD}}$.

4. Results

Part of a fuel assembly is modelled to test the ROM procedure described in the previous section. The domain is $[-1.845, 1.845] \times [-1.845, 1.845] \times [-5, 5]$. There are 8 fuel pins and one control rod of radii 0.48, surrounded by a moderator which in this case is water (see figure 1).

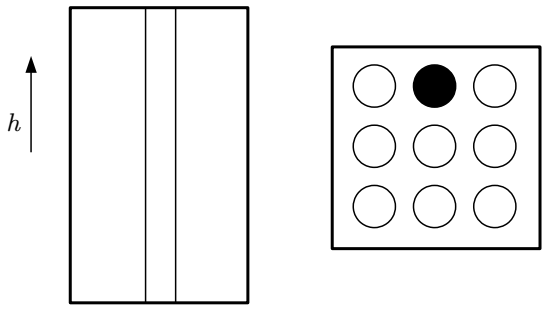

Figure 1: *Left,* part of a fuel assembly showing the region where the control rod is located. *Right,* view from above of the assembly showing fuel pins and control rod (shaded). (Not to scale.)

The cross-sections were generated using the ANSWERS software, WIMS, and some values are reported in table 1. The mesh used has 431883 tetrahedral elements and 76712 nodes. The snapshots were taken for a control rod at heights of $\{-5, -3, -1, 1, 3, 5\}$. Each energy group had 6 POD basis functions so the reduced order system is of size 12×12. For the same heights the reduced order model gives values of k^{eff} which agree with those of the snapshots to within 6 decimal places (see figure 2). For so-called unseen values of the control rod height, the reduced order model predicts k^{eff} to a reasonable accuracy. The computational time to solve the full order model for one parameter was 379.8 seconds, whereas the reduced order model solves in less than 0.1 seconds.

		Σ_1^a	Σ_2^a	$\Sigma_{1\to1}^s$	$\Sigma_{1\to2}^s$	$\Sigma_{2\to2}^s$	Σ_1^f	Σ_2^f
fuel	$300K$	6.003E-03	9.583E-02	3.364E-01	1.336E-03	4.048E-01	3.333E-03	4.994E-02
	$2000K$	6.042E-03	9.499E-02	3.370E-01	1.340E-03	4.079E-01	3.333E-03	4.945E-02
moderator	$300K$	1.447E-04	6.597E-03	3.395E-01	5.957E-02	1.281E+00	0.0	0.0
	$2000K$	1.447E-04	6.584E-03	3.395E-01	5.954E-02	1.279E+00	0.0	0.0

Table 1: Cross-sections for the fuel and moderator at a given temperature are interpolated from the values above.

5. Final remarks

This paper has applied model order reduction to the criticality eigenvalue problem associated with the multigroup neutron diffusion equation. Snapshots were taken for different values of control rod height. When comparing the eigenvalue of the snapshots generated by the full model with that of the reduced order model, the agreement is excellent. For unseen problems, the agreement is reasonable. The full

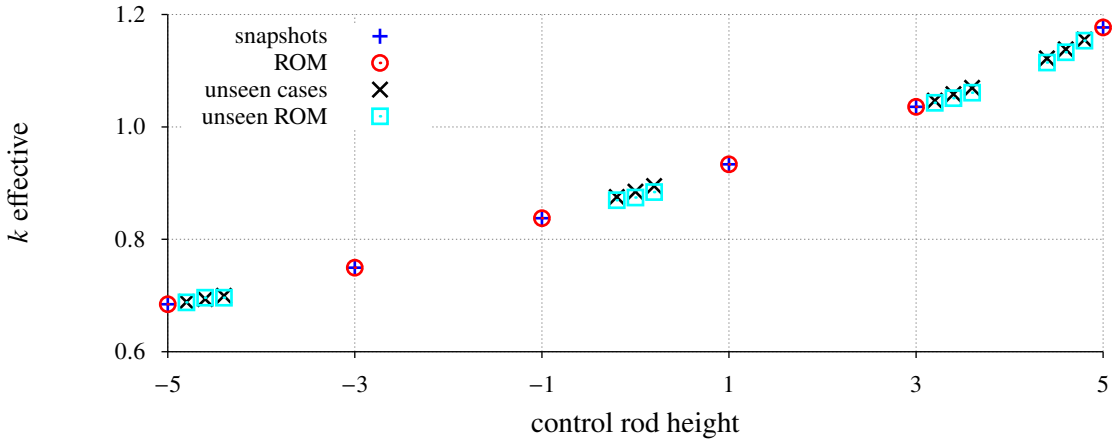

Figure 2: Two comparisons, first of k^{eff} from the snapshots (full model) with k^{eff} from the reduced order model as the control rod height varies (blue crosses and red circles), and second of k^{eff} for full model solutions with k^{eff} of unseen values of the control rod height predicted by ROM (black crosses and cyan squares).

order model has 153424 unknowns whereas the reduced order problem has just 12 and solves in a fraction of the time.

Future work will involve (i) quantifying the error between the reduced order model solution and the full model for unseen problems and (ii) introducing temperature to the ROM as a parameter, as the cross-sections depend on this.

Acknowledgements

The authors gratefully acknowledge financial support from the Defence Academy at HMS Sultan. Dr Andrew Buchan acknowledges support from the EPSRC Fellowship EP/M022684/1.

References

[1] W.H.A. Schilders, H.A. van der Vorst, J. Rommes. *Model Order Reduction: Theory, Research Aspects and Applications.* Springer: Berlin, 2008.

[2] V. Buljak. *Inverse Analyses with Model Reduction: Proper Orthogonal Decomposition in Structural Mechanics (Computational Fluid and Solid Mechanics)*. Springer: Berlin, 2011.

[3] L. Sirovich. Turbulence and the dynamics of coherent structures, part III: dynamics and scaling. *Quarterly of Applied Mathematics*, XLV, 583–590, 1987.

[4] J. Delville, S. Bellin, J.P. Bonnet. Use of the proper orthogonal decomposition in a plane turbulent mixing layer. *In Turbulence and Coherent Structures; Selected Papers from Turbulence 89. Kluwer Academic Publishers*, 75–90, 1991.

[5] F. Fang, C.C. Pain, I.M. Navon, G.J. Gorman, M.D. Piggott, P.A. Allison, P.E. Farrell, A.J.H. Goddard. A POD reduced order unstructured mesh ocean modelling method for moderate Reynolds number flows. *Ocean Modelling*, 28, 127–136, 2009.

[6] A.G. Buchan, C.C. Pain, F. Fang, I.M. Navon. A POD reduced-order model for eigenvalue problems with application to reactor physics, *Int. J. Numer. Meth. Engng*, 95, 1011–1032, 2013.

[7] A. Sartori, D. Baroli, A. Cammi, D. Chiesa, L. Luzzi, R. Ponciroli, E. Previtali, M.E. Ricotti, G. Rozza, M. Sisti. Comparison of a Modal Method and a Proper Orthogonal Decomposition approach for multi-group time-dependent reactor spatial kinetics. *Ann. Nucl. Energy*, 71, 217–229, 2014.

FINITE ELEMENT MODELLING FOR PRODUCTIVITY OF GEOTHERMAL RESERVOIRS VIA EXTRACTION WELL

Musa D. Aliyu[1], *Hua-Peng Chen[2],Ouahid Harireche[3]

[1,2,3]Departmentof Engineering Science, University of Greenwich, Chatham Maritime, Kent, ME4 4TB, UK.

*Corresponding author: H.Chen@greenwich.ac.uk

ABSTRACT

The major process in geothermal energy stimulation is the injection and extraction of fluid through wells to generate power. One of the methods utilised in examining the long-term behaviour of such systems is modelling. In this paper, a three-dimensional (3-D) thermo-hydro-mechanical (THM) coupled model of a geothermal reservoir is developed to probe the productivity of the reservoir via the extraction well at different placement locations using a Multiphysics Finite Element (FE) application solver. Coupling between the thermo-hydro (HT) processes was achieved through convective velocity term and thermo-mechanical (MT) coupling through temperature and thermal expansion coefficient. Therefore, the parameters analysed were the total net energy rate, enthalpy and temperature using a boundary probe function and a parametric study step solver. The results showed that when the extraction well was placed nearer to the injection well, the productivity was found to be lower after only a few years of production, on the other hand, further placement of wells gives higher productivity.

Keywords: *Geothermal reservoir; thermo-hydro-mechanical (THM) coupling; FE modelling; productivity.*

1. Introduction

Geothermal energy is a renewable source and as such listed with solar, wind and biomass asalternative energy options[1,2]. To simulate and evaluate the behaviour of a deep geothermal system for commercial viability, one needs a reliable code that can handle the complexity of subsurface flow [3]. In this work, a geothermal reservoir model was developed using a multiphysics finite element (FE) solver (COMSOL) with a link to MATLAB to investigate the productivity of a geothermal reservoir via the extraction well under the effect of a coupled Thermo-Hydro-Mechanical (THM) processes.

2. FE Modelling of Coupled THM Processes

In this work, only a brief description of the formulations of coupled THM processes will be addressed. Detailed mathematical and finite element formulationshavebeen fully discussedin [4].In a fractured porous medium, the governing equations described for fluid flow are the conservation of mass and Darcy's law. For the matrix, the equations areexpressed as,

$$S\frac{\partial P}{\partial t}-\beta\frac{\partial T}{\partial t}+\nabla\cdot q=Q_h,\ q=\frac{k}{\mu}(-\nabla_P+\rho_w g) \tag{1}$$

where$S$is the specific storage, $P$is the pressure, $T$is the temperature, β is the fluid compressibility, $\nabla$is the vector differential operator,$q$is the Darcy's volumetric flux, and $Q_h$is the source term for the matrix.Also, k is the permeability, $\mu$is the dynamic viscosity, $\rho_w$is the density of water, and $g$is the acceleration due to gravity. For the discrete fractures, the equationsare given as,

$$d_f S\frac{\partial P}{\partial t}-\alpha\frac{\partial d_f}{\partial t}+\nabla\cdot(b_h.q_h)-\beta\frac{\partial T}{\partial t}=Q_h,\ q_f=\frac{b_h^2}{\mu}\mathrm{I}(-\nabla_{pf}+\rho_w g) \tag{2}$$

whered_f is the mechanical aperture, $\alpha$is the biot's coefficient, $b_h$is the hydraulic aperture and I is the identity matrix.The equations definedfor heat transport are the conservation of energy and Fourier's law. For the matrix, the equations areexpressed as,

$$C_P\rho\frac{\partial T}{\partial t}+\nabla\cdot q_T=Q_T,\ q_T=-\lambda\nabla T+C_P\rho T \tag{3}$$

whereC_p is the specific heat capacity of the matrix, ρ is the density of the matrix, λ is the thermal conductivity, q_T is the heat flux, C_{pw} and Q_T is the heat source. The equations describing the discrete fractures aregiven as,

$$d_f C_{Pw}\rho_w\frac{\partial T}{\partial t}+\nabla.q_T=0,\ q_T=-\partial_f\lambda\nabla T+b_h C_P\rho qT \tag{4}$$

The governing equation defined for mechanical behaviour are the conservation of momentum and the Biot's poroelastic model, which are expressed as,

$$\nabla\cdot(\sigma^{'}-\alpha P\mathrm{I})+\rho g=0,\ d\sigma^{'}=D\left(d\varepsilon-\alpha_T\Delta T\mathrm{I}\right) \tag{5}$$

in which$\sigma^{'}$is the effective stress, $\alpha_T$is the thermal expansion coefficient, $\Delta T$is the temperature increment,$\varepsilon$is the total strain and $D$is a forth-order material tensor. For nonlinear and isotropic elasticity, the material tensor is given as,

$$D=\lambda\delta_{ij}\delta_{kl}+2G\delta_{ik}\delta_{jl},\ \varepsilon=\frac{1}{2}\left(\nabla u+(\nabla u)^T\right)=\nabla^S u \tag{6}$$

whereδ is the Kronecker delta, G is the shear modulus, u is the displacement vector and the superscript T means the transpose of the matrix.

Furthermore, the green theorem and the method of weighted residuals (MWR) are applied to the governing equations provided above to derive the weak formulation of the problem as

$$\int_\Omega w\rho S\frac{\partial P}{\partial t}d\Omega-\int_\Omega\rho\nabla w^T\cdot qd\Omega+\int_\Gamma w\rho(q\cdot n)d\Gamma-\int_\Omega wQ_h d\Omega=0 \tag{7}$$

$$\int_\Omega w\rho C_P\frac{\partial T}{\partial t}d\Omega+\int_\Omega w\rho C_p q_T\cdot\nabla Td\Omega-\int_\Gamma\nabla w^T\cdot(-\lambda\nabla T)d\Omega+\int_\Gamma w(-\lambda\nabla T\cdot n)d\Gamma-\int_\Omega w^T Q_T d\Omega=0 \tag{8}$$

$$\int_\Omega\nabla\cdot w\left(\sigma^{'}-\alpha P\mathrm{I}\right)d\Omega-\int_\Omega w\rho g d\Omega=0 \tag{9}$$

where$w$ is the weighting function, Ω represents the model domain and Γ denotes the boundary domain. The boundary conditions are specified for all field functions P, T and U. The weak forms of the THM balance equations were spatially discretised using the Galerkin method. Primary variables are pressure P, temperature T, and displacement U and can be approximated by interpolation functions as,

$$P^y=N_P P \tag{10}$$

$$T^y=N_T T \tag{11}$$

$$U^y=N_U U \tag{12}$$

where P and T are the scalars of the nodal values of the unknowns and U is nodal vector. N_P,$N_T$and $N_U$are the shape functions for P, T and U respectively. The finite element formulation of the governing equations can be given in a matrix form as

$$M_h^m P^{'m}+K_h^m P^m-q_h^m=0 \tag{13}$$

$$M_T^m T^{'m} + K_T^m T^m - q_T^m = 0 \tag{14}$$

$$\int_\Omega B^T \sigma^{'} d\Omega - C^m P^m - f_M = 0 \tag{15}$$

where M, K and C are process-specific mass, Laplace and coupling matrices. The term *f* contained the contributions of the coupled processes and B is the strain-displacement matrix.

3. Problem Description

Based on the formulations presented in the previous section, a 3-D FE model of the Urach Spa geothermal reservoir was developed. The model was 800 m long, 300 m wide, with estimated high of 300 m[5]. However, due to symmetry only half of the reservoir was modelledwith two discrete fractures of 2mm thickness each. The initial temperature of the reservoir was given as T_0 =10°C + 0.03[K/m]*z, where 10°C is the surface temperature, 0.03 [K/m] is the geothermal gradient, and z is the reservoir depth in metres. Also, the initial pressure of the reservoir was hydrostatic and initial stresses applied were lithostatic in all directions, and other reservoir parameters utilisedwere available from literature [5]. Moreover, the boundary conditions (BC) used in the model wereDirichlet for both the hydraulic and thermal processes;for the mechanical process, all the reservoir boundarieswere assumed to be roller except the body load applied at the top.

4. Results and Discussions

A comprehensive study was carried out on injection-extraction well separation distance. The positions of the extraction well were varied systematically using a parametric sweep function to examine the location that could yield maximum energy in the reservoir. The parameters investigated were temperature, enthalpy, and the total net energy rate under a long-term simulation of 30 years. The first sets of results presented were the effect of cold water distribution in the matrix and the fractures. The injected fluid mainly flows in the direction of fractures due to their higher permeability and connected the production well effectively. However, the cold water injection decreases the temperature of the rock after nearly seven years of the simulation. Also, the cooling fronts presented showed that the reservoir temperature is 5°C below the initial rock temperature after one year of injection as shown in Figure 1(A), 7°C after five years and 8°C after ten years as presented in Figures 1(B) and 1(C), respectively.

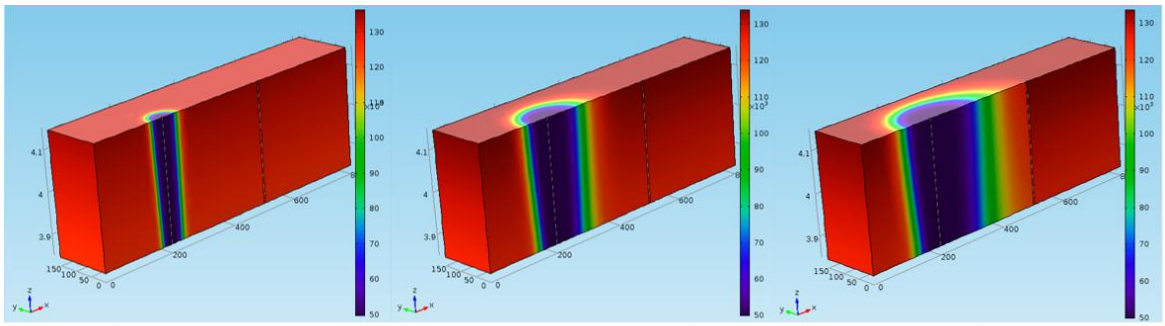

(A) (B) (C)

Figure 1: (A) Cold water distribution after one year of production (ºC), (B) Cold water distribution after five year of production (ºC), (C) Cold water distribution after ten year of production (ºC).

The second sets of results analysed in this work include the temperature, enthalpy and the total net energy rate. The temperature changes at the seven positions of the production wells presented in Figure 2(A) showed a temperature drawdown after six years at the production well that was the closest to the injection (300 m) and ten years at the well that was the second closest (350 m). At twelve and half year drawdown was observed at the well third closest to the injection (400 m) and 17 years at the well that was furthest (450 m). From the furthest position onwards there was no significant drawdown observed because the cold water effect is longer reaching the wells after 30

years of simulation. The enthalpy results presented in Figure 2(B) also showed similar behaviour to that of the temperature due to the close relationship between the two parameters in systems thermodynamics. In the case of the total net energy rate produced at the well head of the reservoir, a significant drop is observed from 5.5 MW to 2.5 MW approximately within the first year of production, because the injected pressure starts to reactivate the existing fractures and also forming new hydraulic fractures (i.e. the breakthrough pressure). The net energy later stabilises after in almost all the cases except for the wells closer to the injection well as shown in Figure 2(C).

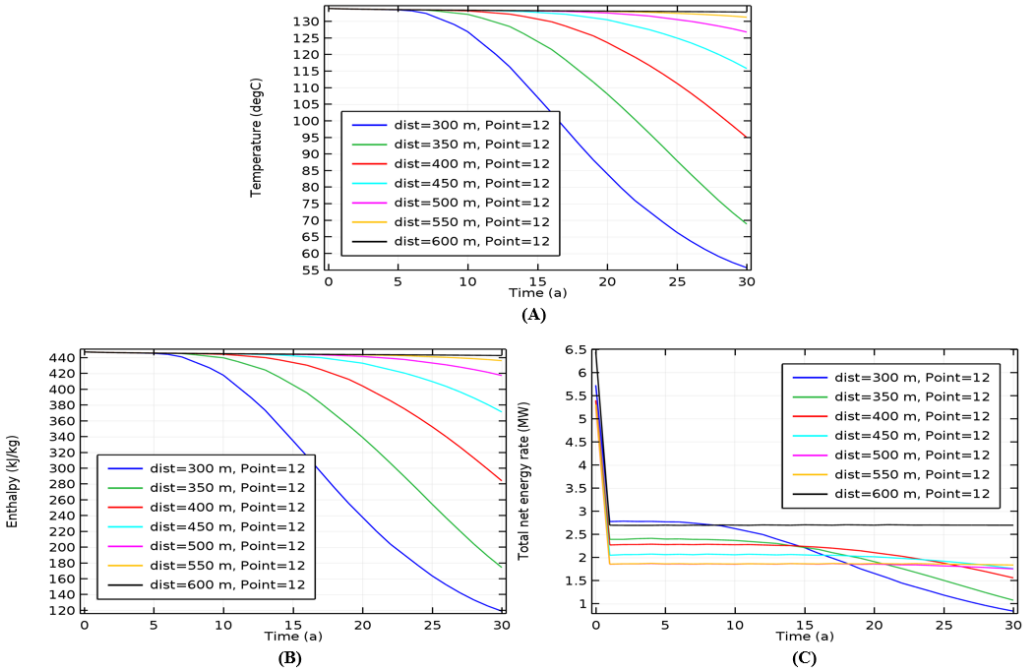

Figure 2: (A) Production temperature, (B)Enthalpy and (C) Total net energy rate

5. Conclusion

A three-dimensional numerical model of a coupled thermo-hydro-mechanical interaction in a naturally fractured reservoir has been developed using the finite element method. The developed model serves as a mechanism for evaluating HDR geothermal reservoir operations and for assessing its long-term performance and energy extraction potential using a parametric sweep solver. The studies reported here have focused attention on the significance of well (i.e. production) placement in HDR geothermal reservoir operations. The model has the potential to serve as a tool for assessing the behaviour of deep subsurface media in the context of other related technologies such as hydrocarbon reservoirs, carbon dioxide (CO_2) sequestration reservoirs and waste disposal reservoirs.

References

[1] J. Burnell, et al., Geothermal Supermodels : the Next Generation of Integrated Geophysical , Chemical and Flow Simulation Modelling Tools, *Proceedings World Geothermal Congress 2015 Melbourne*, Australia, April 2015.

[2] L. Rybach, Geothermal energy: Sustainability and the environment, *Geothermics*, 32(4), 463–470, 2003.

[3] A. E. Croucher and M. J. O'Sullivan, Application of the computer code TOUGH2 to the simulation of supercritical conditions in geothermal systems, *Geothermics*, 37(6), 622–634, 2008.

[4] O. Kolditz, Modelling flow and heat transfer in fractured rocks: Conceptual model of a 3-D deterministic fracture network, *Geothermics*, 24(3). 451–470, 1995.

[5] N. Watanabe, W. Wang, C. I. McDermott, T. Taniguchi, and O. Kolditz, Uncertainty analysis of thermo-hydro-mechanical coupled processes in heterogeneous porous media, *Comput. Mech.*, 45(4), 263–280, 2010.

Proceedings of the 24th UK Conference of the
Association for Computational Mechanics in Engineering
31 March – 01 April 2016, Cardiff University, Cardiff

ARTIFICIAL RECHARGE OF COASTAL AQUIFERS USING TREATED WASTEWATER TO CONTROL SALTWATER INTRUSION

***M. S. Hussain[1], A. A. Javadi[1] and M.M. Sherif[2]**

[1]Department of Engineering, University of Exeter, Exeter, EX4 4QF, UK
[2]Civil and Environmental Engineering Department, UAE University, Al Ain, P.O. Box: 17555, UAE

*mohammed@uod.ac

ABSTRACT

This paper investigates the efficiency of artificial recharge of aquifers with treated wastewater using a surface basin (pond) system to control seawater intrusion (SWI) in coastal aquifers and to increase their safe yield. First a hypothetical case study of an unconfined aquifer is simulated. The effects of the artificial recharge system on inland advancement of saline water in a real case study (Wadi Ham aquifer in the UAE) are outlined in another application. The numerical model of the Wadi Ham aquifer is developed based on the available hydrogeological data in real scale. The 3D variable-density flow and transport numerical models of both case studies are solved using the finite element method. The transient progress of saline water before and after the recharge event is presented in both case studies. Both systems initially suffered from aggressive inland encroachment of saline water due to pumping. However, by implementation of the recharge pond, the treated wastewater starts to infiltrate towards the groundwater table and consequently it helps to alleviate the saltwater intrusion. The results highlight that lower equi-concentration lines are generally more sensitive to recharge and abstraction events.

Keywords: *seawater intrusion; numerical modelling; coastal aquifer; artificial recharge; treated wastewater*

1. Introduction

In coastal areas, usually, there is a relatively small hydraulic gradient of subsurface flow toward sea. But the small density gradient between the seawater and freshwater forces the seawater to penetrate into aquifer and then mixing occurs with the inland freshwater sources. Saltwater intrusion is a serious problem that continuously threats the quality of the groundwater storage in these areas. The groundwater withdrawals can accelerate the rate of saltwater intrusion by disturbing the natural hydrostatic equilibrium state between these two fluids [1]. In order to maintain the seaward hydraulic gradient against SWI a hydraulic barrier should be planned. The artificial recharge approach which is the main focus of this paper is among the most popular techniques that can achieve this. Generally it aims at reducing flood flows, storing the water in aquifer, raising groundwater levels, relieving over-pumping and finally improving water quality and suppressing the saline water [6]. The great potential of this approach in repulsion of intruded saline wedge has been suggested by a number of researches [1-4].

The quality and quantity of the recharge water, the cost and the source of providing the high-quality water for recharge especially in the areas that suffer from scarcity of water and also the operational cost of the recharge system are the factors that should be taken into consideration in the design of recharge systems. Using desalinated seawater is costly and could be difficult to justify. Therefore, application of reclaimed water (treated wastewater) can be highlighted as a reliable strategy with low economic cost and high environmental benefits. The current work attempts to simulate the 3D patterns of evolution of controlling SWI in both hypothetical and real cases of unconfined aquifers using ponded treated wastewater. A density dependent finite element model SUTRA (Saturated-Unsaturated TRAnsport) [5] is used for numerical simulation of both aquifers. The SUTRA code is a FE-based numerical model that employs hybrid finite element and integrated finite difference methods to solve the governing equations of flow and transport processes of solute or energy in aquifer systems. The background information about the SUTRA code and some of its applications in optimal modelling of different SWI management measures can be found in recent papers of the authors [1,8].

2. First Application: Hypothetical Aquifer

The first application is a 3D hypothetical aquifer with 300 m length, 100 m width and 40 m depth (Figure 1). The domain is discretized into 24000 elements and 26691 nodes. Hydrostatic water heads of 24.5 m and 24.0 m are assigned to the left and right sides of the domain respectively to represent the freshwater and seawater boundaries of the simulated unconfined aquifer, where an unsaturated layer overlying a saturated layer. The van Genuchten model [9] is used for simulation of unsaturated flow through top layer. The system is subjected to continuous pumping of 430 m^3/day implemented by the local production well screened at coordinates (70, 40, 15) m. The main input data used for the simulation model include: the coefficient of water molecular diffusion of 1.0×10^{-9} m^2 /s; fluid viscosity of 0.001 kg/(m.s); porosity of 0.35[dimensionless]; transverse and longitudinal dispersivities of 0.5 m and 5.0 m respectively; permeabilities of 1.0×10^{-12} m^2 and 5.0×10^{-11} m^2 for the top and bottom layers; solute mass fractions of 0.0357 and 0 for seawater and freshwater, and densities of 1025 kg/$m^3$and 1000 kg/m^3 for seawater and freshwater respectively.

3. Second Application: Wadi Ham Aquifer, UAE

The second application is the Wadi Ham aquifer located in Fujairah emirate in the UAE country. Figure 2 shows the domain of the Wadi Ham aquifer with the total area of 80.26 km^2 used in the numerical simulation. The figure also illustrates the available hydrological/natural features and the boundary conditions. A hydrostatic pressure boundary condition with a constant head at the mean seawater level is used to define the coastline. The 3D model is generally an anisotropic and heterogeneous system based on hydraulic conductivity field defined through calibration process. The final numerical mesh has 48160 tri-linear hexahedral elements and 55990 nodes. The details about the hydrogeological setting and 3D modelling of this study area can be found in [7-8] where a considerable amount of SWI is reported as the current condition of this aquifer and more specifically due to continuous groundwater withdrawal from available production well located close to the coastline that intensifies the inland encroachment of saltwater.

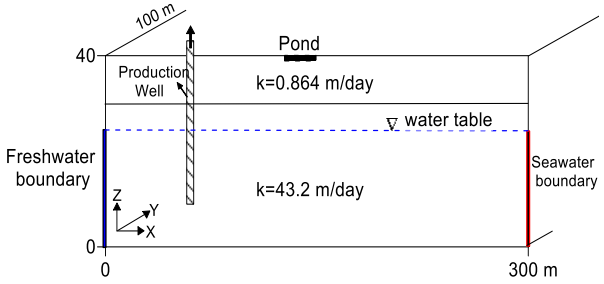

Figure 1: Geometry and boundary conditions of the hypothetical model

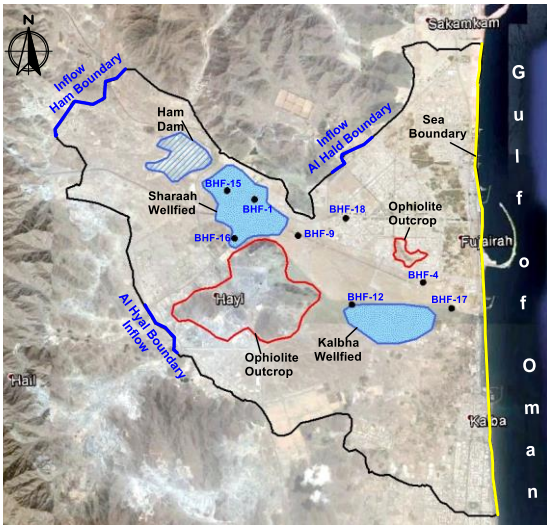

Figure 2: Boundary conditions of Wadi Ham aquifer

4. Results and Discussion

Figure 3 shows the equilibrium salinity distribution of the considered hypothetical aquifer in the first application that is obtained under applied abstraction rate (430 m^3/day) and without any management action. The average inland advancements of the toes of the 10%, 50% and 90% salinity contours along the bottom boundary of the aquifer, measured from the seaside boundary, are 241 m, 232 m and 133 m respectively. These remarkable ingression trends lead to depletion in freshwater sources and thus an essential management action seemed to be necessary in order to protect the aquifer against

SWI. Therefore the system is then subjected to one classical scenario of groundwater management involving artificial recharge of aquifer using the ponded water. However the treated wastewater as an economic and environmentally safe source of water is suggested here and used in a pond to feed the aquifer. The recharge is implemented by an artificial surface pond (40m×10m ×1m) centred at coordinates (150, 65, 39)m. The recharge pond replenishes the aquifer with 1.0 m constant head of water. The corresponding average rate of recharge directly under the pond (calculated by SUTRA) is 0.39 m/day. The transient advancements of 10%, 50% and 90% iso-concentration lines in the reverse direction toward the sea are the evidence of the success of the recharge system to repulse the intruded saline water where the saltwater-freshwater interface will migrate back towards the sea by 8 m, 82 m and 53 m for this set of contour line respectively. This process is followed by recovering a considerable amount of freshwater in the aquifer. The transient variation of the 50% iso-concentration line during the recharge stress period (measured at the bottom boundary from the seaside in the XY plane) is presented in Figure 4. It can be seen that the amount of SWI mitigation is significant in regions away from the pumping well. Also, the retreat of seawater in the central area of the coastal zone is mostly attributed to the positive potential of the recharge system.

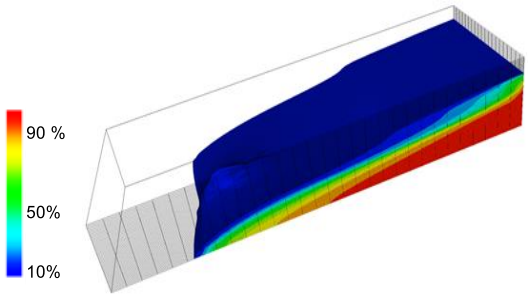

Figure 3: 3D salinity map (%) of hypothetical example prior to recharge process

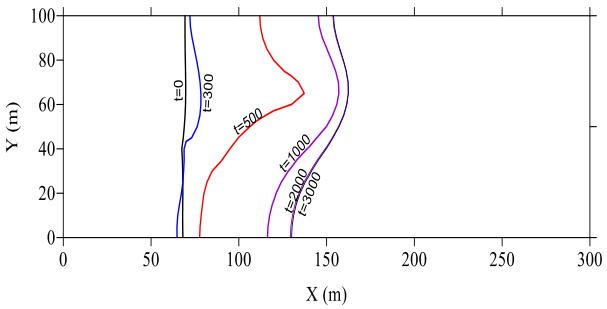

Figure 4: Transient progress of the 50% ischolar across the base of aquifer in XY plane

In the second example, the current condition of flow and salinity in the Wadi Ham aquifer (as a real-world case study) is first obtained. Figure 5 shows the current 3D distribution of salinity throughout this aquifer, pointing out the levels of contamination that are threatening the Kalbha production wells. In the numerical experiment conducted to control SWI in this aquifer, the system is again subjected to an assumed planning of artificial recharge using treated wastewater. For this purpose and by maintaining the current pumping rates (in year 2015) for the next 10 years, three recharge ponds (A,B and C) are assumed in the model to continuously feed the aquifers with an average rate of 0.5 m/day. The 50% iso-salinty contour for this control approach progressing along the base layer of the model is illustrated in Figure 6 and it is compared with the corresponding case with no-management strategy. The projections of the surface ponds' locations are also presented in the figure. In the no-management scenario (first scenario), the system experiences a further inland intrusion of 220 m compared to the results of year 2015 on X-X section. The recharged water subsequently enhances the seaward gradient of water table in the system by raisings the inland piezometric heads. This mechanism works as a countermeasure action against the inland encroachment of saltwater. In comparison to the first (no-recharge) scenario, the 50% iso-contour line will be pushed back in seaward direction by 340 m along section a-a in the second (surface recharge) scenario. The corresponding values of backward movement calculated in the second scenario are 550 m and 240 m along sections b-b and c-c respectively.

In general, there are some limitations in implementing of this scenario of the control methods. Direct application of recharge by ponding or spreading is not applicable in confined aquifers or even relatively thick unconfined aquifers. Under these circumstances, a deep injection by recharge wells may satisfy the design criteria in confined systems. In addition, the application of treated wastewater with large quantities to recharge aquifers requires further attention in terms of sustainability of the host aquifer, and health, environmental and economic risks.

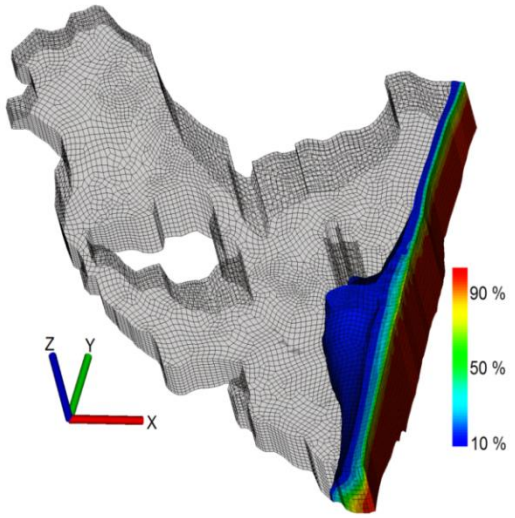

Figure 5: Current condition of salinity distribution (%) in Wadi Ham aquifer

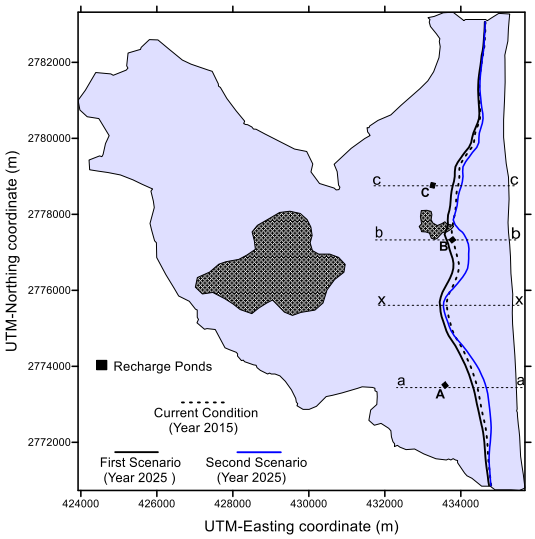

Figure 6: Inland progress of 50% iso-concentration lines across the base of Wadi Ham aquifer

5. Conclusions

3D numerical simulations were performed to outline the effects of the artificial recharge on general inland advancement of saline water into both hypothetical and real-world examples of coastal aquifers. It was shown that a considerable decrease in salinity levels occurs in the aquifers owing to the application of the recharge scenario. This is because the recharged water enhances or maintains the seaward gradient in the system by raising the inland piezometric heads. Therefore, the design of the simple recharge basins to feed the aquifer by collecting the treated wastewater and/or storm water can be considered as an efficient countermeasure against saltwater intrusion and could guarantee the long term sustainability in small unconfined aquifer systems.

References

[1] A. A. Javadi, M. S. Hussain, M. M. Sherif and R. Farmani. Multi-objective optimization of different management scenarios to control seawater intrusion in coastal aquifers. *Water Resources Management*, 29 (6), pp. 1843-1857, 2015.

[2] A. Mahesha. Steady-state effect of freshwater injection on seawater intrusion. *Journal of Irrigation and Drainage Engineering*, 122(3), pp.149-154, 1996.

[3] A. Mahesha and S.H. Nagaraja. Effect of natural recharge on seawater intrusion in coastal aquifers. *Journal of Hydrology*, 174(3–4), pp.211-220, 1996.

[4] A. Vandenbohede, E. van Houtte, and L. Lebbe. Sustainable groundwater extraction in coastal areas: a Belgian example. *Environmental Geology*, 57(4), pp. 735-747, 2009.

[5] C. I. Voss and A. M., Provost. SUTRA-A model for saturated-unsaturated variable-density ground-water flow with solute or energy transport. *U.S. Geological Survey (USGS)*, Report 02-4231, 2010.

[6] D. K. Todd. Salt-water intrusion and its control. *Journal of American Water Works Association*, 66(3), pp. 180-187, 1974.

[7] M. Sherif, A. Kacimov, A. Javadi and A. Ebraheem. Modeling groundwater flow and seawater intrusion in the coastal aquifer of Wadi Ham, UAE. *Water Recourses Management*, 26(3),751-774,2012.

[8] M. S. Hussain, A. A. Javadi and M. M. Sherif. Three dimensional simulation of seawater intrusion in a regional coastal aquifer in UAE. *Procedia Engineering*, 119: pp.1153-1160, 2015.

[9] M. T. van Genuchten. A Closed-form equation for predicting the hydraulic conductivity of unsaturated soils. *Soil Science Society of America Journal*,44(5), pp. 892-898, 1980.

Proceedings of the 24th UK Conference of the
Association for Computational Mechanics in Engineering
08-10 April 2016, Cardiff University, Cardiff

EVALUATION OF WIND POWER OUTPUT INTERMITTENCY THROUGH A SIMULATION METHOD

Amir G.J. Jalalian-Khakshour[1], T.N. Croft[1]

[1]College of Engineering, Swansea University, Singleton Park, Swansea, SA2 8PP

529236@swansea.ac.uk

ABSTRACT

One of the emerging issues with renewable energy technologies, such as wind turbines is the intermittent power output, in response to wind speed variation. Wind speed variation occurs at different timescales, each timescale having a different effect on the power output of the system. The key to understanding the intermittent power output is to understand the temporal dynamics of the systems output.

Vertical Axis Wind Turbine (VAWT) systems are becoming increasingly popular as they have a number of advantages over traditional wind turbines, such as reliability, ease of transportation and manufacture. The performance characteristics of a VAWT differ from that of a traditional horizontal axis wind turbine. Little work has been conducted on the performance of a low tip-speed ratio (0 – 1) VAWT systems in variable wind conditions.

In this study a non-linear, dynamic wind turbine model of a novel VAWT design is created to evaluate the wind power outputs at ms-sec time-scales. The effect that fluctuating wind patterns and the system topology will have on intermittency is of key interest in the study. A key outcome will be to understand the effect of changing particular parameters on power output fluctuations. A computationally inexpensive analytical model was created, from Newton's laws of motion.

Keywords: *Wind Energy; Renewable Energy; Rotordynamics; Vertical Axis Wind Turbines*

1. Introduction

Wind variability is caused by wind speed variations as a result of changing climatic conditions. The classification of wind variability is based on spatial and temporal variations [1]. The time scale of the wind speed variation will have a different effect on the power system [1]. Microscale variations (ms - secs) which can be attributed to wind turbulence can cause power quality and frequency regulation problems when integrated into an electrical power system [1]. Rotor parameters can be altered to alleviate the negative effect of unsteady winds on the system output. Methods to understand and quantify the intermittent output of wind energy will be key to overcoming the technical issues associated with wind speed variation.

A suggested method of evaluating a wind energy systems response in unsteady wind conditions is the use of a dynamic simulation model. L.Ran *et al.* [2] studied the use of a dynamic simulation model of a horizontal axis wind turbine, to optimise the moment of inertia of the rotor, to alleviate output power fluctuations. Y. Hara *et al.* [3] used a similar simulation method to study the effect of moment of inertia in fluctuating wind conditions, deviating around an average wind speed value. T. Wakui *et al.* [4] used a similar model to develop a sensorless condition monitoring technique. A similar simulation technique was adopted in this study to investigate the effect of transient wind on the system.

2. Dynamic Simulation Model

The system model is simplified to include the rotational mass of the turbine and generator, coupled via a shaft with nominal stiffness and damping terms. A Standard model [5] for a double rotational mass was used to create a generic wind turbine model.

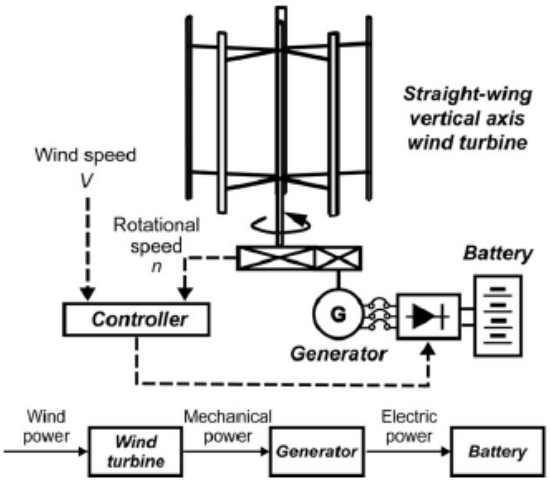

Figure 1: Schematic of the VAWT system model [4]

The equation of motion for a rotational mass is described in (1), where ω_T is the rotational speed of the turbine rotor in rad/sec, ω_G is the rotational speed of the generator in rad/sec, j_T is the moment of inertia of the rotor in Kg.m^2, t is time in seconds, $\dot{\omega}_T$ is the acceleration of the rotor in rad/sec^2 and Γ_T is the aerodynamic torque produced by the turbine in Nm. K and D are the stiffness and damping terms of the shaft, in N/m and N.s/m respectively. θ_T and θ_G are the angular displacement of the rotor and generator respectively in rads.

$$\dot{\omega}_T = \left(\frac{1}{j_T}\right)[\Gamma_T - D(\omega_T - \omega_G) - K(\theta_T - \theta_G)] \quad (1)$$

The net torque value is taken as the net of the aerodynamic torque produced by the rotor and the load torque on the system. The aerodynamic torque is taken as an averaged, instantaneous torque value from CFD data [6], for a particular tip-speed ratio and wind speed. In the model this is taken as a lookup value from a 2D array of data. Previous authors have used Blade Element Momentum methods to generate aerodynamic torque data [4]. This data will be specific to a particular rotor, the dynamic model used is generic.

The numerical model involves integrating the equation of motion, over time, for a given wind speed profile. To integrate the equation of motion an initial value explicit Euler method was used, from the following equations:

$$\Delta\omega_T = \dot{\omega}_T . \Delta t \quad (2)$$

$$\omega_{T_n} = \Delta\omega_{T_{n-1}} + \omega_{T_{n-1}} \quad (3)$$

The model consists of three main sections, the aerodynamic section, mechanical drivetrain section and the control load torque on the system. A number of control load torque regimes can be used. T. Wakui *et al.* [4] employed a constant tip-speed ratio load torque up until a power limit, then a constant speed torque mode was used. This is a typical control algorithm, which tracks the maximum power point at each wind speed up until a rated speed where a power shedding mode is utilised. A flow chart of the model method is shown in Figure 2 below

.

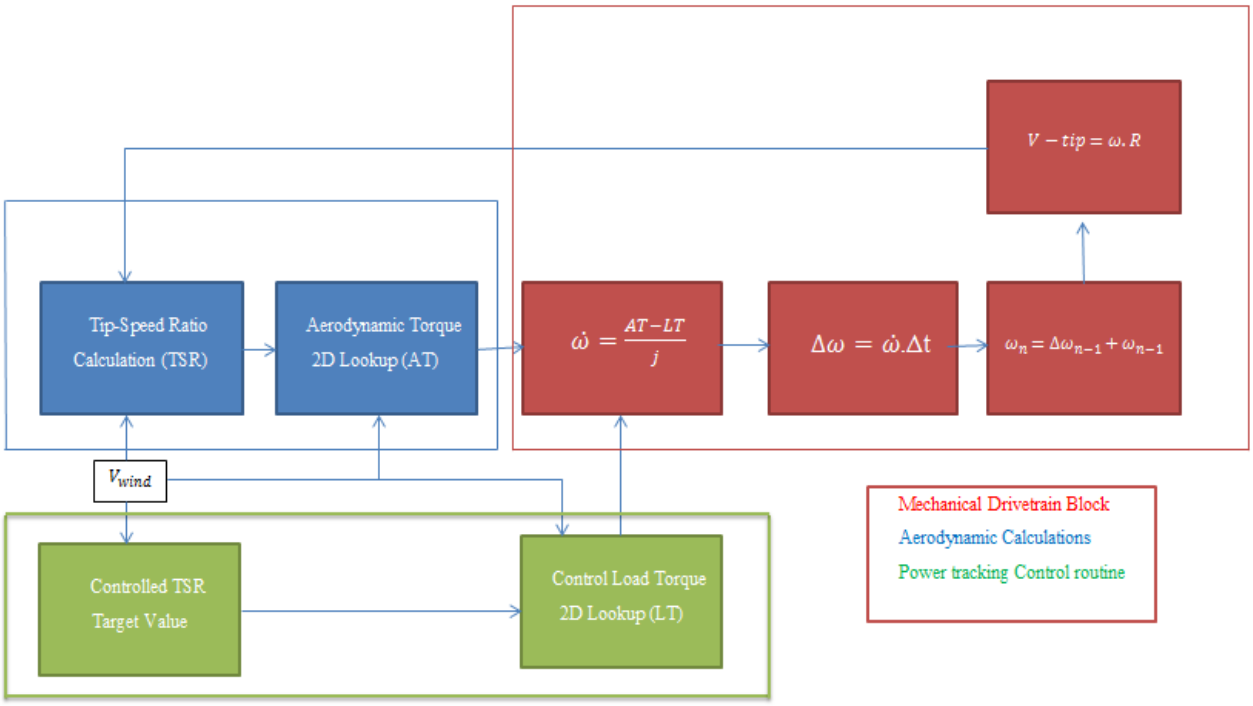

Figure 2: Outline of Dynamic Simulation Model

A number of unsteady wind conditions can be used in the model, high resolution (100 Hz) real wind data and a standard wind gust model prescribed in the British standard (BS EN 61400-2:2006) was used.

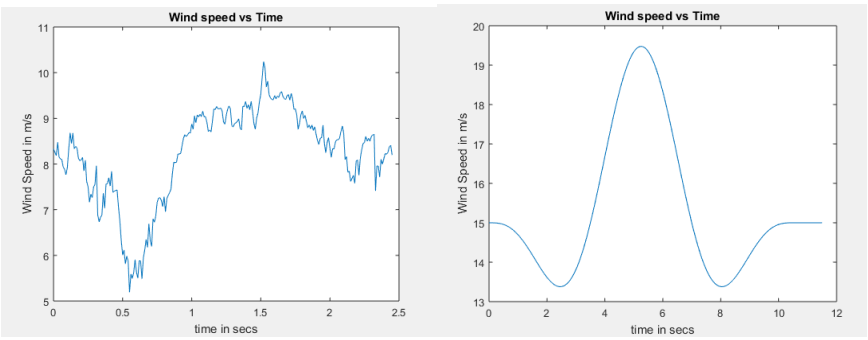

Figure 3: High Resolution (100 Hz) Sample of Wind Data (left), BS EN 61400-2:2006 wind gust model (right)

3. Conclusions

In this work a computational tool to test the effect of unsteady wind on a VAWT was created. The model can utilise a number of input wind conditions and control regimes for different rotors. This makes the model a useful tool for a parametric study of the rotordynamics in a number of wind conditions, at different timescales. The tool will be used for studying the power smoothing potential of the moment of inertia in unsteady wind conditions. Also the future work will look at coupling the VAWT model with other technologies such as wind pumping technology.

Acknowledgements

The author Amir Jalalian-Khakshour would like to acknowledge the funding from the EPSRC (EP/I015507/1) funded EDT MATTER - Manufacturing Advances Through Training Engineering Researchers, C-fec Ltd. and the European Social Fund through the Welsh Government.

References

[1] M. Beaudin, H. Zareipour , A. Schellenberglabe, W. Rosehart, *Energy storage for mitigating the variability of renewable electricity sources: An updated review,* Energy for Sustainable Development 14 (2010) 302–314

[2] L. Ran , J.R. Bumby and P.J Tavner, *Use of Turbine Inertia for Power Smoothing of Wind Turbines with a DFIG*, 11th International Conference on Harmonics and Quality of Power, 2004

[3] Y. Hara, K. Hara, and T. Hayashi, *Moment of Inertia Dependence of Vertical Axis Wind Turbines in Pulsating Winds,* International Journal of Rotating MachineryVolume 2012

[4] T. Wakui, R. Yokoyama, *Wind speed sensorless performance monitoring based on operating behaviour for stand-alone vertical axis wind turbine*, Renewable Energy 53 (2013) 49-59

[5] M. Singh and S. Santoso, *Dynamic Models for Wind Turbines and Wind Power Plants*, National Renewable Energy Laboratory (NREL), Jan 11th, 2008 – May 31, 2011

[6] S.A. Rolland, M. Thatcher , W. Newton a , A.J. Williams , T.N. Croft , D.T. Gethin, M. Cross , *Simulations technique for the design of a vertical axis wind turbine device with experimental validation*, Volume 111, November 2013, Pages 1195–1203

Proceedings of the 24th UK Conference of the
Association for Computational Mechanics in Engineering
31 March – 01 April 2016, Cardiff University, Cardiff

FE modelling of CFRP strengthened steel members under impact loads

***Majid Kadhim[1, 2], Zhangjian Wu[1], Lee Cunningham[1]**

[1]School of Mechanical, Aerospace and Civil Engineering, The University of Manchester
Manchester M13 9PL, United Kingdom
[2]College of Engineering, University of Babylon, Al Hillah, Iraq

*majid.kadhim@postgrad.manchester.ac.uk

ABSTRACT

Recently, the strengthening of steel structures using carbon fibre reinforced polymer has become more attractive for designers due to the advantages of high strength-to-weight ratio and superior environmental durability. Significant research has been performed on the behaviour of CFRP strengthened steel members under static loads. Dynamic behaviour, and in particular impact loading, of CFRP strengthened steelwork has been scarcely studied. In practice, steelwork could be subjected to impact from different events such as road vehicle or ship collisions, and impact by flying debris after an explosion etc.

This study discusses the numerical investigation of the effectiveness of CFRP sheets in strengthening square hollow section (SHS) steel columns under transverse impact loads. The study was conducted using the finite element (FE) programme ABAQUS 6.13. The proposed three-dimensional FE model was validated using existing experimental results. The strain hardening and strain rate effects were accounted for in this model using classical metal plasticity and the Cowper Symonds model respectively, while the CFRP and adhesive material were modelled using the elastic lamina and traction separation model respectively. The effect of different parameters has been investigated in this study such as the compression load level, boundary conditions and CFRP configurations. It has been found that the CFRP can significantly improve column performance for different values depending on the above parameters.

Keywords: *impact; steelwork; carbon fibre reinforced polymer*

1. Introduction

In recent years, there has been an increasing amount of studies on strengthening and repair of steel structures using the technique of adhesively bonded carbon fibre reinforced polymer (CFRP). Most of these studies examined the effectiveness of CFRP strengthening on I' beams such as [1, 2] while hollow structural sections have received less attention from researchers. Photiou [3] found that the ultimate strength of RHS beams with artificial degradation could be restored by using CFRP. In another study, the strengthening of circular hollow section (CHS) beams using CFRP fabric was investigated with emphasis on curing the resin materials under seawater [4]. Different slenderness ratios were examined by Shaat [5] to find out the effect of column slenderness ratio on the strengthened members. During it's life span, a steel structure may be subjected to different types of dynamic loading such as impact. To date only a limited amount of research has been conducted on the behaviour of CFRP strengthened steel members under impact loads. Recently Alam et al [6] examined numerically the effectiveness of fully bonded CFRP plate on SHS columns using ABAQUS. SHS sections with 89×89×3.2 cross section and length 2380 mm strengthened with longitudinal CFRP plates were adopted in the numerical model. According to the aforementioned literature review, the effect of impact load on the CFRP strengthened members needs more study to find out the influence of parameters such as boundary conditions, CFRP configuration and partial bond between the CFRP and steel members. This paper focuses on the behaviour of CFRP strengthened SHS columns under impact load taking into account the boundary conditions, compression load level and different CFRP configurations.

2. Finite element model validation

The simulation model is built using the general finite element software ABAQUS 6.13-1. The steel member was modelled using a four-node shell element S4R, while an eight-node brick element

C3D8R is adopted to model the impactor. In the later simulations, the CFRP and adhesive material were modelled using S4R and the cohesive element COH3D8 respectively. The strain hardening and strain rate effects were accounted for steel using isotropic strain hardening and Cowper Symonds model respectively. The failure behaviour of the materials was defined using the progressive damage and failure models provided by ABAQUS including the shear damage criterion for steel, Hashin's failure criteria for CFRP and the quadratic traction damage criterion for adhesive material.

The proposed finite element model is validated using the experimental test results conducted by Zeinoddini, et al. [7]. Un-strengthened, 1-meter long CHS specimens were tested with one fixed and one sliding end subjected to a 25.54 kg mass with a falling velocity 7 m/s (more detail on the experimental test is given in [7]). The specimens were tested under different compression load levels (P/Py) from 0 to 70% as listed in table 1.

Table 1: comparison between experimental and numerical results

P/Py(%)	Experimental (mm)		Numerical (mm)	
	Permanent deflection	Shortening	Permanent deflection	Shortening
0	15.5	0.3	17.3	0.4
25	21.5	0.8	19.4	1.4
50	25.3	2.3	26.6	3.5
60	28.4	3.1	33.6	5.7
70	-	113	195.1	112

Table 1 summarises the comparison between experimental and numerical permanent deflection and axial shortening. Good agreement was achieved using the numerical model in terms of maximum deformation; shortening and deformation at failure (see Figure 1 (a)). On the other hand, the impact load, which is the interface force developed under the indentor, recorded during the tests for different levels of axial load was compared with corresponding numerical values as shown in Figure 1(b). It can be noticed from this figure that maximum impact load happens with a lower level of axial load while the specimen with 70% P/Py has the minimum value of impact load. This indicates the higher the pre-compression, the less stiff the response.

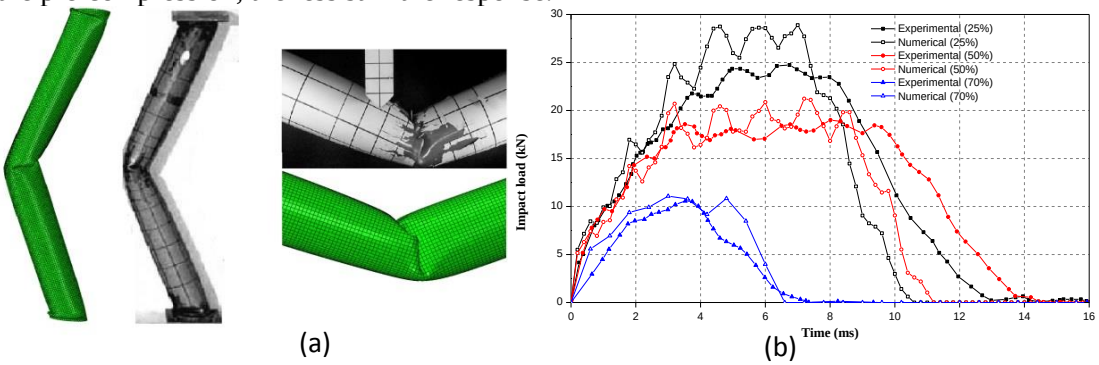

(a) (b)

Figure 1: comparison between experimental [7], and numerical results (a) deformation shape; (b) impact load

3. CFRP strengthened steel columns

In order to investigate the effectiveness of CFRP in strengthening steel members under impact loads, a full-scale column section 3.5 m long was designed according to Eurocode 3 to carry a load consistent with a six storey commercial building. Two different boundary conditions were chosen: simply supported and fixed-fixed to find out the effect of the boundary conditions on the strengthened members. The modulus of elasticity and yield stress of steel were assumed as 200000 and 355 MPa respectively. Different kinetic energies were applied on the designed column (SHS 200×200×8.8) with different components (velocity and mass), while four compression static load levels were suggested as listed in Table 2. It is clear from previous studies[5] that the CFRP orientation has a considerable effect on the strengthening efficiency, therefore three CFRP configurations 6 mm CFRP in the longitudinal direction (L), 6 mm CFRP in the transverse direction (T), 3mm CFRP in the longitudinal direction and 3 mm CFRP in transverse direction (LT), wrapped around the whole

section in all cases) were investigated in this study to ascertain the most efficient. The length of the CFRP was kept constant and is equal to the column length. The material properties of the carbon fibre and the adhesive material gained from Al-Zubaidy, et al. [8].

Table 2: Failure modes for simply supported and fixed-fixed columns

P/Py	BC	Mass=0.5 tonnes												Mass=2 tonnes							
		Impact Velocity (m/s)												Impact Velocity (m/s)							
		5				10				15				5				10			
		U	L	T	LT	U	L	T	LT	U	L	T	LT	U	L	T	LT	U	L	T	LT
0	SS	S	S	S	S	S	S	S	S	S	S	S	S	S	S	S	S	G	S	S	S
	FF	S	S	S	S	S	S	S	S	S	S	S	S	S	S	S	S	S	S	S	S
0.25	SS	S	S	S	S	S	S	S	S	G	S	S	S	G	S	S	S	G	G	G	G
	FF	S	S	S	S	S	S	S	S	S	S	S	S	S	S	S	S	G	S	S	S
0.50	SS	S	S	S	S	G	S	S	S	G	G	G	G	G	S	S	S	G	G	G	G
	FF	S	S	S	S	S	S	S	S	S	S	S	S	S	S	S	S	G	G	G	G
0.75	SS	G	S	S	S	G	G	G	G	G	G	G	G	G	G	G	G	G	G	G	G
	FF	S	S	S	S	G	S	S	S	G	G	G	G	G	S	S	S	G	G	G	G

S: Stable; G: Global buckling failure; U: unstrengthened; L, T, and LT: strengthened columns with CFRP oriented in the longitudinal, transverse and both longitudinal and transverse direction; SS: simply supported; FF: fixed-fixed

As described in section 2 all possible failure modes were included in the validated model. However, in this simulation two main failure modes were investigated namely global buckling failure and transverse shear failure which likely happens when the impact point is close to a support. Therefore, global bucking failure is the unique failure in table 2, while other material failures such as debonding and CFRP rupture were not listed in this table because they are not likely to cause a column failure during this study. It is apparent from Table 2 that the CFRP can enhance the column capacity for the applied compression force in addition to impact load in many cases for the investigated boundary conditions, while for the unstrengthened stable columns the corresponding strengthened column showed less lateral displacement value under the same loading conditions.

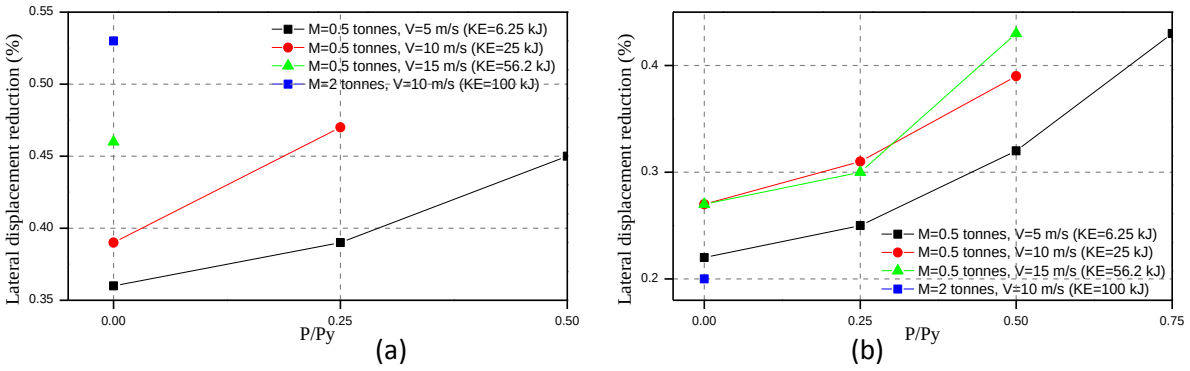

Figure 2: Lateral displacement reduction against pre-loading level for CFRP strengthened columns in longitudinal direction (a) simply supported column; (b) fixed-fixed column.

However, the percentage of lateral displacement reduction is different depending on the CFRP configuration, loading level (P/Py), applied kinetic energy and the boundary conditions. In Figure 2 there is a clear trend of increasing lateral displacement reduction with high levels of P/Py and kinetic energy for simply supported columns strengthened in the longitudinal direction, while for fixed-fixed columns it seems that this trend is slightly different in the last value of kinetic energy (KE). The reason for this difference is related to the severe deformation happening under the impactor for the fixed-fixed columns compared to corresponding simply supported columns, which is caused by the relatively high stiffness of the fixed-fixed member. The above reason may also account for why the CFRP in the transverse direction plays more significant role in fixed-fixed columns, while the enhancement role of the other CFRP configurations reduce with fixed-fixed boundary condition

columns as shown in Figure 3 (a). The above finding is consistent with the study by Shaat [5], which revealed that the CFRP in transverse directions can reduce the local buckling while having fibres oriented in the longitudinal direction can improve the stability of the columns against lateral displacement under static load. It can also be seen from Figure 3(a) that the columns strengthened with CFRP oriented in the longitudinal direction have the highest lateral displacement reduction, whereas the columns strengthened with CFRP in the transverse direction tend to give more severe column response (large displacement) compared to other strengthening configurations. However, these results are significantly different from a similar study by [6] which revealed that CFRP in longitudinal direction can minimise the lateral displacement by about 58% while in this study the average reduction in lateral displacement is about 44%. One reason why that happened may be the result of using partial bond between CFRP and steel in the current study, this being more representative of actual behaviour. Figure 3 (b) proves that CFRP can enhance local buckling resistance of the columns strengthened with CFRP oriented in the transverse direction more than the columns in other directions.

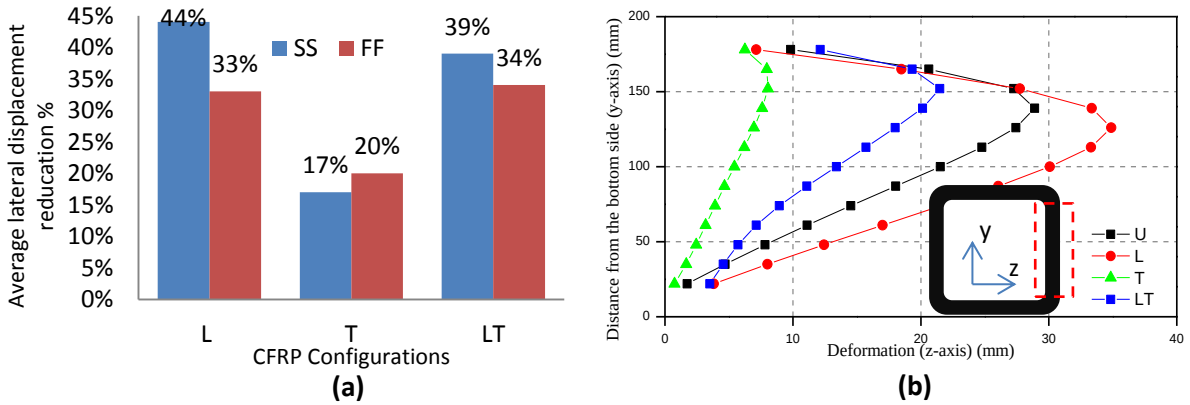

Figure 3: (a) Average lateral displacement reduction against CFRP configuration; (b) Deformation along right side at the point of maximum lateral displacement (Mass=2,V10m/s, fixed-fixed column).

4. Conclusions

Externally bonded CFRP can improve steel column behaviour under impact loads. The numerical results showed that the CFRP could minimise the lateral displacement of the impacted columns with different amounts (44% to 17%) depending on factors such as CFRP configuration, preloading level, boundary conditions and applied kinetic energy.

References

[1] Colombi, P.C. Poggi, *An experimental, analytical and numerical study of the static behavior of steel beams reinforced by pultruded CFRP strips.* Composites Part B: Engineering, 2006. **37**(1): p. 64-73.

[2] Deng, J.M.M. Lee, *Behaviour under static loading of metallic beams reinforced with a bonded CFRP plate.* composite structures, 2007. **78**(2): p. 232-242.

[3] Photiou, N.K., *Rehabilitation of steel members utilising hybrid FRP composite material systems*, 2005, University of Surrey.

[4] Seica, M.V.J.A. Packer, *FRP materials for the rehabilitation of tubular steel structures, for underwater applications.* composite structures, 2007. **80**(3): p. 440-450.

[5] Shaat, A.A.S., *Structural behaviour of steel columns and steel-concrete composite girders retrofitted using CFRP.* 2007.

[6] Alam, M.I.S. Fawzia, *Numerical studies on CFRP strengthened steel columns under transverse impact.* composite structures, 2015. **120**: p. 428-441.

[7] Zeinoddini, M., G. ParkeJ. Harding, *Axially pre-loaded steel tubes subjected to lateral impacts: an experimental study.* International Journal of Impact Engineering, 2002. **27**(6): p. 669-690.

[8] Al-Zubaidy, H.A., X.-L. ZhaoR. Al-Mahaidi, *Finite element modelling of CFRP/steel double strap joints subjected to dynamic tensile loadings.* Composite Structures, 2013. **99**: p. 48-61.

Solids and Structures IV

Proceedings of the 24th UK Conference of the
Association for Computational Mechanics in Engineering
31 March - 01 April 2016, Cardiff University, Cardiff

A PARTITION-OF-UNITY BOUNDARY ELEMENT METHOD FOR TRANSIENT WAVE PROPAGATION

***David Stark[1] and Heiko Gimperlein[1,2]**

[1]Maxwell Institute for Mathematical Sciences and Department of Mathematics, Heriot–Watt University, Edinburgh, EH14 4AS, United Kingdom
[2]Institute for Mathematics, University of Paderborn, Warburger Str. 100, 33098 Paderborn, Germany

*ds221@hw.ac.uk

ABSTRACT

We propose a time domain partition-of-unity boundary element method for wave propagation problems at high frequency. Travelling waves are included as enrichment functions into a space-time boundary element solver. We present some first numerical experiments with this method for high frequencies, and discuss the algorithmic challenges, with a view towards engineering applications.

Key Words: *boundary element method; time domain integral equations; partition of unity method; computational acoustics; traffic noise*

1. Introduction

Boundary element methods provide an efficient, extensively studied numerical scheme for time-independent or time-harmonic scattering and emission problems. Unlike finite element discretisations, they reduce the computation from the three dimensional domain to its two dimensional boundary. Recently, boundary elements have been explored for the simulation of transient phenomena, with applications e.g. to environmental noise [2] or electromagnetic scattering [5]. For the wave equation, time-dependent boundary element methods (TDBEM) were first analysed by Bamberger and Ha-Duong [1].

On the other hand, for time-harmonic wave propagation partition-of-unity, finite and boundary element methods (PUFEM / PUBEM) have emerged as a practically efficient method to achieve engineering accuracy in spite of the numerical pollution at high frequencies [4]. More recently, first results towards time-dependent finite elements with partition-of-unity enrichment in space have been obtained in [3].

This work presents a time domain partition-of-unity boundary element method based on enrichments in space and time. It is the first investigation of a space-time enriched method, here applied to a time-dependent integral equation. The method extends the above works for time-harmonic wave propagation to truly transient problems and, as a space-time Galerkin method, can be proven to be numerically stable and convergent. Practically, it includes travelling plane-wave enrichment functions into an h-version time domain boundary element procedure.

Acknowledgements: H. G. is supported by ERC Advanced Grant HARG 268105.

2. Problem description and time domain PUBEM

This work considers transient sound radiation problems in the exterior of a scatterer Ω^-, where Ω^- is a bounded polygon with connected complement $\Omega = \mathbb{R}^3 \setminus \Omega^-$. The acoustic sound pressure field $u(t,\mathbf{x})$ due to an incident field or sources on $\Gamma = \partial\Omega$ satisfies the linear wave equation for $t \in \mathbb{R}$:

$$c^{-2}\partial_t^2 u(t,\mathbf{x}) - \Delta u(t,\mathbf{x}) = 0 \quad \text{for } \mathbf{x} \in \Omega, \quad u(t,\mathbf{x}) = f(t,\mathbf{x}) \quad \text{for } \mathbf{x} \in \Gamma, \quad u(t,\mathbf{x}) = 0 \quad \text{for } t \leq 0. \quad (1)$$

Here c is the wave velocity, and in the following we set $c = 1$ for simplicity. A single-layer ansatz for u,

$$u(t,\mathbf{x}) = \int_\Gamma \frac{\phi(t-|\mathbf{x}-\mathbf{y}|,\mathbf{y})}{2\pi|\mathbf{x}-\mathbf{y}|} ds_y, \quad (2)$$

results in an equivalent weak formulation of (1) as a coercive integral equation of the first kind: Find ϕ such that for all ψ

$$\int_0^\infty \int_\Gamma (V\phi(t,\mathbf{x}))\partial_t\psi(t,\mathbf{x})\, ds_x\, d_\sigma t = \int_0^\infty \int_\Gamma f(t,\mathbf{x})\partial_t\psi(t,\mathbf{x})\, ds_x\, d_\sigma t\ , V\phi(t,\mathbf{x}) = \int_\Gamma \frac{\phi(t-|\mathbf{x}-\mathbf{y}|,\mathbf{y})}{2\pi|\mathbf{x}-\mathbf{y}|} ds_y, \tag{3}$$

with $d_\sigma t = e^{-2\sigma t}dt$. A theoretical analysis requires $\sigma > 0$, but practical computations use $\sigma = 0$ [1, 2].

We propose a time-dependent boundary element method to solve (3), based on numerical approximations by travelling plane waves:

$$\phi_{h,\Delta t} = \textstyle\sum_i c_i\phi_i, \quad \text{where } \phi_i(t,\mathbf{x}) = \widetilde{\Lambda}_i(t)\Lambda_i(\mathbf{x})\cos(\omega_i(t-t_i) - \mathbf{k}_i\cdot\mathbf{x} + \sigma_i)\ . \tag{4}$$

Here $\omega_i = |\mathbf{k}_i|$, $\sigma_i \in \{0, \frac{\pi}{2}\}$, Λ_i a piecewise polynomial shape function in space and $\widetilde{\Lambda}_i$ a corresponding shape function in time. A first work by Ham and Bathe uses space-enriched FEM for waves in 2d [3].

We obtain a numerical scheme for the weak formulation (3): Find $\phi_{h,\Delta t}$ such that for all $\psi_{h,\Delta t}$

$$\int_0^\infty \int_\Gamma (V\phi_{h,\Delta t}(t,\mathbf{x}))\partial_t\psi_{h,\Delta t}(t,\mathbf{x})\, ds_x\, dt = \int_0^\infty \int_\Gamma f(t,\mathbf{x})\partial_t\psi_{h,\Delta t}(t,\mathbf{x})\, ds_x\, dt\ . \tag{5}$$

From $\phi_{h,\Delta t}$, the sound pressure $u_{h,\Delta t}$ is obtained in Ω by evaluating the integral in (2) numerically. Equation (5) leads to a linear system of equations in space-time, Figure 1, where the stiffness matrix

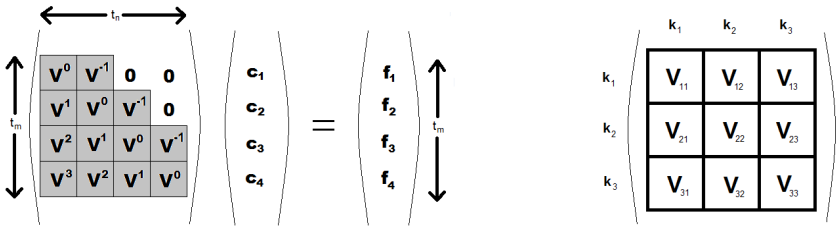

Figure 1: Full PUBEM space-time system and decomposition of the matrices V^j.

$$\mathbf{V}_{mn} = \int_0^\infty \int_\Gamma \int_\Gamma \frac{\phi_m(t-|\mathbf{x}-\mathbf{y}|,\mathbf{y})}{2\pi|\mathbf{x}-\mathbf{y}|}\partial_t\psi_n(t,\mathbf{x})\, ds_y\, ds_x\, dt$$

has a block-banded structure corresponding to the time steps. Each of the time-step blocks decomposes into blocks for the individual enrichments $\mathbf{k}_i$.

A main challenge is the accurate assembly of $\mathbf{V}_{mn}$. After an analytical evaluation of the time integral, the y integral requires integration over geometrically complicated intersections of triangles with light cone shells, with a singular integrand $|\mathbf{x}-\mathbf{y}|^{-1}$. It is evaluated in polar coordinates with a geometrically-graded hp-composite Gauss quadrature [2]. A regular Gauss quadrature is used for the x integral.

Note that the method (5), as a Galerkin method, minimises the energy $E[\phi_{h,\Delta t}] = E(\mathbf{c}) = \frac{1}{2}\mathbf{c}\cdot\mathbf{V}\mathbf{c} - \mathbf{F}\cdot\mathbf{c}$. Stability and convergence are therefore guaranteed, at least for $\sigma > 0$ or sufficiently small times [1, 2].

3. Numerical experiments

Example 1: For a regular icosahedron Γ (Figure 2) of diameter 2 and centered in (0, 0, 0), we use the right hand side $f(t,\mathbf{x}) = \exp(-25/t^2)\cos(\omega_f t - \mathbf{k}_f\mathbf{x})$, a plane wave with $\mathbf{k}_f$=(1.5, 3, 8.5) which is smoothly turned on for times [0,5]. The partition-of-unity TDBEM approximation is compared to h-TDBEM results with 1280 triangles and constant CFL ratio = 0.19. Figure 2 depicts the reference solution ϕ at times 3.8, 4.2 and 4.6 and Figure 3a the PU solution in the centroid of a triangle. The PU TDBEM uses a mesh of 20 triangles and n enrichment functions in each triangle, for $n \le 15$ and $\Delta t = 0.1, 0.2$.

We quantify the numerical error by studying the convergence of the energy $E[\phi_{h,\Delta t}]$.

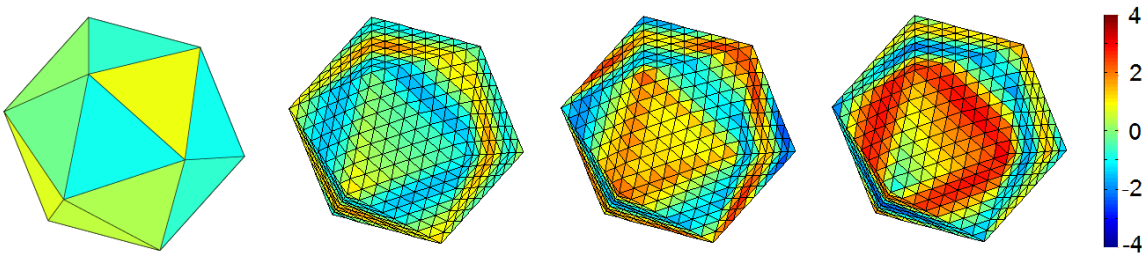

Figure 2: Example 1 - meshes for PU (20 triangles) and h-method (1280 triangles), density at $t = 3.8, 4.2, 4.6$.

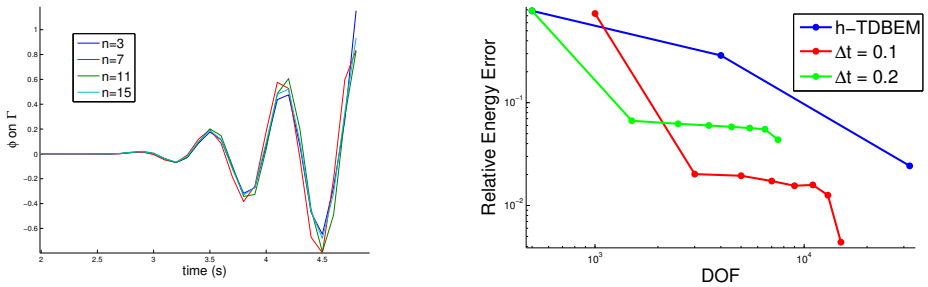

(a) (b)

Figure 3: Example 1 - a) density ϕ, b) relative error in energy: h-method, PU with $\Delta t = 0.1, 0.2$.

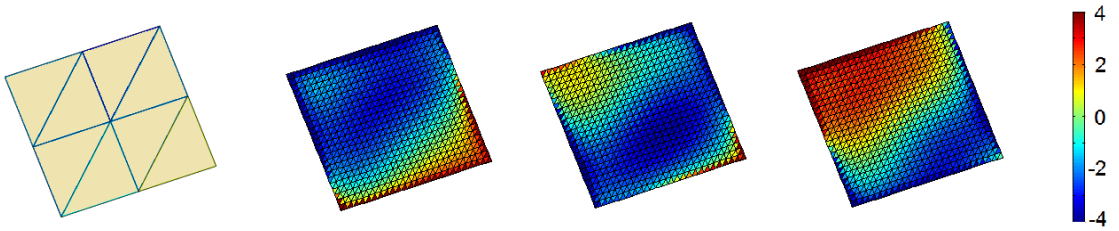

Figure 4: Example 2 - meshes for PU (8 triangles) and h-method (1250 triangles), density at $t = 3.8, 4.2, 4.6$.

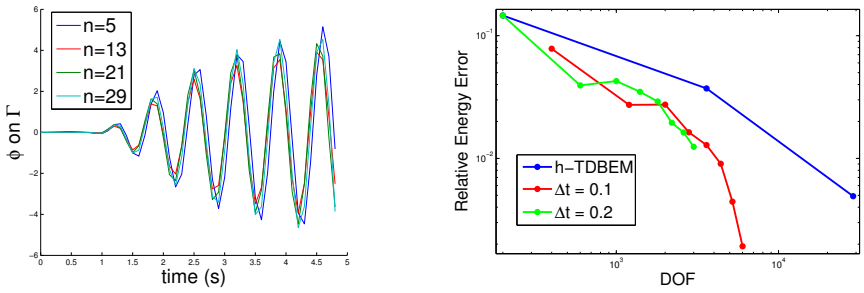

(a) (b)

Figure 5: Example 2 - a) density ϕ, b) relative error in energy: h-method, PU with $\Delta t = 0.1, 0.2$.

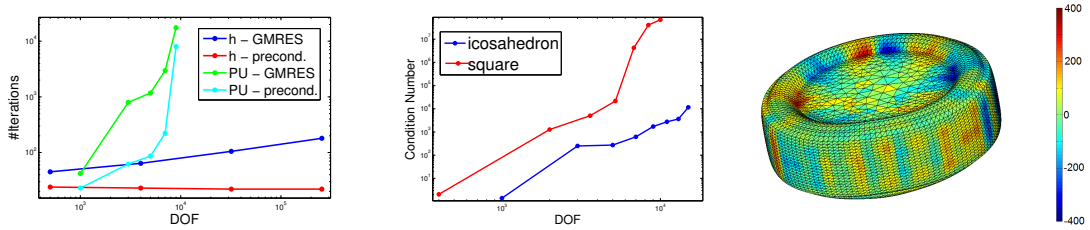

(a) (b) (c)

Figure 6: a) GMRES vs. preconditioned GMRES, b) condition number of $\mathbf{V}^0$ for PU, c) density ϕ on car tyre.

Figure 3b shows a comparison of convergence in the energy, between our h-TDBEM and PU-TDBEM. The PU method reduces the degrees of freedom by a factor up to 8.

Example 2: We now consider a screen $\Gamma = [0,0.5]^2 \times \{z = 0\}$ (Figure 4). We compare a PU method on 8 triangles with $n \leq 30$ enrichment functions to an h-TDBEM with 1250 triangles and CFL ratio 0.56. We use $f(t,\mathbf{x}) = \exp(-4/t^2)\cos(\omega_f t - \mathbf{k}_f \mathbf{x})$, with $\mathbf{k}_f$=(1.5, 3, 8.5) for times [0,5].

Figure 5a shows the density ϕ at the centroid of a triangles, Figure 4 the h-TDBEM density at 3.8,4.2,4.6. Figure 5b depicts the comparison of convergence in energy for h-TDBEM and PU-TDBEM, for Δt = 0.1,0.2. For larger systems, we observe a significant reduction of the degrees of freedom for PU.

Since the memory requirements are too large for solving the large space-time linear system in Figure 1, we use an iterative GMRES solver which allows us to refer implicitly to the memory-intensive stiffness matrix via matrix-vector products only. We have developed a preconditioner for h-TDBEM, which requires less than 25 iterations independent of degrees of freedom (Figure 6a). For PU, the number of iterations is reduced. As known for time-independent PU methods, the stiffness matrix exhibits high condition numbers, here up to 10^8 on the square (Figure 6b).

4. Conclusions and Outlook

This work presents a first step towards space-time enriched methods for the wave equation, here for boundary elements. Even for finite elements such space-time enriched methods are just beginning to be explored. They present a promising approach to efficiently achieve engineering accuracy for rapidly oscillating solutions, with applications from imaging to sound radiation.

Our preliminary results for PU TDBEM already save a factor of 8 for the degrees of freedom compared to the h-method for accuracies as low as a fraction of a percent. We expect further improvements with a more thorough analysis of the time-enrichment, as well as the possibility of using larger time steps.

Outlook: Future work will investigate optimal time enrichments and preconditioning of PU TDBEM. One motivation comes from the sound radiation of tyres [2], Figure 6c.

References

[1] A. Bamberger, T. Ha Duong, *Formulation variationnelle espace-temps pour le calcul par potentiel retard de la diffraction d'une onde acoustique*, Math. Meth. Appl. Sci. 8 (1986), 405-435, 598-608.

[2] H. Gimperlein, M. Maischak, E. P. Stephan, *Adaptive time domain boundary element methods and engineering applications*, invited survey, preprint (2015).

[3] S. Ham, K. J. Bathe, *A finite element method enriched for wave propagation problems*, Computers and Structures 94-95 (2012), 1-12.

[4] E. Perrey-Debain, J. Trevelyan, P. Bettess, *On wave boundary elements for radiation and scattering*, IEEE Trans. Antennas and Propagation 53 (2005), 876-879.

[5] A. E. Yilmaz, J.-M. Jin, E. Michielssen, *Time domain adaptive integral method for surface integral equations*, IEEE Trans. Antennas Propagation 52 (2004), 2692-2708.

Proceedings of the 24th UK Conference of the
Association for Computational Mechanics in Engineering
31 March - 01 April 2016, Cardiff University, Cardiff

A HIGH-ORDER MATERIAL POINT METHOD

***Y. Ghaffari Motlagh [1] and W. M. Coombs [1]**

[1]School of Engineering and Computing Sciences, Durham University
Science Site, South Road, Durham, DH1 3LE

*yousef.ghaffari-motlagh@durham.ac.uk

ABSTRACT

The material point method (MPM) is a version of the particle-in-cell (PIC) which has substantial advantages over pure Lagrangian or Eulerian methods in numerical simulations of problems involving large deformations. Using MPM helps to avoid mesh distortion and tangling problems related to Lagrangian methods and the advection errors associated with Eulerian methods. In this paper a novel high-order material point method within an isogeomeric analysis (IGA) framework is developed. Utilizing high order basis functions enables more accurate determination of physical state variables e.g. stress. Smooth spline function spaces (B-splines) are used to eliminate the non-physical cell-crossing instabilities caused by use of standard finite element basis functions based on Lagrange polynomials.

Key Words: *material point method; implicit time integration; isogeometric analysis; B-splines*

1. Introduction

The material-point method (MPM) is a numerical method for solving continuum problems in fluid and solid mechanics. Its origins are the particle-in-cell (PIC) method developed at Los Alamos in the 1950s [1, 2] to model highly distorted fluid flow such as the splash of a falling drop. In the late 1980s, Brackbill and Ruppel [3] revived the PIC technology with simple modifications that reduced the numerical dissipation and made PIC competitive with current technologies for simulating hydrodynamics. The MPM [4, 5, 6] is a version of this method that is applicable to solids with strength and stiffness and has been applied to model diverse applications such as impact, penetration, fracture, metal forming, granular media and membranes.

In order to combine the advantages of Eulerian and Lagrangian methods, MPM uses two representations of the continuum. First, MPM discretises a continuum body of fluid or solid with a finite set of material points in the original configuration that are tracked throughout the deformation process. Each material point has a mass, position, velocity and stress, as well as material parameters and internal variables as needed for constitutive models or thermodynamics. These material points provide a Lagrangian description of the material that is not subject to mesh tangling because no connectivity is assumed between the points. The latter description, an Eulerian framework, is an often regular background mesh that covers the computational domain. Information is transferred from the material points to the background mesh, the momentum equation is solved on the background mesh, and then information from the mesh solution used to update the material points, at which time the background mesh can be modified if desired, the cycle then repeats.

Despite the MPM being promoted for its ability to solver large deformation problems it suffers from instabilities when material points cross between elements. These instabilities are due to the lack of smoothness of the grid basis functions used for mapping information between the material points and the background grid. By introducing a weighting function with higher degree of smoothness, the generalized interpolation material point (GIMP) method is capable of reducing these errors and improving accuracy [7]. Convected particle domain interpolation (CPDI) is another algorithm developed to improve the accuracy and efficiency of the material point method for problems involving extremely large tensile

deformation and rotation [8]. However, both methods require the basis functions (normally taken to be linear) to be integrated over the domain of the material point of interest, they also do not fully eliminate spurious oscillations due to cell crossing. In this paper an alternative approach is suggested where smooth B-spline function spaces are used to map between the material points and the background grid. The high-order smoothness of the splines eliminates the cell-crossing instability.

2. The quasi-static implicit material point method

Let us start by recalling the elastostatic equations. Let $\Omega \subset \mathbb{R}^d, d = 2,3$, denote the domain occupied by the body, and let $\Gamma = \partial\Omega$ be its boundary. Then

$$\nabla \cdot \boldsymbol{\sigma} + \boldsymbol{f} = \boldsymbol{0} \quad \text{in } \Omega, \qquad \boldsymbol{u} = \boldsymbol{g} \quad \text{on } \Gamma_D, \qquad \text{and} \qquad \boldsymbol{\sigma} \cdot \boldsymbol{n} = \boldsymbol{h} \quad \text{on } \Gamma_N, \tag{1}$$

where $\boldsymbol{\sigma}$ denotes the symmetric Cauchy stress tensor and $\boldsymbol{f}$ is the body force per unit volumeis, $\boldsymbol{u}$ is the displacement, $\boldsymbol{g}$ and $\boldsymbol{h}$ are refered as essential, Dirichlet, and natural, Neumann boundary condition, respectively. Here we restrict ourselves to small-strain analysis, where the small strain approximation, denoted by $\boldsymbol{\epsilon}$, is computed as the symmetric part of the displacement gradient $\boldsymbol{\epsilon} = \left(\nabla \boldsymbol{u} + (\nabla \boldsymbol{u})^T\right)/2$. The constitutive relationship, $\boldsymbol{\sigma} = \boldsymbol{\sigma}(\boldsymbol{\epsilon})$, is necessary to form a complete set of equations for computing the state variable, $\boldsymbol{u}$. Here we assume a linear isotropic relationship between strain and the Cauchy stress.

2.1. Discrete form

The continuum body Ω is discretised by finite set of N_p material points $\{\boldsymbol{x}_p\}_{p=1}^{N_p} \in \Omega$ in the original configuration that are tracked throughout the deformation process. Also, space is discretised by a background mesh defined by a set of N_n control points $\{\boldsymbol{x}_i\}_{i=1}^{N_n}$. The discrete MPM equilibrium equations are constructed by pre-multiplying the strong form of equilibrium (1) by a weighting function and applying integration by parts. A simple one-point quadrature rule is applied over each volume Ω_p associated with the pth material point to give

$$-\sum_{p=1}^{N_p} \left\{ \left(\boldsymbol{\sigma}(\boldsymbol{x}_p) : \nabla \boldsymbol{w}^h(\boldsymbol{x}_p) \right) \Omega_p \right\} + \left(\boldsymbol{h}, \boldsymbol{w}^h \right)_{\Gamma_N} + \sum_{p=1}^{N_p} \left\{ \left(\boldsymbol{f}(\boldsymbol{x}_p) \cdot \boldsymbol{w}^h(\boldsymbol{x}_p) \right) \Omega_p \right\} = \boldsymbol{0}. \tag{2}$$

(2) is solved on a finite dimensional space using functions represented in terms of B-spline basis functions, N_i^q. A B-spline basis is constructed from piece-wise polynomials joined with a prescribed continuity. In order to define a B-spline basis of polynomial order q in one dimension it is necessary to define a *knot vector*. A knot vector in one dimension is a set of coordinates in the parametric space, written as

$$\Xi = \{0 = \xi_1, \xi_2, ..., \xi_{n+q+1} = 1\} \tag{3}$$

where $\xi_1 \leq \xi_2 \leq ...\xi_{q+n+1}$ and n is the total number of basis functions. Given Ξ and q, univariate B-spline basis functions are constructed recursively starting with piecewise

$$N_i^0(\xi) = \begin{cases} 1 & \text{if } \xi_i \leq \xi < \xi_{i+1} \\ 0 & \text{otherwise} \end{cases} \tag{4}$$

For $q = 1,2,3,...$, they are defined by

$$N_i^q(\xi) = \frac{\xi - \xi_i}{\xi_{i+q} - \xi_i} N_i^{q-1}(\xi) + \frac{\xi_{i+q+1} - \xi}{\xi_{i+q+1} - \xi_{i+1}} N_{i+1}^{q-1}(\xi) \tag{5}$$

Note that when $\xi_{i+q} - \xi_i = 0$, $(\xi - \xi_i)/(\xi_{i+q} - \xi_i)$ should be vanished, and similarly, when $\xi_{i+q+1} - \xi_{i+1} = 0$, $(\xi_{i+q+1} - \xi)/(\xi_{i+q+1} - \xi_{i+1})$ is taken to be zero as well. These basis functions have the following properties: (i) they form a partition of unity, (ii) have local support and (iii) are non-negative (for more details see [9]).

The explicit representation of $\boldsymbol{w}^h(\boldsymbol{x})$ in terms of the basis functions and control variables is assumed to take the standard form

$$\boldsymbol{w}^h(\boldsymbol{x}) = \sum_{i=1}^{N_n} N_i^q \boldsymbol{w}_i(\boldsymbol{x}). \tag{6}$$

Substituting the weighting function approximation into (2) and after simplification, the discrete MPM equation is obtained as

$$-\sum_{p=1}^{N_p} \left\{ \Big(\boldsymbol{\sigma}(\boldsymbol{x}_p) \cdot \nabla N_i^q(\boldsymbol{x}_p) \Big) \Omega_p \right\} + \int_{\Gamma_N} \boldsymbol{h} N_i^q \, d\Gamma + \sum_{p=1}^{N_p} \left\{ \boldsymbol{f}(\boldsymbol{x}_p) N_i^q(\boldsymbol{x}_p) \Omega_p \right\} = \boldsymbol{0}. \tag{7}$$

The numerical solution of this quasi-static problem is typically obtained in steps by incrementally imposing displacement boundary conditions, external forces or both in order to obtain increment in displacement, $\Delta\boldsymbol{u}$. Here a fully implicit method is employed to solve the problem. Once the displacement increment is obtained, the material point position, $\boldsymbol{x}_p$, and displacement, $\boldsymbol{u}_p$, are updated as follows

$$\boldsymbol{x}_p^{k+1} = \boldsymbol{x}_p^k + \sum_{i=1}^{N_n} \Delta\boldsymbol{u}_i N_i^q(\boldsymbol{x}_p^k) \qquad \text{and} \qquad \boldsymbol{u}_p^{k+1} = \boldsymbol{u}_p^k + \sum_{i=1}^{N_n} \Delta\boldsymbol{u}_i N_i^q(\boldsymbol{x}_p^k), \tag{8}$$

where k denotes the loadstep number. After each load step, the spatial position of background grid is reset to its original undeformed state.

3. Numerical results

Here we present the numerical results for a one-dimensional elastic column quasi-statically compressed by its own weight through the application of a body force, b_f, per unit mass. The initial material density $\rho_0 = 1$, Young's modulus $E = 10^6$, and initial column height $L_0 = 50$, all in compatible units. The column initially occupies 50 elements and the body force was applied over 20 loadsteps.

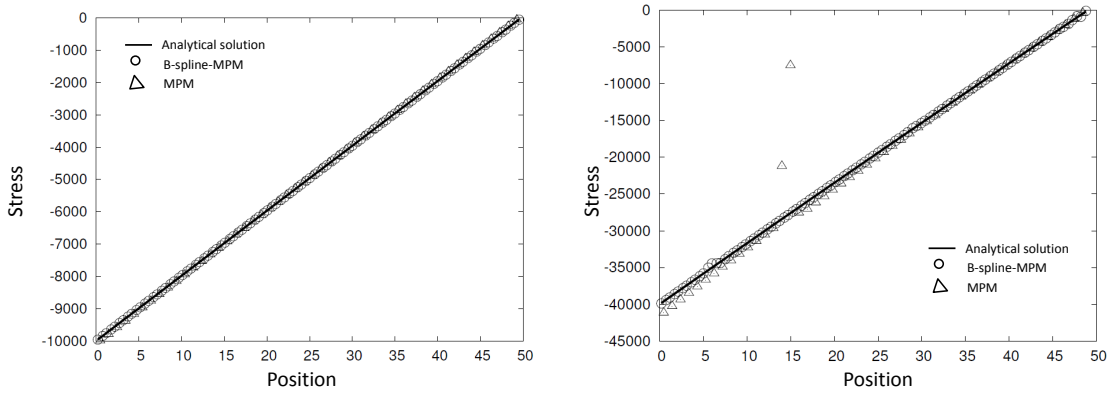

(a) $W = 10000$ (b) $W = 40000$

Figure 1: Numerical and analytical solutions to the one-dimensional elastic column quasi-statically compressed by its own weight under a body force

Figure 1 shows the stress distribution with $b_f = -200$ and $b_f = -800$, that is with a total column weight of $W = \rho_0 |b_f| L_0 = 10000$ and $W = 40000$, respectively. Results are shown for the standard MPM with linear basis functions and for the quadratic B-spline MPM ($q = 2$) and compared against the analytical solution (as provided in [7]). For the MPM the problem is initially discretised with one particle per grid cell as, for this very simple problem, increasing the number of material points reduces the accuracy of the simulation. The B-spline MPM used two particles per grid cell. In both cases the material points are initially located at the appropriate Gauss quadrature locations within the elements. When $b_f = -200$ both the methods provide a reasonable approximation to the analytical solution. However, for $b_f = -800$

spurious oscillations can be seen in the MPM results caused by cell-cross instabilities. These oscillations have been removed by the higher-order basis functions in the B-spline MPM.

Table 1 details the errors in the simulations based on the following error measure and the exact solution at the current particle locations [7]

$$\text{error} = \sum_{p=1}^{N_p} \frac{V_p|\sigma_p - \sigma_A(x_p)|}{WL_0}, \qquad \text{where} \qquad \sigma_A(x_p) = E\left(\sqrt{\frac{2\rho_0 b_f}{E}(L - x_p) + 1} - 1\right) \tag{9}$$

and $L = L_0 + \rho_0 b_f L_0^2/(2E)$ is the current length of the column. x_p is the particle location, V_p is the volume associated with the material point, σ_p is the material point stress. Errors have also been provided for an implicit GIMP implementation with two material points per original grid cell but have not been shown on Figure 1 for the sake of clarity.

total column weight, W	10,000	40,000
MPM	3.667×10^{-3}	2.572×10^{-2}
GIMP	3.680×10^{-3}	2.969×10^{-3}
B-spline MPM ($q = 2$)	6.221×10^{-5}	9.894×10^{-4}

Table 1: One-dimensional elastic column errors

It is clear from Table 1 that the B-spline MPM is an improvement over both the standard MPM and the GIMP method.

4. Conclusions

This paper has presented a MPM where the standard linear basis functions have been replaced by B-splines. The higher order smoothness of the splines significantly improves the accuracy of the method by removing the cell-cross instabilities seen in other MPMs.

Acknowledgements

The authors acknowledge the support of EPSRC grant EP/M017494/1.

References

[1] F. Harlow. Hydrodyanamics problems involving large fluid distortions, *J. Assoc. Compos. Mach.*, 4, 137, 1957.

[2] M. Evans, F. Harlow. The particle-in-cell method for hydrodynamic calculations, *Tech. Rep. LA-2139, Los Alamos Sci. Lab., Los Alamos, N. M.*, 1957.

[3] J. U. Brackbill, H. M. Ruppel. Flip: A method for adaptively zoned, particle-in-cell calculations in two dimensions, *J. Comput. Phys.*, 65, 314, 1986.

[4] D. Sulsky, Z. Chen, H. L. Schreyer. A particle method for history-dependent materials, *Comput. Methods Appl. Mech. Eng.*, 118, 179-196, 1994.

[5] D. Sulsky, S. J. Zhou, H. L. Schreyer. Application of a particle-in-cell method to solid mechanics,*Comput. Phys. Commun.*, 87, 236-252, 1995.

[6] D. Sulsky, H. L. Schreyer. Axisymmetric form of the material point method with applications to upsetting and Taylor impact problems, *Comput. Methods Appl. Mech. Eng.*, 139, 409-429, 1996.

[7] S. Bardenhagen, E. Kober. The generalized interpolation material point method, *CMES-Computer Modeling in Engineering and Sciences*, 5, 477-495. 2004.

[8] A. Sadeghirad, R. M. Brannon, J. Burghardt. A convected particle domain interpolation technique to extend applicability of the material point method for problems involving massive deformations, *Int. J. Numer. Meth. Engng*, 86, 1435-1456, 2011.

[9] L. Piegl, W. Tiller. *The NURBS Book (Monographs in Visual Communication)*, 2nd Edition., Springer-Verlag, New York, 1997.

VIBRATION ANALYSIS OF DAMAGED PLATES BY HYBRID EXACT STIFFNESS AND FINITE ELEMENT METHOD

***Basem Suliman[1], Carol Featherston[1] and David Kennedy[1]**

[1]Cardiff University, Cardiff School of Engineering – Queen's Buildings, The Parade, Cardiff, CF24 3AA, United Kingdom

*SulimanBS@cardiff.ac.uk

ABSTRACT

During preliminary aircraft design when many alternative configurations and load cases need to be considered, fast and reliable analysis tools are required. The specialist software VICONOPT is designed for efficient, accurate buckling and vibration analysis and optimum design of plates and panels. VICONOPT avoids the modelling and computational costs of finite element analysis by employing the exact stiffness analysis and the Wittrick-Williams algorithm. The vibration behaviour of isotropic plates containing through-the-length damages of different sizes and severities is studied using a novel hybrid method. This method, based on a concept that allows VICONOPT to work along with finite elements to improve the ability of VICONOPT to model cases of damaged plates, uses VICONOPT to model the undamaged parts of the structure in combination with finite elements in the area of the damage. The results show the ability of the hybrid method to handle through-the-length damages efficiently. This achievement opens the door for a wide range of more complicated damages that can be studied using this method.

Keywords: *Vibration, isotropic, damages, exact stiffness, finite element*

1. Introduction

Minimizing the mass of an aircraft's structure reduces the cost of materials and manufacturing, as well as fuel consumption and atmospheric emissions. During the preliminary design when many alternative configurations and load cases need to be considered, fast and reliable analysis tools are required. The VICONOPT (VIpasa with CONstraints and OPTimization) program is designed for efficient, accurate buckling and vibration analysis and optimum design of plates and stiffened panels, and is typically about 10 times faster than the equivalent finite element (FE) analysis [1]. This program is based on the exact finite strip method which assumes a continuous distribution of stiffness over the structure. VICONOPT is able to model plates which have different properties in the transverse (y) direction and even different thickness by connecting different plates in this direction. However, all the plates need to have the same length in the longitudinal (x) direction.

VICONOPT is able to model many different cases of damaged plates as long as the damaged region stretches along the whole length of the plate in the x direction. Damghani et al. [2] studied the critical buckling of composite plates with through-the-length delaminations which satisfy these prismatic requirements. This work was extended (Damghani et al. [3]) to study the global buckling behaviour of a composite plate with a single rectangular delamination. This method is based on replacing the longitudinal portion of the plate containing the delamination with an equivalent prismatic structure, which is capable of representing the global buckling behaviour but cannot capture local effects.

The combined VICONOPT and FE method presented here, denoted VFM, is based on using the FE method to model the longitudinal portion of the plate containing the damage as shown in Fig 1. However, the FE method has been merged with VICONOPT process to model the whole plate. This work extends the capability of VICONOPT to use computationally efficient analysis for different cases of plate damage which could not previously be modelled.

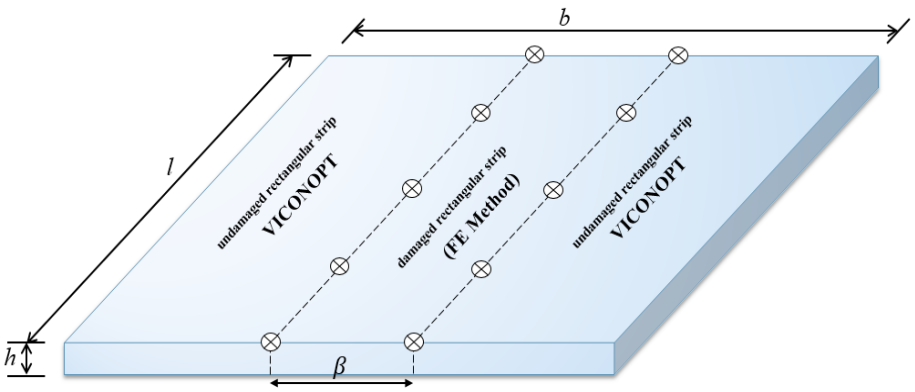

Figure 1: VICONOPT and FE method modelling damaged plate

2. Problem definition

During the early stages of design when many alternative configuration and load cases are considered, fast and reliable analysis tools are required. Finite element analysis (FEA) is capable of handling many combinations of loading and boundary conditions for different cases of damage but it is computationally expensive. These high computational costs are avoided in VICONOPT by employing exact strip solutions and the Wittrick-Williams algorithm [4]. However due to its prismatic requirements, VICONOPT can model damaged plates directly only if the damaged region stretches along the whole length of the plate. The aim of this study is to develop a novel method which can be used to improve the ability of VICONOPT to model more complex cases of damaged plates. For validation purposes and to demonstrate the efficiency of the approach a comparison is first made with FEA for an isotropic plate with through-the-length damage.

3. Theory and Formulation used in VFM

VICONOPT incorporates two earlier programs, VIPASA and VICON. VIPASA provides a powerful analysis for vibration and buckling of prismatic plate assemblies with simply supported ends. However, if the structure is under in-plane shear loading, the mode shapes will be skewed and the end conditions will not be satisfied. Thus the applicability of VIPASA is limited. VICON [5] provides a solution to this problem by coupling the VIPASA stiffness matrices for different wavelength responses through the Lagrangian Multiplier Method [5]. The complete VIPASA generality and capability are thus retained in the VICON program, which satisfies the end conditions through point constraints and also permits attachments to a supporting structure [6]. Thus the VICON stiffness matrix comprises a series of VIPASA stiffness matrices which are coupled by the constraints. It is complex valued and can be expressed as

$$\mathbf{K}_{VICON} = \begin{bmatrix} \mathbf{K}_{Global\,VIPASA} & \mathbf{C}^{H} \\ \mathbf{C} & \mathbf{0} \end{bmatrix} \tag{1}$$

where $\mathbf{K}_{Global\,VIPASA}$ is the global VIPASA stiffness matrix, i.e. a series of uncoupled VIPASA matrices at different half-wavelengths of response, $\mathbf{C}$ is the global plate assembly constraint matrix, and $\mathbf{C}^{H}$ is its Hermitian transpose.

The method proposed in this paper uses the VICONOPT solution procedure for finding the critical buckling loads and natural frequencies for damaged plates, by using a combination of VICONOPT and FE stiffnesses as shown in Fig. 1. Embedded damage is modelled by including finite elements with different stiffness properties within the damaged strip. VICONOPT then assembles the hybrid stiffness matrix of the plate by using Lagrangian Multipliers to couple the VICON and FE components, as follows.

$$\mathbf{K}_{Global} = \begin{bmatrix} \mathbf{K}_{Global\,VIPASA} & \mathbf{0} & \boldsymbol{C}_1{}^H \\ \mathbf{0} & \mathbf{K}_{FE} & \boldsymbol{C}_2{}^T \\ \boldsymbol{C}_1 & \boldsymbol{C}_2 & \mathbf{0} \end{bmatrix} \tag{2}$$

Here, the constraint matrices $\mathbf{C}_1$ and $\mathbf{C}_2$ enforce equal displacements and rotations at the nodes connecting the undamaged and damaged strips. $\mathbf{C}_1$ also includes any end support conditions in the undamaged regions. $\mathbf{C}_2{}^T$ is the transpose of $\mathbf{C}_2$. $\mathbf{K}_{FE}$ is the FE stiffness matrix for the damaged rectangular strip. In the case of vibration problems $\mathbf{K}_{FE}$ takes the form

$$\mathbf{K}_{FE} = \mathbf{k} - n^2\mathbf{m} \tag{3}$$

where n is the frequency, $\mathbf{k}$ and $\mathbf{m}$ are the static stiffness matrix and equivalent mass matrix of the damaged rectangular strip.

4. Numerical results

In this section, plates with through-the-length damage are analysed using VFM, and also pure FEA using ABAQUS/Standard [7]. The rectangular mesh is constructed using an approximate global size of 5mm, homogeneous continuum shell and elements and a linear perturbation procedure is used. The plates are simply supported on all four sides. Natural frequencies are determined for plates containing different sizes and severities of through-the-length damage. Plates are assumed to be isotropic for simplicity, in order to verify the concept of combining VICONOPT and FE analysis. The isotropic plates examined have length l=100mm, width b=100mm, and thickness h=1mm. They have material properties of Young's modulus E=110 kN.mm^{-2} and Poisson's ratio v=0.3. Fig 1 shows a plate containing a centrally located through-the-length degradation of stiffness over a width β. In this parametric study, the width of the damage β is varied and three values of stiffness reduction factor for the damaged region are considered: f=0.75, f=0.50 and f=0.25.

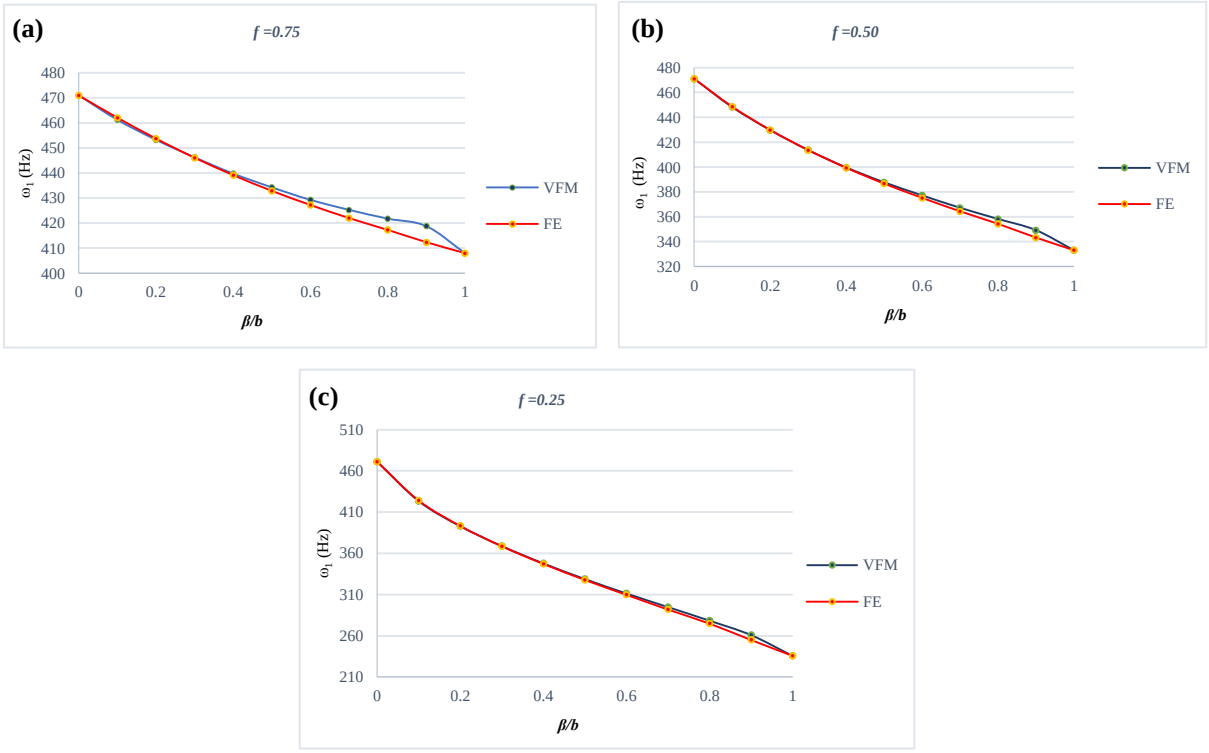

Figure 2: Plots of lowest natural frequency (ω_1) against width β of centrally located through-the-length damage, for different values of stiffness reduction factor f. (a) f =0.75, (b) f =0.50, (c) f =0.25.

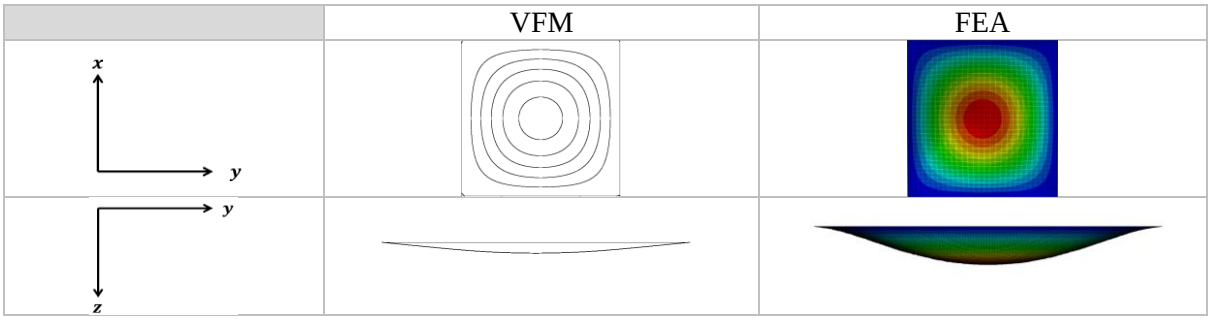

Figure 3: VFM and ABAQUS plots of lowest natural frequency mode for plate with through-the-length damage of β/b=0.2

Fig. 2 shows that there is an excellent agreement between the two methods when $0 \leq \beta/b \leq 0.7$. There is a negligible difference (maximum 2%) between the natural frequencies obtained from FEA (Abaqus) and VFM when $0.7 < \beta/b < 1.0$. Fig. 3 illustrates the vibration mode shapes obtained from VFM and FEA.

5. Conclusions and future work

VFM is based on a concept that allows the computationally efficient program VICONOPT to work along with the finite element method to improve its ability to model cases of damaged plates. This method has been used for the natural frequency analysis of plates containing through-the-length damage. The analysis results are validated against pure FEA. This novel method will be used for more complicated cases of damage that VICONOPT could not previously model directly, such as embedded rectangular damage.

References

[1] D. Kennedy, F.W. Williams, and M.S. Anderson, Buckling and vibration analysis of laminated panels using VICONOPT. *Journal of Aerospace Engineering*, **7**, 245-262, 1994.

[2] M. Damghani, D. Kennedy, and C. Featherston, Critical buckling of delaminated composite plates using exact stiffness analysis. *Computers and Structures*, **89**,1286-1294, 2011.

[3] M. Damghani, D. Kennedy, and C. Featherston, Global buckling of composite plates containing rectangular delaminations using exact stiffness analysis and smearing method. *Computers and Structures*, **134**, 32-47, 2014.

[4] D. Kennedy, and C.A. Featherston, Exact strip analysis and optimum design of aerospace structures. *Aeronautical Journal*, **114**, 505-512, 2010.

[5] F.W. Williams, and M.S. Anderson, Incorporation of Lagrangian Multipliers into an algorithm for finding exact natural frequencies or critical buckling loads. *International Journal of Mechanical Sciences*, **25**, 579-584, 1983.

[6] M.S. Anderson, F.W. Williams, and C.J. Wright, Buckling and vibration of any prismatic assembly of shear and compression loaded anisotropic plates with an arbitrary supporting structure. *International Journal of Mechanical Sciences*, **25**, 585-596, 1983.

[7] DS Simulia Inc. *ABAQUS Standard Manual* (version 6.10), 2012.

Failure and Damage IV

Proceedings of the 24th UK Conference of the
Association for Computational Mechanics in Engineering
31 March - 01 April 2016, Cardiff University, Cardiff

MULTI-SCALE FINITE ELEMENT BASED TIME-DEPENDENT RELIABILITY ANALYSIS FOR LAMINATED FIBRE REINFORCED COMPOSITES

***Xiao-Yi Zhou[1], Peter D. Gosling[1], Zahur Ullah[2], Chris J. Pearce[2] and Lukasz Kaczmarczyk[2]**

[1]School of Civil Engineering & Geosciences, Newcastle University, Claremont road, NE1 7RU
[2]School of Engineering, University of Glasgow, Oakfield avenue, Glasgow, G12 8QQ

*xiaoyi.zhou@newcastle.ac.uk

ABSTRACT

The objective of this paper is to propose a time-dependent reliability analysis method to investigate the durability of fibre reinforced polymer composites. A stochastic multi-scale finite element method, which is based on computational homogenization and perturbation technique, is adopted to propagate uncertainties in both micro- and macro-scale parameters. The influence of water absorption and heat conduction and the induced degradation of mechanical properties, which is estimated through a hygro-thermo-mechanical model that is integrated into the stochastic multi-scale finite method, is then studied in the framework of time-variant reliability analysis. It is shown that the problem reduces to a sequence of time-independent problems that can be solved using the first-order reliability method. A numerical study is carried out to demonstrate the applicability of the proposed method, and the evolution in time of the probability of failure is computed.

Key Words: *Composite; hygro-thermal effect; computational homogenization; durability; reliability*

1. Introduction

Composite materials may provide benifits in terms of reduction of construction time and carbon emission for civil engineering sector, given their success in other sectors. However, civil engineering structures and infrastructures are expected to serve in natural environment for 50 years or more. Accurately quantifying long term durability behaviour is eagerly needed to fully exploit benefits that composite materials could bring to construction sector. In an on-going UK EPSRC funded research project - *Providing Confidence in Durable Composites (DURACOMP)*, pultruded glass fibre reinforced composites, which are typical construction composite materials, have been tested to characterize their ageing behaviours in hot/wet condition. The evolution in time of moisture uptake ratio and mechanical properties has been measured and reported in [1, 2]. To numerical simulate these coupon testing based findings to large scale structures, a coupled hygro-thermo-mechanical model has developed [3] to investigate the long term durability of composites in a deterministic context. Arising from various sources such as manufacturing process, assembly and quality control limits, composite materials exhibit uncertainties in their material properties. Taking these uncertainties into account in designing composites, such as through the use of reliability based structural design, is essential to ensure that the structures perform with sufficient safety during their service and fully realize the advantages offered by composites. In the present study, this coupled hygro-thermo-mechanical is combined with a probabilistic homogenization approach developed in [4] to propagate micro-scale uncertainties to the macro-scale in the mechanical problem. This is subsequently integrated with reliability analysis methods to evaluate the reliability of composite structures.

2. Time-dependent structural reliability analysis

For a stochastic structure system, when stochastic processes or functions of time are explicitly present in the limit state function (LSF), $g(\boldsymbol{x})$, time-variant analysis is required to quantify the probability of failure of the structure. Accordingly, the n-dimensional vector $\boldsymbol{x}$ that collects all random parameters in

the system is split into $\boldsymbol{x}_1$ which is a vector of random variables and $\boldsymbol{x}_2(t)$ which is a vector of random processes. The probability of failure, p_f, of the structure within a time interval $[t_b, t_e]$ is defined as

$$p_f\left(t_b, t_e\right) = Pr\left(\exists t \in [t_b, t_e], g(\boldsymbol{x}_1, \boldsymbol{x}_2(t)) \leq 0\right) \tag{1}$$

In this study, the time effect is present in the problem due to the degradation of material properties, the LSF g thus depends on random variables and functions of time. The computation of p_f as defined in Eq.(1) reduces to

$$p_{f,i} = Pr\left(g\left(\boldsymbol{x}_1, \boldsymbol{x}_2(t)\right) \leq 0\right) \tag{2}$$

which is called instantaneous probability. In a degradation problem, the LSF is monotonously decreasing in time whatever the realizations of the random variables. For each realization of the random vector, the minimum value of $g\left(\boldsymbol{x}_1, \boldsymbol{x}_2(t)\right)$ over a time interval $[t_b, t_e]$ is attained for $t = t_e$. Thus, the time-variant problem is reduced to a time-invariant analysis to calculate the special case of Eq. (2) at t_e. First-order reliability method (FORM) is one of the widely used methods to numerically estimate reliability for time independent problem. Essentially, it requires to transform random variables $\boldsymbol{x}$ from general probability space to standard normal space as $\boldsymbol{u}$, which leads to $G(\boldsymbol{u})$, and to linearly approximate the LSF through the first-order Taylor series expansion, which needs to calculate gradient of G. According to the chain rule of differentiation, the gradient vector of G can be obtained from

$$\nabla G = \frac{\partial G}{\partial \boldsymbol{y}} = \frac{\partial g}{\partial \boldsymbol{s}} \frac{\partial \boldsymbol{s}}{\partial \boldsymbol{x}} \frac{\partial \boldsymbol{x}}{\partial \boldsymbol{y}}, \tag{3}$$

where $\frac{\partial \boldsymbol{x}}{\partial \boldsymbol{y}}$ is Jacobian of the probability transformation, $\frac{\partial g}{\partial \boldsymbol{s}}$ can be analytically obtained since the LSF g is function of components of $\boldsymbol{s}$. Thus, the only unknown is $\frac{\partial \boldsymbol{s}}{\partial \boldsymbol{x}}$ that will be calculated from stochastic finite element method.

3. Stochastic multi-scale finite element analysis

3.1. Degradation model for FRP composites in hot/wet condition

Based on experimental data reported in [1], Zahur et al. [3] proposed a generalized model to characterize the degradation of constitutive matrix of matrix material under hygrothermal condition, which is expressed as

$$\frac{d\mathbb{C}_m}{dt} = -c\eta \log\left(1 - T/T_g\right) \mathbb{C}_m^0 \quad \text{or} \quad \frac{d}{dt}\left(1 - \omega\right) = -c\eta \log\left(1 - T/T_g\right)\left(1 - \omega\right) \tag{4}$$

where $\mathbb{C}_m^0$ is for undegraded material; c is the moisture concentration; η is a model parameter that is obtained from experiment data; T is the temperature; T_g is the glassy transition temperature; and t is the exposure time. Thus, this degradation model is actually to get instantaneous temperature $T(t)$ and moisture concentration $c(t)$, and they are obtained from transient moisture diffusion and heat conduction analyses.

3.2. Computational homogenization for multi-physics problems

Owing to the multi-scale architecture of composite materials, homogenization method should be used to estimate the effective properties of composites. In the present paper, the multi-scale computational homogenization method was used to estimate the effective elastic and physical properties. Thermal and diffusion homogenization were conducted to get the effective conductivity and diffusivity, respectively. These were then supplied to transient heat conduction and moisture diffusion analyses to calculate the instantaneous temperature and moisture concentration for Eq. (4). Finally, the degraded elastic properties of constituent materials were input to the mechanical homogenization to get the effective elastic properties. In the finite element context, the mechanical homogenization is expressed as

$$\begin{bmatrix} \mathbf{K}_\mu & \mathbf{P}^T \\ \mathbf{P} & \mathbf{0} \end{bmatrix} \begin{Bmatrix} \mathbf{u} \\ \boldsymbol{\lambda} \end{Bmatrix} = \begin{Bmatrix} \mathbf{0} \\ \mathbf{D}\bar{\boldsymbol{\varepsilon}} \end{Bmatrix} \quad \text{or} \quad \left[\hat{\mathbf{K}}\right]\{\hat{\mathbf{u}}\} = \left\{\hat{\mathbf{F}}\right\}. \tag{5}$$

where $\boldsymbol{\lambda}$ is the Lagrangian vector, $\bar{\boldsymbol{\varepsilon}}$ is the prescribed or given strain, and $\mathbf{P}$ and $\mathbf{D}$ are constraint matrix and global coordinate matrix.

3.3. Uncertainty propagation with the use of perturbation technique

Considering material properties as random variables, the stiffness matrix $\left[\hat{\mathbf{K}}\right]$ and the nodal displacement vector $\{\hat{\mathbf{u}}\}$ in Eq. (5) are thus stochastic functions. According to the perturbation technique, stochastic function can be approximated by Taylor series expansion. In the present study, only the first order expansion is needed as the first order derivatives of structural responses are required in Eq. (3). By expanding stochastic functions in the form of

$$\phi(\mathbf{b}) = \phi(\bar{\mathbf{b}}) + \epsilon \sum_{i=1}^{n} \left[D_{b_i}\phi(\bar{\mathbf{b}})\right] \delta b_i, \tag{6}$$

substituting them into Eq.(5) and equating terms of equal orders of ϵ, we arrive at the following zeroth- and first-order equations:

$$\left[\hat{\mathbf{K}}\right]\{\hat{\mathbf{u}}\} = \left\{\hat{\mathbf{F}}\right\} \tag{7}$$

$$\sum_{p=1}^{n} \left\{\left[\hat{\mathbf{K}}\right]\left\{D_{b_p}\hat{\mathbf{u}}\right\} + \left[D_{b_p}\hat{\mathbf{K}}\right]\{\hat{\mathbf{u}}\}\right\} = \mathbf{0} \tag{8}$$

In Eq. (5), the block related to stiffness matrix, $\left[\mathbf{K}_\mu\right]$, of the microstructure is function of material properties. It and its first-order partial derivative can be expressed as

$$\mathbf{K}_\mu = \int_{\Omega_\mu^s} \mathbf{B}^T \mathbb{C}_\mu \mathbf{B} dV, \quad \text{and} \quad \left[D_{b_p}\mathbf{K}_\mu\right] = \int_{\Omega_\mu^s} \mathbf{B}^T \left[D_{b_p}\mathbb{C}_\mu\right] \mathbf{B} dV, \tag{9}$$

where $\mathbf{B}$ is the strain-displacement matrix, $\mathbb{C}_\mu$ is the constitutive matrix of constituent material, and $\left[D_{b_p}\mathbb{C}_\mu\right]$ is its first-order partial derivative. Computing Eqs.(7) and (8) successively, the compact displacement vector $\{\hat{\mathbf{u}}\}$ and its first order partial derivative $\left\{D_{b_p}\hat{\mathbf{u}}\right\}$ can be obtained. These were then used to calculated the effective constitutive matrix and its derivatives according to $\bar{\mathbb{C}} = \frac{\bar{\boldsymbol{\sigma}}}{\bar{\boldsymbol{\varepsilon}}}$ (see [4] for details of the derivation). Once the effective constitutive matrix for the composite is obtained, the stochastic structural responses at macro level can be calculated by introducing a perturbation-based stochastic finite element method, and these are input to Eq. (3).

4. Numerical example

A fibre reinforced polymer composite plate is considered in this section to illustrate the time-dependent reliability analysis scheme. The geometry of the plate is shown in Fig 1a. For the macro-level thermal problem, a temperature of $80°C$ is applied to the top and bottom surfaces, and constant heat flux is applied to the left and right surfaces. Similarly, for the moisture transport problem, a constant concentration of 1, which represents 100% relative humility, is applied to the top and bottom surfaces, and constant moisture flux is applied to the left and right surfaces. For the macro-mechanical analysis, a uniform pressure of 1000 MPa is applied along the upper and lower surfaces in the vertical direction to simulate uniaxial tension state. Considering the symmetry of the geometry and boundary conditions for heat transfer, moisture transport and mechanical analysis, only 1/8 of the structure, highlighted in Fig. 1a, needs to be modelled. The plate is made of glass/epoxy plain weave textile composite (see microstructure in Fig. 1b) with elastic and physical properties indicated in [3].

The multi-scale analysis for heat conduction and moisture transport problems were conducted first to get the effective heat conductivity and moisture diffusivity required for performing macro level heat conduction and moisture diffusion analyses. The calculations were conducted in a time interval of 10 days, and a period of 500 days was considered. Thus, a total of 51 times of multi-scale multi-physics calculation were conducted. Using these 51 instantaneous temperature and moisture concentration fields, a series of degradation parameter field was computed by Eq. (4). Then the mechanical computational homogenization was applied to estimate the effective mechanical properties. According to preliminary

study at initial stage, applied load, longitudinal ply strength and longitudinal Young's modulus are the most important parameters in reliability analysis of the considered structures. These three parameters were considered as random variables in the time-dependent reliability calculation, and Tsai-Wu failure theory was used to establish the LSF. Finally, the evolution in time of the reliability index is plotted in Fig. 2. It can be seen that the reliability index decreases about 11% after 500 days degradation.

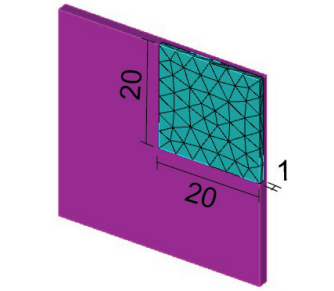

(a) Plate

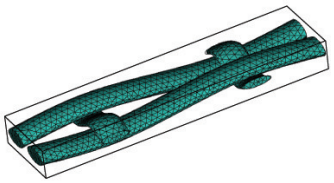

(b) Microstructure

Figure 1: FRP plate and its microstructure

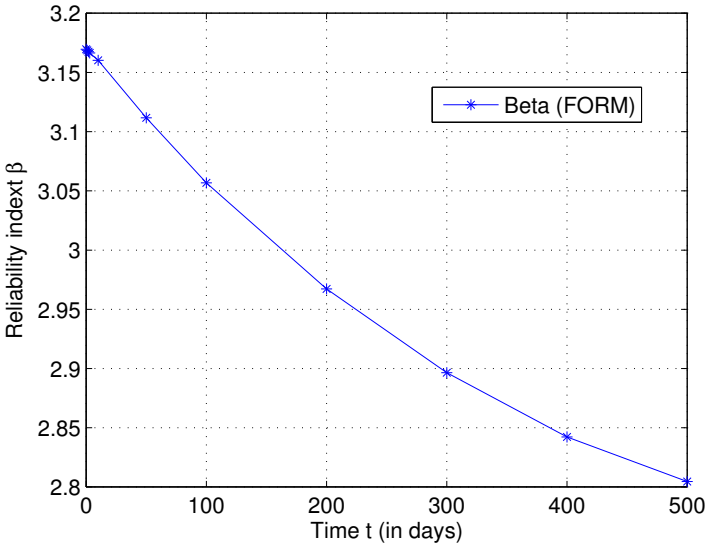

Figure 2: Evolution in time of the reliability index

5. Conclusions

On-going research and early results on the durability of fibre reinforced polymer composite structures, which is investigated by time-dependent reliability analysis, are presented in this paper. The time dependent reliability calculation is realized by integrating a multi-scale finite element reliability method with a hygro-thermo-mechanical model. A numerical study is carried out to demonstrate the applicability of the proposed scheme through the calculation of the evolution in time of the probability of failure.

Acknowledgements

The authors gratefully acknowledge the financial support provided for this study by the UK Engineering and Physical Sciences Research Council (EPSRC) under grant reference EP/K026925/1.

References

[1] S. A. Grammatikos, B. Zafari, M. C. Evernden, J. T. Mottram, J. M. Mitchels, Moisture uptake characteristics of a pultruded fibre reinforced polymer flat sheet subjected to hot/wet aging, Polymer Degradation and Stability 121 (2015) 407–419.

[2] S. A. Grammatikos, M. C. Evernden, J. M. Mitchels, B. Zafari, J. T. Mottram, G. C. Papanicolaou, On the response of hygrothermal aging of pultruded FRPs used in the civil engineering sector, Materials & Design In press.

[3] Z. Ullah, L. Kaczmarczyk, S. A. Grammatikos, M. C. Evernden, C. J. Pearce, Multi-scale computational homogenization to predict the long-term durability of composite structures, Computers & Structures Under review.

[4] X.-Y. Zhou, P. D. Gosling, C. J. Pearce, Z. Ullah, L. Kaczmarczyk, Perturbation-based stochastic multi-scale computational homogenization method for woven textile composites, International Journal of Solids and Structures 80 (2016) 368–380.

Proceedings of the 24th UK Conference of the
Association for Computational Mechanics in Engineering
31 March - 01 April 2016, Cardiff University, Cardiff

3D fatigue fracture modeling by isogeometric boundary element methods

***Xuan Peng[1], Elena Atroshchenko[2], Pierre Kerfriden[1] and Stéphane P. A. Bordas[3,1,4]**

[1]Institute of Mechanics Materials and Advanced Manufacturing, Cardiff University, CF24 3AA, UK
[2]Department of Mechanical Engineering, University of Chile, Santiago, 8370448, Chile
[3]Institute for Computational Engineering, Université du Luxembourg, 6 rue Richard Coudenhove-Kalergi, L-1359, Luxembourg
[4]School of Mechanical and Chemical Engineering, The University of Western Australia (M050), WA 6009, Australia

PengX2@cardiff.ac.uk

ABSTRACT

The isogeometric boundary element method (IGABEM) based on NURBS is adopted to model fracture problem in 3D. The NURBS basis functions are used in both crack representation and physical quantity approximation. A stable quadrature scheme for singular integration is proposed to enhance the robustness of the method in dealing with highly distorted element. An algorithm is outlined and validated to be stable for fatigue crack growth, thanks to the smoothness not only in crack geometry but also in stress/SIFs solution brought by IGABEM.

Key Words: *Isogeometric analysis; NURBS; Linear elastic fracture; Boundary element method; Crack growth*

1. Introduction

The fracture modeling by the boundary element method (BEM) exhibits more advantages than by FEM in terms of mesh/re-mesh efforts as only the boundary discretization is required in BEM in order to approximate the quantity of interest. When cracks evolve, only the boundary surfaces are updated instead of re-generating the volume mesh.

The isogeometric analysis (IGA) was first introduced by Hughes *et al* [1]. The basic idea of IGA is to use the same spline basis functions to represent the CAD geometries and approximate the physical quantities of interest. And the investigation on the joint of IGA and BEM (IGABEM) [2] has increasingly drawn attention recently since only the boundary representation of the geometry is required in IGABEM, which facilitates the integration of design and analysis.

The advantages of the application for fracture based on the IGA framework can be concluded as:

(1) The higher-order continuity of spline basis functions improves the accuracy of the stress field near the crack front which is crucial to fracture analysis and the degrees of freedom is reduced compared to the C^0 Lagrange basis;
(2) The curvature, tangential and normal vectors are exactly retained and evolved for the crack growth thanks to the exact representation of the curved cracks;
(3) The local crack tip (front) system can be constructed directly based on the spline-based curve or surface-represented cracks, which helps to accurately evaluate the fracture parameters;
(4) The concept of integration through design to analysis facilities the mechanical/structural design based on the fatigue fracture analysis.

2. Boundary integral equations (BIE) for crack modeling

Consider an arbitrary domain Ω which contains a crack. The boundary of the domain $\partial\Omega = S \cup S_{c^+} \cup S_{c^-}$, where S is composed of S_u where Dirichlet boundary conditions are prescribed (known displacements $\bar{\mathbf{u}}$), S_t where Neumann boundary conditions are prescribed (known tractions $\bar{\mathbf{t}}$). The displacement BIE

(Equation (1)) is used on one face (S_{c^+}) and on the rest of the boundary S. The traction BIE (Equation (2)) is used on the other crack face (S_{c^-}).

$$\begin{aligned} c_{ij}(\mathbf{s}^+)u_j(\mathbf{s}^+) + c_{ij}(\mathbf{s}_m^-)u_j(\mathbf{s}^+) &= \int_S U_{ij}(\mathbf{s}^+,\mathbf{x})t_j(\mathbf{x})\mathrm{d}S(\mathbf{x}) - \int_S T_{ij}(\mathbf{s}^+,\mathbf{x})u_j(\mathbf{x})\mathrm{d}S(\mathbf{x}) \\ &- \text{⨍}_{S_{c^+}} T_{ij}(\mathbf{s}^+,\mathbf{x}^+)u_j(\mathbf{x}^+)\mathrm{d}S(\mathbf{x}) - \text{⨍}_{S_{c^-}} T_{ij}(\mathbf{s}_m^-,\mathbf{x}^-)u_j(\mathbf{x}^-)\mathrm{d}S(\mathbf{x}) \\ &+ \int_{S_{c^+}} U_{ij}(\mathbf{s}^+,\mathbf{x}^+)t_j(\mathbf{x}^+)\mathrm{d}S(\mathbf{x}) + \int_{S_{c^-}} U_{ij}(\mathbf{s}_m^-,\mathbf{x}^-)t_j(\mathbf{x}^-)\mathrm{d}S(\mathbf{x}), \end{aligned} \tag{1}$$

$$\begin{aligned} c_{ij}(\mathbf{s}^-)t_j(\mathbf{s}^-) + c_{ij}(\mathbf{s}_m^+)t_j(\mathbf{s}^-) &= \int_S K_{ij}(\mathbf{s}^-,\mathbf{x})t_j(\mathbf{x})\mathrm{d}S(\mathbf{x}) - \int_S H_{ij}(\mathbf{s}^-,\mathbf{x})u_j(\mathbf{x})\mathrm{d}S(\mathbf{x}) \\ &- \text{⨎}_{S_{c^-}} H_{ij}(\mathbf{s}^-,\mathbf{x}^-)u_j(\mathbf{x}^-)\mathrm{d}S(\mathbf{x}) + \text{⨎}_{S_{c^+}} H_{ij}(\mathbf{s}_m^+,\mathbf{x}^+)u_j(\mathbf{x}^+)\mathrm{d}S(\mathbf{x}) \\ &+ \text{⨎}_{S_{c^-}} K_{ij}(\mathbf{s}^-,\mathbf{x}^-)t_j(\mathbf{x}^-)\mathrm{d}S(\mathbf{x}) - \text{⨎}_{S_{c^+}} K_{ij}(\mathbf{s}_m^+,\mathbf{x}^-)t_j(\mathbf{x}^+)\mathrm{d}S(\mathbf{x}), \end{aligned} \tag{2}$$

where the U_{ij}, T_{ij} are called fundamental solutions, and

$$H_{ij}(\mathbf{s},\mathbf{x}) = E_{ikpq}\frac{\partial T_{pj}(\mathbf{s},\mathbf{x})}{\partial s_q}n_k(\mathbf{s}), \quad K_{ij}(\mathbf{s},\mathbf{x}) = E_{ikpq}\frac{\partial U_{pj}(\mathbf{s},\mathbf{x})}{\partial s_q}n_k(\mathbf{s}), \tag{3}$$

where ⨍ denotes the integral is interpreted in the *Cauchy Principal Value* sense and ⨎ denotes the *Hadamard Finite Part* integral. $\mathbf{s}_m^-$ denotes the mirror point of $\mathbf{s}^+$ on S_{c^-}, which means $\mathbf{s}_m^-$ and $\mathbf{s}^-$ share the same physical and parametric coordinates but their normal vectors are opposite. The last two terms of both equations and left hand side of Equation (2) are omitted due to the traction-free crack.

3. Singularity subtraction technique (SST) for singular integrals

For the hyper-singular integral

$$I = \lim_{\varepsilon\to 0}\int_0^{2\pi}\int_{\alpha(\varepsilon,\theta)}^{\hat{\rho}(\theta)} H(\rho,\theta)R(\rho,\theta)\bar{J}(\rho,\theta)\rho\mathrm{d}\rho\mathrm{d}\theta, \tag{4}$$

where H is the hyper-singular kernel, R is the NURBS basis function and $\bar{J}$ is the Jacobi transformation from parent space to physical space. The integrand $F(\rho,\theta) = H(\rho,\theta)R(\rho,\theta)\bar{J}(\rho,\theta)\rho$ is expanded as:

$$F(\rho,\theta) = \frac{F_{-2}(\theta)}{\rho^2} + \frac{F_{-1}(\theta)}{\rho} + F_0(\theta) + F_1(\theta)\rho + F_2(\theta)\rho^2 + \cdots = \sum_{i=-1}^{\infty} F_i(\theta)\rho^i. \tag{5}$$

The singularity can be represented explicitly with respect to the parametric distance between the source point and field point ρ. Then the singular terms are subtracted from the integrand, leaving the remaining to be regular for which regular Gaussian rule is applied. the subtracted terms are added back semi-analytically, resulting in:

$$\begin{aligned} I &= I_1 + I_2, \\ I_1 &= \int_0^{2\pi}\int_0^{\hat{\rho}(\theta)} \Big[F(\rho,\theta) - \frac{F_{-2}(\theta)}{\rho^2} - \frac{F_{-1}(\theta)}{\rho}\Big]\mathrm{d}\rho\mathrm{d}\theta, \\ I_2 &= \int_0^{2\pi} I_{-1}(\theta)\ln\frac{\hat{\rho}(\theta)}{\beta(\theta)}\mathrm{d}\theta - \int_0^{2\pi} I_{-2}(\theta)\Big[\frac{\gamma(\theta)}{\beta^2(\theta)} + \frac{1}{\hat{\rho}(\theta)}\Big]\mathrm{d}\theta, \end{aligned} \tag{6}$$

where I_1 is regular and I_2 are regular line integrals, Both can be applied with Gaussian quadrature rule. The evaluation of $\alpha(\varepsilon,\theta)$, $\beta(\theta)$ and $\gamma(\theta)$ as well as the limiting process can be referred in [3].

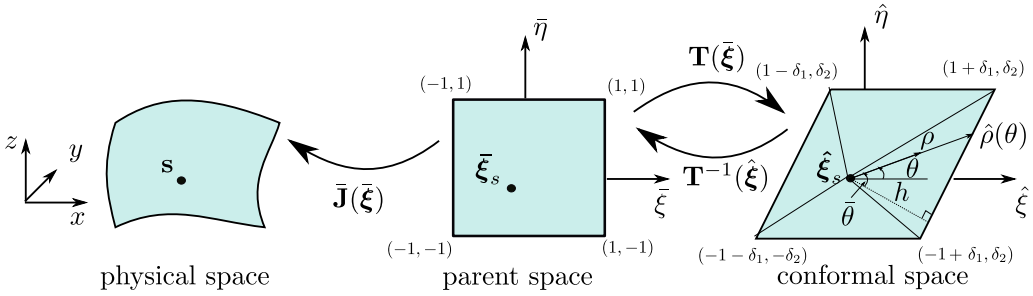

Figure 1: Transformation between coordinate system for SST. The nodal coordinates $\hat{\boldsymbol{\xi}}^I$ are obtained through bilinear interpolation from $(\bar{\xi},\bar{\eta})$ to the new parametric space $(\hat{\xi},\hat{\eta})$ for the quadrilateral element in conformal space

A conformal mapping is proposed to enhance singular integration for distorted elements. The curvilinear basis vectors $\mathbf{m}_i^s = \mathbf{m}_i|_{\bar{\boldsymbol{\xi}}=\bar{\boldsymbol{\xi}}_s}, (i=1,2)$ and are calculated as:

$$\begin{aligned}\mathbf{m}_1 &= \Big[\frac{\partial x}{\partial \bar{\xi}}, \frac{\partial y}{\partial \bar{\xi}}, \frac{\partial z}{\partial \bar{\xi}}\Big],\\ \mathbf{m}_2 &= \Big[\frac{\partial x}{\partial \bar{\eta}}, \frac{\partial y}{\partial \bar{\eta}}, \frac{\partial z}{\partial \bar{\eta}}\Big].\end{aligned} \tag{7}$$

We introduces two parameters $\lambda = |\mathbf{m}_1^s|/|\mathbf{m}_2^s|$, $\cos\psi = \mathbf{m}_1^s \cdot \mathbf{m}_2^s/|\mathbf{m}_1^s||\mathbf{m}_2^s|$. The conformal mapping from the parent space $(\bar{\xi},\bar{\eta})$ to a new parametric space $(\hat{\xi},\hat{\eta})$ can be constructed where the two curvilinear basis vectors in the new parametric space are orthogonal and have identical length. The Jacobian transformation matrix $\mathbf{T}$ from $\bar{\boldsymbol{\xi}} = (\bar{\xi},\bar{\eta})$ to a new parametric space $\hat{\boldsymbol{\xi}} = (\hat{\xi},\hat{\eta})$ is

$$\mathbf{T} = \begin{bmatrix} 1 & \delta_1 \\ 0 & \delta_2 \end{bmatrix}, \text{ so that } \hat{\boldsymbol{\xi}} = \mathbf{T}\bar{\boldsymbol{\xi}}, \tag{8}$$

where $\delta_1 = \cos\psi/\lambda$, $\delta_2 = \sin\psi/\lambda$. Figure 1 illustrates the transformation for singular integration. Now the SST is applied in the conformal space.

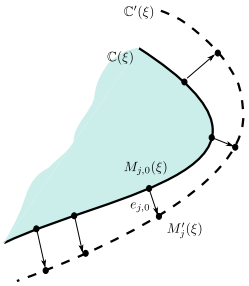

Figure 2: Crack front updating. $\mathbb{C}(\xi)$ is the old crack front curve, $\mathbb{C}'(\xi)$ is the new crack front curve after crack advance

4. Crack growth

In the present work, we use NURBS patches to discretize the crack surfaces. The Paris law is used to calculate the crack advance. A crack surface updating algorithm is outlined to perform the crack growth as in Table 1.

5. Numerical examples

Figure 3(a) shows the convergence study on the relative error in the L_2 norm crack opening displacement (COD) for the penny crack problem with inclination angle $\varphi = 0$. It can be seen that degree elevation

Algorithm 1 Crack front updating algorithm

Data: old crack front curve $\mathbb{C}(\xi)$; sample points M_j; new positions of sample points M'_j
Result: new crack front curve that passes through all M'_j, see Figure 2
$t = 0$;
$tol = 1.e-4$;
$e_{j,0} = \overrightarrow{M_{j,0}M'_j}$; //the initial error vector
while $\|\mathbf{e}_t\| > tol$ **do**
  $t = t + 1$;
  $m_{i,t} = \frac{1}{N}\sum_{j=0}^{N-1} f_{ij}e_{j,t-1}$; //the motion vector at t-th step
  $P_{i,t} = P_{i,t-1} + m_{i,t}$; //the new point on the crack front at t-th step
  $e_{j,t} = e_{j,t-1} - \frac{1}{N}\sum_{k=0}^{N-1}\sum_{i=0}^{n-1} R_{ij}f_{ik}e_{k,t-1}$; //the error vector at t-th step
end

from 2 to 3 improves accuracy. Yet, the convergence rate (oc) keeps almost the same value ($oc = 1$). The deterioated oc is due to the physical singularity along the crack front. Figure 3(b) shows the stress intensity factors (SIFs) for the sample points on the crack front for the penny crack problem with $\varphi = \pi/6$. It can be observed that the numerical SIFs agrees well with the analytical solution. Figure 4 presents the fatigue crack growth for inclined elliptical crack.

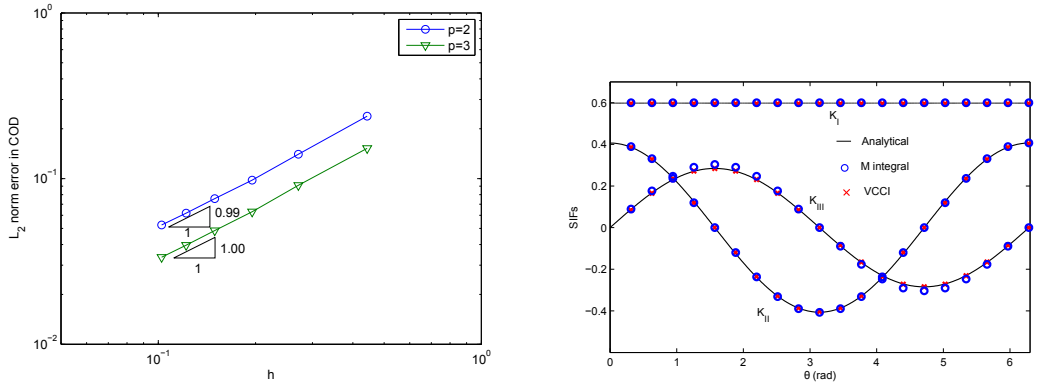

(a) (b)

Figure 3: (a) The relative error in the L_2 norm of COD for penny-shaped crack by uniform mesh refinement in parametric space.; (b) Stress intensity factors for penny crack with inclination angle $\varphi = \pi/6$, θ is the direction angle for the sample points along the crack front

6. Conclusions

The formulation and implementation of isogeometric boundary element methods (IGABEM) for simulating 3D fatigue fracture problem are outlined in this paper. The same NURBS basis functions are used for the discretization of geometry/crack and the approximation of displacement/traction in the isogeometric framework. The highlights of this work include: (1) The proposed singular integration scheme can preserve the quadrature accuracy for highly distorted elements which exist commonly in IGA; (2) The local crack tip system is setup naturally and uniquely thanks to the NURBS representation of the crack surface. With the continuity in stress solution in BEM, the obtained SIFs along the crack front are smooth and accurate; (3) The proposed algorithm for crack propagation is validated to be stable, due to the smoothness in crack front geometry and numerical SIFs.

The future work will focus on the surface cracks problem, where the crack will have intersection with the body geometry.

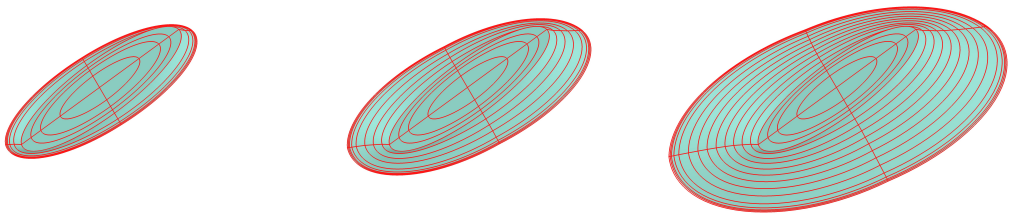

(a) Step 2 (b) Step 5 (c) Step 10

Figure 4: Fatigue crack growth simulation of an elliptical crack with inclination angle $\varphi = \pi/6$ modeled by the dual equations in a finite domain

Acknowledgements

The first and last authors would like to acknowledge the financial support of the Framework Programme 7 Initial Training Network Funding under grant number 289361 'Integrating Numerical Simulation and Geometric Design Technology'.

References

[1] Hughes T J R, Cottrell J A, Bazilevs Y. Isogeometric analysis: CAD, finite elements, NURBS, exact geometry and mesh refinement. *Computer methods in applied mechanics and engineering*, 2005, 194(39): 4135-4195.

[2] Scott, M. A., Simpson, R. N., Evans, J. A., Lipton, S., Bordas, S. P., Hughes, T. J., Sederberg, T. W. (2013). Isogeometric boundary element analysis using unstructured T-splines. *Computer Methods in Applied Mechanics and Engineering*, 254, 197-221.

[3] Guiggiani M. Formulation and numerical treatment of boundary integral equations with hypersingular kernels. *Singular integrals in boundary element methods*, 1998: 85-124.

Proceedings of the 24th UK Conference of the
Association for Computational Mechanics in Engineering
31 March – 01 April 2016, Cardiff University, Cardiff

IMPLEMENTATION OF A COHESIVE ZONE MODEL INTO THE OPEN SOURCE FINITE ELEMENT SOFTWARE ParaFEM

Athanasios G. Tsamos*, Lee Margetts and Andrey P. Jivkov

School of MACE, University of Manchester, Manchester, M13 9PL

*athanasios.tsamos@postgrad.manchester.ac.uk

ABSTRACT

Cohesive elements have proven to be an excellent approach in computational fracture mechanics. Nevertheless, massively parallel computations are required in order to capture damage patterns and evolution meticulously in Carbon Fibre Reinforced Composites (CFRCs). Commercial packages do not exhibit satisfactory scalability in massively parallel computers. Thus, it is essential to implement cohesive elements in suitable codes for large scale simulations. The steps that need to be carried out in order to implement a Cohesive Zone Model (CZM) into the open source finite element (FE) package: ParaFEM (http://parafem.org.uk) are presented. These steps are: (1) a study on the CZM existing in ABAQUS and its key parameters, (2) the generation of a fortran ABAQUS User Element subroutine (UEL) of that particular CZM, (3) the integration of the latter into the source code of ParaFEM as a Cohesive Interface (zero geometrical thickness) Element Subroutine, (4) verification of its accurate functionality with the aid of well established benchmark problems, (5) and finally the culmination of scalability tests and direct comparison between the two programs. The work will be of interest to researchers wishing to perform very large analyses with cohesive elements using supercomputers.

Keywords: *Cohesive Element Subroutine; Modelling of Microstructure; Modelling Damage; Carbon Fibre Composites; Large Scale Simulation*

1. Introduction

The motivation of the work is to enable accurate microstructural simulations to be carried out in composite damage evolution. Composites exhibit a very convoluted response under loading due to the complexity and certain randomness that can be found in their microstructures [1]. Moreover, the interaction of their various damage mechanisms with one another is inordinately important as well. Despite the fact that there are available tools, both analytical and numerical, that can be employed in order to simplify their analysis macroscopically through various homogenization procedures [2] and multiscale approaches [3], these are not fully capable of predicting damage evolution and fracture under various loading conditions.

The systematic application of advanced composite materials in the sensitive aerospace sector (transportation) is probably only inhibited by the lack of serious computational models for the latter. Obviously, physical testing is far more expensive compared with computational modelling and testing. It is a fact that the use of these more efficient materials in contrast to the conventional heavy materials that are currently being used will enact a safer, inexpensive air travel and ultimately will have a beneficial impact on the environment as well.

Cohesive elements have been extensively employed inside FE software in order to predict damage initiation and progression in composite materials. Nevertheless, the use of cohesive elements increases the size of problem that needs to be solved. Thus, they have been used sparingly in areas where fracture is expected to occur, i.e. with pre-defined crack paths. As computational power increases with the introduction of new generations of supercomputers, it is advantageous to possess tools capable of exploiting this potential. A massively parallel and scalability study on damage initiation and evolution in laminate structures can be found in [4], where the exact mesoscale solution was investigated by employing parallel iterative solvers based on the LaTIn mixed domain

decomposition algorithm. Commercial packages such as ABAQUS do not scale well on parallel supercomputers and here we investigate the use of cohesive elements in the open source parallel software ParaFEM [5]. The implementation steps of a well established CZM into this open source software are given below. ParaFEM uses MPI for message passing and has been proven to scale on up to 64,000 cores for problems with >1 billion unknowns [6]. The purpose of this research is to improve the particular CZM, rendering it into a computational tool that will be able to capture damage in a more realistic and physical manner. More specifically, the simulation of damage initiation and propagation in CFRCs emphasizing mixed-mode failure conditions for large models where all the material interfaces include cohesive elements.

2. The CZM

The chosen CZM is the same as the one used in ABAQUS [7], [8]. This particular traction separation law has been proven to effectively capture the mechanics and physics of damage initiation and propagation in CFRCs [9], [10]. More specifically, in the implemented model the damage is assumed to initiate when a Quadratic Nominal Traction Criterion is met. t_n, t_s, t_t indicate the current tractions in the *normal, first shear* and *second shear* directions respectively while the superscript *C* indicates user-defined critical values at damage initiation.

$$\left\{\frac{\langle t_n \rangle}{t^C{}_n}\right\}^2 + \left\{\frac{t_s}{t^C{}_s}\right\}^2 + \left\{\frac{t_t}{t^C{}_t}\right\}^2 = 1 \tag{1}$$

The Macaulay brackets < > imply that compressive forces do not contribute to failure initiation in the normal direction. The recorded traction values and recorded separation values when the quadratic criterion is met are defined as $t_n{}^o$, $t_s{}^o$, $t_t{}^o$ and $\delta_n{}^o$, $\delta_s{}^o$, $\delta_t{}^o$ respectively.

After damage onset, that is after the damage initiation criterion is met, a damage evolution law defines the stiffness degradation of the cohesive element due to damage propagation. It can be represented with a damage scalar variable D, valued between 0 and 1. D = 0 indicates no damage, whereas D = 1 indicates fully developed damage. D is the averaged (mixed mode), overall damage progression state. The mean traction components $\bar{t}_n$, $\bar{t}_s$, $\bar{t}_t$ represent the predicted elastic traction-separation behaviour for the current strains without damage based on user-defined penalty stiffness.

$$t_n = \begin{cases} (1-D)\bar{t}_n & \text{for } \bar{t}_n \geq 0 \\ \bar{t}_n & \text{for } \bar{t}_n < 0 \end{cases} \qquad \text{(no damage due to compressive forces)} \tag{2}$$

$$t_s = (1-D)\bar{t}_s \tag{3}$$

$$t_t = (1-D)\bar{t}_t \tag{4}$$

Now, the fracture energy G_c is the required energy for the formation of a new surface due to fracture and can be employed to define the damage evolution. It is represented by the area under the traction-separation graph (Figure 1). Since in CFRCs the fracture energies along the two shear directions are equal, the Benzeggagh-Kenane (η = *BK exponent*) damage evolution description can be employed to describe the mixed-mode fracture energy [9]. G_n, G_s, G_t indicate the work done (dissipated energy) thus far in the *normal, first shear* and *second shear* directions respectively while the superscript *C* indicates their user-defined critical values at full degradation.

$$G_C = G_n{}^C + \left(G_s{}^C - G_n{}^C\right)\left\{\frac{G_s + G_t}{G_n + G_s + G_t}\right\}^\eta \tag{5}$$

A linear softening (damage evolution) law is adopted.

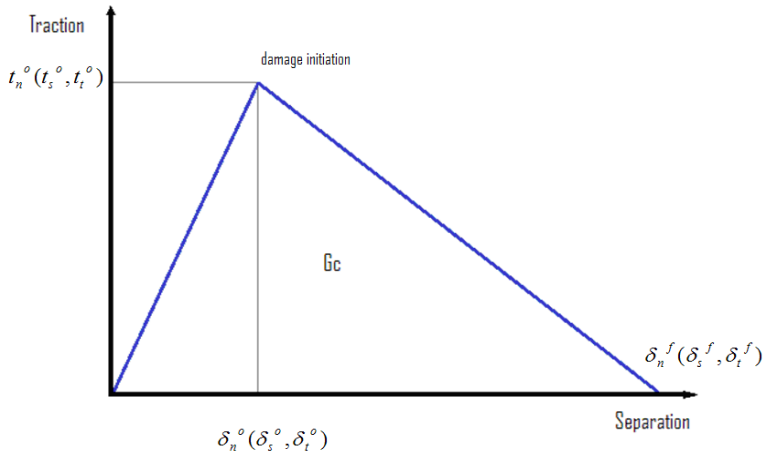

Figure 1: Mixed Mode – Linear Softening Law.

The linear damage evolution, D can be expressed as such:

$$D = \frac{\delta_m^f(\delta_m^{\max} - \delta_m^o)}{\delta_m^{\max}(\delta_m^f - \delta_m^o)} \tag{6}$$

where $\delta_m^f = 2G^C / t_m^o$ (effective displacement at full degradation) (7)

$$t_m^o = \sqrt{\langle t_n^o \rangle^2 + t_s^{o2} + t_t^{o2}} \quad \text{(effective traction at damage initiation)} \tag{8}$$

$$\delta_m^o = \sqrt{\langle \delta_n^o \rangle^2 + \delta_s^{o2} + \delta_t^{o2}} \quad \text{(effective displacement at damage initiation)} \tag{9}$$

The $\delta_m^{\max}$ variable is employed in order to record the damage state of the interface averting the latter to return to its undamaged state during unloading (maximum value of the effective displacement attained during loading history).

3. Method

The first step that needs to be carried out before the implementation of the above CZM into ParaFEM is the generation of an UEL incorporating this cohesive material response. Two different UELs must be programmed for linear 3D meshes. A linear 'wedge' interface cohesive element and a linear 'brick' interface cohesive element. 2D interfaces between hexahedral elements are 'bricks' and 2D interfaces between tetrahedral elements are 'wedges'. The thickness of these cohesive elements can be specified as unity. Therefore, the computed strains from the nodal forces can be equal to the displacements. The actual geometrical thickness of these elements in a FE Model is zero despite the fact they are solid elements. Thus, the geometry of the FE model can remain unaffected.

The second step is the validation of the precision and correctness of these UELs via well established benchmark tests. Based on the work of Camanho & Dávila [8], the original benchmark tests that were undertaken for the validation of the cohesive capabilities of ABAQUS are being adopted. These are: a double cantilever beam (DCB) test, an end notched flexure (ENF) test and a mixed-mode bending (MMB) test. These tests can assess the functionality of the UELs under pure normal decohesion, pure shear decohesion and mixed-mode decohesion respectively. The newly generated numerical results are being compared with the original numerical and experimental results included in [8].

The third step that needs to be carried out is the integration of the UELs into the source code of ParaFEM as a fortran subroutine. The benchmark tests should once more be modelled, this time in ParaFEM, and compared with all the data obtained in step 2, thus confirming the accurate functionality of the new features of ParaFEM.
As a last step, scaling tests must be performed between ABAQUS and ParaFEM. The DCB test is selected as the benchmark test. The test must be run numerous times with a varying mesh/cohesive-elements density, by altering the computational resources employed (number of running cores) and therefore, evaluating the performance of the two solvers (ABAQUS & ParaFEM) on a particular computer based on the overall simulation time. The results of the aforementioned benchmark and scalability tests will be presented in the conference.

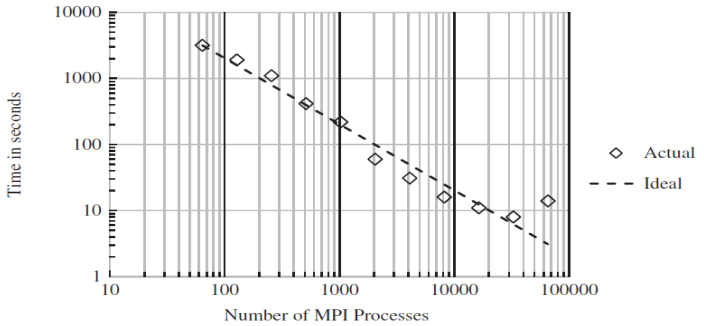

Figure 2: A typical Scaling Graph of a linear problem in ParaFEM (125 million equations: Cray XE6) [6].

4. Discussion

The implementation procedure presented earlier is part of a greater research plan. Its purpose is to improve the particular CZM, rendering it into a computational tool that will be able to capture damage in a more realistic and physical manner on a very large scale. Simulation of real and artificially generated microstructures on large scale has not yet been attempted. Thus, three different interfaces will be modelled (matrix/fiber, matrix/matrix & fiber/fiber) with cohesive interface elements. The mesh geometry along with the diverse interfaces parameters are of special interest and therefore crucial for the delivery of meaningful results from the simulations.

References

[1] R. Talreja. Damage analysis for structural integrity and durability of composite materials, *Fatigue Fract Eng Mater Struct*, 29, 481-506, 2006.

[2] J. C. Halpin, S. W. Tsai. Environmental Factors in Composite Materials Design, *Air Force Materials Laboratory Report*, AFML-TR-64-423, 1967.

[3] C. Soutis, P. W. R. Beaumont, *Multiscale modelling of composite material systems: the art of predictive damage modelling*, Woodhead, 2005.

[4] P. Kerfriden, O. Allix, P. Gosselet. A three-scale domain decomposition method for the 3D analysis of debonding in laminates, *Computational Mechanics*, 44(3), 343-362, 2009.

[5] L. Margetts. *Parallel finite element analysis*, PhD Thesis, University of Manchester, 2002.

[6] I. M. Smith, D. V. Griffiths, L. Margetts, *Programming the Finite Element Method*, 5th Edition, Wiley, 2014.

[7] ABAQUS/CAE, *User's Manual,* 6.13.

[8] P. P. Camanho, C. G. Davila. Mixed-mode decohesion finite elements for the simulation of delamination in composite materials, *Tech rep. NASA/TM*, 2002-211737, 2002.

[9] Y. Shi, C. Pinna, C. Soutis. Modelling impact damage in composite laminates: A simulation of intra- and inter-laminar cracking, *Composite Structures*, 114, 10-19, 2014.

[10] A. Atas, C. Soutis. Application of cohesive zone elements in damage analysis of composites: Strength prediction of a single-bolted joint in CFRP laminates, *Int. Journal of Non-Linear Mech*, 66, 96-104, 2014.

Proceedings of the 24th UK Conference of the
Association for Computational Mechanics in Engineering
31 March - 01 April 2016, Cardiff University, Cardiff

Energy minimizing multi-crack growth in linear elastic fracture using the extended finite element method

***Danas Sutula[1], Pierre Kerfriden[2], Stephane P. A. Bordas[3]**

[1,2]Cardiff University, School of Engineering, The Parade, Cardiff, CF24 3AA, Wales, UK
[3]University of Luxembourg, Engineering, 6 rue Richard Coudenhove-Kalergi, L-1359 Luxembourg

*sutulad@cardiff.ac.uk

ABSTRACT

We investigate multiple fracture evolution under quasi-static conditions in an isotropic linear elastic solid based on the principle of minimum potential elastic energy in the framework of the extended finite element method. The technique enables a minimization of the potential energy with respect to all crack increment directions. Results show that the maximum hoop stress criterion and the energy minimization approach converge to the same fracture path. It is found that the converged solution lies in between the fracture paths obtained by each criterion for coarser meshes. This presents an opportunity to estimate an upper and lower bound of the true fracture path as well as an error on the crack path.

Key Words: *Energy minimisation ; linear elastic fracture ; crack growth criterion ; XFEM.*

1. Introduction

In computational fracture mechanics as applied, for example, to damage tolerance assessment, it has been common practice to determine the onset of fracture growth and the growth direction by post-processing the solution of the linear elastostatics problem, at a particular instance in time. For mixed mode loading the available analytically derived criteria that can be used for determining the onset of crack growth typically rely on the assumptions of an idealized geometry e.g. a single crack subjected to remote loading [9, 5] and that the kink angle of the infinitesimal crack increment is small [7]. Moreover, the growth direction given by a criterion that is based on an instantaneous local crack tip field can only be valid for infinitesimally small crack growth increments. Consequently, the maximum hoop stress criterion [4] and other similar criteria [2] disregard the changes in the solution that take place as fractures advance over a finite size propagation. Hence, due to the error committed in time-integration, fractures may no longer follow the most energetically favorable paths that theoretically could be achieved for a specific discrete problem.

2. Method

In our approach, we investigate multiple fracture evolution under quasi-static conditions in an isotropic linear elastic solid based on the principle of minimum potential elastic energy, which can help circumvent the aforementioned difficulties. The technique enables a minimization of the potential energy with respect to all crack increment directions taking into consideration their relative interactions. The directions are optimized (in the energy sense) by considering virtual crack rotations to find the energy release rates and its first derivatives in order to determine, via an iterative process, the directions that yield zero energy release rates with respect to all virtual rotations [6]. We use the extended finite element method (XFEM) [1, 8] for discretization of a 2D continuum in order to model an elaborate crack evolution over time, similar in principle to [3], although here we would like to consider hundreds of propagating cracks.

3. Governing equations

The energy release rate with respect to a fracture growth direction θ_i can be obtained by differentiation of the potential energy Π of the system:

$$Gs_i = -\frac{\partial \Pi}{\partial \theta_i} \tag{1}$$

Considering a general case of multiple fractures, the rate of the energy release rate can be obtained as:

$$Hs_{i,j} = \frac{\partial Gs_i}{\partial \theta_j} = -\frac{\partial^2 \Pi}{\partial \theta_i \partial \theta_j} \tag{2}$$

In a discrete setting, the potential energy of a static system can be written as:

$$\Pi = \frac{1}{2} u' K u - u' f \tag{3}$$

where u, K, and f are the displacement vector, the stiffness matrix, and the applied force vector. The energy release rate with respect to an arbitrary crack incitement angle θ_i is defined as the negative variation of the potential energy:

$$Gs_i = -\frac{1}{2} u' \delta_i K u + u' \delta_i f - \delta_i u' (K u - f) \tag{4}$$

in which case the last term in (4) disappears due to assumed equilibrium of the discrete system i.e. $Ku = f$. Hence, the expression for the energy release rate becomes:

$$Gs_i = -\frac{1}{2} u' \delta_i K u + u' \delta_i f \tag{5}$$

where $\delta_i f$ only needs to be accounted for if the applied loads influence the virtual crack rotation, e.g. due to crack face tractions and body-type loads. The rates of the energy release rate, Hs_{ij} are obtained by differentiating Gs_i in (5) with respect to θ_j:

$$Hs_{ij} = -\left(\frac{1}{2} u' \delta_{ij}^2 K u - u' \delta_{ij}^2 f \right) - \delta_j u' \left(\delta_i K u - \delta_i f \right) \tag{6}$$

The variations of displacements $\delta_j u$ in (6) are global, and can be determined from the equilibrium condition and that the variation must vanish, i.e. $\delta_j (Ku - f) = 0$ and thus:

$$\delta u = -K^{-1} (\delta K u - \delta f) \tag{7}$$

Substituting (7) in (6) gives:

$$Hs_{ij} = -\left(\frac{1}{2} u' \delta_{ij}^2 K u - u' \delta_{ij}^2 f \right) + (\delta_j K u - \delta_j f)' K^{-1} (\delta_i K u - \delta_i f) \tag{8}$$

In (8) the second order mixed derivatives $\delta_{ij}^2 K$ and $\delta_{ij}^2 f$ capture the local interaction between the rotations of different crack increments. However, if the crack tips are sufficiently far apart such that no geometrical interactions exist between different rotations, then for $i \neq j$ the interacting terms vanish, i.e. $\delta_{ij}^2 K = 0$ and $\delta_{ij}^2 f = 0$. As such, it only becomes necessary to retain the non-zero self-interactions i.e. $\delta_{ii}^2 K$ and $\delta_{ii}^2 f$. Consequently, by leaving out the cross-interactions, equation (8) reads as:

$$Hs_{ij} = -\left(\frac{1}{2} u' \delta_{ii}^2 K u - u' \delta_{ii}^2 F \right) + (\delta_j K u - \delta_j f)' K^{-1} (\delta_i K u - \delta_i f) \tag{9}$$

Equations (5) and (9) can be used to determine the energy release rates and the rates of the energy release rates associated with the rotation of different crack increments. The problem of finding the most energetically favorable growth directions for the candidate finite length crack increments, denoted by a set I_{inc}, is one requiring that the corresponding energy release rates must vanish i.e. $Gs_i = 0,\ \forall i \in I_{\text{inc}}$. The solution procedure at every time step, t^{n+1} can be cast as Newton-Raphson iterations:

$$\boldsymbol{\theta}_{k+1} = \boldsymbol{\theta}_k - \boldsymbol{H}_k{}^{-1}\boldsymbol{G}\boldsymbol{s}_k \tag{10}$$

where k is the iteration count. The converged solution is attained when $|\boldsymbol{\theta}_{k+1} - \boldsymbol{\theta}_k| \leq \epsilon$, ϵ being the tolerance in the change in the angle of the finite crack increment, e.g. $\epsilon = 0.1^\circ$.

4. Implementation

Although XFEM facilitates mesh independent fracture propagation the enrichment must be updated at each time step. In the current implementation this is achieved by means of a systematic book-keeping of the element enrichment data, addition and removal of enrichment only where necessary, and a consistent updating of the global system of equations. Consequently, moderate computational times are obtained, even in our *Matlab* implementation. In the problems we solve, the greatest cost, by far, is in the solution of the linear system of equations rather than in the assembly/updating.

5. Results and discussion

We compare the fracture paths obtained by different criteria for problems consisting of multiple cracks and verify that, with mesh refinement, both criteria converge to the same fracture path provided the criterion for growth is the same. However, the convergence rate of the energy minimization technique to the converged crack path is found to be only marginally superior to that of the maximum hoop stress criterion. It is found that the converged fracture path lies in between the fracture paths obtained by each criterion for coarser meshes. This presents an opportunity to estimate an upper and lower bound of the true fracture path as well as an error on the crack path. It is found that a more accurate approximation of the fracture path for coarser meshes can be obtained by averaging the directions determined by each criteria individually at every time step. Some results are demonstrated in Appendix A. Although there is no limitation on the number of cracks in the implementation, the example cases presented consider only few cracks as it is sufficient to demonstrate the key idea clearly.

6. Conclusions

Convergence of the maximum hoop stress criterion and the energy minimization towards the true fracture path is found to be similar. However, from numerical experiments it is found that the converged fracture path lies in between the fracture paths obtained by each criterion for coarser meshes. Besides the opportunity to estimate the error on the fracture path for a given mesh, a more accurate approximation of the true fracture path can be obtained by taking the average of the propagation directions given by each criterion separately at every time step.

References

[1] T. Belytschko and T. Black. Elastic crack growth in finite elements with minimal remeshing. *International Journal for Numerical*, 620(July 1998):601–620, 1999.

[2] P. O. Bouchard, F. Bay, and Y. Chastel. Numerical modelling of crack propagation: automatic remeshing and comparison of different criteria. *Computer Methods in Applied Mechanics and Engineering*, 192(35-36):3887–3908, August 2003.

[3] E. Budyn, G. Zi, N. Moës, and T. Belytschko. A method for multiple crack growth in brittle materials without remeshing. *International Journal for Numerical Methods in Engineering*, 61(10):1741–1770, November 2004.

[4] F. Erdogan and G. C. Sih. On the crack extension in plates under plane loading and transverse shear. *Journal of basic engineering*, 85:519, 1963.

[5] K. Hayashi and S. Nemat-Nasser. Energy-release rate and crack kinking under combined loading. *Journal of Applied Mechanics*, (September 1981):520–524, 1981.

[6] M. A. Hussain, S. L. Pu, and J. Underwood. Strain Energy Release Rate for a Crack Under Combined Mode I and Mode. *Fracture analysis*, 560:1, 1974.

[7] B. L. Karihaloo, L. M. Keer, and S. Nemat-Nasser. Crack kinking under nonsymmetric loading. *Engineering Fracture Mechanics*, 13(4):879–888, 1980.

[8] N. Moës, J. Dolbow, and T. Belytschko. A finite element method for crack growth without remeshing. 150(February):131–150, 1999.

[9] R. J. Nuismer. An energy release rate criterion for mixed mode fracture. *International journal of fracture*, 11(2):245–250, 1975.

Appendix A. Figures

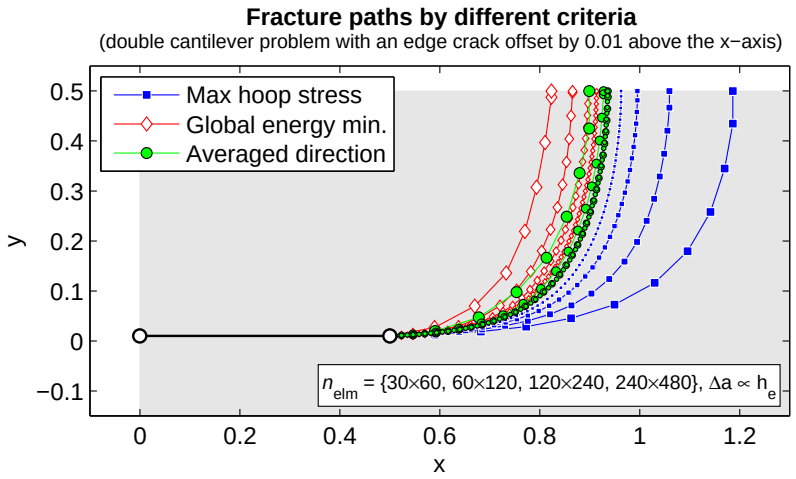

Figure A.1: Fracture paths considering different growth criteria for the double cantilever problem with the initial crack positioned 0.01 above the x-axis. The prying action is exerted by prescribed displacements on the left edge.

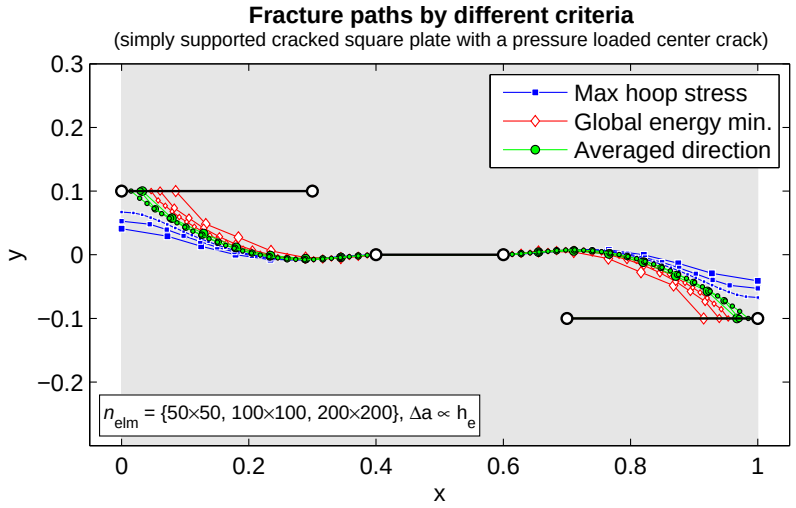

Figure A.2: Fracture paths considering different growth criteria for a simply supported square plate with three pre-existing cracks, where the center crack is subjected to a pressure load acting normal to the crack surface.

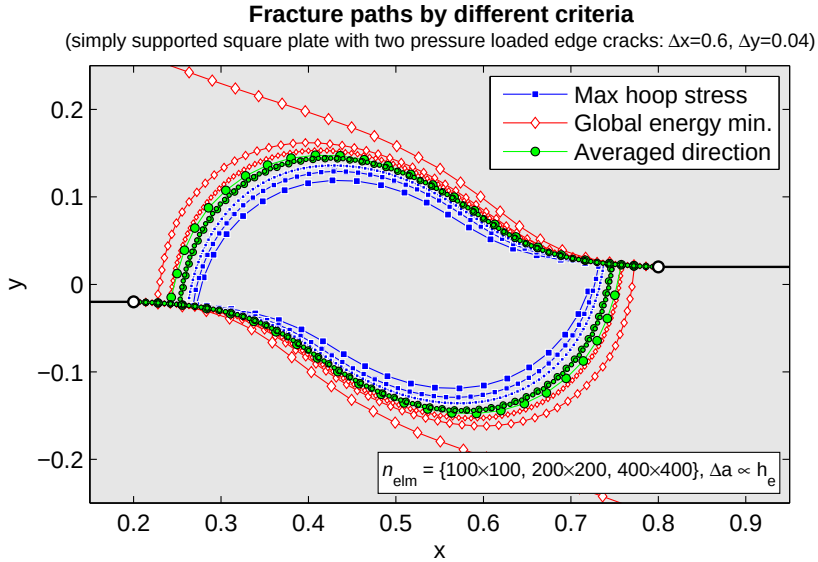

Figure A.3: Fracture paths considering different growth criteria for a simply supported square plate with two initial edge cracks that are loaded by pressure acting normal to the crack surface.

Fluid mechanics and F/S interaction II

Proceedings of the 24th UK Conference of the
Association for Computational Mechanics in Engineering
31 March - 01 April 2016, Cardiff University, Cardiff

Acoustic Wave Propagation in Microfluidic Application with Hierarchical Finite Element

***X. Meng[1], J. Reboud[1], C.J. Pearce[1] and Ł. Kaczmarczyk[1]**

[1] School of Engineering, Rankine Building, The University of Glasgow, Glasgow, G12 8LT, UK

*E-mail: m.xuan.1@research.gla.ac.uk

ABSTRACT

In this paper, we introduce a new computational method for the analysis of fluids subjected to high frequency mechanical forcing. We focus attention on surface acoustic wave droplet microfluidics. In these problems, we distinguish three time scales 1) the fast (μs) time scale of Rayleigh waves on the solid surface, 2) medium (μs-ms) time scale of acoustic wave in the fluid droplet, and 3) slow (ms-s) time scale of capillary wave propagation on the fluid-air surface. Finite element modelling of such problems has been limited in its ability to handle the broad range of timescales. In particular, direct time integration techniques are computationally expensive because of the need to resolve the smallest timescale.

Here we solve the Helmholtz equation in the frequency domain, applying hierarchical finite element approximation based on unstructured meshes [2], where both pressure field and geometry are independently approximated with arbitrary and heterogeneous polynomial order. We demonstrate convergence of the numerical scheme and illustrate model performance using the example of a surface acoustic wave actuation of a droplet, which has applications in microfluidics and microrheology at high frequency.

Key Words: *acoustic modelling ; polychromatic waves ; discrete Fourier transform ; hierarchical shape functions*

1. Introduction

Acoustic problems have a wide range of uses in different physical applications, albeit numerical results can suffer from poor resolution and be computationally expensive. Here we focus on the development of a computational tool to aid the design of acoustic diagnostic devices (lab-on-a-chip). To avoid the need of solving the 4D wave equation, the problem is expanded to polychromatic waves via discrete Fourier transformation in both the spatial and frequency domain with respect to the input signal, solving the 3D Helmholtz equation instead. As shown in Figure 1b, it is presumed that the computational domain of a droplet (shown in purple) is a hemispherical shape with contact angle 90 degree. A surface acoustic wave (SAW) passes along a substrate that then interacts with the droplet. To determine the boundary conditions (BCs) on the droplet, the incoming Rayleigh waves are expressed as a closed form analytical equation based on developments from [3] and [4] (Figure 1a). A Fourier transform is then applied to the analytical equation to establish the BCs. This allows us to solve for the propagation of the acoustic waves in the fluid droplet in the frequency domain. This yields the pressure and velocity fields in the fluid which serves to calculate the radiation acoustic forces. These forces can be applied to solve the problem in the slow time scale using a direct time integration of Navier Stokes equation for droplet, specifically taking care of the surface tension. This final part of the problem is strongly nonlinear as a result of the evolving droplet geometry; thus, the calculations of the acoustic wave in the fluid droplet are repeated for each time step at the slow time scale.

Initially, the problem of a plane wave impinging on the sound hard surface of a cylinder is considered, where solution convergence is studied for both geometry and multiple physical fields. Moreover, error estimators and the numerical efficiency of the *hp*-adaptivity in the context of the Helmholtz equation is investigated. The application of hierarchical finite element approximation improves the computational efficiency and accuracy of the acoustic solver [2]. Subsequently, the problem of SAW actuation of a fluid droplet is considered. The proposed finite element technology is implemented in the open-source finite element University of Glasgow in-house parallel computational code, MoFEM (Mesh Oriented Finite Element Method).

2. Model components

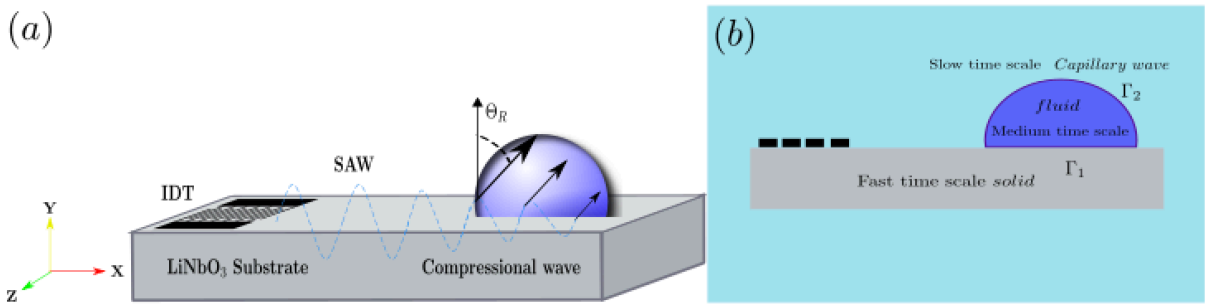

Figure 1: Surface acoustic waves application. (a) SAW actuation of a liquid drop on a $LiNbO_3$ piezoelectric surface, showing the leaky Rayleigh waves in the drop. (b) Illustration of the different timescales.

2.1. Boundary conditions

Let Ω be a domain in $\mathbb{R}^3$ with the smooth boundary and outward unit normal n. The complete form of Helmholtz equation for the acoustic problem is defined as

$$\nabla \cdot \nabla\Phi(\mathbf{r}) + k^2\Phi(\mathbf{r}) = f(\mathbf{r}) \text{ in } \Omega \tag{1a}$$

$$\left(\frac{\partial\Phi(\mathbf{r})}{\partial n} + i\sigma\Phi\right) = g \text{ on } \Gamma \tag{1b}$$

$$\Phi = \Phi_S + \Phi_I \tag{1c}$$

where Φ is the total acoustic potential, (Φ_S and Φ_I denote radiation and incident wave respectively) and the variation of $f(\mathbf{r})$ in (1a) can be regarded as a point source of acoustic wave. (1b) shows the mixed BC with constant σ and g, which can be used to describe any BCs by modifying the parameters. If $g = 0$, the Robin BC can be either Dirichlet or Neumann BC in extreme cases. $\sigma = \rho c$ is called the dimensionless admittance coefficient. When $\sigma \to \infty$ the boundary is soft, conversely, when $\sigma \to 0$, the boundary becomes rigid [1].

2.2. Application on microfludics

Rayleigh waves are a type of surface wave first proposed by Lord Rayleigh (1887), it is propagating along a free surface and the amplitude decays exponentially away from the surface. Rayleigh wave consist two types of surface acoustic waves, their potentials are: longitudinal wave φ and transverse wave $(0, \psi, 0)$. The closed form solution of Rayleigh waves on solid surface is given by

$$\varphi = A_0 e^{-q|y|} e^{ik\mathbf{x}} \tag{2a}$$

The attenuation coefficients in analytical form are:

$$q^2 = k^2 - k^2\frac{c_s}{c_l} > 0 \tag{3a}$$

where $k = \frac{\omega}{c_s}$ and c_s is the phase velocity (speed) of Rayleigh wave ($c_s = c_L$ for leaky Rayleigh wave), c_l denotes the speed of longitudinal wave on solid surface.

As illustrated in Figure 1(a) when SAW pass beneath droplet, it leaks energy into droplet, this phenomena is called the leaky SAW. In addition, longitudinal waves propagate into the droplet, with a complex wavenumber $k_L = k + ik_i$ and speed c_L, form Rayleigh angle $\Theta_R = \arcsin(\frac{c_L}{c_s})$ with horizontal axis. In [4], the leaky SAW number $k_i = 2768$ for Y-X $LiNbO_3$ is provided.

2.3. Polychromatic wave

The detailed procedures devised to treat the case of polychromatic waves are shown in Figure 2.

$$\begin{cases} \text{Find } u \in H^1(\Omega), & \text{such that} \\ \mathfrak{a}(u_{k_n}, v_{k_n}) = \mathfrak{f}(v_{k_n}) & \forall v_{k_n} \in H^1(\Omega) \end{cases}$$

where $\mathfrak{a}(\cdot,\cdot)$ is the symmetric bilinear form based on $H^1(\Omega) \times H^1(\Omega)$ (u_{k_n} is the finite element solution of $\Phi_S(k_n)$) expressed as

$$\mathfrak{a}(u_{k_n}, v_{k_n}) = \int_\Omega \nabla u_{k_n} \nabla v_{k_n} d\Omega - k^2 \int_\Omega u_{k_n} v_{k_n} d\Omega \tag{4a}$$

$$+ \sigma_1 \int_{\Gamma_2} u_{k_n} v_{k_n} dS + \sigma_2 \int_{\Gamma_1} u_{k_n} v_{k_n} dS \tag{4b}$$

$$\mathfrak{f}(v_{k_n}) = \int_\Omega f v_{k_n} d\Omega + (\Phi_I(k_n) + \frac{\partial \Phi_I(k_n)}{\partial r}) \int_{\Gamma_1} v_{k_n} dS \tag{4c}$$

where σ_1 and σ_2 are admittance coefficients corresponding to surfaces Γ_1, Γ_2. The system of linear equations required to be solved

$$\mathbf{K}_n \mathbf{U}_n = \mathbf{F}_n \tag{5}$$

this equation is solved for n frequency where n frequencies is considered here. Once the results are computed, we then apply the inverse Fourier Transform to transfer the acoustic potential back to the time domain. With that at hand, we can calculate radial stress where it drives fluid into motion at the slow time scale. The radial stress is calculated from acoustic potential by averaging velocities [5].

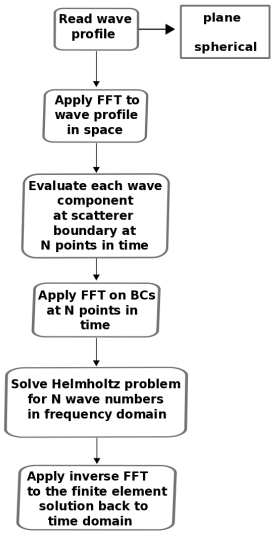

Figure 2: Diagram of polychromatic wave problem solved by Helmholtz equation

3. Computational procedure and results

a

In the pre-processor, a parameterised geometry with uniform mesh containing tetrahedras is made in Cubit. Problem is solved using MUltifrontal Massively Parallel sparse direct Solver (Mumps). In this work, hierarchical Legendre type shape functions are used. The l_2 norm of solution error is calculated for different approximations and various frequencies, plots of convergence analysis were compared.

Figure 3(a) shows the absolute acoustic potential of computational domain around the hard cylinder. Figure 3(b) and (c) present the convergence of the relative error. In 3(b) the polynomial order p is fixed to 2, the mesh size h is gradually decreased. In 3(c) we increase approximation order from 1 to 7 but keep the mesh density constant.

In Figure 3(d) and (e), we have absolute acoustic pressure and radial stress for micro-droplet with 440966 number of degrees of freedoms (DOFs) and 4th order polynomials, and in Figure 3(f) the values of stress components on nodes along x-axis are plotted.

As we can notice from the plots (b), (c) of Figure 3, the convergence speed of p enrichment is nearly two times faster than h refinement. Notably, the convergence speed of relative error in plot (c) started to decrease up to certain percentages (k=3, 5, 10. 0.44%, 0.32%, 0.26% respectively), this reveals the fact

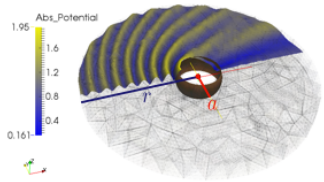

(a) Solution for hard cylinder with coarse mesh, p = 2

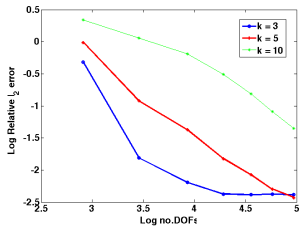

(b) Relative error of h convergence analysis in l_2 norm for impinging cylinder (a=0.5 r=4)

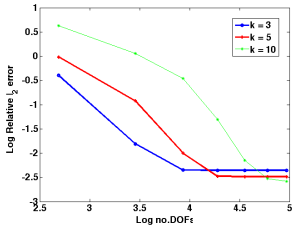

(c) Relative error of p convergence analysis in l_2 norm for impinging cylinder (a=0.5 r=4)

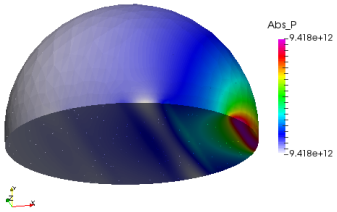

(d) SAW actuation of droplet with diameter&SAW width 0.002 m, RF power 14dBm, 5.3 MHz frequency, t = 1.2830e-07 s out of 1.8868e-07 s

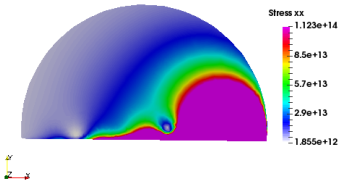

(e) Cross-sectional of x-y plane radial stress σ_{xx} in droplet

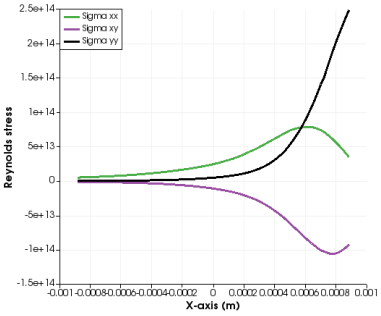

(f) Plot data over x-axis of radial stress in droplet

Figure 3: Numerical results

that the remaining error could be due to non-reflection BC . This errors can be minimised by increasing the domain of computation or implementing exact BCs.

In Figure 3-(d)&(e) the distribution of acoustic pressure and radial stress of droplet is presented [3], the energy of LSAW is attenuated with height and distance travelled. the radial stress derived from pressure can be further employed as the input source stress into separated microfluidic equations in future research.

4. Conclusions

A computational framework for polychromatic waves based on the time dependant Helmholtz equation is described for microfluids applications. In this paper we show that improving solution quality by increasing approximation order is more efficient than making mesh denser. Moreover we calculated radial stresses in droplet subjected to Leaky SAW.

References

[1] Ihlenburg, F. Finite element analysis of acoustic scattering, *Springer Science & Business Media,*, Vol. 132. 2006.

[2] Ainsworth, M. & Coyle, J. Hierarchic finite element bases on unstructured tetrahedral meshes.*International journal for numerical methods in engineering*, 58(14), 2103-2130. 2003

[3] Reboud, J., Bourquin, Y., Wilson, R., Pall, G.S., Jiwaji, M., Pitt, A.R., Graham, A., Waters, A.P. & Cooper, J. M. Shaping acoustic fields as a toolset for microfluidic manipulations in diagnostic technologies. *Proceedings of the National Academy of Sciences,* 109(38), 15162-15167. 2012

[4] Vanneste, J., & Buhler, O. Streaming by leaky surface acoustic waves. *In Proceedings of the Royal Society of London A: Mathematical, Physical and Engineering Sciences*, (Vol. 467, No. 2130, pp. 1779-1800). The Royal Society. 2011

[5] Lighthill, J. Acoustic streaming. *Journal of sound and vibration,* 61(3), 391-418. 1978

Proceedings of the 24th UK Conference of the
Association for Computational Mechanics in Engineering
31 March – 01 April 2016, Cardiff University, Cardiff

Two Droplets interaction on substrate

***A. Jameel, BJ. Bowen and K. Yokoi**

School of engineering, University of Cardiff, 14-17 The Parade, Cardiff, CF243AA

*jameelas@cardiff.ac.uk

ABSTRACT

Dynamics of two droplets interactions on a substrate (droplet impact on a sessile droplet) are numerically investigated using OpenFOAM. The impact speed, location of the impacting droplet, viscosity and surface tension were varied in the numerical studies. We found that when the surface tension dominates the flow, the mass canter of two droplets moves to impacting droplet side. When the inertia dominates the flow, the mass centre moves to the opposite direction.

Keywords: *two droplets; composite location; mass centre; OpenFOAM.*

1. Introduction

Accurate and controlled deposition of droplets on solid surfaces or solid surface with another pre-located sessile droplet is a principle in many of industrial processes or applications such as solid inkjet printing, micro-fabrication, rapid prototyping and electronic packaging [1]. Droplets in touch must overlap and coalesce during the impact process to avoid breaks in the pattern being fabricated. However, surface tension-driven flows that happen when contacted droplets touch can shift droplets location after they have been deposited and such unpredictable movements may make lines break or vary in thickness. Although great progress has been made in the recent coalescence studies on a solid substrates, there are still a few issues to be addressed in the context of its wide applications. To the best of our knowledge, no information in literature on the trend of final footprint location between two consecutively deposited drops which is limited on the variety of impact speed at different lateral displacement, substrate wettability and liquid parameters. The contributions of this work are to study the location trend at different impact velocities, liquid properties, surface wettability and centre to centre displacements. Composite droplet edges will be tracked with time at one displacement case and different velocities to identify coalescence mechanism and its effect on final location.

2. Numerical method and setup

A hemispherical cap sessile droplet deposited with initial diameter D_s=4.4 mm, and located in a steady flow field with static contact angle equal 63°. Glycerol-water mixture liquid used here with density ρ=1220 kg/m^3, viscosity μ=85.8 mPa.s, and surface tension σ=67.1 mN/m. computational domain opened to atmospheric air at 23C° presenting no walls except substrate showing no boundaries influence on the droplet dynamics. A spherical droplet with initial diameter D_o=2.8 mm, generated right to sessile for an overlap ratio $\lambda = 1 - L/D_s$ [1] defined as in Fig.1 and given an impact speed U. The computational domain has given zero initial condition, while the boundary condition was no slip for velocity at substrate and zero gradient for other geometrical boundaries. For pressure, zero gradients applied for substrate, total pressure equal zero are applied on other boundaries. The mesh used was 166*166*45=1,240,020 cells for a domain size 14*14*3.8 (mm) in x, y and z direction respectively. Cell size Δx is 8.4*10^{-5}, which provides 52 mesh nodes for sessile and 34 nodes for impacting droplet. This mesh resolution considered high enough for our physical demands and our resources abilities.
The governing equations for the two isothermal, incompressible, and immiscible fluids include the continuity, momentum, and interface capturing advection equations based on the VOF method:

$$\nabla . \vec{u} = 0 \tag{1}$$

$$\rho\left(\frac{\partial \vec{u}}{\partial t} + \vec{u}.\nabla\vec{u}\right) = -\nabla p + \nabla.(2\mu S) + \vec{F}_\sigma \tag{2}$$

$$\frac{\partial \alpha}{\partial t} + \nabla.(\vec{u}\alpha) + \nabla.[\vec{u}_r \alpha(1-\alpha)] = 0 \quad (3)$$

Where ρ is the fluid density, $\vec{u}$ the fluid velocity vector, S the viscous stress tensor defined as $S_{ij} = \left(\partial_i u_j + \partial_j u_i\right)/2$, μ is the dynamic viscosity, p is the scalar pressure, and $\vec{F}_\sigma$ is the volumetric surface tension force. The volume fraction function α is used to represent a space mesh cell whether is occupied by the dispersed phase or the continuous phase. When the cells are full of the dispersed phase, the value of α is unity; the continuous phase corresponds to zero; when the mesh cells contain both the dispersed phase and the continuous phase, the value of α is between 0 and 1, which denotes an interface between the two phases. $\vec{u}_r$ Is the liquid–gas relative velocity, compressing the interface to improve its resolution [2]. The term α (1- α) limits the effect of the $\vec{u}_r$ to the interface region. Moreover, $\vec{u}_r$ can be calculated as follows:

$$\vec{u}_r = min\left(C_\alpha|\vec{u}|, max(|\vec{u}|)\right)\frac{\nabla\alpha}{|\nabla\alpha|} \quad (4)$$

Where the default value of $C_\alpha = 1$ was used; however, a larger value of C_α can enhance the compression of the interface. The boundedness of α function is guaranteed by a special solver named Multidimensional Universal Limiter for Explicit Solution (MULES) [3]. A new level set field is introduced to provide a more precise interface reconstruction and then reduce the parasitic currents. The LS field is estimated from the VOF field in each time step by $\emptyset = (2\alpha - 1)\Gamma$, Γ is a small non-dimensional number whose value depends on the mesh step size (Δx) at the interface of the two fluids, and it is defined as Γ = 0.75Δx [4]. The LS field is corrected by solving the re-initialization equation:

$$\frac{\partial \emptyset}{\partial t} = sign(\emptyset)(1 - |\nabla\emptyset|) \quad (5)$$

Where $\emptyset$ should satisfy $|\nabla\emptyset| = 1$ by its definition. The normal vector of the interface $\hat{n} = \nabla\emptyset/|\nabla\emptyset|$ can be accurately determined due to the continuity of the LS function. Thus, more precise and smoother interface curvature $\kappa = \nabla \cdot \hat{n}$ can be obtained. Based on the Continuum Surface Force (CSF) model [5], the volumetric surface tension force can be calculated as:

$$\vec{F}_\sigma = \sigma\, \kappa(\emptyset)\delta(\emptyset)\nabla\emptyset \quad (6)$$

Where σ is the surface tension coefficient, and δ is the Dirac function used to limit the influence of the surface tension to a narrow region around the interface. The function of δ is cantered at the interface and takes a zero value in both fluids as:

$$\delta(\emptyset) = \begin{cases} 0 & |\emptyset| > \varepsilon \\ \frac{1}{2\varepsilon}\left(1 + cos\left(\pi\emptyset/_\varepsilon\right)\right) & |\emptyset| \le \varepsilon \end{cases} \quad (7)$$

Where ε is the interface thickness which is chosen as ε = 1.5Δx. The physical properties and the fluxes across the cell faces can be defined using a smoothed Heaviside function:

$$H(\emptyset) = \begin{cases} 0 & \emptyset < -\varepsilon \\ \frac{1}{2}\left[1 + \frac{\emptyset}{\varepsilon} + \frac{1}{\pi}sin\left(\frac{\pi\emptyset}{\varepsilon}\right)\right] & |\emptyset| \le \varepsilon \\ 1 & \emptyset > \varepsilon \end{cases} \quad (8)$$

$$\rho = \rho_g H + \left(\rho_l - \rho_g\right)H \quad (9)$$

$$\mu = \mu_g H + \left(\mu_l - \mu_g\right)H \quad (10)$$

Results and discussion

Three overlap ratios **λ** = 0.5, 0.34 and 0.18 respectively are implemented in this study as shown in Fig.2. Increasing impact velocity expected to force the final composite droplet to be located on the opposite

side of impact. From results, for small impact velocity, droplet composite location was moving gradually towards impact direction (to right), this trend changed at specific critical velocity and composite located away from direction of impact for higher value of velocity. Fig 3 shows the final (steady state, T=0.5s) edges and mass centre location at different values of velocity compared with the mass centre location of two droplets at zero condition for case $\boldsymbol{\lambda}$ = 0.34. Comparing mass centre at before impact, mass centre always located to the right side for a velocity range U= 0.2 - 1.5(m/s). We noticed max location to the right at a critical impact speed U=0.5(m/s) where location trend deflected to the left but still located at the right side of initial mass centre. Mass centre located to the left side of initial mass centre for U=1.5(m/s) and above. To understand the reason behind such non trivial trend of composite location, the right and left edge displacement $X_L, X_R = |d_{L,R}|/D_S + L$ [1] of composite droplets have been tracked with time as shown in Fig.4. For velocity range U= 0.2 - 0.5 (m/s), tracking right edge with time showed spread to right, this spread increase due to increasing velocity. The left edge stayed pinned with substrate showing no spread because of no sensible effect reached from the impact droplet within this range of velocity.

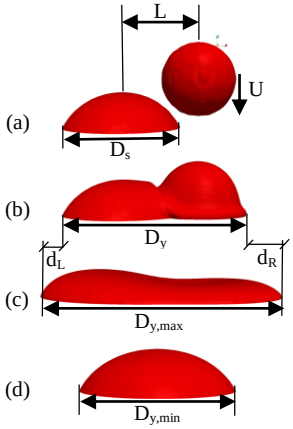

Figure 1: Deposition of two droplets on a solid surface (a); Spread length Dy (b); maximum spread length Dy,max (c); minimum spread length Dy,min (d).

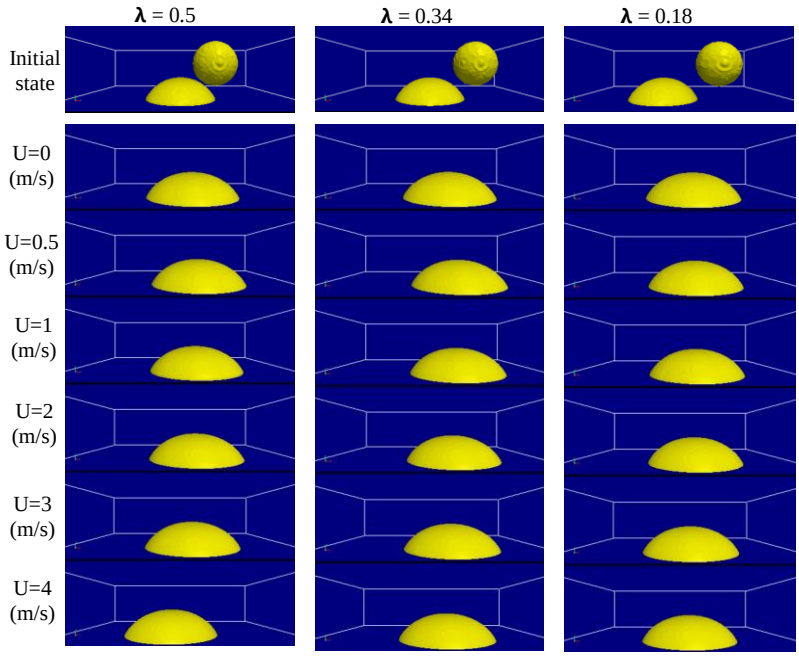

Figure 2: Contour of composite of two droplets at steady state for three different overlap ratios ($\boldsymbol{\lambda}$) and different impact speeds.

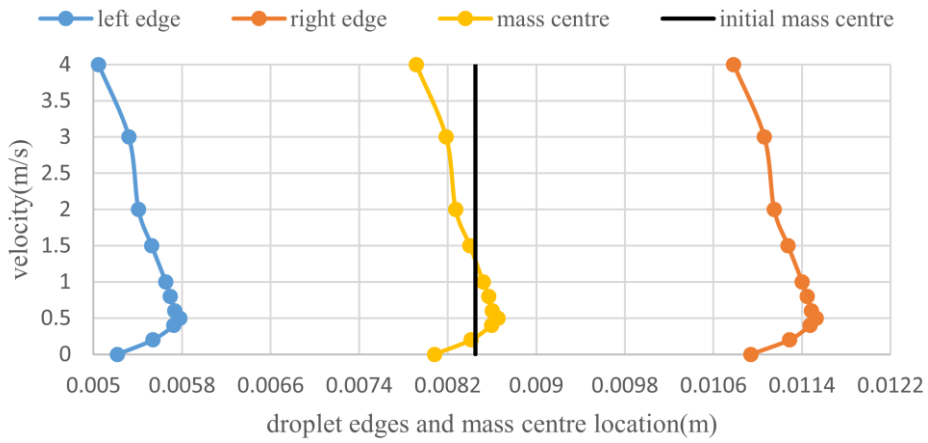

Figure 3: Final edges and mass centre location of composite droplets at different impact speed.

When maximum spread reached, capillary forces effected to recoil the composite due to surface tension.

This recoiling reflected on retracting both right and left edges and considered the reason of locating composite droplet on the side of impact droplet. For bigger impact velocity (U > 0.5 m/s), impact droplet influenced on the left edge of sessile due to bigger liquid wave transferred from the right. Sessile left edge unpinned and exhibited spread to the left, this spreading increases with bigger impact velocity. Sessile left edge unpinned and exhibited spread to the left, this spreading increases with bigger impact velocity. Recoiling due to surface tension represented in retracting of both edges towards equilibrium condition.

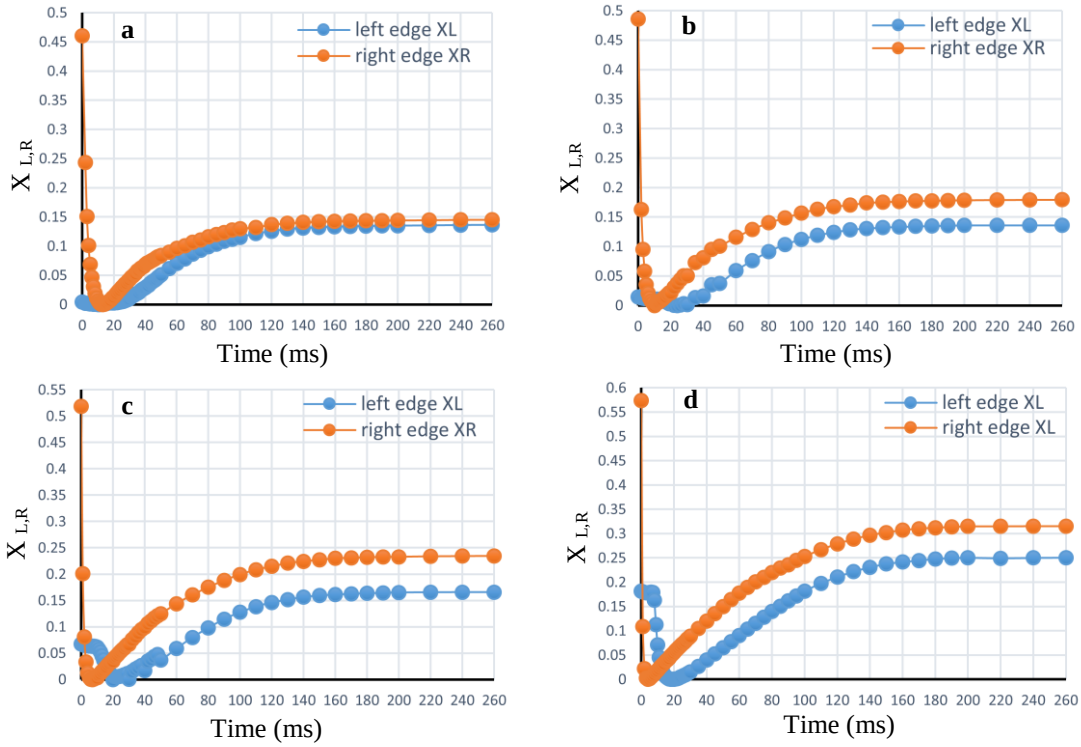

Figure 4: displacement of the right and left edges relative to maximum points.
(a) U= 0.5 (m/s); (b) U= 0.8 (m/s); (c) U= 1.5 (m/s); (d) U= 3 (m/s).

Conclusions

Effect of lateral separation, impact speed and liquid properties on composite droplet location was conducted numerically using OpenFOAM. We found that composite droplet location relative to initial condition controlled by the impacting droplet velocity and liquid properties but showing same non-trivial final location movement for different overlap ratios used in this research. For high value of surface tension, no inertia effect, composite droplet always located to impact side. Opposite happens for lower value of surface tension, inertia dominates and mass centre moves to the opposite direction.

References

[1] Li, R., Ashgriz, N., Chandra, S., Andrews, J. R., and Drappel, S., 2010. "Coalescence of two droplets impacting a solid surface". *Experiments in Fluids,* **48**(6), Jun, pp. 1025–1035.

[2] Weller HG. A new approach to VOF-based interface capturing methods for incompressible and compressible flows. Technical Report No. 2008 TR/HGW/04.

[3] Zalesak ST. Fully multidimensional flux-corrected transport algorithms for fluids. J Comput Phys 1979; 31:335–62.

[4] Albadawi A, Donoghue DB, Robinson AJ, Murray DB, Delauré YMC. Influence of surface tension implementation in volume of fluid and coupled volume of fluid with level set methods for bubble growth and detachment. Int J Multiphase Flow 2013; 53:11–8.

[5] Brackbill JU, Kothe DB, Zemach C. A continuum method for modeling surface tension. J Comput Phys 1992; 100:335–54.

Parallel implementation of numerical modelling of concentration polarisation and cake formation in membrane filtration processes

Bun Lo[1]*, Oubay Hassan[1] and Jason Jones[1]

[1]College of Engineering, Swansea University, Bay Campus, Swansea SA1 8EN
*839372@swansea.ac.uk

ABSTRACT

An existing model[1] capable of predicting concentration polarisation and cake formation in crossflow membrane filtration is implemented on different parallel platforms. The governing equations, Navier Stokes equations for the hydrodynamics and convection diffusion equation for suspended particles, are solved numerically using the lattice Boltzmann method. The equations are coupled through velocity, viscosity and diffusion coefficient, which are assumed to vary with the solute concentration.

The sequential algorithm is analysed to identify potential parallelisation sections and is implemented in C++ with OpenMP for multicore CPU, MPI for distributed memory CPUs clusters and CUDA for GPUs clusters. For each parallel implementation, optimisation is carried out too remove all identified bottlenecks. In general, these optimisations aim to fully utilise pipelines concurrently and eliminate unnecessary workload.

The parallelised algorithms are validated by comparing the results obtained for a number of problems with the predictions produced by other computational models and experimental results available in literature. With the current setup, the algorithms are both memory bound and compute bound, which allow them to scale well with increasing number of computing units. The paper will demonstrate the bottlenecks, effectiveness of optimizations and the performance of the parallel codes.

The parallel implementation of the modelling process demonstrates the potential of the computational technique to be deployed for the prediction of concentration polarisation and cake formation in a fast and efficient manner. Simulations can be done with higher resolution in a much faster timeframe, which allows better optimization of membrane filtration processes.
Keywords: *filtration; parallel computing; optimization*

1. Filtration Model

The lattice Boltzmann method(LBM) is used to solve the Navier Stokes equations for fluid and convection diffusion equation for solute particles[1]. The general formulation of LBM is as follow.

$$f_\alpha(x_i + e_\alpha, t+1) - f_\alpha(x_i, t) = \Omega(f)$$

The left hand side represents the streaming step as each partial distribution function(PDF) shifts to a neighbour cell. The right hand side represents the collision step, where the collision operator rebalances each PDF to simulate change in direction due to particle collision. The details of the collision operator depend on the type of flow. For fluid flow we adopt the multiple relaxation time method by d'Humieres et al[2], for porous cells, such as membranes and cake formation, we adopt the modified BGK operator by Freed[3], and for solute particles the BGK operator is applied with variables altered to suit the convection diffusion equation.

To couple the Navier Stokes equations and convection diffusion equation the viscosity and diffusion coefficient are subject to changes according to the local concentration and shear rate.

When the local concentration of particles reaches a pre-set value, a lattice cell is considered to be a cake layer and modelled as a porous cell.

2. Code Restructuring

The first and foremost problem to identify is the dependencies of the simulation, as parallel computing involves multiple computational units it is vital to assign workload that does not clash with each other.

The collision step in LBM is completely local, as it only uses local information. Different processors can work on different lattice cells without interference. However at a processor level, reordering instructions can also improve performance, this is achieved by fully utilising all pipelines available. By calculating variables such as density, momentum and concentration at the beginning of a time step, most calculations in the collision step can be issued independent of each other, thus able to use all available pipelines and achieve a higher performance. Below is a comparison between the original and revised algorithm.

Solve fluid collision	Compute concentration and update viscosity
Compute macroscopic variables	Compute macroscopic variables
Solve solute collision	Solve fluid collision
Compute concentration and update viscosity	Solve solute collision

Algorithm 1: Original code

Algorithm 2: Revised version

In algorithm 1, each section of calculation is dependent on the previous section, which means there are three bottlenecks that the processor cannot proceed before every current workload is completed. In the updated version (Algorithm 2) calculations are independent of the last section of code, which means that as soon as a pipeline becomes free, it can carry out the next set of calculations instead of waiting for all other pipelines.

In a naive approach to perform the streaming step, one would shift the data to the neighbouring cells. This means reading data from the original location and saving to a new location, altering the value that was stored there. It requires a specific shifting order to ensure data correctness, and prohibits proper parallelisation. Moreover streaming is no more than a read and write operation to the processor, which is also exactly what the collision step has to do. By combing the two steps together only half as many memory transactions are required.

To accommodate these issues we adopt the AA pattern by Bailey et al.[4] There are two schemes for odd and even time steps. Figure 1 shows the memory operations for the cell in the centre. In odd time steps data is read as normal (first from left), but the PDFs are stored in the memory space of the opposite direction PDF (second from left). Even time steps perform a pull - collision - push, reading data from the neighbouring cells(second from right) and then storing similar to the previous step, swapping back to the natural memory space in the neighbours (first from right). The memory operations of this scheme is then completely local for each cell at each time step, since the processor read and write at the same location, and is inherently parallel.

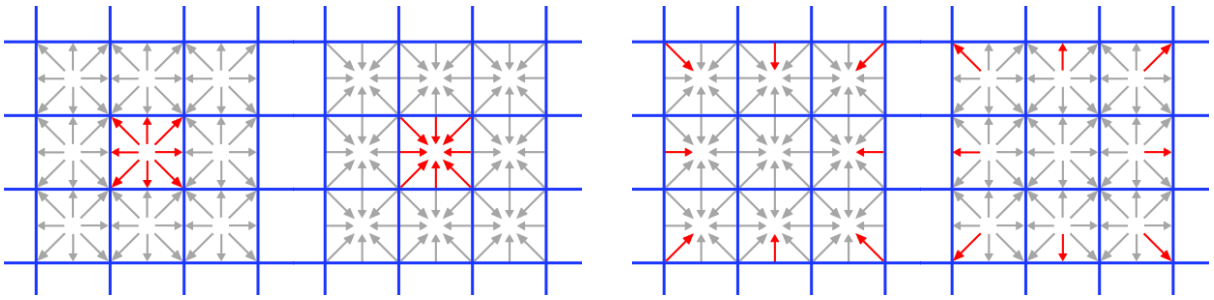

Figure 1: Read and write operations with AA pattern. Left: Odd time steps. Right: Even time steps.

The restructuring on the previous code has improved the performance by a factor of two.

3. Grid Division

For a cluster of CPUs or GPUs it is essential to divide the grid so that each CPU or GPU have equal workload and know which processors to communicate with. The current work concerns 2D problems and there are two different methods on grid division; dividing the grid along the longest axis, or dividing the grid along both axes. The former method is simpler and each processor has up to two neighbours, but has a longer boundary, the latter attempts to divide the grid into squares, thus having a smaller boundary but can have up to eight neighbours.

In GPU programming the simple grid division is clearly superior, due to coalesced memory access. On the other hand CPUs are less reliant on memory access pattern and a test was conducted to find out the differences.

Figure 2 shows the performance of 60 CPU cores on filtration simulation of various gird sizes, the performance in presented in terms of million lattice update per second (MLUPS), given by

$$\text{MLUPS} = \text{number of cells/time taken for a step}$$

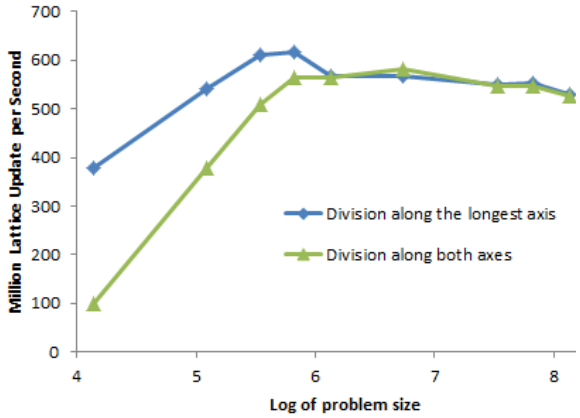

Figure 2: Performance of 60 CPU cores, using different grid division methods

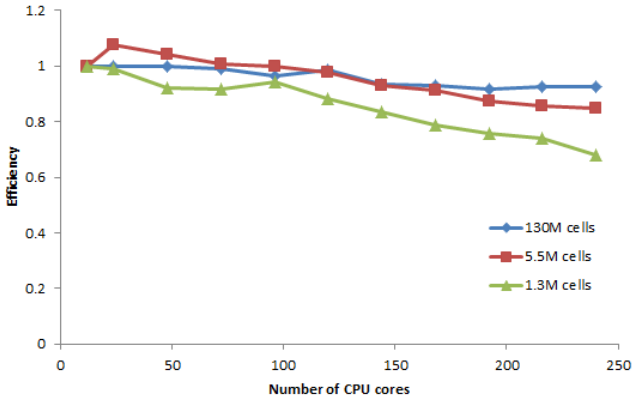

Figure 3: Efficiency of CPU cores on 3 grid sizes

The simple approach performs much better on small grids due to smaller communication overheads, and on large grids where the complex method communicates faster, the differences are minimal since calculations took much more time compare to communication. This shows that the simple grid division is better on CPU clusters as well.

4. Results and Discussion

Results on CPUs

Table 1 shows the speed up when fully utilising an 8-core CPU instead of just 1 core, the grids tested ranged from small 2D problem to large 3D problem. Up to 7.49 times was achieved which is equivalent to 93.75% efficiency.

Table 1: Factor of speed up on an 8-core CPU

Number of cells	13,680	123,120	1,368,000	5,472,000	34,200,000	136,800,000
Speed up	5.78	7.29	7.05	7.16	7.49	7.39

On a cluster of CPUs we tested the larger grids due to the scale of computing power when compared to one CPU. Figure 3 shows the efficiency of up to 240 CPU cores, which is over 85% and 92% for the 5.5million cells and 130million cells grid, whereas the 1.3million cells grid scale well with over 80% efficiency until over 140 cores were deployed. This is because the time taken for each time step falls under 1 millisecond, and the communication time becomes significant.

Bottleneck on CPUs:
While many other LBM simulations are described as memory bound, the current model includes coupling the fluid and solute particles, which introduced a long dependency chain and doubles the amount of calculations. Thus to a certain degree it is compute bound, which is why our multicore code is able to scale well with additional processors. However as it is necessary to inspect whether a cell is a fluid cell or porous cell, it requires reading information before any calculations can begin, which incur a section of code that is memory bound. This can be observed in Figure 2 as some of the smaller grids have the highest performance due to data fitting in the CPU cache and has a higher bandwidth.

Results on GPUs:
The current code was tested on a Titan Z and Quadro K5200. The Titan Z is a dual GPU with 5760 CUDA cores and 1:3 ratio of double precision units to single precision units. The Quadro K5200 has 2304 CUDA cores and 1:24 ratio of double to single units. Due to the difference in double precision capability, our code is compute bound on the Quadro and memory bound on the Titan. Kernels are launched with blocks of 512 threads, which allow each thread to have up to 128 registers and give optimal performance.

Table 2 shows the speed up compared to a sequential code. The Quadro K5200 GPU has a much lower performance at all stages than a single GPU on Titan Z due the lack of computing power. When both GPUs on the Titan Z are used, the communication between the two devices incurs a ~0.35ms penalty between time steps, which makes small grids very slow to process. On the larger grids the Titan Z is able to perform 72.7 times faster than a sequential code.

Table 2: Factor of speed up on two GPUs

Number of cells	13,680	123,120	1,368,000	5,472,000	34,200,000
Quadro K5200	9.2	17.5	19.1	20.1	20.4
Titan Z (1 GPU)	24.5	34.9	37.8	38.8	38.7
Titan Z (2 GPU)	1.8	40.1	55.1	70.5	72.7

5. Conclusion

An existing filtration simulation code was rewritten to make use of multiple processing units available in modern computer structures. The programmes are able to scale efficiently with increasing number of processors and provide performance that enable the simulation of industrial problems in an acceptable time scale.

References

[1] M. Paipuri, S.H. Kim, O. Hassan, N. Hilal and K. Morgan, Numerical modelling of concentration polarisation and cake formation in membrane filtration processes, *Desalination* 365 (2015), 151 – 159.

[2] D. d'Humieres, B. D. Shizgal, D. P. Weaver, Generalized lattice Boltzmann equations. In Rarefied gas dynamics: theory and simulations, Prog. Aeronaut. Astronaut. 159 (1992) 450 - 458.

[3] D. M. Freed, International Journal of Modern Physics C 9 (8)(1998), 1491 - 1503.

[4] P. Bailey, J. Myre, S.D.C. Walsh, D.J. Lilja, M.O. Saar, Accelerating lattice Boltzmann fluid flow simulations using graphics processors, *International Conference on Parallel Processing* (2009).

Proceedings of the 24th UK Conference of the
Association for Computational Mechanics in Engineering
31 March - 01 April 2016, Cardiff University, Cardiff

A 3rd Order ENO-Like Multi-Moment Method for Solving Hyperbolic Conservation Laws

***Syazana Omar[1], Kensuke Yokoi[2]**

[1]School of Engineering, Cardiff University, Queen's Buildings, The Parade, Cardiff CF24 3AA, UK

*omars2@cardiff.ac.uk

ABSTRACT

We propose a conservative multi-moment method based on 3rd order polynomial interpolation functions and the essentially non-oscillatory (ENO) scheme. Based on CIP-CSL3, the proposed method employs two multi-moment based 3rd order polynomial interpolation functions; CIP-CSL3D where three constraints are used in the upwind cell with one constraint in the downwind cell-centre, and a new, complementary method CIP-CSL3U, which uses a constraint in the upwind cell-centre instead. Based on the ENO (Essentially Non-Oscillatory) scheme, either CSL3D or CSL3U is chosen using a local smoothness indicator.

Numerical results from common benchmark tests in one dimension (both linear and non-linear) show that this scheme maintains 4th order accuracy for smooth profiles while successfully reducing numerical oscillation around discontinuity without giving way to numerical diffusion. Its competitive results show that this is a promising high-order method for CFD applications given its algorithmic simplicity, and can be extended for multi-dimensions.

Key Words: *CIP-CSL; multi-moment; ENO; upwind scheme*

1. Introduction

Many numerical schemes have been developed for solving hyperbolic equations [1][2][3]. A way to improve order of accuracy is by increasing the stencil size or by employing the multi-moment method, where at least two types of moments are used and each is updated using a different formulation. For example, the CIP-CSL2 (constrained interpolation conservative semi-Lagrangian) method solves the conservation equation by using two boundary values updated using the finite difference formulation and a cell integrated average moment updated using the finite volume formulation.

Several variants of the CIP-CSL method have been proposed thus far (CSL3 [4], CSL3D [5]). We propose a variant of CIP-CSL3 method with an ENO-like formulation [6].

2. Numerical Method

The CIP-CSL method solves the conservation equation

$$\frac{\partial \phi}{\partial t} + \frac{\partial (u\phi)}{\partial x} = 0 \tag{1}$$

where ϕ is the property being transported at a constant velocity u along the x axis.

2.1. CIP-CSL3D method

The CIP-CSL3D uses 3 moments in the upwind cell (i.e. 1 cell average $\bar{\phi}_{i-1}$ and 2 cell boundary values $\phi_{i-\frac{1}{2}}$ and $\phi_{i-\frac{3}{2}}$) and 1 moment in the downwind cell centre ($\hat{\phi}_i$) which is itself interpolated from the downwind cell's boundary values and cell integrated average. Consequently it yields a cubic interpolation function as such, for $u > 0$

$$\Phi_{i-1}^{CSL3D}(x) = C_{3,i-1}^{CSL3D}(x - x_{i-\frac{1}{2}})^3 + C_{2,i-1}^{CSL3D}(x - x_{i-\frac{1}{2}})^2 + C_{1,i-1}^{CSL3D}(x - x_{i-\frac{1}{2}}) + \phi_{i-\frac{1}{2}} \tag{2}$$

to interpolate between $\phi_{i-\frac{1}{2}}$ and $\phi_{i-\frac{3}{2}}$.

Using this interpolation function, the boundary value $\phi_{i-\frac{1}{2}}$ is updated by the conservation equation in a finite difference form

$$\frac{\partial \phi}{\partial t} + u\frac{\partial \phi}{\partial x} = -\phi\frac{\partial u}{\partial x} \tag{3}$$

and the cell average is updated by

$$\frac{\partial}{\partial t}\int_{x-\frac{1}{2}}^{x+\frac{1}{2}} \phi dx = -\frac{F_{i+1/2} - F_{i-1/2}}{\Delta x} \tag{4}$$

where $F_{i-1/2}$ is the flux at cell boundary $x_{i-1/2}$.

2.2. CIP-CSL3U

This is a proposed variant of CIP-CSL3 complementary to CIP-CSL3D, where an upwind moment in the cell centre ($\hat{\phi}_{i-2}$) is used as a constraint. The cubic interpolation function used to interpolate between $\phi_{i-\frac{1}{2}}$ and $\phi_{i-\frac{3}{2}}$ is similar as that used for CSL3D

$$\Phi_{i-1}^{CSL3U}(x) = C_{3,i-1}^{CSL3U}(x - x_{i-\frac{1}{2}})^3 + C_{2,i-1}^{CSL3U}(x - x_{i-\frac{1}{2}})^2 + C_{1,i-1}^{CSL3U}(x - x_{i-\frac{1}{2}}) + \phi_{i-\frac{1}{2}} \tag{5}$$

for $u > 0$. The cell boundary and cell integrated average are updated in the same manner as CSL3D.

2.3. ENO-like Combination of CSL3D and CSL3U

The ENO scheme proposed a way to avoid interpolating across discontinuities to avoid oscillations. A hierarchy is developed beginning with 1 or 2 cells, and 1 cell is added at a time to the stencil from two candidates on the left and right based on its local smoothness determined by some smoothness indicator. Our proposed method departs from the ENO method by instead having 2 fixed stencils, which is selected depending on their respective smoothness.

The smoothness indicator used to select between the 2 stencils is a modified version of the indicator proposed by Zhang and Shu (2007) [7].

$$S_{CSL3U} = \int_{x-\frac{1}{8}}^{x+\frac{1}{8}} \Delta x\left(\frac{\delta \phi^{CSL3U}(x)}{\delta x}\right)^2 dx - \frac{7}{9}\int_{x-\frac{1}{8}}^{x+\frac{1}{8}} \Delta x^3\left(\frac{\delta^2 \phi^{CSL3U}(x)}{\delta^2 x}\right)^2 dx \tag{6}$$

$$S_{CSL3D} = \int_{x-\frac{1}{8}}^{x+\frac{1}{8}} \Delta x\left(\frac{\delta \phi^{CSL3D}(x)}{\delta x}\right)^2 dx - \frac{7}{9}\int_{x-\frac{1}{8}}^{x+\frac{1}{8}} \Delta x^3\left(\frac{\delta^2 \phi^{CSL3D}(x)}{\delta^2 x}\right)^2 dx \tag{7}$$

3. Results

We validate the proposed method using both linear and non-linear scalar transport problems. In this paper, the results by CSL3 and CSL3D are also included in this section for comparison.

3.1. Complex wave propagation

We test the proposed methodology using the complex wave propagation problem, with $u(x) = 1$, grid size $N = 200$, $\Delta t = 0.4\Delta x$, $\Delta x = 2/N$, and periodic boundary conditions.

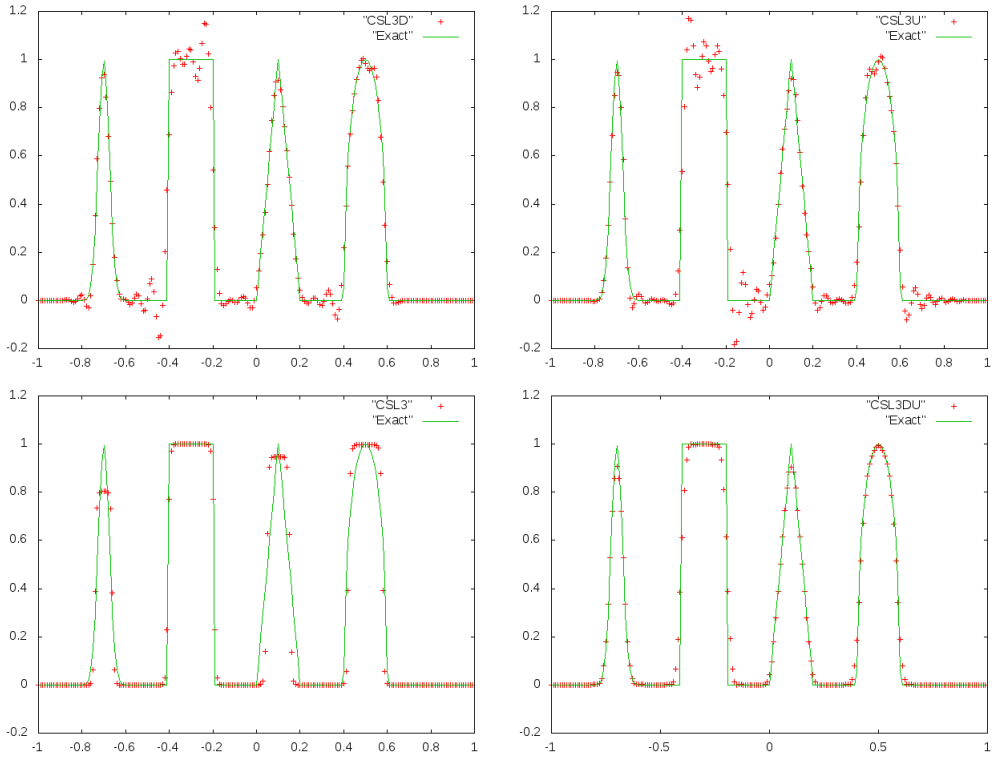

Figure 1: Numerical results of the complex wave propagation test at t=16 (4000 time steps) with N=200

Figure 1 shows that unlike CSL3, CSL3D and CSL3U capture sharp edges well. It is also evident that the oscillations generated by CSL3D and CSL3U are on opposite sides of each other (i.e. where CSL3D has oscillation on the downwind side, CSL3U has the same oscillation on the upwind side). CSL3DU successfully combines CSL3D and CSL3U by preserving sharp edges and suppressing oscillations.

3.2. Square wave propagation in a non-uniform velocity field

In this test, a square wave is transported in the following non-uniform velocity field

$$u(x,0) = \frac{1}{1 + 0.4sin(2\pi x)} \tag{8}$$

Figure 2 shows that while individually, CSL3D and CSL3U generate large oscillations near discontinuities similar to Test 1, the combination of both eliminates oscillations to the same degree as CSL3 without giving way to diffusion.

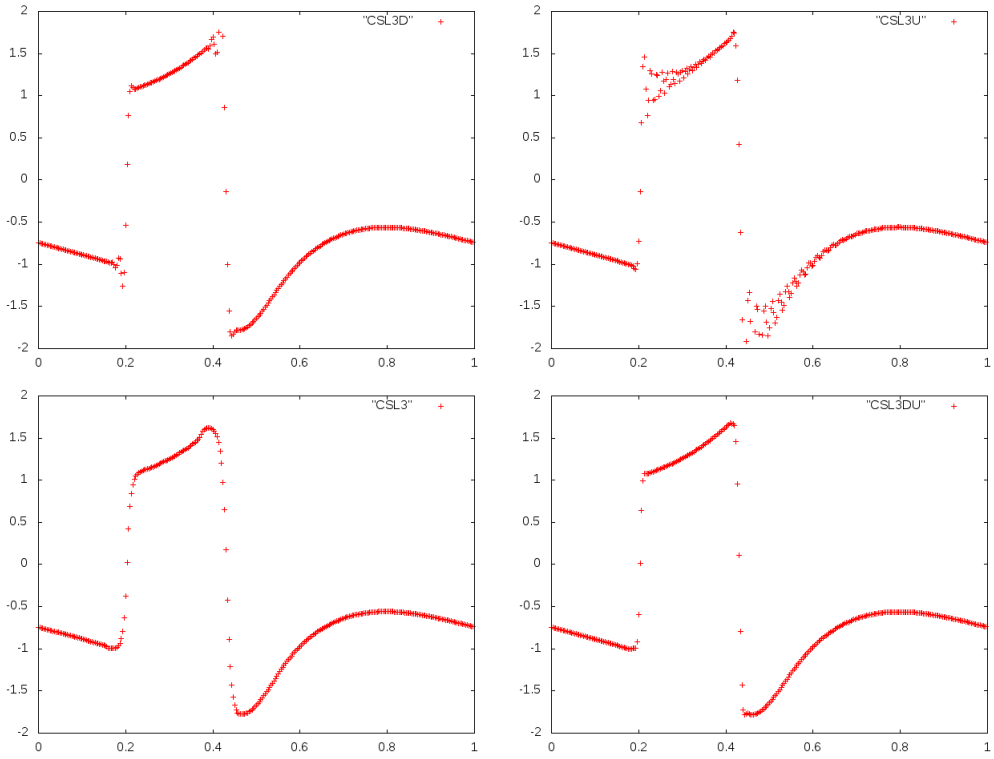

Figure 2: Numerical results of square wave propagation in a non-uniform velocity field at t = 1.8 and N = 300

4. Conclusions

We proposed the CIP-CSL3DU method which employs two 3rd order polynomial interpolation functions. One interpolation function is constructed based on 3 constraints in the upwind cell and 1 constraint in the downwind cell (CIP-CSL3D) and one interpolation is based on 3 constraints in the upwind cell and 1 constraint in the further upwind cell (CIP-CSL3U). By selecting the smoother of these two stencils, we produce CIP-CSL3DU which successfully suppresses Gibbs oscillation while maintaining numerical viscosity.

References

[1] G. Jiang and C. Shu. Efficient Implementation of Weighted ENO Schemes. *J. Comput. Phys*, 126, 202, 1996.

[2] S. Lele. Compact Finite Difference Schemes with Spectral-Like Resolution. *J. Comput. Phys*, 103, 16, 1992.

[3] Y. Morinishi, T. Lund, O. Vasilyev, and P. Moin. Fully Conservative Higher Order Finite Difference Schemes for Compressible Flow. *J. Comput. Phys*, 143, 90, 1998.

[4] F. Xiao and T. Yabe. Completely Conservative and Oscillationless Semi-Lagrangian Schemes for Advection Transportation. *J. Comput. Phys*, 170, 498, 2001.

[5] N. Onodera, T. Aoki, K. Yokoi. A Fully Conservative High-Order Multi-Moment Method Using Moments in Both Upwind and Downwind Cells. *Int. J. Num. Methods*, 2015.

[6] A. Harten and S. Osher. Uniformly High Order Accurate Non-Oscillatory Schemes. *I. SIAM J. Numer. Anal.*, 24, 279, 1987.

[7] S. Zhang and C. Shu. A New Smoothness Indicator for the WENO Schemes and Its Effect on the Convergence to Steady State Solutions. *J. Scientific Comp.*, 31, 2006.

Proceedings of the 24th UK Conference of the
Association for Computational Mechanics in Engineering
31 March – 01 April 2016, Cardiff University, Cardiff

MODELING INTERTIAL FORCES ON CYLINDERS IN CROSS FLOW USING MOVING FRAME OF REFERENCE

Seyed Hossein Madani, Jan Wissink, Hamid Bahai
College of Engineering Design and Physical study - Brunel University London

Abstract

Fluid-Structure interaction (FSI) problems have received significant attention in many applications in the recent decade. An FSI problem can be simulated either in an inertial frame of reference or in a moving (non-inertial) frame of reference. In the latter case, which is mainly applicable when there is only one moving body, the frame of reference in which the governing equations are solved is attached to the moving body.
In this paper, an immersed boundary (IB) interpolation approach is used to simulate fluid flow. A comprehensive parametric study is performed to find the optimum mesh size and computational domain extent. In addition, the effect of the fluid inertial force in a moving frame of reference is investigated by studying hydrodynamic forces. It is shown that the difference between the governing equations in the relative and inertial frames of reference are the fluid inertial forces which can be added separately to the simulation results. In addition, results of simulations using two frames of reference are contrasted. It is shown that the main sources of noise in the lift coefficient are the pressure fluctuations in the non-inertial frame of reference.

Key words: Immersed-Boundary, interpolation/Reconstruction method, pressure gradient, Vortex shedding, FSI

1. Introduction

Fluid flow around a moving bluff body with an irregular geometry has been extensively studied and can be categorised in various ways [1,2]. Regardless of the simulation approach (conforming grid, e.g. ALE or non-conforming grid, e.g. IB), it is possible to simulate moving boundaries in either inertial or non-inertial frames of reference. Here an immersed boundary (IB) method is applied in both frames of references [3].
Paskin [4] was the first to employ the immersed-boundary method for solving flow problems in regions with complex/moving boundaries. These methods are normally classified, by the way that the solid boundary is enforced, into continuous and discrete forcing approaches. In the later scenario, the interpolation/reconstruction method is a popular approach: When the boundary does not align with a mesh line, the solution algorithm is locally replaced by a velocity interpolation to enforce the boundary conditions on the flow field [5]. Note that in order to fulfil the conservation of mass near the immersed boundary, extra measures need to be taken (more detail see [5]).
When there is only one moving body, employing a relative frame of reference that is attached to the body could improve non-conforming grid approaches significantly as there is no need to update the IB formulation due to movements of the body relative to the background computational grid.
To solve the governing equation in the relative frame of reference two fundamental changes are necessary. First of all, the governing equation should be adapted for usage in the relative frame of reference [6] by adding additional terms to compensate for the effect of the moving frame in the calculation. Also, the boundary conditions should be transformed for usage in the relative reference. Here, only movements in the transverse direction are considered.

2. Numerical model

This section briefly outlines the theory and governing equations necessary to simulate a moving body in inertial and non-inertial frames of reference. For reasons of simplicity and easiness of generalization of the solution algorithm, the non-dimensional form of the Navier-Stokes equation is used. The non-dimensional Navier-Stokes equations in primitive variable are given in equation (1). In the moving frame of reference the acceleration of the structure needs to be added to the governing equations and the velocity boundary conditions will also need to be transformed to the relative frame (for more details see [6]).
The flow governing equations in both frames of reference are solved by the fractional step (Chorin projection approach) method. The intermediate velocity is calculated at first instance using a Runge-Kutta method for integrating the momentum equations in time. The velocity is subsequently projected

onto a solenoidal space by adding the pressure obtained by solving the pressure Poisson equation (PPE), which is solved using a SIP solver. The Neumann condition for the PPE should be updated by projecting the momentum equation at the immersed boundary to account for the solid acceleration [6].

$$\frac{\partial \mathrm{V}}{\partial \mathrm{t}} + \mathrm{V} \cdot \nabla \mathrm{V} = -\nabla \mathrm{p} + {}^{1}/_{Re}\, \nabla^2 \mathrm{V} \qquad (1)$$
$$\nabla . \mathrm{V} = 0$$

3. OSCILLATION OF A BODY IN CROSS FLOW DIRECTION

In this problem, the body oscillates with a prescribed motion in the cross flow direction at specific range of oscillations where the frequency of vortex shedding around the body becomes similar to the oscillation frequency ('lock-in' phenomenon). Here, the prescribed motion is defined in equation (**2**), where $y_c(t)$ is the location of the centre of the cylinder and A_{0y}, ω and f are the amplitude, the frequency in rad/s and the frequency in Hz of the prescribe oscillation, respectively.

$$\boldsymbol{y_c(t) = A_{0y} Sin(\omega t) = A_{0y} Sin(2\pi f t)} \qquad (2)$$

In the moving frame of reference approach the reference frame is attached to the moving body and the boundary conditions are transformed accordingly. Note that the flow about a circular cylinder forced to oscillate in the cross flow direction is kinematically the same as the flow about a fixed cylinder in a free stream with a superimposed oscillatory cross flow. It should be noted, however, that these two flows differ dynamically due to the inertial effects. This effect is known as the Froude-Krylov force in the literature [7]. To simulate flow over a moving body using an IB approach in an inertial frame of reference the interpolation formula needs to be regularly updated, while in the moving frame of reference the interpolation formula remains unchanged. The main advantage when using an IB approach is the ability to simulate the Fluid-Structure-Interaction (FSI) for a moving/deforming object on a fixed grid.

4. Results

Various parameters, which could potentially affect the hydrodynamic forces exerted by the uniform stream on an oscillating cylinder, are studied. According to the parametric study for flow around a moving cylinder with prescribe motion, the mesh size, the domain size upstream of the cylinder and the domain size in the cross stream direction are the most influential factors. Here, these effects are studied for a cylinder oscillating in the cross flow direction with an amplitude of A/D=0.2, while the frequency of excitation is fe=1.05fs. The parametric study is performed at Re=100, based on the free stream velocity and the cylinder diameter, where fs=0.167 is the Strouhal frequency for a stationary cylinder.

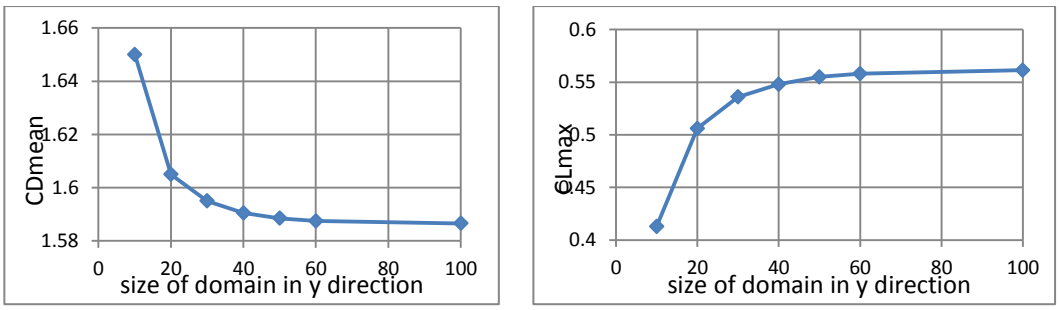

Figure 1: The effect of domain size in the y direction on the mean drag and maximum lift

The numerical results show that lift and drag coefficient changes become negligible (less than 1%) for the grid sizes finer than 0.025D. Also, if the size of the domain upstream of the cylinder is increased from 20D from 30D, the mean drag and maximum lift coefficients only change by 0.2% and -1.5% respectively. In addition, the blockage effect on the lift and drag coefficient is less than 1% when the size of the domain in the transverse direction exceeds 40D (Figure 1).

4.1 Effect of inertial forces

When the flow governing equation is solved using relative velocities rather than absolute ones, without deriving the equations in a moving frame, inertia effects need to be added to the relative hydrodynamic forces (case A). On the other hand, if the flow governing equations are derived in the moving reference frame the flow forces will include inertia effects (case B). This has been shown Figure 2, where in both simulations, Re=150, $F = f_e/f_s$=0.9 and the relative velocities are defined at the inlet and far-field boundaries (top and bottom).

In both cases (Case A and B) the pressure, the lift due to shear, the drag coefficient due to pressure and the shear stress are found to be identical (**Error! Reference source not found.**). The only difference is in the lift due to the pressure which is caused by the inertial force. In Figure 2 (left), the red line and the green line show the lift coefficient (due to pressure) for cases A and B, respectively. In this figure, once the lift in case A (red line) and the inertial effect (orange line) are added together (back dots), the results become in good agreement with the lift coefficient obtained in the case B (Green line).

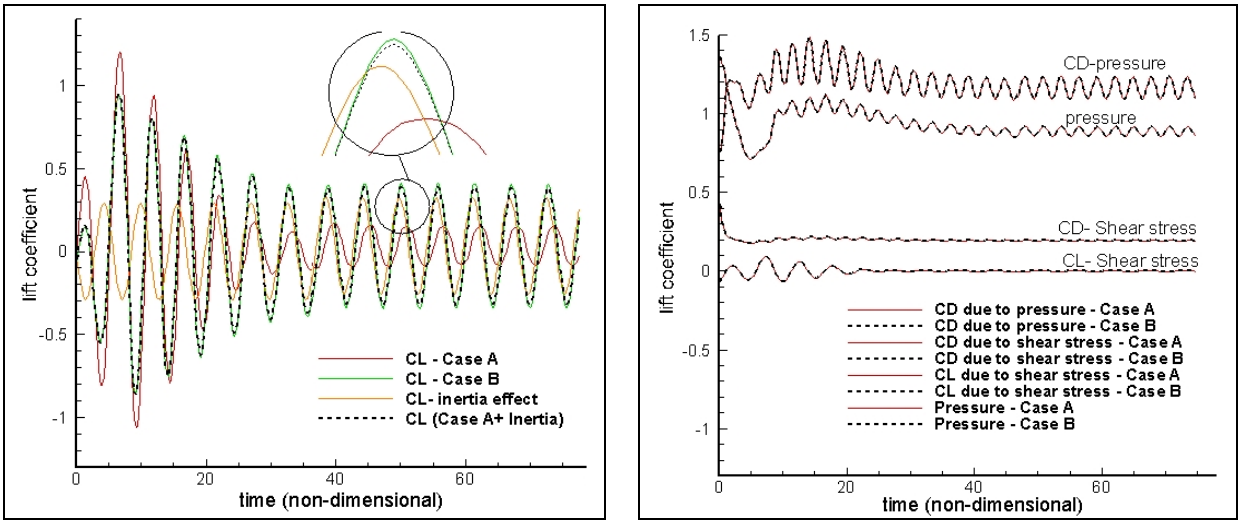

Figure 2: inertial effect to correct lift coefficient calculated in moving frame of reference

4.2 Moving frame verses inertial frame of reference

The governing equations are solved in both the moving frame of reference and the inertial frame of reference. In both approaches an IB interpolation method is used to enforce the immersed boundary. In the moving frame of reference, however, the interpolation formulas are not updated so that the simulation is less time consuming and the results are much smoother. In both cases a cylinder is forced to oscillate in the cross flow direction, the Reynolds number is 100 (Re=100), the amplitude of the oscillation is 0.2D and the frequency of the oscillation is 1.05 times the vortex shedding frequency (0.167). The Reynolds number is based on the free stream velocity and the cylinder diameter, D.

The lift and drag due to pressure for both approaches (moving and fixed frame of reference) are shown in the Figure 3. The results from the inertial frame of reference simulations show noise in the lift and drag signals due to pressure (dotted line). The reason for this is that the interpolation formulas are updated at each time step.

The lift and drag due to shear stress for both non-inertial and inertial frames of reference are similar and do not show any noise (Figure 3, right). It can be concluded that the noise in the lift and drag coefficients are due to the calculation of the pressure. Also this possibly explains why the inertial frame of reference approach is so time consuming. Not only updating the interpolation formulas is taking extra simulation time but also the Pressure Poisson equation needs more iteration to converge due to the noise in the pressure.

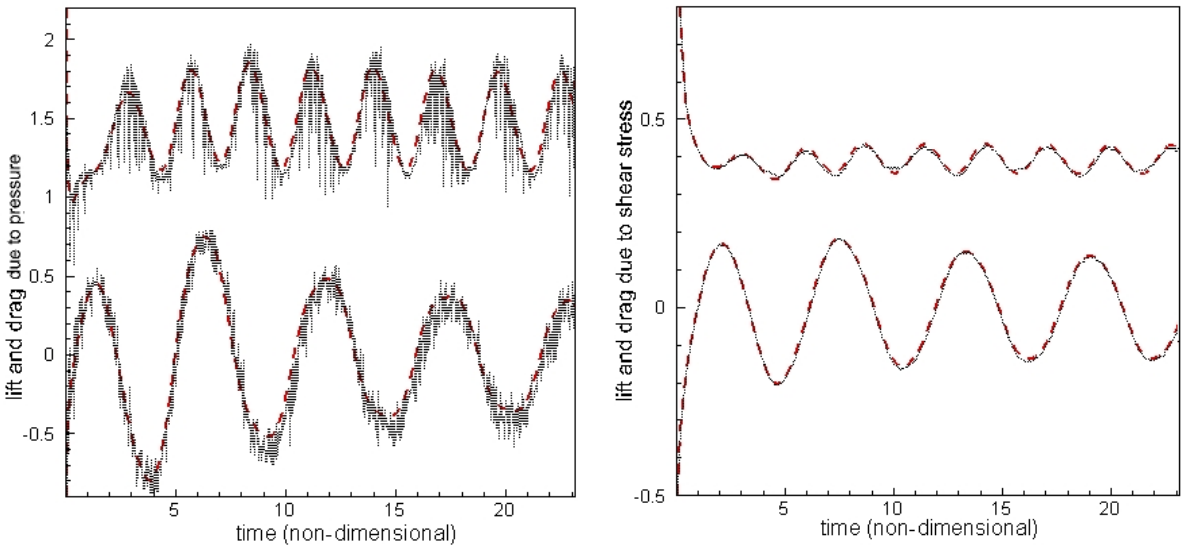

Figure 3: dotted lines, inertia frame of reference; dash lines, moving frame of reference

5. Conclusion

The flow around a circular cylinder with a prescribed motion in cross flow using an IB approach is studied in inertial and non-inertial frames of reference. A comprehensive parametric study is performed to find the optimum mesh size and to define the size of the computational domain. The effect of flow inertial forces is presented in both frames of reference. Also the lift and drag coefficients were compared in detail and source of the noise in the lift and drag coefficients was identified to be due to spurious pressure fluctuations caused by the regular changes of interpolation parameters at the IB.

Acknowledgement

The funding provided by EPSRC (grant number EP/K034243/1) and BP for this research is gratefully acknowledged.

REFERENCES

1. Jaiman RK, Sen S, Gurugubelli PS. A fully implicit combined field scheme for freely vibrating square cylinders with sharp and rounded corners. *Comput Fluids*. 2015;112:1-18.
2. Mittal R, Seshadri V, Udaykumar HS. Flutter, tumble and vortex induced autorotation. *Theor Comput Fluid Dyn*. 2004;17(3):165-170.
3. Madani SH, Wissink J, Bahai H. A comparative study of immersed-boundary interpolation methods for a flow around a stationary cylinder at low reynolds number. . 2013.
4. Peskin CS. Flow patterns around heart valves: A numerical method. *Journal of computational physics*. 1972;10(2):252-271.
5. Kang S, Iaccarino G, Moin P. Accurate immersed-boundary reconstructions for viscous flow simulations. *AIAA J*. 2009;47(7):1750-1760.
6. Li L, Sherwin S, Bearman PW. A moving frame of reference algorithm for fluid/structure interaction of rotating and translating bodies. *Int J Numer Methods Fluids*. 2002;38(2):187-206.
7. Meneghini J, Bearman P. Numerical simulation of high amplitude oscillatory flow about a circular cylinder. *J Fluids Struct*. 1995;9(4):435-455.

Advanced Applications III

Proceedings of the 24th UK Conference of the
Association for Computational Mechanics in Engineering
31 March – 01 April 2016, Cardiff University, Cardiff

Fracture models for hydraulic fracturing stimulation:

Comparison between Numerical method and an EPR-based method

***Reza Naseri-Karim-Vand, Akbar A. Javadi, and Mohammed S. Hussain**

Computational Geomechanics Group, University of Exeter, Exeter, UK

*rn265@exeter.ac.uk

ABSTRACT

In this paper, the behaviour of fractures and their effect on the stress state in a reservoir is investigated as one of the key factors to predict fractures evolution throughout the process. For the numerical modelling, an Extended Finite Element (XFEM Model) has been developed. Also, a model based on an EPR-based (data mining) method has been adopted to predict the fracture behaviour. The data collected from numerical simulations are used to train the EPR-based Models [1].

Keywords: *Fracture model, XFEM, EPR*

1. Introduction

Stress state in geological formations going through hydraulic fracturing is significantly different from stress state in a normal geological formation especially in the zones near a wellbore. The drilling of a well or injecting high pressured fluid into a formation can form a complex stress regime close to a wellbore [6]. In order to study this near wellbore stress state, it is necessary to investigate the evolution of hydraulic fractures in a formation.

This research attempts to make a comparison between a numerical model and a data mining model to capture the fracture behaviour. First, an Extended Finite Element (XFEM) model has been developed to simulate the fracture response and calculate the stress fields and displacement in a fractured medium. The XFEM model is an elastic 2D model under plain strain and quasi-static conditions. Fracturing process is modelled based on linear elastic fracture mechanics (LEFM) theory. XFEM allows discontinuities to be modelled within the finite element mesh and fracture geometry can evolve in any step of the simulation without any need of re-meshing of the finite element mesh [3,4]. Also, a new method is adopted to model the fracture response by applying evolutionary polynomial regression technique. The results obtained by the proposed EPR-based model illustrate very good agreement with the numerical results and available analytical solutions. It is possible to generate more than one model for a specific case using EPR approach. These models could have different accuracy their predictions. More detailed discussion regarding the method can be found in [1].

2. Extended Finite Element Model

Different numerical methods have been proposed by researchers to simulate the crack growth problem such as discrete element methods and boundary element methods. In the past, several strategies have been developed within the finite element framework in order to address the feasibility of numerical simulation. Most effective one is the extended finite element method (XFEM). In this approach, discontinuities such as cracks are permitted to propagate independently of the finite element mesh by allowing the crack to cross the elements. In XFEM, the finite element mesh will be enriched by additional degrees of freedom on the nodes affected by the cracks (figure 1).

XFEM will allow you to preserve the symmetry and sparsity of stiffness matrix, arbitrary crack geometry to the mesh and employing automatic enforcement of continuity [3,4]. The extended finite element (XFEM) approximation to calculate the displacement of a certain point (x) in a domain with a discontinuity is [2]

$$u(x) = u^{FE} + u^{enr} \tag{1}$$

$$u(x) = \sum_{I \epsilon N} N_I(x) u_I + \sum_{I \epsilon N^{cr}} \tilde{N}_I(x)(H(x) - H(x_I))a_I + \sum_{I \epsilon N^{tip}} \tilde{N}_I(x) \sum_{k=1}^{4} (F^k(r, \theta) - F^k(x_I))b_I^k \tag{2}$$

Where x is the position vector; N_I and $\tilde{N}_I$ are the standard and enriched shape functions; N is the number of nodes in the finite element domain; N_{tip} is the number of nodes of elements containing a crack tip; N_{cr} is the number of nodes of elements cut by a crack but do not contain a crack tip.

In XFEM, The nodes of an element cut by a discontinuity are enriched by Heaviside function [2]

$$H(x) = \begin{cases} -1, & x < 0 \\ 1, & x > 0 \end{cases} \tag{3}$$

And the nodes belong to an element containing a crack tip are enriched by the crack tip enrichment functions defined as [2]

$$F^1(r, \theta) = \sqrt{r}\sin\frac{\theta}{2}, F^2(r, \theta) = \sqrt{r}\cos\frac{\theta}{2}, F^3(r, \theta) = \sqrt{r}\sin\frac{\theta}{2}\sin\theta, F^4(r, \theta) = \sqrt{r}\cos\frac{\theta}{2}\sin\theta \tag{4}$$

Where r and θ are local polar coordinate system at the crack tip.

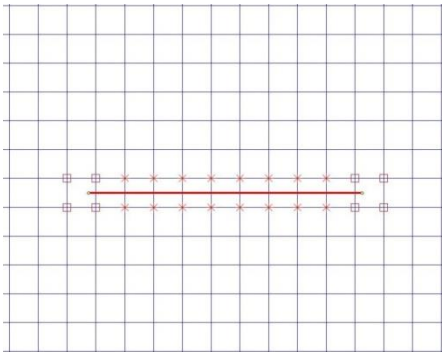

Figure **1.** Enriched finite element mesh. Nodes enriched by tip functions are marked with red squares. Nodes enriched by step function are marked with red crosses.

3. Evolutionary Polynomial Regression Model

Evolutionary polynomial regression (EPR) is a data mining method based on evolutionary algorithms. EPR is designed to search for polynomial structures representing a system. A general EPR formulation can be presented as [1]:

$$y = \sum_{j=1}^{n} F(X, f(X), a_j) + a_0 \tag{5}$$

Where y is the estimated vector of output of the process; a_j is a constant; F is a function constructed by the process; X is the matrix of input variables; f is a function defined by the user; and n is the number of terms of the target expression. In EPR algorithm, the evolutionary starts with computing a constant mean of output values. The number of parameters in the model equations will increase by the raise in the number of evolutions in the process. The accuracy of each EPR model can be determined based on coefficient of determination (COD) as the fitness function [1]:

$$\mathrm{COD} = 1 - \frac{\sum_{\mathrm{N}}(\mathrm{Y_a} - \mathrm{Y_p})^2}{\sum_{\mathrm{N}}(\mathrm{Y_a} - \frac{1}{\mathrm{N}}\sum_{\mathrm{N}}\mathrm{Y_a})^2} \tag{6}$$

Where Y_a is the real output value; Y_p is the output predicted by EPR model and N is the number of data points used to determine the COD. Any EPR-model which does not reach an adequate value of fitness or other termination conditions, maximum number of generation and maximum number of terms, needs to go through another evolution loop to obtain a new model [5].

4. Results

A number of conventional fracture mechanics problems are simulated by XFEM. Figure 2 shows a tensile plate with an edge crack. The analytical solution for the mode I stress intensity factor for this example is

$$K_I = [1.12 - 0.23(c) + 10.56(c)^2 - 21.74(c)^3 + 30.42(c)^4]P\sqrt{\pi a} \tag{7}$$

Where P is the applied tensile stress; $2a$ is the crack length and c is the ratio between the crack length and width of the plate. The following range of inputs are used in the XFEM simulation, $250 \leq P \leq 2500\ psi$ with increment of $\Delta P = 10\ psi$ which will provide 226 unique values for the stress value. Also, $0.05 \leq c \leq 0.45$ and increment of $\Delta c = 0.025$ gives 17 different values. The EPR-based models are computed based on the results determined by XFEM. The size of the dataset used in the EPR-based analysis is 3842. About 85% of the data is used to train the EPR model and 15% for validation of the models.

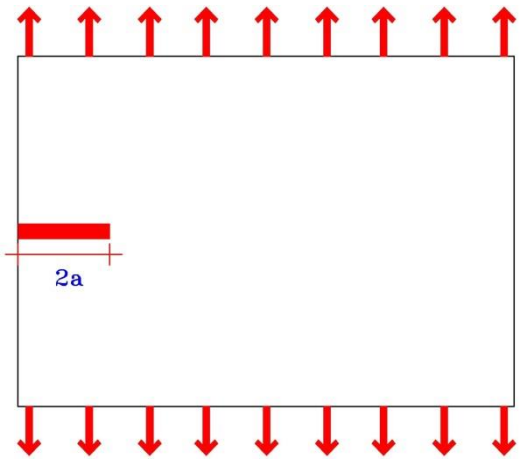

Figure 2. Tensile Plate with an edge crack.

Table 1 Shows 6 models produced by EPR. The EPR model with higher COD and less complexity is the best choice [5]. Stress intensity factor (K) values predicted by best EPR model show a good agreement with the numerical results and exact analytical solutions (see Figure 3).

Conclusion

Fracture models have been developed using evolutionary polynomial regression method. Models predict stress intensity factor values at crack tips. The results demonstrate that EPR models can predict stress intensity factor values effectively and accurately. EPR-based fracture models can be implemented into numerical calculations to decrease the computational time and effort.

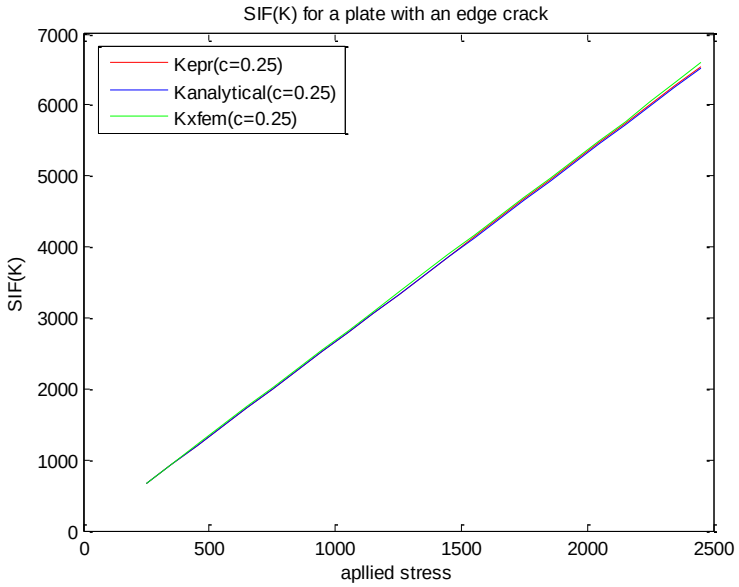

Figure 3. Stress intensity factor (K) vs applied stress

Table 1: EPR expressions

EPR-based equation	COD
$K = 114.72P^{0.5}$	60.91
$K = 5.598Pc^2 + 179.9$	96.31
$K = 234.06P^{0.5}c^{0.5}$	80.64
$K = 1.9758P + 11.067Pc^2$	99.96
$K = 400.53c^3 + 1.9776P + 10.96Pc^2$	99.96
$K = 1.8862P + 2.06Pc + 16.08Pc^3$	99.96

References

[1] Giustolisi O, Savic D. A symbolic data-driven technique based on evolutionary polynomial regression. J Hydroinform 2006;8(3):207–22.

[2] Mohammadi, S. (2008). Extended finite element method for fracture analysis of structure. Blackwell Publishing, UK.

[3] N. Moës, J. Dolbow and T. Belytschko. A finite element method for crack growth without remeshing. Int. J. Numer. Meth. Engng., Vol. 46, 135–150, 1999.

[4] T. P. Fries. The extended/generalized finite element method: An overview of the method and its applications. Int. J. Numer. Meth. Engng., Vol. 84, 253–304, 2010.

[5] Rezania, M., Javadi, A.A. & Giustolisi, O. (2008), *"An Evolutionary-Based Data Mining Technique for Assessment of Civil Engineering Systems",* Journal of Engineering Computations, 25(6), pp 500–517.

[6] Valkó, P. and M.J. Economides, 1995, Hydraulic Fracture Mechanics, Wiley.

Proceedings of the 24th UK Conference of the
Association for Computational Mechanics in Engineering
31 March – 01 April 2016, Cardiff University, Cardiff

Mechanical characterisation and strain rate sensitivity of rubber shockpad in 3G artificial turf

Moura Mehravar [1]*, Paul Fleming[2], David Cole[1], Steph Forrester[1]

[1]Wolfson School of Mechanical, Manufacturing and Electrical Engineering, Loughborough University, UK
[2]School of Civil and Building Engineering, Loughborough University, UK

*M.Mehravar@lboro.ac.uk

ABSTRACT

Artificial turf systems are increasingly prolific, and are typically comprised of multi-components. Their responses to interactions with users and equipment can be relatively complex under different loading conditions as they tend to be polymeric and elastomeric and hence can exhibit non-linear and strain rate dependent behaviour. To further study and better understand the behaviour of these systems, the development of a numerical model to accurately predict individual layers' behaviour as well as the overall system's response under different loading conditions is necessary. Such a model can be used to better optimise surface design such as material choices and layer thickness, also possibly reducing construction costs. The purpose of this study was to model the mechanical behaviour of the rubber shockpad layer used in 3G artificial turfs using finite element (FE) analyses. Shockpad layers in artificial turf play a vital role in the shock absorption and ball interactions, and affect user safety. The rubber shockpad used in this study was an elastic prefabricated mat comprised of recycled rubber shreds approximately 2 to 8 mm in size bonded with polyurethane.

A series of 3D finite element dynamic analyses were carried out using ABAQUS applying compressive cyclic loading to simulate the shockpad behaviour under different loading frequencies. The frequencies were based on biomechanical data for an athlete walking, running and sprinting. Arruda-Boyce hyperelastic constitutive model was employed to best describe the stress-strain response of the rubber shockpad under compressive loading. A series of uniaxial compression tests were conducted and the results were employed to characterise the mechanical behaviour of the material. The best Arruda-Boyce's coefficients, for different strain rates were obtained using initial estimation (IEM) method and trial-and-error approach. The FE results showed the best-fit hyperelastic material model which can describe and predict the material behaviour under various strain rates. Finally, using finite element results a series of models were proposed to accurately predict the stress-strain behaviour of the material in different loading frequencies relevant to athlete.

Keywords: *Rubber shockpad, Finite element modelling, Hyperelastic, ABAQUS, Mechanical Properties.*

1. Introduction

Third generation (3G) artificial turf was developed in the late 1990s, and designed to better simulate natural turf [7]. Most of 3G turf surfaces have a similar structure comprising the key components of an artificial carpet, a shockpad layer and an engineered aggregate foundation (Fig 1). Shockpad layer creates desired playing characteristics for the particular sport in addition to maintain the initial qualities of the artificial pitches during their service life. There are three types of shockpads on the market: integral shockpad, in-situ and prefabricated [6]. Cast in-situ shockpads are constructed from recycled rubber particles bonded together using polyurethane binder. Design and mechanical features of the prefabricated shockpads are very similar to the in-situ type; however, the prefabricated shockpads are manufactured in factories based on specific requirements. Their significant advantage is the uniformity of their mechanical properties and thickness as a result of the controlled construction environment. The principal force applied to a shockpad layer in artificial turf systems is mainly vertically compressive. Physical and mechanical behaviour of rubber-like material when subjected to compressive loading have been investigated by different researchers using experimental, analytical and numerical studies [10]. Thomson et al. [8] attempted to create a finite element model (FEM) of experimentally measured quasi-static response of a particular treadmill surface made of flexible rubber mat under compressive loading using ABAQUS. Song et al. [2] assessed the strain rate dependency of ethylene–propylene–diene monomer (EPDM) rubber for a range of 0.0015 to 4700 s^{-1} and concluded rubber becomes increasingly non-linear by increasing strain rate. Andena et al.

[5] studied the possibility of predicting the force reduction (FR) and shock absorbing capability of running tracks using ABAQUS software. However, no studies have looked at different components of 3G artificial turfs in particular their behaviour under complex dynamic loading conditions.
The purpose of the present study was to investigate the mechanical characterisation and strain rate dependency of rubber shockpad layer used in third generation artificial turf using finite element method. To that end, the mechanical response of the material under various loading frequency were characterised by a series of uniaxial compression tests and then Arruda-Boyce's hyperelastic model which is already implemented into ABAQUS was selected to fit the experiments. Arruda-Boyce's parameters were estimated firstly using an initial estimation method (IEM) and subsequently improved by trial-and-error approach. Finally, based on the finite element analyses, a series of equations were proposed combining the Arruda-Boyce's material model parameters with a new parameter to consider strain rate dependency of the material behaviour for various loading frequencies ranging between 0.9 to 10 Hz.

2. Material characterisation and compression test

The shockpad used in this study was an elastic premanufactured mat made from rubber aggregates bonded with polyurethane. The rubber particles were graded ranging between 2 to 8 mm, and the average density of the rubber shockpad was 557 kg/m^3. The uniaxial compression behaviour of the material under different cyclic loading frequencies (0.9, 3.3 Hz and 10 Hz) relevant to athlete walking, running and sprinting was measured using electropuls instron compression machine. The peak vertical impact force for all dynamic cyclic loadings was controlled within the range of 1800N±15%. This load was applied by a cicular loading feet (50 mm diameter) to simulate a shod adult's heel [10].

3. Model geometry and mesh

To achieve precise results, three-dimensional finite element analyses of above experiments were carried out using ABAQUS. Taking advantage of the symmetrical nature of the problem, only a quarter of the entire system was modelled. Figure 2 represents the typical finite element mesh for the rubber shockpad layer, used in this study. A number of different mesh densities in which element sizes around and under the loading area are refined were performed to obtain accurate results in a reasonable computational time. The mesh is extended 5B (B=50mm is the diameter of loading area) from the layer centre line. Boundary conditions were defined according to the adopted experimental condition. In order to model the rubber, first-order, eight-node linear brick, reduced integration with hourglass control element (C3D8R) was employed.

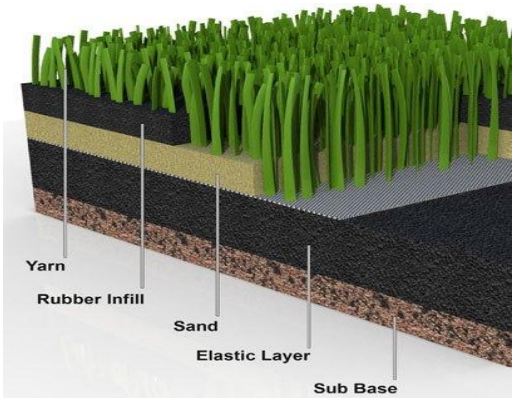

Figure 1: Schematic of a 3G artificial turf system [11]

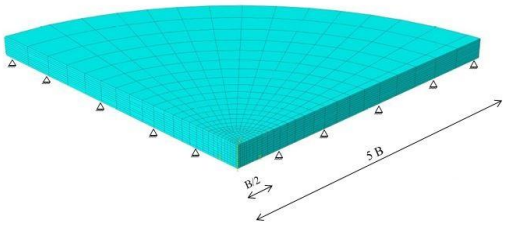

Figure 2: finite element mesh and boundary conditions

4. Constitutive hyperelastic modelling

Generally, rubber like material can exhibit instantaneous elastic response up to large strains without permanent set, and are defined by stored energy function as hyperelastic material. In this paper, the 8-chain Arruda-Boyce hyperelastic constitutive model including compressibility has been selected to simulate rubber shockpad behaviour under various dynamic loading conditions. Arruda-Boyce

constitutive model has been preferred because it has been shown to accurately capture the large strain equilibrium response of several types of elastomers [4], and it is the most successful expression of a strain energy function using the non-Gaussian method of the statistical molecular theory [3]. The form of Arruda-Boyce strain energy potential in fifth order approximation is expressed as following [9]:

$$W = \mu \sum_{i=1}^{5} \frac{Ci}{\lambda_m^{2i-2}} (I_1^{'i} - 3^i) + \frac{1}{D} \left(\frac{J^2 - 1}{2} - \ln J \right) \quad (1)$$

where I_1 and J are the first deviatoric strain invariant and the elastic volume ratio respectively; and

$$\mu = \mu_0 \left(1 + \frac{3}{5\lambda_m^2} + \frac{99}{175\lambda_m^4} + \frac{513}{875\lambda_m^6} + \frac{42039}{67375\lambda_m^8}\right)^{-1} \quad (2)$$

$$C_1 = \frac{1}{2}, C_2 = \frac{1}{20}, C_3 = \frac{11}{1050}, C_4 = \frac{19}{7000}, C_5 = \frac{519}{673750} \qquad D = \frac{2}{k_0}$$

in this formulation, μ_0 and k_0 are the initial shear and bulk modulus of the material, and λ_m is the locking stretch.

5. Material parameters determination

The difficulty of hyperelastic material models is determination of the coefficients in their functions which should be determined via experiments. On the other hand, hyperelastic models should be combined with a rate dependent model to demonstrate the strain rate dependency trait of rubber, since the experimental results revealed strain rate dependency behaviour of the material even at low strains (Fig 3). The large strain uniaxial compression test results were employed to estimate an initial value for the Young's modulus (E_0) as well as the locking stretch (λ_m) of the material for each frequency. Poisson's ratio of the material is also required for initial estimation of D and μ_0 and it cannot be determined from a uniaxial compression test. Using the proposed value for initial Poisson's ratio of rubber particles approximately 2 to 10 mm in size, ρ=585kg/m^3 and porosity, i.e. n = 49%, an initial Poisson's ratio about 0.3 was adopted [1]. This initial estimation method (IEM) for determining Arruda-Boyce's parameters prevents extra effort to find appropriate material parameters to be implemented in ABAQUS. The linear elastic part (initial slope) of the stress-strain curve (Fig 3) can determine approximate value of initial Young's modulus (E_0), and initial approximation of λ_m can be obtained from the following formulation [4]:

$$\lambda_m = \sqrt{\frac{1}{3}\left(\lambda_l^2 + \frac{2}{\lambda_l}\right)} \quad (3)$$

in which λ_l is the stretch when the stress increases without any further significant changes in the strain (Fig 3).

6. Finite element analyses results

Firstly, a series of dynamic FE models were created in which the material parameters were calculated and implemented into ABAQUS based on IEM predictions. All finite element simulations were conducted by applying compressive loads on the same loading area as in the experiments. The finite element results based on IEM's predictions for Arruda-Boyce's coefficients showed an acceptable prediction for stress-strain behaviour, however in order to achieve the best agreement between the FEA results and experimental data, trial and error approach was utilised to improve the material parameters as suggested. The results of numerical simulations and experimental data are presented in Fig 3. It should be noted that the excellent agreement between experimental and FE results simply confirms the choice of a suitable model, since the experimental results were used to define the input parameters to the FE analysis. Using the obtained values for Arruda-Boyce's coefficients (μ, λm and D) a series of equations are proposed to take into account the strain rate dependency of material which is an essential characteristic of the material behaviour. The proposed equations cover the 0.9 – 10 Hz frequency range.

$$\mu = 107.25 \times 10^3 f^{0.295} \qquad D = 3 \times 10^{-9} f^2 - 9 \times 10^{-8} f + 2.7 \times 10^{-6} \qquad \lambda_m = 1.0152 f^{0.0587} \quad (4)$$

In which f is frequency, and the unit of μ and D are Pa(N/m^2) and Pa^{-1} respectively.

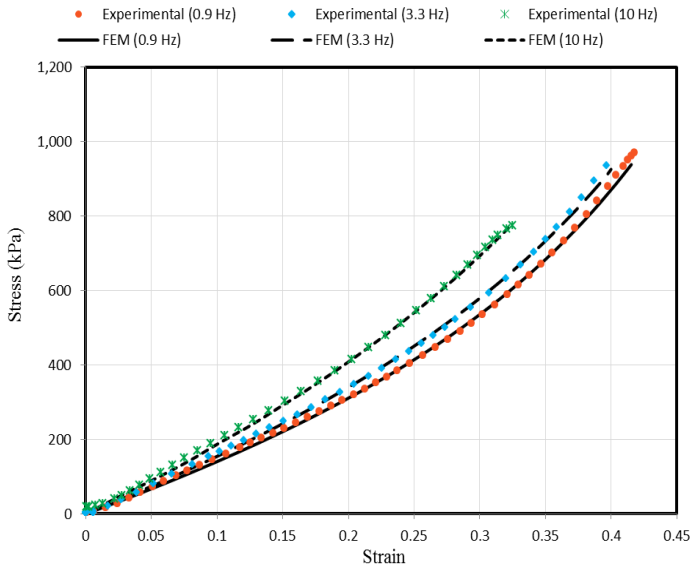

Figure 3: Comparison between FE results and experimental data for 0.9, 3.3 and 10 Hz loading frequency

7. Summary and conclusions

In this paper a series of finite element models are developed to study the behaviour of rubber shockpad layer under dynamic compression loading. A hyperelastic material model, i.e. Arruda-Boyce was adapted to simulate the constitutive behaviour of the shockpad. The results of the FE simulations were used to propose a model to predict the strain rate dependent material behaviour. This model combines the existing Arruda-Boyce's parameters with an additional parameter, i.e. load-frequency, to describe strain rate sensitivity of the material under different loading rate. The proposed new model, once implemented in FE, will enhance the accuracy and capability of the future FE analyses hence improving our understanding and design of such materials.

References

[1] A. Yang, R. Lohnes and H. Kjartanson, Mechanical Properties of Shredded Tires, Geotechnical Testing Journal, vol. 25, no. 1, 2002.

[2] B. Song, W. Chen and M. Cheng, Novel Model for Uniaxial Strain-Rate-Dependant Stress-strain Behaviour of Ethylene-Propylene-Diene Monomer Rubber in Compression or Tension, *Journal of Applied Polymer Science*, vol. 92, pp. 1553-1558, 2004.

[3] G. Montella, A. Calabrese and G. Serino, Mechanical characterization of a Tire Derived Material: Experiments, hyperelastic modelling and numerical validation, *Construction and Building Materials*, pp. 336-347, 2014.

[4] J. S. Bergstrom, Determination of Material Parameters for 8-Chain Model for Use with ABAQUS, LS-DYNA and ANSYS.

[5] L. Andena, F. Briatico-Vangosa, E. Cazzoni, A. Ciancio, S. Mariani and A. Pavan, Modelling of shock absorption in athletics track surfaces, *Sports Eng*, pp. 1-10, 2015.

[6] L. J. Anderson, Elastomeric Shockpads for Outdoor Synthetic Sports Pitches, PhD thesis, Loughborough University, Loughborough, 2007.

[7] P. Fleming, Artificial turf systems for sport surfaces: current knowledge and research needs, 2011.

[8] R. D. Thomson, A. E. Brikbeck and T. D. Lucas, "Hyperelastic modelling of nonlinear running surfaces," vol. 4, 2001.

[9] Simulia, Dassault Systems 2012, Abaqus analysis user's manual.

[10] X. Wang, Advanced measurement for sports surface system behaviour under mechanical and player loading, PhD thesis, Loughborough University, Loughborough, 2013.

[11] http://blog.sidelinesportsdoc.com

Proceedings of the 24th UK Conference of the
Association for Computational Mechanics in Engineering
31 March – 01 April 2016, Cardiff University, Cardiff

MODELLING SCHEME FOR RAILWAY VEHICLE/TRACK/GROUND DYNAMIC INTERACTION IN THE TIME DOMAIN

J. Y. Shih[1*], D.J. Thompson[1], A. Zervos[2]

[1]Institute of Sound and Vibration Research, Faculty of Engineering and the Environment, University of Southampton, Southampton, SO17 1BJ, UK.
[2]Infrastructure Research Group, Faculty of Engineering and the Environment, University of Southampton, Southampton, SO17 1BJ, UK.

*js10e12@soton.ac.uk

ABSTRACT

Modelling of vehicle/track/ground dynamic interaction is an important issue for railway design. Better understanding of how the moving dynamic loads are distributed through the track components to the ground can be derived from these numerical results to improve the stability of the moving train and decrease the cost of the maintenance. Nonlinear models of the ground may be required due to the large displacements induced by heavier and/or high-speed trains. The aim of this research is to develop a general modelling approach for predicting the dynamic behaviour for a variety of situations.
A three-dimensional vehicle/track/ground approach in the time domain is presented. The finite element method is used to model the track/ground vibration. The equations of motion of a multi-body vehicle are implemented to couple with the ground/track system. An alternative approach to the commonly used infinite elements is proposed for modelling the far-field, based on the use of mass-proportional damping to suppress the reflections from model edges. Improved results are shown and better efficiency can be found compared to the results from models with infinite elements. Furthermore, two different geometries for the ground model, a hemispherical and a cuboid one, are discussed. The issue of transients developed by the moving load is discussed and it is shown that long models are required for load speeds close to the wavespeed in the ground to allow the results to achieve steady state. Finally, the results are benchmarked against the results from a wavenumber FE/BE model.

Keywords: *Vehicle/track interaction; Finite Element (FE); viscous damping; ground vibration; track dynamics*

1. Introduction

To achieve better understanding of the ground-borne vibration induced by high-speed trains, numerical simulation has become very important, allowing investigations of the dynamic behaviour of the track/ground system when the train is passing. Assessment of critical speed, ballast and soil degradation, and environmental impact all rely on results from such simulations. To prevent spurious reflections from the domain boundaries, a semi-infinite domain model is required for the soil. Several numerical methods have been developed recently that incorporate absorption at the boundary. Boundary elements (BE) directly include the infinite medium and these can be combined with finite elements (FE) either in a fully three-dimensional FE/BE method [1], or in a so-called 2.5D FE/BE method [2]-[5]. However, these methods mostly operate in the frequency domain and consequently cannot account for the nonlinear behaviour that may occur due to heavy axle loads or higher train speeds. Therefore, an alternative scheme has become common for modelling ground vibration induced by moving loads in which the FE domain is bounded by infinite elements [6]–[9]. Infinite elements form a typical local boundary method that uses viscous dashpots to absorb the incident waves at the boundary. They are defined based on the following equation

$$\begin{cases} c_{Ni} = \rho c_p \\ c_{Ti} = \rho c_s \end{cases} \tag{1}$$

where c_{Ni} and c_{Ti} are the damping values for the normal and tangential direction, respectively. ρ is the material density and c_p, c_s are the wave speeds of the P-wave (longitudinal wave) and the S-wave (shear wave). However, infinite element method does not generally have perfect absorption at the boundary. The absorption efficiency of the infinite elements relies on the domain geometry and the incident wave field. Usually they should be located in the far field and orientated perpendicular to the incident waves. The aim of the present study is to investigate the limitations of the use of infinite elements and to determine the optimum modelling approach for track/ground vibration induced by moving dynamic loads. Comparisons are made with a 2.5D FE/BE approach [5].

2. Numerical models

The purpose of the study is to investigate critical velocity effects, when the load speed approaches the speed of waves in the ground. First, however, the model is considered for a stationary harmonic load.
Two different geometries for the ground model are used for modelling the soil: a hemispherical one (Fig. 1(a)) and a cuboid one (Fig. 1(b)). Infinite elements are applied around the boundary of the hemispherical model. Even though a hemispherical model can show better absorption efficiency of outgoing waves, incorrect artificial displacements of the whole model occur due to the fact that the infinite elements are statically unconstrained [10]. The cuboid model therefore has a fixed bottom to avoid this incorrect displacement. Fixed boundaries are also used at the ends of the model while along the sides infinite elements are considered as an alternative to fixed boundaries. In all cases symmetry of the model is used along the track centreline. Furthermore, when the load speed approaches the critical speed, a relatively long model is required to allow the results to achieve steady state, especially for homogeneous soil models [10]. As a result, the cuboid model is preferred for the moving load problem as the required geometry can be generated relatively easily.
A viscous damping model, based on Rayleigh damping, is used here for the calculations with the FE model. The Rayleigh damping is based on two parameters α and β, which allow the damping matrix **C** to be determined from the mass and stiffness matrices, **M** and **K**:

$$\mathbf{C} = \alpha\mathbf{M} + \beta\mathbf{K} \tag{2}$$

This allows the equivalent loss factor η or damping ratio ξ to be obtained as a function of frequency:

$$\frac{\eta}{2} = \xi = \frac{\alpha}{2\omega} + \frac{\beta\omega}{2} \tag{3}$$

where ω is the circular frequency at which the loss factor η applies. For a plane harmonic wave at circular frequency ω propagating in an elastic medium at a constant wave speed c, the wavenumber k is given by $k = \omega/c$. In the presence of damping with a damping ratio ξ the wavenumber becomes complex with the form $\bar{k} = k(1-i\xi)$. The imaginary part is related to the decay with distance which can be expressed in dB/m as

$$D = -20\log_{10}\left(\left|e^{i\bar{k}}\right|\right) = -8.69\,\mathrm{Im}(\bar{k}) = 8.69k\xi \tag{4}$$

From Eq. (3), the decay with distance for stiffness-proportional damping is proportional to the square of the frequency, $D = 4.34\omega^2\beta / c$. So, for example, for β = 0.000636 (equivalent to η = 0.05 at 12.5 Hz) the decay with distance is around 0.002 dB/m at 1 Hz rising to 5 dB/m at 50 Hz. For the case of a constant loss factor $\eta = 2\xi$, the decay with distance is found to be $D = 4.34\omega\eta / c$ which increases in proportion to the frequency. For mass-proportional damping D is independent of frequency, $D = 4.34\alpha / c$. Thus, e.g. for α = 0.98, D is 0.075 dB/m for all frequencies. As a result it can be expected that mass-proportional damping will be equally effective at suppressing reflections from the domain boundaries at all frequencies.
Fig. 2 shows the point receptance of the rail due to a harmonic load for the various different ground models shown above. The soil is a homogeneous half-space with shear wave speed 60 m/s. The hemispherical domain has a radius 40 m; the cuboid models have a length of 80 m and width of 40 m for the case without the infinite elements and 20 m width for the one with infinite elements. In each

case the force is applied at the centre of the rail. Two different viscous damping models are used: stiffness-proportional damping with α=0 and β=0.000636 and mass-proportional damping with α=0.98 and β=0. The results from a 2.5D FE/BE model are shown for comparison, in this case with constant loss factor η = 0.05. This shows that the hemispherical model with infinite elements gives much better results than the cuboid model particularly at low frequency. Furthermore, the results with mass-proportional damping agree better than the results with stiffness-proportional damping. Even though the results from the cuboid model with infinite elements show less fluctuation than those without the infinite elements, some small oscillations still can be found. The cuboid model without infinite elements is preferred as, although the model with infinite elements gives improved results, it is much less efficient for the moving load problem. For example, for a load speed of 57m/s, the 40 m wide cuboid model requires 7.8 hr calculation time compared with 19 hr for the 20 m wide model with infinite elements and 12.5 hr for the 40 m radius hemispherical model.

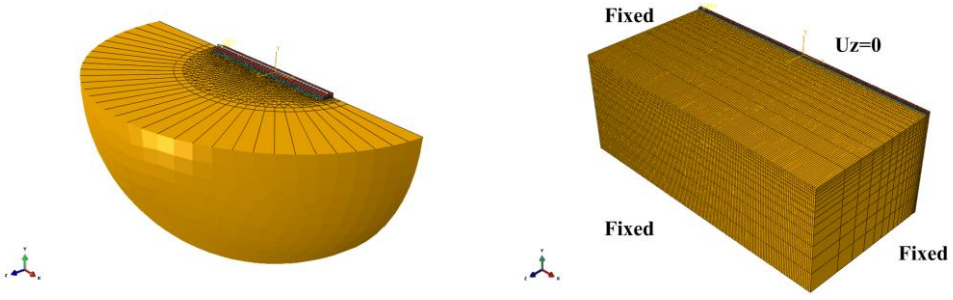

(a) (b)

Figure 1. Ground model; (a) hemispherical ground model; (b) cuboid ground model

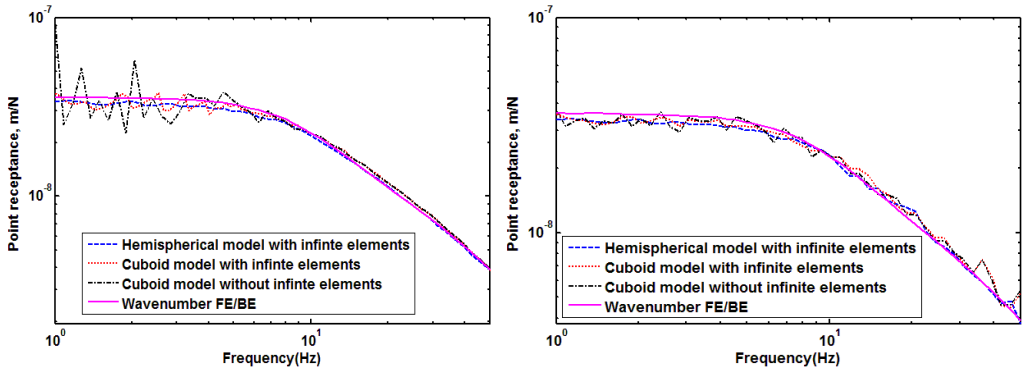

(a) (b)

Figure 2. Point receptance on the rail for homogeneous half-space; (a) stiffness-proportional damping; (b) mass-proportional damping

Finally, results are shown from a time-domain analysis for various speeds. Fig. 3 shows results for the homogeneous half-space (shear wave speed 60 m/s) whereas Fig. 4 shows results for a layered half-space with a 2 m deep upper layer of the same soft soil overlying a stiffer soil with a shear wave speed of 120 m/s. Good agreement can be seen with the results from the wavenumber FE/BE model [5], except close to the critical speed 57 m/s (equal to the Rayleigh wave speed in the ground) as shown in Fig. 3a. On the other hand, for the results from the layered half-space good agreement is seen even close to the critical speed (which here is around 85 m/s).

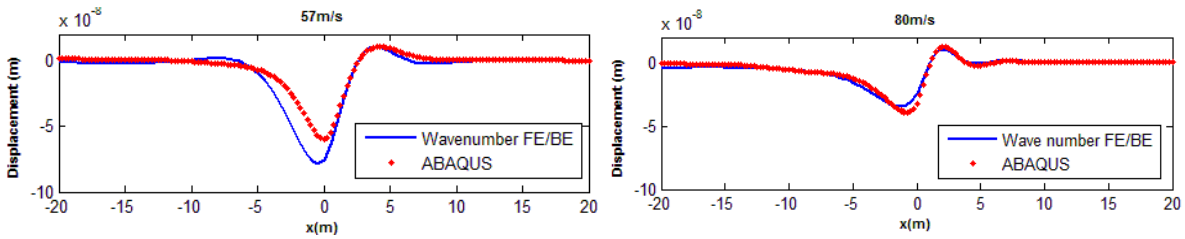

Figure 3. Comparison between the results from FE model and the results from wavenumber FE/BE for homogeneous half-space; (a) V=57 m/s; (b) V=80 m/s

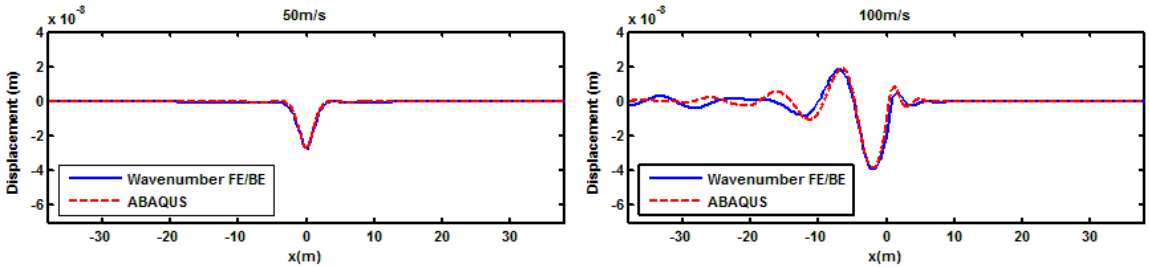

Figure 4. Comparison between the results from FE model and the results from wavenumber FE/BE for layered half-space; (a) V=50 m/s; (b) V=100 m/s

3. Conclusion

An investigation has been presented of the use of the time-domain finite element approach to represent a load moving along a railway track on a flexible ground. The results from a hemispherical model with infinite elements show better absorption efficiency than a cuboid model. However, incorrect displacements are found due to the infinite elements. A cuboid model with fixed boundaries with mass-proportional damping is recommended for modelling the moving load problem due to its relatively accuracy and efficiency. Although the results shown are for linear soil models, the time-domain approach can be readily extended to consider nonlinear soil models.

Acknowledgements

The work described has been supported by the EPSRC under the programme grant EP/H044949/1, 'Railway Track for the 21st Century'.

References

[1] P. Galvín, A. Romero, and J. Domínguez, "Fully three-dimensional analysis of high-speed train–track–soil-structure dynamic interaction," *J. Sound Vib.*, vol. 329, no. 24, pp. 5147–5163, 2010.

[2] P. A. Costa, R. Calçada, and A. S. Cardoso, "Track–ground vibrations induced by railway traffic: In-situ measurements and validation of a 2.5D FEM-BEM model," *Soil Dyn. Earthq. Eng.*, vol. 32, no. 1, pp. 111–128, 2012.

[3] S. François, M. Schevenels, P. Galvín, G. Lombaert, and G. Degrande, "A 2.5D coupled FE–BE methodology for the dynamic interaction between longitudinally invariant structures and a layered halfspace," *Comput. Methods Appl. Mech. Eng.*, vol. 199, no. 23–24, pp. 1536–1548, 2010.

[4] P. Galvín, S. François, M. Schevenels, E. Bongini, G. Degrande, and G. Lombaert, "A 2.5D coupled FE-BE model for the prediction of railway induced vibrations," *Soil Dyn. Earthq. Eng.*, vol. 30, no. 12, pp. 1500–1512, 2010.

[5] X. Sheng, C. J. C. Jones, and D. J. Thompson, "Modelling ground vibration from railways using wavenumber finite- and boundary-element methods," *Proc. R. Soc. A Math. Phys. Eng. Sci.*, vol. 461, no. 2059, pp. 2043–2070, Jul. 2005.

[6] G. Kouroussis, O. Verlinden, and C. Conti, "Ground propagation of vibrations from railway vehicles using a finite/infinite-element model of the soil," *Proc. Inst. Mech. Eng. Part F J. Rail Rapid Transit*, vol. 223, no. 4, pp. 405–413, 2009.

[7] D. Connolly, A. Giannopoulos, and M. C. Forde, "Numerical modelling of ground borne vibrations from high speed rail lines on embankments," *Soil Dyn. Earthq. Eng.*, vol. 46, pp. 13–19, Mar. 2013.

[8] A. El Kacimi, P. K. Woodward, O. Laghrouche, and G. Medero, "Time domain 3D finite element modelling of train-induced vibration at high speed," *Comput. Struct.*, vol. 118, pp. 66–73, Mar. 2013.

[9] L. Hall, "Simulations and analyses of train-induced ground vibrations in finite element models," *Soil Dyn. Earthq. Eng.*, vol. 23, no. 5, pp. 403–413, Jul. 2003.

[10] J. Shih, D. Thompson, and A. Zervos, "Assessment of track-ground coupled vibration induced by high-speed trains," in *The 21st International Congress on Sound and Vibration*, 2014, no. July, pp. 13–17.

Proceedings of the 24th UK Conference of the
Association for Computational Mechanics in Engineering
31 March – 01 April 2016, Cardiff University, Cardiff

Rock Mass Quality Determination in Blasting at Jalal-Abad Iron Ore Mine

M. Nikzad[1], A. Wetherelt[2], A. B. Yasrebi[2, 3], A. Javadi[3], *P. Afzal[2, 4], N. Karim[5]

[1] Young Researchers Club, South Tehran Branch, Islamic Azad University, Tehran, Iran
[2] Camborne School of Mines, University of Exeter, Penryn, UK
[3] Computational Geomechanics Group, University of Exeter, Exeter, UK
[4] Department of Mining Engineering, South Tehran Branch, Islamic Azad University, Tehran, Iran
[5] Senior Mining Engineer, Kavoshgaran Consulting Engineers (KCE), Tehran, Iran

* peymanafzal@yahoo.com

ABSTRACT

Blasting is believed to be one of the most important operations in mining extraction. One of the main parameters which has to be considered in blasting is rock mass quality. Dynamic strengths of rocks, their spacing and orientation of joints planes and cracks as well as lithology and thickness of bedding are thought to be the most influential factors in blast design. A recognised method to combine these geological characteristics within blast design is Blasting Index (BI) which has subsequently been computed for the Jalal-Abad iron mine in Iran. Consequently, blasting patterns were designed using the following four principal methods, namely; Ash, Thumb, Anderson and Konya. Following a comparative analysis, Konya was found to provide the best correlation with regard to BI. As a result of this study it can be shown that around 30% and 70% of the specific charge and drilling metres respectively can be reduced. This can be shown to translate into reducing the drilling and blasting costs by approximately $50 million over the life of the mining operation.

Keywords: *Blasting; rock mass quality; Specific charge; Jalal-Abad iron ore mine*

1. Introduction

The main purpose of drilling and blasting is to break and prepare the fragmented rocks for transportation and crushing purposes. The degree of rock fragmentation plays an important role in order to control and minimise the total production cost [1, 4]. The fragments produced by blasting should be small enough to be easily loaded and transported by transportation equipment. Geological characteristics and rock mechanics properties are fundamental keys in blast design. In recent years, works in the field of rock mass classification and different rock mass strength criterions have been developed. The problem of characterising a rock mass for blasting purposes is so complicated that analytical solutions are not possible, but Lilly (1986) developed a new approach called Blasting Index (BI) which considers joint spacing and orientation, rock density and hardness [3, 7]. The results of this paper show that the Konya was found to provide the best correlation with respect to the calculations for BI in the Jalal-Abad iron mine based on nearly fifty studied blasts.

2. Jalal-Abad iron ore mine

The Jalal-Abad iron mine situated approximately 36 km NW of Zarand, with 200 Mt iron ore resources with an average grade of 38.5% is one of the important iron deposits in Kerman Province, SE Iran [5, 6]. The deposit occurred in the intersection of Urumia-Dokhtar magmatic zone and Sanandaj-Sirjan structural metamorphic zone. There are gabbro, diorite and diabasic rocks as mass and dykes. Moreover, sedimentary rocks consisting of dolomitic limestone, siltstones and sandy-siltstones are present in the area. Main ores include magnetite and hematite which were altered and formed to goethite and limonite in the central and NW parts of the area. In addition, there are sulfidic ore minerals especially pyrite and chalcopyrite [5].
There is at least one blast every day carried out in the studied mine. Blasting parameters have been summarised in Table 1. Several problems have arisen during the investigation such as back break, high explosives and ground vibration. In addition, there are some boulders after the blasts. ANFO is

mixed with Pentaerythritol tetranitrate (PETN) and filled as column charge. Each hole contains about 0 to 12 Kg of high explosive and is charged with a primed cartridge at the bottom with Shock-tube for detonation [6].

Table 1: Blasting parameters

Parameter	Value	Unit
Bench height	12	m
Sub-drilling	1.5	m
Spacing	4 to 4.5	m
Burden	3 to 3.5	m
Weight of ANFO per hole	100 to 150	Kg
Blast hole diameter	165	mm
Stemming length	6.5 to 8.5	m

Subsequently, specific charge and specific drilling are calculated which vary between 0.7 to 1 kg/m^3 and 0.065 to 0.09 m/m^3, respectively.

3. Blasting Index

A blasting index (BI) developed by Lilly in (1986), correlates powder factors for blasting in mines. The blasting index is based on strength, structure, density and hardness of the rock. Equation. 1 describes the BI, Equation. 2 shows the proper specific charge and the input parameters and their ratings are given in Table 2.

$$BI = 0.5(RMD + JPS + JPO + SGI + HD) \quad \text{Equation. 1}$$

$$Specific-charge(Kg/ton) = 0.004 \times BI \quad \text{Equation. 2}$$

Table 2: Description of BI parameters [3, 7]

Geomechanical parameters	Rating
Rock Mass Description (RMD)	
Powdery/friable	10
Blocky	20
Totally massive	50
Joint Plane Spacing (JPS)	
Close (< 0.1m)	10
Intermediate (0.1 to 1m)	20
Wide (> 1m)	50
Joint Plane Orientation (JPO)	
Horizontal	10
Dip out of face	20
Strike out of face	30
Dip into face	40
Specific Gravity Influence (SGI)	SGI=25 SG – 50 (SG in tons/cu metre)
Hardness, Mohs scale, (HD)	1-10

More than 35 faces in the mine were surveyed and determined with respect to the above-mentioned parameters in table 2 in order to calculate BIs. BI varies from 50 to 80 however; BI equal to 60 has more frequency among the calculated values. As the extraction goes further and the mine becomes deeper, possibly, BI trends 70 in the future [2, 6]. Based on Equation. 2, proper specific charge according to Lilly model is about 0.7 Kg/m^3.

4. Blasting Design

In order to design the blasting pattern, 4 methods of the well-known blast models were selected namely; Ash, Thumb, Anderson and Konya and subsequently calculated (Table 3). The calculation has been done for the 12 m bench height and 250 mm blasthole diameter which is advisable for 7 Mt ore production per year.

Table 3: Calculation results

Parameters	Units	Ash	Thumb	Anderson	Konya
Burden	m	6.3	7.5	6.0	6.0
Spacing	m	7.8	9.2	7.5	7.8
Stemming	m	5.9	5.3	5.7	4.5
Sub drilling	m	2.8	2.3	2.7	2.4
Total charge	Kg	392.09	397.61	397.61	437.23
Specific charge	Kg/m^3	0.67	0.48	0.74	0.78
Specific drilling	m/m^3	0.025	0.017	0.027	0.026

5. Conclusions

Comparative analysis between the results from the blasting methods shows that the Ash and Konya have the best correlation with the results for BI. For rock fragmentation point of view, the use of Konya blasting model results proper crushed rocks in term of size. Moreover, the economical evaluation has been done to find how the proposed pattern would affect the cost. Considering the remaining mine life (roughly 30 years), decreasing specific charge (from about 1 to 0.78 kg/m^3) and specific drilling (from about 0.07 to 0.02 m/m^3) and 15% inflation each year, the discounted saved money will be about $50 million.

Acknowledgements

The authors would like to hugely acknowledge Mr. Mahdizadeh and Mr. Masoudian from the Jalal-Abad iron mine for their valuable cooperation and remarks.

References

[1] A. Karamia, S. Afiuni-Zadehb. Sizing of rock fragmentation modeling due to bench blasting using adaptive neuro-fuzzy inference system and radial basis function. *International Journal of Mining Science and Technology*; 22, 459–463, 2012.

[2] A.B. Yasrebi, A. Wetherelt, P. Foster, J. Coggan, P. Afzal, F. Agterberg, D. Kaveh Ahangaran. Application of a Density–volume Fractal Model for rock Characterisation of the Kahang Porphyry Deposit. *International Journal of Rock Mechanics and Mining Sciences*, 66, 188-193, 2014.

[3] CL. Jimeno, EL. Jimeno, FJA. Carcedo, *Drilling and Blasting of Rocks*. Rotterdam, Netherlands: CRC Press, A.A. Balkema; 1995.

[4] F. Faramarzi, H. Mansouri, M. Ebrahimi. A rock engineering systems based model to predict rock fragmentation by blasting. *International Journal of Rock Mechanics & Mining Sciences*; 60, 82-94. 2013.

[5] M. Badel, S. Angorani, M. Shariat Panahi. The application of median indicator kriging and neural network in modeling mixed population in an iron ore deposit. *Computers & Geosciences*; 37(4) 530-540, 2011.

[6] M. Nikzad. Classification of blast fragmentation using number-size (N-S) fractal method in production blasting of Open pit mining method (Case study: JalalAbad Iron mine), *MsC thesis in South Tehran Branch, Islamic Azad University, Tehran, Iran*, 2013.

[7] PA. Lilly, An empirical method of assessing rock mass blastability. *In: Proceedings of the large open pit mining conference, Melbourne, Australia*, pp. 89–92, 1986.

EXPLICIT DYNAMICS FINITE ELEMENT ANALYSIS OF ENERGY ABSORPTION CHARACTERISTICS OF THIN-WALLED ULTRASTEEL COLUMNS

C. Liang[1], C.J. Wang[1], V.B. Nguyen[2] and D.J. Mynors[1]

[1]Department of Engineering and Design, University of Sussex, Brighton BN1 9RH
[2]Hadley Industries plc, PO Box 92, Downing Street, Smethwick, West Midlands, B66 2PA

ABSTRACT

UltraSTEEL material has been reported to have higher yield and ultimate strengths than plain mild steel under quasi-static loads. This project aims to study the energy absorption characteristics of UltraSTEEL thin-walled structures when subjected to axial impact loads. The numerical modelling starts from duplicating the UltraSTEEL dimpling process and defining the resultant material properties by taking strain hardening and strain rate sensitivity into consideration. Features including element type, mesh density, symmetric boundary conditions and imperfections are then studied. The responses of 1mm gauge plain and UltraSTEEL columns to the same impact load are compared by conducting explicit dynamics finite element simulations. Comparing to the plain columns, the effect of gauge on the UltraSTEEL columns' failure mode and specific energy absorption (SEA) are analysed through a parametric study.

Keywords: *Explicit dynamics analysis; UltraSTEEL; Axial crushing; Thin-walled Structure*

1. Introduction

The UltraSTEEL process, developed by Hadley Industries plc, is to cold-roll form plain sheet mild steel into dimpled sheet steel. During the process, a pair of rolls with specially shaped teeth that stretch the surface forming the dimpled shape is used, and the plain sheet steel is progressively fed into this pair of rolls [3]. Quasi-static tensile test results showed that the UltraSTEEL dimpling process can increase the yield and ultimate strengths of the plain steel material by up to 51% and 34%, respectively [3]. The UltraSTEEL process and subsequent quasi-static tensile tests were duplicated on a generic finite element model [3].

Thin-walled structures are widely used as kinetic energy absorbers because of their low cost, light weight and high energy absorbing capacity. Within various dynamic loading conditions, representative axial impact load is of particular interest. In order to analytically predict the response of thin-walled square tubes to axial crushing loads, the super fold element (SFE) method was proposed [1]. This method was then modified by taking effective crushing distance and strain rate effect into account, and verified experimentally [1]. Light weight and high mean crushing force are desired in general applications, therefore, specific energy absorption (SEA) is employed to describe a certain structure's energy absorbing performance. In recent years, SEA has been improved mainly by introducing alternative cross-section profiles, fillers and high strength materials [2, 4, 5].

To understand the energy absorption characteristics of UltraSTEEL structures when subjected to dynamic axial crushing loads, explicit finite element simulations were conducted. Failure modes and SEA of plain and UltraSTEEL columns were compared. Effect of the gauge was also analysed through parametric studies.

2. Numerical modelling

Explicit dynamics method was selected to complete the numerical simulations. The closed square hollow cross section with 60×60mm outer dimensions was adopted in this study, with a slenderness ratio of 5 (i.e. length is 300mm), to avoid global bending. The hollow columns were fully fixed at one end. Both plain and UltraSTEEL models were meshed with shell elements (Element Type 181). According to the convergence study, for the plain columns used in this research, an element size of 1.25mm is capable of providing converged results, and 1mm element size was used in plain models.

However, due to the nature of UltraSTEEL dimpled geometry, the element size was specified to be 0.55mm in UltraSTEEL models. Since the element size is uniform throughout the whole column model, time scaling method is not applicable.
In non-linear dynamic analysis, material properties are critical. According to existing researches, the dynamic mean crushing force is greater than the quasi-static crushing force by up to 30%, when a mild steel column is subjected to low velocity axial loads. In this study, the impactor was treated as a rigid body, while the Cowper-Symonds material model was assigned to plain and UltraSTEEL columns. By applying the Cowper-Symonds material model as shown in Equation 1, the materials were assumed to be strain rate sensitive and purely plastic. The parameters in the strain hardening term were determined based on experimental tensile tests, while the parameters in the strain rate term were obtained based on theoretical models.

$$\sigma^d = \left[\sigma_y + B{\varepsilon_{pl}}^n\right]\left[1 + \left({\dot{\varepsilon}_{pl}}/{D}\right)^{1/q}\right] \quad (1)$$

where σ^d represents equivalent dynamic stress flow, B represents hardening constant, ε_{pl} represents equivalent plastic strain, n represents hardening exponent, $\dot{\varepsilon}_{pl}$ represents equivalent plastic strain rate, D and q represent strain rate constants.
In the modelling process, the columns were simplified by modelling a quarter of the original closed square hollow cross section with the longitudinal dimension unchanged, since the stress wave is dominantly propagating along the longitudinal direction. The rationality of this simplification was justified by comparing the responses (failure modes and force-displacement curves) of the original and simplified models. The force-displacement curves presented in Figure 1 indicate that phase lag appears as the axial displacement increasing. However the SEA curves of two models agree very well. The numerical results showed that after simplifying the model, failure modes are the same, the difference in SEA and peak crushing force are 0.65% and 0.02%, respectively.

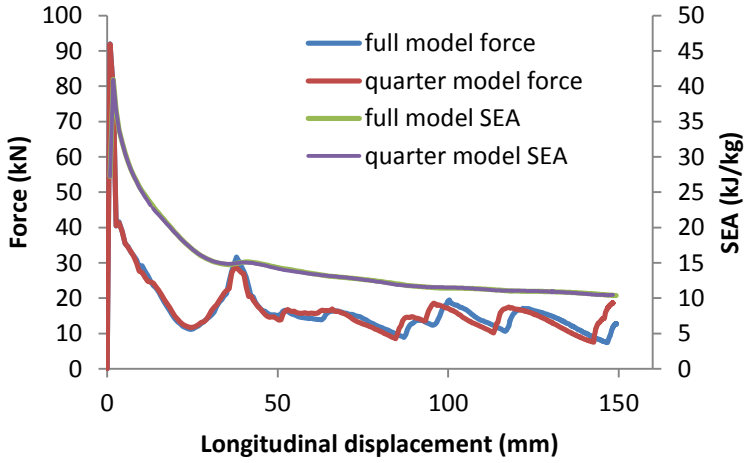

Figure 1 Crushing force and SEA vs longitudinal displacement of full and simplified quarter models

Another important feature of the numerical models is the artificially introduced imperfection. Since the column is initially regarded by the programme to be perfectly perpendicular to the impactor plane, two rigid triggers were introduced to initiate the deformation at the top of the column. A sensitivity study reveals that the effect of triggering on the initial peak crushing force can be neglected.

3. Results and discussion

Figure 2 shows failure modes of 1mm gauge plain and UltraSTEEL columns. It can be observed that failure modes of 1mm gauge plain and UltraSTEEL columns are similar. Following the

Abramowicz's theoretical model [1], each layer of folds has been initiated after the last layer of folds has been fully developed.

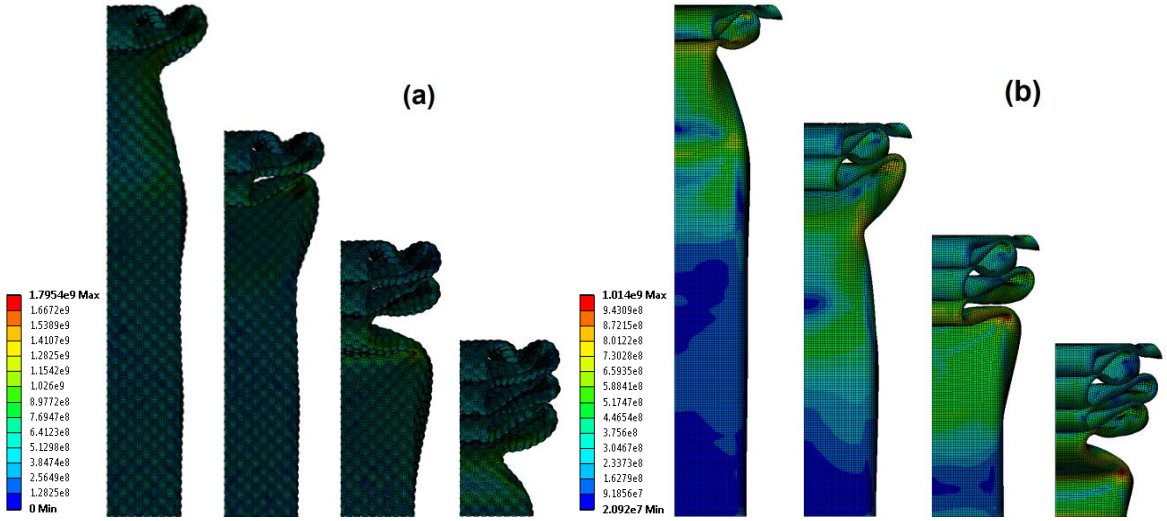

Figure 2 Failure modes of 1mm gauge (a) UltraSTEEL column and (b) plain column

In lightweight design, specific energy absorption (SEA) is the primary variable used to describe a column's energy absorption characteristics. Equation 2 is the definition of SEA.

$$SEA = \frac{\int P d\delta}{\rho A \delta_{total}} \tag{2}$$

where P represents the instantaneous crushing force, δ represents the reduction of the column's length in axial direction, ρ represents density of the material, and A represents the cross-sectional area of the column. Results presented in Figure 3 reveals that SEA converges at the beginning of the second fold. It is also revealed that SEA of the 1mm gauge UltraSTEEL column is 12.4% higher than the same gauge plain column. The increase in SEA is not as high as static yield strength due to the following reasons:

1. Impactors have not been stopped, which results in a higher average strain rate in the UltraSTEEL. Therefore, the strain rate sensitivity effect on the UltraSTEEL column is less significant;
2. The average plastic strain in the UltraSTEEL column is lower due to a greater longitudinal distance between two adjacent layers of folds.

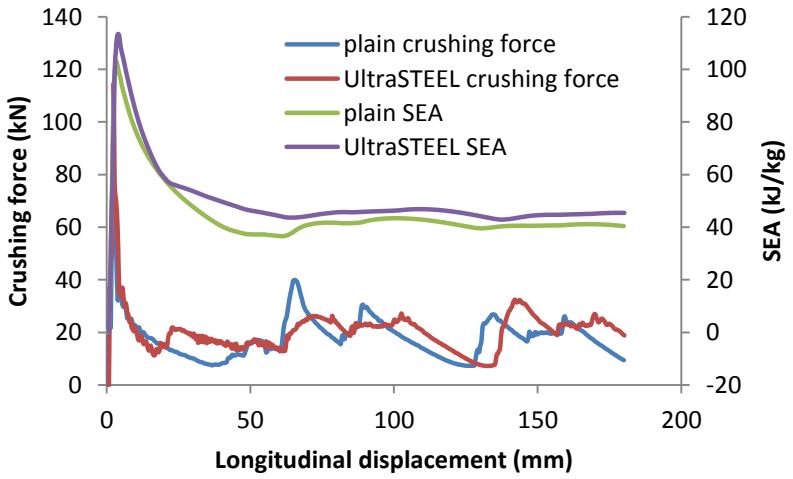

Figure 3 Crushing force and SEA vs longitudinal displacement of 1mm gauge plain and UltraSTEEL columns

The parametric study on gauge reveals that, in terms of failure mode, UltraSTEEL columns are more sensitive than plain columns. Failure modes do not vary significantly in plain columns of 0.7mm to 1.3mm gauge. However, as the gauge increasing, failure modes of UltraSTEEL columns are different. Taking 0.8mm, 1.0mm and 1.2mm gauge UltraSTEEL columns as an example (failure modes shown in figure 4), it is noticed that position of the first fold is different on the 1.2mm gauge column. This is due to a greater cross-sectional modulus. Moreover, a certain layer of folds is initiated to different extend by its previous layer of folds, as highlighted in Figure 4. Since the pre-initiation will reduce the energy absorption capacity, the advantage of UltraSTEEL columns compared to plain columns is predicted to gradually diminished as the gauge increasing. This prediction is then justified by the data shown in Figure 4(d).

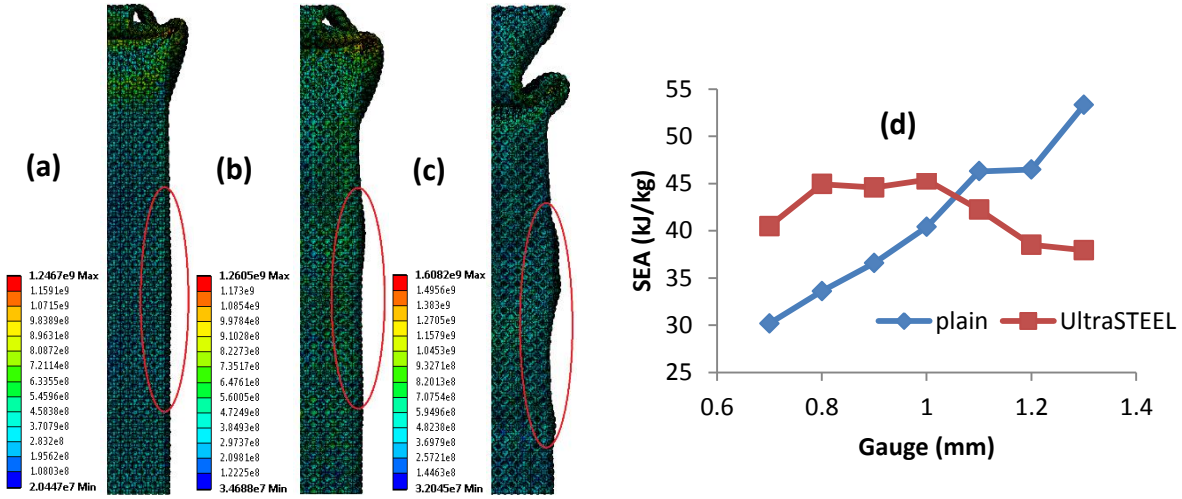

Figure 4 Failure modes of (a) 0.8mm (b) 1.0mm (c) 1.2mm gauge UltraSTEEL columns after the first fold and (d) SEA vs gauge of plain and UltraSTEEL columns

4. Conclusion

In this paper, explicit dynamics finite element simlations were conducted to analyse responses of UltraSTEEL columns to axial impact loads. Cowper-Symonds material models was used to reflect the effect of strain rate sensitivity. It is found that SEA is increased by 12.4% in UltraSTEEL material than plain mild steel closed square section columns, while both types of columns have similar failure modes. The dimpled geometry has made UltraSTEEL column more sensitive than plain columns to its gauge. As a result, the advantage of UltraSTEEL columns in SEA is more significant at small gauges. sensitive than plain columns to its gauge. As a result, the advantage of UltraSTEEL columns in SEA is more significant at small gauges.

References

[1] Abramowicz, W. and Jones, N. Dynamic Axial Crushing of Square Tubes. *International Journal of Impact Engineering*, 2(2), 179-208, 1984.

[2] Jusuf, A., Dirgantara, T., Gunawan, L. and Purta, I.S. Crashworthiness analysis of multi-cell prismatic structures. *International Journal of Impact Engineering*, 78, 34-50, 2015.

[3] Nguyen, V.B., Wang, C.J., Mynors, D.J., English, M.A. and Castellucci, M.A. Compression tests of cold-formed plain and dimpled Steel columns. *Journal of Constructional Steel Research*, 69, 20-29, 2012.

[4] Tarigopula, V., Langseth, M., Hopperstad, O.S. and Clausen, A.H. Axial Crushing of Thin-Walled High-Strength Steel Section. *International Journal of Impact Engineering*, 32, 847-882, 2006.

[5] Zarei, H.R. and Kroger, M. Optimization of the foam-filled aluminium tubes for crush box application. *Thin-Walled Structure,*. 46, 214-221, 2008.

Author Index